2023

Proceedings of the 4th International Conference on Modelling and Optimisation of Ship Energy Systems

Delft University of Technology
Delft, The Netherlands
26-27 October 2023

Editors:
Andrea Coraddu and Luca Oneto

Publisher:

TU Delft OPEN

Proceedings of the 4th International Conference on Modelling and Optimisation of Ship Energy Systems

Delft University of Technology
Delft, The Netherlands
26-27 October 2023

Editors:
Andrea Coraddu and Luca Oneto

Publisher:

TU Delft OPEN

Colophon

Proceedings of the 4th International Conference on Modelling and Optimisation of Ship Energy Systems

Authors:
Andrea Coraddu[1], Luca Oneto[2]
[1] Delft University of Technology, Faculty of Mechanical Engineering, Department of Maritime and Transport Technology | a.coraddu@tudelft.nl ORCID 0000-0001-8891-4963

[2] Università degli Studi di Genova, Department of Informatics, Bioengineering, Robotics and Systems Engineering | luca.oneto@unige.it | ORCID 0000-0002-8445-395X

Keywords:
Alternative Fuels, Efficiency, Systems Optimization, Modeling and Control, Data Driven Methods, Ship Design, System Integration, Efficiency Optimization, Emissions Reduction.

Published by:
TU Delft OPEN Publishing | Delft University of Technology, The Netherlands

DOI: https://doi.org/10.59490/mg.94

ISBN: 978-94-6366-915-3

Copyright statement:

This work is licensed under a Creative Commons Attribution 4.0 International (CC BY 4.0) licence
© 2024 published by TU Delft OPEN Publishing on behalf of the authors

Electronic version of this book is available at:
https://books.open.tudelft.nl

Cover design made by Andrea Coraddu

Copyright clearance made by the TU Delft Library copyright team

Conflict of Interest: *no conflict of interest to disclose.*

Disclaimer:
Every attempt has been made to ensure the correct source of images and other potentially copyrighted material was ascertained, and that all materials included in this book have been attributed and used according to their license. If you believe that a portion of the material infringes someone else's copyright, please contact a.coraddu@tudelft.nl.
The Organising Committee of MOSES 2023 is not responsible or accountable for any statements or opinions expressed in the papers printed in the conference proceedings. The papers have been prepared for final reproduction and printing as received by the authors, without any modification, correction, etc. therefore, the authors are fully responsible for all information contained in their papers. Although all care is taken to ensure integrity and the quality of this publication and the information herein, no responsibility is assumed by the authors for any damage to the property or person as a result of operation or use of this publication and/or the information contained herein.

Table of Contents

Preface

On behalf of the Organizing Committee, it is with great pleasure that we welcome you to the MOSES 2023 - the 4th Conference on Modelling and Optimisation of Ship Energy Systems (MOSES 2023), held in Delft, the Netherlands from 26-27 October 2023. This conference is organized by the Faculty of Mechanical Engineering, Department of Maritime and Transport `technology of the Delft University of Technology.

MOSES continues to be a crucial platform for sparking innovation and promoting essential discussions about the future of energy. It was a privilege to host MOSES 2023, a conference that has stood at the forefront of ship energy system development for the past decade. Following the successful establishment of the MOSES steering committee after the 1st MOSES workshop in 2017, we continue to foster a vibrant scientific community committed to the modelling and optimisation of ship energy systems. Recognizing the need for a specialized conference to serve as a nexus for the exchange of ideas and the advancement of knowledge in our field, the committee has committed to organizing MOSES conferences on a biannual basis. These events particularly encourage the participation of PhD students and young researchers, cultivating the next generation of innovators in ship energy systems. This event highlights the excellence of our field and celebrates the contributions from academia and industry across the globe. In our efforts to expand the boundaries of energy research and embrace the latest technology, this year's conference has added exciting new topics.

The significance of research in ship energy systems is underscored by the ongoing challenges and opportunities in ship design and operation. Innovations aimed at reducing fuel consumption, minimizing environmental impact, and optimizing life-cycle costs of shipping are more crucial than ever. Furthermore, the landscape of our industry is shaped by stringent environmental regulations, fluctuating fuel prices, the exploration of alternative fuels, and the rise of emerging technologies like artificial intelligence, big data analytics, and autonomy concepts from the fourth industrial revolution.

MOSES 2023 aims to address these contemporary challenges and stimulate interest among scientists, researchers, and professionals in the field of ship energy systems design and operation. The conference serves as a forum for sharing innovative ideas, techniques, methods, and experiences across topics including system modelling, optimisation, control, maintenance, safety, autonomy, environmental sustainability, and policymaking. This year's event brought together distinguished academics and industry experts as well as young researchers from various institutions, promoting a rich dialogue that spans continents and disciplines. A key feature this year was the introduction of a round table discussion on Data and Digitalisation. This discussion brought together industry leaders, academic experts, and research institutes to delve into cutting-edge technologies like IoT, AI, and blockchain in the maritime sector. The conversation focused on how these technologies affect operations, safety, and efficiency, and tackled challenges such as data integration, privacy, and cybersecurity in today's digital era.

The 2023 conference was particularly enriched by its setting in Delft, a city celebrated for its deep cultural heritage and significant contributions to technology and academia. Hosting the event in the home city of one of the world’s leading technical universities, Delft University of Technology, highlighted the city’s role as a hub of innovation and research. The picturesque canals, iconic blue

pottery, and historic links to figures like Johannes Vermeer, combined with a vibrant academic community, fostered a collaborative and inspiring atmosphere for all attendees.

We extend our heartfelt gratitude to all presenters, attendees, and members of the MOSES steering and scientific committees, whose dedication and expertise were instrumental in the success of this conference. Special thanks go to our sponsors and the local organizing committee, whose tireless efforts made MOSES 2023 a memorable and impactful gathering. We are excited about the future of the MOSES conferences and confident in their continuing role as a cornerstone for international scientific collaboration and advancement in ship energy systems.

Andrea Coraddu and Luca Oneto

Delft, 8th June 2024

Conference Committees

Conference Chair
Dr. Andrea Coraddu

Faculty of Mechanical Engineering
Delft University of Technology
a.coraddu@tudelft.nl

Conference Co-chair
Prof. Gerasimos Theotokatos

Maritime Safety Research Centre
Department of Naval Architecture, Ocean & Marine Engineering
University of Strathclyde
gerasimos.theotokatos@strath.ac.uk

Conference Local Organising Committee

Dr. Henk Polinder
Dr Lindert van Biert
Mr Jake Walker
Mr Foivos Milio
Ms Charlotte Loeffler
Prof Rudy Negenborn
Prof Klaas Visser
Dr Perter de Vos
Mr Marjn Postma
Ms Sara Tamburello

Scientific Committee

Dr Alessio Tei, Università degli Studi di Genova, Italy
Dr Udai Shipurkar, Maritime Research Institute, Netherlands
Prof Alan J Murphy, University of Southampton, UK
Dr Jeroen Pruijn, Delft University of Technology, Netherlands
Dr Austin Kana, Delft University of Technology, Netherlands
Prof Robert van de Ketterij, Netherlands Defence Academy, Netherlands
Dr Rinze Geertsma, Netherlands Defence Academy, Netherlands
Prof Kari Tammi, Aalto University, Finland
Prof Luca Oneto, Universita Degli Studi di Genova, Italy
Prof Massimo Figari, Universita Degli Studi di Genova, Italy
Dr Francesco Baldi, ENEA, Italy
Dr Christos Gkerekos, Ninety Percent of Everything, UK
Ms Mia Elg, Deltamarin, Finland

Organisers

Delft University of Technology (TU Delft) is esteemed worldwide for its contributions to engineering and technology. The Faculty of Mechanical Engineering at TU Delft stands at the forefront of innovation, educating and inspiring future leaders in engineering to address global challenges with cutting-edge research and sustainable solutions. Within this faculty, the Department of Maritime and Transport Technology is distinguished for its specialized focus on the design and analysis of ship systems and maritime operations. This department pioneers in advancing maritime engineering, encompassing everything from naval architecture to transport logistics. It is dedicated to enhancing the safety, efficiency, and sustainability of maritime transport through research and collaboration with industry leaders. As a crucial part of TU Delft, this department plays a key role in shaping the future of global maritime and transport technologies, making it an ideal host and organizer for conferences such as MOSES 2023, where academia and industry converge to push the boundaries of maritime energy system optimization.

Golden Sponsor

RH Marine RH Marine is a leading system integrator and innovator of electrical and automation systems in the maritime industry, and delivers tailored solutions for complex Defence, Safety & Security ships, and Yachts. Our in-house capabilities include project management, consultancy, system design, engineering, commissioning, installation, site management, training, and service support. With a strong focus on sustainability, we actively contribute our knowledge to various alliances in the global maritime industry. These alliances focus on the development of autonomous and low-emission solutions for all types of ships. At RH Marine we focus on making ships smarter and easier to operate. With our innovative solutions and integrated systems, we reduce life cycle costs and decrease the impact on our environment. RH Marine has decades of experience in working with batteries onboard specialised vessels. In addition to that we have developed an award-winning Energy Management System (EMS) to fully align the additional power from batteries and other power sources with the installation onboard. The self-learning artificial intelligence algorithm automatically distributes the power demand over the available energy sources to ensure optimal operation based on an operational goal. In addition to that we continuously work with our industry partners to encourage the adoption of new technologies in our market. One of the most significant contributions is our commitment to the MENENS project (Methanol as an Energy Step towards Zero-Emission Dutch Shipping). Within this project RH marine focuses on digital twins capable to capture current and future states of the system by developing virtual simulation models and digital solutions to create platforms to perform system integration studies and verify concept designs and innovations in power, propulsion and energy systems.

Silver Sponsors

MARIN is a globally recognised top institute for hydrodynamic, nautical, and marine power systems research. Our mission is 'Better Ships, Blue Oceans': we stand for clean, smart, and safe shipping and sustainable use of the sea. We do this as an independent knowledge partner for the maritime sector, government, and society.

DAMEN provides unprecedented maritime solutions, through design, shipbuilding, ship repair and related services. We offer versatile platforms that enable our customers to be successful and that raise the standard in terms of safety, reliability, efficiency, and sustainability. We want to become the most sustainable shipbuilders in the world.

Authors Index

(This page has been intentionally left blank)

PROCEEDINGS OF MOSES2023 CONFERENCE
4TH INTERNATIONAL CONFERENCE ON MODELLING AND OPTIMISATION OF SHIP ENERGY SYSTEMS
26-27 OCTOBER 2023, DELFT, NETHERLANDS

Establishing the Influence of Methanol Fuelled Power Propulsion and Energy Systems on Ship Design

A.S. Souflis - Rigas[a,*], J.F.J. Pruyn[a], and A.A. Kana[a]

[a]Delft University of Techonology, Delft, the Netherlands
[*]a.s.r.souflis-rigas@tudelft.nl

Abstract

The adoption of alternative energy carriers is one of the key ways to meet the increasingly stricter emission regulations faced by shipping vessels from the international maritime organisation (IMO) and European Commission. To support this objective, this study examines the challenges and uncertainties associated with implementing a methanol power propulsion and energy (PPE) system on the design of a vessel. This paper argues that new fuels, such as methanol, should be treated as disruptive innovations due, in part, to the uncertainties surrounding their implementation. Their integration causes challenges regarding systems selection, layout design, and maintaining strict safety measures. In the case of methanol, current research treats the fuel as a system conversion based on diesel fuel. This paper provides a review of the state-of-the-art on the design of methanol fuelled vessels, and identifies a research gap related to the need for a new suitable design method for the design of ships integrating future alternatively fuelled PPE systems. A design approach inspired by model-based systems engineering integrating uncertainty modelling is proposed to examine the influence of uncertainty on the design of the vessels. The impact of uncertainty on the design is investigated through a case study of a simplified engine room layout utilizing a genetic algorithm to produce layouts for variable PPE systems dimensions within a Monte Carlo simulation.

Keywords: Methanol; Ship design; Uncertainty propagation; Systems Integration; Alternative power propulsion and energy systems.

1 INTRODUCTION

The energy transition and the effort towards the decarbonization of the shipping industry is an important step towards addressing climate change as the maritime industry accounts for approximately 3% of greenhouse gas (GHG) emissions [1]. The International Maritime Organization (IMO) has set a target of net zero GHG emissions in 2050 compared to 2008 [2]. Accordingly, the European Commission is introducing a set of policy actions that target a climate neutral Europe in 2050 [3] and the European Parliament council has announced the target of mitigating GHG intensity by 80% by 2050 [4].

To address this, the IMO has introduced various performance indicators that assess a vessel's CO_2 emissions, including the Energy Efficiency Design Index (EEDI), the Energy Efficiency Existing Ship Index (EEXI) and the Carbon Intensity Index (CII) [5] (MEPC 76). In addition, vessels also need to conform to regulations for SO_X [6] and NO_X [7] which may require the adoption of further technology. Technological innovation is thus required to meet these upcoming regulations and climate goals.

One of the key ways to meet this demand is by adopting alternative fuels [1]. Several studies have compared alternative fuel options from a lifecycle perspective both economically and environmentally, such as [8]–[10]. Transitioning to alternative fuels is not without trouble, as Lindstad [11] demonstrated that adopting alternative fuels can lead to an energy consumption increase on a well to wake (WTW) basis between 100% and 200%. Additionally, the decreased energy densities of alternative fuels lead to an increased volume demand increase by a factor of 2.3 for methanol and 7.1 for liquid hydrogen[12].This inevitably leads to an increased demand for voluminous storage areas and challenges in their integration into the vessel. Various studies comparing alternative fuels integration have generated different outcomes regarding space requirements owing to various assumptions about future fuels. New challenges arise from alternative fuel integration due to storage and handling, vessel performance, space allocation, safety equipment, and safe handling of the fuel [12]. In combination with the existing complexity of conceptual ship design [13], the need arises to understand the influence of the novel power propulsion and energy (PPE) sys-

@2023 Souflis - Rigas, A. S. et al. published by TU Delft OPEN Publishing on behalf of the authors. Licensed under a Creative Commons Attribution CC BY license.
DOI: https://doi.org/10.59490/moses.2023.658

tems on the design of the vessels as early as possible in the design process.

This paper focuses specifically on methanol as a fuel, since it eliminates almost all SO_X, drastically reduces NO_X in comparison to conventional marine diesel [14], and can be produced in clean ways from biomass or water electrolysis. This means that it can potentially turn into an almost carbon neutral fuel [15], [16]. The environmentally clean versions of methanol, biomethanol and e-methanol, prove highly cost competitive in comparison to other alternative fuels [10].

The PPE systems required for methanol differ from traditional fuels and may even require the adoption of additional technologies throughout the ship lifecycle. Section 2 reviews the challenges of methanol PPE systems integration. This review is complemented by a case study in Section 4 that investigates the influence of the uncertainty in the size, dimensions, and logical connections of PPE components and layout arrangements on a simplified engine room.

2 PROBLEM FORMULATION

To formulate the problem of the influence of future methanol PPEs on the design of ships, it is helpful to first define the main categories of the systems and to identify their associated challenges. The categories are split based on the work of [17]:

- The *energy storage system (ESS)* describes the systems used to safely store and handle the fuel such as tanks, pipes and safety systems such as cofferdams, as described in Section 2.1.
- The *auxiliary power generation systems* describe the systems used to generate electric power and auxiliary loads such as pumps and generators, discussed in Section 2.2.
- The *main propulsion engine power (MPE)* includes the engines used for the propulsion. The primary options are internal combustion engines (ICE), fuel cells (FC) and hybrid configurations including electric power generation and batteries, discussed in Section 2.2.

Additionally, the State of the Art of the design approaches attempting to integrate methanol PPEs is looked into and based on the identified research gaps, a suitable design framework is proposed.

2.1 Storage challenges due to methanol fuel properties

It is important to understand the properties of the fuel, to comprehend the integration of methanol energy storage systems. Methanol is a low flashpoint fuel and is handled according to the interim guidelines of IMO's International Code of Safety for Ships using Gases or other Low-flashpoint Fuels (IGF) [18], [19]. This code has been developed for gas or low flashpoint fuels and leads to the requirement of cofferdams around the tanks, except for the areas that are adjacent to the shell plating below the minimum waterline [20]. This leads to a considerable space demand that must be handled within the hull.

IMO [21] has established guidelines especially for methyl alcohol fuels that are under constant review based on the knowledge gained through operation [22]. In terms of storage and handling, methanol shares more common traits with diesel fuel than LNG (see Table 1) meaning that it can be stored in conventional tanks [8], [23].

Table 1: Comparative chemical properties of diesel oil, methanol, and LNG (adopted from [15]).
LHV: Lower Heating Value

Properties	Diesel Oil	Methanol	LNG
LHV (MJ /kg)	42.6	19.9	$48-50$
Boiling point ($^\circ C$)	$180-360$	65	-161.4
Flash point ($^\circ C$)	78	11	-136

The tank volume storage becomes critical in the case of methanol, because it has approximately half the energy density of conventional diesel, as illustrated in Table 1. Kries [24] showed that a 50% increase in the usable tank volume can be achieved by adopting a smaller cofferdam. Furthermore, Ban and Bebić [12] implemented a hazard identification study (HAZID) to be able to store methanol fuel in ballast tanks in a retrofit case and found that small adjustments on sailing range or speed are required. Additionally, [25] argued that for a diesel fuel capacity of 600 m^3, an equivalent 1300 - 1500 m^3 methanol fuel capacity is necessary. These findings indicate a level of uncertainty in the additional storage space requirement.

Safety concerns arise from the use of methanol as an energy carrier because of its toxic and flammable properties [26] (its flames are invisible during daylight [18] and form no smoke [27]), which leads to additional safety equipment requirements [26]. Thus, methanol cannot be placed adjacent to any manned or freely accessible space of the vessel for

fire safety. This poses limitations to the layout of the systems within the vessel. Methanol also presents a corrosive behaviour that increases when metallic materials such as aluminium and titanium alloys exist in the same environment. Thus, stainless steel and appropriate protective coating (such as zinc) are among the solutions applied to the tank interior [18]. This raises a concern regarding the cost and the maintenance demands for the vessels and means that careful materials selection is necessary.

2.2 State-of-the-art of methanol fuelled PPE systems

This section provides a review of the various technologies that are already available or under development to facilitate the shift towards methanol as an energy carrier. Methanol can be burned in an engine, a high temperature fuel cell or be used as a hydrogen carrier in fuel cells. Each propulsion option has relative advantages. Table 2 presents that engines offer a known technology, easy to adapt, with a long lifetime [28], but also with higher emissions, especially NO_X, and lower efficiencies, when compared to fuel cells. This has lead to the consideration of hybrid systems, next to the individual systems, so no propulsion choice is currently absolute.

Methanol combustion in internal combustion engines (ICE), drastically reduces SO_X and particulate matter (PM) emissions [16], [27], [29]. When green or e-methanol is adopted [11] they provide a profound reduction in CO_2 emissions on a Well-to-Wake (WTW) scope. Methanol generated from natural gas barely reduces [28] or even slightly increases CO_2 emissions on a WTW level [11], [30]. Even worse on a WTW level, approximately 6 kWhs of e-methanol are required to generate 1 kWh on the propeller [31]. Looking into the details of the engine many more variations can be observed. Methanol does not burn by itself, it requires a pilot fuel to achieve this [16]. As a result, variations can be found in the location in the process where methanol is mixed with the pilot fuel, but also the choice of pilot fuel and engine type (e.g. compression vs spark) vary in the chosen solutions. The two main combustion concepts are the spark ignited (SI) engine and the compression ignited engine (CI) engine. The SI engine operates only on methanol and has been proven to comply with tier III NO_X emissions levels [16]. On the other hand, the CI engine can offer fuel flexibility and has been more widely used on projects to date. However, CI engines only comply with tier II NO_X emission levels [27], thus requiring an after-treatment such as a selective catalyst reduction (SCR) unit, water fuel mix technique, or an exhaust gas recirculation system (EGR) [16]. SCR and EGR systems take up additional internal volume in comparison to the fuel - water blending technique. Recent studies show that methanol engines operate at the same efficiency (η) as diesel engines or even higher [27], at approximately 40% [8].

In combination with the fact that a dual fuel strategy requires tanks for both methanol and diesel, the size and shape of the PPEs becomes even more unclear, causing uncertainty in the actual layout arrangement of the PPEs. In addition, waste heat recovery (WHR) systems may be part of the PPE to use the waste energy of exhaust gases and produce further mechanical energy. However, these WHR systems are voluminous [16]. On the one hand, improvements in efficiency are expected for methanol fuel cells, but on the other hand, the configurations of large-scale systems (including cooling, control, etc.) are still under development, making the size of the system debatable. Technology readiness level (TRL) [32] is low and they have not been yet commercially applied [8]. In combination with their shorter lifecycle [24], they become a less attractive option to consider. Therefore, they were not further investigated within the scope of this study.

Table 2: Overview of main methanol propulsion options [8], [16]

Properties	**ICE**	**Fuel Cells**
Advantages	High TRL Reliability Easy conversion	Efficiency (η) (60%) Lower emissions
Disadvantages	Efficiency (η) (40%) More emissions	Low TRL Lifecycle (8 - 10) Years

Recent studies on the effect of alternatively fuelled PPE configurations on the size of navy vessels have provided inconsistent findings (see Table 3), not only within a single study but also between studies. One of the primary assumptions in the studies [33], [34] is that the additional weight by the integration of methanol fuelled systems does not lead to an increase in power demand. Snaathorst [35] investigated the effect of alternative fuels integration by using a parametric tool based on empirical equations and ship data, computed the impact on the size and consequently the resistance of the vessel that leads to increased power demand. He found that the increase in size can vary from 2,4 - 6%

which leads to an additional powering demand of 2,7% on average.

Table 3: Effect of displacement of methanol fuelled PPE systems on navy vessels

Propulsion Configuration	Estimated Δ increase [%]	Design Tool	Reference
Hybrid, ICE FC, Gas	18 - 25 %	Parametric tool	[33]
Hybrid, ICE Gas	1,4 - 20 %	Layout modelling	[34]
Hybrid, ICE FC, Gas	8 - 15 %	Parametric tool	[36]

Lastly, a unanimous trend in conversions and retrofits to methanol is to first lengthen the vessel to generate additional space [24], [34], [35]. This is rational as increasing the length can have a limited effect on the resistance [37]. However in most retrofit cases, they maintain the existing hull shape and explore alternative placement options for the additional methanol tanks [15], [30], [34]. This paper argues that:

- There is a large variety of systems under development that need to be integrated into the vessel.
- The exact shapes and quantities of these components are unknown. This study refers to the components as the *building blocks* (BB) of the PPEs.
- Different propulsion choices lead to different PPE shapes that are not yet fully defined. Thus, the overall impact on ship design is not yet fully deterministic.

2.3 State-of-the-Art of the design approaches of methanol fuelled ships

Maersk is currently investing in methanol fuelled vessels [38], underlining the interest for alternative fuels adoption in the maritime sector. The dimensions of the PPE systems are largely influenced by the operational requirements set for the vessel. The intended range and sailing speed largely dictate the fuel consumption ,required fuel storage space and the required installed power. As shown in Table 4 vessels with different missions and sailing speeds, but similar sizes, require highly different installed power. Zuidgeest [30] showed that a 30% increase in speed can lead to an 80% increase in fuel consumption, as also logically follows from the speed power relationship [39]. Considering that slow steaming [40] and engine derating [16] have proven to be effective measures for emission mitigation, there is a decrease in the installed power demand [41]. This has a large effect on the size of the machinery equipment and the overall size of the ship. Therefore the size of the ship depends, in part, on the operational requirements set for it.

The requirements regarding sailing speed and range may still be under discussion and thus uncertain during the design phase while they simultaneously have a large influence on the systems layout of the vessel. Therefore the relationship between the operational, functional, and physical requirements of methanol PPE systems must be captured within the design process.

To date, research projects have primarily focused on conversion and retrofits of diesel fuelled vessels. The retrofit as a process leads to having a vessel with a given hull shape and inner system layout arrangement. This indicates an already set design space for the systems, that rather limits the alternatives for reconfiguration as shown below. These projects have mainly adopted a dual fuel 4 stroke engine and have essentially tried to fit in the extra tanks for methanol in the conversion process. Such a case is the Stena Germanica [23], [29] that applied a new high pressure common rail system, high pressure pumps, and the corresponding safety equipment. Consequently the integration of so many systems leads to large connection costs between the systems, meaning new control systems and cable lengths [29] and if their layout logic is wrong, can lead to unwanted connection costs. Thus, the manner in which the systems are placed and the proximity between relevant systems has an influence on the size of the ESS and the engine room.

Zuidgeest [30] explored the general arrangement of an existing vessel and potential propulsion alternatives.Pothaar [34] used a 3D modelling tool to evaluate the effect of methanol integration in reference to an existing ship. Ban [12] performed a HAZID risk design approach to integrate the additional methanol tanks into the ballast tanks location with minimized effect. The Green Maritime Methanol project [43] investigated a variety of vessels such as those listed in Table 4, focusing on the placement of the extra fuel tanks and safety measures within an existing hull. The above mentioned studies follow a sequential approach resembling to the design spiral approach and only explore an existing design space to place the methanol tanks, meaning that the design choices are rather limited. There is the need to design and explore the design space without strict initial conditions that limit the possible solutions.

Table 4: Comparison of principal characteristics of methanol fuelled vessels

Vessel Type	Vessel size [t]	Sailing Speed [kn]	Installed Power [kW]	Reference
TSHD	DWT 4200	11	4600	[12]
Stena Germanica ferry	GT 52000	22	24000	[29], [42]
General Cargo Vessel	DWT 7000	9.5	1600	[30]
Navy Vessel	Δ 7200	18	50000	[34]
Cable laying vessel	DWT 8400	12.4	11000	[43]

The use cases of green maritime methanol (GMM) [43] have demonstrated that a retrofit can prove more complex and expensive. In case of limited space, the conversion can become more complex and unfeasible as was the case for an inland patrol vessel. The conversions were categorized as either major or minor. Major conversions demanded an enlargement with several frames for the installation of the methanol system, while minor conversions included adjustments in the general arrangement of the vessel. The case of a small port patrol vessel proved unsuitable for conversion. Furthermore, the operation on a dual fuel strategy using both methanol and diesel can lead to a mitigated decrease in the range [43] in excess of 20%.

For different vessel types, the sailing range was reduced approximately 40% - 50%, when integrating methanol [30], [34], [43]. In contrast, Ban [12] found that the range for a two-week mission remains almost identical. Consequently treating the methanol integration just as a modification in an existing design rationale leads to bottlenecks and unexpected compromises in the design and operation of the vessel.

2.4 Requirements for Design Framework

The proposed Design Framework is necessary to integrate the uncertainty, as inconsistencies have been found regarding the size of the PPE subsystems and their effect on the overall ship design, as presented in sections 2.1, 2.2, 2.3. As categorized [44], uncertainties can be divided into two main categories:

- *Epistemic*: is generated by insufficient knowledge regarding a problem or technology and is mitigated by gaining more information and understanding via simulations, experiments etc..
- *Aleatory*: is caused by the randomness of outcomes in the nature and cannot be mitigated via modelling.

The uncertainty type addressed in this problem is epistemic. Further knowledge regarding technology development can lead to mitigation of the uncertainty regarding the sizing and dimensioning of the building blocks (BB) - size of the subsystems. Consequently, modelling the uncertainty of the parameters related to these systems is a prominent requirement.

To establish the design method required for this research, it is essential to clarify both the main research gaps identified above and the matching method requirements, which are presented in Table 5. Because many PPE systems are still under development, the level of complexity increases.

As stated in the [45] there is the need to handle the ship as part of a larger system towards more environmentally sustainable vessels. The design should thus be interconnected with the requirements of the stakeholders, such as: regulatory authorities, shipowners, shipyards, or class societies. There is also a need to investigate various scenarios regarding technical, economic, environmental and safety performance from a lifecycle perspective [45].

Relevant studies have been evaluated to shape the proposed method (see Table 6). Therefore, it is clear that different aspects of each methodology need to be combined to meet all the requirements. The design approach that shows the most promise and satisfies most requirements is model based systems engineering (MBSE), as it provides the traceability of changes and interaction between the various requirements in design highlighted in Table 7 [46], [47]. In Table 6, the MBSE approach is only found at a basic level on the work of Rehn [13] and on the application of the Ship Power and Energy Concept (SPEC) tool developed by MARIN to a hydrogen fuelled vessel [46]. The approach is based on the analysis of the design process into 4 main layers inspired by systems engineering (SE) [48]

- *Operational Analysis*, from which the basic requirements for the operation of the vessel are established
- *Functional Requirements* which defines the functions expected to be fulfilled by the system

Table 5: Research Method Requirements

Research Gap	Method Requirement
Uncertainty on influence of PPE on ship design	Traceability of changes Uncertainty modelling
Accurate size effect consideration	Layout integration
Uncertainty on operational requirements	Interaction between operational requirements and physical space
Variation of new environmental regulations requirements	Lifecycle assessment

- *Logical Architecture*, which defines in further detail the system technologies that are to be used to fulfil the above requirements and their possible interconnections to comply with different regulations requirements [46].
- *Physical Architecture* defines the actual placement of the systems in the physical space (e.g. with a general arrangement plan).

The uncertainties outlined above are categorized within these layers, as listed in Table 7. As a first step in this research, this paper focuses on the integration of uncertainty within the physical layer, while considering variations in the logical architecture and their effect on the overall shape of the engine room design.

Table 7: Uncertainties found per MBSE Layer

MBSE Layer	Uncertainty
Requirements	Range, speed
Functional	Safety measures required
Logical	Placement and connection patterns systems due to safety
Physical	Actual size and amount of required PPE systems

3 PROPOSED DESIGN FRAMEWORK

Based on the findings in Tables 6 and 7, there is the need to integrate uncertainty into the layout design process of machinery spaces owing, in part, to uncertainty in the size and amount of integrated systems. This can also be due to the uncertainty in the original design requirements regarding ship speed and range parameters, which influence the installed power and sizing of the main propulsion equipment. Dimensions uncertainty can root also from the functional requirement for safety as relevant regulations and technology are still under development. Additionally the safety requirements owing to the properties of methanol pose limitations on spaces not being adjacent to each other due to fire risks. For this reason the logical architecture is taken into account within the layout modelling at a high level in this research, posing layout boundary conditions for the integrated components. Requirements from different levels trace back to uncertainty in the physical space.

The proposed modelling process is illustrated in Figure 1. The emphasis is on the physical architecture layer of the MBSE coupled with variations in logical architecture. The layout generation algorithm (based on [51]) has been integrated into a Monte Carlo simulation (MCS) to capture the already discussed uncertainty aspects. Poullis [51] set up a layout algorithm for the engine room of a hybrid methanol fuelled yacht. This study extended this model to turn the layout algorithm into a stochastic model to generate the distributions of the output variables.

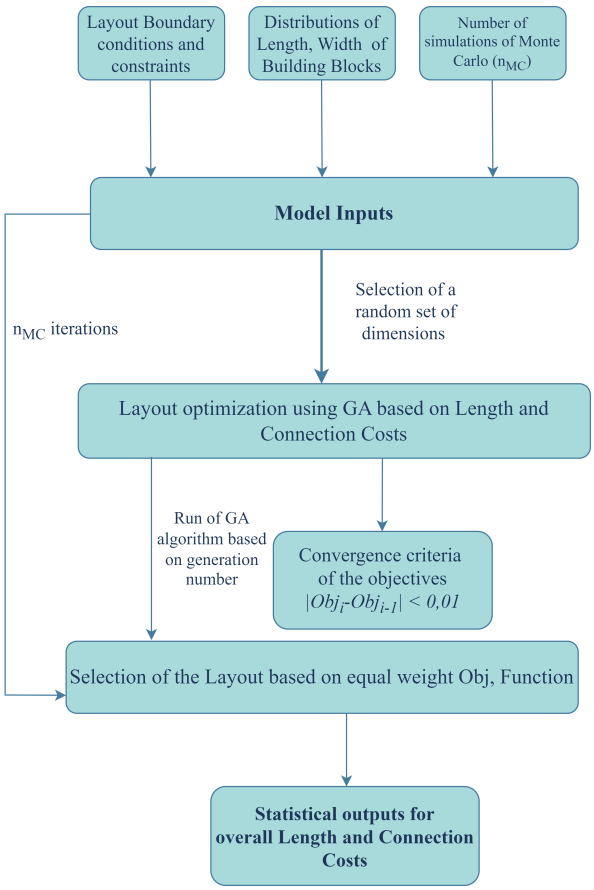

Figure 1: Proposed design model process

Table 6: Relevant literature for method requirements

Traceability of changes	Uncertainty modelling	Layout integration	Requirements and physical design interaction	Lifecycle evaluation	Approach name
X	X	✓	✓	✓	Design Parametric tool [24]
X	X	X	✓	X	Design spiral for retrofit [43]
X	X	✓	X	✓	Lifecycle choices analysis [49]
✓	✓	X	X	✓	SE design under uncertainty [13]
✓	X	X	X	✓	MBSE application [46]
X	X	✓	X	✓	Stochastic parametric tool [50]
X	X	✓	X	X	Machinery layout tool [51], [52]

The MCS is applied to understand the impact of variable dimensions to the simplified engine room of a vessel, which potentially affects the size of the vessel. MCS has previously been applied by Kana [53] to establish an understanding of the way that different emission regulations scenarios influence the conversion decision for an LNG powered containership. Coraddu [54] integrated a MCS to approximate the EEOI while having two stochastic inputs Δ (displacement) and v_s (sailing speed). Dall'armi [55] followed this approach to apply a MCS analysis to investigate influence of the fuel cells costs to the optimal operation of a hydrogen ferry. Curto [56] applied MCS to determine the influence of various uncertainty types on the behaviour of project costs. Thus MCS is a promising method for exploring this type of problem, whilst being simple to implement.

Using this model, the design space is explored probabilistically to gain an understanding of the influence of different PPE systems physical dimensions (length, width) on the overall length of a simplified engine room. A uniform distribution has been selected for the input variables (length and width of BBs), as it appoints equally likely outcomes to all the variables within the defined interval.

3.1 Layout Algorithm within Monte Carlo simulation

The layout modelling approach selected is based on solving the facility layout problem (FLP), used by [51] to model the shipboard layout of a machinery space. As defined in [57], the FLP can be described as the arrangement of units (BBs in this case) in a plant area to attain the most effective layout in accordance with predefined objectives and constraints. In the model proposed by Poullis[51], and extended in this paper, the FLP is framed as a multi-objective problem with non linear constraints. The objectives of the problem are the minimization of *length* and *connection costs*.

The proposed model generates layouts for a simplified engine room with fixed width. Integer constraints are introduced to tune the rotational ability of the BBs, by using a value of 1 for rotational ability and 0 for non-rotation. A coordinate-based system is used for the layout generation. The BBs are modelled as boxes as depicted in Figure 3. They have an input and output point that coincide with the start and the end of the box respectively, as defined in [51]. The minimum length is computed by finding the right most BB coordinate.

Connection costs (CCs) refer to the various connections such as pipe routing and cable links that need to be implemented to connect the various PPE systems. The CCs are based on computing the euclidean distances between the various systems and multiplying with the corresponding cost factor (Equation 1) [52]. The cost of each connection is allocated using a connection matrix (CM) that includes weighting factors for connecting either to the input or the output of the BB.

$$\sum_{i=1}^{N}\sum_{j=1}^{N} CM_{ij}\cdot d_{ij} = \sum_{i=1}^{N}\sum_{j=1}^{N} CM_{ij}\cdot(\mid d_{i_{out}} - d_{j_{in}}) \mid \tag{1}$$

The multi-objective optimisation is implemented using Deb's NSGA-II [58] incorporated into the MATLAB global optimisation toolbox [59]. The critical parameters to define the optimization process are listed in Table 8. The population size is set to 400 by trial and error. Each BB has a set of three decision variables: length, width and rotational freedom. Five BBs are selected for this case study. Therefore, there are 15 decision variables ($n_{variables}$) in this case study.

Table 8: GA parameters definition, $n_{variables}$ refers to the number of decision variables.

Parameter	Value
Population	400
Maximum Generations	$200 \cdot n_{variables}$
Maximum Stall Generations	100

A convergence criterion has been applied to compare the outcome of the objective functions

based on Equation 2:

$$|Obj_{j,i} - Obj_{j,i-1}| \leq 0.01, j = 1, 2 \quad (2)$$

The convergence criterion (Equation 2), regarding the values of the objectives: length, connection costs is applied to reduce computational time when the GA cannot provide fundamental layout improvements. GA produces more than one solutions per set of inputs. The maximum value of the objectives out of these solutions per MC run has been used to normalize the values of the objectives in Equation 3 and thus receive values in the range of 0 to 1. Each set of inputs needs to match one layout output to generate a distribution of engine room length and connection costs outputs within the MC simulation. This technique allows to observe the influence of variable dimensions on the overall size of the engine room. Therefore, the selection equation in Equation 3 is applied, which allocates equal weight factors to the objectives of the problem:

$$minObj = min(\sum_{i=1}^{2} w_i \cdot \frac{Obj_i}{maxObj_i}), w_i = 0.5 \quad (3)$$

The GA output that minimizes the value of Equation 3 is integrated into the MC simulation output. Equal weight factors have been assigned to the Objectives of the problem and the objectives are normalized by dividing with the maximum value of each objective respectively per GA run. The objectives compared in the minimization Equation 3 receive values in the range of 0 to 1, which makes the length and connection costs values equally important.

The solution minimizing Equation 3 is selected and is part of the output statistical data of the MC simulation, regarding length and connection cost. For the case study two main concepts are examined:

1. Impact of variable BB dimensions on the length and connection costs of the engine room with a standard logical architecture
2. Impact of alternative logical architectures on the length and connection costs of the engine room

4 CASE STUDY

The proposed model is used to generate multiple layouts of a simplified engine room with main components. Five BBs that constitute an engine room were selected, as defined in [39], [51], with their variable dimensions (between 15-20 $\%$) provided in Table 9:

- Main Engine
- Fuel Cells
- Fuel Handling room
- Generators
- Control Switchboard room

Table 9: Case Study Dimensions

Building Block	Width [m]	Length [m]
Methanol Fuel Preparation[1]	1.6 - 2.1	2.6 - 3.5
Fuel Cell [2]	0.6 - 0.9	1.1 - 1.4
Main Engine [3]	1.2 - 1.5	1.4 - 1.9
ESM Machine [4]	0.6 - 0.9	1.1 - 1.4
DC Distribution [5]	0.8 - 1.1	3.8 - 5.1

$$CM_{baseline} = \begin{bmatrix} 0 & 0 & 2 & 0 & 0 \\ 1 & 0 & 0 & 0 & 0 \\ 0 & 0 & 0 & 5 & 0 \\ 0 & 0 & 0 & 0 & 1 \\ 0 & 2 & 0 & 0 & 0 \end{bmatrix} \quad (4)$$

The connection matrix, CM_{normal}, expresses the importance of the connection between the different components, with 0 meaning a connection of minimum importance and 5 a highly important connection and thus components should be in close proximity. The definition of the specific connections was elaborated on in [51]. The matrix in Equation 4 introduces to the layout algorithm, whether BBs should be adjacent or apart, based on the connection costs. To an extent, this reflects the logical architecture that can be implemented. The output variables of the simulation are the Length and the Connection Costs of the simplified engine room, which are also the objectives of the GA algorithm.

4.1 Effect of Uncertainty

Before exploring the results, the convergence of the MCS was determined. Here, 1% was deemed sufficient convergence, and was evaluated based on the cumulative incremental difference (CID) defined in Equation 5. CID expresses the alteration of the mean value (μ) of length and connection cost respectively per MC simulation. As shown in Figure 2 acceptable convergence was achieved within the 400 simulation runs, because the CID values remained within acceptable range of the 1% accuracy. The same accuracy was selected in Equation 2 for

the GA convergence, because it is reasonable for both parts of the simulation to have the same level of accuracy. For this set up, the simulation duration was approximately 2 hours per scenario using the Delft Blue supercomputer [60]. A representative layout of the simulation is shown in Figure 3. The presented layout has values similar to the mean values of the length and connection costs in the MC simulation with the baseline logical architecture defined by Equation 4.

$$CID = \frac{\mu_{Objective(i)} - \mu_{Oblective(i-1)}}{N} \quad (5)$$

N:number of runs

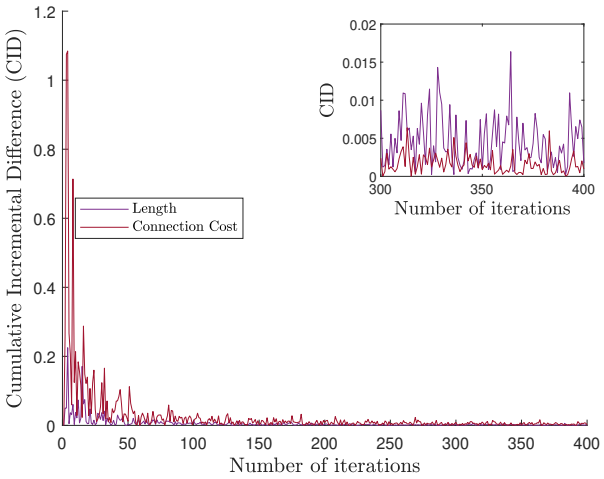

Figure 2: Convergence of the Monte Carlo simulation

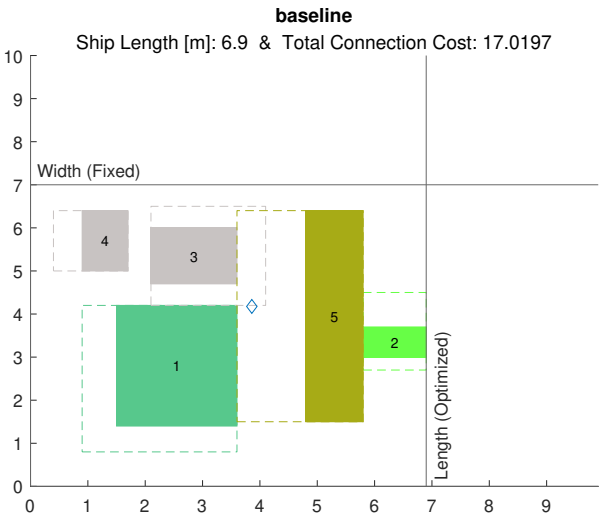

Figure 3: Representative layout generated during simulation with the baseline logical architecture and the mean length

The MC solution space of the 400 runs is presented in Figure 4, where there is no clear correlation between the length and connection costs. Although there is a concentration of points around the mean values of the experiment, simultaneously there are points with an inconsistent behaviour. Figure 5 complements this observation as the distribution especially of the length, does not clearly relate to any of the standard distributions. The solution points are widely spread and exhibit significant variability compared with an evenly spread uniform distribution.

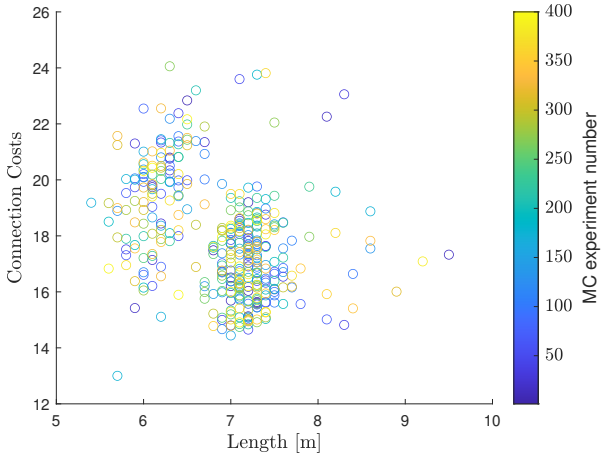

Figure 4: Solution space of the Monte Carlo simulation

Figure 5 presents the histograms of the length and connection costs, where the distributions of the outputs show a clear non-uniform behaviour contrary to the inputs. This underscores the complex relationship uncertainty plays in the integration of methanol fuelled systems and its influence on the design space. When considering the variety of PPE systems to be included in a full-scale ship design, the complexity of the design process increases.

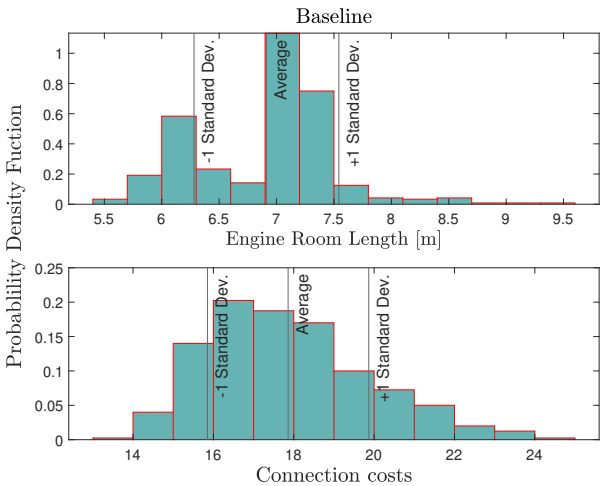

Figure 5: Histogram of engine room length and connection costs

4.2 Effect of uncertainty with varied logical architectures

The aim of this experiment is to explore the influence of uncertainty within the logical architectures by applying two additional connection matrices, namely:

1. *Zero constraints*, meaning that a zero constraint matrix is implemented, and
2. *Full constraints*, which has minor adjustments compared to the baseline CM in Section 4.1. Changes were made to allocate higher CCs between the BBs that potentially limit the layout options and are implemented in Equation 6.

$$CM_{fullconstraints} = \begin{bmatrix} 0 & 0 & 2 & 0 & 0 \\ 2 & 0 & 0 & 1 & 1 \\ 0 & 0 & 0 & 5 & 0 \\ 0 & 0 & 1 & 0 & 1 \\ 0 & 2 & 0 & 1 & 0 \end{bmatrix} \quad (6)$$

Similar to the baseline case, the solution space is generated to compare the behaviour of the different logical architecture scenarios. Figure 6 shows the data clustered depending on the logical architecture scenario. It is natural that the *zero constraints* scenario generates a flat line and is therefore not included in the comparison of connection costs below. The full constraints scenario generates a considerable increase in connection costs, but also a shift of points towards the left meaning a lower overall length. This pattern is similarly observed in Figure 7, in which many points are outliers, meaning that they fall outside the consistent box plot pattern. The existence of outliers is confirmed by the kurtosis values in Tables 10 and 11. This points to an inconsistent and complex impact of the logical architecture and BBs size uncertainties even in a very simplified case study, which cannot be logically explained and requires further research.

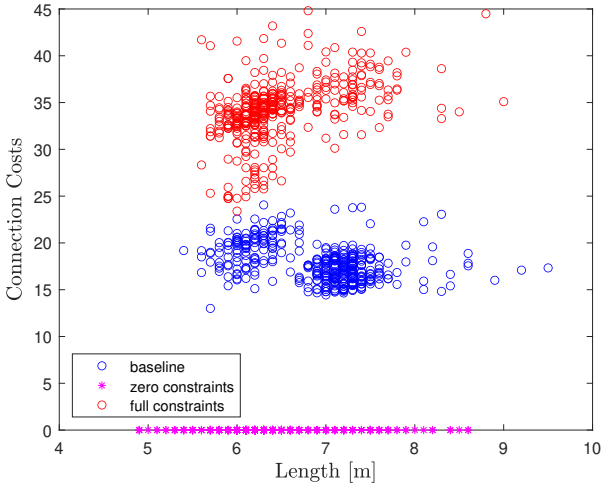

Figure 6: Solution Space for different logical architectures

Similarly, Figures 7 and 8 show how the length distribution varies between the different experiments. *Full* and *zero constraints* scenarios appear to have different behaviours despite the minor modifications per logical architecture scenario. Both of them lead to a reduced engine room length compared to the baseline scenario.

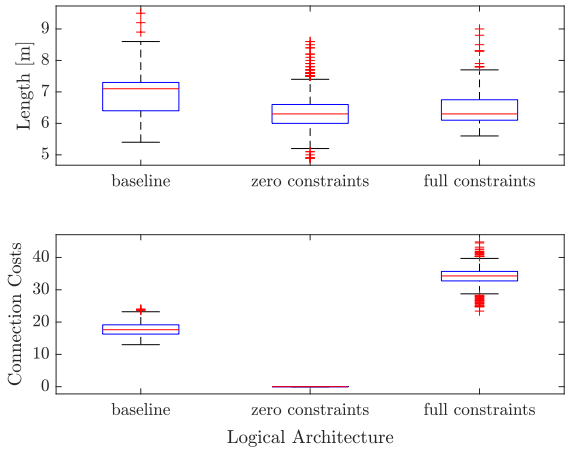

Figure 7: Variation of length and connection costs depending on the allocated connection matrices

Figure 8 shows that the distributions of the variables vary. The statistics of length and connection costs provided in Tables 10 and 11 show the variation of the possible outcomes depending on the connection matrices defined, as well as the skew of the distributions. As a result, there is no consistent distribution to describe the outcomes of the experiment, meaning that the alteration in PPE systems generates uncertainty in the design process and needs further investigation to minimize the risks propagated throughout the design process.

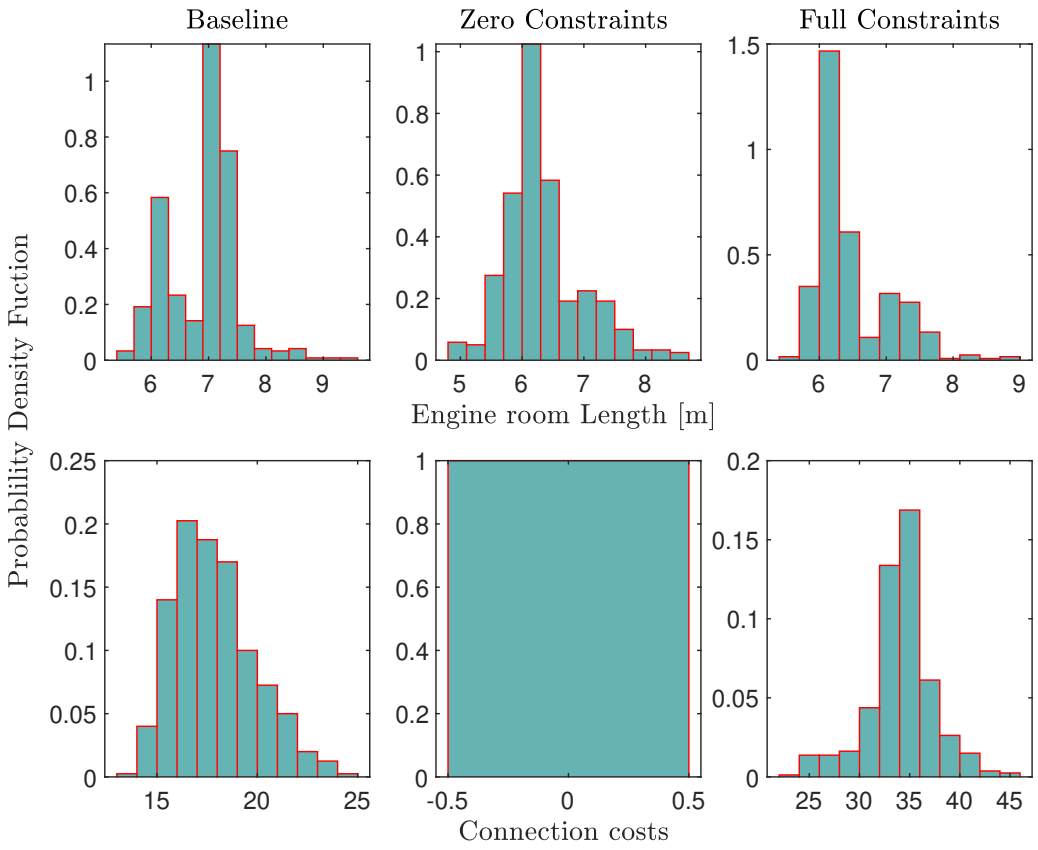

Figure 8: Length and Connection Cost distribution per different scenario

Table 10: Length [m] statistics per scenario

Measure	baseline	zero	full constraints
μ	6.91	6.39	6.49
σ	0.63	0.64	0.57
kurtosis	3.65	4.00	4.63
skewness	0.13	0.78	1.28

Table 11: Connection costs statistics per scenario

Measure	baseline	full constraints
μ	17.86	34.16
σ	2.01	3.29
kurtosis	2.95	4.51
skewness	0.60	-0.36

4.3 Discussion and Results

This study represents an attempt to study the influence of uncertainty in the design process due to the integration of alternative fuelled PPE systems. The integration of a multi-objective optimisation process in Monte Carlo simulations leads to increased computational modelling cost and complexity. For this reason, a simplified case study is developed to increase the ease of application. As discussed in Section 2, there is lack of knowledge regarding the actual size and shape that alternative fuelled PPEs are going to be,due to the technological advancements and the safety regulations under development. In combination with the case study, it is clear that there is no consistent pattern regarding the properties of the design space. The logical architecture in the form of the connection matrix proved a highly influential parameter that differentiates the design space more than the actual dimensions uncertainty.

In terms of the actual layout, margins for the BBs were included to account for possible corridors and safe spaces that need to exist within the engine room. The layout integration aims not to find the optimal configuration of the engine room, but instead to establish insights into the variation of the generated designs under uncertain conditions. It stands out that either *zero constraints* or *full constraints* lead to a smaller overall length, meaning that there is no linear behaviour depending on the number of constraints applied. Lastly, the method is not yet able to fully model the uncertainty propagation within all of MBSE layers and the case study was mostly limited to the physical and logical architecture layers.

5 CONCLUSIONS

The presented study establishes the uncertainties relating to power propulsion energy (PPE) systems that are generated from technical and regulatory factors. The review of the state-of-the-art in methanol fuelled vessels and the state-of-the-art on systems showed that more elements should be combined in the design process to fully understand the influence of the PPE systems on ship design. The uncertainties that were presented in Table 7 can prove critical design drivers. Based on these, a design framework is proposed (Figure 1), which centers around the inclusion of uncertainty and its propagation through the model-based systems engineering (MBSE) layers, as shown in Table 7.

Complementary to the review of the state-of-art, a case study is set up to evaluate the uncertainties within the physical space combined with different logical architectures. This case study investigates the effect of variable dimensions and connection costs of the building blocks on the overall size of the engine room. The outcome confirms the findings reported in the literature. The distribution shapes of the output variable differ from the uniform input distribution, meaning that the size alteration does not always prove to be fully influential. Furthermore, modifications to logical architectures result in distinct distribution patterns, leading to inconsistencies in the outcomes. Therefore, there is the need to gain a better understanding on the way that PPE systems are integrated into the vessel and the constraints imposed on the design because of safety or performance demands. Future research will therefore focus on the percolation of the established uncertainties within the layers of MBSE with a particular emphasis on understanding the effect of the different design choices on the overall design.

ACKNOWLEDGEMENTS

This work is part of the MENENS project, funded by the Netherlands Enterprise Agency (RVO) under the grant number MOB21012.

REFERENCES

[1] IMO, *Fourth Greenhouse Gas Study 2020 International Maritime Organisation*, https://www.imo.org/en/ourwork/Environment/Pages/Fourth-IMO-Greenhouse-Gas-Study-2020.aspx, 2021.

[2] IMO, *Revised GHG reduction strategy for global shipping adopted*, https://www.imo.org/en/MediaCentre/PressBriefings/pages/Revised-GHG-reduction-strategy-for-global-shipping-adopted-.aspx, Jul. 2023.

[3] E. Commission, *A European Green Deal*, https://commission.europa.eu/strategy-and-policy/priorities-2019-2024/european-green-deal_en, 2021.

[4] E. Union, *Press releases - Fuel EU Maritime*, https://www.waterborne.eu/documents/press-releases, 2023.

[5] IMO, *UN body adopts climate change strategy for shipping*, https://imopublicsite.azurewebsites.net/en/MediaCentre/PressBriefings/Pages/06GHGinitialstrategy.aspx, 2023.

[6] IMO, *Sulphur oxides (SOx) and Particulate Matter (PM) – Regulation 14*, 2020. [Online]. Available: https://www.imo.org/en/OurWork/Environment/Pages/Sulphur-oxides-(SOx)-%E2%80%93-Regulation-14.aspx.

[7] IMO, *Nitrogen Oxides (NOx) – Regulation 13*, 2020. [Online]. Available: https://www.imo.org/en/OurWork/Environment/Pages/Nitrogen-oxides-(NOx)-%E2%80%93-Regulation-13.aspx.

[8] Y. Wang and L. A. Wright, "A Comparative Review of Alternative Fuels for the Maritime Sector: Economic, Technology, and Policy Challenges for Clean Energy Implementation," *World*, vol. 2, no. 4, pp. 456–481, Oct. 2021.

[9] B. Lagemann, E. Lindstad, K. Fagerholt, A. Rialland, and S. Ove Erikstad, "Optimal ship lifetime fuel and power system selection," *Transportation Research Part D: Transport and Environment*, vol. 102, pp. 103–145, Jan. 2022.

[10] A. D. Korberg, S. Brynolf, M. Grahn, and I. R. Skov, "Techno-economic assessment of advanced fuels and propulsion systems in future fossil-free ships," *Renewable and Sustainable Energy Reviews*, vol. 142, May 2021.

[11] E. Lindstad, G. M. Gamlem, A. Rialland, and A. Valland, "Assessment of Alternative Fuels and Engine Technologies to Reduce GHG," SNAME Maritime Convention 2021 Assessment of Alternative Fuels, 2021.

[12] D. Ban and J. Bebić, "An introduction of future fuels on working ship for GHGs reduction: Trailing suction hopper dredger case study," *Journal of Cleaner Production*, vol. 405, p. 137 008, Jun. 2023.

[13] C. F. Rehn, "Ship Design under Uncertainty," Ph.D. dissertation, 2018.

[14] B. Zincir, P. C. Shukla, and A. K. Agarwal, *Decarbonization of Maritime Transport*. 2023.

[15] J. Harmsen, "Green Maritime Methanol. Towards a zero emission shipping industry," Tech. Rep., 2021.

[16] B. Zincir and C. Deniz, *Methanol as a Fuel for Marine Diesel Engines*. 2021.

[17] P. de Vos, de Van der Schueren, S. Los, and K. Visser, "Effective Naval Power Plant Design Space Exploration," in *Conference Proceedings of International Naval Engineering Conference and Exhibition INEC*, 2022.

[18] Bureau of Shipping, American, *Sustainability-Methanol-as-Marine-Fuel*, https://absinfo.eagle.org/acton/media/16130/sustainability-whitepaper-methanol-as-marine-fuel, 2021.

[19] IMO, *IGF Code (MSC.391(95) Code of safety for ships using gases or other low-flashpoint fuels) - Netherlands Regulatory Framework (NeRF) – Maritime*, https://puc.overheid.nl/nsi/doc/PUC_80736_14/1/, 2015.

[20] A. Bureau of Shipping, *Requirements for Methanol and Ethanol Fueled Vessels 2022*, https://ww2.eagle.org/content/dam/eagle/rules-and-guides/current/other/328-requirements-for-methanol-and-ethanol-fueled-vessels/328-methanol-and-ethanol-fueled-vessels-reqts-july22.pdf, 2022.

[21] I. M. O. (IMO), "MSC.1-Circ.1621 - Interim Guidelines For The Safety Of ShipsUsing MethylEthyl Alcohol As Fuel - Netherlands Regulatory Framework (NeRF) – Maritime," Guidelines, Oct. 2020. [Online]. Available: https://puc.overheid.nl/nsi/doc/PUC_641671_14/1/.

[22] J. Ellis, "Study on the use of ethyl and methyl alcohol as alternative fuels in shipping," en, Tech. Rep., 2016.

[23] K. Andersson and C. M. Salazar, "FCBI Methanol Marine Fuel Report Final English — PDF — Fuels — Chemical Energy Sources," Tech. Rep., Oct. 2015. [Online]. Available: https://www.scribd.com/document/413836055/FCBI-Methanol-Marine-Fuel-Report-Final-English.

[24] M. J. W. Kries, "A methanol impact tool for yachts," en, M.S. thesis, Mar. 2021.

[25] M. Pothaar, R. Geertsma, and J. Reurings, "Energy transition for the replacement Air Defense and Command Frigate," in *Conference Proceedings of International Naval Engineering Conference and ExhibitionINEC*, Oct. 2022.

[26] Ç. Karatuğ, E. Ceylan B. O.and Ejder, and Y. Arslanoğlu, "Investigation and Examination of LNG, Methanol, and Ammonia Usage on Marine Vessels," in *Decarbonization of Maritime Transport*, ser. Energy, Environment, and Sustainability, B. Zincir, P. C. Shukla, and A. K. Agarwal, Eds., 2023, pp. 65–85.

[27] J. Harmsen, N. Nesterova, C. Bekdemir, and K. J. van Kranenburg, "Green Maritime Methanol. WP2 Initiation and Benchmark analysis," Tech. Rep., 2020.

[28] G. Voniati, A. Dimaratos, S. Kyklis, G. Koltsakis, and L. Ntziachristos, "The Potential of Methanol and Ammonia to Decarbonize Shipping: Impact on GHG and Other Pollutants," en, in *8th International Symposium on Ship Operations, Management and Economics (SOME 2023)*, OnePetro, Mar. 2023. (visited on 04/06/2023).

[29] K. Portin, "WÄRTSILÄ GAS ENGINE DEVELOPMENT & METHANOL ADAPTATION," Tech. Rep., 2015.

[30] S. Zuidgeest, "Alternative fuel selection and operational performance assessment for a 7000 DWT general cargo vessel: Impact assessment of methanol as alternative fuel on the operational performance of the LABRAX sersies vessels," M.S. thesis, 2022.

[31] E. Lindstad, B. Lagemann, A. Rialland, G. M. Gamlem, and A. Valland, "Reduction of maritime GHG emissions and the potential role of E-fuels," *Transportation Research Part D: Transport and Environment*, vol. 101, p. 103 075, Dec. 2021.

[32] DNV, *Decarbonize shipping*, https://www.dnv.com/CustomHeader, 2023.

[33] R. Pawling, R. Bucknall, and A. Greig, "Considerations For Future Fuels in Naval Vessels," in *Conference Proceedings of International Naval Engineering Conference and Exhibition (INEC) 2022*, Meeting Name: International Naval Engineering Conference and Exhibition, 2022.

[34] M. Pothaar, "Assessing the impact of sustainable fuels for Large Surface Combatants: A comparison between sustainable methanol and diesel for the Future Air Defender of the Royal Netherlands Navy," M.S. thesis, 2022.

[35] A. Snaathorst, "Alternative marine energy carrier impact on ship powering and the environment: A comparative conceptual LCA of the operational stage of ship types with alternative marine energy carriers," M.S. thesis, 2023.

[36] J. Streng, A. Kana, J. Verbaan, I. Barendregt, and J. Hopman, "Alternative Energy Carriers in Naval Vessels," in *Conference Proceedings of International Naval Engineering Conference and Exhibition (INEC) 2022*, vol. 16, 2022.

[37] S. Liu and A. Papanikolaou, "Approximation of the added resistance of ships with small draft or in ballast condition by empirical formula," *Proceedings of the Institution of Mechanical Engineers, Part M: Journal of Engineering for the Maritime Environment*, vol. 233, no. 1, pp. 27–40, Feb. 2019, Publisher: SAGE Publications.

[38] A.P. Moller - Maersk, *Maersk continues green transformation with six additional large container vessels*, https://www.maersk.com/news/articles/2022/10/05/maersk-continues-green-transformation, Oct. 2022.

[39] H. J. Klein Woud and D. Stapersma, *Design of Propulsion and Electric Power Generations Systems*. 2003.

[40] Maritime Knowledge Center (MKC), TNO, TU Delft, "Framework CO2 reduction in shipping.pdf," Tech. Rep. MIIP019-2016, 2017. [Online]. Available: https://www.koersenvaart.nl/files/Framework%20CO2%20reduction%20in%20shipping.pdf.

[41] MAN, "Propulsion trends in bulk carriers," Tech. Rep., 2022.

[42] *Stena Germanica ferry (STENA LINE)*, https://www.cruisemapper.com/ships/Stena-Germanica-ferry-1897, 2023.

[43] GMM consortium partners, "Green Maritime Methanol. WP 5 - System Design for Short Sea Shipping — TNO Publications," Tech. Rep., May 2020.

[44] E. Esmailian, S. Steen, and K. Koushan, "Ship design for real sea states under uncertainty," *Ocean Engineering*, vol. 266, p. 113 127, Dec. 2022.

[45] S. O. Erikstad and B. Lagemann, "Design Methodology State-of-the-Art Report," in *IMDC Day 3 Tue, June 28, 2022*, Vancouver, Canada: SNAME, Jun. 2022, D031S000R001.

[46] C. Veldhuis, A. Grasman, J. Willemsen, and U. Shipurkar, "Systematic design of future marine power & energy systems," in *The 15th International Symposium on Practical design of ships and other floating structures*, 2022.

[47] P. Roques, *Systems Architecture Modeling with the Arcadia Method: A Practical Guide to Capella*. Jan. 2017, pp. 1–277.

[48] A. Kossiakoff, W. N. Sweet, S. J. Seymour, and S. M. Biemer, *Systems Engineering Principles and Practice*, en. 1991, ISBN: 978-1-118-00102-8.

[49] A. A. Kana, "Forecasting design and decision paths in ship design using the ship-centric Markov decision process model," *Ocean Engineering*, vol. 137, pp. 328–337, Jun. 2017.

[50] K. Terün, A. A. Kana, and R. Dekker, "Assessing Alternative Fuel Types for Ultra Large Container Vessels in Face of Uncertainty," B. Volker, Ed., 21st International Conference on Computer and IT Applications in the Maritime Industries, Pontignano, 21-23 June 2022, Hamburg, Hamburg University of Technology, 202, 2022.

[51] I. Poullis, "Application of Model Based System Engineering (MBSE) with Ship Design Arrangement Tool of advanced zero emissions Power, Propulsion and Energy Systems in Maritime Technology," M.S. thesis, Delft University of Technology, 2022.

[52] R. van der Bles, "A Design Tool for Machinery Space Arrangement," M.S. thesis, Delft University of Technology, 2019.

[53] A. A. Kana and B. M. Harrison, "A Monte Carlo approach to the ship-centric Markov decision process for analyzing decisions over converting a containership to LNG power," *Ocean Engineering*, vol. 130, 2017.

[54] A. Coraddu, M. Figari, and S. Savio, "Numerical investigation on ship energy efficiency by Monte Carlo simulation," pp. 220–234, Aug. 2014.

[55] C. Dall'armi, D. Pivetta, and R. Taccani, "Health-conscious optimization of long-term operation for hybrid pemfc ship propulsion systems," *Energies*, vol. 14, no. 13, Jul. 2021.

[56] D. Curto, F. Acebes, J. M. González-Varona, and D. Poza, "Impact of aleatoric, stochastic and epistemic uncertainties on project cost contingency reserves," *International Journal of Production Economics*, vol. 253, p. 108 626, Nov. 2022.

[57] H. Hosseini nasab, S. Fereidouni, s. Fatemi Ghomi, and M. Fakhrzad, "Classification of facility layout problems: A review study," *The International Journal of Advanced Manufacturing Technology*, vol. 94, Jan. 2018.

[58] K. Deb, "Multi-objective Optimisation Using Evolutionary Algorithms: An Introduction," in *Multi-objective Evolutionary Optimisation for Product Design and Manufacturing*, L. Wang, A. H. C. Ng, and K. Deb, Eds., 2011, pp. 3–34.

[59] MATLAB, *Global Optimization Toolbox*. [Online]. Available: https://nl.mathworks.com/products/global-optimization.html.

[60] D. H. P. C. C. (DHPC), *DelftBlue Supercomputer (Phase 1)*, 2022. [Online]. Available: https://www.tudelft.nl/dhpc/ark/delftbluephase1.

A Comparative Study on the Performance of Marine Diesel Engines Running on Diesel/Methanol and Diesel/Natural Gas Mode

Weihe Yao[a], Yu Ding[a], Shuai Guan[a], Hongkai Ben[a], La Xiang[a*]

[a] Harbin Engineering University, Harbin, China
* Corresponding Author e-mail: xiangla@hrbeu.edu.cn

Abstract

With the increasingly stringent requirements of international decarbonization regulations, the shipping industry has accelerated the pace of exploiting low-carbon fuels. Methanol is one of the most prospective substitute fuels featured with low-carbon content, clean combustion and easy storage. For marine diesel/methanol dual-fuel engine applications, a certain quantity of diesel is typically used to ensure a stable ignition and combustion. However, the combustion and emission characteristics as well as the stable operation window of marine diesel/methanol dual-fuel engines under different operating loads have not yet been well investigated. In this study, a marine diesel/natural gas dual-fuel engine was used as a prototype to develop a 3D simulation model using CONVERGE, which was then validated using experimental data under different operating loads. The validated model was then employed to investigate the effects of methanol substitution rate (MSR) on the combustion and emission characteristics under the diesel/methanol operation mode. By monitoring the abnormal combustion phenomena such as misfire and knocking, the maximum MSR under different operating conditions was identified. Finally, the engine performances of diesel/natural gas and diesel/methanol modes were compared in terms of combustion and emission characteristics. The results show that the maximum MSR tends to increase first (from 5% to 43% under operation load from 25% to 75%) and then decrease (from 43% to 20% under operation load from 75% to 100%) with increasing operating load owing to the misfire limitation at low load and knocking limitation at high load, respectively. Comparing to the prototype diesel/natural gas mode, the diesel/methanol mode exhibited a shorter combustion duration with increased NOx emissions. The results obtained from this study are expected to guide the operation management of marine diesel/methanol dual fuel engines, and thus help reduce ships' CO_2 emissions.

Keywords: Diesel/methanol, Diesel/natural gas, Operating load, Combustion characteristics, Emissions, Substitution rate.

1. INTRODUCTION

With increasingly stringent emission regulations, a number of methods, such as using alternative fuels, optimizing the combustion process, and adding after-treatment equipment, have been employed to reduce carbon emissions in the marine shipping industry. Methanol is one of the most prospective alternative fuels for marine engines due to its low-carbon, clean-combustion, easy-storage and renewable characteristics [1].

When applied in internal combustion engines, methanol can be used alone [2-3] or in combination with other fuels, such as methanol-diesel engines, methanol-gasoline engines, methanol-hydrogen engines, etc [4-5]. For marine application, methanol-diesel engines are more widely used, which can be divided into three classifications: direct blending, port injection, and direct injection. Direct blending means methanol is emulsified and mixed with diesel to form a diesel-methanol mixture as an engine fuel [6-8]. Port injection methanol-diesel engine is to inject methanol into the intake port, where it is mixed with air before entering the cylinder during the intake process, while the diesel fuel is injected directly into the cylinder before the top dead center (TDC) for igniting the methanol [9-12]. Direct injection methanol-diesel engine is to inject both methanol and diesel directly into a cylinder. Two separate nozzles are used to inject methanol and diesel, with diesel generally injected before the TDC, while there are a number of methanol injection strategies [13-15]. However, the combustion and emission characteristics as well as the operational stability of marine diesel/methanol dual-fuel engines under different operating loads are seriously affected by misfire and knocking [16].

In this area, Duan et al. [3] investigated the causes of knocking in methanol engines, showing that the premature ignition due to hot spots causes severe knocking which can be suppressed by using a fractional direct in-cylinder injection strategy.

@2023 Weihe Yaoa et al., published by TU Delft OPEN Publishing on behalf of the authors. Licensed under a Creative Commons Attribution CC BY license.
DOI: https://doi.org/10.59490/moses.2023.656

Yin et al. [13] investigated the effects of methanol direct injection strategies on engine performance. The results show that injection of methanol during the compression stroke could result in a large in-cylinder fuel concentration gradient, thus reducing the combustion duration. The ignition delay and combustion duration increased with the increase of methanol blending ratio, whilst the combustion stability was improved. Li et al. [16] compared the diesel/methanol dual-fuel engine knocking in port injection and direct injection mode. The results show that direct injection mode can effectively inhibit the occurrence of knocking, while the port injection mode is relatively serious, however, it can be suppressed by optimizing the diesel injection strategy or increasing exhaust gas recirculation. Sun et al. [17] improved the knocking of a diesel-methanol dual-fuel engine in direct injection mode based on the optimization of the in-cylinder injection strategy. The results show that the optimized injection strategy can improve the economy while reducing the intensity of knocking. To summarize, the research related to knocking has been relatively intensive, while the research related to misfire is still unclear.

Previous studies on methanol have been relatively comprehensive. However, in terms of evaluating misfire phenomenon, the most widely used index is the cyclic fluctuation rate of the indicated mean effective pressure (IMEP), which is inappropriate for CFD modelling within one cycle. Thus, a new method of misfire evaluation (PCC) is proposed in this study, which can provide new ideas for the operating boundary exploration of dual-fuel engines. In addition, methanol and natural gas are good choices for marine dual-fuel engines. The application technologies of the diesel/natural gas mode have been well developed, whilst those of the diesel/methanol mode are still under development. Therefore, it is of great significance to investigate the convention from diesel/natural gas mode to diesel/methanol mode.

To explore the combustion and emission characteristics as well as the steady operation window of a port injection marine diesel/methanol engine, a CFD model was chosen because of its high accuracy in predicting the knocking and misfire phenomena as well as engine emissions. By monitoring the abnormal combustion phenomena such as misfire and knocking, the maximum methanol substitution rate under different operating conditions was identified. Finally, the engine performances of diesel/natural gas and diesel/methanol modes were compared in terms of combustion and emission characteristics. This study can provide guidance for the conversion of diesel/natural gas dual-fuel engines to diesel/methanol dual-fuel engines and help reduce CO_2 emissions of ships in the future.

2. MODELLING METHODOLOGY

In this study, a 3D CFD simulation model was developed using CONVERGE software, which has the advantages of autonomous meshing and abundant sub-models. Since n-heptane can describe the ignition and combustion characteristics of diesel fuel well [31], it was chosen to simulate the diesel injection and combustion processes in this study. The properties of n-heptane and methanol are presented in Table 1.

Table 1. Properties of methanol and n-heptane

	Methanol	N-heptane
Molecular Formula	CH_3OH	C_7H_{16}
Molecular weight (g/mol)	32	100
Density（g/cm^3,at 20℃）	0.79	0.683
Boiling temperature (℃)	64.7	98.8
Flashpoint (℃)	11	-4
Auto-ignition temperature (℃)	470	204
Viscosity (mPa s at 298.15K)	0.59	0.4
Stoichiometric fuel-air ratio	0.154	0.069
Cetane number	3-5	56
Lower heating value (MJ/kg)	19.95	44.60
Carbon content (wt%)	37.5	84
Hydrogen content (wt%)	12.5	16
Oxygen content (wt%)	50	0

The sub-models used for developing the 3D CFD model are listed in Table 2.

Table 2. Sub-models used in this study

Name	Sub-model
Turbulence model	RNG k-ε model [18]
Liquid injection	Blob injection model [19]
Spray breakup model	KH-RT model [20]
Drop/wall interaction	Rebound/slide model
Droplets collision model	NTC model [21]
Evaporation model	Frossling model [22]
Wall heat transfer model	O'Rourke and Amsden model [23]
Combustion model	SAGE model [24]
Reaction kinetics	Diesel/methanol dual-fuel mechanism [25]
Soot mechanism	Hiroyasu-NSC model [26]
NO_x mechanism	Extended Zeldovich NO_x model [27]

Although in-cylinder combustion is complex, the three conservation equations of mass (1), momentum (2), and energy (3) constitute the basis for combustion process simulation.

$$\frac{\partial \rho}{\partial t} + \frac{\partial \rho u_i}{\partial x_i} = S \tag{1}$$

$$\frac{\partial \rho u_i}{\partial t}+\frac{\partial \rho u_i u_j}{\partial x_j}=-\frac{\partial P}{\partial x_i}+\frac{\partial \sigma_{ij}}{\partial x_j}+S_i \quad (2)$$

$$\frac{\partial \rho e}{\partial t}+\frac{\partial u_j \rho e}{\partial x_j}=-P\frac{\partial u_j}{\partial x_j}+\sigma_{ij}\frac{\partial u_i}{\partial x_j}+\frac{\partial}{\partial x_j}(K\frac{\partial T}{\partial x_j}) +\frac{\partial}{\partial x_j}(\rho D\sum_m h_m\frac{\partial \Upsilon_m}{\partial x_j})+S \quad (3)$$

The RNG k-ε model was selected to characterize the turbulence, which significantly contributes to the combustion process. The turbulent kinetic energy k and turbulent dissipation rate ε were calculated according to Equations (4) and (5), respectively.

$$\frac{\partial \rho k}{\partial t}+\frac{\partial \rho u_i k}{\partial x_i}=\tau_{ij}\frac{\partial u_i}{\partial x_j}+\frac{\partial}{\partial x_j}\left(\frac{\mu+\mu_t}{\mathrm{Pr}_k}\frac{\partial k}{\partial x_j}\right) -\rho\varepsilon+\frac{C_s}{1.5}S_s \quad (4)$$

$$\frac{\partial \rho \varepsilon}{\partial t}+\frac{\partial(\rho u_i \varepsilon)}{\partial x_i}=\frac{\partial}{\partial x_j}\left(\frac{\mu+\mu_t}{\mathrm{Pr}_\varepsilon}\frac{\partial \varepsilon}{\partial x_j}\right)+C_{\varepsilon 3}\rho\varepsilon\frac{\partial u_i}{\partial x_i} +\left(C_{\varepsilon 1}\frac{\partial u_j}{\partial x_j}\tau_{ij}-C_{\varepsilon 2}\rho\varepsilon+C_s S_s\right)\frac{\varepsilon}{k} +S-\rho R_\varepsilon \quad (5)$$

The SAGE model was chosen to simulate the combustion process based on the skeleton kinetic mechanism for the methanol/n-heptane dual-fuel combustion proposed by Liu et al., which includes 52 species and 182 reactions, and exhibits high accuracy for characterizing dual-fuel combustion [25].

In order to quantify the knocking phenomenon under different operating conditions, the indicator knock index (KI) is chosen, which denotes the average value of PP_{max}(peak-to-peak value of the vibration signal of filtered pressure) for local pressure monitoring points at N different locations [28].

$$KI=\frac{1}{N}\sum_{n=1}^{N}PP_{\max,n} \quad (6)$$

For CFD models that simulate the combustion process with one cycle, it is inappropriate to use the cyclic fluctuation rate of the IMEP to evaluate misfire occurrence. Therefore, referring to the definition of CA10 (combustion initiation angle) and CA90 (combustion termination angle), a new parameter, the Percentage of Combustion Completion (PCC), which is defined as the ratio of the accumulated heat released at the end of the simulation to the theoretical energy input, was introduced to evaluate the misfire phenomenon for CFD modelling. In this study, PCC= 10% and PCC= 90% were set as the boundaries for complete misfire and partial misfire, respectively.

$$PCC=\frac{Q}{m\cdot LHV}\times 100\% \quad (7)$$

3. MODEL SETUP AND VALIDATION

3.1 Model setup

The main engine specifications are presented in Table 3. It is worth mentioning that a number of experiments have been conducted on the investigated dual-fuel engine, while corresponding data acquisition and post-processing can be found in reference [29].

Table 3. Engine specifications.

Parameter	Specification
Engine type	6-cylinder
Displacement (L)	12.149
Bore×stroke (mm)	129×155
Compression ratio	16.5
IVC (°CA ATDC)	-150
EVO (°CA ATDC)	129
Nozzle (number×nozzle diameter) (mm)	8×0.22

In this study, the complete engine model was developed by using the *Make engine sector surface* tool, and the grid was generated automatically using the CONVERGE software. The simulation starts with the -150° CA intake valve closed and ends with the 129° CA exhaust valve open. Because the injector contains eight uniformly distributed nozzles, a one-eighth model of the combustion chamber was constructed to reduce the computational cost by utilizing axial symmetry. According to Figure 2, the simulation results of the two simulation models do not show a significant difference, indicating that both models can satisfy model accuracy validation.

Therefore, after considering the model accuracy and computational cost, the one-eighth model was selected for the subsequent research. Six local pressure monitoring points were set inside the computational domain, as shown in Figure 3.

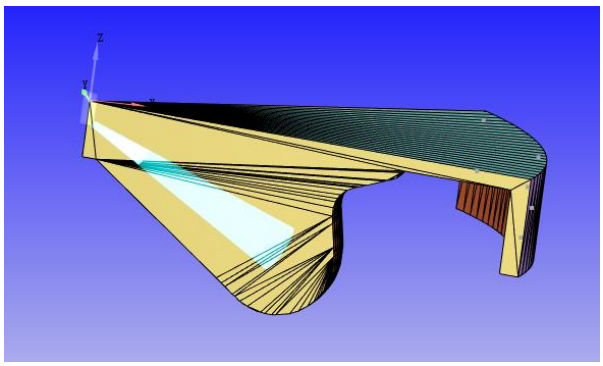

Figure 1: Complete model of the combustion chamber and one-eighth model at TDC.

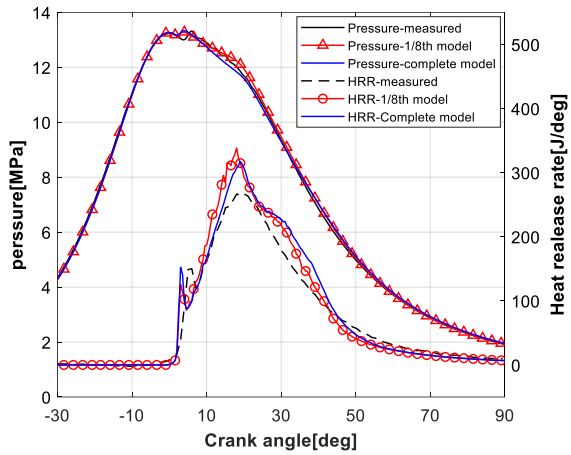

Figure 2: In-cylinder pressure and HRR comparison at 100% operation loads.

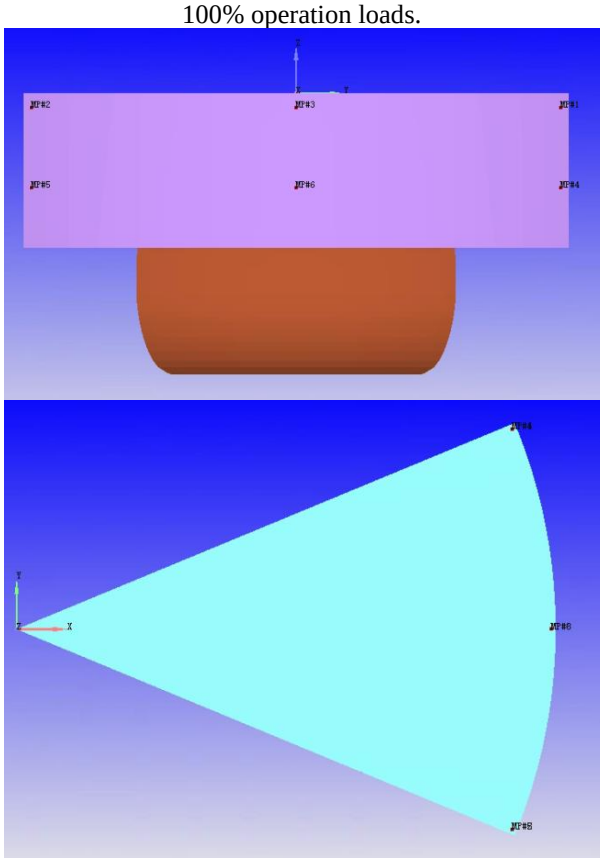

Figure 3: Location of the monitoring points.

3.2 Model validation

Before validating the developed CFD one-eighth model, it is necessary to verify the mesh grid size independence. To determine the appropriate basic grid size, four grid schemes (1.5, 2.0, 2.5, and 3.0 mm) were compared in terms of in-cylinder pressure. Figure 4 shows the comparison results of the pressure for four basic grid sizes. Balancing the prediction accuracy and computation cost, a 2 mm basic grid size and 33689 basic cells were ultimately selected in this study.

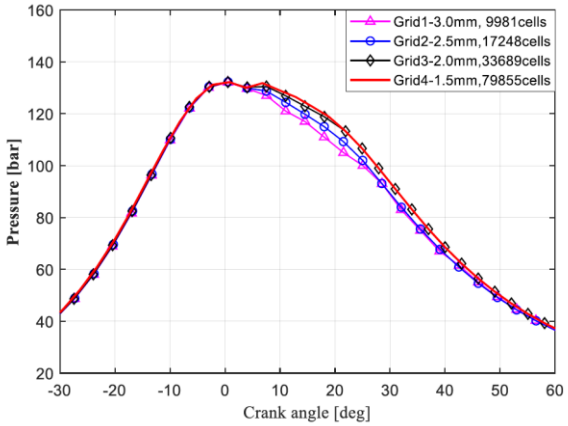

Figure 4: In-cylinder pressure comparison with 4 base grid sizes.

To validate the model accuracy, the simulation results were compared with the experimental data under operation loads of 32%, 53%, 74%, and 100%. However, due to page limitations, the results are not fully presented.

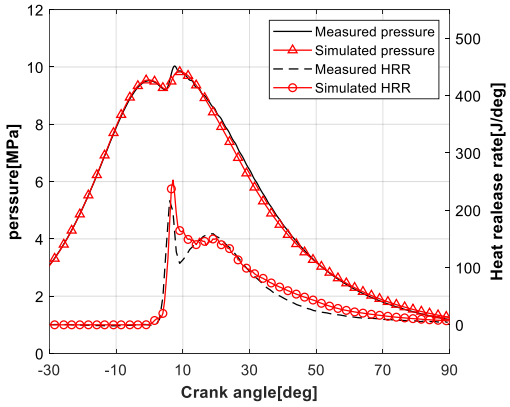

Figure 5: In-cylinder pressure and HRR comparison at 53% operation loads.

The simulated and measured pressures and heat release rate (HRR) at 100% operating conditions are shown in Figures 2, which clearly demonstrate good agreement with each other. It can be observed that under 100% operating conditions the predicted results match the experimentally obtained data with adequate accuracy. Figures 5 and 6 show the accuracy verification of the pressure and HRR at 53% and 32% of the operation loads, respectively.

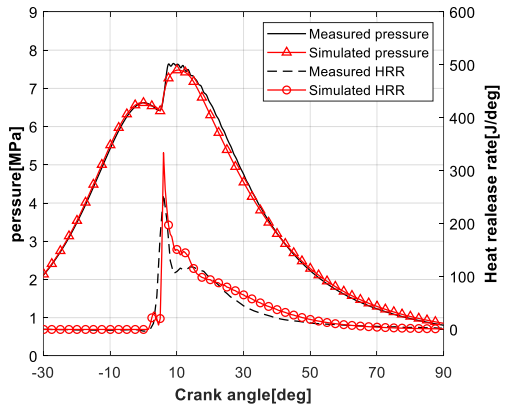

Figure 6: In-cylinder pressure and HRR comparison at 32% operation loads.

This study quantitatively compared the simulated and measured p_{max}, and the corresponding angles (α_1), p_{com}, and IMEP. Comparisons of the simulated and measured in-cylinder parameters at 4 different loads are presented in Table 4. It can be seen that under 100% load, the simulated peak pressure was 132.8 bar, compared with the measured peak pressure of 133.1 bar, the error is only 0.2%, and the corresponding angle difference is 1.89 °CA. The simulated p_{com} was 132.6 bar, which is very close to the experimental data of 132.4 bar, with an error of 0.2%. The relative errors of all the parameters at the other operating loads were less than 5%, and the angles were less than 3°CA, indicating that the model was more accurate in terms of combustion.

Table 4. Quantitative Comparison between the simulated and measured in-cylinder parameters

Load	Parameters	p_{max} (bar)	α_1	p_{com} (bar)	IMEP (bar)
100%	Simulation	132.8	4.03	132.6	19.78
	Experiment	133.1	5.92	132.4	18.90
	Error	0.2%	1.89	0.2%	4.6%
74%	Simulation	128.4	5.64	128.1	17.89
	Experiment	128.0	6.23	127.4	18.00
	Error	0.3%	0.59	0.5%	0.6%
53%	Simulation	99.37	9.02	94.87	11.84
	Experiment	100.1	7.80	95.06	12.39
	Error	0.7%	1.22	0.2%	4.4%
32%	Simulation	74.81	10.5	66.15	9.37
	Experiment	76.05	9.49	65.59	9.70
	Error	1.6%	1.01	0.9%	3.4%

A comparison of the simulated and measured emissions under 4 different operating conditions is presented in Table 5. It can be observed that the relative errors for both NOx and CO are less than 10%, whereas HC has larger relative errors, except at the100% load. Combined with the higher simulated NOx emissions, the overestimated temperature may have been the main cause. Overall, the accuracy of emission predictions of the model was acceptable.

Table5. Comparison between the simulated and the measured emissions.

Load	Parameters	NOx (g/kWh)	CO (g/kWh)	HC (g/kWh)
100%	Experiment	1.83	6.82	17.67
	Simulation	1.67	7.47	18.8
	Error(%)	8.74	9.53	6.4
74%	Experiment	1.34	9.36	32.45
	Simulation	1.47	8.55	28.40
	Error(%)	9.70	8.65	12.48
53%	Experiment	1.50	7.21	24.93
	Simulation	1.62	6.50	22.30
	Error(%)	8.80	9.85	10.55
32%	Experiment	1.62	3.77	10.30
	Simulation	1.70	3.45	8.90
	Error(%)	4.94	8.49	13.59

In summary, by comparing the p_{max}, HRR, IMEP, and emissions obtained from the simulation and experiments, it was proven that the developed model has sufficient accuracy and can be used in subsequent research.

4. RESULTS AND ANALYSIS

In this section, the validated 3D model is used to investigate the maximum methanol substitution rate under different operating conditions, the effects of the MSR on engine performance, and a comparison between diesel/methanol and diesel/natural gas dual-fuel modes.

4.1 Maximum methanol substitution rate under different operating loads

In this study, the maximum methanol substitution rate (MMSR) under four operating conditions (25%, 50%, 75%, and 100% load) was identified by considering the misfire and knocking occurrences. Figure 7 shows that the MMSR tended to increase from 5% to 43% when the operating load increased from 25% to 75% and then decreased to 20% at 100% operating load. Misfire and knocking were the main factors constraining the MMSR at low and high operating loads, respectively, as shown in Figures 8 and 9.

Figure 8 presents the PCC variation with methanol substitution rate (MSR) at different operating loads. As described in Equation (7), the partial misfire and complete misfire limits are defined as PCC = 90% and PCC=10%, respectively. In this study, the partial misfire limit was used to determine the maximum methanol substitution rate at low operating loads. At 25% and 50% operating loads, the PCC showed a decreasing trend with increasing MSR, which constrained the MMSR to 5% and 25%, respectively. For the case of 25% operating load, the PCC drops below 10% at

approximately 50% MSR, indicating complete misfire occurrence. At 75% and 100% operating loads, the PCC exhibited an increasing trend with increasing MSR, which was probably caused by the increasing intake pressure and temperature. This means that the methanol addition stimulates combustion; thus the partial misfire limit is no longer the MMSR constraint at high operating loads.

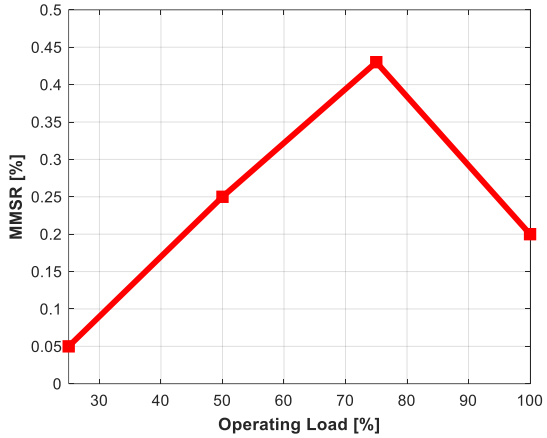

Figure 7: MMSR variation with engine operating load.

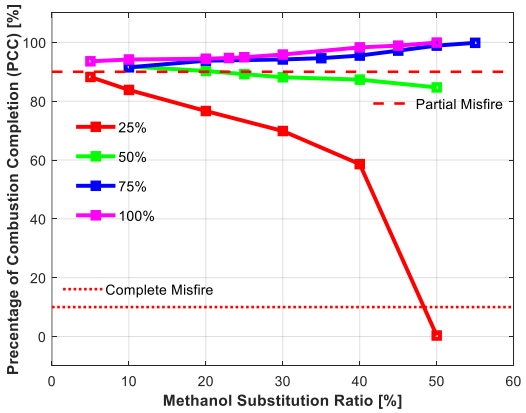

Figure 8: PCC variation with MSR under different operating loads.

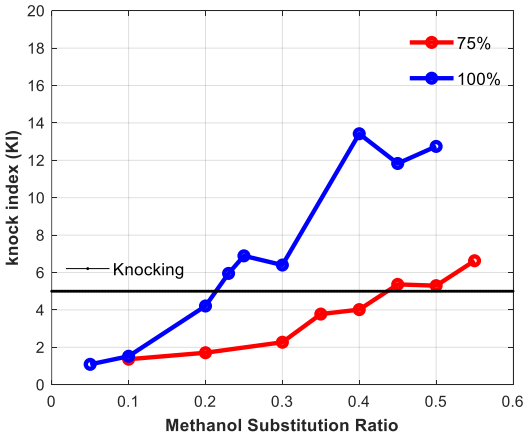

Figure 9: Knocking condition of engine.

However, with an increase in the operating load, the combustion becomes more violent with increasing MSR, which makes the knocking index (KI) the main factor constraining the MMSR at high operating loads. Figure 9 shows the KI variation with MSR under 75% and 100% operating loads. At high operating loads, the MMSR can be obtained by identifying the knocking index. Currently, the setting of KI is mainly based on SI engines and is not applicable to this study. In this study, first, the monitoring points were all close to the cylinder wall, resulting in a larger KI; second, in the pure diesel mode KI=2.52, so KI of the knocking limit should be larger. Finally, it was concluded from the analysis of the results that a significant difference in the cylinder pressure curves (shown in Figure 10) was observed at the 75% work and 50% MSR condition, which was considered to be closer to the knockout boundary (KI=5). In summary, KI=5 was tentatively selected as the limiting value for this study. As shown in Figure 9, the MMSR at the 75% and 100% operating loads were approximately 43% and 20%, respectively.

4.2 Effects of methanol substitution rate on engine performance and emissions

Among the investigated 4 operating loads, the largest MMSR was achieved under 75% operating load, which was the most economical operating point for engine management. Thus, the effects of different MSR on engine combustion and emissions were analyzed under a 75% operating load.

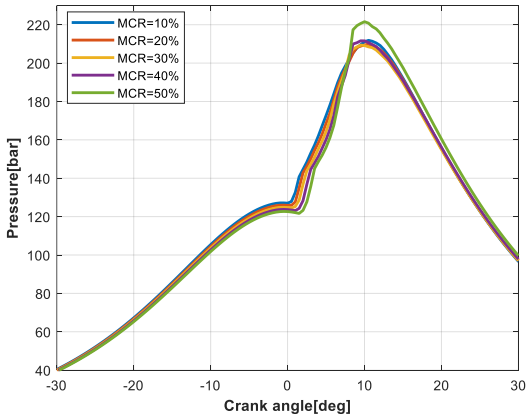

Figure 10: Comparison of in-cylinder pressure.

As shown in Figures 10 and 11, both the in-cylinder temperature and pressure during the compression stage decrease with increasing MSR, which is caused by the increase in the specific heat capacity of the in-cylinder gas owing to the increase in methanol. After diesel injection, it can be observed that as the MSR increases, the ignition delay period increases with a shorter combustion duration, indicating that the in-cylinder combustion becomes more intense, which can also be observed from KI. The two factors together resulted in a

decrease and then an increase in the maximum pressure and temperature.

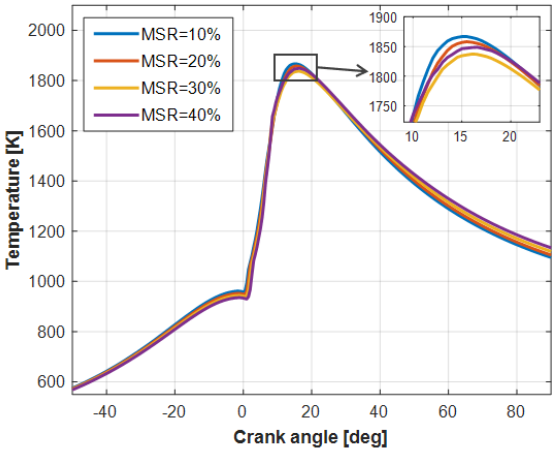

Figure 11: Comparison of in-cylinder temperature.

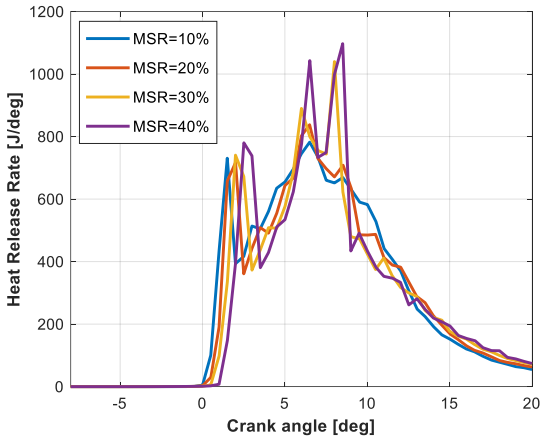

Figure 12: Comparison of heat release rate.

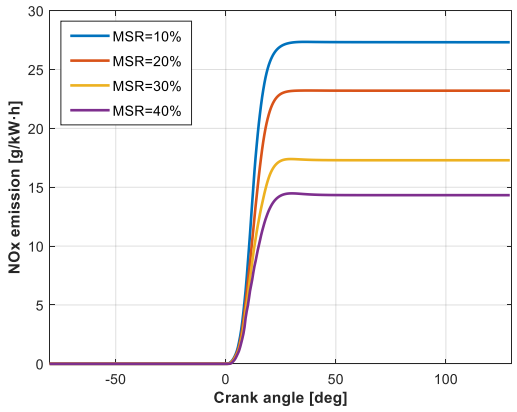

Figure 13: Comparison of NO_x emission.

A comparison of the HRR is shown in Figure 12, which shows that the HRR gradually changes from double to triple peaks as the MSR increases. It was observed that when the MSR was small, the combustion process mainly consisted of two stages: premixed combustion and diffusion combustion of diesel fuel. With a gradual increase in the MSR, the premixed combustion of methanol played a more important role in the combustion process, which contributed to the change from double to triple peaks. The HRR and KI analyses suggest that the engine is already at slight knocking at approximately 40% MSR, which might be beneficial to the output power [30]. Figure 13 shows the NO_x emission variation with MSR. It can be seen that NOx emissions decreased significantly with increasing MSR. There are two possible reasons for this: first, the reduction in diesel injection leads to a reduction in the hot zone at the flame front, and second, methanol combustion has an inhibitory effect on NOx production.

4.3 Comparison of diesel/methanol and diesel/natural gas dual fuel mode

In this section, a comparison is made between the diesel/methanol and diesel/natural gas dual-fuel modes in terms of combustion and emissions performance. Because the largest MMSR was achieved at 75% operating load, the operation mode comparison was conducted at 75% operating load. In addition, a maximum methanol substitution rate of 43% was used for the diesel/methanol mode, whereas a maximum natural gas substitution rate of 90% was used for the diesel/natural gas prototype mode.

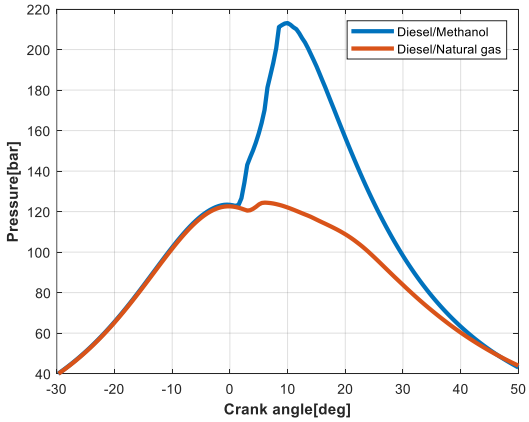

Figure 14: Comparison of in-cylinder pressure.

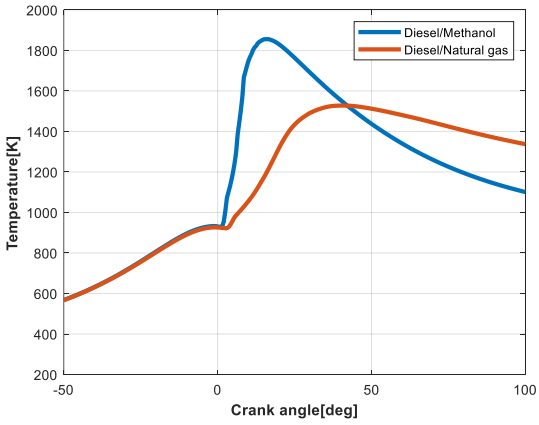

Figure 15: Comparison of in-cylinder temperature.

As shown in the Figures 14 and 15, the maximum pressure and temperature of the

diesel/methanol mode are much higher than those of prototype mode, which could probably increase the engine's mechanical and thermal loads. Figure 16 shows a comparison of the HRR. With the same pilot injection timing, the diesel/methanol mode exhibited shorter ignition delay and combustion duration. Besides, the combustion phase advanced with three HRR peaks in diesel/methanol mode. Compared with the diesel/natural gas mode, the higher temperature resulted in a significant increase in NO_x emissions in the diesel/methanol mode, as shown in Figure 17.

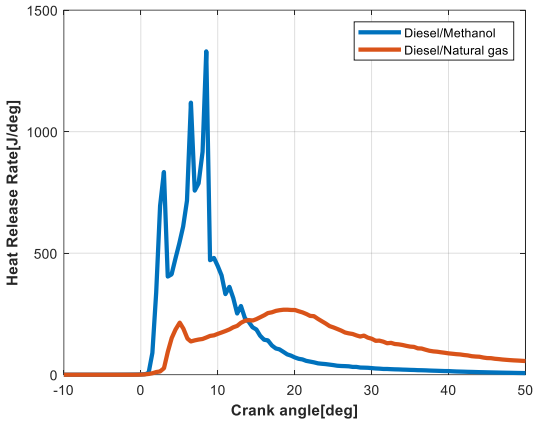

Figure 16: Comparison of heat release rate.

Figure 18 shows a comparison of the in-cylinder temperature distributions of the diesel/methanol and diesel/natural gas modes. As diesel is used mainly as a pilot fuel (approximately 10% energy percentage) in the diesel/natural gas mode, the diesel penetration distance is much smaller than that in the diesel/methanol mode, which uses 57% diesel for combustion. Owing to the shorter diesel spray penetration, the diesel/natural gas mode exhibited a significant afterburning phenomenon. However, diesel accounts for 57% of the total heat release; thus, the injection mass and spray penetration are much larger than those in the diesel/natural gas mode. Therefore, the combustion phase was advanced, thereby improving the afterburning phenomenon. It can also be observed that the main factor responsible for the high NO_x emissions in the methanol mode is excessive diesel injection.

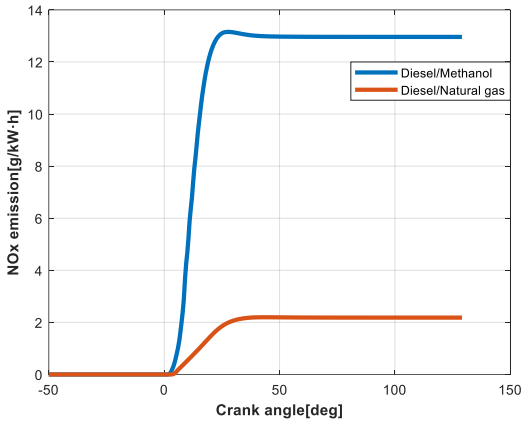

Figure 17: Comparison of NO_x.

Combining the simulation results of Figures 16 and 18, it can be found that for the diesel/methanol dual-fuel engine, the combustion was completed at approximately 20° CA; but from the three-dimensional results, there still exists a considerable amount of space in the low-temperature state (approximately 1500 K). For a diesel/natural gas dual-fuel engine, the temperature of the burned zone of the natural gas is very high (approximately 2000 K). In summary, it was concluded that methanol combustion contributes very little to the temperature increase, and therefore, NO_x generation can be effectively suppressed.

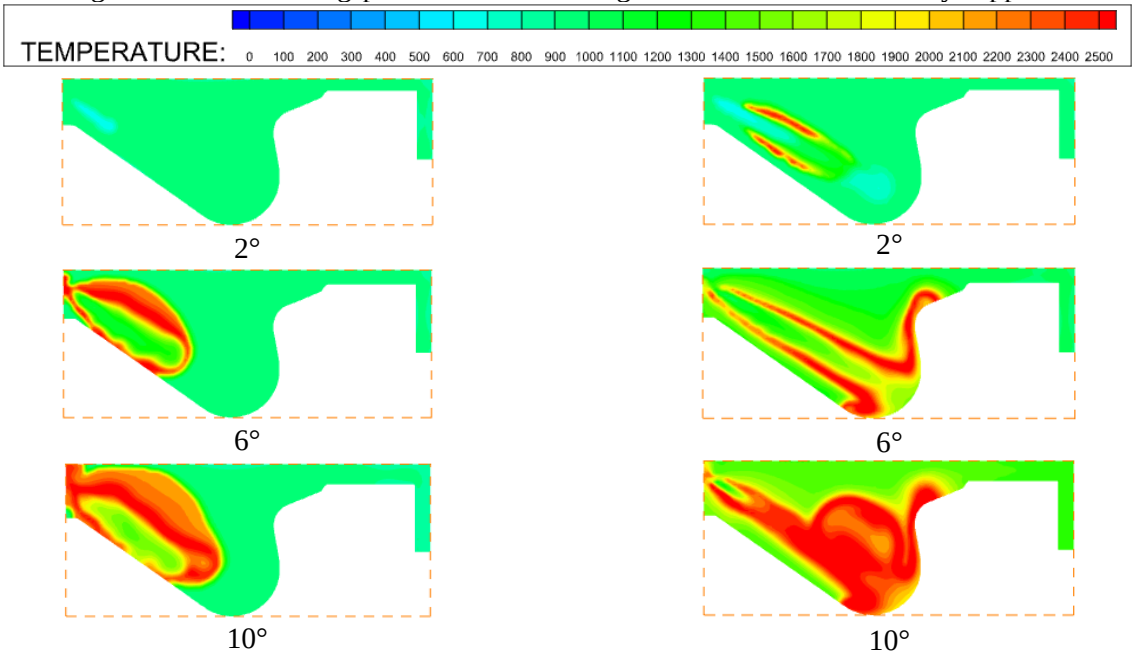

a.Natural gas-diesel dual fuel engine. b.Methanol-diesel dual fuel engine.

Figure 18: In-cylinder temperature distribution of different fuel engines.

5. CONCLUSION

In this study, a 3D CFD simulation model of a diesel/methanol dual-fuel engine was developed to investigate the maximum methanol substitution ratio under different operating conditions, the effects of the MSR on engine performance, and a comparative study with the diesel/natural gas dual-fuel operation mode. The conclusions are as follows.

1. For the diesel/methanol dual-fuel engine in the inlet port injection mode, the MMSR tended to increase and then decrease with an increasing operating load. The MMSRs at 25%, 50%, 75% and 100% loads are 5%, 25%, 43% and 20%, respectively.

2. At 75% operation condition, with the increase in MSR, the ignition delay period increased and the combustion duration decreased, resulting in more complete combustion and better emissions.

3. Compared with the prototype, the ignition delay and combustion duration of the diesel/methanol dual-fuel mode were significantly shorter, resulting in better engine dynamics for the same total heat release. Higher pressures and average temperatures mean increased mechanical and thermal loads, which may limit the engine's operating range. In addition, diesel/methanol dual-fuel engines have worse NO_x emissions.

4. In the diesel/methanol mode, methanol combustion is very rapid and the contribution to the temperature increase after combustion is not obvious; at the end of combustion, there is still a considerable space in the cylinder at approximately 1500 K. Therefore, the application of methanol in the engine can effectively inhibit the generation of NO_x.

5. As fuel, methanol can reduce NO_x generation in two ways: first, the use of methanol to replace diesel fuel can reduce the in-cylinder hot zone caused by diesel fuel combustion; second, the combustion of methanol does not have a significant effect on the temperature increase, and the relatively low temperature of the combusted zone can inhibit NO_x generation.

Owing to the limitations of knocking and misfire, there is an upper limit to the substitution rate of methanol, which is much lower than that of natural gas without changing the original engine structure. Nevertheless, as a new alternative fuel, methanol still exhibits unique advantages such as a faster combustion speed and stronger NOx suppression ability. In response to these findings, future research will focus on a diesel/methanol dual-fuel mode with direct in-cylinder injection to improve engine combustion and emission performance while increasing the methanol substitution rates.

6. ACKNOWLEDGMENTS

This study was supported by the National Key Research and Development Program of China (No. 2022YFE0107200).

REFERENCE

[1] Tian Z et al, “The effect of methanol production and application in internal combustion engines on emissions in the context of carbon neutrality: A review,”. *Fuel*, vol.320, no.123902, Jul.2022.

[2] Gong C et al, “Numerical study of twin-spark plug arrangement effects on flame, combustion and emissions of a medium compression ratio direct-injection methanol engine,”. *Fuel*, vol.279, no.118427, Nov.2020.

[3] Duan Q et al, “Experimental study of knock combustion and direct injection on knock suppression in a high compression ratio methanol engine,”. *Fuel*, vol.311, no.122505, Mar.2022.

[4] Yang S et al, “Combustion and emissions characteristics of methanol/gasoline CISI engines under different injection modes,”. *Fuel*, vol.333, no.126506, Feb.2023.

[5] Tian Z et al, “Numerical comparative analysis on performance and emission characteristics of methanol/hydrogen, ethanol/hydrogen and butanol/hydrogen blends fuels under lean burn conditions in SI engine,”. *Fuel*, vol.313, no.123012, Apr.2022.

[6] Zhang Z et al, “Investigation on the combustion and emission characteristics of diesel engine fueled with diesel/methanol/n-butanol blends,”. *Fuel*, vol.314, no.123088, Apr.2022.

[7] Fan C et al, “Chemical feature of the soot emissions from a diesel engine fueled with methanol-diesel blends,”. *Fuel*, vol.297, no.120739, Aug.2021.

[8] EL-Seesy A I et al, “Enhancement of the combustion and stability aspects of diesel-

methanol-hydrous methanol blends utilizing n-octanol, diethyl ether, and nanoparticle additives,". *Journal of Cleaner Production*, vol.371, no.133673, Oct.2022.
[9] Xu C et al, "Effect on the performance and emissions of methanol/diesel dual-fuel engine with different methanol injection positions,". *Fuel*, vol.307, no.121868, Jan.2022.
[10] Tao W et al, "The effect of diesel pilot injection strategy on combustion and emission characteristic of diesel/methanol dual fuel engine,". *Fuel*, vol.324, no.124653, Sep.2022.
[11] Liu J et al, "Experimental study on effects of pilot injection strategy on combustion and emission characteristics of diesel/methanol dual-fuel engine under low load,". *Energy*, vol.247, no.123464, May.2022.
[12] Panda K et al, "Diesel injection strategies for reducing emissions and enhancing the performance of a methanol based dual fuel stationary engine,". *Fuel*, vol.289, no.119809, Apr.2021.
[13] Yin X et al, "A comparative study on operating range and combustion characteristics of methanol/diesel dual direct injection engine with different methanol injection timings,". *Fuel*, vol.334, no.126646, Feb.2023.
[14] Li Z et al, "An exploratory numerical study of a diesel/methanol dual-fuel injector: Effects of nozzle number, nozzle diameter and spray spacial angle on a diesel/methanol dual-fuel direct injection engine,". *Fuel*, vol.318, no.123700, Jun.2022.
[15] Wang Y et al, "Study on the performance of diesel-methanol diffusion combustion with dual-direct injection system on a high-speed light-duty engine,". *Fuel*, vol.317, no.123414, Jun.2022.
[16] Li Z et al, "To achieve high methanol substitution ratio and clean combustion on a diesel/methanol dual fuel engine: A comparison of diesel methanol compound combustion (DMCC) and direct dual fuel stratification (DDFS) strategies,". *Fuel*, vol.304, no.121466, Nov.2021.
[17] Sun W et al, "Numerical study of injection strategies for marine methanol/diesel direct dual fuel stratification engine,". *Journal of Cleaner Production*, vol.421, no.138505, Oct.2023.
[18] Han Z et al, "Turbulence modeling of internal combustion engines using RNG κ-ε models,". *Combustion Science and Technology*, vol.106, no.4, pp.267-295, Mar.1995.
[19] Reitz R D et al, "Structure of high-pressure fuel sprays,". *SAE Transactions*, vol.96, no.5, pp.492-509, 1987.
[20] Beale J C et al, "Modeling spray atomization with the Kelvin-Helmholtz/Rayleigh-Taylor hybrid model,". *Atomization and Sprays*, vol.9, no.6 pp.623-650, 1999.
[21] Naber J D et al, "Modeling engine spray/wall impingement,". *SAE Transactions*, vol.97, no.6, pp.118-140, 1988.
[22] Amsden, O'Rourke, and Butler, "KIVA-II: A Computer Program for Chemically Reactive Flows with Sprays," Los Alamos National Laboratory Technical Report LA-11560-MS, 1989.
[23] Amsden, "KIVA-3V: A Block Structured KIVA Program for Engines with Vertical or Canted Valves," Los Alamos National Laboratory Technical Report LA-13313-MS, 1997.
[24] Senecal P K et al, "Multi-dimensional modeling of direct-injection diesel spray liquid length and flame lift-off length using CFD and parallel detailed chemistry,". *SAE Transactions*, vol.112, no.3, pp.1331-1351, 2003.
[25] Liu S, Sun T et al, "A new skeletal kinetic model for methanol/n-heptane dual fuels under engine-like conditions,". *Energy*, vol.263, no.125648, Jan.2023.
[26] Hiroyasu H et al, "Models for combustion and formation of nitric oxide and soot in direct injection diesel engines,". *SAE Transactions*, vol.85, no.1, pp.513-526, 1976.
[27] Heywood J B, "Internal combustion engine fundamentals," 2018.
[28] Liang L et al, "Modeling knock in spark-ignition engines using a G-equation combustion model incorporating detailed chemical kinetics," Tech. rep. 2007-01-0165. Ford Research and Advanced Engineering, University of Wisconsin-Madison, Wisconsin, United States, 2007.
[29] Xiang L et al, "Parametric investigation on the performance-emissions trade-off and knocking occurrence of dual fuel engines using CFD,". *Fuel*, vol.340, no.127535, May.2023.
[30] Bi F et al, "Knock detection based on the optimized variational mode decomposition," *Measurement*, vol.140, pp.1-13, Jul.2019.
[31] Li Y et al, "Thermodynamic energy and exergy analysis of three different engine combustion regimes,". *Applied Energy*, vol.180, pp.849-858, 2016.

Feasibility Analysis of a Methanol Fuelled Bulk Carrier

Giorgia Adami[a,*], **Massimo Figari**[a]

[a] Università di Genova, DITEN, Genoa, Italy
* giorgia.adami@edu.unige.it

Abstract

Emissions restrictions are growing worldwide due to climate change concern. In the maritime sector different fuels are under scrutiny to identify the best option toward a carbon free transport. Methanol, the simplest alcohol, is one of the most discussed alternative fuels. This work aims at investigating the use of this chemical as fuel on board from different perspectives in order to provide a complete picture. A 34000 DWT bulk carrier has been used as case study including both the hypothesis of a retrofit and a newbuilding. From the technical point of view the attention has been focussed on the ship general arrangement finding space for methanol tanks and fuel systems, in agreement with the existing ABS rules. A carbon footprint emission assessment has been performed, taking into account both IMO's and EU's regulations. To have a more complete overview, a preliminary economic evaluation is also performed with the estimation of OpEx and CapEx related to the methanol system on board. Results showed the technical feasibility with respect to the ship conversion and some criticality related to safety measures and the energy content of methanol. From the polluting impact point of view, the study highlights the importance of a Well to Wake (WtW) approach instead of considering only Tank to Wake (TtW) emissions. From this perspective, with a global decrease in GHG emissions of about 85% with respect to HFO, green methanol appears to be the only viable ecological solution. The use of bio methanol on board significantly affects OpEx, with an estimate increase of more than 250%, due to the high costs of methanol produced from renewable feedstocks and its small production worldwide.

Funding Statement: This work was carried out under research program BIPE 2021 of Genoa University supported by the Foundation Compagnia San Paolo.

Author Contributions: GA and MF equally contributed to the design and implementation of the research, to the analysis of the results and to the writing of the manuscript.

Keywords: Bulk Carrier, CapEx-OpEx Evaluation, Carbon Footprint, Methanol, Technical Feasibility

1. INTRODUCTION

Climate change and environmental protection are the most discussed issues for the future.

One of the major problems is Air Pollution, especially from Greenhouse Gases (GHG) emissions. The shipping sector, with a fleet almost entirely powered by fossil fuels, in 2018 was responsible of 2.89% of global anthropogenic emissions [1].

In light of these conditions, major ruling bodies are imposing increasingly restrictive regulations on the maritime sector; this leads to the need to find alternative solutions to fossil fuels.

This work aims to investigate one of the possible alternative fuels, the methanol, using a 34000 DWT bulk carrier well proven design as a case study including both the hypothesis of a retrofit and a newbuilding. The main focus is on developing a methodology that allows to verify the feasibility of the methanol solutions proposed. The methodology is based on three main pillars: technical, environmental and economic feasibility.

From the technical point of view, the attention has been focused on the ship general arrangement finding space for methanol tanks and fuel system following the ABS's "Requirements for Ethanol and Methanol fuelled Vessels".

The environmental impact of methanol used as marine fuel has been assessed following International Maritime Organization's (IMO) Annex VI and an approach based on European Union's (EU) FuelEU Maritime regulation. This allows to highlight differences and peculiarities of both the decarbonization strategies.

A preliminary economic evaluation has been carried out with the Operational Expenditure (OpEx) and Capital Expenditure (CapEx) calculation related to the fuel system on board in order to give a complete overview of this alternative solution.

The methanol solutions have been compared in every aspect to the original ship to highlight the differences with a fossil fuel propulsion.

@2023 Adami & Figari published by TU Delft OPEN Publishing on behalf of the authors. Licensed under a Creative Commons Attribution CC BY license.
DOI: https://doi.org/10.59490/moses.2023.654

1.1 State of the Art

Methanol, the simplest alcohol, is a chemical widely traded worldwide as a commodity; in recent years its characteristics have led to a growth of interest in its use as an alternative marine fuel [2].

Methanol is liquid under atmospheric conditions, which facilitates transport and storage; this advantage is limited by the low lower heating value (LHV 20 MJ/kg [3]) compared with traditional marine fuels. As a consequence, approximately twice as much fuel by weight must be bunkered to store the same energy on board [3]. In addition to being volatile, colourless, and extremely flammable, methanol is also toxic for humans and has a low flashpoint (12°C [3]). These peculiarities lead to the need for strict and dedicated regulations. In 2020, IMO published and adopted the "Interim Guidelines for the Safety of Ships Using Methyl/Ethyl Alcohols as Fuel" with a more prescriptive approach compared to the previous IGF code (2015). On that basis, some of the most important Classification Societies (DNV-GL, ABS, Lloyd's Register, IRS) developed their own guidelines for methanol and ethanol fuelled vessels.

Methanol's characteristics allow its use in traditional Compression Ignition engines with some modifications regarding injection and feeding system; moreover, a minimum amount of Diesel Oil (DO) should be used as pilot oil [4].

Major marine engine manufacturers (e.g., MAN, Wartsila) have expanded their portfolio with methanol dual fuel solutions; they also provide the possibility of retrofitting and adapting to methanol existing engines [5].

Analysing the context of the production, methanol can be produced efficiently from various sources including some fossil products but also form agricultural waste, biomass, urban garbage and other ecological feedstocks [3]. Methanol is classified according to the type of raw material used for its production in: Grey Methanol when Natural Gas is the feedstock, Brown Methanol if produced from Coal, Blue Methanol when produced from both fossil and bio-feedstocks, Green Methanol that is obtained exclusively from green sources, this category includes also e-methanol from carbon capture. This distinction is really important for the emissions evaluation; in fact, the environmental impact is different between the various paths of production.

Presently two different metrics have been in use to define the GHG emissions: the ones produced on board from combustion process are the so-called Tank to Wake (TtW) or end-life emissions, and the Well to Tank (WtT) emissions are those related to raw material extraction, fuel production, transport and storage onshore. The WtW emissions include the entire chain.

The methanol produced from different raw materials has the same chemical properties, thus TtW emissions are the same because they are based on the methanol molecule: for each gram of fossil-based methanol 44 /32 gram of CO2 are emitted.[6]

Considering other on-board pollutant emissions, the use of methanol, a sulphur free chemical, eliminates 99% of Sulphur Oxides (SOx) emissions compared to fossil fuels; this allows to comply with SECA areas restriction [6]. With regards to Nitrogen Oxides (NOx) emissions are still present but reduced by approximately 60% [6] compared with traditional fuels and there are easy solutions that allows to respect Tier III regulation. Particulate matters emissions are reduced by about 95% compared to HFO [3]. From a technical point of view the low NOx and SOx emissions avoid having to install Scrubbers or other exhaust gas treatment devices with a saving in economic terms and space on board.

With the focus on Carbon Footprint or GHG emissions, the emissions to consider having a complete overview are the WtW and from this point of view differences arise between the different path of methanol production.

The fossil-based methanol produces, over the entire chain, carbon dioxide (CO2) emissions comparable to fossil Diesel Oil (DO). Full lifecycle emissions for natural gas-based methanol, are 103 - 110 gCO2/MJ LHV or 2.05 - 2.20 kg CO2eq/kg while the carbon footprint of methanol produced from coal is nearly 300 gCO2eq/MJ, which is about 3 times higher than the previous one [6].

Considering methanol obtained by green sources, TtW emissions are considered climate neutral resulting in a significant reduction in overall carbon emissions of about 60-80% [6]. The Methanol Institute suggest that the TtW emissions of this type of methanol count as zero because they were previously absorbed from the atmosphere [6]. Some production paths even allow to negativize CO2 emissions [6].

In light of these considerations, the only option that effectively reduce GHG emissions, is the use of methanol from green feedstocks.

Green methanol is a small reality compared to the total global production; only 0.2 Mt/year of renewable methanol are produced worldwide [7] by a handful of commercial producers. This fact leads to incredibly high costs as well as not having, nowadays, enough to meet the possible demand of the maritime sector.

Looking at the State of the Art with regards to existing vessels and new orders, from 2015, with the Stena Germanica conversion to methanol, the

global interest in the use of methanol as marine fuel has grown exponentially. Some important Companies e.g., Methanex Waterfront Shipping, CMA-CGM and A.P. Moller-Maersk, have started to enlarge their fleet with methanol powered ships.

A.P Moller-Maersk has 19 methanol dual fuel ships on order and the first feeder vessel of 2100 teu will arrive in autumn 2023 [8]. The strategy of this colossal deserves attention; in fact, they engage in strategic partnership across the globe to scale green methanol production by 2025 [9]. This highlight that collaboration and investments in innovative projects are the most important ways to reach a net zero fuel value chain.

Additionally, the academic and research interest on this fuel solution and on the importance of techno-economic-environmental analysis is high and the following papers have been useful for this work. Denitz et al. [10] studied environmental and economic performance of methanol, ethanol, liquefied natural gas, and hydrogen as marine fuels. Horvath et al. [11] analysed the most cost-effective combination of synthetic fuels and fuel cells or internal combustion engines to replace fossil oil as the main propulsion fuel in the shipping industry in 2030 and 2040. Ammar [12] studied the application of methanol dual-fuel engine for a cellular container ship from environmental and economic points of view.

The rest of the paper is structured as follows: Section 2 contains the description of the methodology, Section 3 is related to the Case Study, in Section 4 the results have been analysed and the Section 5 is dedicated to the conclusions.

2. MATERIAL AND METHODS

This section aims to describe the proposed methodology used to identify a feasibility metric for methanol fuelled bulk carriers.

2.1 Pillar 1: Technical requirements for the safe use of methanol as fuel on board

The technical requirements used in this work for evaluating the installation of methanol fuel tanks and supply system are dictated by ABS's guideline for methanol and ethanol fuelled vessels [13] that incorporates IMO's MSC.1/Circ.1621. The most significant points have been highlighted below.

Methanol can be stored on board in integral, independent and portable tanks; each of these options are considered in the Rules.

Fire and explosion safety is one the most important aspects to consider for a low flashpoint fuel; for this reason, integral methanol tanks are surrounded by protective cofferdams. The cofferdam is not mandatory on those surfaces bounded by shell plating below the waterline, other methanol tanks or fuel preparation spaces ("Sect 5, 3.2 ABS's guideline"). The distance between the tank and the cofferdam should be at least 600 mm with A-60 insulation.

Methanol has also a corrosive nature, for this reason stainless steel is the proposed material for fuel storage tanks; however, for large structural tanks or in case of a retrofit, silicate coatings on structural steel can be used.

Storage tanks need to be ventilated and inerted at any time during normal operation; a nitrogen inert system is required on board.

The ABS's guide dedicates section 8 to bunkering. The key aspects for the positioning of the bunker station are ventilation and safety; in particular is important to analyse the risk of fuel exposure in case of spillage during ordinary operations.

Methanol as fuel needs a system of valve trains, pumps, filters and heat exchangers to supply the engine at specific conditions. Pumps submerged in methanol tanks should be arranged with double barriers preventing from being directly exposed to the fuel. The space for the fuel supply system must be separate from the engine room although an entrance is permitted via airlock.

In non-hazardous enclosed areas stainless steel double-walled pipes are necessary for fire safety reasons.

The location of the vent mast requires a minimum safety distance to deck, air intake, opening to accommodation, service spaces, and ignition sources.

It is present practice with dual fuel engines to have on board an amount of diesel oil as safety measure. This is required to ensure a safe return to port with fuel oil propulsion in case of failure of the methanol system. This requirement makes even more difficult to find volumes for methanol on board, especially in the case of a retrofit.

This work provides an amount of DO to ensure 7 days of navigation in oil-only mode.

2.2 Pillar 2: Environmental KPI

IMO in 2018 adopted the Initial Strategy on reducing GHG emissions from ships with the ambition to impose a regulatory framework that effectively reduces the global fleet's environmental impact. [14]

With this purpose various technical and operational indexes and tools have been set including Energy Efficiency Design Index (EEDI) and Carbon Intensity Indicator (CII) that will be evaluated in this paper.

The EEDI is used to calculate a vessel's energy efficiency with a complex formula taking the ship emissions, capacity and speed into account. [14] The equation can be summarised with:

$$EEDI\ [\frac{gCO_2}{t\ Nm}] = \frac{\sum P\ \times C_f \times SFC}{Capacity\ \times Speed} \quad (1)$$

where P is the Power, Cf is a conversion factor, and SFC is Specific Fuel Consumption. For bulk carriers the capacity means Deadweight [15].

Equation (1) allows to evaluate the Attained EEDI (EEDIa) that has to be compared with the so called Required EEDI (EEDIr) [16].

$$EEDI_a \leq EEDI_r \quad (2)$$

$$EEDI_r = \left(1 - \frac{x}{100}\right) \cdot Ref.Line\ Value \quad (3)$$

where x is the reduction factor that varies with time [16]. The reference line value must be evaluated with the following equation:

$$Ref.Line\ Value = a \cdot b^{-c} \quad (4)$$

The parameters a, b, c are provided by IMO's regulation [16] depending on ship types and size.

The CII is a rating scheme (A-E) developed by the IMO to measure the annual performance in terms of CO2 per DWT and distance covered [17]. Even in this case the CII of the ship, the Attained CII (CII a), has to be compared with the Required Annual one (CII ar) [18].

$$CII_a = \frac{M}{W} \quad (5)$$

Where M is the Mass of CO2 emissions in grams and W represents the transport work Tons x Nautical Miles [t Nm].

$$M = FC_j \times C_{f_j} \quad (6)$$

FCj is the total mass in grams of consumed fuel oil of type j in the calendar year while Cfj represents the fuel oil mass to CO2 mass conversion factor for fuel oil type [18].

Transport work W can be evaluated as follows [17]:

$$W = C \times D_t \quad (7)$$

C represents the ship capacity and is different for ship types (for bulk carrier=DWT); Dt is the total distance traveled [Nm].

The Required Annual CII (CIIar) equation is the following [19]:

$$CII_{ar} = \left(1 - \frac{Z}{100}\right) CII_{ref} \quad (8)$$

Z is an annual reduction factor

$$CII_{ref} = a\ Capacity^{-c} \quad (9)$$

The parameters are tabled in IMO's requirement [20].

The requirement also provides the boundaries for determining a ship's annual operational carbon intensity performance from the year 2023 to 2030.

The boundaries are determined by the required annual operational CII in conjunction with the so called "dd vectors"; by comparing the attained annual operational CII of a specific ship with the four boundaries, a rating from A to E is assigned. [21]

In this work an estimate of the EEDI and CII is presented for both the original ship and the methanol propelled vessel.

In 2021, European Commission adopted the "Fit for 55" package that is a series of legislative proposal with the objective of reducing GHG emissions. [22]

The maritime sector is included in this path of decarbonization with the FuelEU Maritime proposal. In March 2023, the European Council and Parliament agreed that FuelEU will come into force from January 2025 [22].

This regulation includes a technical annex with the methodology for establishing the GHG Intensity Limit on the energy used on board by a ship.

The peculiarity of this index is that it considers the emissions over the entire chain, the so called Well to Wake emissions [23].

$$GHG\ Intensity\ Index\ \left[\frac{g\ CO_{2eq}}{MJ}\right] = WtT + TtW \quad (10)$$

From 2025, the average GHG intensity of the energy used on-board during the reference period shall be calculated and not exceed the target value otherwise a penalty has to be paid. Such target value will be reduced over the years.

EU's regulation focusses the attention also to the energy needed by the ship moored at the quayside; only onshore power supply or zero emissions technologies are allowed.

In this work an estimate of WtW emissions is calculated for both the original ship case and the methanol propelled vessel (instead of the GHG

Intensity Index). The calculation is based on data from literature and equations from regulations with the hypothesis to ignore the contribution of marine gas oil for electric generation. The small amount of DO used as pilot oil has been neglected, too.

For both HFO and methanol propulsion the WtT emissions data have been selected from literature while the TtW emissions, for the fossil fuelled case, have been calculated in accordance with (11) from Annex I [21] of EU COM (2021) 562 [24].

$$CO_{2eq,TtW,j} = (Cf_{CO2} \times GWP_{CO2} + Cf_{CH4} \times GWP_{CH4} + Cf_{N2O} \times GWP_{N20})/\text{LCV} \quad (11)$$

According to [6], the TtW emissions from bio methanol (for example from solid biomass), have been considered climate neutral, and therefore not accounted for. The following table summarises the emissions data available in literature for Green Methanol.

Table 1. Green Methanol Emissions [6]

Green Methanol Emissions		
Well to Tank	13.5	gCO2/MJ
Tank to Wake	0	gCO2/MJ
Well to Wake	13.5	gCO2/MJ

2.3 Pillar 3: Economic KPI

In this work CapEx and OpEx have been estimated to provide a preliminary economic assessment.

The attention has been focussed on the costs related to the Fuel and Engine Systems, in order to better highlight the variations in comparison to traditionally fuelled vessels.

CapEx are initial and fixed costs that are not dependant on the intensity of the operation of the vessel. The data required for their evaluation are the costs of the Engine and the Storage that include the Supply System.

An EMSA's Report [25] suggests the costs in terms of EUR/kW for engine and storage in case of newbuilding (reported in Table 2).

Engine cost can be considered almost equal in case of retrofit and newbuilding while the Storage and Supply system costs in case of retrofit should be more expensive. EMSA suggests, on the base of best engineering judgement, an increment of about 13-17% to newbuild CapEx [25].

The sum of costs in EUR/kW has been multiplied by the main engine power [kW]. Moreover, following a further in-depth analysis on available data, an amount of EUR 500000 has been added to the Methanol CapEx to improve the accuracy of the calculations.

OpEx are variable costs that depend on ship lifetime and its operativity. The OpEx considered for this work are only related to the Fuel and the Engine systems; they have been divided in: Bunkering costs, Maintenance and Repair (M&R) costs.

Table 2. Engine and Storage Costs

Ship Category	Fuel Type	Engine Cost (EUR/kW)	Storage Cost (EUR/kW)
Large Vessels	Fuel Oil	200	60
Deep Sea Vessels	Bio-Methanol	280	100

Additionally, the Diesel Oil amount considered for the OpEx evaluation is only the one related to the use as Pilot Oil in methanol dual fuel engine.

The original vessel used as case study in this project is HFO fuelled, contract data specifications shows that specifically the fuel is IFO 380 so this type of fossil fuel has been considered. The mean value of Global Average Bunker Price (GABP) for the last three years (2019-22) has been used; and this value is of 414.75 USD/mt [26] or 403 EUR/mt (based on change 1EUR=1.03USD-17 Nov.22).

For M&R costs of a 2T fuel oil engine, the literature suggests costs of about 1.2-7.3 €/MWh/year [25]; a value of 1.5 has been chosen after analyzing some reports. Also considering tanks, fuel preparation, and supply system a final cost of 2.5 €/MWh/year has been used for M&R costs calculations for the original ship.

The EMSA's report on biofuels [25] provides a cost table of green methanol from different feedstocks for 2020 and a forecast for 2030 and 2050 that is summarised in Table 3; the first price scenario has been selected for the work.

Table 3. Green Methanol Costs [24]

Ship Category	2020 [€/MWh]	2030 [€/MWh]	2050 [€/MWh]
Green Methanol "bio-e methanol"	131	103	82
Green Methanol CCU	161.5	120	84.5
Green Methanol DAC	190	147.5	100.5

For DO costs the same procedure as IFO380 has been used; this allows to find a cost of 673 €/mt [26]. Through the specific consumptions and the hypotheses made on the hours of ship operativity and lifetime of the ship (Table 5), it has been

possible to estimate the tons of fuels necessary during the whole life of the ship.

A market survey has shown the M&R costs that amount to approximately 30 EUR/kW/year divided in 20 EUR/kW/year attributable to main engine and the remaining to Storage and Supply.

After defining the specific consumption of the main engine in the two cases of propulsion, with simple operations of sums and multiplications, the OpEx costs have been evaluated.

3. CASE STUDY

The original ship's fuel oil tanks are located aft inside Engine Room (Fig. 1) and in this area is positioned also the separator room.

Table 4. Original Ship Data

Item	Value
Length Overall, max	180.00 m
Breadth moulded at design, max	30.00 m
Depth moulded to upper deck at side	14.70 m
Scantling Draught	9.75 m
DWT Scantling Draught	34000 t
Total Cargo Volume	45500 m^3
Heavy Fuel Oil tanks total volume	1700 m^3
Diesel tanks total volume	200 m^3
Service Speed at Scantling Draught	14 knots
Engine Output at CSR (80% MCR)	6100 kW
CMCR Main Engine	7600 kW
Daily Consumption of HFO at CSR	26.4 t
Auxiliary Engines Daily Consumption	2 t
Endurance	18500 Nm
SFOC Main Engine	170g/kWh

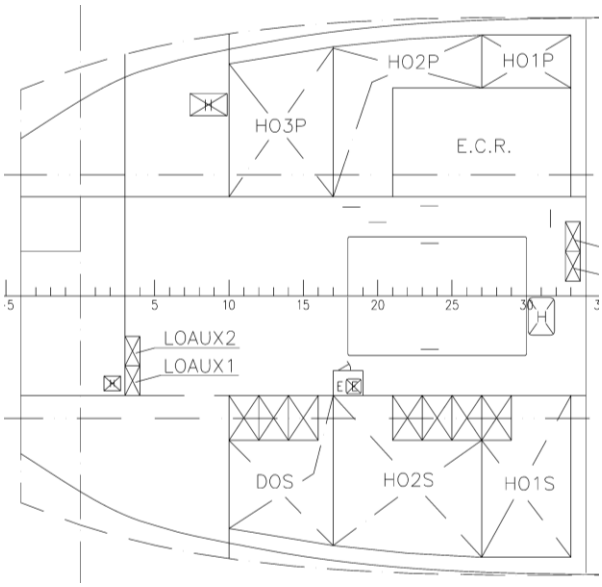

Figure 1: Original Ship's Fuel Tanks Layout

For the various calculation that will follow for both original ship and methanol solutions the operativity data used are listed in Table 5.

Table 5. Operational Data

Operational Data		
Ship Lifetime	20	years
Operating Time	6000	h/year
Distance Travelled in one year	60000	Nm

The data and formulas presented in chapter 2 have been used to evaluate costs and environmental parameters for the original fossil fuelled vessel. The results, which are presented in Table 6, have been used as comparison parameters with the methanol solutions.

The vessel under analysis has been designed before IMO's regulations for emissions control; this lead to have results in term of EEDI and CII that do not comply with actual standards. This problem has been solved by comparing the new solutions in percentage terms with the HFO solution.

Table 6. Original Ship Index and Parameters

Emission Indexes for Original Ship		
EEDI	6.70	gCO2/tNm
CII	10.86	gCO2/tNm
WtT Emission HFO	13.5 [14]	gCO2eq/MJ
TtW Emission HFO	78	gCO2eq/MJ
WtW Emissions HFO	91.5	gCO2eq/MJ
Economical Parameters for Original Ship		
CapEx	1976000	EUR
OpEx	64524000	EUR

3.1 Methanol Solutions

In this work both cases of retrofit and newbuilding have been proposed; the following considerations must be applied to both solutions.

It has been hypothesized that the changes made on fuel system for the methanol use are not such as to modify the power request for the propulsion; thus, the main engine power of 7600 kW has been maintained. With methanol propulsion a Specific Gas Consumption (SGC, that represents methanol consumption) of 350 g/kWh and a Specific Pilot Oil Consumption (SPOC) of about 8.35 g/kWh have been considered. The data just defined are based on information about MAN B&W ME-LGIM, CEAS Engine Data Reports [4].

Moreover, in this study the attention has been focused on the main propulsion; for this reason, the Auxiliary Engines are considered diesel fuelled also in the new solutions.

As regards the Methanol Supply System, the footprint has been estimated based on the size of

one of the currently commercially available [27]; the selected volume is of about 65 m^3.

It is nowadays a customary practice to store on-board an amount of diesel oil for safety purpose; for this reason, a volume of 210 m^3 is dedicated to ensuring 7 days endurance in fuel oil-only mode.

For the Retrofit case, the simplest solution has been selected: the methanol tanks have been positioned in the spaces originally dedicated to HFO tanks, trying to use all available volumes and limiting the changes. All the safety measures mentioned before (section 2.1) have been considered for the installation.

This solution provides to accommodate the Methanol Supply System in a volume previously used as a tank, providing a direct access from the open deck.

The proposed layout, represented in Fig. 2, admits storing 1120 m3 of Methanol divided in four tanks. Moreover, 280 m^3 diesel oil are provided for pilot oil and safety purposes. The yellow dashed spaces in the retrofit tank layout figure represent safety cofferdams.

The lower LHV of methanol compared to fossil fuels, combined with the reduction of volumes dedicated to primary fuel due to safety and operational needs, lead to an inevitable reduction in ship's endurance.

The techno-economic-environmental results of the proposed retrofit solution are summarized in Section 4, Table 7(a,b,c).

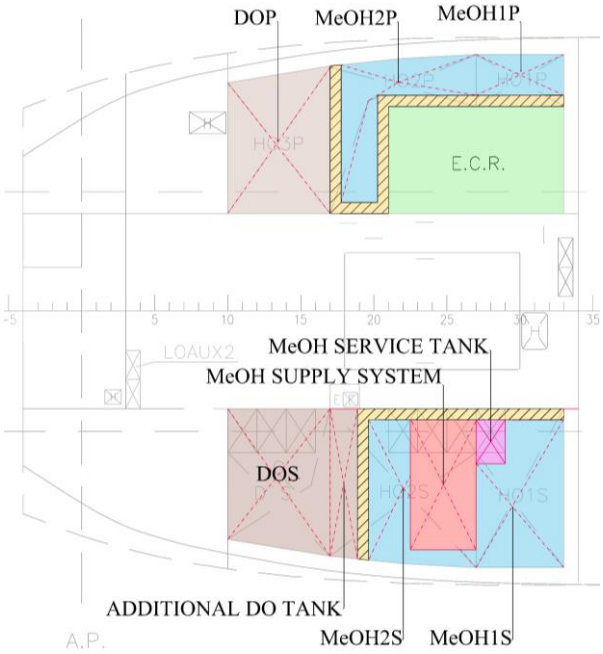

Figure 2: Methanol Retrofit Tanks Layout

In case of newbuilding no changes in the main dimensions of the vessels have been considered. The proposed solution is based on the hypothesis of a rearrangement of the original fuel tank area merged with finding spaces for methanol from the cargo hold n° 5 that is the closest to the engine room.

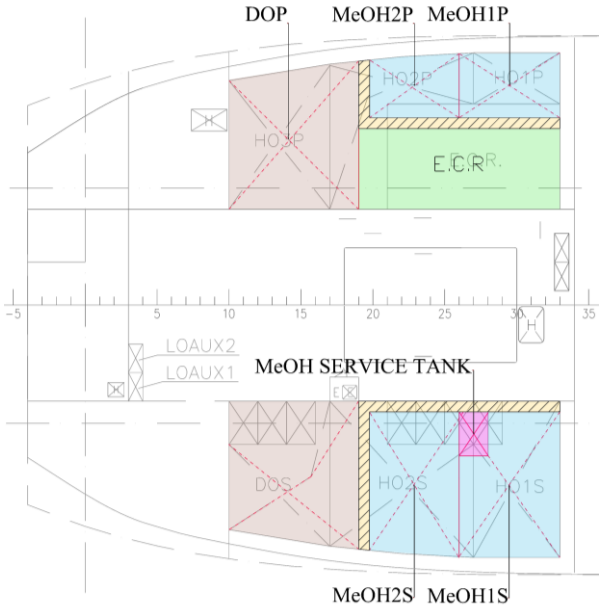

Figure 3: Newbuilding Tank Layout Engine Room

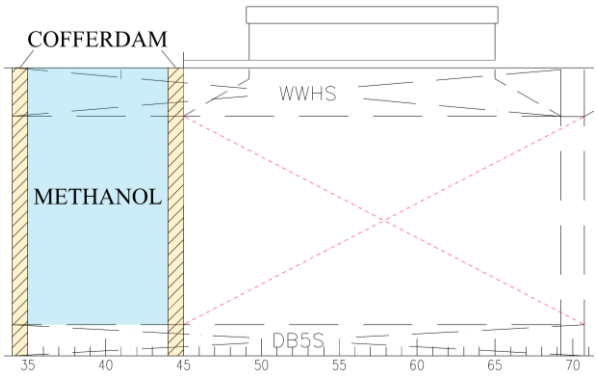

Figure 4: Newbuilding Tank Layout Cargo Area

In figs 3 and 4 the yellow dashed areas represent the cofferdams installed for safety purposes.

The Methanol Supply System has been located inside the engine room where the HFO separator room was originally positioned. This is possible ensuring the access to this area via airlock.

The newbuilding case layout allows to obtain 3557 m3 of methanol storage volume and an additional Diesel volume of about 430 m3. This methanol solution ensures a ship's range similar to the original HFO powered vessel.

The main drawback of this option is the cargo volume reduction of about 8%. Reasoning on equal freeboard with the original vessel, the cargo reduction would be more problematic in the case of light cargo while it might not be impacting in the case of heavy cargo.

4. RESULTS

This chapter has the purpose to summarise the results obtained in this work.

Tables 7 (a,b,c) shows the comparison between the original HFO fuelled ship and the new solutions powered by methanol. It is worth mentioning that both solutions have been designed avoiding variations on ships main dimensions and that the costs are related only to the engine and fuel storage & supply system.

Table 7a. Methanol Solutions Comparison Pillar 1

Pillar 1: Technical Feasibility		
HFO Volume "Original Ship"	1700	m3
Methanol Volume "Retrofit"	-34%	
Methanol Volume "Newbuilding"	+109%	
Endurance "Original Ship"	18500	Nm
Endurance Methanol "Retrofit"	-69%	
Endurance Methanol "Newbuilding"	0%	
Cargo Volume "Original Ship"	45500	m3
Cargo Volume Methanol "Retrofit"	0%	
Cargo Volume Methanol "Newbuilding"	-8%	

Table 7b. Methanol Solutions Comparison Pillar 2

Pillar 2: Environmental Feasibility		
EEDI "Original Ship"	6.70	gCO2/tNm
EEDI "Methanol"	-9%	
CII "Original Ship"	10.86	gCO2/tNm
CII "Methanol"	-4%	
WtW Emissions "Original Ship"	91.5	gCO2eq/MJ
Well to Wake Emissions "Green Methanol Ship"	-85%	

Table 7c. Methanol Solutions Comparison Pillar 3

Pillar 3: Economic Feasibility		
CapEx* "Original Ship"	1976000	EUR
CapEx Methanol "Retrofit"	+94%	
CapEx Methanol "Newbuilding"	+71%	
OpEx "Original Ship"	64524000	EUR
OpEx "Green Methanol 2020"	+269%	
OpEx "Green Methanol 2030"	+193%	
OpEx "Green Methanol 2050"	+173%	

* CapEx only related to Propulsion Equipment

The retrofit results show that, with the purpose of limiting the structural changes and following the rule safety requirements, the storage volume dedicated to methanol is limited. Consequently, taking into account the low LHV of the alternative fuel, the energy stored on board and the ship's endurance are considerably reduced compared to the original vessel. This disadvantage could be mitigated by a frequent bunkering given that 88 of the world's largest 100 ports can supply methanol [24].

Considering the newbuilding solution, it is evident form table 7a that the modifications allow to store the same energy on board and consequently to reach the same endurance of the fossil powered ship. This is possible with a cargo reduction of about 8%. The loss of cargo volume may not be too impactful when carrying heavy loads, but more accurate considerations need to be made in this regard.

Paying attention to GHG emissions and carbon footprint both IMO's and EU's strategy for decarbonisation have been considered.

What emerged in this work is that, focussing on TtW emissions with the IMO's approach, EEDI and CII have a limited improvement (in the order of -5%/-10%) with respect to the HFO fuelled ship; this fact is also confirmed in the literature. This consideration, together with the yearly increasing restrictive limits for IMO's indexes, lead to consider methanol as a viable alternative marine fuel mainly for the short term.

However, following the EU's strategical path to decarbonisation thus considering WtW emissions methanol could be also considered as a long-term solution.

With a complete overview of the emissions over the entire fuel chain differences arise between the different type of methanol production, which is not evident from the IMO perspective.

Considering grey/brown methanol, total emissions could be equivalent or slightly higher compared to fossil fuels based on the different raw materials.

In light of the evidence, green methanol is the only real option to effectively reduce GHG emissions in fact allows their reduction of 85% compared to HFO; and this is valid and unchanged even for a long-term analysis.

Proceeding with the analysis of the economic sphere, methanol fuelled vessels, like every new solution or idea, need an intensive design phase with an accurate risk analysis and shipyards must cope with new demands and special features. This inevitably leads to an increase in CapEx in both retrofit and newbuilding cases but in the first the proportional increase is greater. This could

probably be overcome or reduced after a series of newbuilding or retrofits and with the help of pilot projects and academic studies.

In the OpEx evaluation fuel costs represent the greater part and the high price of green methanol nowadays is a barrier to its expansion as alternative marine fuel. As mentioned above and as read in various papers, forecasts for the future price of bio-methanol are optimistic: in 2050 could be halved [24].

5. CONCLUSIONS

In this chapter a summary of what emerged during the drafting of this project is presented.

This work has been focussed on finding a methodology that allows to evaluate the technical, economic and environmental feasibility of the use of methanol as fuel for bulk carrier vessels.

From the technical point of view, there are several options to store methanol on board but here two of the simplest and less invasive solutions have been presented.

The results show that it is not too difficult to convert a bulk carrier to methanol in both retrofit and newbuilding cases. The major difficulty is to find enough space for methanol tanks, due to the low energy content of this chemical and some additional safety requirements such as cofferdams. The liquid condition of methanol at ambient pressure and temperature allows an easy bunkering and the storage in conventional fuel tanks.

The current common practice to store a large amount of DO to ensure a safe return to port, in case of methanol system failure, is a barrier for methanol fuelled vessels especially in case of retrofit. More projects and experience with different ships applications would lead to safer and more reliable systems for methanol and, as result, lower diesel storage.

The environmental results highlight the importance of the strategic path to decarbonisation and the difference between a Tank to Wake and a Well to Wake approach. This aspect is really important because if emissions continued to be regulated only on a TtW basis the effectiveness of the methanol will be only on the short-term period.

Considering the results on a WtW basis, green/bio methanol from renewable feedstocks appears to be the only true feasible option to reduce the carbon footprint.

The methodology used in this work shows an overall feasibility for the use of methanol for small size bulk carrier with a major criticality related to operating costs. Additionally, the methodology account for the price reduction of bio methanol as suggested by literature; this will be possible only if demand from ship operators will rise at the same pace of the green methanol production [28].

REFERENCES

[1] IMO, “Fourth Greenhouse Gases Gas Study 2020”, 2021. [Online]. Available: https://wwwcdn.imo.org/localresources/en/OurWork/Environment/Documents/Fourth%20IMO%20GHG%20Study%202020%20-%20Full%20report%20and%20annexes.pdf

[2] ABS, “Sustainability whitepaper: Methanol as Marine Fuel”, 2021. [Online]. Available: https://safety4sea.com/wp-content/uploads/2021/02/Sustainability-Methanol-as-Marine-Fuel.pdf 2021

[3] J. Ellis, K. Tanneberger, “Study on the use of ethyl and methyl alcohol as alternative fuel in shipping”. Report prepared for the European Maritime Safety Agengy, Rep. no. 20151204.5, 2017. Accessed 2023. [Online]. Available: https://emsa.europa.eu/air-pollution/alternative-fuels/items.html?cid=329&id=2726

[4] MAN, CEAS Engine data report for MAN B&W ME-LGIM. [Online] Available: https://www.man-es.com/marine/products/planning-tools-and-downloads/ceas-engine-calculations

[5] Longspur Research. “All at Sea: Methanol in Shipping”, 2022. [Online]. Available: https://www.methanol.org/wp-content/uploads/2022/01/Methanol-and-Shipping-Longspur-Research-25-Jan-2022.pdf

[6] Methanol Institute, “Carbon footprint of methanol”, 2022. [Online]. Available: https://www.methanol.org/wp-content/uploads/2022/01/CARBON-FOOTPRINT-OF-METHANOL-PAPER_1-31-22.pdf

[7] IRENA and Methanol Institute, “Innovation Outlook: renewable methanol”,International Renewable Energy Agency, 2021, Abu Dhabi. [Online]. Available: https://www.irena.org/-/media/Files/IRENA/Agency/Publication/2021/Jan/IRENA_Innovation_Renewable_Methanol_2021.pdf?rev=ca7ec52e824041e8b20407ab2e6c7341

[8] A.P. Moller-Maersk Press Release, 05 Oct. 2022. [Online]. Available: https://www.maersk.com/news/articles/2022/10/05/maersk-continues-green-transformation

[9] A.P. Moller-Maersk. Press Release, 10 Mar. 2022. [Online]. Available: https://www.maersk.com/news/articles/2022/03/10/maersk-engages-in-

strategic-partnerships-to-scale-green-methanol-production

[10] C. Deniz, B. Zincir. "Environmental and economical assessment of alternative marine fuels". In: Journal of Cleaner Production, 113 (2016) pp. 438-449

[11] S. Horvath, M. Fasihi, C. Breyer. "Techno-economic analysis of a decarbonized shipping sector: Technology suggestions for a fleet in 2030 and 2040". In: Energy Conversion and Management 164 (2018) pag. 230-241

[12] N. R. Ammar. "An environmental and economic analysis of methanol fuel for a cellular container ship". In: Transportation Research Part D, 69 (2019) pp. 66-76

[13] *Requirements for Methanol and Ethanol Fueled Vessels*, American Bureau of Shipping, 2022. [Online]. Available: https://ww2.eagle.org/content/dam/eagle/rules-and-guides/current/other/328-requirements-for-methanol-and-ethanol-fueled-vessels/328-methanol-and-ethanol-fueled-vessels-reqts-july22.pdf

[14] *Initial IMO Strategy on Reduction of GHG Emissions from Ship*, Resoultion MEPC.304(72), IMO, Apr. 2018. [Online]. Available: https://wwwcdn.imo.org/localresources/en/KnowledgeCentre/IndexofIMOResolutions/MEPCDocuments/MEPC.304(72).pdf

[15] MAN energy solutions, "Energy Efficiency Design Index". [Online]. Available: https://man-es.com/docs/default-source/document-sync/eedi-eng.pdf?sfvrsn=23fbab95_3

[16] *2021 Revised MARPOL Annex VI*, Resolution MEPC75/15/Add.1 Annex I, IMO, 2021. [Online]. Available: https://wwwcdn.imo.org/localresources/en/OurWork/Environment/Documents/Air%20pollution/MEPC.328%2876%29.pdf

[17] DNV-GL, "IMO GHG Strategy" https://www.dnv.com/maritime/hub/decarbonize-shipping/key-drivers/regulations/imo-regulations/ghg-vision.html#:~:text=The%20IMO's%20Initial%20GHG%20Strategy,by%202050%2C%20compared%20to%202008.

[18] *2021 Guidelines on Operational Carbon Intensity Indicators and Calculation Methods*, Resolution MEPC.336(76) Annex 10, IMO, 2021. [Online]. Available: https://wwwcdn.imo.org/localresources/en/OurWork/Environment/Documents/Air%20pollution/MEPC.336(76).pdf

[19] *2021 Guidelines on the Operational Carbon Intensity Factors Relative to Reference Lines*, Resolution MEPC.338(76) Annex 12, IMO, 2021. [Online]. Available: https://wwwcdn.imo.org/localresources/en/OurWork/Environment/Documents/Air%20pollution/MEPC.338(76).pdf

[20] *Guidelines on the Reference Lines for use with Operational Carbon Intensity Indicators*, Resolution MEPC.353(78) Annex 15, IMO, 2022 [Online]. Available:https://wwwcdn.imo.org/localresources/en/OurWork/Environment/Documents/Air%20pollution/MEPC.353(78).pdf

[21] *Guidelines on the Operational Carbon Intensity Rating of Ships*, Resolution MEPC.354(78) Annex 16, IMO, 2022. [Online]. Available: https://wwwcdn.imo.org/localresources/en/OurWork/Environment/Documents/Air%20pollution/MEPC.354(78).pdf

[22] ABS Regulatory News No. 08/2023, "EU FIT FOR 55: Maritime FuelEU Regulation". [Online]. Available: https://ww2.eagle.org/content/dam/eagle/regulatory-news/2023/ABS%20Regulatory%20News%20-%20Fit%20for%2055%20-%20FuelEU.pdf

[23] *Annexes to the Proposal for a Regulation of the European and of the Council on the use of renewable and low-carbon fuels in maritime transport and amending Directive 2009/16/EC*, COM (2021)52 final, European Commission, Brussels, 2021. [Online]. Available: https://eur-lex.europa.eu/resource.html?uri=cellar:078fb779-e577-11eb-a1a5-01aa75ed71a1.0001.02/DOC_2&format=PDF

[24] *Directive EU 2018/2001 of the European Parliament and of the Council on the promotion of the use of energy from renewable sources*, Directive (EU) 2018/2001, European Parliament and the Council of EU, 2018.

[25] European Maritime Safety Agency, Update on Potential of Biofuels in Shipping", Rep.no. 4837444, Lisbon, 2022.

[26] Ship & Bunker Website. [Online]. Available: https://shipandbunker.com/prices#IFO380

[27] Alpha Laval, *Alpha Laval Fuel Conditioning Module (FCM) Methanol*. [Online]. Available: https://www.alfalaval.com/products/process-solutions/fuel-conditioning-solutions/fuel-conditioning-modules/fcm-methanol/

[28] S. Warden, "Alternative Marine Fuels Series Wrapped Up", 2018. [Online]. Available: https://www.czapp.com/analyst-insights/alternative-marine-fuels-series-wrapped-up/

PROCEEDINGS OF MOSES2023 CONFERENCE
4TH INTERNATIONAL CONFERENCE ON MODELLING AND OPTIMISATION OF SHIP ENERGY SYSTEMS
26-27 OCTOBER 2023, DELFT, NETHERLANDS

Thermodynamic Evaluation of a Combined SOFC-PEMFC Cycle System

N.G.H. Goselink[a,*], B.J. Boersma[a], and L. van Biert[a]

[a]Delft University of Technology, Delft, The Netherlands
[*]n.g.h.goselink@tudelft.nl

Abstract

Solid oxide fuel cell (SOFC) technology offers a promising way to reduce maritime greenhouse gas (GHG) emissions. Integration with a proton exchange membrane fuel cell (PEMFC) allows unreacted hydrogen, produced in the SOFC stack, to be reused and increase the electrical efficiency of the system. In this study, the Cycle Tempo software is used to model a SOFC-PEFMC combined cycle system operating on methane. The system is thermodynamically analysed to reveal the influence of SOFC fuel utilisation, cell voltage, operating temperature and PEMFC cell voltage on the system performance. A multivariable parametric analysis is applied to generate contour plots of net electrical efficiency and fraction of total power produced by the PEMFC. The analysis shows that increasing the cell voltage of both the SOFC and PEMFC has a positive influence on efficiency, whereas increasing the fuel utilisation reduces the system efficiency. Efficiencies in the range of 50-68% can be achieved. Model assumptions for PEMFC operating parameters are verified to exert little influence on the system efficiency, which confirms the assumption of constant values for these parameters. This study highlights the high-efficiency potential of the combined system and the difficulties that arise from thermally integrating an SOFC with a PEMFC.

Keywords: SOFC; PEMFC; Combined cycle system; Thermodynamic analysis.

1 INTRODUCTION

The maritime industry is responsible for roughly three percent of global anthropogenic greenhouse gas (GHG) emissions [1]. Therefore, the International Maritime Organisation (IMO) has imposed several guidelines and regulations to achieve net-zero GHG emissions by 2050 [2]. Solid oxide fuel cells (SOFC) have been recognized as a promising technology for use on board ships [3]. The SOFC can achieve efficiencies of up to 60% in a stand-alone configuration [4], [5], which is significantly higher than that of conventional internal combustion engines and gas turbines, as reported in [6]. In addition, the internal reforming capabilities of the SOFC make the system suitable for a variety of alternative fuels, such as methanol, ammonia, hydrogen or (L)NG, while emitting little to no NO_x and SO_x [7].

The stand-alone efficiency of an SOFC is already high at 60% but can be further increased by reusing the fuel and heat within the anode/cathode off-gas streams [8], [9]. Integrating a pressurized SOFC with a gas turbine (GT) increases the net electrical efficiency to 70% [10]. However, direct coupling between the SOFC and gas turbine requires matching of operating points, limiting the system operating envelope and introducing significant control challenges [11]. Another approach is the addition of an internal combustion engine (ICE). The SOFC-ICE combined system can theoretically achieve similar efficiencies ($\sim$70%), with the added benefit of improved transient capabilities and better part-load performance [12], [13] compared to SOFC-GT systems. However, the direct combustion of residual fuel still generates significant amounts of emissions such as NO_x.

More recently, the combination of an SOFC and proton exchange membrane fuel cell (PEMFC) has surfaced as a viable alternative. This approach benefits from both energy generation and hydrogen production within the SOFC. Because the fuel utilisation is smaller than unity, ranging from 0.60 to 0.90, a significant amount of unreacted hydrogen is present in the anode off-gas stream. This hydrogen can be used in a PEMFC to generate additional electricity, thereby increasing the overall system efficiency [14], [15]. In addition to H_2, the syngas includes major species such as CO, CO_2 and H_2O. Because the PEMFC has a limited CO tolerance, a few parts per million (ppm) can already cause cell performance degradation [16], this component must

@2023 Goselink, N. G. H. et al. published by TU Delft OPEN Publishing on behalf of the authors. Licensed under a Creative Commons Attribution CC BY license.
DOI: https://doi.org/10.59490/moses.2023.659

be removed from the syngas stream. The commonly applied approaches are water gas shift (WGS), preferential oxidation (PrOX) and pressure swing adsorption (PSA) [6]. The combined SOFC-PEMFC cycle system is reported to be potentially competitive with other combined cycle systems in terms of efficiency [17]. However, because this specific system layout remains relatively unstudied, a structured review of its performance potential is lacking. This represents the knowledge gap that this study aims to address.

Thermodynamic analysis is an established approach to compare the efficiency of combined system architectures with stand-alone SOFCs or between different combined cycles. However, because most thermodynamic analyses are performed at arbitrary design points, it is difficult to compare these systems. Therefore, van Biert et al. [9] investigated the thermodynamic efficiencies of four different solid oxide fuel cell-combined cycle system across their entire operating envelope. The selected systems were a steam turbine combined cycle, two gas turbine combined cycles at ambient and elevated pressure, and a reciprocating engine combined cycle. The operating parameters, e.g., fuel utilization, cell voltage and stack temperature are varied to achieve more meaningful results, as the stack operating parameters are similar for all cases investigated.

To investigate the performance potential of the SOFC-PEMFC combined cycle system, this study follows a similar approach, by analysing the systems' efficiency across an operating envelope of typical SOFC operating parameters. To the best of the authors knowledge, this is the first time that such a complete analysis of the SOFC-PEMFC system performance is performed.

The proposed configuration is presented and modeled in sections 2-3. The results of the multivariable parameter analysis are analysed and discussed in section 4. Finally, the conclusions of the preliminary analysis are presented in section 5 and future work is discussed in 6. This work will thus present a basis for the comparison of the SOFC-PEMFC combined cycle performance with other combined cycle systems and stand-alone configurations.

2 CONFIGURATION OF THE PROPOSED SOFC-PEMFC COMBINED CYCLE

A schematic of the SOFC-PEMFC combined cycle system is shown in figure 1. The system consists of different modules: the SOFC subsystem, gas cleaning equipment and PEMFC subsystem.

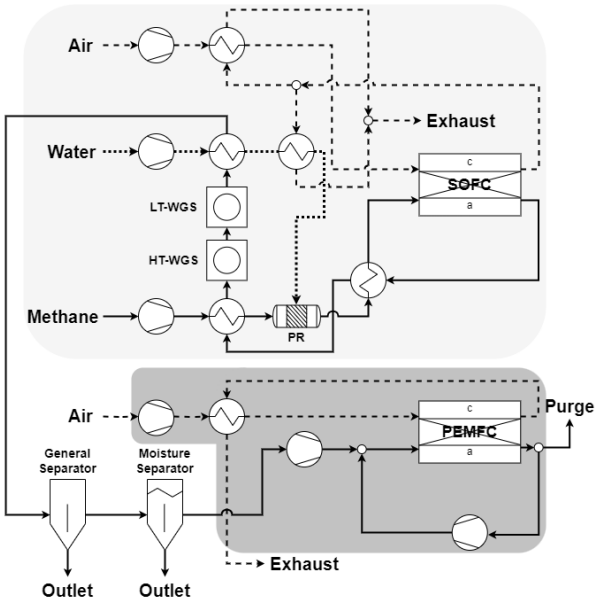

Figure 1: SOFC-PEMFC combined cycle system layout

The SOFC layout is based on the configuration reported by Riensche et al. [18]. Air is supplied by a compressor to overcome the pressure losses in the system and is preheated before it enters the SOFC cathode. The fuel, in this case methane, is compressed, preheated, and partly reformed in a pre-reformer (PR) before it is fed to the anode side. Within the pre-reformer, methane steam reforming and water gas shift reactions convert methane into hydrogen. A pre-reforming temperature of 450°C is chosen, such that it matches the pre-reformer outlet temperature. A pre-reform ratio of 20% is assumed, the minimum amount as specified by a SOFC manufacturer [19]. The anode and cathode off-gas (AOG) and (COG) are reused to preheat the reactant flows. The COG is used to preheat the airflow and superheat the water. In contrast to the stand-alone case, the AOG is not recirculated and burnt but is used to directly preheat the fuel and evaporate the water. Subsequently, the AOG is cleaned and purified such that the remaining chemical energy contained within the hydrogen-rich gas is converted into electricity in the PEMFC. The generated steam is used for methane reforming and water gas shift processes. A steam-to-carbon ratio (S/C), the ratio of moles of steam to moles of carbon at the anode inlet, of 2.25 is assumed to prevent the formation of solid carbon inside the SOFC [20]. The AOG is cleaned to remove CO, CO_2, and H_2O before it can be fed to the PEMFC. CO removal is achieved in a high- and low-

temperature water gas shift (WGS) reactor (350 and 180°C respectively) [21]. At higher temperatures, the kinetics are faster, whereas at lower temperatures the H_2 yield is larger and the equilibrium concentration of CO is lower [6]. Because WGS alone cannot meet the requirement of CO $<$ 10 ppm [22], another purification step is required to remove the remaining trace CO. Various methods are available for this purpose. However, because the identification and analysis of the most suitable method is outside the scope of this research, a general separator is assumed. This component is modeled to remove 99.5 mole % CO_2 and all the remaining CO. In the last step, water vapor is separated from the gas flow in a moisture separator. The purified gas flow (designated H_2 in figure 2) contains a high concentration of hydrogen and small concentrations of impurities and water vapor. The compositions of the different process flows shown in figures 1 and 2, are listed in table 1.

For the PEMFC subsystem model, a simple architecture is assumed that consists of a water-cooled stack operating at 60°C, fed with reactant flows at 40°C. The air is compressed and preheated by residual heat in the PEMFC COG stream before entering the cathode. The hydrogen-rich gas flow is cooled to 40°C before being compressed, such that it can be directly connected to the anode side. Because the fuel utilisation in the PEMFC is lower than unity (85% under nominal conditions), the anode off-gas is recirculated and mixed with fresh gas at the anode inlet. Consequently, CO_2 in the anode gas stream might accumulate in the system. While CO_2 itself is inert, the reverse WGS reaction can create CO in such amounts (CO $>$ 10ppm) that it can poison the anode, thereby reducing the stack efficiency. To remove this CO_2, a continuous purge is modeled, that vents 20% of the anode off-gas to the environment. This maintains the level of CO_2 at the anode inlet at such a level that the performance degradation is less than 5% under nominal conditions [23]. Because purging hydrogen also introduces system losses, the chosen value of 20% represents an efficiency trade-off.

3 METHODOLOGY

The flow-sheet program *Cycle-Tempo*, an in-house software developed at TU Delft, is used for the thermodynamic evaluation of this system. The program contains a library of components such as a pump, compressor, fuel cell stack, reformer, combustor and heat exchangers. Combining these, a complete fuel cell system is created. In Cycle-Tempo, these components form a system matrix consisting of mass and energy equations, which are solved to determine the pressure, mass flow, temperature and flow composition of each component. The results can be used to analyse the performance of power plants, for example, the system efficiency and exergy analysis [24]. This modeling software is commonly used in SOFC-based power plant research [25]–[27]. The model assumptions and governing equations for the different subsystems are given below. Cycle-Tempo employs a Gibbs free energy minimisation routine for equilibrium calculations in the cell models.

3.1 Model assumptions

1. Pressure drops over the pipes are neglected.
2. The system operates in steady-state.
3. The fuel cell, heat exchanger and chemical reactor components are all assumed to be well insulated. There is no heat transfer between those components and the ambient.
4. Humidification of the PEMFC cathode is not included.
5. 99.5 Mole % of CO_2 is removed from the AOG in the general separator.
6. 100 Mole % of CO is removed from the AOG in the general separator.

3.2 SOFC model

The SOFC module uses the mole flow and conditions (composition and temperature) at the cell inlet to calculate the outlet mole flows and conditions. The operating point of the fuel cell is defined by specifying the power generation $P_{el,AC}$ and the cell voltage V_{cell}. The other parameters such as current I and power generated by the stack $P_{el,DC}$ are calculated from the input data. These processes are assumed to occur at constant internal pressure, gas composition and temperature. The required fuel mass flow at the anode inlet m_a^{in} is calculated from the total current I, and fuel utilisation u_f, according to [25]

$$m_a^{in} = \frac{IM_a}{2F(y_{H_2}^{in} + y_{CO}^{in} + 4_{CH_4}^{in})u_f} \qquad (1)$$

where, y_i^{in} is the anode gas concentrations at the inlet, M_a the molar mass of the anode gas and F is the Faraday constant. The oxygen mass flow from the cathode to the anode $m_{O_2,c\to a}$ is also calculated

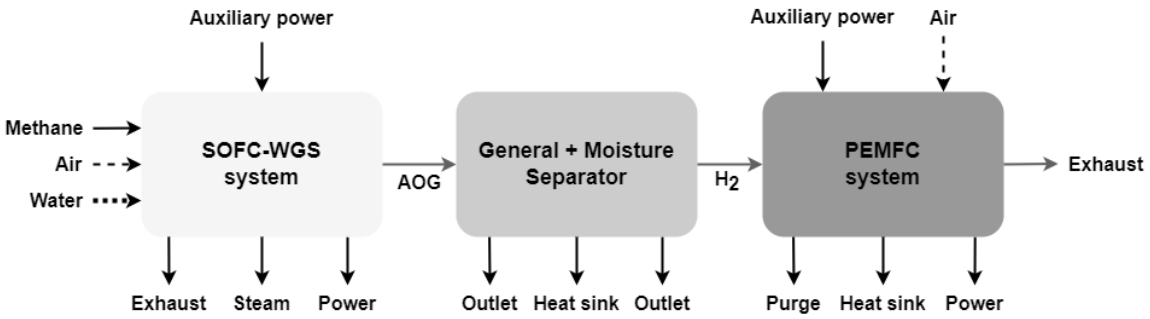

Figure 2: Schematic of the energy inputs and outputs of the SOFC-PEMFC combined system. AOG represents the anode off-gas of the SOFC, that is being cleaned to generate a high-purity hydrogen mixutre (H_2 stream).

from the total current I,

$$m_{O_2,c\to a} = M_{O_2}\frac{I}{4F} \tag{2}$$

where M_{O_2} is the oxygen molar mass. The cathode mass flow is determined from the energy balance over the fuel cell because the temperature at the outlet is an input and the anode and cathode outlet temperatures are assumed to be identical.

A simplified isothermal model is used for the fuel cell, to limit the computational time and convergence to acceptable levels for flow sheeting modeling purposes. The fuel cell model calculates the local processes along the direction of the flow, with all processes occurring at a constant temperature T. Internal profiles are obtained for the concentrations and current density to determine the local reversible voltage. To calculate these profiles, the cell is discretised in the direction of the flow such that pressure and gas composition are assumed constant in the cross-section perpendicular to the flow. The position of the local variables along the profiles is indicated by subscript x. The reversible, no loss, voltage $V_{rev,x}$ is calculated according to [25]:

$$V_{rev,x} = V^0_{rev} + \frac{\bar{R}T}{2F}\ln\left\{\frac{y^{1/2}_{O_2,c}y_{H_2,a}}{y_{H_2O,a}}\times p^{1/2}_{cell}\right\} \tag{3}$$

with standard reversible voltage V^0_{rev}, universal gas constant $\bar{R}$, temperature T, mole fraction y and pressure p_{cell}. In reality, irreversibilities that occur within the cell will result in a cell voltage, V_x, smaller than the reversible voltage. This difference is indicated by the voltage loss ΔV_x. Because the model assumes that the voltage losses are negligible at the electrode level in the x-direction, the cell voltage is assumed to be constant over the fuel cell:

$$V = V_x = V_{rev,x} - \Delta V_x \tag{4}$$

The current density in the flow direction along the cell is:

$$i_x = \frac{\Delta V_x}{R_{eq}} \tag{5}$$

where R_{eq} denotes the equivalent cell resistance. Therefore, for the entire cell, the total current I is calculated according to:

$$I = \frac{u_f A}{R_{eq}\int_0^{u_f} d\lambda/(V_{rev}-V)} \tag{6}$$

Table 1: Composition of SOFC-PEMFC system process flows

Gas stream	**Composition [mole %]**
Methane	CH_4=100%
Air	Ar=0.92%, CO_2=0.03%, H_2O=1.01%, N_2=77.29%, O_2=20.75%
Water	H_2O (l)=100%
AOG	H_2O=66.29% , CO_2=17.72%, H_2=13.72%, CO=2.26%
H_2	H_2O=7.29%, CO_2=0.58%, H_2=92.14%
SOFC exhaust	Ar=0.95%, CO_2=0.03%, H_2O=1.05%, O_2=17.98%, N_2=79.99%
PEMFC exhaust	Ar=0.82%, CO_2=0.03%, H_2O=20.93%, O_2=9.26%, N_2=68.96%
PEMFC purge	CH_4=0.12%, CO_2=15.55%, H_2=84.32
General separator outlet	CO=0.01%, CO_2=99.99%
Moisture separator outlet	H_2O (l)=100%

where A is the cell area and λ is the dimensionless reaction coordinate. The cell power can be calculated using the known current and voltage.

The system operates on pure methane, CH_4, of which 20% is bypassed to be converted externally in an adiabatic pre-reformer. The remaining methane is converted internally in the SOFC into a hydrogen-rich gas. Methane reforming occurs through steam reforming and the water gas shift reaction (Eqs. 7 and 8).

$$\mathrm{CH_4 + H_2O \rightleftharpoons CO + 3\,H_2} \tag{7}$$

$$\mathrm{CO + H_2O \rightleftharpoons H_2 + CO_2} \tag{8}$$

The steam reforming reaction requires water, which is vaporised by heat recovered from the SOFC exhaust stream.

3.3 SOFC anode off-gas cleaning model

In WGS reactors, the equilibrium water gas shift reaction occurs (Eq. 8). The equilibrium is calculated by means of the equilibrium constant K_{react}, as a function of temperature T_{react}, according to

$$K_{react} = \frac{(\partial p_{CO_2} + y)(\partial p_{H_2} + y)}{(\partial p_{CO} - y)(\partial p_{H_2O} - y)} \tag{9}$$

where y is the reaction coordinate of the water gas shift reaction and ∂p_x is the partial pressure of component x. The outlet temperature and gas composition are calculated using equilibrium, energy and mass balances.
The flow is subsequently cooled in the moisture separator, where condensation occurs and is separated via a separate pipe.

3.4 PEMFC model

The PEMFC module calculations followed an approach similar to that described in Section 3.2, for the SOFC module. Only this time, the fuel mass flow is specified instead of the power generation. For low-temperature fuel cells, it is assumed that only H_2 is present in the fuel and that a shift reaction does not occur. Equation 2 can be rewritten as follows:

$$I = \frac{m_{a,in}}{M_a} 2F y^0_{H_2} u_f \tag{10}$$

The PEMFC is modeled with a cooling circuit, which is assumed to be under environmental conditions at the inlet of the pump (20°C, p_{amb}=1.103 bar).

3.5 System analysis

The main performance metric is the net electrical efficiency of the combined system, $\eta_{el,AC}$, which is calculated as

$$\eta_{el,AC} = \frac{P_{el,tot} - P_{aux}}{m_f LHV_{CH_4}} \tag{11}$$

In Equation 11, $P_{el,tot}$ is the net electrical power output of the system, calculated from the direct current (DC) power produced by both the SOFC and PEMFC, multiplied by the efficiency of converting DC into AC according to:

$$P_{el,tot} = (P_{SOFC,_{DC}} + P_{PEMFC,_{DC}})\eta_{DC/AC} \tag{12}$$

In addition, P_{aux} is defined as the total power consumption of all auxiliary components, such as pumps and compressors used in both the SOFC and PEMFC systems. The net electrical efficiency is calculated based on the lower heating value (LHV) of methane.

An additional metric of interest is the fraction of the total power delivered by the PEMFC, defined as

$$f_{P,_{PEMFC}} = \frac{P_{PEMFC,_{AC}}}{P_{PEMFC,_{AC}} + P_{SOFC,_{AC}}} \tag{13}$$

An overview of the operating parameters used in this study is provided in table 2.

3.6 Model verification

Figure 2 shows a schematic overview of the energy inputs and outputs of the combined cycle system. The SOFC and WGS reactors are integrated because the heat of the exothermic WGS reaction is used to evaporate the water required for the steam reforming reaction in the SOFC system. In figure 2, AOG stands for the anode off-gas stream and syngas containing residual hydrogen. The H_2 stream represents a high-purity hydrogen stream, which is suitable for fueling the PEMFC.

Model verification can be achieved at various levels. In this study, the energy balance of the complete system is calculated as a verification method. The SOFC power output is set to $P_{el,AC}$ = 200 kW, with the input parameters as presented in table 2, resulting in a PEMFC power output of $P_{el,AC}$ = 48,29 kW. It is verified that all components assumed adiabatic (e.g., nodes, reactors, heat exchangers) have zero energy losses.

Table 2: Input parameters used for analysis of the combined cycle system

Parameter	Value
General	
Heat exchanger pressure drop, Δp_{HEX}	0.05 [bar]
Economiser pressure drop, Δp_{ECO}	0.5 [bar]
Isentropic efficiency compressor, η_{is}	0.7 [-]
Mechanical efficiency compressor, η_{me}	0.8 [-]
DC-AC converter efficiency, $\eta_{converter}$	0.95 [-]
SOFC	
Average stack temperature, $T_{stack,SOFC}$	700 [°C]
Stack inlet temperature, $T_{in,SOFC}$	$T_{stack,SOFC}$ -50 [°C]
Stack outlet temperature, $T_{out,SOFC}$	$T_{stack,SOFC}$ +50 [°C]
Anode pressure drop, Δp_{an}	0.03 [bar]
Cathode pressure drop, Δp_{ca}	0.05 [bar]
Power output, $P_{SOFC,AC}$	200 [kW]
Operating pressure, p_{SOFC}	1.013 [bar]
Pre-reformer temperature, T_{reform}	450 [°C]
Syngas cleaning	
HT-WGS reaction temperature, T_{HT-WGS}	350 [°C]
LT-WGS reaction temperature, T_{LT-WGS}	180 [°C]
Fraction of CO separated, χ_{CO}	100 [mole %]
Fraction of CO_2 separated, χ_{CO_2}	99.5 [mole %]
PEMFC	
Average stack temperature, $T_{stack,PEMFC}$	60 [°C]
Anode pressure drop, Δp_{an}	0.03 [bar]
Cathode pressure drop, Δp_{ca}	0.03 [bar]
Operating pressure, p_{PEMFC}	1.013 [bar]
Fuel utilisation, u_f	0.85 [-]
Oxygen utilisation, u_{ox}	0.5 [-]
Anode purge percentage x_{purge}	20 [%]

Moreover, comparing the energy inputs and outputs, an absolute error of 0.01 kW and a relative error of 0.05% is observed. This is considered negligible small, such that the system is assumed to be verified for the energy balance.

4 RESULTS

The performance of the combined SOFC-PEMFC system is first evaluated for the nominal operating conditions of the SOFC power output of P_{SOFC} = 200 kW, under nominal conditions (table 3). This results in a methane mass flow rate of 0.00781 kg/s. The power output of the PEMFC is dependent on the amount of H_2 present in the SOFC anode off-gas stream. For the nominal operating point, the resulting hydrogen flow reads 0.00079 kg/s, producing 48.29 kW of PEMFC power. The total net power generated by the system $P_{el,tot}$ = 200 + 48.29 = 248.29 kW. The net efficiency is $\eta_{el,AC}$ = 59.7% and the fraction of power produced by the PEMFC is $f_{P,PEMFC}$ = 0.19 [-].

4.1 Multivariable parametric analysis

The SOFC-PEMFC system is subjected to a parametric analysis of typical SOFC and PEMFC operating variables. For the SOFC, the cell voltage is varied in the range 0.6-0.8 V, the fuel utilisation in the range 0.6-0.9 [-] and the stack temperature is between 600-900 °C; for the PEMFC, the cell voltage is varied in the range 0.6-0.8 V, while the stack temperature is kept constant. The analysis is performed with a finite parameter interval, the details are provided in table 3.

Table 3: Overview of the parameters varied in the analysis, with their respective range, interval and nominal values.

Parameter	Range	Interval	Nominal value
$V_{cell,SOFC}$ [V]	0.6-0.8	0.025	0.7
u_f [-]	0.6-0.9	0.025	0.8
$T_{stack,SOFC}$ [°C]	600-900	50	700
$V_{cell,PEMFC}$ [V]	0.6-0.8	0.025	0.7

4.1.1 SOFC cell voltage

Figure 3a shows the contours of net electrical efficiency and the fraction of total power delivered by the PEMFC for various SOFC fuel utilisations and cell voltages at a constant SOFC stack temperature of 700°C and PEMFC cell voltage of 0.7 V. At lower fuel utilisation levels, the fuel flow increases for a constant power output, enhancing the cooling effect owing to the internal reforming process. Therefore, less air is required to cool the stack such that the airflow is reduced, which negatively affects the waste thermal energy available in the cathode off-gas. This trend is accelerated at higher cell voltages because less waste heat is available owing to the reduction in electrochemical losses in the fuel cell. Consequently, the cathode off-gas stream does not contain sufficient thermal energy to preheat the cathode air stream and superheat the water stream. Hence, the system is unable to sustain itself which represents an invalid operating point. The entire invalid operating regime is indicated by the gray area in figure 3a. Within the valid operating envelope, the system efficiency is primarily affected by the cell voltage, whereas it only slightly increases for a decrease in fuel utilisation. The electrochemical losses in the SOFC are reduced by increasing the cell voltage. The required airflow is reduced by reducing the fuel utilisation, lowering the power consumption of the air compressors. Because the air compressor is the primary power consumer, the net electrical efficiency of the system is increased. The fraction of the total power produced by the PEMFC is primarily affected by fuel utilisation as the hydrogen availability for the PEMFC is increased for higher fuel flows. The influence of cell voltage is less prominent. The $f_{P_{PEMFC}}$ slightly reduces with an increase in cell voltage because less fuel is required to achieve the

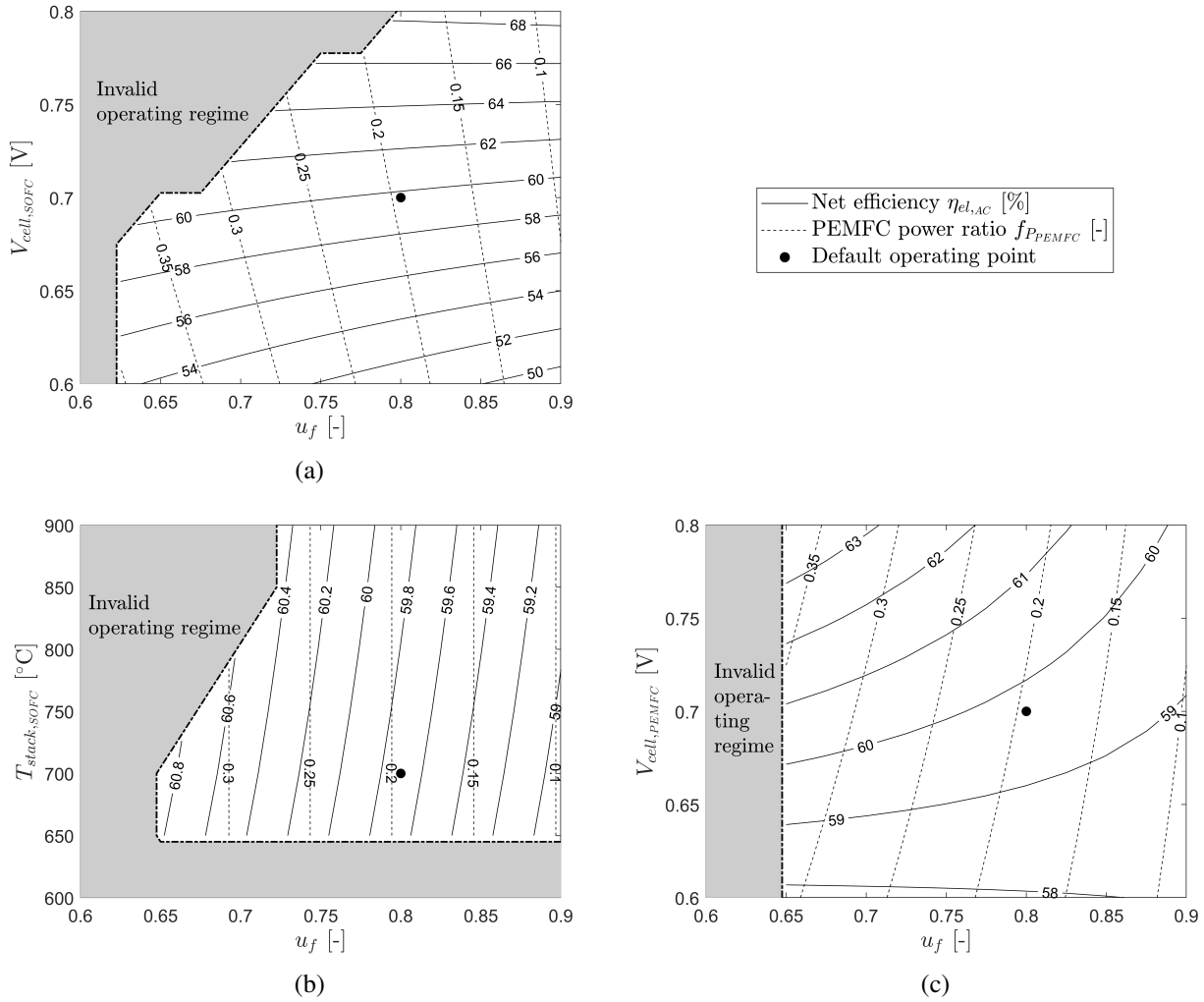

Figure 3: Contour plots of net electrical efficiency and fraction of power delivered by the PEMFC for various SOFC fuel utilisations, SOFC cell voltage (3a), SOFC stack temperature (3b) and PEMFC cell voltage (3c) at a constant PEMFC stack temperature of 60°C

same power output at higher cell efficiency. The maximum net electrical efficiency is 68.8%, for a cell voltage of 0.8 V and fuel utilisation of 0.9 [-]. This corresponds to the minimum PEMFC power production ratio of 0.085 [-].

4.1.2 SOFC stack temperature

Figure 3b shows contours of net electrical efficiency and the fraction of total power delivered by the PEMFC for various SOFC fuel utilisations and SOFC stack temperatures, at a constant SOFC cell voltage of 0.7 V and PEMFC cell voltage of 0.7 V. At $u_f < 0.65$ [-], the cathode off-gas did not contain sufficient thermal energy to sustain stable operation. In this case, this trend is enhanced by increasing the stack temperature, because less air is required for cooling. Owing to the reduction in the cathode mass flow, insufficient energy is available to preheat the airflow and superheat the water. Furthermore, the invalid operating regime extends over the entire range of u_f values, for $T_{stack_{SOFC}} < 650$°C. At these low temperatures, the anode off-gas does not contain sufficient thermal energy to preheat the fuel flow and evaporate the water stream. Increasing the stack operating temperature has a negligible effect on the system efficiency and power production ratio. Because operational conditions imposed on the stack, such as the operating temperature and pressure, do not affect the cell voltage, this does not affect the stack efficiency. This behaviour deviates from reality, where an increase in temperature will result in decreased voltage losses and an increased efficiency. Nonetheless, a marginal efficiency increase is observed for increasing SOFC stack temperatures, as less cooling air is required, reducing the auxiliary power consumption. The fraction of total power produced by the PEMFC is only seen to increase with a reduction in fuel util-

isation, as more hydrogen is available to be fed to the PEMFC. The maximum net electrical efficiency ($\eta_{el_{AC}}$ = 60.9%) is achieved for medium-low stack temperatures (650-700°C) and low fuel utilisation levels.

4.1.3 PEMFC cell voltage

Figure 3c displays contours of net electrical efficiency and fraction of the total power produced by the PEMFC as a function of SOFC fuel utilisation and PEMFC cell voltage, for a constant SOFC cell voltage of 0.7 V and SOFC stack temperature of 700°C. A fuel utilisation factor of 0.65 limits the valid operating regime. Because the electrical efficiency is seen to increase with an increase in the PEMFC cell voltage and a decrease in SOFC fuel utilisation, the maximum efficiency ($\eta_{el_{AC}} \approx 64\%$) is achieved for the maximum cell voltage and minimum fuel utilisation. At lower PEMFC cell voltages ($V_{cell_{PEMFC}}$ <0.625 V), this trend is reversed. The electrical efficiency decreases with a decrease in fuel utilisation. This is because of the increased hydrogen flow to the PEMFC, which increases the auxiliary power demand of the PEMFC system. This trend is further enhanced by the reduction in PEMFC efficiency with increased electrochemical losses. Because the SOFC operating parameters are kept constant in this case, the increase in net electrical efficiency follows directly from an increase in the PEMFC efficiency, combined with an increase in the PEMFC power output. The fraction of total power produced by the PEMFC primarily increases with a reduction in fuel utilisation and only slightly with an increase in the PEMFC cell voltage.

4.2 Sensitivity analysis

The PEMFC operating parameters that were kept constant during the foregoing analysis are investigated to analyse their influence on the system performance. The parameters investigated are the anode purge percentage x_{purge} as well as the fuel utilisation $u_{f,PEM}$. The influence of these parameters on the net electrical efficiency $\eta_{el,AC}$ and the fraction of power delivered by the PEMFC $f_{P_{PEMFC}}$ is presented in table 4. For every parameter, the nominal values and variations are provided. The last two columns provide the percentage changes according to

$$\text{Percentage change} = \frac{X_{new} - X_{nominal}}{X_{nominal}} \times 100\% \tag{14}$$

with X representing the system performance indicators $\eta_{el,AC}$ and $f_{P_{PEMFC}}$.

Both the PEMFC purge percentage and fuel utilisation are verified to have little influence on the system efficiency. At x_{purge}=0 and $u_{f,PEM}$=0.9, the net electrical efficiency is 60.3%, which is only slightly higher that under nominal conditions. The influence on the PEMFC power production is larger. As expected, the power produced by the PEMFC is directly influenced by the fuel utilisation and purge percentage. Nonetheless, varying these parameters did not change the conclusions presented in this study. Owing to the lack of physical feedback from the PEMFC to the SOFC, the PEMFC can be optimised without affecting the SOFC performance. Based on these observations, the assumed constant parameter values are considered acceptable.

5 CONCLUSION

A thermodynamic analysis of the SOFC-PEMFC combined cycle system is presented in this paper. The SOFC fuel utilisation, cell voltage and operating temperature were varied in addition to the PEMFC cell voltage. The calculated net electrical efficiency $\eta_{el_{AC}}$, varies in the range of 50-68%. The net electrical efficiency increases with SOFC and PEMFC cell voltages as electrochemical losses are reduced. The efficiency further increases with a decrease in SOFC fuel utilisation, as less air is required to cool the stack. The fraction of the total power produced by the PEMFC is seen to decrease with an increase in SOFC cell voltage and fuel utilisation, as the SOFC losses are reduced and less hydrogen is available for the PEMFC. An increase in the PEMFC cell voltage results in an increase in the power produced by the PEMFC. This analysis shows the high-efficiency potential of the combined SOFC-PEMFC system and highlights the interaction between SOFC and PEMFC. The PEMFC is influenced by changing the conditions upstream in the SOFC; however, because there is no physical feedback from the PEMFC to the SOFC, the PEMFC can be optimised independently of the SOFC. The hydrogen purification system presented herein is based on WGS reactors and a general separator. Details on the specific method or approach for trace CO and CO_2 removal are not included. As the choice of AOG post-treatment and purification method is beyond the scope of this research, this level of detail is deemed sufficient. However, in future research, the model should be expanded with a more detailed purification system to improve the credibility of the

Table 4: Percentage change in net electrical efficiency and fraction of total power produced by the PEMFC compared to nominal values as a function of x_{purge} and $u_{f_{PEM}}$.

Parameter	Nominal value	Set value	Percentage change $\eta_{el,AC}$ [%]	Percentage change $f_{P_{PEMFC}}$ [%]
x_{purge}	20	0	0.754	3.063
		10	0.353	1.396
		30	-0.342	-1.356
$u_{f,PEM}$	0.85	0.6	-1.774	-7.092
		0.7	-0.944	-3.770
		0.8	-0.282	-1.121
		0.9	0.257	1.032

proposed setup. Figures 3(a-c) show the invalid operating regimes (gray areas) to cover significant sections of the simulation matrix. This highlights the precarious balance between increasing the SOFC efficiency (reducing thermal losses) and retaining sufficient waste energy in the anode/cathode off-gas streams for preheating the different reactant flows. This shows the trade-off that must be made between optimising the design point efficiency and retaining a sufficiently large operating envelope.

6 FUTURE WORK

This work presents a basis for the comparison of the SOFC-PEMFC combined cycle with other SOFC-based combined cycle systems and different stand-alone SOFC system layouts. In future research, the purification step should be modeled in more detail, after which a more in-depth analysis can be performed, such as an investigation of exergy losses in the system. Moreover, the effects of using different alternative fuels other than methane will also be included in the next stage of this research. To do this, different fuel pre-processing models will be developed and included within the currently developed model. Moving forward, off-design conditions such as part-load operation will also be investigated to identify the operating envelope and operational constraints of the system.

ACKNOWLEDGEMENTS

This research is supported by the SH_2IPDRIVE project, which aims to accelerate the introduction of hydrogen as an alternative energy carrier in the Dutch maritime sector. The main goal is to develop reliable, safe, standardized, and scalable solutions for zero-emission propulsion and energy systems on board ships. The project is funded by the Rijksdienst voor Ondernemend Nederland (RVO) under the R&D Mobiliteitssectoren regulation.

REFERENCES

[1] IMO, "Fourth imo ghg study 2020 executive-summary," Report, 2020.

[2] IMO, "2023 imo strategy on reduction of ghg emissions from ships," Report, 2023.

[3] F. Baldi, S. Moret, K. Tammi, and F. Maréchal, "The role of solid oxide fuel cells in future ship energy systems," *Energy*, vol. 194, 2020, ISSN: 03605442.

[4] R. Payne, J. Love, and M. Kah, "Generating electricity at 60% electrical efficiency from 1-2 kwe sofc products," in *ECS Transactions*, vol. 25, pp. 231–239.

[5] A. C. Power, *Alma clean power announces breakthrough in direct ammonia fuel cells*, Web Page, 2023. [Online]. Available: `https://almacleanpower.com/news/alma-clean-power-announces-breakthrough-in-direct-ammonia-fuel-cells`.

[6] L. van Biert, M. Godjevac, K. Visser, and P. V. Aravind, "A review of fuel cell systems for maritime applications," *Journal of Power Sources*, vol. 327, pp. 345–364, 2016, ISSN: 03787753.

[7] B. N. van Veldhuizen, L. van Biert, P. V. Aravind, and K. Visser, "Solid oxide fuel cells for marine applications," *International Journal of Energy Research*, vol. 2023, p. 35, 2023.

[8] T. Tronstad, H. Hogmoen Astrand, G. Haugom, and L. Langfeldt, "Study on the use of fuel cells in shipping," European Maritime Safety Agency, Report, 2017.

[9] L. van Biert, T. Woudstra, M. Godjevac, K. Visser, and P. V. Aravind, "A thermodynamic comparison of solid oxide fuel cell-combined cycles," *Journal of Power Sources*, vol. 397, pp. 382–396, 2018, ISSN: 03787753.

[10] D. Cocco and V. Tola, "Externally reformed solid oxide fuel cell–micro-gas turbine (sofc–mgt) hybrid systems fueled by methanol and di-methyl-ether (dme)," *Energy*, vol. 34, no. 12, pp. 2124–2130, 2009, ISSN: 03605442.

[11] V. He, M. Gaffuri, J. Van herle, and J. Schiffmann, "Readiness evaluation of sofc-mgt hybrid systems with carbon capture for distributed combined heat and power," *Energy Conversion and Management*, vol. 278, 2023, ISSN: 01968904.

[12] F. D. F. Chuahy and S. L. Kokjohn, "Solid oxide fuel cell and advanced combustion engine combined cycle: A pathway to 70% electrical efficiency," *Applied Energy*, vol. 235, pp. 391–408, 2019, ISSN: 03062619.

[13] H. Sapra, J. Stam, J. Reurings, *et al.*, "Integration of solid oxide fuel cell and internal combustion engine for maritime applications," *Applied Energy*, vol. 281, 2021, ISSN: 03062619.

[14] A. Dicks, R. Fellows, C. Mescal, and C. Seymour, "A study of sofc-pem hybrid systems," *Journal of Power Sources*, vol. 86, pp. 501–506, 2000.

[15] L. J. Tan, C. Yang, and N. Zhou, "Performance of the solid oxide fuel cell (sofc)/proton-exchange membrane fuel cell (pemfc) hybrid system," *Chemical Engineering & Technology*, vol. 39, no. 4, pp. 689–698, 2016, ISSN: 09307516.

[16] X. Cheng, Z. Shi, N. Glass, *et al.*, "A review of pem hydrogen fuel cell contamination: Impacts, mechanisms, and mitigation," *Journal of Power Sources*, vol. 165, no. 2, pp. 739–756, 2007, ISSN: 03787753.

[17] Z. Wu, Z. Zhang, and M. Ni, "Modeling of a novel sofc-pemfc hybrid system coupled with thermal swing adsorption for h2 purification: Parametric and exergy analyses," *Energy Conversion and Management*, vol. 174, p. 802, 2018, ISSN: 0196-8904 0196-8904.

[18] E. Riensche, U. Stimming, and G. Unverzagt, "Optimization of a 200 kw sofc cogeneration power plant part 1: Variation of process parameters," *Journal of Power Sources*, vol. 73, pp. 251–256, 1998.

[19] B. N. van Veldhuizen, L. van Biert, A. Amladi, T. Woudstra, K. Visser, and P. V. Aravind, "The effects of fuel type and cathode off-gas recirculation on combined heat and power generation of marine sofc systems," *Energy Conversion and Management*, vol. 276, 2023, ISSN: 01968904.

[20] C. Stiller, B. Thorud, S. Seljebø, Ø. Mathisen, H. Karoliussen, and O. Bolland, "Finite-volume modeling and hybrid-cycle performance of planar and tubular solid oxide fuel cells," *Journal of Power Sources*, vol. 141, no. 2, pp. 227–240, 2005, ISSN: 03787753.

[21] A. Ghenciu, "Review of fuel processing catalysts for hydrogen production in pem fuel cell systems," *Current Opinion in Solid State nd Materials Science*, vol. 6, no. 5, pp. 389–399, 2002.

[22] E.-S. Bang, M.-H. Kim, and S.-K. Park, "Options for methane fuel processing in pemfc system with potential maritime applications," *Energies*, vol. 15, no. 22, 2022, ISSN: 1996-1073.

[23] F. de Bruijn, D. Papageorgopoulos, E. Sitters, and G. Janssen, "The influence of carbon dioxide on pem fuel cell anodes," *Journal of Power Sources*, vol. 110, pp. 117–124, 2002.

[24] A. de Groot, "Advanced exergy analysis of high temperature fuel cell systems," Thesis, 2004.

[25] P. V. Aravind, T. Woudstra, N. Woudstra, and H. Spliethoff, "Thermodynamic evaluation of small-scale systems with biomass gasifiers, solid oxide fuel cells with ni/gdc anodes and gas turbines," *Journal of Power Sources*, vol. 190, no. 2, pp. 461–475, 2009, ISSN: 03787753.

[26] N. Woudstra, T. van der Stelt, and K. Hemmes, "The thermodynamic evaluation and optimization of fuel cell systems," *Journal of Fuel Cell Science and Technology*, vol. 3, pp. 155–164, 2006.

[27] K. Hemmes, A. Patil, and N. Woudstra, *Internal reforming sofc system for flexible coproduction of hydrogen and power*, Conference Paper, 2005.

Diesel Substitution with Hydrogen for Marine Engines

Panagiotis Karvounis, Gerasimos Theotokatos

Maritime Safety Research Centre, Department of Naval Architecture, Ocean, and Marine Engineering, University of Strathclyde, Glasgow, Scotland, United Kingdom
* Corresponding Author panagiotis.karvounis@strath.ac.uk

Abstract

Zero-carbon fuels are expected to catalyse the decarbonisation of the maritime industry, with hydrogen being considered a long-term solution. This study aimed to investigate the feasibility of using hydrogen as a secondary fuel in marine diesel engines. A marine four-stroke engine with a nominal power output of 10.5 MW at 500 rpm was investigated, whereas the hydrogen injection at the engine port was considered. A CFD model was set up in CONVERGE for both diesel and the diesel-hydrogen operating modes to investigate the effects of 20% hydrogen fuel fraction (by energy) on engine performance, emissions, and combustion characteristics. This model was validated against experimental data for the diesel operating mode. Based on a parametric study, the mesh characteristics were selected to compromise between the prediction error and the computational effort. The impact of 20% hydrogen energy fraction on the heat release rate (HRR) and NO_x emissions is comparing with the diesel mode. The results demonstrate that despite the reduction in carbon emissions when using hydrogen, the NO_x emissions increase by 2.5 times, whereas the lower compression ratio allows for engine free-knock operation. This study contributes to the identification of efficient and reliable combustion conditions for diesel-hydrogen dual-fuel marine engines.

Keywords: CFD model, Hydrogen, Combustion, Marine engines, Decarbonisation.

1. INTRODUCTION

Hydrogen, as an environmentally friendly fuel, has emerged as a promising long-term solution for achieving sustainability goals and advancing decarbonisation efforts within the maritime industry [1]. Recent empirical studies have provided valuable insights into the feasibility of hydrogen-powered engines operating under real-world conditions [2]. These investigations underscore the techno-economic viability of adopting hydrogen-based propulsion systems, particularly when considering specific incentivisation mechanisms such as carbon taxation. However, the investigation of hydrogen combustion for marine compression ignition engines presents a range of challenges [3], which predominantly arise from the distinctive physical properties of hydrogen compared to conventional diesel fuels.

One notable difference is the elevated auto-ignition temperature of hydrogen, which necessitates the use of significantly higher compression ratios when employed as the primary fuel source [4]. Consequently, to address ignition-related issues, a dual-fuel operational strategy has been proposed [11]. In this approach, a fuel with a higher reactivity, typically diesel, is directly injected to initiate combustion. Most investigations of dual-fuel engines have considered the direct injection of diesel fuel close to the top dead centre (TDC). Other combustion methods include premixed combustion involving hydrogen injection into the port manifold, in-cylinder diesel injection, and diffusion combustion, which includes both diesel and hydrogen in-cylinder direct injection [5]. The former also involves low-pressure hydrogen injection during the compression stroke, whereas the latter considers high-pressure injection near TDC, each resulting in distinct effects on performance and emission parameters [6].

The literature lacks studies that examine the use of hydrogen in marine engines and hydrogen port injection in compression ignition engines. The latter has been identified as an attractive case for retrofitted marine engines and hence is expected to attract interest in the maritime sector [7].

This study aims to comparatively investigate the impact of hydrogen use in compression ignition marine engines by employing CFD modelling. The large marine four-stroke engine operation in the diesel and diesel-hydrogen dual fuel (DF) modes was simulated to reveal the effects of hydrogen use on the combustion, performance, and emissions parameters. This study contributes to the identification of settings that require optimisation in hydrogen fuelled marine dual-fuel engines.

2. METHODOLOGY

This study investigated a nine-cylinder marine four-stroke engine with 10.5 MW nominal power.

@2023 Karvounis, P. et al., published by TU Delft OPEN Publishing on behalf of the authors. Licensed under a Creative Commons Attribution CC BY license.
DOI: https://doi.org/10.59490/moses.2023.657

The engine bore and stroke were 460 and 580 mm, respectively, and the compression ratio was 14:1.

The CONVERGE CFD commercial code is used in this study. The methodological steps are illustrated in Fig. 1. The diesel mode operation, as well as the geometrical characteristics and settings of the engine, are first considered. A grid dependency study was conducted. The validation of the CFD model-derived results for the diesel mode is performed against datasets acquired from onboard experimental campaigns and manufacturers shop test trials. A comprehensive description of the data-acquisition process was reported by Stoumpos et al. [8].

The investigated case studies included baseline diesel mode operation (D) at a medium load. n-Heptane fuel was directly injected into the cylinder. The injection pressure was 1400 bar, and the injection start was 6ºCA BTDC. In the dual-fuel mode (DF), hydrogen is injected into the intake ports, and the hydrogen-air mixture at the inlet valve close (IVC) is considered fully premixed (hence homogeneous). Diesel fuel was injected using the same settings as the diesel mode.

To identify stable combustion conditions (knock free) in the DF mode, a set of parametric studies was conducted, including exhaust gas recirculation (EGR), diesel start of injection (SOI) retard, and compression ratio (CR) decrease. Following a parametric investigation (not reported herein for brevity), the CR of 11 (instead of 14 for the diesel mode) was identified to lead to knock-free combustion, although it was associated with lower engine efficiency. This parametric investigation yielded the operational parameters shown in Fig. 2. It is worth noting that an increased in-cylinder temperature at the IVC (compared with the diesel mode) is required for effective hydrogen combustion. Further investigation of optimal conditions is required so that the engine can operate in both diesel and dual-fuel modes with the same compression ratio.

Hydrogen requires specific storage conditions and is expected to occupy seven times the gross tank volume of conventional MGO fuels [18]. Considering this, along with the decarbonisation targets for shipping operations, it is expected that marine dual-fuel engines will be adopted with partial hydrogen fuel use. Hence, this study considers a 20% hydrogen energy fraction (HEF), defined by equation (1), to identify trade-offs between engine performance and emissions parameters.

$$HEF = \frac{m_{H_2} LHV_{H_2}}{(m_D LHV_D)+(m_{H_2} LHV_{H_2})} \quad (1)$$

where $m_{D,}$ m_{H2} denote the injected masses of diesel and hydrogen, respectively, and *LHV* is the lower heating value of these fuels.

Lastly, comparative evaluation is conducted between diesel and the dual-fuel modes.

Table 1 presents the physical properties of the diesel and hydrogen fuels. The high auto-ignition temperature of hydrogen poses challenges for its stable combustion in compression ignition engines.

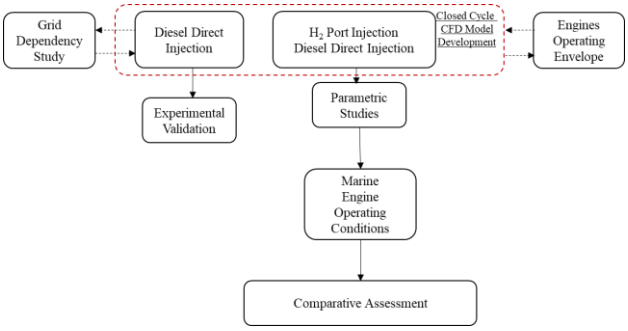

Figure 1. Methodology flowchart.

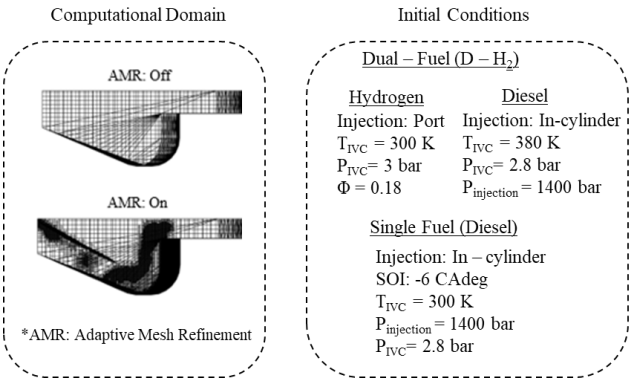

Figure 2. Computational domain and initial conditions of the CFD model.

Table 1. Fuel characteristics

Property	Diesel	Hydrogen
Density [kg/m^3] at 20ºC	847	0.083
Flash Point [ºC]	52	570
Auto-ignition temperature [ºC]	300	858
Viscosity [mPa] at 298.15 K	3.35	
Stoichiometric fuel–air ratio	0.069	0.029
Cetane number	55	–
Lower heating value [MJ/kg]	42.7	120
Latent heat of vaporisation [kJ/kg]	359	461
Laminar burning velocity [cm/s]	30	265–325

2.1 Computational Domain & Grid Sensitivity Study

A segment of one engine cylinder based on in-cylinder and diesel fuel injector (diesel jet deployment) symmetry was selected to reduce the computational cost of the model. The employed

computational domain is shown in Figure 2. The (sub)models employed to develop the CFD model are presented in Table 2.

Table 2. Simulation models.

Mechanisms	**Model**
Turbulence model	RANS k-ε
Droplet breakup model	KH-RT [13]
Spray/Wall interaction model	Han [14]
Droplets collision model	Nordin [15]
NO_x mechanism	Extended Zeldovich [16]
Reaction mechanism - Diesel	Rahimi [17]

A grid sensitivity analysis was performed to compromise between accuracy and computational time. The grid characteristics are presented in Table 3. For all grids, adaptive mesh refinement was used in conjunction with fixed embedding within the injector area to achieve higher resolution. Fig. 3 shows the in-cylinder pressure variations for the three grids. The G-1 grid was selected because it led to smaller errors (considering the measured in-cylinder pressure).

Table 3. Computational grid characteristics.

Parameter	**G3**	**G2**	**G1**
Element size [mm]	0.01	0.005	0.002
Maximum cells number (at TDC)	19242	153940	2460000
Error at Pmax (%)	2	0.8	0.3
Solution duration [h]	6	14	55

3. RESULTS

Fig. 4 shows the measured and derived in-cylinder pressure and heat release variations for the diesel mode. Slight deviations were observed between the measurements and CFD predictions. The estimated error for the in-cylinder peak pressure is approximately 1%, whereas the crank angle at the peak pressure exhibits an error of 6%.

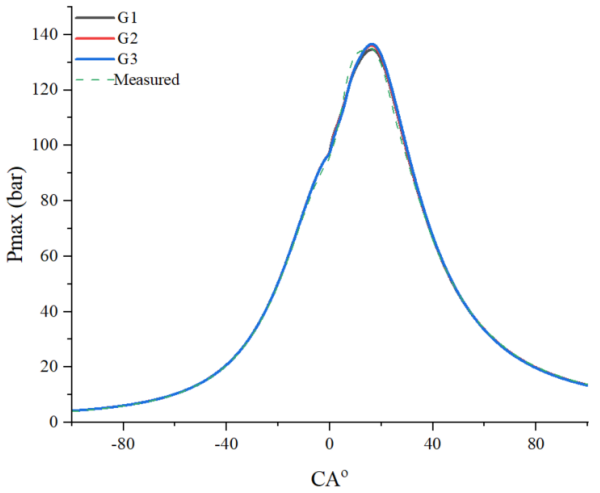

Figure 3. Derived in-cylinder pressure variations for different grids.

Figure 5 presents the measured and derived (by CFD model) NO concentration at the engine cylinder exhaust gas for the three engine loads. Errors of 3%, 8%, and 10% were estimated for 100%, 75%, and 50% loads, respectively, and the CFD model resulted in slight overprediction of the NO concentration. Furthermore, during the shop tests, NO was measured after the turbocharger turbine, whereas the simulated values corresponded to the cylinder at the exhaust valve opening, which also contributed to the deviations. Nevertheless, these errors are considered acceptable; hence, it is inferred that the CFD model is validated for the engine diesel mode. The measured data for the hydrogen fuelled mode were not available to further validate the CFD model. However, the developed model adequately represents the trade-offs for engine performance and emission parameters.

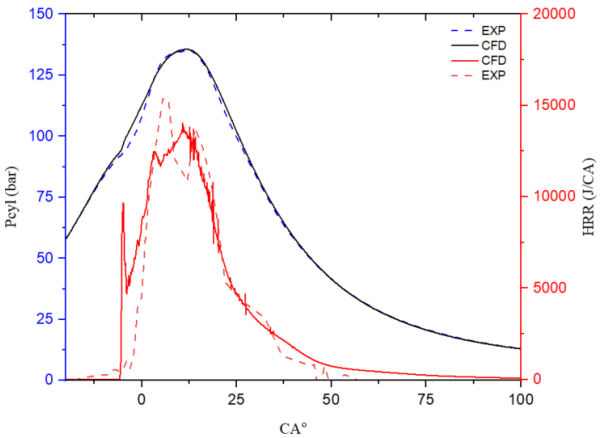

Figure 4. In-cylinder pressure and HRR variations.

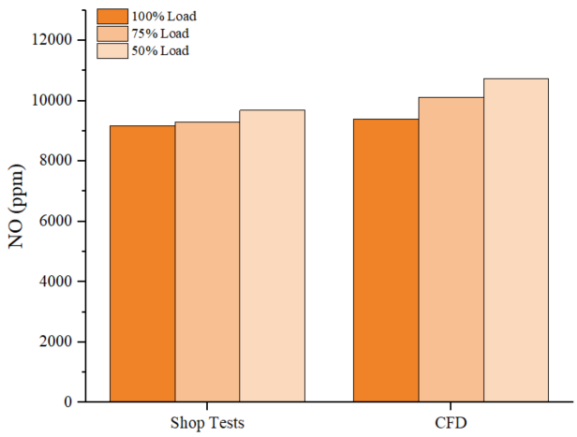

Figure 5. Measured and derived NO concentration.

Previous studies [9–10] have reported that hydrogen exhibits enhanced flame velocity compared to diesel, resulting in pronounced knocking phenomena within the engine, particularly at high loads, which leads to severe mechanical loading.

Fig. 6 shows the in-cylinder pressure variations in the diesel and DF modes. The maximum cylinder pressure was 136 bar and 100 bar for the D and DF cases, respectively, whereas the CA at Pmax shifted from 13.5 15.7ºCA ATDC.

Fig. 7 shows the derived heat release rate (HRR) for the diesel and dual-fuel modes. Owing to diesel dominance, the HRRs exhibited similar trends with some notable differences. The initial spike (3.7–0.3ºCA BTDC) is attributed to diesel premixed combustion. For the DF mode, the premixed hydrogen mixture along with the smaller injected diesel amount resulted in a slightly advanced start of combustion (SOC) at 5ºCA BTDC with a lower rate (HRR rate slope), leading to a lower spike peak value.

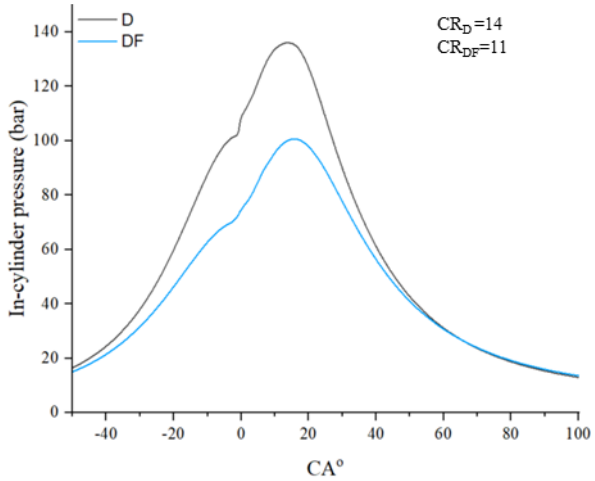

Figure 6. In-cylinder pressure variations for diesel and DF modes.

Following SOC, the hydrogen-air homogenous mixture burns under premixed conditions (flame front progressing in the combustion chamber). Simultaneously, the prepared diesel-air fuel mixture burns based on the diffusion combustion principles. Additionally, it is evident that in the DF mode, the combustion process in the 20–30ºCA ATDC evolves faster compared to the diesel mode (higher HRR), whereas most of the hydrogen (approximately 70% of the total amount) is burnt during this period. Notably, approximately 6% of the hydrogen remained unburnt.

The hydrogen-air mixture ignition occurs by the flame of diesel combustion at approximately 5ºCA ATDC, as can be observed in Fig. 11. From the variation in the hydrogen mass fraction (red line in Figure 7), the hydrogen combustion efficiency was estimated to be 93.7%. Between 0ºCA ATDC and 3ºCA ATDC, there was an increase in the mass fraction of hydrogen stemming from the diesel combustion products.

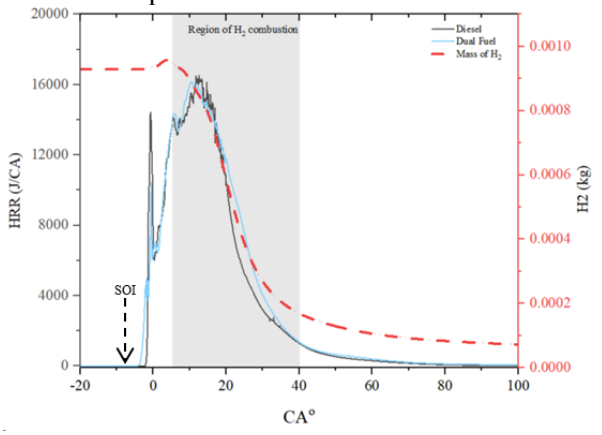

Figure 7. Heat release rates for the diesel and DF mode with 20% HEF. (b) represents the oxygen mass fraction at 5ºCA TDC where the hydrogen combustion initiates.

Fig. 8 illustrates the NO_x emissions in the diesel and dual-fuel modes. Hydrogen use requires a higher in-cylinder temperature to achieve satisfactory combustion efficiency. This leads to more favourable conditions for NO_x formation (compared to the diesel mode). The temperature threshold for thermal NO_x generation typically ranges between 1600 K and 1800 K. NO formation typically commences at 700 K. For the DF mode, a longer duration of residence above this temperature range leads to higher concentrations of thermal NO_x. To effectively reduce NO_x emissions, optimisation of the engine settings is required.

However, it is evident that the use of hydrogen primarily focuses on CO_2 reduction proportional to the HEF employed. The indicated thermal efficiency decreased from 43% in the D case to 41% in the DF case because of the increase in the heat transfer losses and CR reduction.

Potential pathways to mitigate NOx formation include the use of exhaust gas recirculation, engine setting optimisation, or the use of other lean combustion concepts.

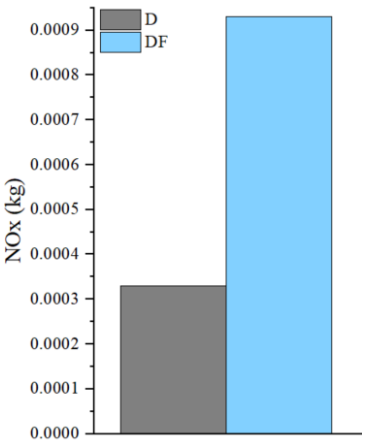

Figure 8. Derived NOx mass for the diesel mode and the DF mode with 20% HEF.

Fig. 9 shows the in-cylinder NO_x mass and temperature for different crank angles for the diesel and DF modes. As diesel is injected close to the TDC (6ºCA BTDC) and combustion occurs, the NO_x mass is zero as the temperature is not sufficiently high (>1800 K) to accommodate the oxidation of atmospheric nitrogen to NO and NO_2. At 3ºCA BTDC, the most volatile species of the diesel jet evaporated owing to the high-pressure, high-temperature regime.

The latter is also observed in Fig. 10, which shows the in-cylinder NOx mass and temperature variations for the diesel and DF modes. In the DF mode, the in-cylinder contents remained for a longer period at high temperatures (prolonged combustion duration), thus yielding a higher NOx concentration.

Fig. 11 shows the in-cylinder hydrogen mass fraction, which illustrates the progression of the hydrogen-air mixture combustion process. At 3ºCA BTDC, the hydrogen-air mixture combustion has not commenced, indicating that the heat release rate (HRR) spike (Fig. 7) is solely attributed to the injected diesel premixed combustion (prepared diesel-air mixture within the region 5–3.7ºCA BTDC). Notably, at 5ºCA ATDC, a considerable hydrogen fraction was noted in the near-wall region; this was attributed to the diesel combustion reactions leading to hydrogen production. The increased temperature in proximity to the diesel jet initiates hydrogen-air mixture combustion. The hydrogen mass fraction is considerably reduced in the period of 20–30ºCA ATDC with the flame front moving, whereas the remaining diesel fuel is burned via a diffusion combustion approach.

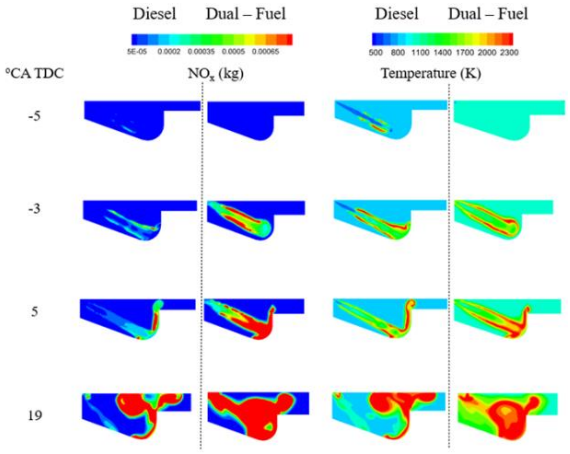

Figure 9. CFD contours of NOx concentration and in-cylinder temperature for single and dual – fuel operation

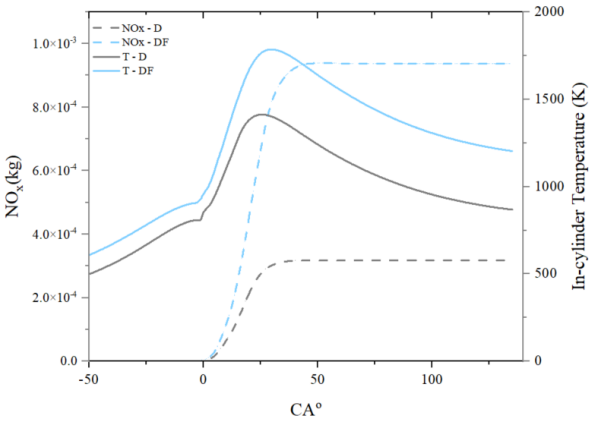

Figure 10. D, DF NOx emissions and temperature in-cylinder.

Fig. 11 shows the in-cylinder hydrogen mass fraction, which illustrates the progression of the hydrogen-air mixture combustion process. At 3ºCA BTDC, the hydrogen-air mixture combustion has not commenced, indicating that the heat release rate (HRR) spike (Fig. 7) is solely attributed to the injected diesel premixed combustion (prepared diesel-air mixture within the region 5–3.7ºCA BTDC). Notably, at 5ºCA ATDC, a considerable hydrogen fraction was noted in the near-wall region; this was attributed to the diesel combustion reactions leading to hydrogen production. The increased temperature in proximity to the diesel jet initiates hydrogen-air mixture combustion. The hydrogen mass fraction is considerably reduced in the period of 20–30ºCA ATDC with the flame front moving, whereas the remaining diesel fuel is burned via a diffusion combustion approach.

4. CONCLUSIONS

This study employed CFD modelling to investigate the impact of hydrogen use in a large marine dual-fuel engine, considering hydrogen port injection and a 20% hydrogen energy fraction. The engine performance and emission parameters were compared for diesel and dual-fuel modes. The developed CFD model was validated using

experimental data for the diesel mode. The study concluded the following.

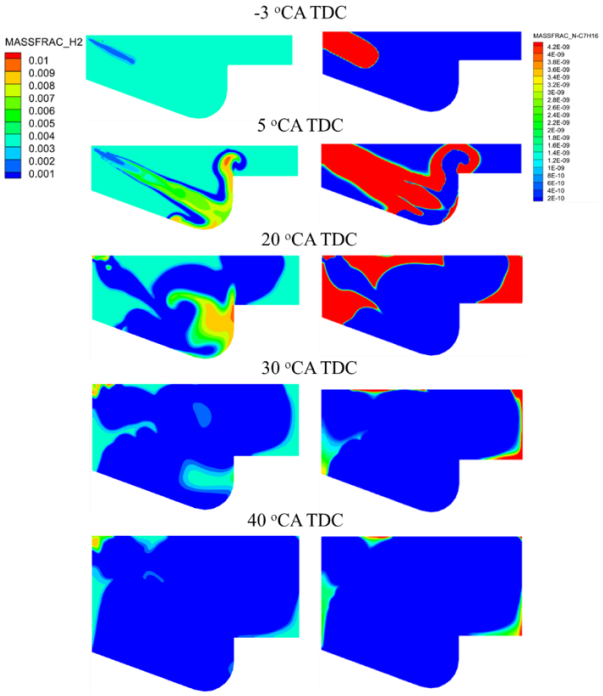

Figure 11. In-cylinder hydrogen and diesel mass fraction variations.

- Maximum in-cylinder pressure reduces from 136 bar to 100 bar due to CR reduction, whereas the CA at maximum pressure retards from 13.5°CA TDC in single fuel to 15.7°CA TDC, for the diesel and dual-fuel modes, respectively.
- The dual-fuel mode exhibits reduced ignition delay and a prolonged diffusion phase in the region 20–30°CA ATDC.
- Indicated thermal efficiency reduces by 2% as heat transfer losses increase under hydrogen operation.
- The hydrogen combustion efficiency was estimated at 93.7%, which indicates that measures to reduce unburnt hydrogen must be further investigated.
- NO_x emissions at the dual fuel mode increased by 260% due to higher in-cylinder temperature.
- The HRR analysis indicated that the premixed hydrogen combustion took place along the diesel diffusion combustion in the range 5–40°CA ATDC.

Future studies could focus on the optimisation of engine settings to accommodate contradicting effects and higher hydrogen energy fractions while maintaining knock-free conditions, minimising unburnt hydrogen, and reducing NO_x emissions, thereby simultaneously providing efficiency improvement and emissions reduction.

FUNDING STATEMENT

The study was carried out in the framework of the AUTOSHIP project (AUTOSHIP, 2022), which is funded by the European Union's Horizon 2020 research and innovation programme under agreement No 815012.

ACKNOWLEDGMENTS

The authors greatly acknowledge the funding from DNV AS and RCCL for the MSRC establishment and operation. The opinions expressed herein are those of the authors and should not be construed to reflect the views of EU, DNV AS and RCCL.

REFERENCES

[1] L. M. Wong, "Hydrogen as marine fuel–feasibility, prospects, and challenges," 2023.

[2] P. Karvounis, J. L. Dantas, C. Tsoumpris, and G. Theotokatos, "Ship Power Plant Decarbonisation Using Hybrid Systems and Ammonia Fuel—A Techno-Economic–Environmental Analysis," Journal of Marine Science and Engineering, vol. 10, no. 11, p. 1675, 2022.

[3] P. Karvounis, C. Tsoumpris, E. Boulougouris, and G. Theotokatos, "Recent advances for sustainable and safe marine engines operation with alternative fuels," Frontiers in Mechanical Engineering, vol. 8, 2022.

[4] P. Dimitriou and T. Tsujimura, "A review of hydrogen as a compression ignition engine fuel," International Journal of Hydrogen Energy, vol. 42, no. 38, pp. 24470-24486, 2017.

[5] J. Gao, X. Wang, P. Song, G. Tian, and C. Ma, "Review of the backfire occurrences and control strategies for port hydrogen injection internal combustion engines," Fuel, vol. 307, p. 121553, 2022.

[6] V. Kumar, D. Gupta, and N. Kumar, "Hydrogen use in internal combustion engine: A review," International Journal of Advanced Culture Technology, vol. 3, no. 2, pp. 87-99, 2015.

[7] A. Ritari, J. Huotari, and K. Tammi, "Marine vessel powertrain design optimization: Multiperiod modeling considering retrofits and alternative fuels," Proceedings of the Institution of Mechanical Engineers, Part M: Journal of Engineering for the Maritime Environment, p. 14750902221145747, 2023.

[8] S. Stoumpos, G. Theotokatos, E. Boulougouris, D. Vassalos, I. Lazakis, and G. Livanos, "Marine dual fuel engine modelling and parametric investigation of engine settings effect on performance-emissions trade-offs," Ocean Engineering, vol. 157, pp. 376-386, 2018.

[9] S. Verhelst and T. Wallner, "Hydrogen-fueled internal combustion engines," Progress in Energy and Combustion Science, vol. 35, no. 6, pp. 490-527, 2009.

[10] N. Castro, M. Toledo, and G. Amador, "An experimental investigation of the performance and emissions of a hydrogen-diesel dual fuel compression ignition internal combustion engine," Applied Thermal Engineering, vol. 156, pp. 660-667, 2019.

[11] P. Dimitriou and T. Tsujimura, "A review of hydrogen as a compression ignition engine fuel," International Journal of Hydrogen Energy, vol. 42, no. 38, pp. 24470-24486, 2017.
[12] "San Diego Mech, 2006," [Online]. Available: http://www.mae.ucsd.edu/combustion/cermech-21.
[13] L. M. Ricart, R. D. Reitz, and J. E. Dec, "Comparisons of diesel spray liquid penetration and vapor fuel distributions with in-cylinder optical measurements," J Eng Gas Turb Power, vol. 122, no. 4, pp. 588–95, 2000.
[14] Z. Y. Han, Z. Xu, and N. Trigui, "Spray/wall interaction models for multidimensional engine simulation," Int J Eng Res, vol. 1, no. 1, pp. 127–46, 2000.
[15] N. Nordin, "Complex chemistry modeling of diesel spray combustion," Ph.D. thesis, Chalmers University, 2001.
[16] A. M. Mellor, J. P. Mello, K. P. Duffy, W. L. Easley, and J. C. Faulkner, "Skeletal Mechanism for NOx Chemistry in Diesel Engines," SAE transactions, pp. 786-801, 1998.
[17] A. Rahimi, E. Fatehifar, and R. K. Saray, "Development of an optimized chemical kinetic mechanism for homogeneous charge compression ignition combustion of a fuel blend of n-heptane and natural gas using a genetic algorithm," Proceedings of the Institution of Mechanical Engineers, Part D: Journal of Automobile Engineering, vol. 224, no. 9, pp. 1141-1159, 2010.
[18] M. Dadashzadeh, S. Kashkarov, D. Makarov, and V. Molkov, "Risk assessment methodology for onboard hydrogen storage," International Journal of Hydrogen Energy, vol. 43, no. 12, pp. 6462-6475, 2018.

PROCEEDINGS OF MOSES2023 CONFERENCE
4TH INTERNATIONAL CONFERENCE ON MODELLING AND OPTIMISATION OF SHIP ENERGY SYSTEMS
26-27 OCTOBER 2023, DELFT, NETHERLANDS

Evaluation of Methanol Sprays in Marine Internal Combustion Engines: a Case Study for Port Fuel Injection Systems

Konstantinos Zoumpourlos[a,*], Andrea Coraddu[a], Rinze Geertsma[a,b], and Robert van de Ketterij[b]

[a]Delft University of Technology, Delft, Netherlands
[b]Netherlands Defence Academy, Den Helder, Netherlands
[*]k.zoumpourlos@tudelft.nl

Abstract

Methanol has emerged as a cost-effective and scalable alternative fuel for the maritime sector. However, the use of methanol in marine engines is limited by the unknown characteristics of methanol sprays when introduced through retrofitted port fuel injection (PFI) systems. The present study investigates the characteristics of methanol sprays under relevant conditions for marine engines, such as low injection pressure PFI. The primary objective of this research is to advance knowledge into key spray characteristics, including spray penetration, droplet size, atomization quality, and evaporation. The proposed methodology evaluates the efficacy of state-of-the-art computational fluid dynamics (CFD) models in simulating PFI marine engine spray conditions. Moreover, the study compares the performance of the Kelvin-Helmholtz (KH-RT) and Taylor Analogy Breakup (TAB) droplet breakup models under low injection pressure conditions. The results demonstrated that the KH-RT model does not predict any droplet breakup occurrence suggesting that the TAB model is more suitable for the given conditions. Furthermore, the liquid penetration of the spray was observed to align with the outcomes reported in previous experimental literature on methanol sprays. Nevertheless, the droplet sizes for low pressure injectors appear relatively large, indicating poor spray atomization, which impedes rapid evaporation and increases the risk of wall wetting in the inlet manifold and combustion chamber.

Keywords: Methanol; Internal Combustion Engine; Computational Fluid Dynamics; Spray Penetration; Droplet Size; Atomization Quality; Evaporation.

1 INTRODUCTION

Increased greenhouse gas emissions from the maritime industry contribute to climate change [1]. These emissions are mostly produced during the combustion of fossil fuels in internal combustion engines (ICEs) that are used for power and propulsion [2]. To address this issue, there is a growing need to shift towards sustainable energy solutions, such as electrified propulsion [3], [4]. However, most of these energy solutions are not yet mature enough for implementation at a scale due to their low energy density and range limitation, therefore enlarging the reliance on ICEs [3], [5], [6]. Hence, to reduce emissions, leveraging alternative fuels is urgent to decarbonize ICE-powered vessels [7], [8].

Methanol is identified as a potential alternative fuel for the maritime sector, demonstrating scalable production, adequate properties, and low cost [9], [10]. Moreover, the integration of methanol in state-of-the-art marine ICEs is achieved through different injection strategies, namely port fuel injection (PFI) and direct injection (DI) [9], [11]. Among these techniques, PFI systems are commonly favored in the maritime sector as an easy retrofitting solution for existing natural gas and diesel engines [9], [12]. These systems introduce fuel into the engine's intake manifold and are preferred because of their affordability and simple installation process [9].

However, integrating methanol into marine ICEs presents a significant challenge owing to its high latent heat of vaporisation [9]. Compared to diesel, methanol exhibits nearly half the lower heating value, adding another degree of complexity to its integration [11], [13], [14]. Consequently, longer injection duration and increased mass quantities are required to achieve the same power output. In addition, operation under PFI conditions is limiting because of the unknown characteristics of methanol sprays [9]. Therefore, a thorough understanding of methanol's injection and evaporation process is crucial for comprehending its combustion characteristics and emissions.

This study examines the impact of methanol PFI

@2023 Zoumpourlos et. al. published by TU Delft OPEN Publishing on behalf of the authors. Licensed under a Creative Commons Attribution CC BY license.
DOI: https://doi.org/10.59490/moses.2023.655

systems on spray characteristics and evaporation. The methodology involves computational fluid dynamics (CFD) modeling, with validation from dedicated spray experiments under PFI conditions [15]. Moreover, the efficacy of state-of-the-art spray models was evaluated, leading to selecting of the most appropriate droplet breakup and turbulence models. Particularly, under PFI conditions, the droplet interactions with the surrounding ambient air differ significantly from DI sprays. This differentiation arises from the fact that the ambient pressure and temperature conditions impose less intensive interactions between the liquid spray and the ambient air. Hence, using CFD, methanol spray behaviour in PFI conditions can be studied and analyzed in detail.

The paper is structured as follows. Section 2 provides a concise overview of the literature and the problem related to low-pressure methanol PFI sprays. In Section 3, the CFD numerical methodology is described in detail. Furthermore, Section 4 presents the experimental conditions on which the model is based, including information on the initial and boundary conditions and the employed computational mesh. The comparison of turbulence and breakup models, along with relevant discussions on the performance of each model, is presented in Section 5. Finally, Section 6 provides the conclusions drawn from the study.

2 PROBLEM STATEMENT & RELATED WORK

The phase transition process of methanol presents unique thermodynamic properties, necessitating an elevated amount of thermal energy for evaporation compared to traditional fuels. This phenomenon is attributable to its significantly higher latent heat of vaporization: $h_{lg,MeOH} \approx 4 \cdot h_{lg,Diesel}$ as reported in [9]. Considering also methanol's lower heating value being half that of diesel, approximately eight times the amount of thermal energy is required for complete evaporation while maintaining the same power output. Experimental research in this domain has been predominantly confined to DI conditions, which are characterized by high ambient and injection pressures, along with high temperature [16]–[19]. Particularly, these experimental efforts have tried to characterize spray parameters such as penetration length, cone angle and vapor penetration under these conditions. Consequently, a knowledge gap exists on the behavior of methanol sprays at inlet manifold conditions, predominantly characterized by near atmospheric ambient conditions coupled with low injection pressures. Further research is required to fill this gap, which would contribute to a better understanding of the fuel-air mixture formation process in methanol engines.

Previous research on conventional fuels demonstrated that certain spray sub-models and boundary conditions such as the liquid droplet breakup model, the turbulence model [20]–[22], and the mass Rate Of Injection (ROI) [23] significantly affect the transient response of the spray. However, under low injection pressure, it is still unclear whether the state-of-the-art models can accurately predict spray penetration and droplet breakup.

A factor that is greatly affecting the breakup behavior of the droplets is the Weber (We) number, which is the ratio of the aerodynamic drag force imposed from the ambient air onto the droplet and the droplet surface tension force [24]:

$$\mathrm{We} = \frac{\rho_g u^2 r_d}{\sigma} \tag{1}$$

where ρ_g is the ambient air density, u is the droplet velocity, r_d is the droplet radius, and σ is the droplet surface tension. Since the Weber number of low injection pressure sprays is significantly lower than in high pressure sprays, the droplet surface tension significantly impacts the liquid breakup submodel and, therefore, the liquid penetration [25], [26]. Hence, this research aims to investigate the influence of the Taylor Analogy Breakup (TAB) model [24], which is recommended for low Weber number droplets in the vibrational breakup mode [27]. Consequently, the TAB model was compared with the Kelvin Helmholtz - Rayleigh Taylor (KH-RT) model [28], which is widely adopted in DI spray research.

3 NUMERICAL SETUP

This computational study employed the commercial CONVERGE v3.0 CFD code [29], which contains a framework for the numerical analysis of multiphase flow studies. The framework utilizes the finite volume approach to solve the compressible conservation equations of mass, momentum, and energy, coupled with a variable time-step control algorithm based on the Courant-Friedrichs-Lewy (CFL) criterion [30]–[32]. The conservation of mass, momentum, and energy are formulated according to Equations 2, 3, and 5 respectively:

$$\frac{\partial \rho}{\partial t} + \frac{\partial (\rho u_i)}{\partial x_i} = 0 \tag{2}$$

$$\frac{\partial(\rho u_i)}{\partial t} + \frac{\partial}{\partial x_j}[\rho u_i u_j + P\delta_{ij} - \sigma_{ij}] = 0 \quad (3)$$

where σ is the viscous stress tensor

$$\sigma_{ij} = \mu(\frac{\partial u_i}{\partial x_j} + \frac{\partial u_j}{\partial x_i}) + (\mu_\nu - \frac{2}{3}\mu)\frac{\partial u_k}{\partial x_k}\delta_{ij} \quad (4)$$

$$\frac{\partial(\rho e_0)}{\partial t} + \frac{\partial}{\partial x_j}[\rho u_j e_0 + u_j P - K\frac{\partial T}{\partial x_j} - u_i\sigma_{ij} - \rho\sum_m D_m h_m \frac{\partial Y_m}{\partial x_j}] = 0 \quad (5)$$

where the total specific energy is $e_0 \equiv e + \frac{u_k u_k}{2}$, ρ is the fluid density, u is the velocity in each axis, P is the pressure, μ is the viscosity, μ_ν is the dilatational viscosity (set to zero), δ_{ij} is the Kronecker delta, T is the temperature, K is the thermal conductivity, m are the species, Y_m is the mass fraction of species, D_m is the species mass diffusion coefficient, and h_m is the species specific enthalpy.

Moreover, the density-based solver [30] was utilized using the Pressure Implicit with Splitting of Operators (PISO) method [33]. The fluids comprising the simulation, including air and methanol, were modeled based on the Redlich-Kwong equation of state [34]. Finally, the simulations were run in parallel utilizing the DelftBlue supercomputer [35] with the Message Passing Interface (MPI) [36]. An advantageous feature of CONVERGE is its scalability to many cores, resulting in a substantial acceleration in the solution process [30].

Regarding turbulence modeling, the present study employed the RNG and the Standard $k-\epsilon$ turbulence models in the modeling process [37]. Those $k-\epsilon$ models are based on the Reynolds-Averaged-Navier-Stokes (RANS) equations which approximate the velocity field as a summation of a mean and a fluctuating velocity ($u = \bar{u} + u'$). The result of this assumption generates a turbulence induced Reynolds-stress tensor in the Navier-Stokes equations. Resolving the stress tensor leads to modeling two additional transport equations accounting for the turbulent kinetic energy (k), and the rate of dissipation of turbulent kinetic energy (ϵ) [32], [38]. The transport equations for k and ϵ are as follows [30]

$$\frac{\partial(\rho k)}{\partial t} + \frac{\partial(\rho u_i k)}{\partial x_i} = \tau_{ij}\frac{\partial u_i}{\partial x_j} + \frac{\partial}{\partial x_j}\frac{\mu + \mu_t}{Pr_k}\frac{\partial k}{\partial x_j} - \rho\epsilon \quad (6)$$

and

$$\frac{\partial(\rho\epsilon)}{\partial t} + \frac{\partial(\rho u_i \epsilon)}{\partial x_i} = \frac{\partial}{\partial x_j}\left(\frac{\mu + \mu_t}{Pr_\epsilon}\frac{\partial \epsilon}{\partial x_j}\right) + C_{\epsilon 3}\rho\epsilon\frac{\partial u_i}{\partial x_i} + (C_{\epsilon 1}\frac{\partial u_i}{\partial x_j}\tau_{ij} - C_{\epsilon 2}\rho\epsilon)\frac{\epsilon}{k} - \rho R_\epsilon \quad (7)$$

where ρ is the fluid density, u is the velocity in each axis, τ_{ij} is the modeled Reynolds stress, μ is the viscosity, μ_t is the turbulent viscosity, Pr is the Prandtl number, $C_{\epsilon 1}, C_{\epsilon 2}$, and $C_{\epsilon 3}$ are turbulence model parameters.

Additionally,

$$k = \frac{1}{2}\overline{u_i' u_i'}, \quad (8)$$

$$\mu_t = C_\mu \rho \frac{k^2}{\epsilon}, \quad (9)$$

and

$$R_\epsilon = \frac{C_\mu \eta^3(1 - \eta/\eta_0)}{1 + \beta\eta^3}\frac{\epsilon^2}{k} \quad (10)$$

where C_μ, η, η_0 and β are turbulence model parameters. For the Standard $k-\epsilon$ model the last term $R_\epsilon = 0$.

The Lagrangian Particle Tracking (LPT) technique was utilized for modeling the multiphase flow through a Lagrangian-Eulerian (LE) two-way coupling approach [39], [40]. The LPT technique treats the liquid droplets as Lagrangian particles tracked based on their position in the computational domain. On the contrary, the gaseous phase is treated using an Eulerian representation, which treats the flow parameters based on a fixed mesh grid. The coupling between the droplets and the surrounding gaseous medium is ensured through the exchange of momentum, energy (heat transfer), and mass (evaporation) [39]. In addition, various phenomenological sub-grid models are implemented to resolve the physical phenomena that occur in the sub-grid length scales [21], [39]. The sub-grid models account for a wide range of physical phenomena that occur during the life cycle of a droplet, starting from the initial injection from the nozzle until its complete evaporation.

The injection of parcels was performed using the Reitz and Diwakar [41] model, which assumes the initial discrete spherical droplets ('blobs') to be the same size as the nozzle diameter. The droplet breakup process was modeled using the KH-RT model, widely used in high pressure DI sprays [28], [42], [43]. The KH-RT model is based on two separate mechanisms that occur during the primary and secondary phases of the breakup of droplets.

Kelvin-Helmholtz hydrodynamic instabilities dominate the primary breakup phase, attributed to the unstable waves of the droplet-air interface [41]. Moreover, the secondary breakup is mainly caused by the aerodynamic drag force between the droplets and the air on the tip of the spray, attributed to Rayleigh-Taylor instabilities [41]. In addition, the TAB model was utilized, which assumes the droplet distortion and breakup to be proportional to a spring-mass-damper system [24]. Hence, the foundation of the model is based upon the analogy of the following parameters:

- Spring force $\cong$ Droplet surface tension
- External force $\cong$ Aerodynamic drag force
- Damping force $\cong$ Viscosity force

Consequently, droplet breakup occurs when the external aerodynamic force surpasses the droplet's internal forces from surface tension and viscosity. The two breakup models were compared and evaluated based on spray penetration and breakup occurrence.

The spray droplets interact through collisions and coalescence. The No Time Counter (NTC) algorithm [44] estimated the collisions between droplets, while the model of Post and Abraham [45] predicted the post-collision outcome, including bouncing, stretching, reflective separation, and coalescence. The droplet aerodynamic drag force was modeled using a dynamic drag model [46]. Lastly, the evaporation model is based on the Frossling correlation, assuming a uniform temperature distribution within each individual droplet [30], [47]. The correlation provides a link between the Reynolds (Re) and Schmidt (Sc) numbers with the Sherwood (Sh) number of the droplet. The Sherwood number quantifies the mass transfer rate from the droplet to the ambient environment playing a fundamental role in the evaporation process. Hence, the droplet radius rate of change is calculated as follows:

$$\frac{\mathrm{d}r_0}{\mathrm{d}t} = -\frac{\alpha_{spray}\rho_g D}{2\rho_l r_0} B_d Sh_d \qquad (11)$$

where r_0 is the initial drop radius, α_{spray} is a user-specified scaling mass transfer coefficient, D is the mass diffusivity, ρ_g and ρ_l are the gas and liquid densities respectively, and B_d is the fraction of vapour's mass fraction at the drop surface to the vapour mass fraction of the droplet. The Frossling correlation estimates the Sherwood number (Sh) as indicated by the following equation:

$$Sh_d = (2.0 + 0.6 {Re_d}^{\frac{1}{2}} Sc^{\frac{1}{3}}) \ln \frac{1 + B_d}{B_d} \qquad (12)$$

where Re_d is the droplet Reynolds number and Sc is the Schmidt number of air. The numerical models utilised in the computational study are summarised in Table 1.

Table 1: Numerical models

Physical Phenomena	Numerical Models
Fluid Flow	Navier Stokes, density-based solver [30]
Turbulence	RNG and Standard $k-\epsilon$ model [37]
Droplet Injection	Blob model [41]
Liquid Breakup	KH-RT model [28] & TAB model [24]
Droplet Drag Force	Dynamic Drag Model [46]
Droplet Collision	NTC model [44]
Droplet Coalescence	Post Collision Outcome model [45]
Droplet Evaporation	Frossling correlation-based model [30]

4 PORT FUEL INJECTION CONDITION STUDY

The employed numerical CFD study was based on the conditions reported in the experimental methanol PFI study by Liu, Chen, Su, *et al.* [15]. In their experiments, the authors utilized backlight imaging and high-speed photography to capture the spray morphology of methanol under low injection pressure conditions (constant $6\,\mathrm{bar}$ injection pressure). The study deployed a 14-hole injector with the intention of investigating the effect of varied ambient and fuel temperatures and ambient pressures on spray penetration. Based on their experimental study, Liu, Chen, Su, *et al.* [15] concluded that higher ambient and fuel temperatures result in faster evaporation time and larger penetration and cone angle.

4.1 Computational Study Initial & Boundary Conditions

The validation of the CFD model originates from the reported experimental spray penetration length under the $2\,\mathrm{bar}$ ambient air pressure and $25\,^{\circ}\mathrm{C}$ ambient air temperature condition [15]. Moreover, for the optimal performing model, a brief comparison of the $1\,\mathrm{bar}$ and $2.5\,\mathrm{bar}$ cases was conducted to demonstrate the robustness of the method. The selection of these ambient pressure conditions was closely related to the intake manifold conditions of turbocharged marine engines.

Detailed information about the initial conditions is presented in Table 2. The modeling included assumptions about the injected mass and nozzle di-

ameter, while the injector was modeled as a single-nozzle. These quantities have a significant influence on the spray structure and penetration. Therefore, their selection was conducted through trial and error resulting in a rational spray penetration prediction. Moreover, the order of magnitude of the values was in the context of automotive injection quantities and nozzle diameters [48]–[50]. The nozzle hydraulic characteristics were also tuned to match the experimental injection pressure.

Table 2: Low pressure PFI case conditions

Item	Value	Unit
Ambient Pressure	2	[bar]
Injection Duration	10	[ms]
Injection Pressure	6	[bar]
Injection Quantity (Assumed)	4.67	[mg]
Ambient Temperature	25	[°C]
Fuel Temperature	25	[°C]
Nozzle Diameter (Assumed)	0.15	[mm]
Nozzle Discharge Coefficient	0.87	[]

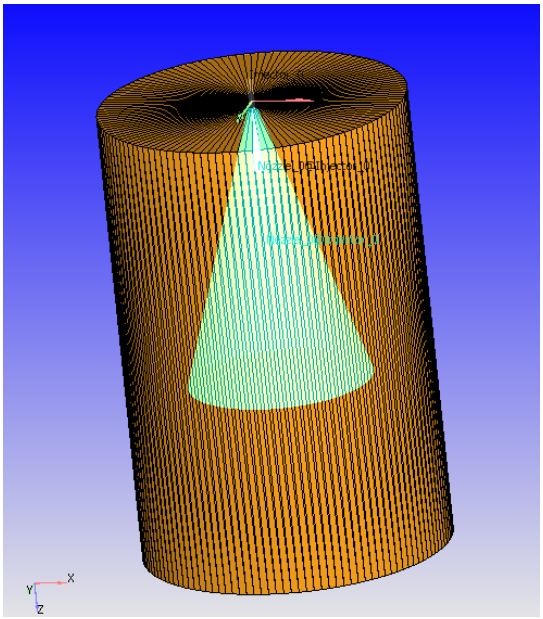

Figure 1: Simulation control volume

In this study, a cylindrical shaped control volume was adopted for the numerical computations (fig. 1) with a $60\,\mathrm{mm}$ radius and $180\,\mathrm{mm}$ height. The dimensions of the geometry were chosen in accordance with the literature of CFD spray studies for marine engines [20], [21]. The boundaries of the control volume were set as a wall-type condition with Neumann boundary conditions for the temperature and the turbulent kinetic energy. The numerical results considered 95% of liquid fuel mass fraction for calculating the liquid penetration. In the experiment, the liquid penetration was regarded as the vertical distance between the nozzle and the identified spray edge [15]. Moreover, the liquid penetration definition was slightly different between experimental and numerical data. However, the error in the comparison was sufficiently smaller than the other induced experimental uncertainties.

4.2 Mesh Convergence Study

A coarse mesh was employed with a uniform mesh grid having a base cell size of $4\,\mathrm{mm}$. The mesh grid was refined in the spray cone region to better resolve the flow field and the interactions between the droplets and the ambient air while keeping the overall cell count low for faster computation. As depicted in light green color in Fig. 1, the finer grid area encloses the cone of the spray area where the refinement was performed.

A grid convergence study was conducted for both turbulence models. Five different uniform cell sizes were tested for the spray cone area, ranging from $2\,\mathrm{mm}$ to $0.125\,\mathrm{mm}$. The liquid penetration length was monitored as the criterion for the convergence of the CFD model. The comparison with the liquid penetration results from the experiment showcased that the $0.5\,\mathrm{mm}$ grid was the most adequate for the study, aligning with spray-mesh guidelines from the literature [51]. Hence, the $0.5\,\mathrm{mm}$ grid was selected as the balanced trade-off for maintaining a grid-convergent and computationally viable mesh for the LE coupling.

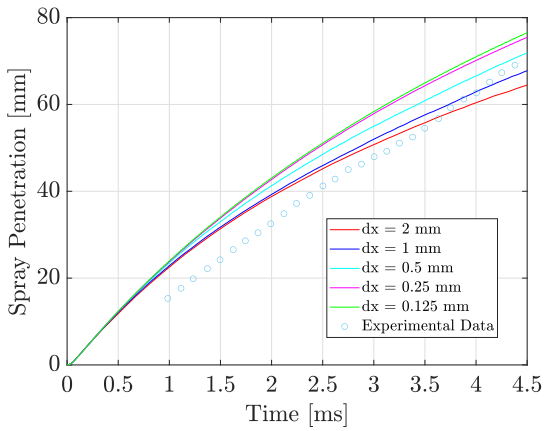

Figure 2: Grid convergence study

5 RESULTS & DISCUSSION

The comparison of the turbulence models demonstrated that the RNG $k-\epsilon$ is overpredicting spray penetration, aligning with the recommendations from diesel spray literature [20]. Therefore,

the Standard $k-\epsilon$ model coupled with the TAB liquid breakup model yielded reasonable predictions of the experimental liquid penetration values, accounting for the inherent uncertainties and unknowns in the experimental study (fig. 3).

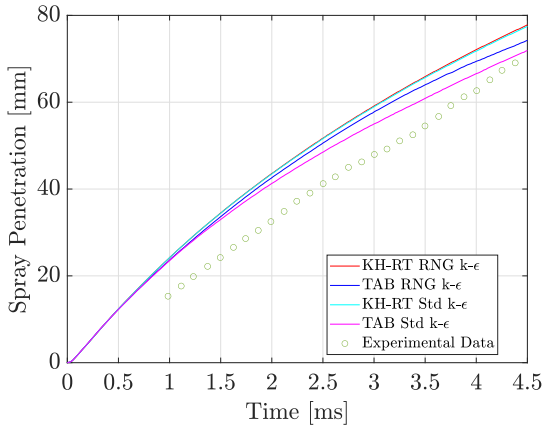

Figure 3: Influence of turbulence model & droplet breakup model on spray penetration

Moreover, in fig. 4, the coupling of the TAB model with the Standard $k-\epsilon$ turbulence model demonstrated satisfactory predicting capabilities for the other ambient pressures from the paper. However, accurately tuning the CFD model is impossible due to incomplete information on the reported experimental conditions. The primary objective of this study is to compare the droplet breakup model rather than assess the predictive capability of the numerical method. Therefore, the obtained computational results were considered rational for the scope of this research.

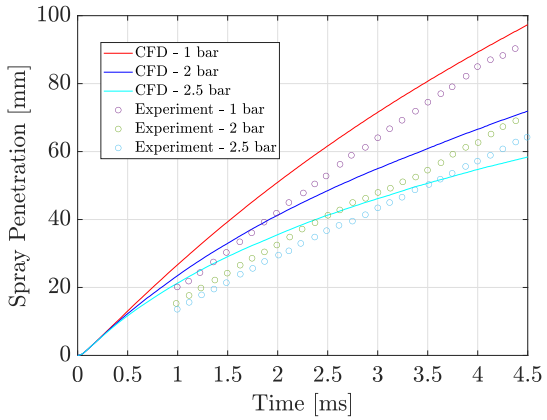

Figure 4: CFD model results for different ambient pressure conditions

5.1 Comparison of Droplet Breakup Model

In the section, the results considering the outcome of the droplet breakup model are demonstrated. Since there is a significant difference in the liquid penetration length between the TAB and the KH-RT models, this will greatly impact the resulting droplet sizes after breakup occurrence and, thus, the evaporation rate and the mixture fraction. Fig. 5 illustrates the Sauter Mean Diameter (SMD)[1], calculated for the entire spray structure, using each breakup model. The results indicate that the KH-RT model does not predict the occurrence of rational droplet breakup since the SMD remains approximately constant.

The opposite happened for the TAB model, demonstrating the presence of lower mean diameter length scales. Consequently, the higher SMD in the KH-RT model justifies the difference in the liquid penetration length due to the higher momentum of the larger droplets. It is also worth noting that the KH-RT model exhibited a slight increase in SMD due to droplet coalescence.

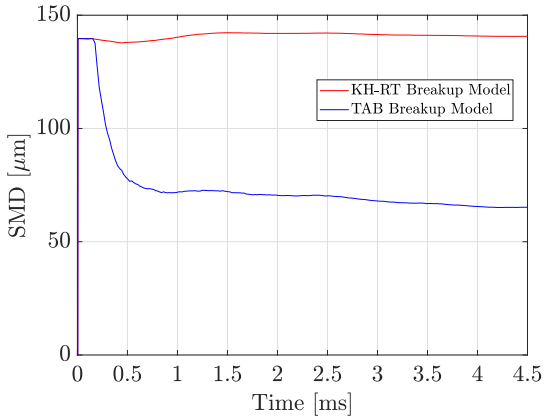

Figure 5: Comparison of Droplet Breakup Model (non evaporating conditions) - SMD

5.2 Evaporating Conditions

The conditions reported in this paper include a relatively low ambient temperature, which hinders spray evaporation. In this section, a set of higher ambient and fuel temperature conditions was examined to facilitate evaporation of the methanol spray (shown in Table 3).

[1]The SMD is interpreted as the diameter of a drop having the same volume to surface area ratio as the entire spray [52].

Table 3: Evaporating conditions

Item	Value	Unit
Ambient Temperature	100	[°C]
Fuel Temperature	80	[°C]

The previous study's adopted models were used to examine the performance of the KH-RT and TAB breakup models under evaporating condition. As before, the KH-RT model predicted higher liquid penetration length (fig. 6) due to diminished droplet breakup occurrence (fig. 7). This difference in penetration length was more pronounced due to the decreased evaporation rate of large droplets in the KH-RT case.

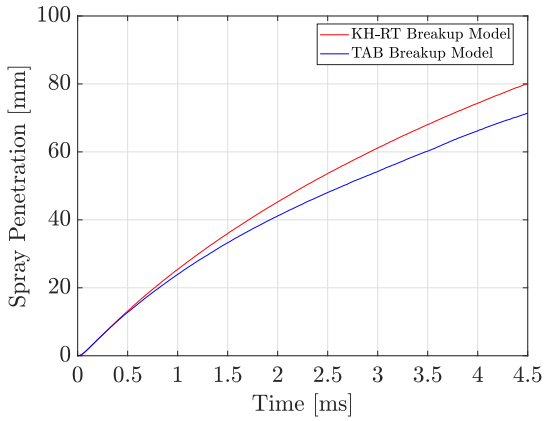

Figure 6: Comparison of Droplet Breakup Model (under evaporating conditions) - Spray Penetration

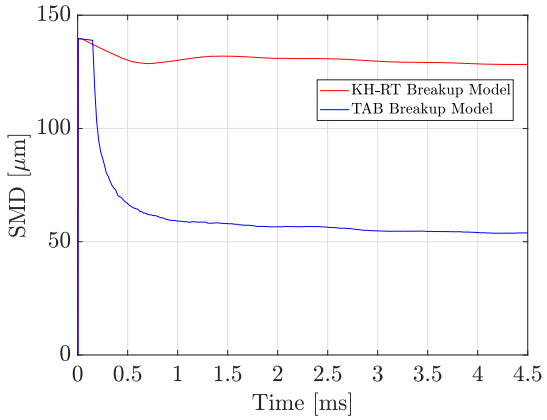

Figure 7: Comparison of Droplet Breakup Model (under evaporating conditions) - SMD

Figure 8 illustrates a comparison of 3D droplet diameters between the droplet breakup models. The plot displays the individual diameters of each particle in the computational domain. The comparison highlights the discrepancy in the SMD, with droplet sizes ranging from 120 µm to 160 µm for the KH-RT model. In contrast, the TAB model exhibits smaller droplet sizes ranging from 40 µm to 80 µm microns.

As mentioned before, the difference in the outcome particles after droplet breakup significantly influences the evaporation rate. Mass fraction contours illustrate the extent of methanol evaporation and mixing with the surrounding air. Fig. 10 confirms higher predicted mass fractions for the TAB case, supporting the initial hypothesis of evaporation prediction.

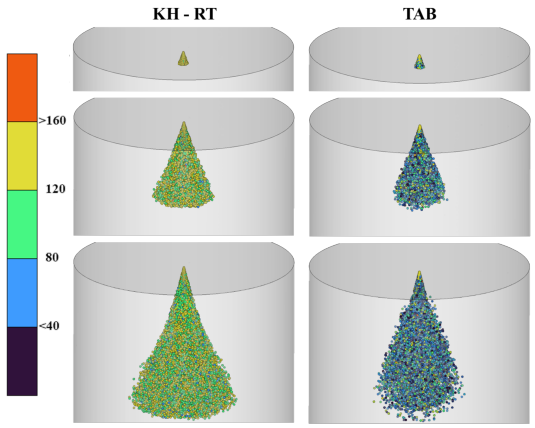

Figure 8: Droplet Diameter comparison, for $t = 0.27, 2, 4.5$ ms - Diameter in μm.

Furthermore, fig. 9 presents the total mass of evaporated methanol. This result emphasizes the importance of selecting the appropriate droplet breakup model for simulating low pressure PFI sprays.

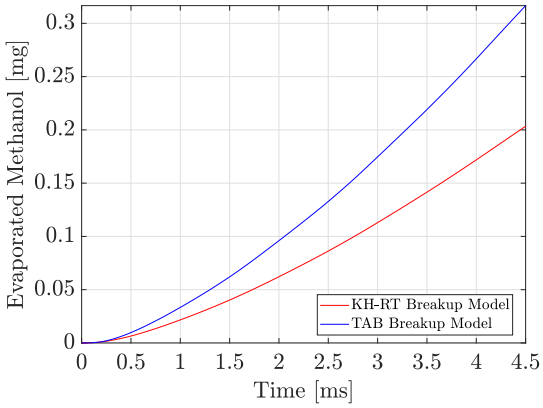

Figure 9: Comparison of Droplet Breakup Model (under evaporating conditions) - Evaporated Methanol

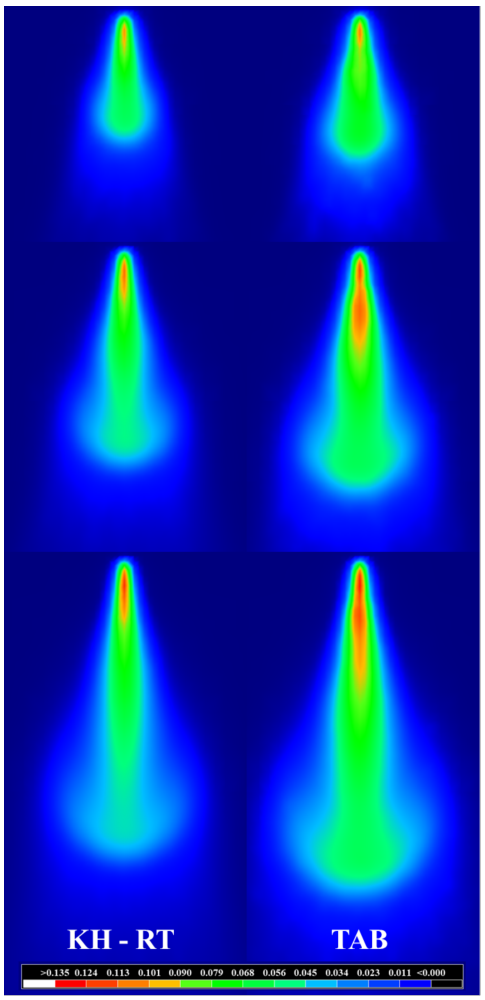

Figure 10: Methanol mass fraction contours plot - Comparison between KH-RT and TAB model, for $t = 1.5$, 3.0, and 4.5 ms.

Finally, examining the We number during the initial phase of the injection is crucial. According to O'Rourke and Amsden [24], the critical We number for vibrational breakup is 12. Therefore, it is important to maintain a value below this threshold for the TAB model's validity. Since the liquid jet is injected into an ambient environment with zero initial velocity, the drag force will naturally decelerate the droplets, resulting in a decrease in their We number. Consequently, the initial velocity of the "blobs" exiting the nozzle is the primary condition for selecting the appropriate breakup model. In fig. 11, the visualization of the We number confirms the rationality of choosing the TAB model.

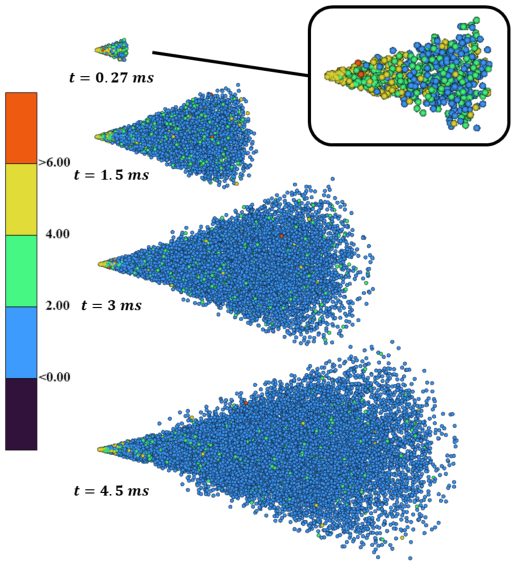

Figure 11: Weber number in TAB model injection

6 CONCLUSIONS

This study aimed to conduct a preliminary assessment of the impact of spray submodels on CFD spray predictions. The study examined the influence of the droplet breakup mechanism and the turbulence model under low injection pressure. The KH-RT and TAB models were compared, along with an investigation into the performance of the RNG and Standard $k - \epsilon$ turbulence models. The results demonstrated a satisfactory prediction of the spray penetration, consistent with experimental observations reported by Liu, Chen, Su, *et al.* [15]. This analysis provides a valuable initial step towards selecting appropriate models for maritime methanol PFI spray simulations. Therefore, the utilization of the TAB breakup model and the Standard $k - \epsilon$ model provided rational predictions for PFI conditions, which is in line with the previous findings in the literature [20], [25], [26]. This simulation step could be instrumental in shaping future studies in marine engines encompassing predictive CFD modeling to assess atomization quality and minimize wall wetting. Moreover, this study's predicted droplet sizes demonstrated poor spray atomization under low injection pressure in intake port conditions. Hence, the relatively large droplets hindered the evaporation process and increased risk of wall wetting of the inlet manifold.

In conclusion, this study highlights the importance of investigating spray submodels for PFI conditions. Understanding the specific droplet breakup mode is crucial for selecting an appropriate modeling technique that accurately captures the underlying physics. Specifically, in low-pressure PFI

sprays, the dominant breakup mode is characterized by droplet vibration, which can be effectively modeled using the TAB model. CFD analysis confirmed this by observing low Weber numbers indicating the prevalence of vibrational breakup. Additionally, the TAB model outperformed the KH-RT model in capturing breakup behavior under these conditions. However, further investigation is required to assess the limitations of the TAB model in PFI scenarios. This investigation should consider the critical Weber number and compare the droplet breakup regimes predicted by each model. Specifically, the evaluation should be conducted under modified droplet breakup regimes at higher injection pressures in PFI conditions. Lastly, appropriate experimental data, including spray images and SMD measurements, are necessary to sufficiently validate the proposed modeling approach.

ACKNOWLEDGEMENTS

The present research is part of the MENENS project (Methanol als Energiestap Naar Emissieloze Nederlandse Scheepvaart). The project is funded by the Netherlands Enterprise Agency (RVO: Rijksdienst voor Ondernemend Nederland). We would like to thank Convergent Science [29], and BETA CAE Systems [53] for offering their software (CONVERGE, ANSA & META) and their technical support for the accomplishment of this research. ANSA was used for geometry creation and pre-processing of the CFD model, CONVERGE for the CFD simulations, and META for post-processing and visualisation of the results.

REFERENCES

[1] *International Maritime Organization: Fourth Greenhouse Gas Study 2020*, 2020. [Online]. Available: https://www.imo.org/en/OurWork/Environment/Pages/Fourth-IMO-Greenhouse-Gas-Study-2020.aspx.

[2] D. G. Kessel, "Global warming—facts, assessment, countermeasures," *Journal of Petroleum Science and Engineering*, vol. 26, no. 1-4, pp. 157–168, 2000.

[3] L. C. Law, B. Foscoli, E. Mastorakos, and S. Evans, "A comparison of alternative fuels for shipping in terms of lifecycle energy and cost," *Energies*, vol. 14, no. 24, p. 8502, 2021.

[4] M. Perčić, N. Vladimir, and A. Fan, "Life-cycle cost assessment of alternative marine fuels to reduce the carbon footprint in short-sea shipping: A case study of Croatia," *Applied Energy*, vol. 279, Dec. 2020. (visited on 05/23/2022).

[5] R. D. Reitz, H. Ogawa, R. Payri, *et al.*, "IJER Editorial: The future of the internal combustion engine," *International Journal of Engine Research*, 2020. DOI: 10.1177/1468087419877990.

[6] C. J. McKinlay, S. R. Turnock, and D. A. Hudson, "Route to zero emission shipping: Hydrogen, ammonia or methanol?" *International Journal of Hydrogen Energy*, vol. 46, no. 55, pp. 28 282–28 297, 2021.

[7] M. Tuner, "Review and Benchmarking of Alternative Fuels in Conventional and Advanced Engine Concepts with Emphasis on Efficiency, CO2, and Regulated Emissions," *SAE Technical Papers*, 2016.

[8] A. Ait Allal, K. Mansouri, M. Youssfi, and M. Qbadou, "Toward an evaluation of marine fuels for a clean and efficient autonomous ship propulsion energy," *Materials Today: Proceedings*, vol. 13, pp. 486–495, 2019. (visited on 05/23/2022).

[9] S. Verhelst, J. W. Turner, L. Sileghem, and J. Vancoillie, "Methanol as a fuel for internal combustion engines," *Progress in Energy and Combustion Science*, vol. 70, pp. 43–88, Jan. 2019.

[10] A. D. Korberg, S. Brynolf, M. Grahn, and I. R. Skov, "Techno-economic assessment of advanced fuels and propulsion systems in future fossil-free ships," *Renewable and Sustainable Energy Reviews*, vol. 142, May 2021. (visited on 07/15/2022).

[11] J. Singh, A. Dhar, and P. Kumar, "Methanol Fuel in Compression Ignition Engines," in *Energy, Environment, and Sustainability*, Springer Nature, 2022, pp. 71–101. (visited on 05/19/2022).

[12] J. Dierickx, J. Verbiest, T. Janvier, J. Peeters, L. Sileghem, and S. Verhelst, "Retrofitting a high-speed marine engine to dual-fuel methanol-diesel operation: A comparison of multiple and single point methanol port injection," *Fuel Communications*, vol. 7, p. 10, 2021.

[13] B. Zincir and C. Deniz, "Methanol as a Fuel for Marine Diesel Engines," in *Energy, Environment, and Sustainability*, Springer Nature, 2021, pp. 45–85. (visited on 05/23/2022).

[14] M. Pipicelli, G. Di Luca, R. Ianniello, A. Gimelli, and C. Beatrice, "Alcohol Fuels in Compression Ignition Engines," in *Energy, Environment, and Sustainability*, Springer Nature, 2022, pp. 9–31.

[15] K. Liu, C. Chen, M. Su, *et al.*, "Experimental study of the macroscopic characteristics of methanol low-pressure injection spray," en, *International Journal of Energy Research*, er.8625, Aug. 2022. (visited on 11/01/2022).

[16] Y. Gong, S. Liu, and Y. Li, "Investigation on methanol spray characteristics," *Energy and Fuels*, vol. 21, no. 5, pp. 2991–2997, Sep. 2007.

[17] A. Matamis, S. Lonn, M. Tuner, O. Andersson, and M. Richter, "Optical Characterization of Methanol Sprays and Mixture Formation in a Compression-Ignition Heavy-Duty Engine,"

en, Sep. 2020, pp. 2020–01–2109. (visited on 09/01/2022).

[18] A. Ghosh, P. Boggavarapu, and R. V. Ravikrishna, "MEASUREMENT OF LIQUID AND VAPOR PENETRATION OF EVAPORATING METHANOL SPRAYS," *Atomization and Sprays*, vol. 30, no. 10, pp. 741–757, 2020.

[19] Y. Wang, P. Dong, W. Long, *et al.*, "Characteristics of Evaporating Spray for Direct Injection Methanol Engine: Comparison between Methanol and Diesel Spray," *Processes*, vol. 10, no. 6, p. 1132, Jun. 2022. (visited on 07/13/2022).

[20] H. Li, T. Beji, and S. Verhelst, "Improving the calculation of evaporating sprays for medium-speed marine-engine-like conditions," *Atomization and Sprays*, vol. 31, no. 8, 2021.

[21] N. Maes, N. Dam, B. Somers, T. Lucchini, G. D'Errico, and G. Hardy, "Experimental and numerical analyses of liquid and spray penetration under heavy-duty diesel engine conditions," *SAE International Journal of Fuels and Lubricants*, vol. 9, no. 1, pp. 108–124, 2016.

[22] R. Reitz *et al.*, "Modeling atomization processes in high-pressure vaporizing sprays," *Atomisation and Spray technology*, vol. 3, no. 4, pp. 309–337, 1987.

[23] L. M. Pickett, J. Manin, R. Payri, M. Bardi, and J. Gimeno, "Transient rate of injection effects on spray development," SAE Technical Paper, Tech. Rep., 2013.

[24] P. J. O'Rourke and A. A. Amsden, "The tab method for numerical calculation of spray droplet breakup," SAE Technical Paper, Tech. Rep., 1987.

[25] G. C. Papageorgakis and D. N. Assanis, "A spray breakup model for low injection pressures," *International communications in heat and mass transfer*, vol. 23, no. 1, pp. 1–10, 1996.

[26] F. Balduzzi, G. Vichi, L. Romani, *et al.*, "Development of a low pressure direct injection system for a small 2s engine. part i-cfd analysis of the injection process," *SAE International Journal of Engines*, vol. 8, no. 4, pp. 1885–1897, 2015.

[27] D. D. Joseph, J. Belanger, and G. Beavers, "Breakup of a liquid drop suddenly exposed to a high-speed airstream," *International Journal of Multiphase Flow*, vol. 25, no. 6-7, pp. 1263–1303, 1999.

[28] J. C. Beale and R. D. Reitz, "Modeling spray atomization with the kelvin-helmholtz/rayleigh-taylor hybrid model," *Atomization and sprays*, vol. 9, no. 6, 1999.

[29] *CONVERGE CFD Software Website*, 2023. [Online]. Available: `https://convergecfd.com/`.

[30] Convergent Science Inc, *CONVERGE MANUAL v3.0*. 2022.

[31] J. H. Ferziger, M. Perić, and R. L. Street, *Computational methods for fluid dynamics*. Springer, 2002, vol. 3.

[32] P. K. Kundu, I. M. Cohen, and D. R. Dowling, *Fluid mechanics*. Academic press, 2015.

[33] R. I. Issa, "Solution of the implicitly discretised fluid flow equations by operator-splitting," *Journal of computational physics*, vol. 62, no. 1, pp. 40–65, 1986.

[34] A. Horvath, "Redlich-kwong equation of state: Review for chemical engineering calculations," *Chemical Engineering Science*, vol. 29, no. 5, pp. 1334–1340, 1974.

[35] D. H. P. C. C. (DHPC), *DelftBlue Supercomputer (Phase 1)*, 2022. [Online]. Available: `https://www.tudelft.nl/dhpc/ark/delftbluephase1`.

[36] W. Gropp, E. Lusk, N. Doss, and A. Skjellum, "A high-performance, portable implementation of the mpi message passing interface standard," *Parallel computing*, vol. 22, no. 6, pp. 789–828, 1996.

[37] Z. Han and R. D. Reitz, "Turbulence modeling of internal combustion engines using rng κ-ε models," *Combustion science and technology*, vol. 106, no. 4-6, pp. 267–295, 1995.

[38] S. B. Pope and S. B. Pope, *Turbulent flows*. Cambridge university press, 2000.

[39] C. Baumgarten, *Mixture formation in internal combustion engines*. Springer Science & Business Media, 2006.

[40] S. Subramaniam, "Lagrangian–eulerian methods for multiphase flows," *Progress in Energy and Combustion Science*, vol. 39, no. 2-3, pp. 215–245, 2013.

[41] R. D. Reitz and R. Diwakar, "Structure of high-pressure fuel sprays," *SAE transactions*, pp. 492–509, 1987.

[42] H. Li, R. Verschaeren, G. Decan, and S. Verhelst, "Evaluation of breakup models for marine diesel spray simulations," in *29th Conference on Liquid Atomization and Spray Systems (ILASS-Europe 2019)*, Centre pour la Communication Scientifique Directe, 2020.

[43] R. D. Reitz, "Mechanism of breakup of round liquid jets," *Encyclopedia of fluid mechanics*, vol. 10, 1986.

[44] D. P. Schmidt and C. J. Rutland, "A new droplet collision algorithm," *Journal of Computational Physics*, vol. 164, no. 1, pp. 62–80, 2000.

[45] S. L. Post and J. Abraham, "Modeling the outcome of drop–drop collisions in diesel sprays," *International Journal of Multiphase Flow*, vol. 28, no. 6, pp. 997–1019, 2002.

[46] A. B. Liu, D. Mather, and R. D. Reitz, "Modeling the effects of drop drag and breakup on fuel sprays," *SAE Transactions*, pp. 83–95, 1993.

[47] R. Miller, K. Harstad, and J. Bellan, "Evaluation of equilibrium and non-equilibrium evaporation models for many-droplet gas-liquid flow simulations," *International journal of multiphase flow*, vol. 24, no. 6, pp. 1025–1055, 1998.

[48] T. Lucchini, G. D'Errico, D. Ettorre, and G. Ferrari, "Numerical investigation of non-reacting and reacting diesel sprays in constant-volume ves-

sels," *SAE International Journal of Fuels and Lubricants*, vol. 2, no. 1, pp. 966–975, 2009.

[49] *Engine Combustion Network Spray-G Conditions*, 2023. [Online]. Available: https://ecn.sandia.gov/gasoline-spray-combustion/target-condition/spray-g-operating-condition/.

[50] *Engine Combustion Network*, 2023. [Online]. Available: https://ecn.sandia.gov/.

[51] T. Lucchini, G. D'Errico, and D. Ettorre, "Numerical investigation of the spray–mesh–turbulence interactions for high-pressure, evaporating sprays at engine conditions," *International Journal of Heat and Fluid Flow*, vol. 32, no. 1, pp. 285–297, 2011.

[52] S. McAllister, J.-Y. Chen, A. C. Fernandez-Pello, S. McAllister, J.-Y. Chen, and A. C. Fernandez-Pello, "Droplet evaporation and combustion," *Fundamentals of Combustion Processes*, pp. 155–175, 2011.

[53] *BETA CAE Systems Website*, 2023. [Online]. Available: https://www.beta-cae.com/.

PROCEEDINGS OF MOSES2023 CONFERENCE
4TH INTERNATIONAL CONFERENCE ON MODELLING AND OPTIMISATION OF SHIP ENERGY SYSTEMS
26-27 OCTOBER 2023, DELFT, NETHERLANDS

A 0D Model for the Comparative Analysis of Hydrogen Carriers in Ship's Integrated Energy Systems

E.S. van Rheenen[a,*], J.T. Padding[a], and K. Visser[a]

[a]Delft University of Technology, Delft, The Netherlands
[*]E.S.vanRheenen@tudelft.nl

Abstract

Hydrogen carriers are attractive alternative fuels for the shipping sectors. They are zero-emission, have high energy densities, and are safe, available, and easy to handle. Sodium borohydride, potassium borohydride, dibenzyltoluene, n-ethylcarbazole, and ammoniaborane are interesting hydrogen carriers, with high theoretical energy densities. The exact energy density of these hydrogen carriers depends on the integration of heat and mass with the energy converters. This combination defines the energy efficiency and, thus, the energy density of the system. Using a 0D model, we combined the five carriers with two types of fuel cells (PEM and SOFC), an internal combustion engine and a gas turbine. This resulted in 20 combinations. Despite the limitations of the 0D model and the occasional difficulty of validating input values, this model still produces exciting findings, which are valuable for further research. For the dehydrogenation of both dibenzyltoluene and n-ethylcarbazole, an external hydrogen burner is required if no waste heat resources from the integrated system are available. For the borohydrides, on the other hand, energy integration is essential for reducing cooling power. Dehydrogenation produces substantial energy, but only a fraction of this energy can be used for internal preheating. Dehydrogenation of ammoniaborane produces less energy. Among all hydrogen carriers, both ammoniaborane and sodium borohydride provide energy densities comparable to that of marine diesel oil. In particular, ammoniaborane possesses a remarkably high energy density. Thus, we conclude, that hydrogen carriers are attractive alternative fuels that deserve more attention, including their potential performance for hydrogen imports.

Keywords: Alternative fuel; Energy analysis; Hydrogen carrier; Hydrogen generation.

1 INTRODUCTION

The shipping sector, which uses oil-based fuels, emits 3% of global greenhouse gases [1]. Currently, the sector is not on track to reach net-zero greenhouse gas emissions by 2050 [1], [2]. Alternative low- and zero-carbon fuels such as ammonia, methanol, LNG and hydrogen, are considered as convenient methods of reduction [3]. The diversity of ship types makes it impossible for a single alternative fuel to meet all of their requirements for now. Ammonia and methanol are toxic. Methanol and LNG still emit CO_2 and other harmful emissions, and LNG is a fossil fuel, making it unsustainable. Gaseous hydrogen has a low volumetric energy density and pure hydrogen is extremely flammable. However, hydrogen is the only fuel with zero-emission performance as it emits only water when used. The major issues with hydrogen, the low energy density and high flammability, can be resolved by storing hydrogen in hydrogen carriers.
Hydrogen carriers are liquid or solid substances that can store and release hydrogen when required. They store hydrogen by chemically bonding it or adsorbing it into their structure. Thus, no hydrogen gas is present onboard anymore. We previously identified five hydrogen carriers that meet the before-mentioned requirements: two liquid organic hydrogen carriers (LOHCs): N-ethylcarbazole (NEC) and dibenzyltoluene (DBT) and three boron-based carriers: $NaBH_4$, KBH_4, and ammoniaborane [4]. However, we only evaluated whether these hydrogen carriers comply with the requirements on a theoretical level. In contrast, the energy density of these hydrogen carriers depends on much more than just the theoretical energy density. Examples include packing factors, different densities depending on particle size and energy loss in the dehydrogenation process. Most research focuses only on LOHCs combined with fuel cells and is not in a maritime context [5]–[9]. Only one study, focusing on KBH_4 conducted an integration within a maritime context [10].
This study aims to obtain the practical density values of the previously identified hydrogen carriers when the dehydrogenation process is included. Our study will utilize a zero-dimension integration model of the five before-mentioned hydrogen carriers combined with four different energy converters to find

@2023 van Rheenen, E. S. et al. published by TU Delft OPEN Publishing on behalf of the authors. Licensed under a Creative Commons Attribution CC BY license.
DOI: https://doi.org/10.59490/moses.2023.669

the efficiency of the combinations. The practical energy density of the different hydrogen carrier and energy converter combinations follows from this efficiency. This contribution will give insight into which hydrogen carriers should be considered as alternative fuels in the maritime industry.

2 SELECTION OF HYDROGEN CARRIERS AND ENERGY CONVERTERS

Table 1: Theoretical volumetric and gravimetric energy densities of hydrogen carriers for explicit application onboard ships[4]

Carrier	MJ/kg	MJ/L
Ammoniaborane	23.52	14.4
$NaBH_4$ (hydrolysis)	25.56	27.34
KBH_4 (hydrolysis)	17.76	20.78
LOHC: NEC	6.98	6.63
LOHC: DBT	7.44	7.0
MDO	29	30

We consider five different hydrogen carriers, namely two LOHCs (DBT and NEC), two borohydrides ($NaBH_4$ and KBH_4) and ammoniaborane. These hydrogen carriers fulfil the aforementioned requirements to a certain extent. As energy converters, that is the machines that convert chemical energy into either electrical or mechanical energy, we consider four different types. On the one hand we look at conventionally used energy converters such as internal combustion engines (ICE) and gas turbines (GT) and on the other hand at innovative fuel cells, specifically solid oxide fuel cells (SOFC) and proton exchange membrane fuel cells (PEMFC).

2.1 Hydrogen carriers

In this section, we will give a very short description of the used hydrogen carriers (of which an overview including the energy densities can be seen in table 1) and specific properties that are needed to calculate the overall efficiency of a hydrogen carrier-energy converter system, such as the energy required for dehydrogenation. For a more thorough description of hydrogen carriers and the corresponding references, as well as more detailed selection criteria, we refer to [4].

2.1.1 LOHCs

DBT and NEC are chosen because DBT has one of the highest energy densities of LOHCs and NEC has a relatively low release temperature. LOHCs release hydrogen endothermically, at elevated temperatures. Equation 1 shows the general release mechanism of LOHCs.

$$\mathrm{LOHC^{+}} + \mathrm{Energy} \rightarrow \mathrm{LOHC^{-}} + \mathrm{H_2} \quad (1)$$

The exact release temperature depends on the LOHC and the corresponding catalyst. For DBT, the temperatures lie between 553 and 593K and, for NEC, the temperatures lie between 453 and 523K [8]. The dehydrogenation and decomposition temperatures of DBT are similar, requiring careful heat control and possible gaseous stream cleanup. Additionally, external heat may be required for complete dehydrogenation. NEC has better dehydrogenation kinetics [8], [11]. However, its spent fuel is solid at room temperature, requiring continuous heating until it enters the tank.

2.1.2 Borohydrides and ammoniaborane

Ammoniaborane, $NaBH_4$, and KBH_4 are solid powders with similar chemical properties at ambient conditions, including a high theoretical density and hydrogen release through hydrolysis. The release of hydrogen through hydrolysis with the borohydrides ($NaBH_4$ and KBH_4) is very similar, taking the example of $NaBH_4$:

$$\mathrm{NaBH_4} + (2+x)\mathrm{H_2O} \rightarrow 4\mathrm{H_2} + \mathrm{NaBO_2}.x\mathrm{H_2O} \quad (2)$$

The reaction is exothermic; energy is released during the dehydrogenation process and thus cooling is required. A drawback of borohydrides is that the spent fuel is heavier than the fuel. Because the weight of the spent fuel depends on the exact dehydrogenation reaction, it is not considered here.
The dehydrogenation mechanism of ammoniaborane is very similar, although it forms different products. Equation 3 describes the dehydrogenation reaction.

$$\mathrm{NH_3BH_3} + 3\mathrm{H_2O} \rightarrow 3\mathrm{H_2} + \mathrm{B(OH)_3} + \mathrm{NH_3} \quad (3)$$

However, next to the metaborate, the hydrolysis reaction also produces the toxic gas ammonia. This gas can either be burned in a heat engine, decomposed into N_2 and H_2 for use in a fuel cell or stored on board. The final option is considered impractical for ships because it requires a completely different, additional, storage system, significantly reducing the energy density of the system. This study disregards the second option (cracking) due to its complexity and additional space requirements. Thus, in this study, we will work with the resulting mixture of H_2 and NH_3 as input fuel for the energy converters when using ammoniaborane.

2.2 Energy converters

Energy converters are defined as devices that convert chemical energy into either electrical or mechanical energy. Ships typically use compression ignition ICEs, but these have challenges when using hydrogen as a single fuel due to its high auto ignition temperature. Thus, the sector is considering alternative energy converters, such as spark ignition ICE and fuel cells. We have identified four promising energy converters for the maritime sector: spark ignition ICEs, gas turbines (GTs), PEMFCs and SOFCs. Spark ignition ICEs are similar to current engines, while GTs have been used on ships previously due to their high power density [12]. Both can be run on alternative fuels such as hydrogen, and their high outlet temperatures make them suitable for heat integration. Fuel cells have gained attention because of their modularity and high efficiency. PEMFCs are low-temperature fuel cells that require pure hydrogen, whereas SOFCs operate at much higher temperatures and are less sensitive to poisoning. Both have high efficiencies, but only produce electricity, so an electrical conversion system is required.

3 MODEL

To assess the efficiency and thus the total energy density of the hydrogen carrier, we constructed a simplified 0D thermodynamic model. The electricity or mechanical energy produced in the energy converter is not converted to the same type of power output to keep the playing field as level as possible. Each energy converter converts energy the way they are the most efficient.

3.1 Endothermic model

Fig. 1 shows the basic model of an endothermic-release hydrogen carrier system. The system has an additional heat exchanger set that uses heat from the coolant, spent fuel, and exhaust to preheat the LOHC. Heat from the exhaust is used for the final preheating and dehydrogenation of the LOHC. If more heat is required, a hydrogen burner with an efficiency of 90% is used. The hydrogen required for the burner is tapped off before it reaches the energy converter.

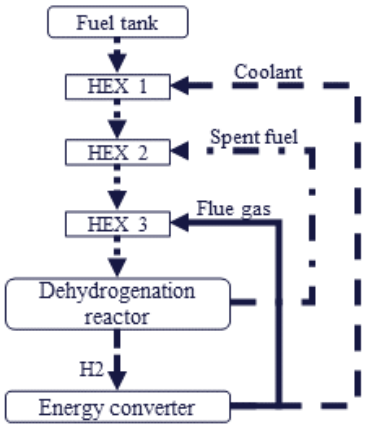

Figure 1: Simplified display of the endothermic model. HEX stands for heat exchanger

3.2 Exothermic model

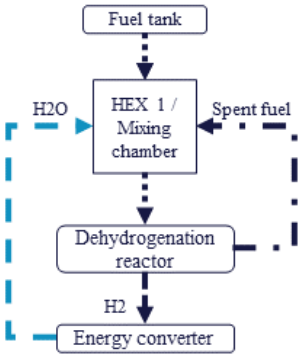

Figure 2: Simplified display of the exothermic model. HEX stands for heat exchanger

The exothermic model has a single heat exchanger that also serves as the mixing chamber. The heat exchanger is heated with the spent fuel, which has sufficient energy and also needs to be cooled down. Ammonia is poisonous to PEMFCs, therefore we do not consider this energy converter for ammonia-borane.

3.3 Input values for model

Table 2 gives an overview of the parameters used in the energy converter section of the model and table 3 shows the parameters used in the dehydrogenation reactor, preheating and mixing chamber sections of the model.

Table 2: Parameters of energy converters including sources.

Parameter	SI-ICE	PEMFC	SOFC	GT
T coolant [K]	363	348	0	0
P coolant [%]	30	44.8	0	0
P effective [%]	35	42.9	48	37.5
T flue gas [K]	623*	0	1023	790
P flue gas [%]	25	0	42.1	29
P losses [%]	10	12.3	9.9	33.5
Sources	[13]	[14]	[15]	[16], [17]

With P percentages of overall power distribution, mainly based on Sankey diagrams.
* Flue gas temperature of SI-ICE largely fluctuates depending on operating conditions and can range from 423 to 773K

Table 3: Parameters of hydrogen carriers

Parameter	DBT	NEC	$NaBH_4$	KBH_4	Ammoniaborane
Hydrogen yield per molecule of hydrogen carrier [-]	9	6	4	4	3
Molecular weight [g/mol]	290.54	207	37.8	53.94	30.8
Heat capacity fuel (pure) [kJ/kgK]	1.58	1.49	2.23	1.2	2.7
Heat capacity spent fuel (pure) [kJ/kgK]	1.49	1.50	0.6221	1.0512*	0.7937*
Dehydrogenation temperature [K]	573	503	333	333*	333*
Dehydrogenation energy [kJ/mol Fuel]	558	318	-210	-21	-220
Sources	[6], [18]	[19]–[21]	[22]–[24]	[25]	[26], [27]

Values denoted with * are estimated by the authors as no precise information was available

For the SOFC we have set the cooling to zero, as in the model this is treated as low-temperature cooling. SOFCs are air-cooled, at relatively high temperatures. This cooling is called "flue gas" in the model. For the overall heat capacity of mixtures, we calculate the heat capacity using the rule of mixtures. We assume 100% conversion. In instances where precise or accurate data was not available, estimated values were derived based on analogous processes or chemical structures.
Unfortunately, sources looking at ammonia-hydrogen dual-fuel options usually consider only a small amount of hydrogen and can thus not be directly used. However, no alterations are considered in terms of overall efficiencies or outlet temperatures for the mixture of ammonia and hydrogen compared to hydrogen only. This assumption is based on the substantial quantity of hydrogen present in the feed (75% mole fraction which contributes approximately 70% of the total energy) and the similarity of the efficiencies of hydrogen only and ammonia only [15], [28].

4 RESULTS AND DISCUSSION

This section provides an overview and a discussion of the results of the model. Subsection 4.1 provides a validation of the results, while subsection 4.2 gives an overview of the efficiency and distribution of energy of the whole cycle, including the dehydrogenation process. The hydrogen carrier quantity necessary for a 5000kW power output and its corresponding energy distribution are discussed in subsection 4.3. Additionally, subsection 4.4 gives an overview of required additional water to the system in the case of borohydrides, depending on the efficiency of the recycling system. Finally, subsection 4.5 gives the effective energy densities for each of the systems, compared to MDO, and subsection 4.6 discusses the limitations of the model and provides recommendations for further research.

4.1 Validation of results

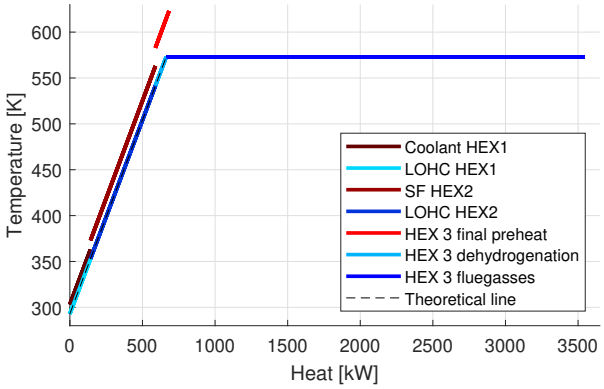

Figure 3: Pinch analysis of heat exchangers with DBT and ICE

To verify whether the results are physically possible, we performed a pinch analysis on each of the total heat-exchanging systems. Fig. 3 gives an example of such a pinch analysis. The pinch analysis shows the hot and cold flows, their temperatures and the amount of heat they contain. A physically possible process will never have the hot and cold flows cross within a pinch analysis, because the hot flows must always remain hotter than the cold flows for heat transfer to occur. Fig. 3 confirms that this is the case for the analyzed systems.

4.2 Energy efficiency analysis

The energy analysis, represented in Fig. 4 to 7 shows the energy distribution throughout the sys-

tem, organised per hydrogen carrier. These figures show the delivered power, energy in the coolant and in the flue gases, additional energy added through a burner and absolute or irrecoverable losses that are unavoidable.

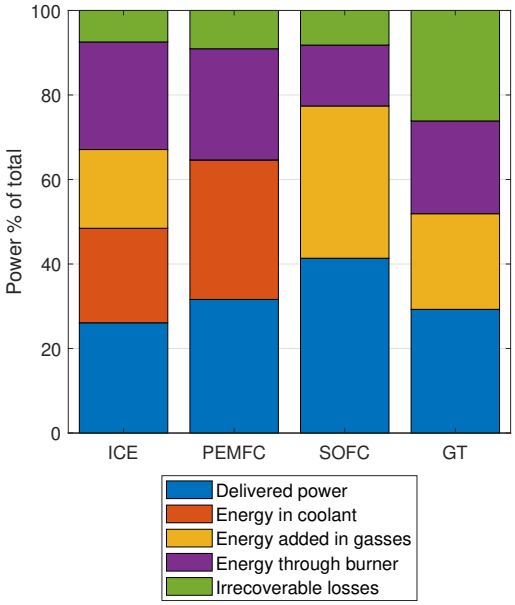

Figure 4: Efficiency and heat distribution as percentage of total available energy for DBT

Fig. 4 shows the LOHC DBT coupled to four different energy converters. Irrespective of the energy converter, an additional burner is always necessary when using DBT as a hydrogen carrier. As expected, the energy added through the burner is higher for systems operating at lower temperatures. A similar trend can be seen for NEC, (Fig. 5). However, the overall heating requirements are lower for NEC than for DBT, therefore, the amount of energy added through the burner is also lower. Even when using an SOFC or GT, a burner is still necessary to provide the heat required for the dehydrogenation process. Despite the higher heating requirements for DBT, the overall efficiency is still higher compared to NEC, due to the higher hydrogen content of DBT.

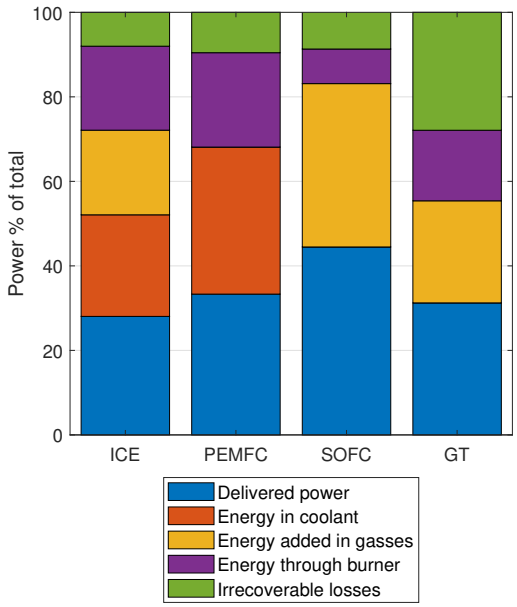

Figure 5: Efficiency and heat distribution as percentage of total energy for NEC

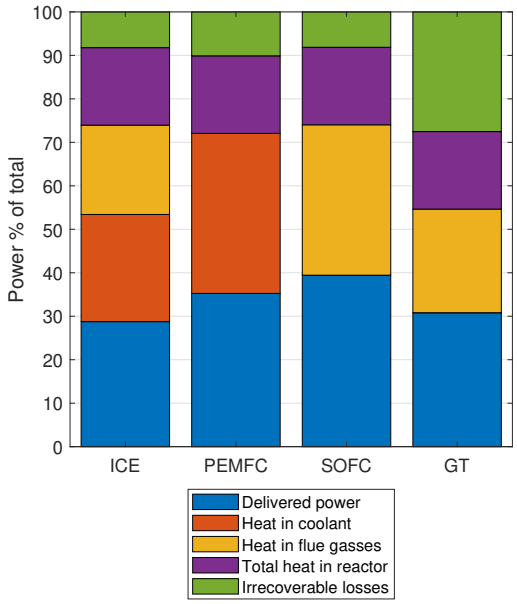

Figure 6: Efficiency and heat distribution as percentage of total energy for $NaBH_4$

The hydrolysis reaction of borohydrides produces additional energy, which can be used to preheat the fuel and reduce the external cooling requirements. To avoid overheating, the reactor must to be cooled constantly. It should be noted that the total heat in the reactor for both $NaBH_4$ and KBH_4 includes the premixing, dehydrogenation and spent fuel heat, and is reduced due to the preheating. Section 4.3 goes into more detail on this, but it is important to consider the cooling requirement when designing a system using borohydrides.

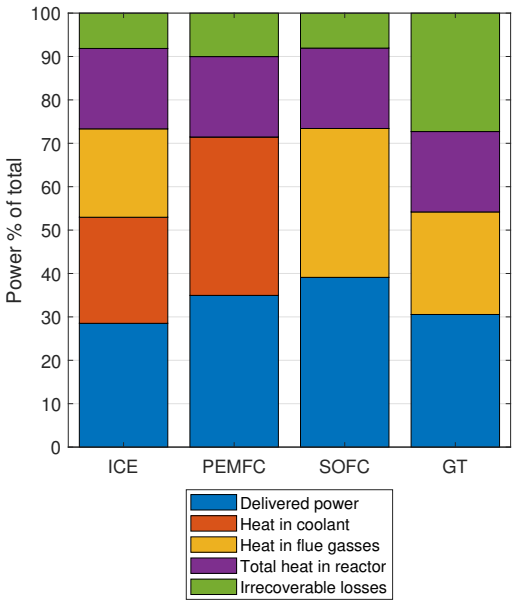

Figure 7: Efficiency and heat distribution as percentage of total energy for KBH_4

The heat produced in the reactor is percentage-wise less for ammoniaborane, compared to the heat produced in the coolant and the flue gases (see Fig. 8). The combination of NH_3 and H_2 produces more power in an absolute sense, thus reducing the relative heat produced by the reactor. The percentage of power that goes to useful power is significantly higher than that of $NaBH_4$ or KBH_4.

4.3 Detailed use of heat

Figs 9 to 12 show a detailed heat and power distribution, for a similar output power (5000kW). The resulting mass flows are listed in table 4.

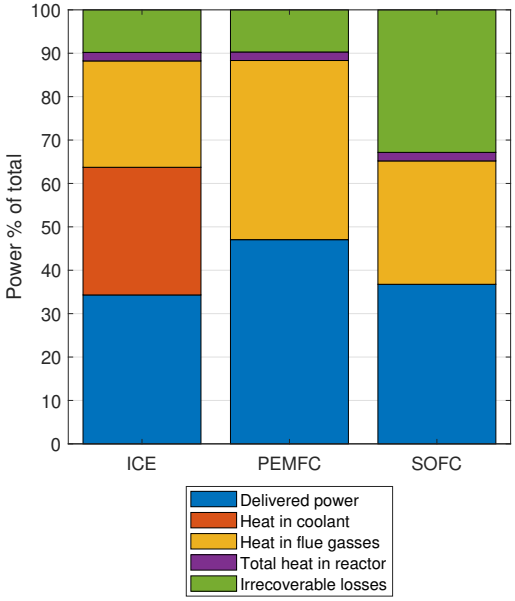

Figure 8: Efficiency and heat distribution as percentage of total energy for ammoniaborane

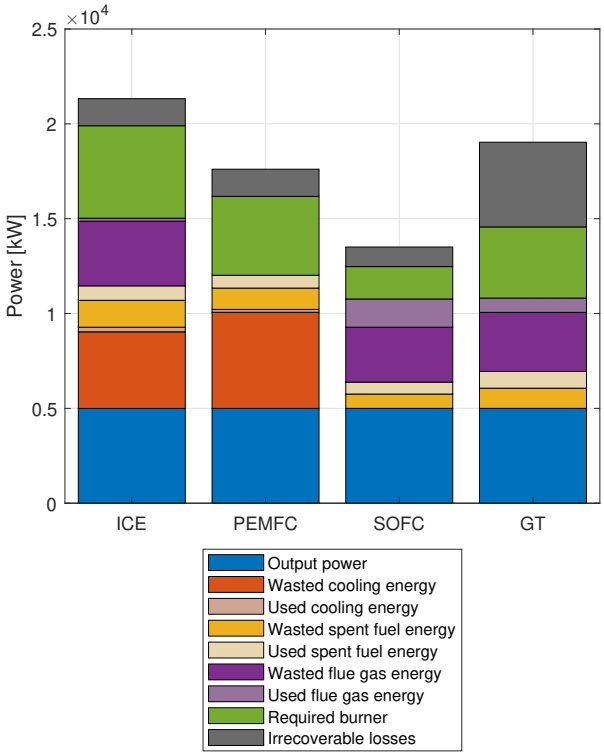

Figure 9: Detailed distribution of heat and energy in the whole system. Hydrogen carrier is DBT

Unused heat is often present in heat integration, although it is undesirable. Low-temperature heat is more difficult to use than high-temperature heat. Preheating relies on lower-temperature heat sources to make optimal use of these heat sources.

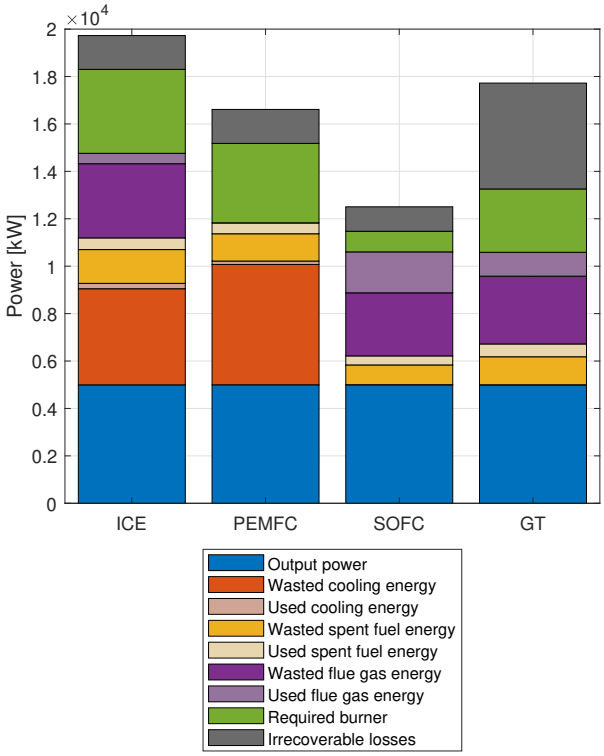

Figure 10: Detailed distribution of heat and energy in the whole system for NEC

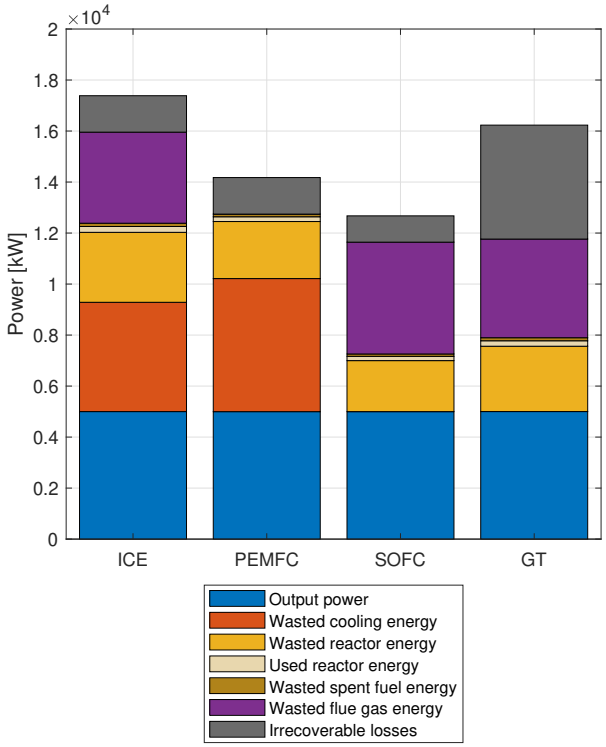

Figure 11: Detailed distribution of heat and energy in the whole system. The hydrogen carrier is $NaBH_4$

Figs 9 and 10 show the unused heat in coolants and flue gases. Flue gas heat is the only heat available for dehydrogenation, but not all of it can be used because it can only be cooled down to the dehydrogenation temperature.

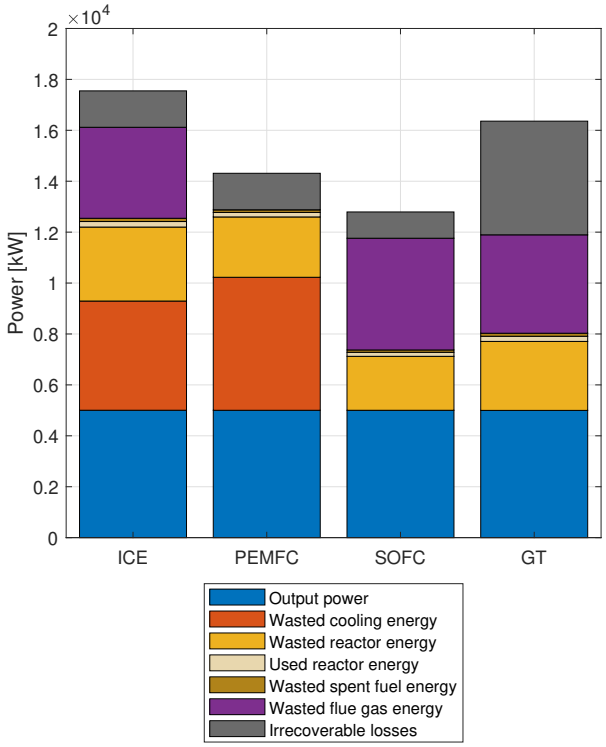

Figure 12: Detailed distribution of heat and energy in the whole system. The hydrogen carrier is KBH_4

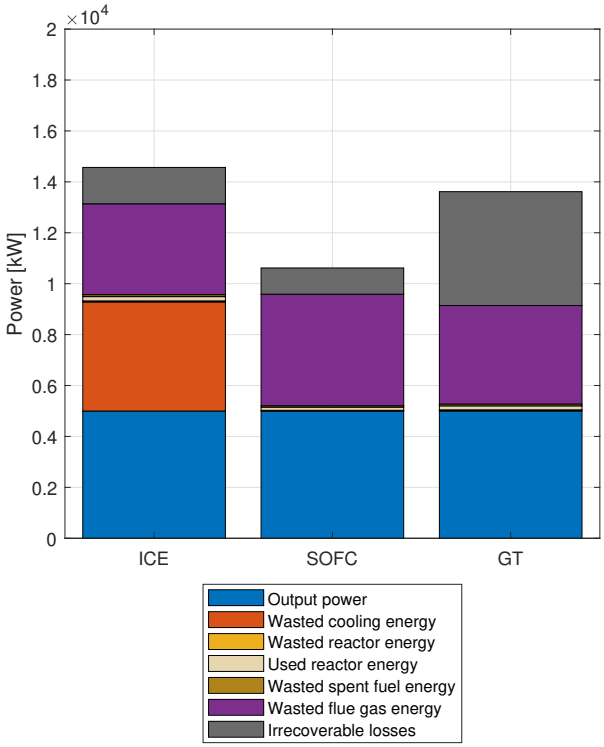

Figure 13: Detailed distribution of heat and energy in the whole system. The hydrogen carrier is ammoniaborane

Boron-based carriers yield higher power outputs. However, as only a small fraction of the reactor's energy can be used for preheating, active cooling is necessary, reducing the overall power output.
Table 4 shows the different mass flows required to reach the 5000kW. It is clear from this table that there is very little difference in the LOHCs, as the different energy densities are countered by the different dehydrogenation requirements. Additionally, $NaBH_4$ requires less mass flow than KBH_4, irrespective of the energy converter and ammoniaborane requires the least mass flow, with differences of up to 6 times less mass flow compared to the LOHCs.

Table 4: Mass flows [kg/s] required to to reach 5000kW output

Parameter	H2-ICE	PEMFC	SOFC	GT
DBT	2.56	2.11	1.62	2.28
NEC	2.54	2.14	1.61	2.82
$NaBH_4$	0.56	0.46	0.41	0.52
KBH_4	0.78	0.65	0.58	0.74
Ammoniaborane	0.42		0.30	0.39

4.4 Additional water requirements

The hydrolysis dehydrogenation reaction requires water. Theoretically, this water could be recycled from the outlet of the energy converter and

could satisfy the overall water requirements completely for all boron-based hydrogen carriers. However, as this recycling is most likely not 100%, we examined the amount of water required for different recycling rates. Fig. 14 shows the different recycling rates. For borohydrides, it is likely that an external pure water source is needed, because if the recycling is less than 100%, additional water is necessary. For ammoniaborane, however, this external water source is only necessary for less than 75% of water recycling. This is because the conversion of hydrogen and ammonia both result in water.

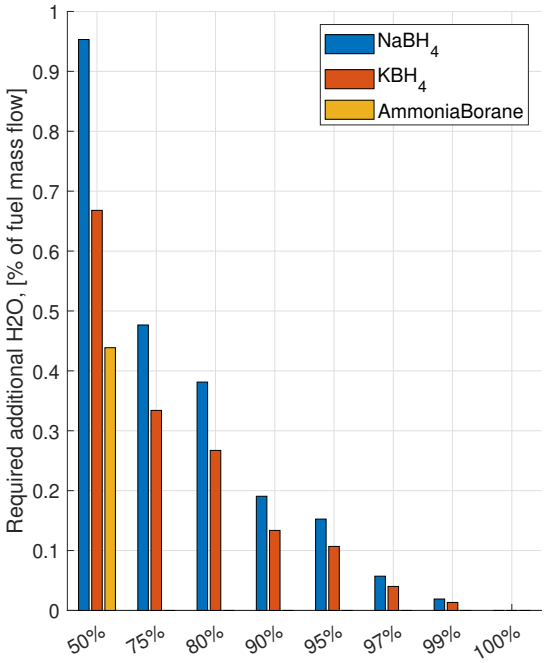

Figure 14: Effect of the water recirculation rate of water from exhaust gases on the amount of water that needs to be added to the system from an external source.

4.5 Effective energy density

Fig 15 shows the effective energy density of each fuel. The effective energy density is the amount of effective mechanical or electrical energy that can be taken out of 1 kg of fuel. This definition includes the energy converter, as heat and mass integration is necessary for the efficient use of hydrogen carriers. Additionally, from fig. 15, we can conclude that there is very little difference between the LOHCs after heat integration. This suggests that the choice of LOHC may not be as important as the efficiency of the energy converter. Fig 15 also highlights the high potential of $NaBH_4$ and ammoniaborane, as these can reach effective energy densities close to that of MDO.

4.6 Model limitations and further research

The current model provides a simplified, but well-founded, overview of the energy efficiency and density of the different combinations of hydrogen carriers and energy converters. This overview could be improved with more specific temperature and heat distributions of the energy converters, as well as by looking at load factors. These parameters largely depend on the operating conditions and the power requirements of ships, making them different for different ship types and different operational profiles.

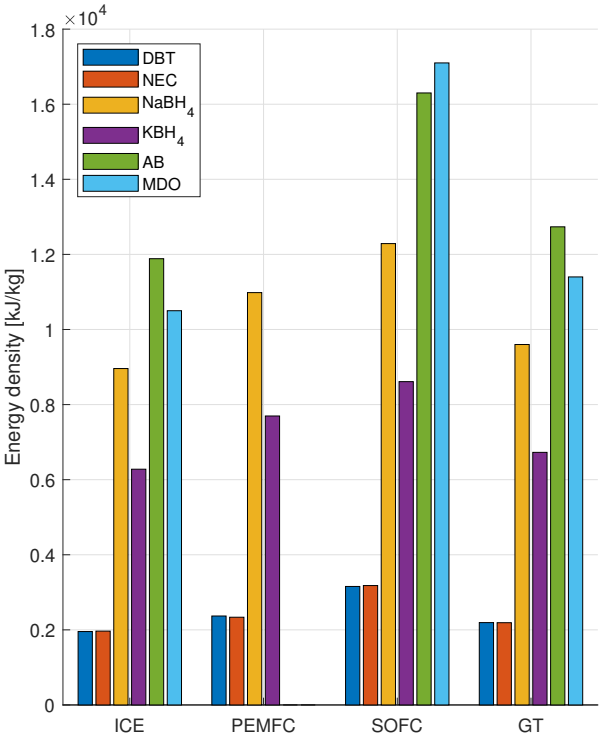

Figure 15: Effective energy density of hydrogen carriers compared to MDO for each of the energy converters. Data for MDO conversion from [15], [16]

In addition to the energy density, the power density is also important for all ships. To provide a more complete overview, the power density of each of the options should be evaluated. However, the technology readiness levels of the hydrogen carriers are not yet sufficient for this power density analysis. Besides power density, other properties of hydrogen carriers influence the possible use of fuel, such as safety, handling, availability and costs, the latter of which is closely related to the recycling process of the spent fuel.
Moreover, for borohydrides, the additional weight of the spent fuel must be considered. The spent fuel is much heavier (up to 3.7 times) than the original

fuel. To calculate the effective energy density regarding the weight and volume onboard a ship, the weight (and volume) difference should be taken into account.
The model can be enhanced for more detailed results. In the exothermic model, cooling of waste heat is currently not considered, even though cooling pumps will cost power. Using this waste heat for other purposes, such as co-generation or hotel loads can also enhance the energy efficiency of the system, particularly for boron-based carriers. Additionally, the cracking of ammonia could be considered. It would also add the PEMFC as an option for ammoniaborane. The endothermic model could be enhanced by optimizing the heat integration, as done in [7]. They demonstrated that a burner is not always necessary for endothermic hydrogen carriers. Thus, a better heat integration in our model would be advisable. However, all combined, the model provides a good first overview of the possibilities that hydrogen carriers and energy converters can provide.

5 CONCLUSION

The objective of this study was to evaluate the effective energy density of hydrogen carriers as alternative fuels. We accomplished this goal by examining the efficiency of the overall energy cycle when using alternative fuels. Our model can calculate different efficiencies in a simple, yet accurate manner, enabling us to draw conclusions on the efficiency and thus, on the practicability of hydrogen carriers.
The model consists of two main types, as the dehydrogenation process can be either endothermal or exothermal. However, this dehydrogenation process always requires either energy (in the form of heat) or mass (e.g. water). To determine the overall energy density of the system., we built a thermodynamic 0D model which integrates the heat and mass flows of the system. This model provided a first indication of the overall energy densities of five hydrogen carriers combined with four energy converters, which are as follows.
First, the high efficiency of the SOFC makes it a compelling energy converter, independent of the alternative fuel source. Of the hydrogen carriers, the following have the highest energy densities: $NaBH_4$ and ammoniaborane. Without taking the spent fuel into account, these energy densities are close to (and may in some cases, even surpass) the energy density of diesel. Although both LOHCs have lower energy densities, other characteristics may still make them interesting. KBH_4, on the other hand, is not as favourable as $NaBH_4$.
Our study highlights the importance of heat and mass integration of hydrogen carriers and energy converters for the overall energy density. Although the 0D model only provides estimates, it shows interesting findings, which should be investigated in more detail in future research. Hydrogen carriers can achieve overall energy efficiencies similar to those of conventional fuels, thereby considerably enhancing the attractiveness of more sustainable options.

ACKNOWLEDGEMENTS

This work was supported by the project SH2IPDRIVE, which has received funding from the Ministry of Economic Affairs and Climate Policy, RDM regulation, carried out by the Netherlands Enterprise Agency (RvO)

REFERENCES

[1] International Energy Agency, "International shipping," *Paris*, 2021, Accessed on 22nd June 2022. [Online]. Available: `https://www.iea.org/reports/international-shipping`.

[2] IMO, *Revised ghg reduction strategy for global shipping adopted*, `https://www.imo.org/en/MediaCentre/PressBriefings/pages/Revised-GHG-reduction-strategy-for-global-shipping-adopted-.aspx`, 2023.

[3] M. D. Kass, C. S. Sluder, and B. C. Kaul, "Spill behavior, detection, and mitigation for emerging nontraditional marine fuels," 2021.

[4] E. Van Rheenen, J. T. Padding, J. C. Slootweg, and K. Visser, "A review of the potential of hydrogen carriers for zero emission, low signature ship propulsion systems," *Conference Proceedings of INEC*, Nov. 2022.

[5] L. Li, P. V. Aravind, T. Woudstra, and M. van den Broek, "Assessing the waste heat recovery potential of liquid organic hydrogen carrier chains," *Energy Conversion and Management*, vol. 276, p. 116 555, Jan. 2023.

[6] S. Lee, T. Kim, G. Han, *et al.*, "Comparative energetic studies on liquid organic hydrogen carrier: A net energy analysis," *Renewable and Sustainable Energy Reviews*, vol. 150, Oct. 2021.

[7] P. Preuster, Q. Fang, R. Peters, *et al.*, "Solid oxide fuel cell operating on liquid organic hydrogen carrier-based hydrogen – making full use of heat integration potentials," *International Journal of Hydrogen Energy*, vol. 43, pp. 1758–1768, 3 Jan. 2018.

[8] M. Niermann, A. Beckendorff, M. Kaltschmitt, and K. Bonhoff, "Liquid organic hydrogen carrier (lohc) – assessment based on chemical and economic properties," *International Journal of Hydrogen Energy*, vol. 44, pp. 6631–6654, 13 Mar. 2019.

[9] K. Müller, S. Thiele, and P. Wasserscheid, "Evaluations of concepts for the integration of fuel cells in liquid organic hydrogen carrier systems," *Energy and Fuels*, vol. 33, pp. 10 324–10 330, 10 Oct. 2019.

[10] A. Düll, P. Rohlfs, O. Deutschmann, and M. Börnhorst, "Performance evaluation of kbh4 as energy carrier for shipping applications," *Chemie Ingenieur Technik*, vol. 94, pp. 747–759, 5 May 2022.

[11] R. Peters, R. Deja, M. Engelbracht, *et al.*, "Efficiency analysis of a hydrogen-fueled solid oxide fuel cell system with anode off-gas recirculation," *Journal of Power Sources*, vol. 328, pp. 105–113, Oct. 2016.

[12] A. Fatsis, "Gas turbine performance enhancement for naval ship propulsion using wave rotors," *Journal of Marine Engineering & Technology*, vol. 21, no. 5, pp. 297–309, 2022.

[13] X. Wang, B.-G. Sun, and Q.-H. Luo, "Energy and exergy analysis of a turbocharged hydrogen internal combustion engine," *International Journal of Hydrogen Energy*, vol. 44, pp. 5551–5563, 11 Feb. 2019.

[14] L. Zhao, J. Brouwer, S. James, *et al.*, "Dynamic performance of an in-rack proton exchange membrane fuel cell battery system to power servers," *International Journal of Hydrogen Energy*, vol. 42, no. 15, pp. 10 158–10 174, 2017.

[15] B. van Veldhuizen, L. van Biert, A. Amladi, T. Woudstra, K. Visser, and P. Aravind, "The effects of fuel type and cathode off-gas recirculation on combined heat and power generation of marine sofc systems," *Energy Conversion and Management*, vol. 276, p. 116 498, 2023.

[16] M. M. E. Gohary and I. S. Seddiek, "Utilization of alternative marine fuels for gas turbine power plant onboard ships," *International Journal of Naval Architecture and Ocean Engineering*, vol. 5, pp. 21–32, 1 Mar. 2013.

[17] D. M. Rosado, S. R. Chavez, and J. de Carvalho Jr, "Determination of global efficiency without/with supplementary burning of a thermoelectric plant with combined cycle of natural gas.," Oct. 2019.

[18] Y. Kwak, J. Kirk, S. Moon, *et al.*, "Hydrogen production from homocyclic liquid organic hydrogen carriers (lohcs): Benchmarking studies and energy-economic analyses," *Energy Conversion and Management*, vol. 239, p. 114 124, Jul. 2021.

[19] K. Stark, V. N. Emelyanenko, A. A. Zhabina, *et al.*, "Liquid organic hydrogen carriers: Thermophysical and thermochemical studies of carbazole partly and fully hydrogenated derivatives," *Industrial and Engineering Chemistry Research*, vol. 54, pp. 7953–7966, 32 Aug. 2015.

[20] K. Stark, P. Keil, S. Schug, K. Müller, P. Wasserscheid, and W. Arlt, "Melting points of potential liquid organic hydrogen carrier systems consisting of n-alkylcarbazoles," *Journal of Chemical and Engineering Data*, vol. 61, pp. 1441–1448, 4 Apr. 2016.

[21] D. Teichmann, K. Stark, K. Müller, G. Zoettl, P. Wasserscheid, and W. Arlt, "Energy storage in residential and commercial buildings via liquid organic hydrogen carriers (lohc)," *Energy Environ. Sci.*, vol. 5, pp. 9044–9054, Sep. 2012.

[22] J. Zhang, T. S. Fisher, J. P. Gore, D. Hazra, and P. V. Ramachandran, "Heat of reaction measurements of sodium borohydride alcoholysis and hydrolysis," *International Journal of Hydrogen Energy*, vol. 31, pp. 2292–2298, 15 Dec. 2006.

[23] Y. Kojima, "Hydrogen storage materials for hydrogen and energy carriers," *International Journal of Hydrogen Energy*, vol. 44, pp. 18 179–18 192, 33 Jul. 2019.

[24] L. Ye, D. Li, Y. P. Dong, B. Xu, and D. Zeng, "Measurement of specific heat capacity of nabo2(aq) solution and thermodynamic modeling of nabo2 + h2o, nabo2 + nacl + h2o, and nabo2 + na2so4 + h2o systems," *Journal of Chemical and Engineering Data*, vol. 65, pp. 2548–2557, 5 May 2020.

[25] L. Damjanović, S. Bennici, and A. Auroux, "A direct measurement of the heat evolved during the sodium and potassium borohydride catalytic hydrolysis," *Journal of Power Sources*, vol. 195, pp. 3284–3292, 10 May 2010.

[26] U. Sanyal, U. B. Demirci, B. R. Jagirdar, and P. Miele, "Hydrolysis of ammonia borane as a hydrogen source: Fundamental issues and potential solutions towards implementation," 2003.

[27] M. Chandra and Q. Xu, "Room temperature hydrogen generation from aqueous ammonia-borane using noble metal nano-clusters as highly active catalysts," *Journal of Power Sources*, vol. 168, pp. 135–142, 1 May 2007.

[28] C. Tornatore, L. Marchitto, P. Sabia, and M. de Joannon, "Ammonia as green fuel in internal combustion engines: State-of-the-art and future perspectives," *Frontiers in Mechanical Engineering*, vol. 8, p. 944 201, Jul. 2022.

Improved Control of Propeller Ventilation Based on POA-XGBoost and Ship Dynamics/Control Model

Shengping Ma [a*], **Yu Ding** [a], **Congbiao Sui** [a]

[a] Harbin Engineering University, Harbin, China
*mashengping@hrbeu.edu.cn

Abstract

Under adverse sea conditions, propeller ventilation caused by in-and-out water can decrease the reliability of the ship power grid and the lifespan of the propulsion shaft system. Predicting the development of propeller ventilation severity while identifying it can contribute to improving propeller ventilation control. In this study, the eXtreme Gradient Boosting (XGBoost) algorithm combined with a ship dynamics/control model is proposed as a propeller ventilation identification and prediction method. Meanwhile, the Pelican optimization algorithm (POA), particle swarm optimization (PSO), and genetic algorithm (GA) are applied to determine the optimal hyperparameters of the XGBoost algorithm. The results indicate that the method can effectively identify the current propeller ventilation state and predict whether a full ventilation state will occur after experiencing a partial propeller ventilation state. The comparison results indicate that the POA has a better optimization effect on the XGBoost algorithm for propeller ventilation identification and prediction. The method proposed in this study provides crucial technical support for the effective switching of propulsion control strategies for ship electric propulsion systems under adverse sea conditions.

Keywords: Adverse sea condition, Propeller ventilation, Propulsion control switching strategy, POA-XGBoost model, Propeller ventilation identification and prediction method.

1. INTRODUCTION

Under adverse sea conditions, the dynamic behavior of the propeller in waves causes fluctuations in the ship-integrated power system. In particular, propeller ventilation caused by frequent in-and-out-of-water movements leads to fluctuations as high as 80–100% of the rated load [1]. Propeller ventilation can not only accelerate the wear and tear of the ship's propulsion equipment but also lead to significant fluctuations in the voltage and frequency of the shipboard power network caused by an imbalance between the "source" and "load" power [2]. Severe fluctuations in the shipboard power network can adversely affect the operational performance and efficiency of electrical equipment and even lead to accidents where the entire ship loses power. To solve this issue, Smogeli et al. [3] proposed an anti-spin control strategy that can switch between adverse sea conditions and normal conditions for propulsion control strategies. This switch was based on the propeller ventilation state identified by the ventilation identification module. Without considering the predicted development of ventilation severity, ineffective propulsion control strategy switching may occur. Therefore, predicting the severity of ventilation while identifying it is important for ensuring the safety and stability of ship operations.

Machine Learning (ML) algorithms have been widely applied in the identification of propeller ventilation in recent years. Califano et al. [4] and Luca Savio et al. [5] adopted a support vector machine and a single Kalman filter to identify whether propeller ventilation occurred, both of which have achieved high identification accuracy. Gao et al. [6] and Zhang et al. [7] proposed adopting an evidence reasoning rule based on the Adaboost. ML and maximum likelihood evidential reasoning rule to identify the partial ventilation state. This is a transitional state between the non-ventilated and fully ventilated states. However, there are some limitations to the existing methods. They can only identify the current propeller ventilation state as the moment for switching propulsion control strategies without considering whether a full ventilation state will occur after experiencing the partial propeller ventilation state. If the propeller does not fully transition from a partial ventilation state to a full ventilation state, it quickly returns to the non-ventilation state. This can result in the frequent and ineffective switching of propulsion control strategies under adverse sea conditions. The propeller may return to the non-

@2023 Ma, S. et al., published by TU Delft OPEN Publishing on behalf of the authors. Licensed under a Creative Commons Attribution CC BY license.
DOI: https://doi.org/10.59490/moses.2023.662

ventilation state before completing the switch to the propulsion control strategy, or it immediately needs to switch back to the normal condition control strategy after completing the switch to the adverse sea condition control strategy. The method proposed in this study can identify the current propeller ventilation state and predict whether a full ventilation state will occur after experiencing the partial propeller ventilation state. The propulsion control strategy is switched only when the full ventilation state is predicted, resulting in a reduction in ineffective switching of propulsion control strategies.

To address the aforementioned issues, this study proposes predicting the severity of ventilation development and identifying it to enhance the control of propeller ventilation. If the propeller reached the full ventilation state, the propulsion control strategy was switched. If it does not, it does not switch. Propeller ventilation identification and prediction are classification problems. Currently, the main algorithms used for classification include KNN, neural networks, SVM, and decision trees. The XGBoost algorithm proposed by Chen [8] is based on the CART regression tree and belongs to the boosting ensemble learning method. By incorporating L2 regularization terms and second-order derivatives into the objective function of the gradient augmented decision tree, the ability to generalize and avoid overfitting of XGBoost is improved. The XGBoost algorithm has an excellent ability to handle large-scale data. The comparison results of the KNN, BP neural network, SVM, and XGBoost on the problem of propeller ventilation identification and prediction by the author indicate that XGBoost achieves better performance. However, the XGBoost algorithm without parameter optimization has a low degree of fit with the existing dataset, which leads to its poor generalization performance and adaptability [9]. Therefore, this study adopts POA, PSO, and GA to optimize the hyperparameters of XGBoost.

This paper is organized as follows. In Section 2, the ship dynamics/control model is developed to simulate the dynamic response of a ship propulsion system under adverse sea conditions of different wind and wave conditions. In Section 3, the current and speed signals of the propulsion motor are collected, and their characteristics are extracted for training the POA-XGBoost, PSO-XGBoost, and GA-XGBoost algorithms. These algorithms were designed to accurately identify and predict the propeller ventilation. Section 4 focuses on the identification and prediction performance of the model. Finally, the conclusions and recommendations for future research are presented in Section 5.

2. SHIP DYNAMICS/CONTROL MODEL

To simulate the dynamic characteristics of ship electric propulsion systems under adverse sea conditions, an integrated simulation model including a mechanical module, electrical module, and hydrodynamic module is introduced in this section, as shown in Fig. 1. The integrated simulation model is mainly categorized into three main subsystems: electrical propulsion system, the 3 DOF (degree of freedom) motion system, and the sea state interference system. The electrical propulsion system includes a propulsion motor, propulsion controller, and propeller models. The 3 DOF motion system can calculate the ship heading angle and speed according to the interaction between the thrust generated by the propeller, pod angle, and external interference of wind and waves. The sea state interference system, which includes the first-order wave force model, second-order wave force model, wind force model, and in-and-out-of-water model, was used to simulate the external environmental interference of ships under adverse sea conditions.

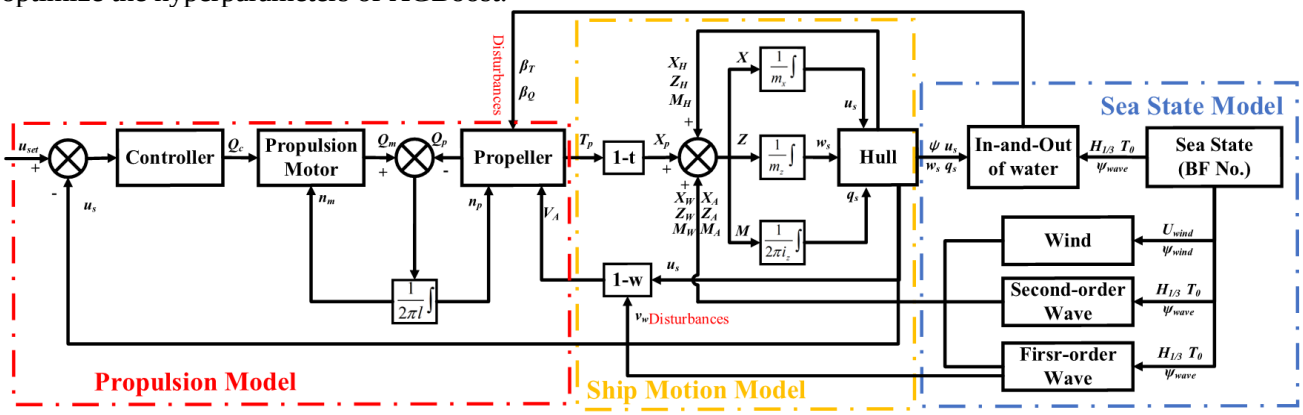

Figure 1: block diagram of the integrated simulation model structure

2.1 Electric propulsion system

2.1.1 The propulsion motor model

Because the electrical time constant is much smaller than the mechanical time constant in an electric propulsion system, the first-order equation in. Equation (1) is used to simplify the motor dynamic equation [10].

$$\frac{dQ_m}{dt} = \frac{1}{T_m} \cdot (Q_c - Q_m) \tag{1}$$

where Q_c is the target torque provided by the controller, Q_m is the output torque of the propulsion motor, T_m is the time constant of the motor.

The torque balance equation between the propeller and the propulsion motor can be simplified using (2).

$$I_s \cdot \frac{d\omega}{dt} = Q_m - Q_p - k_\omega \cdot \omega \tag{2}$$

where I_s is the moment of inertia, k_ω is the friction coefficient of the transmission shaft, ω is the propeller angular velocity, Q_p is the propeller torque.

2.1.2 Propeller model

When determining the geometric parameters of a fixed-pitch propeller, the torque and thrust coefficients of the propeller are dependent only on the advance coefficient. The torque and thrust of the propeller are expressed by (3).

$$\begin{cases} Q_p = \mathrm{sgn}(n) \cdot \beta_Q \cdot K_Q \cdot \rho_w \cdot n^2 \cdot D^5 \\ T_p = \mathrm{sgn}(n) \cdot \beta_T \cdot K_T \cdot \rho_w \cdot n^2 \cdot D^4 \end{cases} \tag{3}$$

where T_p is the propeller thrust; K_Q and K_T represent the propeller torque coefficient and the propeller thrust coefficient, respectively; β_Q and β_T represent the torque loss coefficient and the loss thrust coefficient, respectively, which are used to characterize the variation of propeller torque and thrust with propeller submergence; ρ_w is the water density; n and D represent the revolution speed and the diameter of the propeller, respectively.

The goal of ship propulsion control is to maintain the stability of a ship's velocity. A motor speed control strategy was adopted in this study.

2.2 3 DOF ship motion system

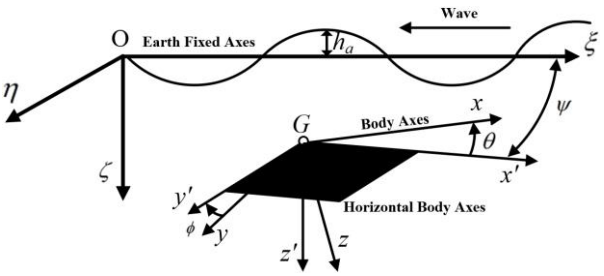

Figure 2: ship motion coordinate system [11]

As shown in Fig. 2, a ship motion coordinate system [11], which includes the earth-fixed coordinate system *O-ξηζ*, the body-fixed coordinate system *G-xyz* and the motion coordinate system *G-x'y'z'*,' is developed to explore the effects of wind and waves on ship forces in adverse sea conditions.

In this study, it was assumed that the forces generated by the wind and waves on the ship were in the same direction. The ship sails against wind and waves under adverse sea conditions. Therefore, only surge, heave, and pitch motions were considered in this study, whereas sway, roll, and yaw motions were ignored.

According to the separation concept of MMG school [12], surge motion can be expressed by (4).

$$(m + m_{11}) \cdot \left(\frac{du}{dt} + q \cdot w \right) = X_H + X_P + X_A + X_W \tag{4}$$

where m and m_{11} are the mass of the ship and the added mass of the entrained water in the longitudinal direction, respectively, u is the ship longitudinal velocity, w is the ship vertical velocity, q is the angular speed of the pitch motion. The subscripts *H*, *P*, *A* and *W* represent the external forces and moments contributed by the hull, pod thruster, wind, and waves, respectively.

According to [13], a simplified response equation derived from a semi-analytical approach was proposed by Jørgen Juncher Jense et al. to calculate the pitch and heave motion of monohull ships induced by waves, which can be expressed by (5).

$$\begin{cases} 2\dfrac{k \cdot d}{\omega^2} \cdot \dfrac{d^2 w}{dt^2} + \dfrac{A^2}{k \cdot B \cdot \alpha^3 \cdot \omega} \cdot \dfrac{dw}{dt} + w = Z_p + Z_A + Z_W \\ 2\dfrac{k \cdot d}{\omega^2} \cdot \dfrac{d^2 \theta}{dt^2} + \dfrac{A^2}{k \cdot B \cdot \alpha^3 \cdot \omega} \cdot \dfrac{d\theta}{dt} + \theta = M_p + M_A + M_W \end{cases} \tag{5}$$

where θ is ship trim angle, B is breadth, d is draught, L is length, $k = 2\pi/\lambda$ is the wave number, λ is the wave length, V_s is the ship velocity, χ_w is the relative wave direction that is taken as π when moving against the waves, Z is the vertical force, M is the longitudinal moment, A is the sectional hydrodynamic damping, which can be modelled by the dimensionless ratio between the incoming and diffracted wave amplitudes [14].

2.3 Sea state interference system

2.3.1 Wind force model

As recorded in [15], the force and moments generated by the wind usually have a significant impact on the surge, sway, and yaw motions of ships on the horizontal plane, with little impact on the heave, pitch, and roll motions. Therefore, only the longitudinal force generated by the wind was

considered in this study, which can be calculated using the steady velocity of the ship.

$$X_A = 1/2 \cdot \rho_A \cdot U_A^2 \cdot C_{XA}(\chi_A) \cdot A_X \quad (6)$$

where ρ_A is the air density, U_A is the relative wind speed, C_{XA} is the longitudinal wind coefficient, χ_A is the relative wind direction, A_X is the projected frontal area of the ship above water.

2.3.2 First-order waves force model

The Froude-Krenov hypothesis states that the pressure distribution in regular waves is not influenced by the presence of ships [13]. The first-order wave force generated by regular waves can be expressed by (7) by considering the ship to be a hexahedron.

$$\begin{cases} X_W^1 = \dfrac{-4\rho_A \cdot g \cdot h_a}{k^2 \cdot \sin^2 \chi_W} \cdot \left(1 - e^{-k \cdot d}\right) \cdot \sin\left(\dfrac{k \cdot L \cdot \cos \chi_W}{2}\right) \\ \cdot \sin\left(\dfrac{k \cdot B \cdot \sin \chi_W}{2}\right) \cdot \sin(\omega_e \cdot t) \\ Z_W^1 = h_a \cdot \kappa \cdot \sqrt{(1 - k \cdot d)^2 + \left(\dfrac{A^2}{k \cdot B \cdot \alpha^2}\right)^2} \\ \cdot \dfrac{2}{k_e \cdot \cos \chi_W} \cdot \sin\left(\dfrac{k_e \cdot L}{2}\right) \cdot \cos(\omega_e \cdot t) \\ M_W^1 = h_a \cdot \kappa \cdot \sqrt{(1 - k \cdot d)^2 + \left(\dfrac{A^2}{k \cdot B \cdot \alpha^2}\right)^2} \\ \cdot \left[\sin\left(\dfrac{k_e \cdot L}{2}\right) - \dfrac{k_e \cdot L}{2} \cdot \cos\left(\dfrac{k_e \cdot L}{2}\right)\right] \cdot \sin(\omega_e \cdot t) \end{cases} \quad (7)$$

where χ_w is the relative wave direction, h_a is the amplitude of the wave, k is the wave number, λ is the wavelength, ω_e is the frequency of encounter, k_e is the effective wave number, κ is the Smith correction coefficient.

2.3.3 Second-order waves force model

According to [15], the second-order wave force has a significant impact on ship surge motion, with little impact on heave and pitch motions. The longitudinal force generated by second-order waves can be expressed as (8).

$$X_W^2 = \rho_w \cdot g \cdot H_{1/3}^2 \cdot \left(B^2/L\right) \cdot C_{XW}(U, T_v, \chi_W) \quad (8)$$

where g is the gravity acceleration, $H_{1/3}$ is the significant wave, approximately 1.6 times the average wave height, T_v is the averaged wave period, C_{XW} is the longitudinal second-order force coefficient.

2.3.4 In-and-out-of-water model

Under adverse sea conditions, the loss of thrust and torque in the propeller caused by the in- and out-of-water effects can be expressed by the thrust loss factor and torque loss factor, respectively. Equation (9) was used to calculate the thrust loss factor.

$$\beta_T = \begin{cases} 0, & \dfrac{h}{R} \le -0.48 \\ 1 - 0.675\left(1 - 0.769\dfrac{h}{R}\right)^{1.258}, & -0.48 < \dfrac{h}{R} < 1.3 \\ 1, & 1.3 < \dfrac{h}{R} \end{cases} \quad (9)$$

Where, h is the propeller submergence; R represents the radius of propeller.

The torque loss factor can be expressed as the thrust loss factor, as shown in (10).

$$\beta_Q = (\beta_T)^m \quad (10)$$

Where, m is a coefficient with the value of 0.85 in this paper.

2.3.5 Propeller wake fluctuation model

The inflow velocity of the propeller continuously fluctuates under the combined influence of ship speed, maneuvering, and waves [16]. This study comprehensively considers the influence of the ship maneuvering motion on the average inflow velocity of the propeller and the influence of regular waves on the oscillation inflow velocity of the propeller. The inflow velocity of the propeller is expressed as (11).

$$\begin{aligned} V_a = {} & u \cdot (1 - w_p) + \alpha \cdot \omega \cdot h_a \cdot \exp(-k \cdot z_p) \\ & \cdot \cos \chi_W \cdot \cos(\omega_e \cdot t - k \cdot x_p \cdot \cos \chi_W) \end{aligned} \quad (11)$$

where x_p and z_p represent the longitudinal and vertical positions of the propeller, respectively, in the ship-fixed coordinate system.

2.4 Model validation

Because the ship dynamic/control model is used to simulate the dynamic response of the ship propulsion system, the simulation accuracy must be validated.

By comparing the experimental results obtained from the propeller model test in the deep-water towing tank of the benchmark cruise ship, the accuracy of the ship surge motion model was validated, as shown in Fig. 3.

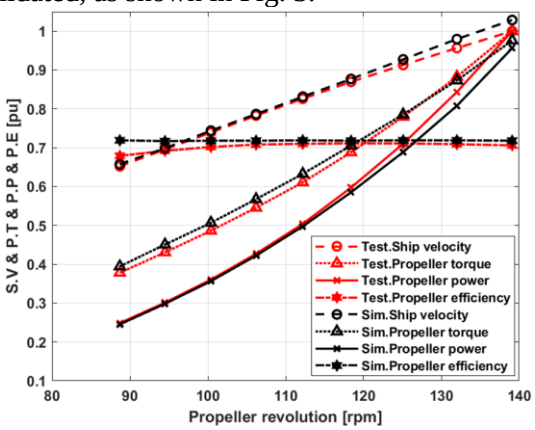

Figure 3: Validation of ship surge motion model

According to the data from the ship seakeeping test recorded in [17], the ship pitch motion, heave motion, and first-order wave models were validated, as shown in Fig. 4.

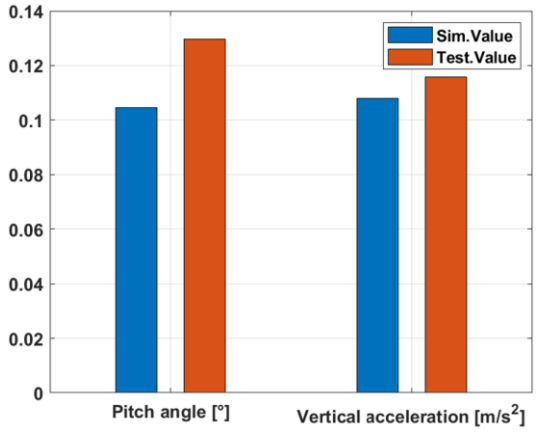

(a) Double significant amplitude of cruise motion response in head wave (sea state 4)

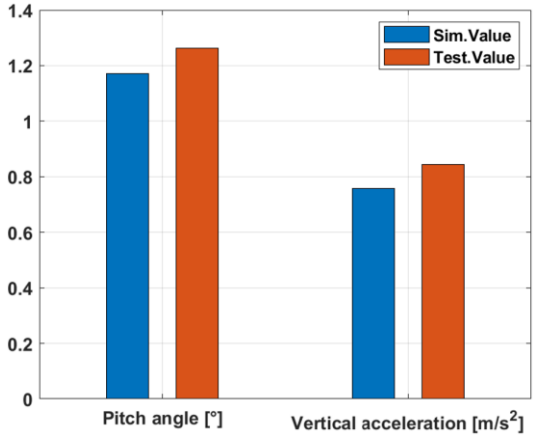

(b) Double significant amplitude of cruise motion response in the head wave (sea state 6)

Figure 4: Validation of pitch motion, heave motion and first-order waves models

To simulate the longitudinal forces caused by the wind and second-order wave forces, the longitudinal and second-order wave force coefficients are shown in Figure 5. Note that the coefficients recorded in [15] were directly used in this study. The uncertainties caused by directly using these coefficients for the cruise ship are assumed to be acceptable for the following reasons: first, both ships are cruise ships with similar hull shapes; second, the longitudinal wind and second-order wave force coefficients are nondimensional.

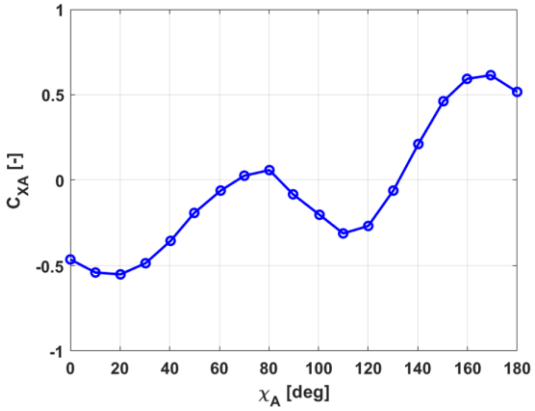

(a) Longitudinal wind force coefficient

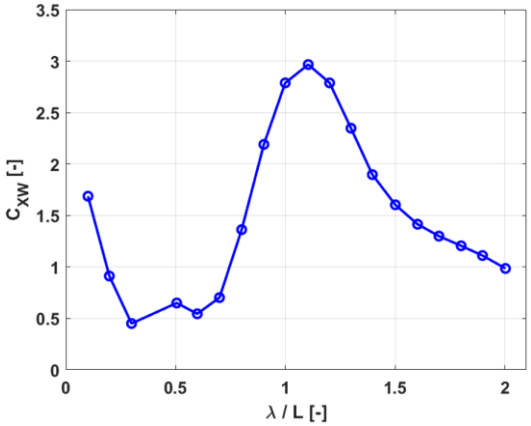

(b) Longitudinal second-order waves force coefficient

Figure 5: Wind and second-order waves force coefficients

3. THE PROPELLER VENTILATION IDENTIFICATION AND PREDICTION METHOD BASED ON XGBOOST

3.1 Design of the ventilation identification and prediction model

There are challenges in directly measuring the changes in propeller performance parameters under adverse sea conditions. Because the propulsion motor is directly connected to the propeller, its state parameters of the propulsion motor can be used for propeller ventilation identification and prediction.

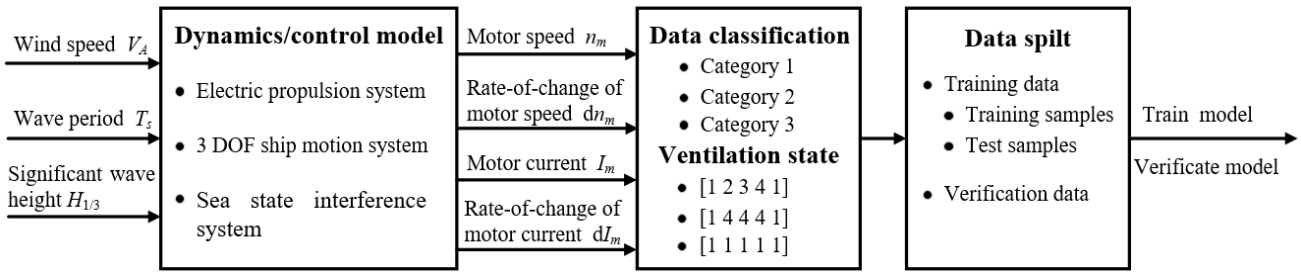

Figure 6: Block diagram of the identification and prediction method

Wang et al. [18] used propulsion torque data to train a model for identifying propeller ventilation, while Zhang [7] incorporated both propulsion torque and speed data. The parameters of the propulsion motor can be divided into electrical and mechanical parameters. Comprehensively considering both the electrical and mechanical parameters may result in better performance. Gao [6] utilized the propulsion torque data and the root mean square value of the electric current. However, to a certain extent, the electric current of the motor varies with torque. In other words, they exhibited the same change trend. Therefore, the electrical and mechanical parameters of the propulsion motor were selected in this study, specifically, the root mean square of the current and speed signals.

The design process of the propeller ventilation identification and prediction model is illustrated in Fig. 6. The dynamics/control model is introduced in Section 2. First, in the simulation model, the ship velocity was set to 6 kn. The operational parameters of the ship propulsion motor under 32 different wind and wave conditions were obtained by adjusting the wind and wave parameters, such as the wind speed, wave period, and significant wave height, as presented in Table 1. The wind speed can be set to 19.0 m/s and 21.0 m/s. The wave period can be set to 9.0 s, 11.0 s, 13.0 s and 15.0 s. The significant wave height can be set to 4.5 m, 5.0 s, 5.5 m and 6.0 m. Then, 32 different conditions can be obtained by cross combining the values of above parameters. The propulsion motor parameters include the motor speed, rate of change of the motor speed, root mean square of the motor current, and rate of change of the root mean square of the motor current. Second, according to the maximum ventilation level that the propeller can develop, 32 sets of simulation results were divided into three categories. Different propeller ventilation states are set for the three categories, which are introduced in Section 3.2. Then, the 32 sets of simulation results were divided into training data and verification data, among which the training data were further divided into training and test samples. Training data were used to train and test the learning and prediction performance of the intelligent algorithm. Verification data were used to demonstrate the generalization ability of the trained intelligent algorithm. Finally, POA-XGBoost, PSO-XGBoost, and GA-XGBoost are developed to achieve a function that can identify the current ventilation state and predict the development of ventilation severity. POA, PSO, and GA were used to select the optimal hyperparameters of the XGBoost algorithm.

Table 1. Input parameters and applications of the 32 sets of data.

NO.	Wind speed (m/s)	Wave period (s)	Significant wave height (m)	Application
1	19.0	9.0	4.5	Training
2			5.0	Training
3			5.5	Training
4			6.0	Training
5		11.0	4.5	Test
6			5.0	Training
7			5.5	Training
8			6.0	Training
9		13.0	4.5	Training
10			5.0	Training
11			5.5	Training
12			6.0	Training
13		15.0	4.5	Training
14			5.0	Training
15			5.5	Training
16			6.0	Training
17	21.0	9.0	4.5	Training
18			5.0	Training
19			5.5	Training
20			6.0	Training
21		11.0	4.5	Training
22			5.0	Training
23			5.5	Training
24			6.0	Training
25		13.0	4.5	Training
26			5.0	Test
27			5.5	Training
28			6.0	Training
29		15.0	4.5	Training
30			5.0	Training
31			5.5	Test
32			6.0	Training

3.2 Data classification and ventilation state

The method of setting different propeller ventilation states for different categories proposed by the author in [19] will be used again in this study.

According to the maximum ventilation level that the propeller can develop, 32 sets of simulation results were divided into three categories. Category 1 indicates the occurrence of full ventilation. Category 2 indicates that the maximum ventilation level within a wave period corresponds to a partial ventilation. Category 3 indicated that ventilation did not occur.

Different propeller ventilation states were set for different categories. State 1 indicates that the propeller is in a nonventilated state. State 2 indicates that the propeller is currently in a partial ventilation state, and the full ventilation state is predicted to occur immediately. State 3 indicates that the propeller is in a fully ventilated state. State 4 indicates that the propeller is currently in the partial ventilation state; however, the full ventilation state is predicted not to occur immediately.

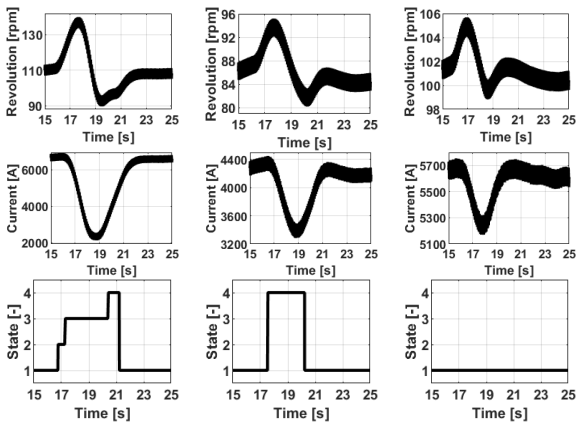

(a) Category 1 (b) Category 2 (c) Category 3

Figure 7: Different propeller ventilation states setting based on different categories [19]

3.3 Hyperparameters optimization of XGBoost

3.3.1 Pelican optimization algorithm

The POA developed by Pavel Trojovský [20] in 2020 is a random heuristic algorithm. The POA simulates the behavior and strategies of pelicans during hunting and is divided into two stages: moving towards prey and winging on the water surface. In the stage of moving towards prey, the pelicans determine the position of the prey and then move towards the determined area. It is worth mentioning that the position of the prey is randomly generated in the search space, leading to an increase in the exploration ability of the POA in the exact search of the problem-solving space. In the stage of winging on the water surface, after reaching the surface of the water, the pelicans spread their wings to move the fish upward and then collected prey in their throat pouch. This behavior can lead to more prey being caught in the attacked space. A POA can increase its local search capability by simulating its behavior. POA has better global search ability and best local area recognition ability in engineering problems, which has been proven in several reports [21], [22].

3.3.2 Particle swarm optimization

The PSO, developed by Eberhart and Kennedy [23] in 1995, is an evolutionary computation. PSO is a simplified model established using swarm intelligence, which was initially inspired by the regularity of bird clustering activities. The PSO simulates the sharing of information among individuals in an animal population. This process leads to an evolutionary progression from disorder to order in the problem-solving space, ultimately resulting in identification of the optimal solution.

3.3.3 Genetic algorithm

The GA, proposed by Holland in 1973 [24], is a modern intelligent algorithm that draws inspiration from Darwin's theory of evolution and Mendel's theory of genetics. The aim is to simulate the survival of the fittest and natural genetic mechanisms observed in the biological world. The GA transforms practical problems into evolutionary problems by starting with an initial population and generating new populations through repeated genetic operations of selection, crossover, and mutation until the termination conditions are met. Because of its advantages of good robustness, strong global optimization ability, and no limitations on derivatives and function continuity, GA is often adopted in the field of objective optimization.

3.3.4 XGBoost algorithm

The prediction model of XGBoost can be expressed by (12).

$$\hat{y}_i = \sum_{t=1}^{K} f_t(x_i),\ f_t \in F \tag{12}$$

where x_i represents the i-th input sample, $\hat{y}_i$ is the predicted value of the i-th sample, f_t represents the t-th decision tree, F is the set of all regression trees.

The objective function of the XGBoost algorithm consists of a loss function and regularization, which can be expressed as (13).

$$obj = \sum_{i=1}^{m} l(y_i, \hat{y}_i) + \sum_{j=1}^{K} \Omega(f_i),\ f_i \in F \tag{13}$$

where y_i represents the true value of the i-th sample, $\sum_{i=1}^{m} l(y_i, \hat{y}_i)$ is the loss function, and $\sum_{j=1}^{K} \Omega(f_i)$ is the regularization function, which can be specifically represented by (14).

$$\Omega(f_i) = \gamma \cdot T + \frac{1}{2}\lambda \sum_{j=1}^{T} \omega_j^2 \tag{14}$$

where T is the number of leaf nodes in the decision tree, ω represents the leaf node output score of each decision tree, λ is the coefficient of the leaf node, γ is the punish regularization term for the leaf weights.

In the XGBoost algorithm, the error generated by the model combined with the previous (t-1) trees is used as a reference to build the t-th tree, leading to a decrease in the value of the loss function. Therefore, the objective function can be rewritten as (15):

$$obj^t \approx \sum_{i=1}^{m} \left(g_i \cdot f_t(x_i) + \frac{1}{2} h_i \cdot f_t^2(x_i) \right) + \gamma \cdot T + \frac{1}{2}\lambda \sum_{j=1}^{T} \omega_j^2 \tag{15}$$

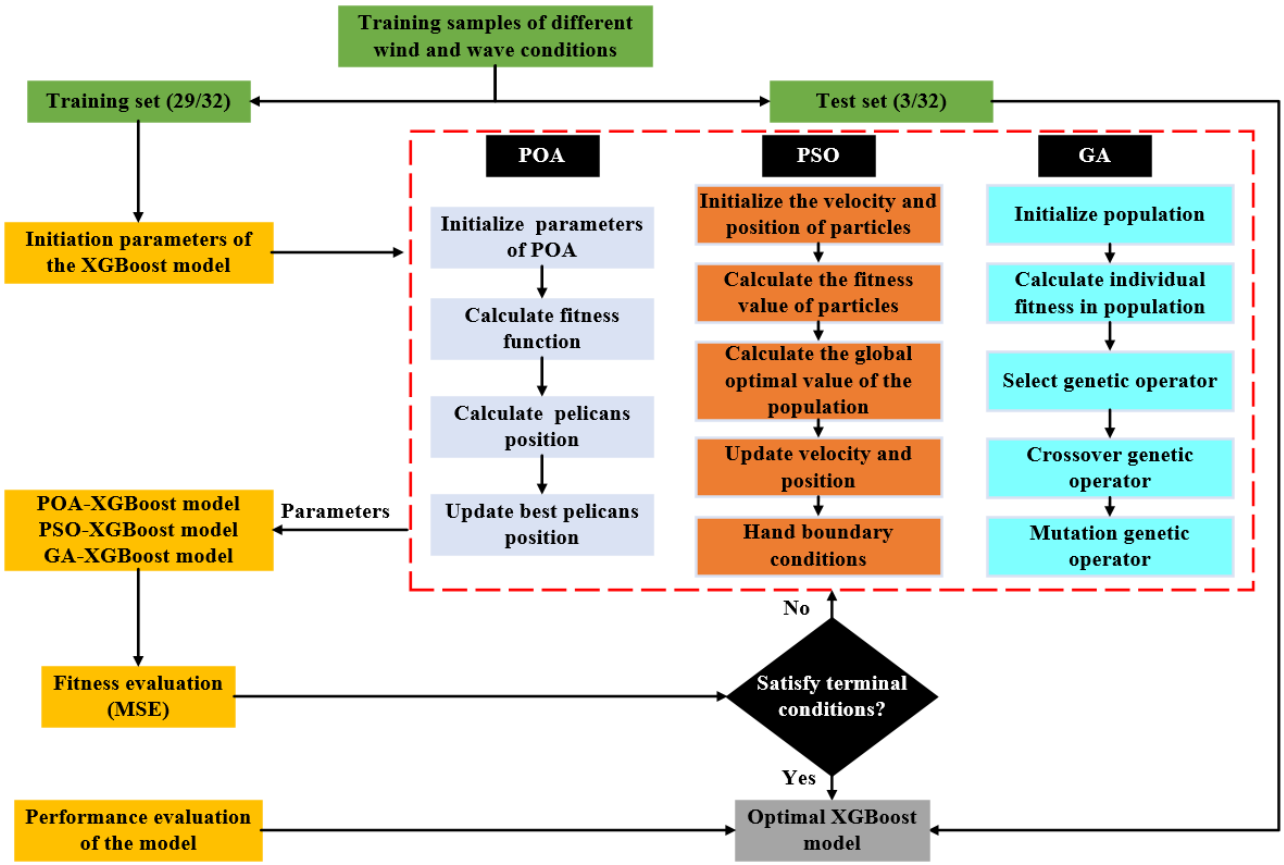

Figure 8: Propeller ventilation identification and prediction process

where $g_i = \frac{\partial l\left(y_i, \hat{y}_i^{(t-1)}\right)}{\partial \hat{y}_i^{(t-1)}}$ and $h_i = \frac{\partial^2 l\left(y_i, \hat{y}_i^{(t-1)}\right)}{\partial^2 \hat{y}_i^{(t-1)}}$ represent the first- and second-order derivatives of the objective function, respectively.

When the tree structure is determined, the optimal weight is obtained by setting its first-order derivative to 0.

$$\omega_j^* = -\frac{G_j}{H_j + \lambda} \tag{16}$$

The optimized objective function can be obtained by substituting the optimal weight expressed in Equation (16) into the objective function.

$$obj^t = -\frac{1}{2}\sum_{j=1}^{T}\left(\frac{G_j^2}{H_j + \lambda}\right) + \lambda \cdot T \tag{17}$$

Where, $G_j = \sum_{i \in I_j} g_i$, $H_j = \sum_{i \in I_j} h_i$ and $I_i = \left\{ i \middle| q(x_i) = j \right\}$ are the sample sets that falls into leaf node j.

3.3.5 POA- XGBoost, PSO- XGBoost, and GA- XGBoost

The 32 sets of data were divided into training and test datasets. Meanwhile, the 32 sets of data were divided into three categories. Therefore, three sets of data, including one set from each category, were selected as test data, whereas the remaining 29 sets of data were selected as training data.

Table 2. Hyperparameters to be optimized.

Hyperparameter	Meaning
max_depth	Maximum depth of trees
min_child_weight	Minimum sum of the instance weights contained in child nodes
n_estimators	Number of boosted trees
alpha	Regular term of weight L1
lambda	Regular term of weight L2
gamma	Minimum loss reduction required to make a further partition
subsample	Sampling rate of training samples
colsample_bytree	Column sampling rate of features when building each tree

In this study, POA, PSO, and GA were selected to adjust the hyperparameters of the XGBoost algorithm. The baseline algorithm for propeller ventilation identification and prediction was XGBoost, whereas the POA, PSO, and GA were used to search for the optimal hyperparameters of the Xgboost algorithm. The hyperparameters that need to be optimized are listed in Table 2, which include max_depth, min_child_weight, n_estimators, alpha, lambda, gamma, subsample, and colsample_bytree.

The modeling process of the propeller ventilation identification and prediction model

based on POA-Xgboost, PSO-Xgboost, and GA-Xgboost is shown in Fig. 8. POA, PSO, and GA are used to optimize the XGBoost algorithm to find the hyperparameters that can maximize the classification performance of the XGBoost algorithm. The classification error of the XGBoost algorithm was used as the fitness function of the POA, PSO, and GA. The optimal hyperparameters of the Xgboost algorithm can be obtained by comparing the fitness values to those obtained by continuous iteration and update.

4. RESULT AND ANALYSIS

The training data consisted of 29 sets of simulation results comprising 20,967 sample points. Among these, 14,667 sample points were randomly selected to form the training samples, and the remaining 6,300 were selected to form the test samples.

The MAPE, MSE, and MAE values of the XGBoost, POA-XGBoost, PSO-XGBoost, and GA-XGBoost models are listed in Table 3. It can be seen that the POA, PSO, and GA can improve the classification accuracy of Xgboost, whereas the POA performs better for propeller ventilation identification and prediction problems.

Table 3. MAPE, MSE and MAE values of the different Xgboost model.

Category	Algorithm	MAPE	MSE	MAE
Category 1	Xgboost	0.045	0.332	0.156
	POA-Xgboost	0.028	0.122	0.093
	PSO-Xgboost	0.037	0.234	0.117
	GA-Xgboost	0.036	0.298	0.122
Category 2	Xgboost	0.134	0.684	0.228
	POA-Xgboost	0.144	0.594	0.198
	PSO-Xgboost	0.119	0.612	0.204
	GA-Xgboost	0.177	0.720	0.240

To further demonstrate the generalization ability of the POA-Xgboost model for propeller ventilation identification and prediction, the remaining three sets of verification data were used as the inputs for the trained model. Meanwhile, the GA and PSO are used to optimize the hyperparameters of XGBoost through the same process as POA-XGBoost. The identification accuracy of the POA-XGBoost model was compared with the results of the XGBoost, GA-XGBoost, and PSO-XGBoost models, as shown in Fig.7 and Fig. 8. Note that owing to the extremely obvious features of category 3, all models in this study can be easily identified and have a high identification accuracy. The results for Category 3 are not displayed here.

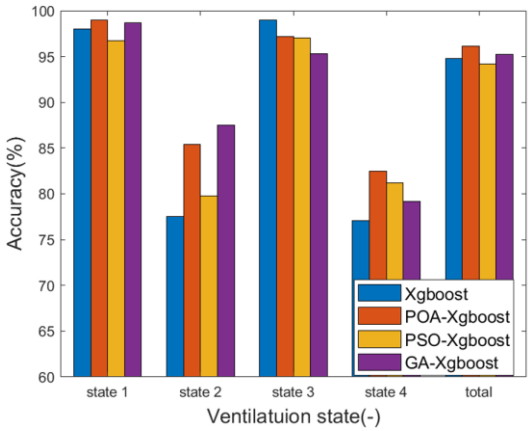

Figure 10: Comparison results identification accuracy for category 1

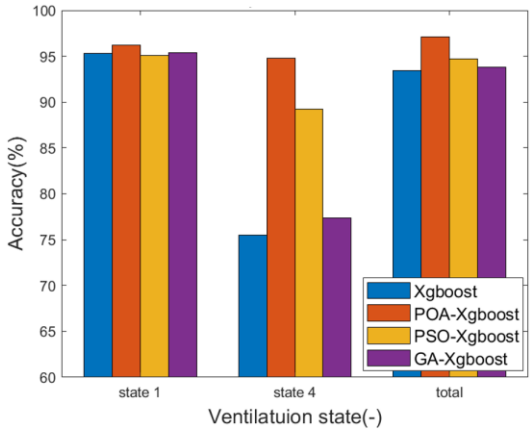

Figure 11: Comparison results identification accuracy for category 2

There is a sample imbalance problem for the remaining verification data of both Category 1 and Category 2. For category 1, the proportion of sample points of state 1 to all samples was 57.6%, 5.8% for state 2, 26.6% for state 3, and 10.0% for state 4. For Category 2, the proportion of the sample points of State 1 to all samples was 90.2%, while that of State 4 was 9.8 %. Accurately identifying states 2 and 4 is most important, as it relates to the switching of propulsion control strategies. From Fig. 10 and Fig. 11, it can be seen that the POA-XGBoost model has the highest total identification accuracy among all the models for both category 1 and category 2. For category 1, although the GA-XGBoost model achieves better identification accuracy for state 2, POA-XGBoost performs better when considering the identification accuracy of states 2 and 4 comprehensively. For category 2, the identification accuracy of state 4 of the POA-XGBoost model is far higher than that of the other models.

The test samples were used to test the accuracy of the trained POA-XGBoost model, as shown in Fig. 6. A confusion matrix is presented in Table 3. From Table 4, it can be seen that the total identification accuracy of POA-XGBoost for the

test samples was 99.38%. This indicates that the POA-XGBoost model has excellent learning ability.

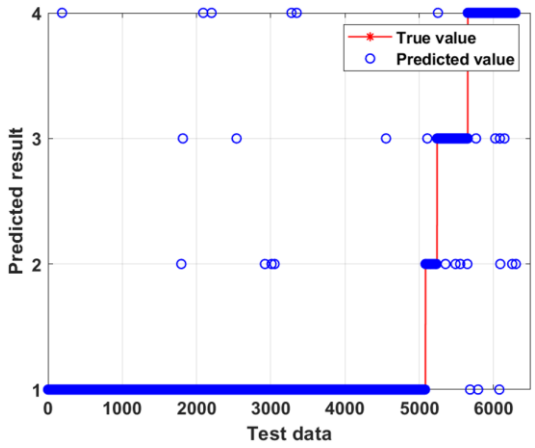

Figure 12: Comparison results between test samples and predicted values

Table 4. Error metrics of POA-XGBoost model for test samples.

		Prediction results				Total	Acc (%)
		D_1	D_2	D_3	D_4		
True values	D_1	5074	2	3	4	5083	99.8
	D_2	3	150	3	0	156	96.2
	D_3	0	4	406	3	413	98.3
	D_4	7	3	7	631	648	97.4

As state 1 has a large sample size and high prediction accuracy, it was excluded from the calculation of the confidence interval for the prediction results, as shown in Table 5. The confidence interval results further demonstrate the effectiveness of the POA-XGBoost model.

Table 5. Confidence interval of prediction accuracy of POA-XGBoost model.

	Category 1	Category 2
Mean error (-)	0.964	0.934
Standard deviation (-)	0.022	0.018
90% CI	[0.950,0.977]	[0.916,0.952]
95% CI	[0.947,0.980]	[0.912,0.956]
99% CI	[0.943,0.985]	[0.905,0.963]

5. CONCLUSION

Considering the important role of propeller state identification and prediction in the safety of ships sailing in adverse sea conditions, as well as the powerful classification performance of the XGBoost algorithm, a method of combining the simulation model with the XGBoost algorithm to design a propeller ventilation identification and prediction model is proposed in this paper. Then, POA, PSO, and GA are adopted to optimize the hyperparameters of the XGBoost algorithm. The results indicate that the proposed method can achieve the function of predict whether a full ventilation state will occur after experiencing a partial propeller ventilation state, which can improve the control of ship propeller ventilation in adverse sea conditions. Meanwhile, the POA has a better optimization effect on the XGBoost algorithm for propeller ventilation identification and prediction.

The proposed method provides a basis for switching propulsion control strategies to improve the stability of ship-integrated power systems. Therefore, in the next step, a model predictive control strategy will be developed based on the propeller ventilation identification and prediction model. We will further develop a propeller ventilation effect prediction model to improve its real-time performance.

REFERENCES

[1] J. Hou, J. Sun, and H. Hofmann, "Adaptive model predictive control with propulsion load estimation and prediction for all-electric ship energy management," *Energy*, vol. 150, pp. 877-889, Jan. 2018.

[2] H. Alafnan *et al*, "Stability Improvement of DC Power Systems in an All-Electric Ship Using Hybrid SMES/Battery," *IEEE Transactions on Applied Superconductivity*, vol. 28, no. 3, pp. 1-6, Nov. 2018.

[3] Ø. N. Smogeli *et al*, "The concept of anti-spin thruster control," *Control Engineering Practice*, vol. 16, no. 4, pp. 465-481, Apr. 2008.

[4] A. Califano, S Steen, "Identification of ventilation regimes of a marine propeller by means of dynamic-loads analysis," *Ocean Engineering*, vol. 38, pp. 1600-1610, Oct. 2011.

[5] L. Savio, S. Steen, "Identification and analysis of full-scale ventilation events," *International Journal of Rotating Machinery*, vol. 2012, pp. 1-19, Jul. 2012.

[6] H. Gao, L. Liao, and Y. He, "Improved control of propeller ventilation using an evidence reasoning rule based Adaboost. M1 approach," *Ocean Engineering*, vol. 209, pp. 107329, Aug. 2020.

[7] X. Zhang, X. Xu, and X. Xu, "Intelligent Sea states identification based on maximum likelihood evidential reasoning rule," *Entropy*, vol. 22, no. 7, pp. 770, Jul. 2020.

[8] T. Chen, and C. Guestrin, "XGBoost: A scalable tree boosting system," in *Proceedings of the 22nd Acm Sigkdd International Conference on Knowledge Discovery and Data Mining*, 2016, pp. 785-794.

[9] Y. Zhang, B. Feng, and Y. Chen, "Fault diagnosis method for oil-immersed transformer based on XGBoost optimized by genetic algorithm," *Electric Power Automation Equipment*, vol. 41, no. 2, pp. 200-206, 2021.

[10] M. Blanke, K. Lindegaard, and T. I. Fossen, "Dynamic model for thrust generation of marine propellers," *Ifac Proceedings Volumes*, vol. 33 no. 21, pp. 353-358, Aug. 2000.

[11] H. Masami, and K. Yoon-Soo, "A New Coordinate System and the Equations Describing Manoeuvring Motion of a Ship in Waves," *Journal of the Japan Society of Naval Architects & Ocean Engineers*, vol. 1993, no. 173, pp. 209-220, Jan. 2010.

[12] Z. Ayaz, O. Turan, and D. Vassalos, "A 6 DOF manoeuvring model for controlled ship motions of pod-driven ships in astern seas," *Ifac Proceedings Volumes*, vol. 36, no. 21, pp. 193-198, Sep. 2003.

[13] J. J. Jensen, A. E. Mansour, and A. S. Olsen, "Estimation of ship motions using closed-form expressions," *Ocean Engineering*, vol. 31, no. 1, pp. 61-85, Jan. 2004.

[14] Y. Yamamoto, K. Sugai, and H. Inoue, "Wave loads and response of ships and offshore structures from the viewpoint of hydroelasticity," in *Advances in Marine Structures Conference*, 1986.

[15] T. Fujiwara, "Cruising Performance of a Large Passenger Ship in Heavy Sea," in *The Sixteenth International Offshore and Polar Engineering Conference*, 2006.

[16] M. Ueno, Y. Tsukada, and K. Tanizawa, "Estimation and prediction of effective inflow velocity to propeller in waves," *Journal of Marine Science and Technology*, vol. 18, pp. 339-348, Feb. 2013.

[17] X. Zhou *et al*. "Research on cruise ship navigation simulation under the action of wave field (in Chinese)," *Ship science and technology*, vol. 43, no. 9, pp. 80-84, 2021.

[18] W. Hao, S. Fossen, and H. Fang, "Towards Data-driven Identification and Analysis of Propeller Ventilation," in *Mts/ieee Oceans Conference 2016*, 2016.

[19] S. Ma, Y. Ding *et al*. "Identification and Prediction of Propeller Ventilation Based on Stacked LGBM-LSTM-RF-XGB Model,". *Submitted to a journal (Ocean Engineering)*, 2023.

[20] P. Trojovský, and M. Dehghani. "Pelican optimization algorithm: A novel nature-inspired algorithm for engineering applications," *Sensors*, vol. 22, no. 3, pp. 855, Jan. 2022.

[21] N. Alamir, S. Kamel, and T. F. Megahed *et al*. "Developing hybrid demand response technique for energy management in microgrid based on pelican optimization algorithm," *Electric Power Systems Research*, vol. 214, pp. 108905, Jan. 2023.

[22] Y. R. Naidu. "Multi-objective Pelican Optimization Algorithm for Engineering Design Problems," in *International Conference on Distributed Computing and Intelligent Technology: Springer*, 2023, pp. 362-368.

[23] J. Kennedy, and Russell Eberhart, "Particle swarm optimization," *Proceedings of Icnn 95-th international Conference on Neural Networks: Ieee*, 1995, pp. 1942-1948.

[24] S. Mirjalili, "Genetic algorithm," *Evolutionary Algorithms and Neural Networks: Theory and Applications*, vol. 780, pp. 43-55, 2019.

PROCEEDINGS OF MOSES2023 CONFERENCE
4TH INTERNATIONAL CONFERENCE ON MODELLING AND OPTIMISATION OF SHIP ENERGY SYSTEMS
26-27 OCTOBER 2023, DELFT, NETHERLANDS

Shallow and Deep Learning Models for Vessel Motions Forecasting during Adverse Weather Conditions

Jake M. Walker[a], Andrea Coraddu[a,*], Stefano Savio[b], and Luca Oneto[b]

[a]Delft University of Technology, Delft, Netherlands
[b]University of Genoa, Genoa, Italy
[*]a.coraddu@tudelft.nl

Abstract

Accurately forecasting vessel motions is a critical step towards achieving fast and accurate intelligent vessel control systems. Intelligent vessel control relies on accurate predictions of vessel motion to make informed decisions regarding control, maneuvering, and positioning, particularly during times of exogenous loading caused by adverse weather conditions. Hence, by accurately forecasting vessel motion accurately, the control system can anticipate potential issues (i.e., excessive trim or roll) and prescribe corrective actions before they become problematic. In this study, the authors propose two approaches to address the problem of vessel motion forecasting. The first approach relies on classical shallow learning models, whereas the second approach involves the use of state-of-the-art deep learning models for improved accuracy at further forecast horizons. Unlike shallow models, deep models can learn the required features directly from the data and therefore do not require *a priori* knowledge or additional features engineering. By leveraging deep learning models, the authors show that vessel motions can be forecasted further into the future without a significant loss in accuracy, thereby improving the overall effectiveness of the intelligent vessel control system. To support their statements, the authors use real operational data and compare the performance of the shallow and deep learning models. The results show that deep learning outperforms shallow learning models in terms of accuracy without a significant increase in the computational demand. Additionally, the authors demonstrate that their models remain accurate even under adverse weather conditions, indicating that they have practical applicability for vessel motions forecasting and can potentially improve the overall effectiveness of intelligent vessel control systems.

Keywords: Autonomous Vessels; Intelligent Control; State Prediction; Time-Series Forecasting, Signal Processing, Supervised Learning, Shallow Models, Deep Models.

1 INTRODUCTION

Intelligent and autonomous vessels have been proposed as an important step towards mitigating emissions from shipping, alleviating seafarers' fatigue, and enhancing safety measures at sea [1]. Nonetheless, the deployment of fully autonomous vessels across intricate mission scenarios remains a formidable challenge [2], [3]. According to the International Maritime Organization (IMO), achieving full autonomy for a vessel requires a control system capable of independently determining the most optimal course of action [4]. Therefore, prior to the deployment of fully functional autonomous vessels, concerted efforts must be directed towards developing intelligent control systems. Although numerous motion control systems have been documented in the literature [5], substantial work remains to bridge the gap between the predicted behavior and the actual responses of vessels to their surroundings [6].

To consider the behavior and dynamics of a vessel in six Degrees of Freedom (DoF), contemporary physics-based models can be leveraged [7], which account for three translational motions (surge, sway, and heave) as well as three rotational motions (roll, pitch, and yaw) and are often characterized by a high accuracy and interoperability. Real-time solutions provided by numerical models such as [7] are a necessary step towards intelligent control systems and can accurately describe the state of the vessel while incorporating external disturbances, and determine the optimal force distributions needed to meet mission criteria. However, vessel control systems frequently operate under challenging conditions and intricate mission environments such as close proximity situations, densely populated areas, station keeping, mooring, automatic docking, and helicopter operations.

Irrespective of the application, for fully autonomous vessels to operate independently and prescribe the optimal course of action even in situations of high exogenous loading (e.g., high wind

@2023 Walker & Coraddu & Savio & Oneto published by TU Delft OPEN Publishing on behalf of the authors. Licensed under a Creative Commons Attribution CC BY license.
DOI: https://doi.org/10.59490/moses.2023.660

speeds and sea swells). It is essential for intelligent control to accurately predict the short-term future state of the vessel (i.e., forecast) and not just at the present moment (i.e., nowcast) during these conditions. In the context of intelligent vessel control systems, state prediction facilitates protocols such as model predictive control where the horizon prediction is coupled with the real-time solution of a multiobjective optimization problem [6]. Hence, within the intelligent vessel control framework, the control system can anticipate potential issues (i.e., excessive trim or roll) due to short-term motions forecasting over a sufficiently large horizon and prescribe corrective actions (i.e., optimal force distributions) before they become problematic.

Existing control systems often rely on observers and state predictors such as the Kalman Filter [8]. However, real-time implementation issues frequently arise because of disparities between actual and forecasted motion attributed to simplified vessel or environment models. To address this disparity, contemporary sensor technology data can be combined with automatic control systems to enhance autonomous operations, assess mission feasibility, and determine optimal control strategies to ensure mission success.

Additionally, the complexity of the optimization problem increases with the forecast horizon (i.e., extending further into the future), which results in the computational complexity of physics-based solutions increasing significantly. Therefore, state prediction will benefit from a fast, novel, and accurate solution that leverages state-of-the-art machine learning models. For these reasons, this paper centers its focus on Shallow and Deep Learning models for vessel motions forecasting, which is a pivotal element for formulating intelligent control strategies and realizing the potential of fully autonomous intelligent vessel control systems. Additionally, this study demonstrates how these models can be developed to remain reliable even during adverse weather conditions characterized by periods of high exogenous loading.

The rest of this paper is organized as follows: Section 2 presents an overview of related work on machine learning models for vessel motions forecasting, Section 3 describes the problem at hand and the available data, Section 4 presents the proposed methodology, Section 5 outlines the results, and finally, Section 6 concludes the work.

2 RELATED WORK

For the sake of completeness, the authors have reported the current state-of-the-art approaches to vessel motion prediction using machine learning in this section with a tabulated summary of the related works found in Table 1.

In [8], the authors developed a model that yielded satisfactory performance in forecasting heave motion, with a forecast horizon of 15-30 [s] and a Root Mean Square Error (RMSE) between $\sim 0.05 - 0.2$ $[m]$. Additionally, the prediction of pitch and roll motion up to a 50s horizon was executed using a hybrid Nonlinear AutoRegressive (NAR) wavelet framework. The models displayed an accuracy of RMSE ~ 0.05 $[^\circ]$ for pitch and RMSE ~ 0.13 $[^\circ]$ for roll. Despite the promising results, they were derived from a rather limited dataset (650 samples), providing only a single day's motion description for an inertial platform.

In [9], the authors predicted the roll motion of a floating production unit using an Autoregressive Integrated Moving Average (ARIMA) deep learning model. They used of synthetic data captured at an extremely high frequency (15 Hz), and a hybrid model with a forecast range of 3-16 $[s]$ resulted in an RMSE of ~ 0.04 $[^\circ]$.

In [10], the authors conducted a study where they forecasted the heading angle with a horizon of 1s, resulting in an RMSE of ~ 0.2 $[^\circ]$. The authors leveraged a time-delay wavelet Neural Network (NN). When the horizon was extended to 3 $[s]$, the RMSE increased to ~ 0.37 $[^\circ]$.

In [11], the authors formulated a state prediction algorithm for an Autonomous Underwater Vehicle (AUV) by leveraging Extreme Learning Machines (ELMs). They conducted tests on models of the pitch (θ), pitch rate ($\dot{\theta}$), heave (Z), and heave velocity (w) of an underwater vehicle. They employed a Nonlinear AutoRegressive Moving Average with eXogenous input (NARMAX) framework, which proved effective in forecasting selected Key Performance Indicators (KPIs) over brief periods. The selected data sample period was 0.56 $[s]$, and the study's findings demonstrated acceptable performance with a time delay of less than 1s.

In [12], the authors presented a Deep Neural Network (DNN) method for the prediction of 6-DoF ship motions under real conditions. This method uses a transformer neural network to learn the relationship between ship motions and environmental conditions. The model was trained on a dataset of AIS data records with a period of 1 $[s]$ and bathymetry data, and it was validated by predicting

the motions of a Ro-Pax Passenger ship between two ports in the Gulf of Finland. The results show that the proposed method can predict the rate of ship motions (surge, sway, heave, roll, pitch, yaw) in real conditions with a Mean Absolute Error of $0.49\ [m/s]$, $0.10\ [m/s]$, $0.001\ [m/s]$, $0.005\ [^\circ/s]$, $0.0005\ [^\circ/s]$, and $0.01\ [^\circ/s]$ respectively. The proposed model is suggested for use in collision avoidance and automatic ship control applications.

Table 1: Summary of related work according to reference, forecasted motions, machine learning algorithms, and resulting accuracy.

Reference	Motions	Algorithm	RMSE
[8]	θ, φ, Z	NAR	0.1, 0.05, 0.05
[9]	φ	ARIMA	0.04
[10]	ψ	NN	0.2
[11]	$\theta, \dot{\theta}, Z, w$	ELM	[-]
[12]	$\theta, \varphi, \phi, X, Y, Z$	DNN	0.0161, 0.005, 0.00055, 0.4959, 0.1173, 0.001

3 PROBLEM DESCRIPTION AND AVAILABLE DATA

In this study, the authors investigate the problem of short-term motions forecasting for vessel roll (φ) and trim (ψ). To this end, the authors leverage real-world operational data gathered over a period of one year for a twin diesel engine commercial vessel. The features in the data set can be grouped into two categories: (i) exogenous data, which describes the weather conditions through a number of climate and metocean features; and, (ii) endogenous data, which describes the on-board behaviors, such as the state of the propulsive system, the current position, and the trajectory of the ship. The vessel motions, that is, the roll (φ) and trim (ψ), are a subset of the endogenous data. The dataset is summarized according to source, category, feature, and unit in Table 2, but there are 49 time series features in total (because some features have more than one data-stream).

Additionally, the data are non-continuous, and characterized by 175 portions of varying lengths. There are approximately $500,000$ examples sampled over a period of 3 $[s]$. In fact, for each of the 175 portions, we can determine the weather conditions in which the vessel operates by comparing two common metrics: (i) the wind speed (e.g., according to the Beauford wind scale [13]) and (ii) the sea swell (e.g., according to the Douglas sea state [14]). This allows us to characterize the operating conditions into a number of classes based on quantitative metrics. Figure 1 summarizes this approach by showing the average wind speed and average sea swell across the 175 time series portions, which can be categorized into 10 classes of weather conditions. Additionally, qualitative descriptions for the Beauford wind scale and the Douglas sea state are included in the figure legend.

Table 2: Dataset summary according to the source, category, feature, and unit. Note that: there are 49 time series features in total (due to some features having more than one data-stream).

Source	Category	Feature	Unit
Exogenous	Climate	Air Temperature	$[^\circ C]$
		Relative Air Humidity	$[-]$
		Relative Wind Speed	$[m/s]$
		True Wind Speed	$[m/s]$
		Relative Wind Angle	$[^\circ]$
		Mean Wind Angle	$[^\circ]$
	Metocean	Mean Wave Period	$[s]$
		Mean Swell Period	$[s]$
		Swell + Wave Height	$[m]$
		Mean Wave Angle	$[^\circ]$
		Mean Swell Angle	$[^\circ]$
Endogenous	Main Engine	Speed	$[rpm]$
		Fuel Consumption	$[m^3/s]$
	Diesel Generators	Fuel Consumption	$[m^3/s]$
		Load	$[\%]$
		Power	$[kW]$
	Thrusters	Absorbed Power	$[kW]$
	Propeller	Pitch Ratio	$[-]$
		Speed	$[m/s]$
		Torque	$[Nm]$
	Rudder	Angle	$[^\circ]$
	Speed	Speed Over Water	$[m/s]$
		Speed Over Ground	$[m/s]$
	Position	Drift Angle	$[^\circ]$
		Draft at Bow	$[m]$
		Draft at Stern	$[m]$
	Motion	Roll Angle	$[^\circ]$
		Trim Angle	$[^\circ]$

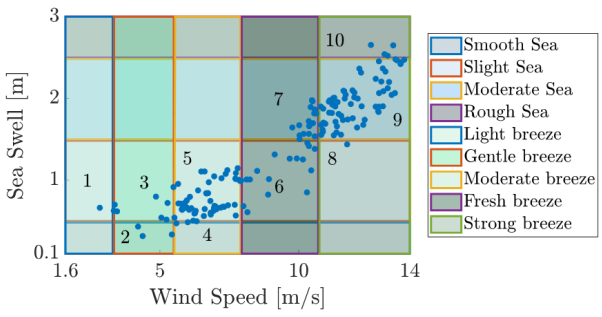

Figure 1: Average wind speed and average sea swell across the 175 time series portions which can be categorized into 10 classes of weather conditions.

4 METHODOLOGY

The approach in this study begins by mapping the problem of vessel motion prediction into a regression framework using Machine Learning. We begin with the conventional framework represented by an input space $\mathcal{X} \subseteq \mathbb{R}^d$, output space $\mathcal{Y} \subseteq \mathbb{R}^b$, and a target phenomenon $\mu : \mathcal{X} \rightarrow \mathcal{Y}$ to be learned [15], [16]. For pointwise motion prediction, $\mathcal{X}$ includes exogenous and endogenous vessel data, excluding motions, whereas $\mathcal{Y}$ pertains solely to the vessel motions (φ and ψ).

Furthermore, short-term motions forecasting requires expanding the regression framework by incorporating two temporal model hyperparameters. First, Δ^-, incorporates historical data, extending the input space to encompass past data from the interval $[t-\Delta^-, t]$ (i.e., $[\mathcal{X}, \mathcal{Y}] \subseteq \mathbb{R}^{d+b}$). The second, Δ^+, defines the forecast horizon (i.e., the vessel motions at time $t + \Delta^+$). In addition, reliable feature estimations can be used to further enrich the input space within $(t, t + \Delta^+]$.

Attention towards the correct choice of Δ^- is required to balance the dimensionality of the problem with capturing the dynamic effects [15]–[17]. Conversely, the ideal Δ^+ depends on the specific application [15]–[17]. For short-term vessel motions forecasting, Δ^+ should be in the order of a few seconds to ensure an adequate thrust allocation time for the vessel control system.

When selecting a machine learning algorithm for this application, the no-free-lunch theorem [18] requires testing multiple algorithms to find the best one. For the problem at hand, we test three shallow state-of-the-art algorithms from two different families [19], [20]. From the family of Kernel Methods [21], the authors selected to test Kernel Ridge Regression (KRR) using the Gaussian Kernel for the reason described in [22]. While from the family of Ensemble Methods [23], [24] the authors selected to test Random Forests (RF) and XGBoost (XGB) [25].

KRR requires tuning both the regularisation hyperparameter C and the kernel coefficient γ.

RF requires tuning the number of features to be randomly sampled from the entire set of features at each node n_f and the maximum number of elements in each leaf n_l. Since the performance of the RF improves with the number of trees n_t, we fixed it to 1000 to keep it computationally tractable.

XGB requires tuning the gradient learning rate l_r, the maximum depth of each tree n_d, the minimum loss reduction m_l, the number of points to randomly sample from the entire training set for each tree creation n_b, and the number of features to randomly sample from the entire set of features at each node n_f.

Additionally, in line with the current state-of-the-art approaches [26], the authors selected to test a deep learning approach: Temporal Convolutional Network (TCN) [26], [27]. While other deep learning architectures (e.g., the classical and Bidirectional Long Short-Term Memory network [28]) are also suitable candidate architectures for the problem at hand, previous studies have shown that the TCN generally outperforms the other deep learning models while also addressing several of their weaknesses [26], [27]. The TCN architecture illustrated in Figure 2 shows the proposed deep learning model architecture based on the TCN. The general architecture outlined in Figure 2(a), shows the 8 layer TCN block. The first TCN block serves as the input for the original time series signals and, as shown in Figure 2(b), the output of the network was the targets (i.e., the vessel motions) at the desired forecast horizons. For TCN, there are a number of hyperparameters to consider: the learning rate l_r, the dropout rate $d_{r,0}$ of each TCN layer and the last layer, the regularization coefficient C, the number of TCN blocks h_l, the number of filters on each block n_i, and the kernel size for each series and block $k_{s,i}$. For each algorithm, a summary of the hyperparameters with the associated search space is reported in Table 3.

Regarding the implementation of the algorithms for KRR and RF, the models were developed using an in-house custom Python toolbox, for XGB the models relied on the implementation found at [29].

Table 3: Hyperparameters and associated hyperparameter space for each algorithm tested in this work.

	Algorithm	Hyperparameters
Shallow	KRR	γ: $\{0.1, 0.01, 0.001, 0.0001\}$
		C : $\{0.001, 0.01, 0.1, 1, 10, 100\}$
	RF	n_f : $\{d^{1/3}, d^{1/2}, d^{3/4}\}$
		n_l : $\{1, 3, 5, 10\}$
		n_t : $\{1000\}$
	XGB	l_r : $\{0.01, 0.02, 0.03, 0.04, 0.05\}$
		n_d : $\{3, 5, 10\}$
		m_l : $\{0, 0.1, 0.2\}$
		n_b : $\{0.6n, 0.8n, 1n\}$
		n_f : $\{0.5d, 0.8d, 1d\}$
Deep	TCN	l_r: $\{0.0001, 0.0005, 0.001, 0.005, 0.01\}$
		$d_{r,0}$: $\{0.1, 0.15, \ldots, 0.5\}$
		C : $\{0.00001, 0.00005, 0.000001\}$
		h_l : $\{1, 2, 3, 4\}$
		n_i : $\{16, 32, 64, 128, 256\}$
		$k_{s,i}$: $\{3, 5, 7, 9, 11\}$

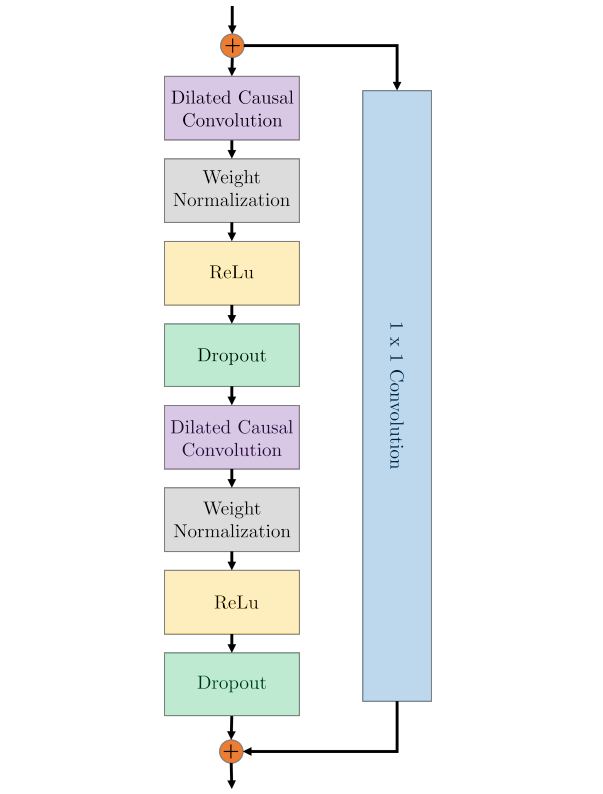

(a) TCN block layers.

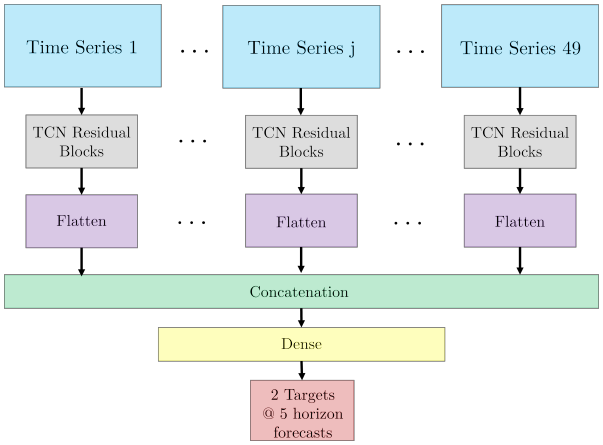

(b) Model architecture using the TCN.

Figure 2: TCN block and model architecture.

To implementat the TCN, the models were developed using custom software relying on the TensorFlow [30] Python module.

To tune the models' hyperparameters and assess the performance of the algorithms, the following Model Selection (MS) and Error Estimation (EE) procedures were employed [17].

For EE, based on the fact that the desired model should be able to extrapolate over unseen weather conditions, the data were divided into Training $\mathcal{D}_n$ and Test $\mathcal{T}_t$ sets using the Leave One Out (LOO) principle applied to different classes of weather conditions (see Section 3). For example, all the data corresponding to a single class of weather conditions were allocated into $\mathcal{T}_t$ while the remaining ones are kept in the $\mathcal{D}_n$.

It is then possible to use $\mathcal{D}_n$ to train the model and select the associated best hyperparameters, and use $\mathcal{T}_t$ to assess the performance of the final model. Repeating this procedure multiple times gives us the average performance in different scenarios (i.e., LOO). Furthermore, because the complexity of this problem increases with the adversity of the weather conditions, we reserved the most complex scenario (class 10) from the learning procedure for the final performance testing to present an unbiased and realistic test of the proposed approach.

Instead, for the MS, namely tuning the hyperparameters of the different algorithms, the following procedure was applied. First, $\mathcal{D}_n$ was split into Learning $\mathcal{L}_l$ and Validation $\mathcal{V}_v$ sets using the same LOO principle as previously described for the EE. Then, for all of the possible hyperparameter configurations (see Table 3), a model was trained on $\mathcal{L}_l$ and its performance was assessed on $\mathcal{V}_v$ according to the Mean Absolute Error (MAE). This procedure was then repeated for each LOO scenario, and the chosen hyperparameter configuration is the one with the lowest MAE when the performance was averaged across all the validation sets. Finally, just before the EE, the model is retrained using the entire $\mathcal{D}_n$ and the best hyperparameter configuration.

This approach is summarized in Figure 3.

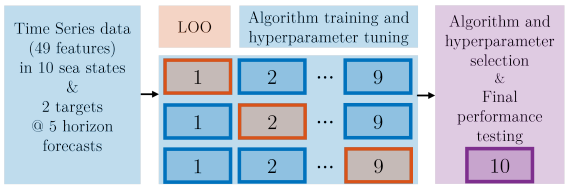

Figure 3: Leave One Out (LOO) methodology for algorithm and hyperparameter selection (on weather classes 1–9) and final performance testing (on weather class 10).

5 RESULTS

This section presents the results obtained by following the methodology proposed in Section 4 using the data described in Section 3.

For the first part, the LOO resampling procedure was carried out with weather condition classes $1-9$ to determine how each algorithm (KRR, RF, XGB, TCN) performs when forecasting short-term motions while extrapolating over weather conditions. The experiments considered $\Delta^- \in \{3, 12, 48, 64, 128\}$ $[s]$ and $\Delta^+ \in \{3, 6, 12, 24, 48\}$

$[s]$. The results of this experiment are presented in Tables 4 and 5 for the Trim (ψ) and Roll (φ) motions, respectively. The tables report the MAE for different forecast horizons (Δ^+) with the optimal model and temporal (Δ^-) hyperparameters for each of the algorithms, along with the interval of confidence evaluated according to the t-student's distribution with 95% confidence and $n-1$ degrees of freedom (where $n=9$ because of the number of classes in the LOO scenario). Note that a factor of 1×10^{-2} was removed from the results to ensure readability.

Table 4: Trim motion (ψ): MAE $[\times10^{-2\circ}]$ in LOO conditions for weather condition classes $1-9$ for different forecast horizons (Δ^+) with the optimal model and temporal (Δ^-) hyperparameters for each of the algorithms (KRR, RF, XGB, TCN).

Algorithm		Δ^+ [s]				
		3	6	12	24	48
Shallow	KRR	2.09 ± 0.30	2.51 ± 0.42	2.53 ± 0.55	2.54 ± 0.57	2.54 ± 0.53
	RF	2.10 ± 0.41	2.49 ± 0.45	2.49 ± 0.52	2.54 ± 0.59	2.56 ± 0.56
	XGB	2.07 ± 0.38	2.48 ± 0.41	2.49 ± 0.51	2.49 ± 0.54	2.54 ± 0.55
Deep	TCN	2.01 ± 0.29	2.50 ± 0.44	2.52 ± 0.50	2.53 ± 0.55	2.53 ± 0.58

Table 5: Roll motion (φ): MAE $[\times10^{-2\circ}]$ in LOO conditions for weather condition classes $1-9$ for different forecast horizons (Δ^+) with the optimal model and temporal (Δ^-) hyperparameters for each of the algorithms (KRR, RF, XGB, TCN).

Algorithm		Δ^+ [s]				
		3	6	12	24	48
Shallow	KRR	1.32 ± 0.12	1.44 ± 0.15	1.47 ± 0.16	1.73 ± 0.22	1.90 ± 0.28
	RF	1.41 ± 0.14	1.47 ± 0.16	1.51 ± 0.18	1.75 ± 0.25	2.02 ± 0.33
	XGB	1.33 ± 0.11	1.43 ± 0.14	1.45 ± 0.15	1.72 ± 0.20	1.98 ± 0.27
Deep	TCN	1.22 ± 0.09	1.31 ± 0.11	1.41 ± 0.13	1.63 ± 0.18	1.91 ± 0.24

Figures 4 and 5 show the varying MAE versus Δ^+ for each of the possible Δ^- combinations in the LOO scenario applied to the weather classes 1–9. From the results in Tables 4 and 5 and Figures 4 and 5, the best algorithm is defined as the one with the lowest MAE at the Δ^+ which is the furthest in the future, but still exhibits a low error. There are a few observations to make. First, as the forecast horizon increases, the error increases; however, for the trim motion, the error saturates at a forecast horizon of up to 6 [s] which is the point where the predictions are no longer reliable (i.e., MAE(ψ) $\approx 0.025[^\circ]$ using the TCN). Second, in general, as the forecast horizon increases the amount of past information included in the prediction (captured in the window $[t-\Delta^-, t]$) should be increased; although, as seen for the roll motion this saturates at approximately $\Delta^- = 64$ [s]. Finally, it is possible to infer that reasonable forecasts can be obtained for the trim motion (ψ) within a Δ^+ of 6 [s]; whereas for the roll motion (φ) within a forecast horizon (Δ^+) of up to 12 [s] (i.e., MAE(φ) $\approx 0.014[^\circ]$ using the TCN).

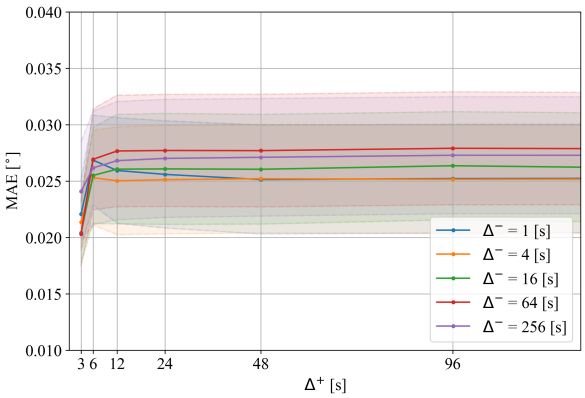

Figure 4: Trim motion (ψ): MAE versus Δ^+ for each of the Δ^- options for the best performing algorithm.

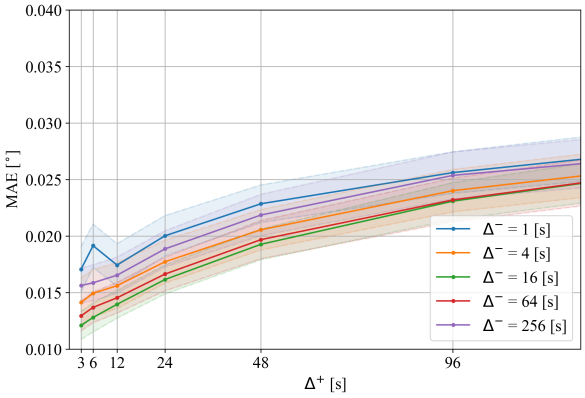

Figure 5: Roll motion (φ): MAE versus Δ^+ for each of the Δ^- options for the best performing algorithm.

Finally, according to the methodology outlined in Section 4, to obtain a more accurate representation of a real world test, the best models will be applied to unseen data coming from the most challenging scenario (weather class 10).

This experiment, aimed at providing an unbiased assessment of the proposed models in a real test scenario, was performed by selecting the best model and temporal hyperparameters for each motion according to Tables 4 and 5 and Figures 4 and 5 for the best possible Δ^+ (i.e., the largest forecast horizon that is still characterized by a low error).

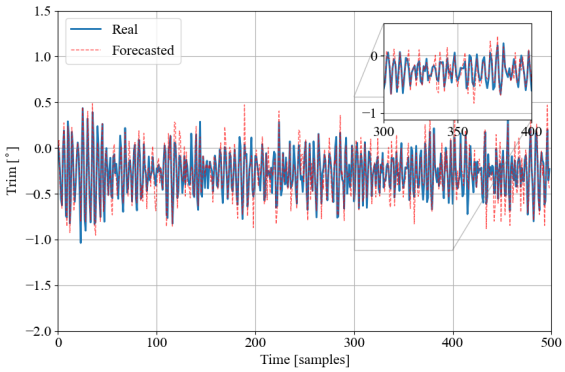

Figure 6: Trim motion (ψ): Real versus Forecasted with $\Delta^+ = 6$ [s] and $\Delta^- = 48$ [s].

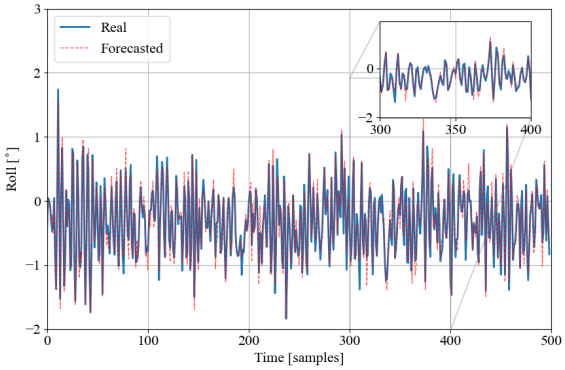

Figure 7: Roll motion (φ): Real versus Forecasted with $\Delta^+ = 12$ [s] and $\Delta^- = 48$ [s].

Table 6: Trim (ψ) and Roll (φ) motions: Best forecast horizons (Δ^+) with the optimal model and temporal (Δ^-) hyperparameters for the best algorithm on weather class 10.

Motion	**Algorithm**	Δ^+ **[s]**	Δ^- **[s]**	**MAE** [°]
ψ	TCN	6	48	0.0251
φ	TCN	12	48	0.0145

Using Tables 4 and 5 and Figures 4 and 5, the horizons are defined as 6 [s] for the roll and 12 [s] for the trim because these forecasts correspond to an error of less than 10% and 5% respectively, which is an acceptable margin for the task at hand.

The results obtained by applying the proposed method to the data left in weather class 10 are shown in Figures 6 and 7, where the real versus forecasted motions are presented for the trim and roll, respectively. Note that, for readability only 500 samples have been reported in the Figures; however, there were approximately 2050 data samples corresponding to weather class 10.

Finally, for a quantitative description of the models' performance, the error metrics are reported in Table 6 (over the entire portion of data belonging to this class).

Figures 6 and 7, and Table 6 demonstrate the efficacy of the proposed TCN-based short-term motions forecasting. Importantly, and distinct from the other approaches in the literature, the authors demonstrate the TCN-based approach is robust to changes in operating conditions and still performs well during periods of high exogenous loading.

6 CONCLUSIONS

In the fast-paced and demanding landscape of maritime technology, where accurate and precise state prediction is of utmost importance to enable intelligent vessel control systems, the proposed models harness the capabilities of both shallow and deep learning algorithms to deliver high accuracy in short-term vessel motion forecasting. The authors showed that the proposed models are robust, maintaining their predictive accuracy even under challenging conditions characterized by high exogenous loading, which is an important step toward developing fast and reliable short-term motions forecasting algorithms. The demonstrated forecasting framework has been subjected to empirical validation using a dataset collected from an operational vessel over a year.

The results of this study are promising. They show that for trim prediction, our models achieve a forecast horizon of up to 6 seconds, accompanied by a mean absolute error of $2.51[\times 10^{-2\circ}]$, which translates to a mean absolute percentage error of 9.12%. However, for the roll prediction, the performance is even more impressive, achieving a 12 seconds forecast horizon with a mean absolute error of $1.45[\times 10^{-2\circ}]$ and a corresponding mean absolute percentage error of 4.64%.

All models, whether based on shallow or deep learning algorithms, exhibited comparable levels of accuracy. There is a noticeable but acceptable decline in accuracy when the prediction horizons are extended to 24 and 48 seconds. For the roll motion, the mean absolute percentage errors at the extended horizons are 9.19% and 12.63%, respectively. Importantly, these errors remain within acceptable margins for making operational-related decisions.

Given the increasing data stream availability at higher sampling rates, the potential for extending these predictive horizons is increasingly likely. While the models developed in this study

are promising, they are validated using data from a single vessel, which poses questions about their generalizability across different types of vessels and operational conditions. Future research should address this by further validating the effectiveness of the deep learning-based approach using more diverse datasets and increased sampling rates for the specific problem at hand.

The next step in this research is the seamless integration of these advanced models into the existing vessel control systems. The successful integration of advanced predictive models into existing vessel control systems offers a unique opportunity to enhance the real-time decision-making processes onboard. In traditional vessel control systems, operators often rely on heuristic methods and past experience to make navigational and operational decisions. The introduction of the proposed models can transform this paradigm by providing data-driven insights that are both fast and accurate. This is particularly crucial in challenging maritime conditions where swift decision making can differentiate between safe navigation and operational hazards.

Moreover, the ability of the proposed models to maintain high levels of accuracy even under conditions of high exogenous loading adds an extra layer of reliability and robustness to the control systems. This is invaluable in scenarios such as heavy weather sailing or navigating through congested waterways, where the margin for error is minimal. Additionally, the models' scalability to longer prediction horizons, while maintaining acceptable error margins, indicates their potential for future applications that require long-term planning, such as route optimization and fuel efficiency calculations.

ACKNOWLEDGMENTS

This research is supported by the *Sustainable Hydrogen Integrated Propulsion Drives (SH2IPDRIVE)* project, which has received funding from RvO (reference number MOB21013), through the RDM regulation of the Ministry of Economic Affairs and Climate Policy. Additionally, the computational portion of this work leveraged the DelftBlue Supercomputer (Phase 1) [31].

REFERENCES

[1] S. Li and K. S. Fung, "Maritime autonomous surface ships (mass): Implementation and legal issues," *Maritime Business Review*, vol. 4, pp. 330–339, 4 Nov. 2019.

[2] E. Jokioinen, J. Poikonen, M. Hyvönen, *et al.*, "Remote and Autonomous Ships - The next step," *AAWA: Advanced Autonomous Waterborne Applications*, pp. 1–87, 2016.

[3] S. Thombre, Z. Zhao, H. Ramm-Schmidt, *et al.*, "Sensors and ai techniques for situational awareness in autonomous ships: A review," *IEEE Transactions on Intelligent Transportation Systems*, vol. 23, no. 1, pp. 64–83, 2022.

[4] International Maritime Organization, *Maritime Safety Committee (MSC), 100th session, 3-7 December 2018*, `https://www.imo.org/en/MediaCentre/MeetingSummaries/Pages/MSC-100th-session.aspx`, Last visited 11th March 2022, 2018.

[5] A. C. Qi, Q. L. Han, and Y. L. Wang, "A survey of motion control for marine vehicles," *Chinese Control Conference, CCC*, vol. 2015-September, pp. 4214–4218, 2015.

[6] R. Skulstad, G. Li, T. I. Fossen, T. Wang, and H. Zhang, "A Co-Operative hybrid model for ship motion prediction," *Modeling, Identification and Control*, vol. 42, no. 1, pp. 17–26, 2021.

[7] T. Fossen and Ø. Smogeli, "Nonlinear time-domain strip theory formulation for low-speed manoeuvering and station-keeping," *MIC Journal of Modeling, Identification and Control*, vol. 25, pp. 201–221, 2004.

[8] G. De Masi, R. Bruschi, and F. Gaggiotti, "Short term vessel motion forecasting based on wavelet neural network for wave feed-forward dynamic positioning," in *Proceedings of the International Offshore and Polar Engineering Conference*, 2012, pp. 915–919.

[9] N. Suhermi, Suhartono, D. D. Prastyo, and B. Ali, "Roll motion prediction using a hybrid deep learning and ARIMA model," *Procedia Computer Science*, vol. 144, pp. 251–258, 2018.

[10] W. Zhang and Z. Liu, "Real-time ship motion prediction based on time delay wavelet neural network," *Journal of Applied Mathematics*, vol. 2014, 2014.

[11] B. N. Rath and B. Subudhi, "Chapter 12 - an extreme learning-based adaptive control design for an autonomous underwater vehicle," in *Cognitive Informatics, Computer Modelling, and Cognitive Science*, G. Sinha and J. S. Suri, Eds., 2020, pp. 213–228.

[12] M. Zhang, G. Taimuri, J. Zhang, and S. Hirdaris, "A deep learning method for the prediction of 6-dof ship motions in real conditions," *Proceedings of the Institution of Mechanical Engineers, Part M: Journal of Engineering for the Maritime Environment*, vol. 0, no. 0, p. 14 750 902 231 157 852, 0.

[13] National Weather Service, *Beaufort Wind Scale*, `https://www.weather.gov/mfl/beaufort`, Accessed August 2023, 2023.

[14] World Meterological Organization, *Marine Frequently Asked Questions: 3. What is the Douglas scale and is it appropriate terminology?* `https:`

//community.wmo.int/en/activity-areas/Marine/About/FAQs, Accessed August 2023, 2023.

[15] S. Shalev-Shwartz and S. Ben-David, *Understanding machine learning: From theory to algorithms*. Cambridge university press, 2014.

[16] J. D. Hamilton, *Time series analysis*. Princeton university press, 1994.

[17] L. Oneto, *Model Selection and Error Estimation in a Nutshell*. Springer, 2020.

[18] S. P. Adam, S. A. N. Alexandropoulos, P. M. Pardalos, and M. N. Vrahatis, "No free lunch theorem: A review," *Approximation and optimization*, pp. 57–82, 2019.

[19] M. Fernández-Delgado, E. Cernadas, S. Barro, and D. Amorim, "Do we need hundreds of classifiers to solve real world classification problems?" *The journal of machine learning research*, vol. 15, no. 1, pp. 3133–3181, 2014.

[20] M. Wainberg, B. Alipanahi, and B. J. Frey, "Are random forests truly the best classifiers?" *The Journal of Machine Learning Research*, vol. 17, no. 1, pp. 3837–3841, 2016.

[21] J. Shawe-Taylor and N. Cristianini, *Kernel methods for pattern analysis*. Cambridge university press, 2004.

[22] S. S. Keerthi and C. J. Lin, "Asymptotic behaviors of support vector machines with gaussian kernel," *Neural computation*, vol. 15, no. 7, pp. 1667–1689, 2003.

[23] L. Breiman, "Random forests," *Machine Learning*, vol. 45, no. 1, pp. 5–32, 2001.

[24] I. Orlandi, L. Oneto, and D. Anguita, "Random forests model selection," in *European Symposium on Artificial Neural Networks, Computational Intelligence and Machine Learning*, 2016.

[25] T. Chen and C. Guestrin, "Xgboost: A scalable tree boosting system," in *ASM SIGKDD international conference on knowledge discovery and data mining*, 2016.

[26] V. D'Amato, L. Oneto, A. Camurri, and D. Anguita, "The importance of multiple temporal scales in motion recognition: When shallow model can support deep multi scale models," in *2022 International Joint Conference on Neural Networks (IJCNN)*, IEEE, 2022, pp. 01–10.

[27] V. D'Amato, L. Oneto, A. Camurri, *et al.*, "The importance of multiple temporal scales in motion recognition: From shallow to deep multi-scale models," in *IEEE International Joint Conference on Neural Networks*, 2022.

[28] L. Zhu, X. Wang, and J. Gao, "Co-occurrence feature learning for skeleton based action recognition using regularized deep lstm networks," *arXiv preprint arXiv:1603.07772*, 2016.

[29] T. Chen and C. Guestrin, "XGBoost: A scalable tree boosting system," in *Proceedings of the 22nd ACM SIGKDD International Conference on Knowledge Discovery and Data Mining*, San Francisco, California, USA: ACM, 2016, pp. 785–794.

[30] M. Abadi, A. Agarwal, P. Barham, *et al.*, *TensorFlow: Large-scale machine learning on heterogeneous systems*, https://www.tensorflow.org/, 2015.

[31] Delft High Performance Computing Centre (DHPC), *DelftBlue Supercomputer (Phase 1)*, https://www.tudelft.nl/dhpc/ark:/44463/DelftBluePhase1, 2022.

PROCEEDINGS OF MOSES2023 CONFERENCE
4TH INTERNATIONAL CONFERENCE ON MODELLING AND OPTIMISATION OF SHIP ENERGY SYSTEMS
26-27 OCTOBER 2023, DELFT, NETHERLANDS

Power Increase due to Marine Biofouling: a Grey-box Model Approach

Matthew de Haas[a,b], Andrea Coraddu[a], Abdel-Ali El Mouhandiz[b], Nikoleta Dimitra Charisi[a], and Austin A. Kana[a*]

[a]Department of Maritime and Transport Technology, Delft University of Technology, Delft, the Netherlands
[b]Feadship, Hoofdorp, the Netherlands
[*]A.A.Kana@tudelft.nl

Abstract

This paper proposes a grey-box modelling approach to predict marine biofouling growth and its effects on ship performance. The approach combines empirical or experimental-based white-box models with data-driven black-box models. First, a white-box model is built to predict ship resistance considering a bare hull. This prediction is based on calm water resistance, wind, waves, and temperature differences. Subsequently, marine biofouling growth is predicted using an experimental model that estimates the level of roughness on the ship hull. Finally, a deep extreme learning machine is used as a black-box model, employing a feedforward neural network technique. To test the approach, a superyacht case study was selected as a category of vessel heavily exposed to fouling. The study used a 2-year dataset obtained through a collaboration with Feadship. Results showed that the black-box approach outperforms the white-box approach in predictive capabilities. However, when the knowledge encapsulated in the white-box model is included in the grey-box approach, the model shows the highest prediction accuracy achieved by leveraging less historical data. This study demonstrates the potential of the proposed grey-box approach to accurately predict marine biofouling growth and its effects on ship performance, which can benefit ship operators and designers in improving operational efficiency and reducing maintenance costs.

Keywords: Marine Biofouling; Power Increase Prediction; Yachts; Deep Extreme Learning Machine; Grey-box Models.

1 INTRODUCTION

Marine biofouling, a phenomenon of the accumulation of micro and macro-organisms on immersed surfaces, has a strong influence on the performance of vessels by increasing surface roughness and consequently increasing fuel consumption and emissions of greenhouse gases [1]. Biofouling creates roughness on the hull and propeller which leads to additional frictional resistance and loss of propeller efficiency, also known as additional sea margin. Research has shown that fuel costs can be increased up to 35% when the ship hull is heavily fouled [2]. Additionally, biofouling threatens ecological balance by transferring invasive aquatic species in waters where they have little to no natural enemies [3]. A trade-off is often made for ship owners and operators between the additional cost of maintenance to keep the ship clean compared to the increase in operational cost of sailing with a fouled hull. The current practice is that the hull and propeller are cleaned when other maintenance is scheduled, which does not guarantee optimal cleaning schedules [4].

Accurate prediction of biofouling may lead to significant benefits for ship design, maintenance and operations. For ship design, the added sea margin is the result of both added hull resistance and decreased propeller efficiency and can be taken into account either within hydrodynamic analysis or within the calculation of the powering of the vessel. Additionally, for ship's maintenance and operation, accurate marine biofouling prediction may lead to optimal maintenance and cleaning schedules.

Marine biofouling is a complex phenomenon because it depends on various variables such as seawater surface temperature, salinity, acidity, speed of water flow, and light intensity [1]. There is currently no accurate and universal method for predicting biofouling and associated added sea margin [5]. The standard approach for estimating the speed loss is by applying ISO 19030 (ISO 19030-2, 2016), which prescribes methods for measuring changes in hull and propeller performance to give an indication for hull and propeller efficiency. However, this approach lacks a clear method on how to predict added sea margin due to fouling for ship design. As such, only low-fidelity analytical expressions ex-

@2023 de Haas, M. et al. published by TU Delft OPEN Publishing on behalf of the authors. Licensed under a Creative Commons Attribution CC BY license.
DOI: https://doi.org/10.59490/moses.2023.661

ist recommended by the Propulsion Committee of the 28th ITTC, having an average error of around 20% [6].

State-of-the-art methods for predicting the additional sea margin and the effect of biofouling on a propeller's performance are based on first-principle experimental based models (e.g., [7]), computational fluid dynamics (CFD) (e.g., [8]–[10], and data-driven modelling [11]. The main strengths of first-principle experimental based models are their interpretability and low computational cost to perform evaluations. Such models can give a good insight into the relevant physics, such as those related to added frictional resistance of a flat plate [12]. However, conventional models cannot represent all fouling situations, and models are often limited to static growth of fouling [13]. On the other hand, CFD can provide accurate predictions of the additional sea margin. However, at a high computational cost, thus limiting results to the chosen ship hull. Authors of [12], [14] have shown promising results with only a few percentage deviation between predicted resistance and power compared to verified results.

Finally, data-driven black-box models are based on Machine Learning (ML) techniques and are able to address complex problems and improve the accuracy of the predictions. These data-driven models show great potential to predict added sea margin by giving new insights and accounting for all variables with limited simplifications [11]. However, data-driven models typically suffer from a lack of interpretability. Authors of [11] developed a data driven digital twin to estimate the speed loss due to marine biofouling, which showed significant improvement compared to ISO 19030.

Authors of [15] investigated and compared the applicability of both Artificial Neural Networks (ANNs) and Gaussian processes (GPs) to the prediction of fuel efficiency in ship propulsion by using sensors' data. White-box modelling trends were applied to account for fouling. The authors concluded that the ANN performed slightly better than the GPs. Additionally, [11] developed a data-driven digital twin using data from on-board sensors to estimate the speed loss due to marine biofouling. The method used was Deep Extreme Learning Machine (DELM), which uses a feedforward neural network. This overcomes the problems resulting from the backward-propagation training algorithm with potentially low convergence rates, critical tuning of optimization parameters, and presence of local minima that call for multi-start and re-training strategies [16].

To the best of the authors' knowledge, the applicability of a grey-box modelling approach, which combines a white- and a black-box model, for the prediction of marine biofouling has not yet been explored. The authors thus propose a grey-box approach to predict the power increase for ships due to marine biofouling. The white-box model is used for the estimation of the required power in a fouled situation, dependent on time and the ship environmental conditions. The collected sensors' data and the white-box power prediction are used as inputs for the black-box model based on DELM.

To test the approach, a superyacht case study was selected because superyachts are particularly heavily exposed to marine biofouling due to their operational profile, which includes longer periods of being stationary compared to commercial vessels, often staying in ports or being anchored for long periods of time [17]. The operational profile of each superyacht can be very different and change over time. With an increasing and diversifying yacht fleet, understanding biofouling and its influence on yacht performance is important to minimizing their environmental footprint.

For this research, the collected data provided by Feadship came from both on-board sensors and company's databases. The available data contains ship design specifications, various captain logs, maintenance, engine, motion, voyage report, and auxiliary power data. Here the voyage report data contains onboard feedback monitoring of the following parameters: ship speed and heading, wave conditions (height, period, and directions), wind conditions (speed and direction), and corresponding measured operational profiles from Feadship fleet.

2 PHYSICS-BASED MODEL FOR BIOFOULING ESTIMATION

This section explains the physical model for predicting the fouled ship power. This contains both a short discussion on the predicted smooth ship resistance in Section 2.1, together with further elaboration on the prediction of fouling roughness in Section 2.2, while the fouled ship power prediction is presented in Section 2.3.

2.1 Smooth Ship Resistance

The ship resistance is predicted based on calm water, wind, and wave resistance together with differences due to temperature. The method proposed is in line with recommendations given by the [18].

As a basis for the resistance prediction in any given condition, the calm water resistance is computed based on the ship's speed. The speed over water is used, rather than the speed over ground as measured with AIS. The relative wind speed is based on the ship's speed, wind speed, and wind direction. The wind resistance coefficient, area of maximum transverse section exposed to wind, air density, and relative wind speed have been used to determine the added resistance due to wind in accordance with the methodology reported in [18].

To determine the added wave resistance, first the added thrust in waves is found based on ship speed, heading, length, displacement, and waterplane coefficient of the foreship [19]. With the added thrust in waves known, the added wave resistance can be found. An actual sea state is normally described by a wave spectrum such as the one proposed by Pierson-Moskowitz [20]. To allow for flexible spectrum shapes, the spectrum is multiplied with the peak enhancement factor, using the JONSWAP spectrum [21]. Next, the directional wave spectrum is found by multiplying the JONSWAP spectrum with the angular distribution function. Last, a correction accounts for the difference in resistance due to change in water temperature and difference in ship draft due to salinity. With this approach, a change of frictional resistance coefficient and change in resistance due to ship displacement can be found [18], [22].

2.2 Fouling roughness

For the prediction of biofouling growth, the model proposed by Uzun, Demirel, Coraddu, *et al.* was used [13]. The model makes use of two main principles: i) a fouling rating and ii) the fouling surface coverage for calcareous fouling. The fouling rating forms a basis for the model, combining slime, non-shells organisms, and calcareous fouling into one overall fouling rating. Together, this gives a good indication of the level of fouling present on the ship and its resulting roughness. However, when calcareous fouling is present on the ship, its level of surface coverage can be a dominant factor. Due to this, the authors introduced the calcareous surface coverage as an additional parameter. For this reason, a different function is used for the biofouling growth when the calcareous surface coverage increases above 5%.

With analyses limited to the given regions, the authors suggest interpolating and extrapolating found patterns based on sea surface temperature as the dominant fouling parameter. With the help of the proposed functions, biofouling growth trends for the Equator and Mediterranean can be inter- and extrapolated for all locations, to obtain the roughness thickness present on the ship. In this case, the roughness is modelled by using the equivalent sand roughness height (k_s). For a full explanation of the model, see [13].

2.3 Fouled Ship Power Prediction

The effects of the obtained roughness on the hull and propeller surface are determined next. First, the added frictional resistance coefficient (ΔC_F) as a result of this roughness can be calculated. This is done based on the equivalent sand roughness height, the ship waterline length (L_{WL}), and Reynolds number (Re) with the function of [23] (Equation 1).

$$\Delta C_F = 0.044 \left[\left(\frac{k_s}{L_{WL}} \right)^{\frac{1}{3}} - 10 \cdot Re^{-\frac{1}{3}} \right] + 0.000125 \tag{1}$$

Next, the added frictional resistance due to biofouling is found via Equation 2.

$$\Delta R_F = \frac{1}{2} \rho S \Delta C_F V_S^2 \tag{2}$$

The approach by [7] was employed to simulate the impacts of biofouling on the ship propeller. With this model, the change in thrust and torque coefficient due to biofouling is computed, and a new open water efficiency is found. This is done by finding the change in drag and lift for both coefficients (see [7] for the full method). However, it can be seen that the changes in the coefficients are a function of the propeller characteristics: propeller pitch, diameter, number of blades, chord length, and maximum thickness, together with fouling roughness. It is important to mention that both chord length and maximum thickness are taken at a radius of 0.75. Next, the drag and lift coefficient can be determined for the propeller in smooth and rough condition. Here, the smooth frictional coefficient can be found by either using Schroenherrs friction line (in Equation 3) or with the ITTC-1957 skin friction line (Equation 4), based on the method of the [24]. For the rough condition, the added frictional resistance coefficient is found using Equation 1, where the plate length (L_{WL}) is taken as the chord length (c) at radius $0.75R$.

$$\frac{0.242}{\sqrt{C_{FS}}} = log(Re \cdot C_{FS}) \tag{3}$$

$$C_{FS} = \frac{0.075}{(log(Re) - 2)^2} \tag{4}$$

With changes found, the open water efficiency for a fouled propeller can be found with the propeller thrust and torque coefficient for rough conditions.

Last, it can be noted that while marine biofouling mainly has an influence on the frictional resistance of the ship, it also has some effects on the wave resistance. One of the key findings by [25] is the decreasing wave resistance with an increasing surface roughness. This trend was later also found and confirmed by others [10], [26], [27]. It is important to mention that these findings go against the traditional view that wave-making resistance is not affected by hull-roughness [28]. The author proposes to use changes in wave coefficients based on [26], and interpolate and extrapolate these between researched speeds and equivalent sand roughness heights.

With a resistance prediction for smooth ship outlined and fouling growth and effects predicted, next a fouled ship power prediction can be made. First, the total resistance (R_T) can be found based on the calm water resistance (R_{calm}), the air drag resistance (R_{AA}), the wave resistance including changes due to biofouling ($R_W + \Delta R_W$), friction changes due to temperature ($\Delta R_{\Delta T}$), changes due to displacement ($R_{\Delta D}$), and added frictional resistance due to biofouling (ΔR_F), as shown in Equation 5

$$R_T = R_{calm} + R_{AA} + R_W + \Delta R_W + \Delta R_{\Delta T} + \Delta R_{\Delta D} + \Delta R_F \quad (5)$$

Next, the fouled brake power (P_{BR}) can be predicted, with the help of the found total resistance for the fouled situation together with ship speed, hull efficiency (η_H), rough open water efficiency (η_{OR}), relative rotative efficiency (η_R), propulsive efficiency (η_D), gearbox efficiency (η_{GB}) and shaft efficiency (η_S) as shown in Equations 6 and 7.

$$P_E = R_T V_S \quad (6)$$

$$P_{BR} = \frac{P_E}{\eta_H \cdot \eta_{OR} \cdot \eta_R \cdot \eta_{GB} \cdot \eta_S} \quad (7)$$

3 GREY-BOX MODEL APPROACH

In this section, a comprehensive description of the grey-box model applied for predicting marine biofouling growth and its effects on ship performance is provided. First, the underlying principles of DELM are detailed in Section 3.1, while the characteristics and parameters of the model's input are described in Section 3.2.

3.1 Deep Extreme Learning Machine

The task of predicting marine biofouling growth and its subsequent impact on ship performance, based on the data delineated in Section 1, can be mapped into the classical ML regression problem [29].

To better comprehend the aforementioned problem, let's recall the fundamental concepts of the ML regression problem. Let us define $\mathcal{X} \subseteq \mathbb{R}^d$ as the input space composed of d distinct features, and $\mathcal{Y} \subseteq \mathbb{R}$ as the corresponding output space.

Consider a sequence of $n \in \mathbb{N}^*$ distinct samples, symbolized as $\mathcal{D}_n = \{(x_1, y_1), \ldots, (x_n, y_n)\}$, where each $x_i \in \mathcal{X}$ and $y_i \in \mathcal{Y}$ for all $i \in 1, \cdots, n$. These samples are independently drawn from an undefined probability distribution μ encompassing $\mathcal{X} \times \mathcal{Y}$. Within this scenario, we opt for a function (or model) $f : \mathcal{X} \to \mathcal{Y}$ from a set $\mathcal{F}$ of potential models. An algorithm, characterized by its hyperparameters $\mathcal{H}$ and denoted as $\mathscr{A}_{\mathcal{H}} : \mathcal{D}_n \times \mathcal{F} \to f$, is employed to choose a model from the suite of possible choices, guided by the available dataset.

The efficacy of the function f in modeling the unobserved system $\mathfrak{S}$ is evaluated by employing a predetermined loss function, $\ell : \mathcal{Y} \times \mathcal{Y} \to [0, \infty)$. Given that the issue at hand is one of regression, the most fitting choice for the loss function is the squared loss, expressed as $\ell(f(\boldsymbol{x}), y) = [f(\boldsymbol{x}) - y]^2$ [30]. Consequently, we can define the true error, or the generalization error, of f as

$$L(f) = \mathbb{E}_{(\boldsymbol{x},y)}\ell(f(\boldsymbol{x}, y)). \quad (8)$$

Since $L(f)$ cannot be computed, its empirical estimator (the empirical error) can be derived as follow

$$\widehat{L}(f) = \frac{1}{n}\sum_{i=1}^{n} \ell(f(\boldsymbol{x}_i, y_i)). \quad (9)$$

When it comes to the selection of an algorithm, this paper capitalizes on the DELM. Various algorithms for tackling regression problems abound in the existing literature [29]. In particular, three principal categories of methods have demonstrated practical effectiveness [29], [31], [32]: kernel methods, ensemble methods, and neural networks. In our study, we leverage insights from [11] to adopt a specific subset of neural networks, namely, the DELM [33]. DELM represents an evolution from the Shallow Extreme Learning Machine (SELM), developed for single-hidden-layer feedforward neural networks, with the aim of creating an algorithm capable of not only learning new features from available raw variables but also building a robust regression model.

SELM were originally developed for the single-hidden-layer feedforward neural networks

$$f(\boldsymbol{x}) = \sum_{i=1}^{h} w_i g_i(\boldsymbol{x}). \tag{10}$$

Here, $g_i : \mathbb{R}^d \to \mathbb{R},\ i \in 1, \cdots, h$ denotes the output from the hidden layer corresponding to the input sample $\boldsymbol{x} \in \mathbb{R}^d$, while $\boldsymbol{w} \in \mathbb{R}^h$ represents the output weight vector linking the hidden layer to the output layer.

The input layer, equipped with d neurons, communicates with the hidden layer (which has h neurons) via a set of weights $W \in \mathbb{R}^{h \times d}$ and a nonlinear activation function. For this study, we selected the $\tanh$ function as the activation function, as suggested in the seminal work of [33]. It is worth noting, however, that the choice of other activation functions, such as the sigmoid function, doesn't significantly impact the final performance, $\varphi : \mathbb{R} \to \mathbb{R}$. Consequently, the response of the i-th hidden neuron to an input stimulus $\boldsymbol{x}$ is given by:

$$g_i(\boldsymbol{x}) = \varphi\left(W_{i,0} + \sum_{j=1}^{d} W_{i,j} x_j\right). \tag{11}$$

In SELM, the parameters W are randomly assigned. A weight vector, $\boldsymbol{w} \in \mathbb{R}^h$, devoid of any bias, bridges the hidden neurons to the output neuron. The comprehensive output function of the network is given by:

$$f(\boldsymbol{x}) = \sum_{i=1}^{h} w_i \varphi\left(W_{i,0} + \sum_{j=1}^{d} W_{i,j} x_j\right). \tag{12}$$

For practicality, we define an activation matrix, $A \in \mathbb{R}^{n \times h}$, in which the element $A_{i,j}$ signifies the activation value of the j-th hidden neuron for the i-th input pattern. Consequently, the A matrix takes the form:

$$A = \begin{bmatrix} \varphi_1(\boldsymbol{x}_1) & \cdots & \varphi_h(\boldsymbol{x}_1) \\ \vdots & \ddots & \vdots \\ \varphi_1(\boldsymbol{x}_n) & \cdots & \varphi_h(\boldsymbol{x}_n) \end{bmatrix}. \tag{13}$$

In SELM models, the weights W are set randomly and remain unmodified, leaving the quantity $\boldsymbol{w}$ in Eq.(12) as the sole degree of freedom. This circumstance simplifies the training to a direct Regularized Least Squares (RLS) problem [34]:

$$\boldsymbol{w}^* = \arg\min_{\boldsymbol{w}} \|A\boldsymbol{w} - \boldsymbol{y}\|^2 + \lambda \|\boldsymbol{w}\|^2, \tag{14}$$

where, $\lambda \in [0, \infty)$ signifies a hyperparameter that requires tuning during the Model Selection (MS) phase [35]. This tuning process establishes a balance between model complexity and accuracy, measured by the square loss and the $L2$ regularizer respectively. As a result, the optimal weight vector, denoted as $\boldsymbol{w}^*$, can be determined as follows:

$$\boldsymbol{w}^* = (A^T A + \lambda I)^+ A^T \boldsymbol{y}, \tag{15}$$

where $I \in \mathbb{R}^{h \times h}$ denotes an identity matrix, and $(\cdot)^+$ refers to the Moore-Penrose matrix pseudoinverse. It's crucial to note that h, the count of hidden neurons, is another hyperparameter requiring fine-tuning, based on the specific problem under consideration. Additionally, other regularizers, such as sparse regularizers, can be employed [36].

Given its shallow architecture, SELM might not offer efficient feature learning, even when h is large. As feature learning frequently enhances the final model's accuracy, multi-layer (deep) solutions are often required. In this context, [37] develops multi-layer learning architectures using ELM-based autoencoder (AE) as the fundamental building block, leading to the creation of DELM. In a DELM, each layer i out of the l layers — each composed of $h_{i \in 1,\cdots,l}$ neurons — strives to reconstruct the input data. The outputs from the previous layer are then utilized as inputs for the next. Consequently, instead of yielding a single output, a sequence of outputs $\hat{x}_j$ is obtained, with $j \in 1, \cdots, d$, such that:

$$\hat{x}_j = \sum_{i=1}^{h} w_{i,j} \varphi\left(W_{i,0} + \sum_{j=1}^{d} W_{i,j} x_j\right) \tag{16}$$

$$\hat{x}_j = \sum_{i=1}^{h} w_{i,j} \varphi_i(\boldsymbol{x}), \tag{17}$$

where $w_{i,j}$ with $i \in \{1, \cdots, h\}$ are found with the same approach of SELM.

In the DELM model, before the supervised regularized least mean square optimization occurs, the encoded outputs are directly channeled to the last layer for decision-making, bypassing any random feature mapping. Unlike SELM, DELM doesn't necessitate fine-tuning for the entire system, enabling much faster training speed than traditional backpropagation-based Deep Learning. Training a DELM is essentially equivalent to training multiple SELMs. Therefore, the advantages of a deep architecture can be harnessed using only the optimization tools designed for the SELM. It's worth noting that the DELM model encompasses numerous hyperparameters: the number of layers, the number of nodes per layer, and the regularization coefficient,

expressed as $\mathcal{H} = \{l, h_1, \cdots, h_l, \lambda\}$. These parameters must be carefully fine-tuned to minimize the final model's generalization error. Accordingly, a model selection phase consistent with [38] has been conducted in this study.

We utilize the nonparametric Bootstrap approach for model selection, a frequently implemented method within the resampling method family. The original dataset $\mathcal{D}_n$ has been resampled once or several times (n_r), either with or without replacement, to create two independent datasets — the training set $\mathcal{L}^r_{n_l}$ and the validation set $\mathcal{V}^r_{n_v}$, respectively. Here, $r \in \{1, \cdots, n_r\}$ and the two sets are mutually exclusive and collectively exhaustive: $\mathcal{L}^r_{n_l} \cap \mathcal{V}^r_{n_v} = \oslash$, $\mathcal{L}^r_{n_l} \cup \mathcal{V}^r_{n_v} = \mathcal{D}_n$. Following this, to perform the model selection phase and identify the optimal combination of hyperparameters $\mathcal{H}$ from a set of possible ones $\mathcal{S}_\mathcal{H} = \{\mathcal{H}_1, \mathcal{H}_2, \cdots\}$ for the algorithm $\mathscr{A}_\mathcal{H}$, we apply the subsequent procedure:

$$\mathcal{H}^* : \quad \min_{\mathcal{H} \in \mathcal{S}_\mathcal{H}} \frac{1}{n_r} \sum_{r=1}^{n_r} \frac{1}{n_v} \sum_{(\boldsymbol{x}, y) \in \mathcal{V}^r_{n_v}} \ell(\mathscr{A}_{\mathcal{H}, \mathcal{L}^r_{n_l}}(\boldsymbol{x}), y), \tag{18}$$

where $\mathscr{A}_{\mathcal{H}, \mathcal{L}^r_{n_l}}$ is a model built with the algorithm $\mathscr{A}_\mathcal{H}$ trained with $\mathcal{L}^r_{n_l}$. Since the data in $\mathcal{L}^r_{n_l}$ is independent of that in $\mathcal{V}^r_{n_v}$, the optimized hyperparameters $\mathcal{H}^*$ should achieve low error rates on a dataset distinct from the one used for training. It's important to note that the nonparametric Bootstrap approach differs from other resampling methods in two key aspects: firstly, $n_l = n$ and secondly, $\mathcal{L}^r_{n_l}$ is sampled with replacement from $\mathcal{D}n$. We also note that $\mathcal{V}^r n_v$ is the complement of $\mathcal{L}^r_{n_l}$ within $\mathcal{D}_n$, that is, $\mathcal{V}^r n_v = \mathcal{D}_n \setminus \mathcal{L}^r n_l$.

3.2 Model Input

Using the selected grey-box approach, all available data, as previously described, has been incorporated into the grey-box model, along with the estimate found from the white-box prediction, following the serial grey-box configuration of [39]. In the white-box biofouling growth approach, the fouling at each anchorage was predicted in conjunction with its corresponding average sea surface temperature, therefore, for the grey-box model, the sea surface temperature is used (see Fig 1). Note that sensor data for the sea surface temperature was not available for the full investigated period, when this was the case an additional dataset with the ships location and time was employed for an estimate of this parameter. The white-box approach contains both the total anchorage days since cleaning that are processed per anchorage and the sailing days since cleaning, and the biofouling growth model does not have a prediction of how this changes during sailing, as the model is based only on static tests. Nonetheless, this parameter is entered into the grey-box model so that possible fouling changes during sailing can be found. Last, the delivered brake power by the ship is taken as the model output at different speeds (Fig 2). An overview of the input and output parameters is shown in Table 1.

Figure 1: Sea surface temperature over time.

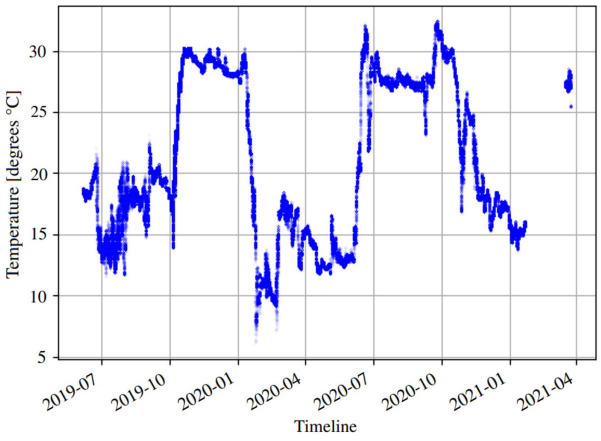

Figure 2: Ship speed vs power.

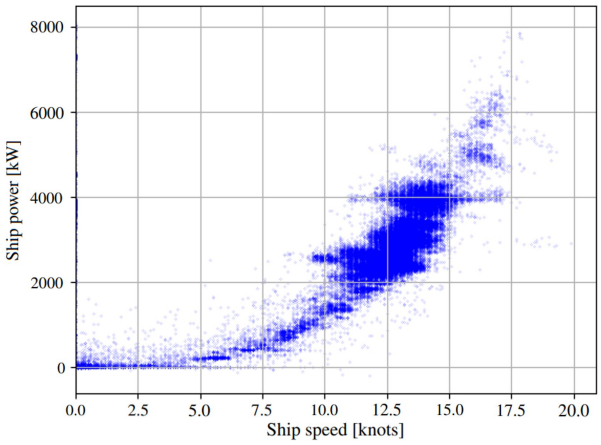

Table 1: Input and output for grey-box model.

Input	Unit
White-box prediction	[kW]
Ship speed	[knots]
Ship direction	[°]
Wave height	$[m]$
Wave direction	[°]
Wave period	$[s]$
Wind speed	$[m/s]$
Wind direction	[°]
Average sea surface temperature	[°C]
Anchorage days since clean ship	[days]
Sailing days since clean ship	[days]
Average ship speed	[knots]
Mean roll	[°]
Mean pitch	[°]
Roll deviation	$[°/s]$
Pitch deviation	$[°/s]$
Output	**Unit**
Fouled ship power	[kW]

Once input and output have been defined, the data still requires preparation for use in the grey-box model. To achieve this, the data was filtered using Chauvenet's criterion [40]. Moreover, a filtering technique that incorporates engineering knowledge to curate the data has been applied. The data selection for these predictions was determined by specific criteria related to ship speed and wind conditions. For ship speed, we incorporated all data exceeding 10 knots. Meanwhile, for wind speed, we restricted the dataset to conditions below 8 m/s to exclude instances of severe weather, which render ship performance difficult to predict. In addition to these factors, changes in ship speed were also considered. Significant speed fluctuations in a short period of time typically indicate that the ship is either accelerating or decelerating. As the current methodology does not account for these motions, they could potentially lead to inaccurate power predictions and adversely affect the quality of analysis data. Therefore, with data sampling every three minutes, we chose to analyze only those ship speeds where the preceding speed was within a one-knot range. This approach led to a total number of 34,448 samples. This approach was adopted based on the study cited in [11].

4 RESULTS AND DISCUSSION

In this section, we will evaluate the performance of the proposed grey-box approach utilizing the validation techniques outlined in Section 3. First, we examine the accuracy of the white-box model, detailed in Section 2, that forms the basis of the grey-box construction. We present its performance through both quantitative and qualitative metrics. The dataset was filtered to focus on a fixed speed of 13.5 knots, one of the most frequently attained speeds, using for the overall prediction accuracy the mean absolute percentage error (MAPE). To give better insight into which extent this number is true, a 95% confidence level interval has been applied. Upon inspection of this filtered data, a noticeable drift in power increase during operation can be discerned, as illustrated in Fig 3. Moreover, after cleaning periods in early 2020, we observe a decrement in power, reverting back to lower values. This observation substantiates the presumption that the visible power increase is attributable to marine biofouling, rather than, for instance, the loss of performces of other propulsion system components.

Figure 3: Power usage over time for 13.5 knots.

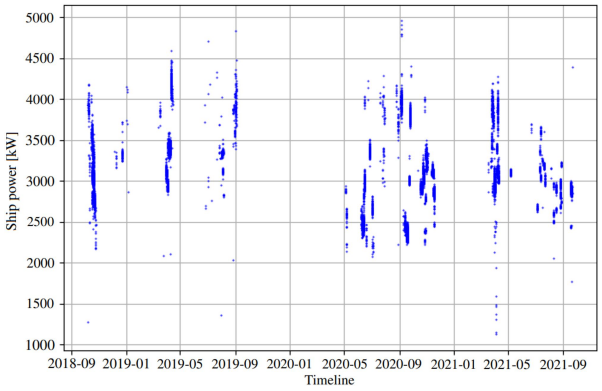

The white-box model's predictions showcased an accuracy of 85%, as shown in Figure 4. This model, grounded in established physical laws and principles, possesses the advantage of being interpretable and reliable under conditions akin to the ones it was formulated for. However, our analysis revealed a consistent trend of underestimation. Even in scenarios shortly following cleaning procedures, the white-box model's predictions fell short of the actual measurements. This systematic bias suggests that certain aspects of the resistance are not being fully accounted for within this model. The degree of this bias is expected to vary across different vessels, underscoring the inherent challenge in formulating a general model suitable for all ship types. Therefore, a pertinent line of inquiry is to determine the extent to which the white-box method can capture the intricacies of ship power prediction. In addition, it's worth investigating whether the introduction of additional parameters or refinement of existing ones

can address this model's underestimation bias.

Moving onto the black-box model, this approach exhibited an accuracy of 90%, as shown in Fig 5. This model has a similar input as the grey-box model as illustrated in Table 1, except for the white-box prediction as an input parameter. Black-box models, being purely data-driven, tend to be highly flexible and can potentially model complex, nonlinear relationships that the white-box models may not adequately capture. However, they are susceptible to high variance error, a problem often associated with overfitting. Thus, although it delivers a marginally improved accuracy compared to the white-box model, it's crucial to evaluate its performance over a wide range of operational conditions and for different ship types to ensure robustness.

Lastly, the grey-box model, a fusion of the principles-based approach of the white-box model and the empirical learning of the black-box model, accomplished the highest prediction accuracy of almost 92%, as shown in Figure 6. By integrating known physical relationships and data-driven elements, the grey-box model can effectively strike a balance between bias and variance, consequently leading to a superior predictive performance. Notably, another crucial advantage of the grey-box model lies in its efficiency with respect to data requirements. While data-driven models, like the black-box model, typically necessitate large quantities of data to attain high accuracy, the incorporation of known physical laws in the grey-box model allows it to achieve comparable, if not superior, performance levels with significantly less data, as it has prior knowledge/assumptions about the problem domain. This trait makes the grey-box model particularly attractive in scenarios where data collection may be expensive, time-consuming, or otherwise challenging. However, caution is advised to avoid over-dependence on the data-driven component in the grey-box model, as this could veer the model towards overfitting. Thus, while leveraging the flexibility offered by the data-driven component, it is critical to continually reference and respect the governing physical principles to maintain the robustness and generalizability of the model.

A comparative analysis of the models, as summarized in Table 2, clearly indicates a hierarchy in performance over the test dataset: Grey-Box $>$ Black-Box $>$ White-Box. Yet, it's important to note that each model's performance should not be evaluated merely on accuracy, but also on bias-variance tradeoff, interpretability, and applicability to diverse ship types and operational conditions.

Table 2: Performance comparison

Model	**MAPE**
White-Box	14.7% $\pm$ 0.3%
Black-Box	10.2% $\pm$ 0.2%
Grey-Box	8.6% $\pm$ 0.2%

Figure 4: Physics-based model predicted and measured power.

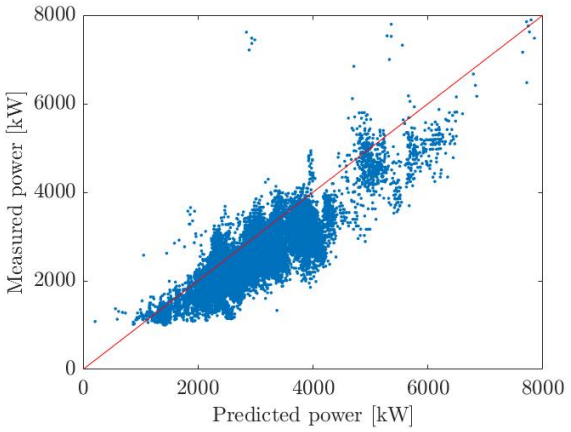

Figure 5: Black-box predicted and measured power.

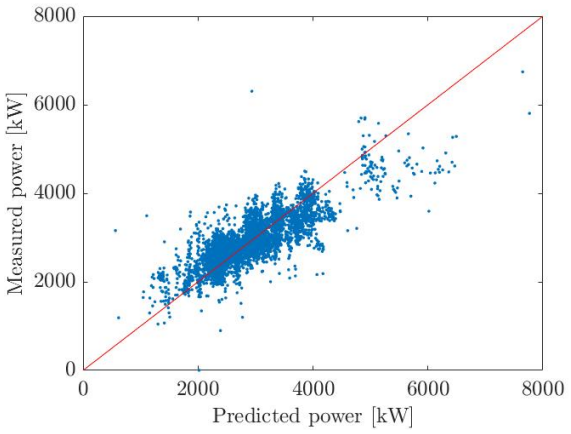

Figure 6: Grey-box predicted and measured power.

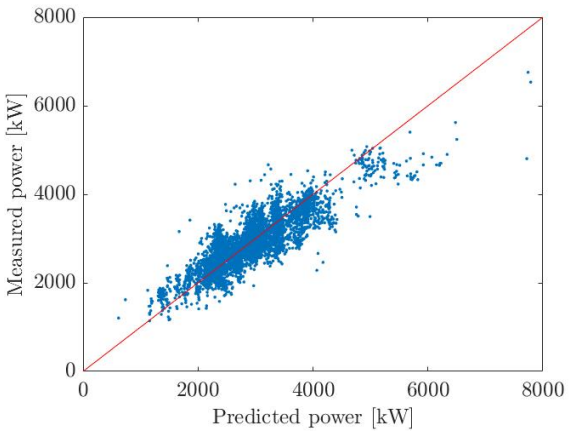

In order to assess the models' predictive performance beyond the confines of the data used for training, validation, and test, a preliminary evaluation was conducted. Fig 7 presents an application of the model over an extended period. To facilitate this, all parameters, with the exception of anchorage days, sailing days, and the predictions from the white-box model, were assumed to be at their mean value. The yacht's activity, characterized by sailing 16% of the time, was used to establish the correlation between anchorage and sailing days. Fig 7 illustrates the mean predictions for the black-box and grey-box models with a line, while the prediction area represents the interval of confidence of the results over 30 repetitions. These repetitions are performed, as deep learning models are stochastic models, making use of randomness while being fit on the data. Employing this approach provides insights into the areas where the predictions are mostly congruent and the regions that exhibit significant inter-model variance in predictions. It highlights models ability to capture the inherent uncertainties associated with real-world conditions, thereby lending confidence to their utility in practical scenarios. Last, the trained anchorage days range is also highlighted in the figure, as it shows a more clear division between the interpolation and extrapolation capacities of the models employed.

Figure 7: Comparison between white-, black-, and grey-box prediction for longer period of time.

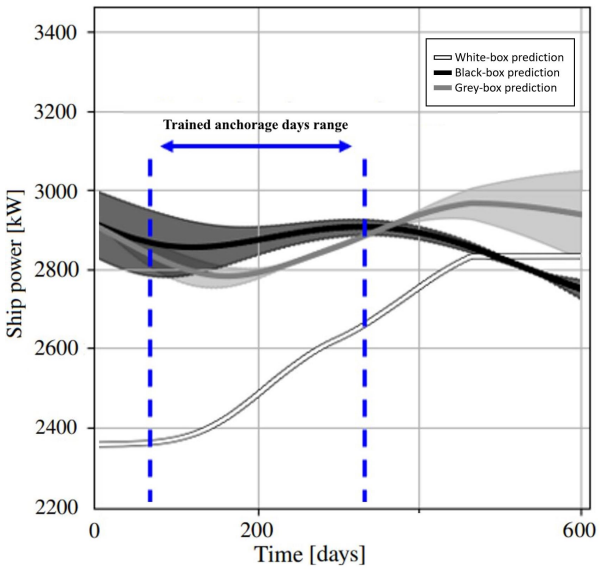

Fig 7 illustrates that the black-box and grey-box models display comparable trends within the range of trained data, whereas the white-box model consistently generates lower predictions. However, upon extrapolating the data-driven models, a significant degree of variance and potential inaccuracy in their results becomes evident. Such observations align with the common understanding that data-driven models often grapple with challenges in the context of extrapolation. The exhibited large variance and outcomes underscore the limitations of such models when applied beyond the bounds of their training data. This highlights the limitations for application of the proposed models, particularly in scenarios when extreme extrapolation is necessary.

Marine fouling growth encompasses various stages, such as the formation of slime, the growth of non-shell organisms, and the occurrence of calcareous fouling. However, given that our model was solely trained on data from the initial year of fouling growth, it remains unfamiliar with the settlement of barnacles and the onset of calcareous fouling. This unfamiliarity becomes evident when the white-box model indicates a significant power increase at more advanced stages of fouling. While the grey-box model attempts to harness the strengths of both white- and black-box models, its effectiveness seems to primarily lie in improving upon the black-box model predictions. Conversely, the white-box model still appears to have the upper hand in extrapolation and in providing transparent and interpretable insights into the fouling process. This underscores the need for a more comprehensive training dataset that spans across the various stages of marine fouling, thereby improving the predictive capacity of the model for long-term and advanced fouling situations.

The white-box model, as employed in this study, is indeed a practical solution that assimilates some of the most relevant research pertinent to this field of application. However, it's critical to underline that this model, despite its theoretical robustness, manifests certain limitations in terms of accuracy. Its predictive performance is low, and the model also demonstrates a higher level of variance, introducing a degree of uncertainty into the predictions. This model also exhibits substantial bias error, which may significantly skew the predictions and result in systematic deviations from the actual data. These aspects, coupled with the limitations in addressing complex, multi-staged fouling processes, call for refinement and enhancement of the white-box model to ensure it's aptly equipped to handle the intricacies of this application.

This observed scatter can be attributed primarily to the inconsistencies between the ship's power, which tends to remain stable, and the ship's speed,

which fluctuates. This disparity introduces inaccuracies across the dataset, despite the overall trend displaying promising prediction potential. Another contributing factor to the data scatter is the derivation process for the ship's speed. Initially extracted from the Automatic Identification System (AIS), the speed was then computed over water using predicted currents. However, it's important to acknowledge that directly measuring the speed over water could potentially improve prediction accuracy. Even slight variations in speed can significantly impact the predicted calm water resistance and the power required, underscoring the need for precise speed measurements in enhancing the predictive accuracy of these models.

5 CONCLUSIONS

The research outlined in this paper introduces a grey-box modeling strategy aimed at predicting marine biofouling growth and its subsequent impact on ship performance. This approach synergistically integrates the empirical insights of white-box models and the data-intensive capabilities of black-box models. Initially, a white-box model is presented to predict ship resistance, considering variables such as calm water resistance, wind, waves, and temperature discrepancies. The prediction of marine biofouling growth is subsequently managed via an experimental model designed to estimate the roughness level of the ship hull. Lastly, a Deep Extreme Learning Machine is utilized as a black-box model, which incorporates a feedforward neural network technique.

With the proposed approach certain limitations inherent in the white-box model can be partially mitigated through the application of trained data-driven models. These models possess the capacity to understand how available input can be utilized to enhance the predictive accuracy of the white-box models.

Moreover, in situations where a fleet of similar ships is available, the correlations discerned by the grey-box model can be leveraged to refine the predictions of full white-box models for other ships. This can be achieved even in the absence of trainable data. This highlights the potential of the grey-box model as a powerful predictive tool that can efficiently use available information to enhance prediction accuracy, thus providing a robust method that can be applied across multiple ships, irrespective of the available data for each vessel.

To validate the proposed approach, a superyacht case study was chosen as the testing ground due to the category's high susceptibility to fouling. This involved the analysis of a 2-year dataset acquired through a partnership with Feadship.

The results presented highlighted that while the black-box model displayed superior predictive capabilities compared to its white-box counterpart, it was the grey-box model that exhibited the best performance. By incorporating the knowledge encapsulated within the white-box model, the grey-box model displayed the highest prediction accuracy whilst requiring less historical data. These findings underline the potential of the grey-box model as a tool for accurately predicting marine biofouling growth and its impact on ship performance. The practical implications of this research extend to ship operators and designers, who could leverage these insights to enhance operational efficiency and minimize maintenance costs.

The results also suggest for a more nuanced understanding of model selection and design in predictive tasks. While black-box models may often deliver higher prediction accuracy in situations where ample historical data is available, the incorporation of domain knowledge via grey-box models can help achieve similar, if not better, performance with less data. This highlights the importance of continued research in hybrid modelling techniques, especially in domains where data may be costly or difficult to acquire. While the data-driven models, and especially the grey-box model showed the highest potential for the capture of the biofouling modeling and ship power prediction within the researched period, its lacking extrapolation capacity was also identified. Enabling the dataset with more vessels, a wider range of operational profiles, and later biofouling growth stages such as barnacle growth, would improve model performance.

From the perspective of ship design, the current approaches towards predicting fouling are either absent or rely heavily on rudimentary approximations. The primary assessments for powering calculations and ship speed are generally conducted for clean hulls, given that the biofouling issue is predominantly addressed during maintenance and operational phases rather than the design stage. Nonetheless, pertinent information that could allow for preliminary predictions on biofouling development is often available even at the early stages of ship design. The present research was initiated with the intention to incorporate and utilize this information effectively. Utilizing the proposed model, it is possible to craft ship-specific predictions grounded on

the prospective operational profile and forecasted environmental conditions. This, in turn, facilitates more informed decisions regarding the selection of antifouling systems and the determination of necessary engine margins or propulsion layouts. When these predictions are coupled with the operational profile of a yacht, it is possible to calculate the fuel penalty in conjunction with the costs of antifouling, docking, and cleaning.

ACKNOWLEDGEMENTS

The authors are grateful for the support of Feadship / De Voogt Naval Architects as the research presented in this paper was generated as part of their sea margin project, where yacht sensor data was shared together with in-house methods.

REFERENCES

[1] C. Bressy and M. Lejars, "Marine fouling : An overview," *Journal of Ocean Technology*, vol. 9, pp. 19–28, Dec. 2014.

[2] Y. Demirel, O. Turan, and A. Incecik, "Predicting the effect of biofouling on ship resistance using CFD," *Applied Ocean Research*, vol. 62, pp. 100–118, 2017.

[3] S. A. Alghamdi and R. A. Quijada Cordova, "The impact of biofouling on marine environment: A qualitative review of the current antifouling technologies," M.S. thesis, World Maritime University, Malmö, Sweden, 2019.

[4] L. Kjær, D. Pigosso, T. McAloone, and M. Birkved, "Guidelines for evaluating the environmental performance of product/service-systems through life cycle assessment," *Journal of Cleaner Production*, vol. 190, Apr. 2018.

[5] ITTC Technical Committee on Resistance and Propulsion. "Review of state of the art." (2021), [Online]. Available: `https://ittc.info/media/9825/resistance-and-propulsion-committee.pdf`.

[6] Propulsion Committee of the 28th ITTC, "1978 ITTC Performance Prediction Method," *ITTC - Recommended Procedures and Guidelines*, 2017.

[7] A. Farkas, N. Degiuli, I. Martić, and I. Ančić, "Performance prediction method for fouled surfaces," *Applied Ocean Research*, vol. 99, Apr. 2020.

[8] A. Farkas, N. Degiuli, and I. Martić, "The impact of biofouling on the propeller performance," *Ocean Engineering*, vol. 219, p. 108 376, Nov. 2020.

[9] D. Owen, Y. Demirel, E. Oguz, T. Tezdogan, and A. Incecik, "Investigating the effect of biofouling on propeller characteristics using cfd," *Ocean Engineering*, vol. 159, Feb. 2018.

[10] S. Song, Y. Demirel, C. De Marco, T. Tezdogan, and M. Atlar, "Fouling effect on the resistance of different ship types," *Ocean Engineering*, vol. 216, p. 107 736, 2020.

[11] A. Coraddu, L. Oneto, F. Baldi, F. Cipollini, M. Atlar, and s. Savio, "Data-driven ship digital twin for estimating the speed loss caused by the marine fouling," *Ocean Engineering*, vol. 186, p. 106 063, 2019.

[12] Y. K. Demirel, S. Song, O. Turan, and A. Incecik, "Practical added resistance diagrams to predict fouling impact on ship performance," *Ocean Engineering*, vol. 186, p. 106 112, 2019, ISSN: 0029-8018. [Online]. Available: `https://www.sciencedirect.com/science/article/pii/S0029801819303087`.

[13] D. Uzun, Y. Demirel, A. Coraddu, and O. Turan, "Time-dependent biofouling growth model for predicting the effects of biofouling on ship resistance and powering," *Ocean Engineering*, vol. 191, 2019.

[14] Y. Demirel, M. Khorasanchi, O. Turan, A. Incecik, and M. Schultz, "A CFD model for the frictional resistance prediction of antifouling coatings," *Ocean Engineering*, vol. 89, pp. 21–31, 2014.

[15] J. P. Petersen, D. J. Jacobsen, and O. Winther, "Statistical modelling for ship propulsion efficiency," *Journal of marine science and technology*, vol. 17, no. 1, pp. 30–39, 2012.

[16] G.-B. Huang, "An insight into extreme learning machines: Random neurons, random features and kernels," *Cognitive Computation*, vol. 6, no. 3, pp. 376–390, 2014.

[17] L. Chambers, K. Stokes, F. Walsh, and R. Wood, "Modern approaches to marine antifouling coatings," *Surface and Coatings Technology*, vol. 201, pp. 3642–3652, 2006.

[18] ITTC, "Analysis of Speed/Power Trial Data," *ITTC - Recommended Procedures and Guidelines*, 2014.

[19] R. Grin, "On the prediction of wave-added resistance with empirical methods," *Journal of Ship Production and Design*, vol. 31, no. 03, pp. 181–191, 2015.

[20] W. J. Pierson Jr and L. Moskowitz, "A proposed spectral form for fully developed wind seas based on the similarity theory of sa kitaigorodskii," *Journal of geophysical research*, vol. 69, no. 24, pp. 5181–5190, 1964.

[21] K. Hasselmann, T. P. Barnett, E. Bouws, *et al.*, "Measurements of wind-wave growth and swell decay during the joint north sea wave project (jonswap).," *Ergaenzungsheft zur Deutschen Hydrographischen Zeitschrift, Reihe A*, 1973.

[22] 26th ITTC Specialist Committee on Uncertainty Analysis, "Fresh Water and Seawater Properties," *ITTC - Recommended Procedures*, 2011.

[23] R. Townsin, "The ship hull fouling penalty," *Biofouling*, vol. 19, no. S1, pp. 9–15, 2003.

[24] ITTC, "Recommended Procedures and Guideline Practical Guidelines for Ship CFD Applications," *ITTC - Recommended Procedures and Guidelines*, 2011.

[25] Y. Demirel, M. Khorasanchi, O. Turan, and A. Incecik, "On the importance of antifouling coatings regarding ship resistance and powering," in *International Conference on Technologies, Operations, Logistics and Modelling for Low Carbon Shipping*, 2013.

[26] D. Oliveira, A. I. Larsson, and L. Granhag, "Effect of ship hull form on the resistance penalty from biofouling," *Biofouling*, vol. 34, no. 3, pp. 262–272, 2018.

[27] P. Kanninen, P. Peltonen, and V. Vuorinen, "Full-scale ship stern wave with the modelled and resolved turbulence including the hull roughness effect," *Ocean Engineering*, vol. 245, p. 110 434, 2022.

[28] W. H. O. Institution and U. S. N. D. B. of Ships, *Marine fouling and its prevention*. United States Naval Institute, 1952.

[29] S. Shalev-Shwartz and S. Ben-David, *Understanding machine learning: From theory to algorithms*. Cambridge university press, 2014.

[30] L. Rosasco, E. De Vito, A. Caponnetto, M. Piana, and A. Verri, "Are loss functions all the same?" *Neural Computation*, vol. 16, no. 5, pp. 1063–1076, 2004.

[31] M. Fernández-Delgado, E. Cernadas, S. Barro, and D. Amorim, "Do we need hundreds of classifiers to solve real world classification problems?" *The journal of machine learning research*, vol. 15, no. 1, pp. 3133–3181, 2014.

[32] M. Wainberg, B. Alipanahi, and B. J. Frey, "Are random forests truly the best classifiers?" *The Journal of Machine Learning Research*, vol. 17, no. 1, pp. 3837–3841, 2016.

[33] G.-B. Huang, Q.-Y. Zhu, and C.-K. Siew, "Extreme learning machine: A new learning scheme of feedforward neural networks," in *IEEE International Joint Conference on Neural Networks*, 2004.

[34] A. Caponnetto and E. De Vito, "Optimal rates for the regularized least-squares algorithm," *Foundations of Computational Mathematics*, vol. 7, no. 3, pp. 331–368, 2007.

[35] L. Oneto, "Model selection and error estimation without the agonizing pain," *WIREs Data Mining and Knowledge Discovery*, 2018.

[36] R. Tibshirani, "Regression shrinkage and selection via the lasso," *Journal of the Royal Statistical Society. Series B (Methodological)*, vol. 58, no. 1, pp. 267–288, 1996.

[37] L. L. C. Kasun, H. Zhou, G.-B. Huang, and C. M. Vong, "Representational learning with elms for big data," *IEEE Intelligent Systems*, vol. 28, no. 6, pp. 31–34, 2013.

[38] L. Oneto, "Model selection and error estimation without the agonizing pain," *Wiley Interdisciplinary Reviews: Data Mining and Knowledge Discovery*, vol. 8, no. 4, e1252, 2018.

[39] L. Leifsson, H. Sævarsdóttir, S. Sigurdsson, and A. Vésteinsson, "Grey-box modeling of an ocean vessel for operational optimization," *Simulation Modelling Practice and Theory*, vol. 16, pp. 923–932, Sep. 2008.

[40] A. F. R. F. Rochim, *Chauvenet's criterion, peirce's criterion, and thompson's criterion (literatures review)*, 2021.

PROCEEDINGS OF MOSES2023 CONFERENCE
4TH INTERNATIONAL CONFERENCE ON MODELLING AND OPTIMISATION OF SHIP ENERGY SYSTEMS
26-27 OCTOBER 2023, DELFT, NETHERLANDS

Topology Generation of Naval Propulsion Architecture

Florian Dugast[a,*], Stéphane Bénac[b], Pierre Marty[a], and Pascal Chessé[a]

[a]Nantes Université, École Centrale Nantes, CNRS, LHEEA, UMR 6598, F-44000 Nantes, France
[b]Naval Group, CEMEP, Technocampus Ocean, Bouguenais, France
[*]florian.dugast@ec-nantes.fr

Abstract

Reducing shipping emissions at an affordable cost is critical and can be achieved through propulsion architecture optimization. The multiple choices of components and constraints to be fulfilled (required speed, fuel consumption, maintenance, ...) make architecture design increasingly complex. Some optimization methods have already been used, for example, to optimize diesel generators (number, type and load) for fuel consumption reduction. More complex architectures have been studied by including the absence or presence of some components in a superconfiguration but in the end the number of configurations remains limited. In this study, the ship architecture is not predetermined but is generated by a list of components associated with constraints and rules, making architecture creation more flexible. The algorithm written for this purpose follows the principles found in hybrid vehicle design but with adapted rules and components for naval applications. The main objective of this paper is to explain in detail the topology generation architecture algorithm rather than to find an optimal architecture for a specific ship. From this perspective, the test cases presented are general to demonstrate that the algorithm can be applied to various system configurations. The components are linked together based on their input and output energy type and the architecture is generated to comply with propulsion and hotel load requirements. Next, physical constraints are added to build realistic designs such as avoiding spurious redundant connections or defining the maximal occurrence for each component. All the constraints and the generation algorithm are written in Prolog. Two numerical applications are presented where the list of components covers different types of propulsion (mechanical and/or electrical with gas turbines and/or diesel engines) along with hotel load or heating requirements.

Keywords: Synthesis design; logic programming; naval propulsion architecture.

1 INTRODUCTION

In engineering design, system architecture can be increasingly complex to establish due to the multiple choice of components and the number of constraints to be fulfilled (performance, cost, environmental impact, energy savings, maintenance, etc) [1], [2]. In this context, the design of naval vessels is particularly critical because of their important role in transportation or military and the need for efficiency to meet greenhouse gas reduction requirements at an affordable cost. In general, the conception of any system relies on different levels such as topology, size and control [3], [4]. The topology refers here to the presence/absence of components and how they are connected to each other. The “size level” determines the number of each component in the architecture whereas some optimal design points are determined at the “control level”. For a naval design, the topology can refer to the type of propulsion (electric, mechanical or hybrid) [5] and how the hotel load is generated (combined with the propulsion system or not) whereas the number of diesel engines, for example, and their load are determined at the size and control level respectively. Note that the terminology ”topology, size, control” is mostly employed in hybrid vehicle design whereas ”synthesis, design, operation” are widely used in ship design literature [6], [7] referring to the same concepts. In this article, we focus on the synthesis level as it is a challenging topic that needs further development [6].

The architecture at the synthesis level is described as a list of components and connections between two components. Network representation is used for ship design in [8] to represent zone decks (e.g hangar, propulsion plant, flight deck) and their connectivity. The arrangement of the different nodes is evaluated based on logical and physical levels, representing the system connectivity and the spatial locations, respectively. The design exploration of the main users in ship architecture was also realized in [9]. The components are similar to those in [8] with some additional details on the propulsion

@2023 Dugast, F. et al. published by TU Delft OPEN Publishing on behalf of the authors. Licensed under a Creative Commons Attribution CC BY license.
DOI: https://doi.org/10.59490/moses.2023.667

system : eight options available (COmbined Diesel And Gas, COmbined Gas And Gas, Hybrid Electric Drive or Integrated Propulsion System) with two main propulsion engines and four secondary engines. In these studies, the entire propulsion system is considered as one object in the ship structure. In our work, we intend to explore in more detail the architecture of the propulsion system as it plays a critical role in ship performance, so the next articles presented will focus on this topic. In [10], the connections in ship energy distribution systems were determined by a combination of an adjacency matrix and a genetic algorithm. The adjacency matrix exhibits unfeasible constraints whereas the genetic algorithm minimizes the number of connections or maximizes system reconfigurability. The number of possibilities for different connections configurations is very important but the number of each component is fixed (i.e 4 DG, 4 switchboards, etc) which can limit design space exploration. Compared to [10], the number of components is not fixed in [11] but calculated using an optimization process. However the absence/presence of components is predetermined by a "superconfiguration" and at the end the flexibility of the topology in the architecture is relatively low, relying only on the presence/absence of HRSG units and with only one HRSG per engine. Some extensions of this work have been published to simulate the use of gas turbines [12] or to add ship resistance for the optimization of ship speed [13]. A superconfiguration is also used in [14] to incorporate ORC, Stirling units or thermal storage systems. Depending on the number of components and interactions between them, the creation of such a superconfiguration can become cumbersome or intractable.

In this article, we propose an algorithm for the creation of architecture topology by searching for both the number of possible components and the connections between them to allow the generation to go over a large design space. The objective is to obtain a ship architecture without the use of a predefined superconfiguration, but with only a list of components and generic constraints included in a constraint-satisfactory problem. Automation of the creation of architecture connections can be useful to handle an important number of components and obtaining ship architecture with all possible configurations in an efficient way. Most of the articles published on this topic have focused on hybrid vehicle design [15]–[19] due to its important market. For example, Wijknet et al. [19] used the Prolog (logic programming) language [20] to implement constraints for powertrain architecture generation in order to reduce the design space. More details regarding the architecture generation algorithms for hybrid vehicles can be found in the review of Hu et al. [18].

In this work, the architecture is generated with similar methods developed for hybrid vehicle design (constraint-satisfaction problem solved in Prolog) but with an application on ship architecture. The connections between components are realized based on identical input/output energy types and the algorithm is written to achieve both propulsion and hotel load requirements. Other constraints are added to obtain feasible and realistic ship architectures. The algorithm for the architecture topology generation is presented in Section 2 and two numerical examples are given in Section 3 as an illustration of the method.

2 ARCHITECTURE TOPOLOGY GENERATION ALGORITHM

The architecture is described by a list of connections between blocks, where a block can be a resource, a component or a user. In this case, a component can be used either for energy conversion or to gather energy from different sources.The block database is user-defined and the list of connections is obtained by logic programming implemented in Prolog. In this section, the constraints and process developed to generate the architecture will be detailed. The reference example used throughout the article is based on the list of blocks in Table 1:

full name	**input**	**output**
Propulsion (prop)	sea	/
Hotel load (hl)	el.network	/
Propeller (ppel)	mech.en	sea
Elec. motor (elm)	el.network	mech.en
Elec. network (eln)	el.en	el.network
Gas turbine (gt)	fuel	mech.en
Diesel engine (de)	fuel	mech.en
Alternator (al)	mech.en	el.en
Fuel tank (fuel)	/	fuel

Table 1: Reference block list

The input and output of a block can be an energy type or a specific interface name. In Table 1, a block with no input is a resource (e.g Fuel tank), a block with no output is a user (e.g Propulsion or Hotel load) and the remaining blocks are components.

This list has been composed to be representative of the components for the energy propulsion system of a large cruise or a naval vessel with possible high requirements on ship velocity or hotel load. With the inputs/outputs listed in Table 1, the electricity supply can be used for either propulsion or hotel load needs.

2.1 Constraints implementation

The different physical or logical constraints used to generate the architecture are :

1. Constraint 1 : Two components are linked together if they share a common input/output, see Fig. 1

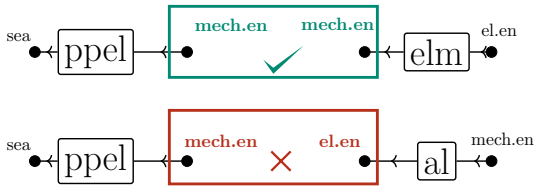

Figure 1: Constraint on connection input/output

2. Constraint 2 : From empirical knowledge, it is assumed that the same connection cannot occur twice in the elementary chain to avoid unrealistic architectures. For example in Fig. 2 on top, if an electric motor is connected to an alternator, this alternator is not allowed to be connected to an electric motor again.

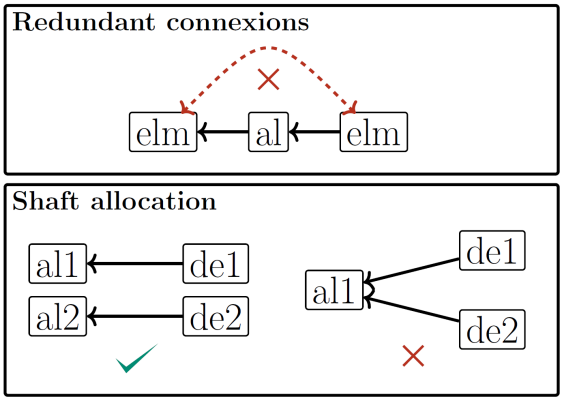

Figure 2: Constraints on redundant connection and shaft allocation

3. Constraint 3 : Only one mechanical component is allowed per shaft; for example two diesel engines cannot be connected to the same alternator (see Fig. 2 at the bottom).

4. Constraint 4 : The configuration of the propellers must exhibit a symmetry pattern, as shown in Fig. 3.

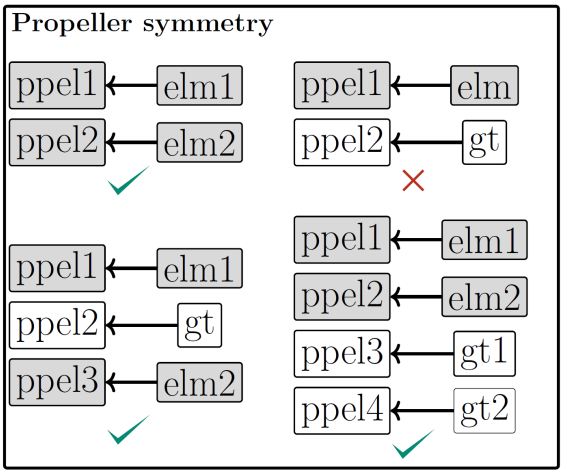

Figure 3: Constraint on propeller arrangement

5. Constraint 5 : A limitation on the maximal number of each component is provided (see Table 2 for the blocks listed in Table 1).

Block name	Max1	Max2	Max3
Propulsion	1	1	1
Hotel load	1	1	1
Propeller	4	2	4
Electrical motor	4	2	4
Electrical network	1	1	2
Gas turbine	4	2	4
Diesel engine	4	6	4
Alternator	4	6	4
Fuel tank	1	1	1

Table 2: Maximal occurrence of the reference block list

The maximal occurrence of users (Propulsion, Hotel load) and resources (Fuel tank) is set to 1. For the components, different cases will be studied :

- Max1 configuration : all the occurrences are arbitrarily set to four apart from the electrical network, as a good compromise between the diversity and compactness of the architecture
- Max2 configuration : the maximal occurrences are based on values found in literature ([13], [21])
- Max3 configuration : identical to Max1 but with two electrical networks

2.2 Architecture construction

The generation of the architecture is divided in five main steps :

1. Research of the elementary chains required for each user, the definition of an elementary chain will be given later;
2. Construction of the architecture structure based on the maximal mutualization (i.e with the smallest possible number of components) of all the elementary chains;
3. Determination of the occurrence of each group found in the architecture structure. This choice considers constraints based on the maximal number of each component;
4. Creation of the architecture connections;
5. Creation of the diagram of nodes and edges for visualization.

In step 3, the system of equations is generated manually from step 2 at this point. Au automation of this step is currently under development. For step 5, the graph generation algorithm has not been deeply investigated at the moment so it is sometimes necessary to manually adjust the node locations to avoid overlapping. Otherwise all the other steps are done automatically by the algorithm. After this process, the architecture is given as a list of connections between components. Each component name is composed of the component key and a unique number to distinguish between all the components.

2.2.1 Creation of elementary chains

An elementary chain (EC) consists of a minimal number of connections that can bring power to a user in the ship architecture, that is, propulsion or hotel load, in the example given above. Starting from a user, the connections are established based on the input and output of each component. Components A and B are connected if the output of A is equal to the input of B based on Constraint 1. If several connections are possible for the block A, each connection creates a different EC. In Table 1, there is only one input and one output for each component but it is possible to specify several inputs or outputs if necessary. The research on the corresponding inputs and outputs is also restrained by Constraint 2 and the EC ends when a block without output is encountered. The list of ECs based on the example in Table 1 is shown in Fig. 4.

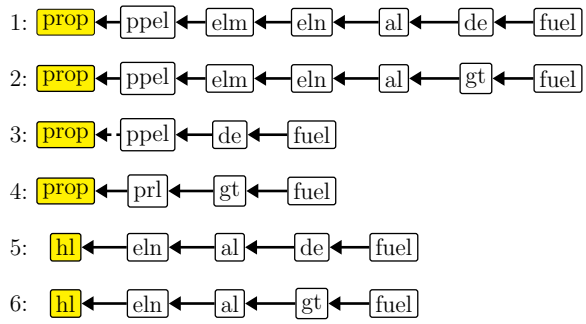

Figure 4: List of ECs for the reference block list

The first four elementary chains represent different ship propulsion alternatives : electric (ECs 1 and 2) or mechanical (ECs 3 and 4). For both options, diesel engines or gas turbines can be used to deliver mechanical power. The last two elementary chains provide an hotel load for the ship, with either diesel engines or gas turbines.

2.2.2 Construction of the architecture structure

The structure is a combination of all the elementary chains found for the set of components. The elementary chains have some components in common so one component can belong to several elementary chains if it does not violate any constraint, it is called mutualization in the following of the article. For example, the components diesel engine and alternator are both in the elementary chains 1 and 5, see Fig. 5.

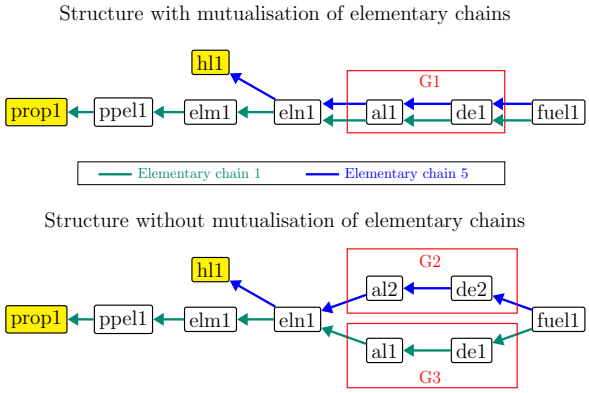

Figure 5: Mutualization of elementary chains in the architecture structure

At this stage, two options are possible to represent it : a mutualization of the diesel-alternator to combine both EC 1 and EC 5 into one group (see G1 on top of Fig. 5) or a separation into two groups for each elementary chain (see G2 and G3 at the bottom of Fig. 5). When this case is encoun-

tered, the mutualization is always chosen to avoid duplicate architectures in the end. Indeed after the creation of the architecture structure, the occurrence of each components is decided and for example, the architecture with one group G2 and no group G3 would be the same than with no group G2 and one group G3. However the same configuration is only represented by one group G1 for the structure with mutualization which is more advantageous. For the set of components indicated in Table 1, the architecture structure is presented in Fig. 6. One can see that for the electricity generation with the diesel engine and the gas turbine, one alternator is dedicated to each component due to Constraint 3. The presence (=1) or absence (=0) of each elementary chain in the architecture structure is summarized in Table 3.

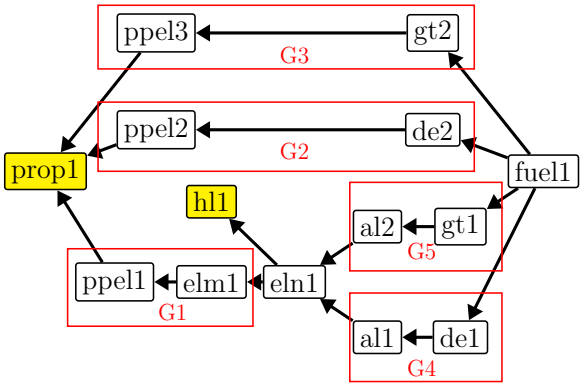

Figure 6: Architecture structure 1

EC	G1	G2	G3	G4	G5
1	1	0	0	1	0
2	1	0	0	0	1
3	0	1	0	0	0
4	0	0	1	0	0
5	0	0	0	1	0
6	0	0	0	0	1

Table 3: Relationships between groups and elementary chains

2.2.3 Occurrence of the architecture structure groups

After the creation of the architecture structure, the next step to obtain a complete definition of the architecture topology is to define the occurrence of each component in the structure based on the maximal number of each component defined by the user and on some constraints. When some components are linked together due Constraint 3, they are linked together in a group because their occurrence must be the same. The different groups are represented by red boxes in Fig. 6 and the number of occurrences of each group Gi is indicated as N_{Gi}. This vector is determined by the following system of equations :

$$\begin{aligned} & N_{Gi} \in [0, \infty],\ i \in [1, 5] \\ & 0 < N_{G4} + N_{G5} \leq N_{\text{al}}^{\max} \\ & 0 < N_{G1} + N_{G2} + N_{G3} \leq N_{\text{ppel}}^{\max} \\ & N_{G2} + N_{G4} \leq N_{\text{de}}^{\max} \\ & N_{G3} + N_{G5} \leq N_{\text{gt}}^{\max} \\ & \text{checkSymmetry1}(N_{G1}, N_{G2}, N_{G3}) \end{aligned} \tag{1}$$

Generally the number of occurrence of one group can be zero in order to indicate the absence of a specific part of the architecture structure. However the users needs (propulsion and hotel load) must always be met, that is why the constraints $N_{G1} + N_{G2} + N_{G3} > 0$ and $N_{G4} + N_{G5} > 0$ exists, due to the propulsion and hotel load requirement respectively. The function *checkSymmetry1* verifies Constraint 4 by counting the number of pairs of each different components connected to the propellers.

From this point, the exhaustive search for the N_{Gi} is performed in Prolog based on the constraints in (1). Note that the N_{Gi} could also be found by an optimization process if a physical model and data are available but it is beyond the scope of this article.

2.2.4 Creation of architecture connections

Once the number of each group is determined, there is a potential last degree of freedom in the architecture generation regarding how two components from different groups are connected together. For example, if there is more than one electrical network in the architecture and several alternators, one could find different ways of connecting these components, as shown in Fig. 7.

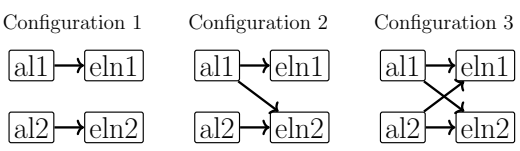

Figure 7: Architecture connections configurations

Note that some configurations are not represented in this figure as there would be similar to one of the three configurations already drawn by assuming that components 1 and 2 are identical. One drawback of these different configurations is the requirement of additional variables, that is the energy

partition between the different components if the architecture is to be calculated with a physical model. In addition, it can lead to identical performance at the end depending on the energy partition. For example, the energy gathered in eln1 and eln2 will be the same for configurations 1 and 3 if the energy is equally balanced in configuration 3. Therefore, the maximal number of electrical networks has been usually set to 1 in Table 2 and Table 6. A study has been added about the use of two electrical networks if redundancy is a critical criterion in the ship design.

3 ARCHITECTURE GENERATION RESULTS

In the following numerical cases, calculations and timings have been performed on a standard laptop computer.

3.1 Reference case

Based on the architecture structure presented in Fig. 6, different architectures are shown in Fig. 8.

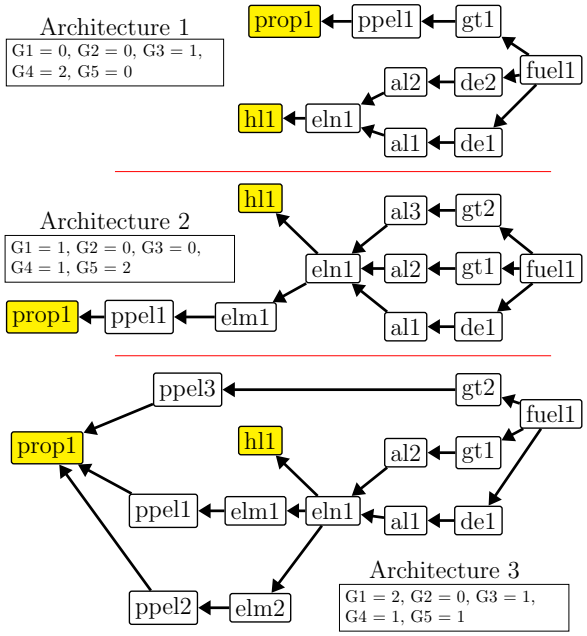

Figure 8: Architecture generation results 1

Architectures 1, 2 and 3 exhibit a pure mechanical, a pure electrical and a mechanical-electrical propulsion, respectively. The number of architectures obtained and the corresponding computational time depend on the maximal occurrence of each components, and the results have been gathered in Table 4.

	Max1	Max2	Max3
Number of architectures	226	82	1888
Computational time (ms)	29	9	98

Table 4: Architecture results for the reference case

3.2 Case 2

The same methodology is applied to a more complex set of components to evaluate the flexibility of the algorithm. This example is referred to as *Case 2* in the following section. The list of components still refers to a standard ship architecture propulsion but it also considers the production and circulation of heat. The heat can be used from the engines to produce steam, which can then be used either for heating or as an input to a steam turbine. The list of components for this second case along with their inputs and outputs are given in Table 5.

full name	input	output
Propulsion (prop)	sea	/
Hotel load (hl)	el.network	/
Heating (heat)	steam	/
Propeller (ppel)	shaft	sea
Shaft (shaft)	mech.en	shaft
Elec. motor (elm)	el.network	mech.en
Elec. network (eln)	el.en	el.network
Gas turbine (gt)	fuel	mech.en,heat
Steam turbine (st)	steam	mech.en,heat
HRSG (hrsg)	water,heat	steam
AB (ab)	fuel,water	steam
Diesel engine (de)	fuel	mech.en,heat
Alternator (al)	mech.en	el.en
Fuel tank (fuel)	/	fuel
Water tank (water)	/	water

Table 5: Case 2 : block list

Figure 9: Elementary chain example for Case 2

HRSG and AB represent the heat recovery steam generator and auxiliary boiler, respectively. One change to the reference case is the use of several keywords for some components in input or output. For example, both water and heat are required to produce steam in the HRSG component. It means that on the elementary chains, one component can have

several connections, as seen in Fig. 9. The number of elementary chains for this case is 18 compared to 6 for the reference case : 10 for propulsion, 5 for hotel load and 3 for heating. Also in this example, multiple components can be connected to the same shaft but the diesel engines and turbines cannot be connected simultaneously on a drive shaft and on a alternator. Based on the list of components and on these rules, the architecture structure is shown in Fig. 10.

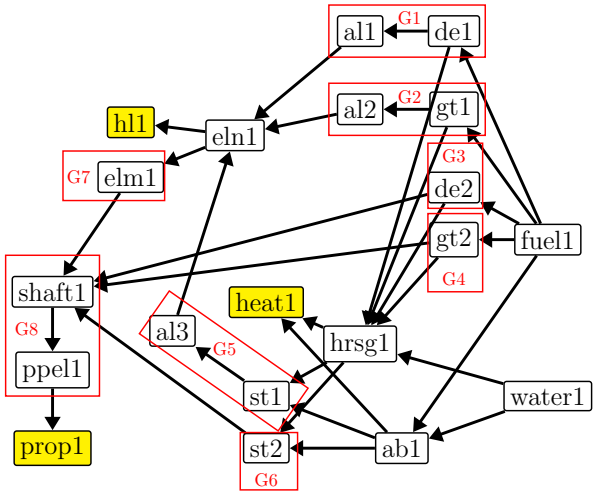

Figure 10: Architecture structure 2

The study about the influence on the maximal occurrence of each component is also performed for this case, see Table 6.

Block name	Max1	Max2	Max3
Propulsion	1	1	1
Hotel load	1	1	1
Heating	1	1	1
Propeller	4	2	4
Shaft	4	2	4
Elec. motor	4	2	4
Elec. network	1	1	2
Gas turbine	4	2	4
Steam turbine	4	2	4
HRSG	1	1	1
AB	1	1	1
Diesel engine	4	2	4
Alternator	4	2	4
Fuel tank	1	1	1
Water tank	1	1	1

Table 6: Maximal occurrence of the block list for Case 2

Apart from the users (heat,p,hl) and the resources (water,fuel), the components ab,hrsg and eln have been set to 1 for simplification. At the end of topology generation, the objective is to evaluate the architecture performance based on its fuel consumption to achieve a user requirement (specified speed, hotel load and heating) and the speed seems the most critical goal so the focus is on the diesel engines and turbines configuration rather than on the steam generation process here.

Based on the structure in Fig. 10, the following system of equations is solved to determine the architecture set :

$$
\begin{aligned}
& N_{Gi} \in [0, \infty],\ i \in [1, 8] \\
& 0 < N_{G8} < \min(N_{\text{ppel}}^{\max}, N_{\text{shaft}}^{\max}) \\
& N_{G6} + N_{G4} + N_{G3} + N_{G7} > 0 \\
& 0 < N_{G1} + N_{G2} + N_{G5} \leq N_{\text{al}}^{\max} \\
& N_{G5} + N_{G6} \leq N_{\text{st}}^{\max} \\
& N_{G7} \leq N_{\text{elm}}^{\max} \\
& N_{G2} + N_{G4} < N_{\text{gt}}^{\max} \\
& N_{G1} + N_{G3} < N_{\text{de}}^{\max} \\
& \text{checkSymmetry2}(N_{G3}, N_{G4}, N_{G7}, N_{G8})
\end{aligned}
\tag{2}
$$

The function *checkSymmetry2* ensure that every driving shaft is connected to the same components by checking $\text{mod}(N_{Gj}, N_{G8}) = 0$ with $j = [3, 4, 6, 7]$. Solving the system (2) leads to the following results in Table 7:

	Max1	Max2	Max3
Number of architectures	11143	3011	420703
Computational time (ms)	440	163	16710

Table 7: Architecture results for Case 2

Compared to the reference case with the Max1 configuration, there are 50 times more architectures in Case 2 but the simulation time only increased by a factor 15 so it demonstrates a good scalability of the algorithm. Three examples are shown in Fig. 11. Architecture 1 represents a mechanical propulsion with two gas turbines on one driving shaft. Architecture 2 is also a mechanical propulsion but with two driving shafts. In this configuration each gas turbine is connected to one shaft only. Finally, Architecture 3 is an electrical propulsion with two gas turbines for the electricity generation and one electric motor for propulsion.

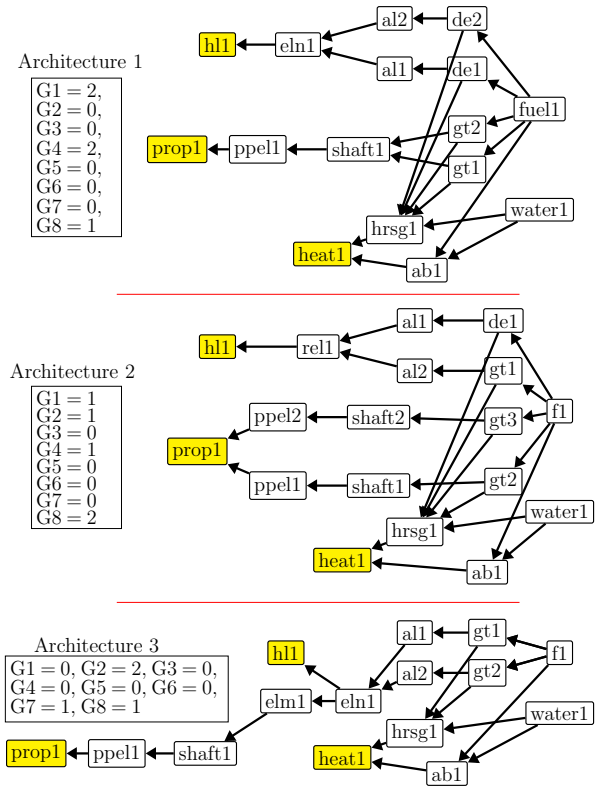

Figure 11: Architecture generation results 2

4 CONCLUSION

An architecture generation algorithm for naval applications has been presented in this article. The presence/absence of components and their connections with each other are determined with some constraints implemented in the logic programming language Prolog. The definition of input/output keywords for each component along with general constraints (prevention of redundant connections, limitation of the maximal number of components) made the algorithm easily adaptable for different configurations. Next, a large number of architectures have been found in a short computational time using constraint logic programming combined with architecture structure construction. Two numerical examples has been provided to illustrate this method, leading to diverse feasible architectures with different properties (mechanical or electrical propulsion, use of diesel engines or gas turbines among others). One perspective of this work is to add components for energy storage (batteries) and for a more detailed description of the mechanical part of the architecture (gearboxes and clutches). Also it is desirable to have more generic keywords for input and output of the components. For example, the keyword "sea" was chosen for the output of the propeller in the reference list in order to get a connection for the block Propulsion but adding custom keywords for specific connections could be difficult to handle for a larger list of components so it will be addressed in future research.

ACKNOWLEDGMENTS

We gratefully thank the Join Laboratory of Marine Technology (J.L.M.T) from Ecole Centrale Nantes and Naval Group for its financial support in this research work.

REFERENCES

[1] G. Doulgeris, T. Korakianitis, P. Pilidis, and E. Tsoudis, "Techno-economic and environmental risk analysis for advanced marine propulsion systems," *Applied Energy*, vol. 99, pp. 1–12, 2012, ISSN: 0306-2619.

[2] A. Batra, S. Sampath, T. Nikolaidis, and P. Pilidis, "Techno-economic model-based design space exploration of combined ship propulsion systems," *Journal of Marine Science and Technology*, Feb. 2023, ISSN: 0948-4280.

[3] E. Silvas, T. Hofman, N. Murgovski, L. F. P. Etman, and M. Steinbuch, "Review of optimization strategies for system-level design in hybrid electric vehicles," *IEEE Transactions on Vehicular Technology*, vol. 66, no. 1, pp. 57–70, 2017.

[4] Z. Qin, Y. Luo, W. Zhuang, Z. Pan, K. Li, and H. Peng, "Simultaneous optimization of topology, control and size for multi-mode hybrid tracked vehicles," *Applied Energy*, vol. 212, pp. 1627–1641, 2018, ISSN: 0306-2619.

[5] O. B. Inal, J.-F. Charpentier, and C. Deniz, "Hybrid power and propulsion systems for ships: Current status and future challenges," *Renewable and Sustainable Energy Reviews*, vol. 156, p. 111 965, 2022, ISSN: 1364-0321.

[6] C. A. Frangopoulos, "Developments, trends, and challenges in optimization of ship energy systems," *Applied Sciences*, vol. 10, no. 13, 2020, ISSN: 2076-3417.

[7] N. L. Trivyza, A. Rentizelas, G. Theotokatos, and E. Boulougouris, "Decision support methods for sustainable ship energy systems: A state-of-the-art review," *Energy*, vol. 239, p. 122 288, 2022, ISSN: 0360-5442.

[8] C. P. Shields, M. J. Sypniewski, and D. J. Singer, "Characterizing general arrangements and distributed system configurations in early-stage ship design," *Ocean Engineering*, vol. 163, pp. 107–114, 2018, ISSN: 0029-8018.

[9] M. A. Parsons, "Network-based naval ship distributed system design and mission effectiveness using dynamic architecture flow optimization," Ph.D. dissertation, Virginia Polytechnic Institute and State University, 2021.

[10] P. de Vos and D. Stapersma, "Automatic topology generation for early design of on-board energy distribution systems," *Ocean Engineering*, vol. 170, pp. 55–73, 2018, ISSN: 0029-8018.

[11] G. N. Sakalis and C. A. Frangopoulos, "Intertemporal optimization of synthesis, design and operation of integrated energy systems of ships: General method and application on a system with diesel main engines," *Applied Energy*, vol. 226, pp. 991–1008, 2018, ISSN: 0306-2619.

[12] G. N. Sakalis, G. J. Tzortzis, and C. A. Frangopoulos, "Intertemporal static and dynamic optimization of synthesis, design, and operation of integrated energy systems of ships," *Energies*, vol. 12, no. 5, 2019, ISSN: 1996-1073.

[13] G. N. Sakalis, G. J. Tzortzis, and C. A. Frangopoulos, "Synthesis, design and operation optimization of a combined cycle integrated energy system including optimization of the seasonal speed of a vlcc," *Proceedings of the Institution of Mechanical Engineers, Part M: Journal of Engineering for the Maritime Environment*, vol. 235, no. 1, pp. 41–67, 2021.

[14] P. Gnes, P. Pinamonti, and M. Reini, "Bi-level optimization of the energy recovery system from internal combustion engines of a cruise ship," *Applied Sciences*, vol. 10, no. 19, 2020, ISSN: 2076-3417.

[15] E. Silvas, T. Hofman, A. Serebrenik, and M. Steinbuch, "Functional and cost-based automatic generator for hybrid vehicles topologies," *IEEE/ASME Transactions on Mechatronics*, vol. 20, no. 4, pp. 1561–1572, 2015.

[16] X. Zhang, H. Peng, J. Sun, and S. Li, "Automated modeling and mode screening for exhaustive search of double-planetary-gear power split hybrid powertrains," Dynamic Systems and Control Conference, vol. 1, 2014.

[17] C. Song, J. Hwang, and D. Kum, "Efficient design space exploration of multi-mode, two-planetary-gear, power-split hybrid electric powertrains via virtual levers," *IEEE Transactions on Intelligent Transportation Systems*, vol. 23, no. 4, pp. 3498–3509, 2022.

[18] X. Hu, J. Han, X. Tang, and X. Lin, "Powertrain design and control in electrified vehicles: A critical review," *IEEE Transactions on Transportation Electrification*, vol. 7, no. 3, pp. 1990–2009, 2021.

[19] J. Wijkniet and T. Hofman, "Modified computational design synthesis using simulation-based evaluation and constraint consistency for vehicle powertrain systems," *IEEE Transactions on Vehicular Technology*, vol. 67, no. 9, pp. 8065–8076, 2018.

[20] I. Bratko, *Prolog Programming for Artificial Intelligence* (International Computer Science Series). Addison-Wesley, 2011, ISBN: 9780321417466.

[21] P. Marty, "Étude de l'efficacité énergétique des navires : développement et application d'une méthode d'analyse," Ph.D. dissertation, Ecole Centrale de Nantes (ECN), 2014.

Improving the Energy Efficiency of Ships: Modelling, Simulation, and Optimization of Cost-effective Technologies

Giovanni Barone[a], Annamaria Buonomano[a,b,*], Gianluca Del Papa[a], Cesare Forzano[a], Giovanni Francesco Giuzio[a], Robert Maka[a], Adolfo Palombo[a], Giuseppe Russo[a] and Raffaele Vanoli[c]

[a] Department of Industrial Engineering, Università degli Studi di Napoli Federico II, Naples, Italy
[b] Department of Building, Civil and Environmental Engineering, Concordia University, Montreal, Canada
[c] Università Mercatorum, Rome, Italy
* *annamaria.buonomano@unina.it*

Abstract

This paper includes a part of the findings of an international research project, called HEMOS, funded by the EU through the Horizon Europe program, with the aim of decarbonizing the maritime sector. This study focuses on the use of dynamic simulation and optimization to identify policies and technologies for reducing carbon emissions and enhancing the energy efficiency of cruise ships. The primary findings of the study, which sought to identify the ideal ship plant topology, are presented with a particular emphasis on the optimization of the thermal and energy behaviour of a case study cruise ship. By exploiting the developed simulation model and the optimization procedure applied to the Allure of the Seas of the Royal Caribbean Group, potential efficiency measures were identified to enhance the overall efficiency of energy utilization. Several scenarios, including diverse energy efficient user technologies, were analysed and optimized with the aim of providing guidelines for the design of future ships. According to the obtained numerical results, the application of thermal devices for the utilization of on-board waste heat and the implementation of a fuel cell powered by bio-LNG can result in significant primary energy savings of up to approximately 17%, demonstrating that workable solutions to improve the energy efficiency of ships are already available.

Keywords: Ship energy efficiency, dynamic simulation, energy optimization, waste heat recovery, green fuels.

1. INTRODUCTION

With the goal of reducing greenhouse gas (GHG) emissions in international shipping, the IMO Marine Environment Protection Committee (MEPC 80) recently established new goals and policies [1]. The transition to cleaner energy sources requires considerable reductions in GHG emissions from ships to be achieved through the implementation of technologies, fuels, and energy sources with low or zero GHG emissions. The updated IMO GHG Strategy, FuelEU maritime initiative, and recent international agreements comprise ambitious goals to achieve net-zero GHG emissions from international shipping by 2050, including a commitment to secure the use of alternative fuels with zero or nearly zero GHG emissions by 2030, and suggested checkpoints for 2030 and 2040 [2], [3].

According to international institutions and governments [1], [2], large ships such as cruise ships are thus required to gradually reduce GHG emissions and air pollutants, use a fuel mix that includes renewable fuels, and consider on-shore power supply when in ports [4]. Despite the technologies and measures that can be implemented to enhance the energy efficiency of cruise ships, particularly in the context of cooling and overall energy management, a holistic approach that combines several strategies will likely yield the best results. From this point of view, the use of sophisticated energy analysis techniques allows for a thorough understanding of the energy behaviour of ships, facilitating the identification of energy-saving opportunities and the implementation of effective design modifications [5].

In the context of cruise ships, *dynamic simulation* can be used to model the ship's energy consumption, heat flows, and cooling requirements under various conditions [6]. The application of dynamic analysis in ship design or refurbishment is crucial for achieving these objectives. Simultaneously, in the context of cruise ship energy efficiency, *optimization techniques* can be applied to maximize energy savings and minimize energy consumption [7].

Dynamic analysis enables the evaluation of the variable behaviour of a ship's energy system, its interaction with the weather, and the variability of its electrical and thermal requirements. The energy efficiency and viability of on-board production systems, including diesel engines and oil-fired boilers, are significantly affected by load variability, particularly the electrical demand

@2023 Barone, G. et al., published by TU Delft OPEN Publishing on behalf of the authors. Licensed under a Creative Commons Attribution CC BY license.
DOI: https://doi.org/10.59490/ moses.2023.665

related to propulsion. Therefore, to properly *model and simulate the ship energy system*, it is vital to thoroughly understand these load behaviours. At the same time, optimization is necessary to investigate several potential layouts while specifying the optimal design parameters and operating conditions for the complete ship system [8]. The exploitation of waste heat from the main engines to power thermally activated technologies and the optimization of the energy management of heat are now becoming the standard for shipowners [9].

Several studies are available in the literature on the sustainability of ship energy systems, taking into account various approaches (such as model based design [10], dynamic simulation [11], optimization [12], analytical analysis [13], multiple techniques [14], life cycle assessment, and experiments [15]), and highlighting the solutions more frequently implemented (evaluation of different propulsion systems, implementation of heat recovery, thermal boilers, electric auxiliary systems, or emission abatement) [16], [17].

Promising results have been obtained by implementing the *dynamic simulation* to achieve a holistic approach to find the most effective and energy efficient technologies and their mix (e.g. absorption chiller, steam turbine, Organic Rankine Cycle machine, fuel cells), the best control logics to be implemented on-board [6, 18], and to provide more knowledge on advanced fuels and relative crucial issues for ship applications [7]. The analysis of the literature highlights that most of the proposed energy efficiency measures for ship applications include the exploitation of the thermal energy produced from the on-board engine system; different level temperature energies are, in fact, available on board to be properly exploited to satisfy users' needs (e.g. domestic hot water, air conditioning, etc.) or to produce energy from thermally activated technologies. Among the technologies that can be used for waste heat recovery, there are Rankine cycle machine [19] also based on organic fluids [20], supercritical Rankine cycle, Kalina cycle [21], exhaust gas turbine systems, absorption chillers, etc.. Obviously, the optimal configuration depends on several aspects (such as the initial configuration, actual energy requirements, and boundary conditions), suggesting that a unique solution cannot be achieved [22]. Moreover, the optimal solution for a specific ship must be properly assessed by using dynamic simulation and optimization [23]. This strategy not only improves energy efficiency, but also reduces the risks associated with operating adjustments and shipowner expenditures in new technologies.

1.1 Aim of the work

The research activity described in this paper is centred in this framework. The study is part of the HEMOS research project on the development of a dynamic simulation tool for the optimization of the on-board waste heat and of the energy efficiency of large cruise ships. The tool is finally used to identify suitable technologies to be implemented on-board an existing ship, the Allure of the Seas, an Oasis class ship of the Royal Caribbean Group (RCG). To this aim, several simulation environments (Revit, EnergyPlus, TRNSYS and MATLAB) were used to model the ship envelope and its energy systems. The developed holistic approach enables the investigation of diverse optimal solutions that can guarantee energy savings and support the on-board implementation. A comprehensive assessment of ship energy performance has been recently published [24], and the optimization procedure and its main findings are described in this paper. The entire procedure enables the evaluation of the proposed solutions and of the set of operating parameters that improve the selected objective functions (minimum fuel consumption) while satisfying some constraints (e.g. comfort levels, fresh water production, ship speed). Multiple configurations were considered to find the most energy efficient and effective layouts and the mix of technologies to be implemented on-board the Allure of the Seas. The ultimate goal of this study is to provide answers to various research concerns regarding how to use current and cutting-edge technologies and fuels to ensure compliance with changing environmental requirements and standards [25]. Some questions can be formulated as follows:

- *What strategies and technologies can enhance fuel efficiency, reduce emissions, and ensure compliance with the evolving environmental regulations and targets?*
- *How can waste heat recovery systems be improved to capture and reuse energy effectively?*
- *What and how can emerging technologies be combined and implemented on ships to improve their energy efficiency?*
- *Which alternative fuels can feasibly support the maritime environmental transition?*

2. MATERIAL AND METHOD

2.1 Modelling and simulation of ship

The ship under investigation was the Oasis class ship Allure of the Seas of Royal Caribbean (RCG). Schematic drawings and data used to develop the ship model were provided by the shipowner and retrieved from public repositories [26], as shown in Figure 1. The energy analysis of the ship,

conducted in previous studies [24], [27], was used as the starting point for the optimization analysis here described.

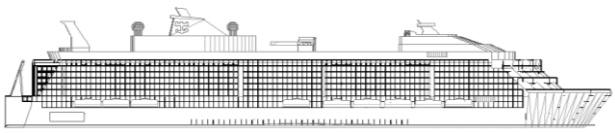

Figure 1. 3D model of the Allure of the Seas.

Dynamic simulations were conducted to assess the energy performance of a ship system by considering the interaction between its envelope, which is seen as a moving building, and its integrated systems. Details about the case study ship envelope are reported in reference [24], whereas key information regarding its energy systems is reported hereinafter. The main geometrical features of the ship, information on the dimensions and capacity, and power systems are summarized in Table 1.

The modelling of the ship was carried out by considering the ship geometry with the aim of assessing the real thermal behaviour of the Allure of the Seas. Several simplifications and assumptions were considered to perform dynamic simulations of a complex ship system, as detailed in reference [24] regarding the ship envelope.

Table 1. Info about the Allure of the Seas.

Built	STX Europe Turku Shipyard, Finland. Delivered on October 28th, 2010. Classification society DNV
Sister ships	Oasis of the Seas (2009), Harmony of the Seas (2016), Symphony of the Seas (2018), Wonder of the Seas (2022), Utopia of the Seas (planned 2024)
Length,	361.82 m
Beam	47 m at waterline (max 65.47 m)
Height	72 m above waterline
Draught	9.15 m (max 9.3 m)
Gross tonnage	225282 GT
Decks	16 passenger decks, 18 decks in total
Capacity	5492 passengers, 2200 crew
Installed power	Diesel-electric type power plant 3×13860 kW (Wärtsilä 12V46D) 3×18480 kW (Wärtsilä 16V46D)
Propulsion	3×20 MW ABB Azipods 4×5500 kW bow thrusters

Autodesk Revit was used for the 3D modelling of the case study ship envelope (to assess its thermal behaviour), whereas *TRNSYS* and *MATLAB* were used to model the heat energy system of the ship. Figure 2 shows the prospects of the Allure of the Seas merged with its Revit model, which was created by zoning the ship considering thermo-hygrometric conditions and usage.

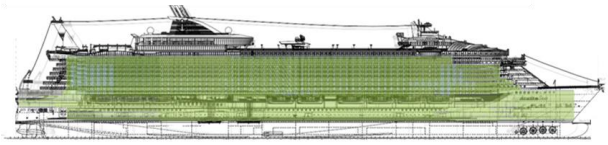

Figure 2. Merge of ship prospect and Revit model.

The existing on-board heat energy system is illustrated in Figure 3, and its main equipment is:

- 3 Wärtsilä 16V46D-CR (DG 1 - 3);
- 3 Wärtsilä 12V46D-CR (DG 4 - 6);
- 3 plate Heat exchangers by Alfa Laval (HEX 1 - 3);
- 3 plate Heat exchangers by Alfa Laval (HEX 4 - 6);
- 3 Exhaust Gas Boiler Unex G-622 (EGB 1 - 3);
- 3 Exhaust Gas Boiler Unex G-533 (EGB 4 - 6);
- 2 Oil Fired Boiler Aalborg MISSION (OFB 1 - 2);
- 4 Multi Stage Flash Evaporators Hamworthy;
- 5 electrical chillers;
- 2 Reverse Osmosis unit by Triton Water;
- Several heat exchangers are used to feed thermal users (e.g. Air Conditioning, Domestic Hot Water).

A simulation model of the ship, which is necessary to assess the heating and cooling demands, was developed and implemented in *Autodesk Revit*, *OpenStudio* and *EnergyPlus*. The obtained electricity, heating and cooling load profiles were processed to simulate the behaviour of the *waste heat recovery system* coupled with *ship engines* and the *heat integration of boilers*, which is necessary to assess the energy performance of the existing energy system, namely the reference layout (RL).

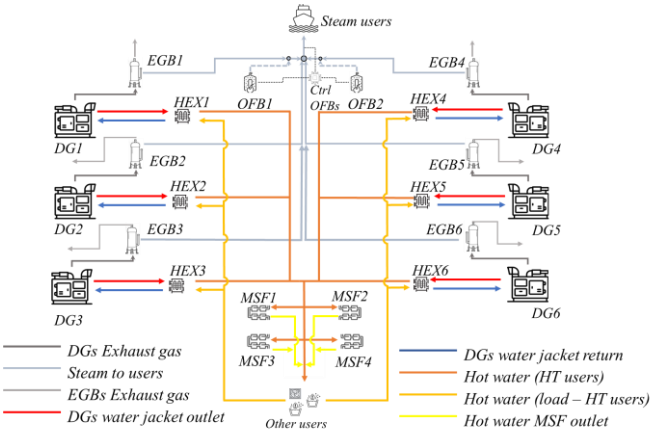

Figure 3. Sketch of the existing heat energy system.

The energy system was modelled in *TRNSYS* and *MATLAB*, where all components and their logical and physical connections were implemented to simulate the operation of the existing ship generation plant. The *MATLAB* tool takes detailed *EnergyPlus* simulation results and the information retrieved by the ship building model developed in the BIM environment as

inputs. The performance curves provided by manufacturers, physical algorithms, and conversion coefficients were considered to account for all operating conditions [27]. For the propulsion power input, a cubic curve was obtained as a function of the ship speed provided by the RCG data measurements [27]. A route was established to evaluate the electrical needs of the most energy intensive user of the ship; its itinerary is depicted in Figure 4.

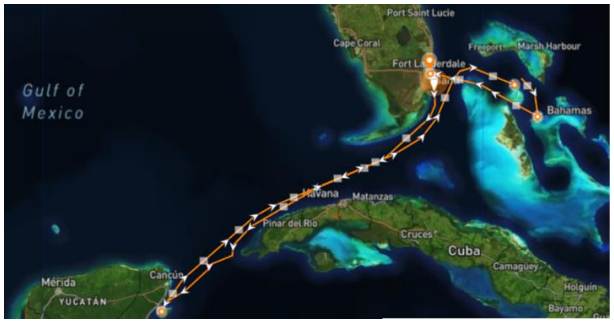

Figure 4. Simulated route of the ship.

Simulations were performed considering a 6-day round trip in the Western Caribbean Seas. The weather files used in the analysis includes historical data for the outdoor temperature, solar irradiance, and other relevant variables.

A brief explanation of the ship system function is reported below. Each main engine (DG) is equipped with an independent low-temperature (LT) cooling system for the generator, lubricating oil, and charge air cooler second stage, as well as a high-temperature (HT) cooling water circuit for the cylinders, charge air cooler first stage, and turbochargers. By carefully mixing with the LT cooling circuit and by heating the waste heat recovery (WHR) circuit, the HT circuit's inlet temperature is maintained between 77 and 79 °C. The sea water pump speed is adjusted by a frequency converter setpoint to maintain the temperature of the LT circuit between 36 and 38 °C (all extra heat discharged into the sea).

Four multi stage flash (MSF) evaporators and two reverse osmosis (RO) systems are used to produce fresh water while the ship is sailing. With a storage capacity of 6216 m^3, the theoretical production capacity is 4100 m^3/day. The WHR secondary circuit and steam booster heaters heat the evaporators. The heating medium of the evaporator, the WHR water, moves through the heat exchangers. According to the design specifications, a steam booster provides extra heat if necessary. RO plants are made up of high-pressure filtering units that filter seawater using semipermeable reverse osmosis membranes; a high-pressure pump aids in the filtration process by forcing water through them.

The heating and cooling needs of the air-conditioning plant are met by the air conditioning system of the ship. The intended summertime cooled water temperature is 6°C, whereas the maximum reheated water temperature is 80/60°C. WHR circuit preheats domestic hot water (DHW). The MSF receives heat from the diesel engines' WHR before being transferred to the AC and DHW heat exchangers. Steam is the main source of heat transfer on the cruise ship. Six exhaust gas boilers (EGB), one for each engine, and two oil fired boilers (OFB), which serve as backups, make up the steam generation system. The EGBs produce steam at a pressure of 8 bar by recovering heat from the main engine exhaust gases. Heavy Fuel Oil (HFO) is used to power diesel engines, and Marine Gas Oil (MGO) to power oil-fired boilers.

According to the simulations, the main energy, economic and environmental parameters of the RL are listed in Table 2.

Table 2. Reference system (RL) key parameters.

Parameter (per itinerary)		unit
Primary energy	8.82	(GWh)
Primary energy w/o propulsion	4.51	(GWh)
Operating cost	477	(k€)
CO_2 emissions	2369	(t)

2.2 Optimization procedure: methodology, investigated technologies, and layouts

To meet the energy efficiency and sustainability goals for the case study ship and, more generally, for the Oasis class ships from RCG, a full design-oriented optimization of the ship-energy system is carried out. The objective of optimization is to identify the best set of technologies and design approaches for a ship's (new or redesigned) construction that will enable energy savings and, thus, achieve stringent environmental goals. Additionally, economic and environmental criteria were considered to simultaneously evaluate the system financial feasibility and cost-effectiveness, as well as its potential in terms of environmental sustainability. An example of the optimization process is reported in Figure 5.

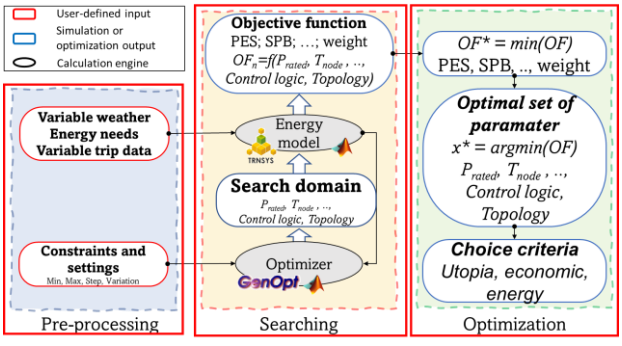

Figure 5. Optimization process

As energy objective function, the Primary Energy Saving (PES) is evaluated as:

$$PES = \sum_t \left(\frac{PE_{RL} - PE_{PL}}{PE_{RL}} \right)_t = \sum_t \left(\frac{m_{RL} - m_{PL}}{m_{RL}} \right)_t \quad (1)$$

where *PE* and *m* are the primary energy referred to the considered fuel and related burned mass, respectively, in the reference (subscript RL) and proposed (subscript PL) system layouts. *PES* can be calculated by considering propulsion (*PES w/ prop.*) or neglecting it (*PES w/o prop.*). This objective function must be maximized to reduce the ship energy needs and its pollutant emissions; accordingly, the associated avoided carbon dioxide emissions (ΔCO_2) are calculated as:

$$\Delta CO_2 = \sum_t f_{HFO}(m_{RL} - m_{PL}) \quad (2)$$

where f_{HFO} is the CO_2 equivalent emission factor of the considered fuel. Note that, similar formulas can be adopted for all pollutants (e.g. SO_x, NO_x, and $PM_{2.5}$) [18].

Conserning the economic evaluation, the Simple Payback Period (SPB) is evaluated as:

$$SPB = J_i \cdot \begin{pmatrix} (m_{RL} - m_{PL})_{HFO} c_{HFO} + \dots \\ \sum_t (m_{RL} - m_{PL})_{MGO} c_{MGO} + \dots \\ (m_{fw,RL} - m_{fw,PL}) c_{fw} + \dots \\ M_{RL} - M_{PL} \end{pmatrix}^{-1} \quad (3)$$

where J_i is the capital cost calculated as in equation (4), *m* is the mass of consumed fuel, c_{HFO} and c_{MGO} are the unitary cost of consumed fuels (HFO and MGO), m_{fw} and c_{fw} are the mass and unitary costs of bunkering freshwater at port, *M* is the maintenance cost. The denominator of equation (3) represents the reduction in operating cost (ΔOPEX).

$$J_i = m_i x_i^{n_i} \quad (4)$$

When compared to the reference layout (RL), each proposed system (PL) involves modifications to the size of the system components or the introduction of new energy-efficient technologies; therefore, similar objective functions should be considered. The expenditure (CAPEX) and operating (OPEX) costs considered in this analysis are reported in Table 3 and Table 4 [13], [28].

Table 3. Capital cost of each technology.

CAPEX	Technology	*m*	unit
J_{RO}	*Reverse osmosis*	4175	(€·d/ m^3)
J_{MSF}	*Multi stage flash*	12035	(€·d/ m^3)
J_{SAC}	*Single stage absorption chiller*	300	(€/kW_c)
J_{DAC}	*Double stage absorption chiller*	390	(€/kW_c)
J_{VCC}	*Vapour compressor chiller*	150	(€/kW_c)
J_{ORC}	*Organic Rankine Cycle system*	6500	(€/kW_e)
J_{MCFC}	*Molten Carbonate Fuel Cell*	4500	(€/kW_e)
J_{ST}	*Steam Turbine*	1140	(€/kW_e)

Table 4. Operative costs.

Operative costs		unit
HFO	627.0	(€/t)
MGO	838.5	(€/t)
Green LNG	2124	(€/t)
LNG	708	(€/t)

A number of *cutting-edge technologies*, including promising thermal and non-thermal devices, have been proposed and investigated to increase the on-board energy efficiency. Starting from RL, the PLs, not fully described for the sake of briefness, are as follows:

1. **Layout 1**: RL + a wet steam turbine (WST) that exploits excess steam otherwise wasted.
2. **Layout 2**: RL + a single effect absorption chiller (SAC) implemented on HT WHR circuit.
3. **Layout 3**: RL + a double effect absorption chiller (DAC) that exploits excess steam otherwise wasted.
4. **Layout 4**: RL + an Organic Rankine Cycle machine (ORC) implemented on HT WHR circuit.
5. **Layout 5**: RL + a combination of a WST, a SAC and a DAC. Here, two scenarios are considered: i) *scenario 1* without an efficient engine activation strategy: the reduction of the electrical power from engines due to the use of WST and SAC/DAC causes lower part load ratios and electrical efficiencies; ii) *scenario 2* with an efficient engine activation strategy: the engines are run in a way that ensures the best electrical efficiency.
6. **Layout 6**: RL + a mix of *different high-performance technologies*, such as WST, SAC, DAC, and a Molten Carbonate Fuel Cell (MCFC), plus *operating logics* for the exploitation of *waste heat recovery from the LT circuit*, the control of the return temperatures on the HT secondary circuit, and the proper and optimal activation of RO and MSF units *for variable freshwater production*. The MCFC also provides heat to high temperature users. Because the fuel cell run on a variety of fuels (hydrogen, natural gas, biofuels, etc), the use of Liquified Natural Gas (LNG) or bio-LNG has been investigated.

A summary of the range of variation, with minimum and maximum values, of all parameters considered in the optimization procedure relative to each investigated Layout (from 1 to 6), is provided in Table 5.

Table 5. Optimization process parameters.

Parameters	Range (min - max)
WST, nominal flowrate (t/h)	3 - 12
WST, outlet pressure (bar)	0.7 - 2
SAC, cooling power (kW)	105 - 4571

DAC, cooling power (kW)	176 - 3868
MCFC, electrical power (kWe)	1400 - 2800
RO, number of units (-)	2 - 4
MSF, number of units (-)	1 - 3
Return tempererature HT secondary circuit (°C)	71 - 74
Return temperature LT circuit (°C)	36 - 40
Use of bio-LNG to power fuel cell (-)	Yes or No

3. RESULTS AND DISCUSSION

Previous layouts were analysed by focusing on three different selection criteria: *economic*, *energy*, and *utopia point*. The latter corresponds to the ideal solution in the objective space, which simultaneously represents the best possible value for all objectives. The *utopia point* may not be reachable in practice but can be considered to find the solution closer to the ideal one. The point of the real optimum is the point on the Pareto front at the minimum geometric distance from the utopia point. Focusing on the entire procedure, the potential PES (w/ prop.) versus CAPEX for each configuration is shown in Figure 6.

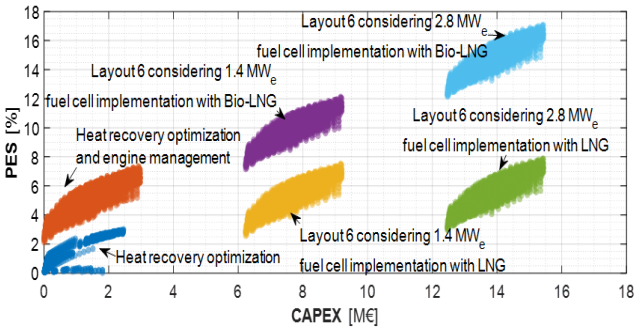

Figure 6. Possible configurations analysed: results.

On the *left side* of Figure 6, it is possible to see two clouds of results:

- *Blue cloud*: it includes the configurations relative to the *heat recovery optimization* obtained considering Layouts 1, 2, 3, 4 and Layout 5 scenario 1 (with no efficient engine activation strategy). PES values range from 0 to 3% corresponding to CAPEX up to 2.5M€.
- *Orange cloud*: it refers to all configurations relative to the *heat recovery optimization* plus the *engine management* control logic; thus, all configurations were obtained considering Layouts 1, 2, 3, 4, Layout 5 scenario 2, and Layout 6 without a FC. The energy management control logic allows for a remarkable increase of PES (from approximately 2 to 7%), without changes in CAPEX with respect to the blue cloud results.

On the *right side* of Figure 6, configurations incorporating the MCFC (two different sizes are considered, 1.4 and 2.8 MW_e), fuelled by either LNG or bio-LNG, are explored:

- *Yellow cloud*: it refers to the configurations of Layout 6 implementing a MCFC of 1.4 MW_e fuelled *with LNG*. These configurations show a similar range of PES (from approximately 2 to 7.5%) obtained by the *heat recovery optimization* plus the *engine management* (orange cloud), while CAPEX is up to four times higher (from approximately 6.2 to 9.2 M€).
- *Violet cloud*: it refers to the configurations of Layout 6 implementing a MCFC of 1.4 MW_e fuelled *with bio- LNG*. The use of bio-LNG offers a large rise in PES, almost doubled (from roughly 7 to 12%), with the same CAPEX.
- *Green cloud*: it refers to the configurations of Layout 6 implementing a MCFC of 2.8 MW_e fuelled *with LNG*. These configurations show a similar range of PES obtained by the *heat recovery optimization* plus the *engine management* (orange cloud) and by *Layout 6 with 1.4 MW_e MCFC fuelled with LNG* (yellow cloud), while CAPEX is significantly higher (from roughly 12.5 to 15.5 M€).
- *Sky-blue cloud*: it refers to the configurations of Layout 6 implementing a MCFC of 2.8 MW_e fuelled *with bio-LNG*. In comparison to the previous configurations (green cloud), the use of bio-LNG allowed PES to increase significantly (from 12 to 17.5%), which was helpful into meeting the strict energy efficiency and environmental targets imposed on the maritime industry and to gross tonnage ships, such as cruise ships (as well as the HEMOS project target of 14% reduction in fossil fuel consumption).

Although there is a remarkable increase in capital costs due to the current stage of fuel cell technology, significant savings in non-renewable primary energy can be observed, particularly with the use of bio-LNG. In any case, it is equally important to evaluate the implementation of these solutions in terms of operating expenses, occupied volume, and fuel availability. From this point of view, it is worth noticing that, with respect to other promising fuels, bio-LNG bunkering, which is necessary to reach medium term targets, is currently available (and scalable for the future) in almost 70 ports in Europe, North America, and Asia, according to the Bunker Navigator tool [29], suggesting that the investigated solutions are immediately applicable.

Although a substantial number (approximately thousands) of configurations were analysed, Figure

6 allows for an immediate comparison of the PES and CAPEX performances of the various systems under consideration; note that the CO_2 emission performance is similar to that of the PES. The results of Figure 6 can be considered for renovation initiatives or *decision-making aims* at the early stages of designing an on-board energy system. From each cloud a Pareto front can be evaluated; an example relative to the configurations that allow achieving medium term EU' emission reduction targets (by 6% by 2030) is depicted in Figure 7. The figure shows non-dominated configurations that provide the Pareto front (highlighted by blue dots) for each subgroup under analysis.

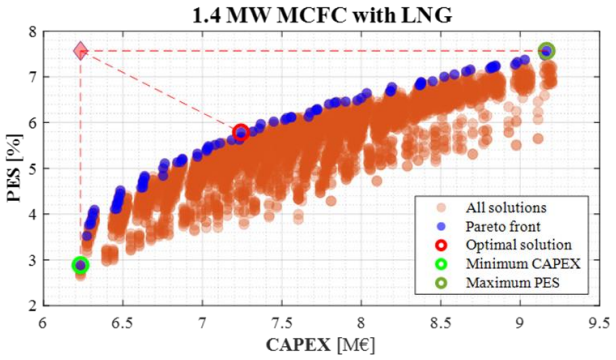

Figure 7. Pareto frons for diverse Layouts.

The optimal solutions depending on the criteria employed are reported in Table 6 for the previously described configurations (defined in the table by FC size and fuel and relative to Layout 6).

Table 6. Optimization results for Layout 6.

FC size and fuel	Index	Utopia	Economic	Energy
(a) 1.4MWe MCFC *LNG*	PES w/ prop (%)	*5.79*	*2.88*	7.57
	PES w/o prop (%)	11.3	*5.64*	**14.8**
	CAPEX (M€)	7.24	6.23	9.17
	ΔOPEX (k€/trip)	27.8	13.9	36.3
	ΔCO_2 (t/trip)	161	91.8	203
	SPB (years)	4.74	8.12	4.59
(b) 1.4MWe MCFC *bio-LNG*	PES w/ prop (%)	10.4	7.48	12.2
	PES w/o prop (%)	**20.3**	**14.6**	**23.8**
	CAPEX (M€)	7.24	6.23	9.17
	ΔOPEX (k€/trip)	-16.1	-29.9	-7.55
	ΔCO_2 (t/trip)	246	177	287
	SPB (years)	-	-	-
(c) 2.8MWe MCFC *LNG*	PES w/ prop (%)	6.42	*3.25*	8.28
	PES w/o prop (%)	12.6	6.36	**16.2**
	CAPEX (M€)	13.6	12.5	15.4
	ΔOPEX (k€/trip)	30.9	15.7	39.7
	ΔCO_2 (t/trip)	199	124	243
	SPB (years)	7.99	14.4	7.06
(d) 2.8MWe MCFC *bio-LNG*	PES w/ prop (%)	**15.6**	12.4	**17.5**
	PES w/o prop (%)	**30.5**	**24.3**	**34.2**
	CAPEX (M€)	13.6	12.5	15.4
	ΔOPEX (k€/trip)	-56.8	-71.9	-48.0
	ΔCO_2 (t/trip)	370	294	413
	SPB (years)	-	-	-

PES values greater than 2%, 6% and 14.5% (associated with fuel consumption and emission savings) are reported in italic, underlined, and bold, respectively. The implementation of the MCFC (Layout 6) significantly affects the CAPEX, due to its remarkable cost. Moreover, the fuel cell electrical efficiency is only marginally higher than that of the currently installed DGs; therefore, the difference in PES is negligible when considering the primary energy of non-renewable fuel cells. Higher PES values can be achieved by considering the use of bio-LNG (configurations (b) and (d) in Table 6), ensuring a reduction in fuel consumption from non-renewable sources, but also a decrease in emissions. These variations in CAPEX and PES and variations in thermal energy recovery (due to different waste heat vectors) are crucial factors in determining the best configuration according to the specific criteria adopted (energy, economic, and utopia criteria).

For each of the above configurations reported in Table 6, Table 7 shows the main operating parameters along with the PES, CAPEX and ΔOPEX, which results refer to the optimization process and utopia criterion. The optimal sizes of the considered technologies (e.g. WST, SAC, DAC, or ORC), along with the required operating parameters (flowrates and pressures), are reported. The table also shows the return temperatures (HT and LT) of the waste heat recovery circuits and the number of RO and MSF units.

Table 7. Layout 6 with FC - utopia criterion results.

	(a)	(b)	(c)	(d)
PES w/ prop. (%)	5.79	10.4	6.42	**15.6**
CAPEX (M€)	**7.24**	**7.24**	13.6	13.6
ΔOPEX (k€)	27.8	-16.1	**30.9**	-56.8
WST steam flowrate (kg/h)	9000	9000	6000	6000
WST outlet pressure (bar)	0.70	0.70	0.70	0.70
WST electric power (kWe)	493	493	328	328
SAC cooling power (kWc)	2391	2391	3428	3428
DAC cooling power (kWc)	527	527	0	0
ORC HT source flowrate (t/h)	-	-	-	-
ORC electric power (kWe)	-	-	-	-
MCFC electric power (MWe)	1.4	1.4	2.8	2.8
HT circuit return temp. (°C)	71	71	71	71
LT circuit return temp. (°C)	38	38	38	38
Engine optimization	Yes	Yes	Yes	Yes
Number of activated RO	3	3	4	4
Number of activated MSF	2	2	1	1
Fuel DG	HFO	HFO	HFO	HFO
Fuel FC	LNG	Bio LNG	LNG	Bio LNG

Through the optimization process, it was possible to see: i) configuration (d), with the highest MCFC size and the use of bio-LNG, shows the highest PES (15.6%); ii) configurations (a) and (b), with the smallest MCFC size, achieves the lowest CAPEX (7.24 M€); and iii) configuration (c), with the highest MCFC size and the use of LNG, shows the best OPEX (30.9 k€). Each design includes a WST, with a capacity of 493 (*a* and *b*) or 328 (*c* and *d*) kW_e (according to the availability of waste heat, with a steam flow rate of 9000 or 6000 kg/h and an output pressure of 0.70 bar).

Layout 6 configurations shown in Table 7 include the exploitation of the waste heat from the LT circuit (used for the preheating of air conditioning and domestic hot water) and the implementation of freshwater production strategies (utilizing thermal energy for MSFs and electrical energy for RO) coupled with a lower return temperature of the HT waste heat recovery circuit. When the latter decreases (from 74°C in the RL to 71°C), an *increase in the availability of thermal energy from the HT circuit* is always observed, allowing for the implementation of larger SAC sizes, due to the better heat exchange inside the heat recovery connected to each engine. It is also noteworthy that by considering the implementation of a MCFC, the number of MSF units decreases from four to two or even one, whereas the number of RO units increases from two to three or four. This suggests that the use of an extra RO unit will also be covered by the MCFC, reducing the need for MSFs and releasing up thermal energy (to be exploited by the SAC or DAC). Finally, due to its low efficiency, the ORC machine was not included in the mix of technologies with the MCFC.

Focusing on the configuration relative to Layout 6 with a 2.8 MWe MCFC powered by bio-LNG, its PES exceeds 30%, excluding propulsion (the higher electric power demand on-board the ship, which is unlikely to vary significantly due to diverse routes and travel times). Although the type of fuel utilized has no effect on capital costs, CAPEX, it does have an impact on operating cost. The cost of bio-LNG (2124 €/t) is now much greater than that of HFO (627 €/t) or even LNG (708 €/t). Therefore, a negative return on investment is obtained in configurations (b) and (d), where the use of bio-LNG is considered because of the greater operating cost reached for each individual route, which leads to a negative variation in the operating costs (ΔOPEX < 0). Figure 8 shows the price point at which bio-LNG becomes economically feasible and competitive with conventional fuels (HFO and LNG). The red dots refer to the target bio-LNG purchase price for achieving OPEX variation of 0% for each HFO purchase cost. Lower bio-LNG costs imply a positive ΔOPEX; these threshold values mark the points at which ΔOPEX becomes null.

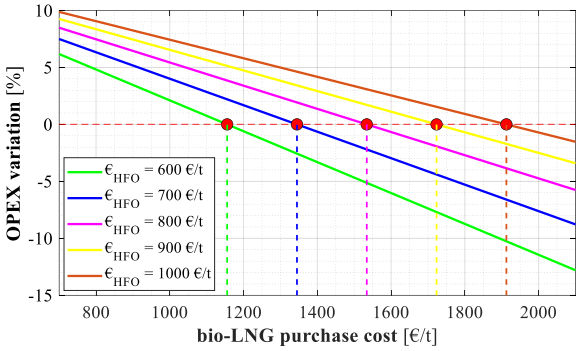

Figure 8. Parametric analysis of operating expenses variation based on fuel purchase costs.

The most energy-efficient technologies currently in use are not economically viable, according to the optimization results, as they have not yet attained a level of widespread adoption and practical use. Therefore, creating a roadmap that defines *realistic goals and activities for the near future* is crucial. The roadmap summarized in Figure 9 and created by exploiting the optimization results presented here, is intended as a guideline to support the sustainable transition of the shipping sector.

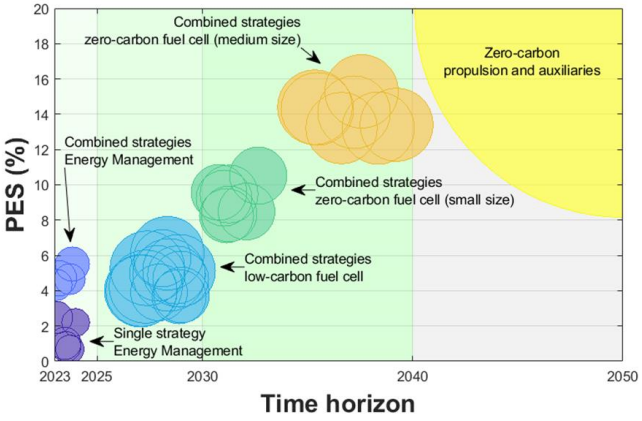

Figure 9. Towards a decarbonised future: roadmap in the maritime sector.

Figure 9 highlights that to accomplish the ambitious environmental targets established for 2040 and 2050, investments in cutting-edge propulsion technologies, such as hybrid systems or the use of alternative fuels, which result in significant fuel savings and emissions reductions, are crucial. The use of renewable energy sources is another viable method. When physically possible, replacing traditional energy sources and significantly reducing the overall fuel usage by integrating solar panels or wind turbines, can be an interesting option. Given that they have the highest PES potential, these solutions are shown in the yellow area (*zero-carbon propulsion and*

auxiliaries) in the top-right corner of Figure 9. The application of these solutions has the potential to reduce non-renewable primary energy use (as well as emissions) by a variety of tens of percentage points, and theoretically even completely decarbonize the ship, depending on the degree of integration with the ship system and the ratio of renewable power to ship required power, which is negligible in the case of cruise ships.

4. CONCLUSION

This paper provides the results of a research study aimed at proposing a holistic approach for the identification of energy efficient technologies and measures for ship applications based on dynamic simulation and optimization. Waste heat recovery technologies and strategies, as well as additional power technologies, are considered to find the set of potential layouts to be implemented on the Allure of the Seas, from Royal Caribbean Group, to increase energy efficiency and reduce fuel consumption.

Based on the numerical results obtained, it was possible to determine the mix of strategies and technologies that enhance fuel efficiency, reduce emissions, and effectively ensure compliance with environmental regulations and targets. For this purpose, the EU's short, medium and long term targets on cleaner maritime fuels are considered: ship emissions must be reduced by 2% by 2025, 14.5% by 2035, and 80% by 2050 in comparison to levels in 2020 [3]. Note that these targets apply to 90% of CO_2 emissions from ships with a gross tonnage exceeding 5000, such as the case study ship, but also to all energy used on board in or between EU ports, 50% of energy used on journeys where the departure or arrival port is outside the EU, and most EU remote areas. So, considering the EU agreement for the maritime transition, for the investigated cruise ship (and for same class ships) the research findings highlight that it is possible to reach emission reduction targets, *in the short and medium term*, by:

- 2% (by 2025) with the *optimization of waste heat recovery on-board* (blue cloud configurations in Figure 6). The implementation of single or combined technologies, which are currently available on the market, including a wet steam turbine, a single or double effect absorption chiller, and an ORC machine, allows for achieving a *PES* higher than 2%.
- 6% (by 2030) with the *optimization of the on-board heat recovery and engine operation*. This enables the achievement of a PES of approximately 8%, including propulsion, which is an impressive result, especially considering that it can be achieved by optimizing engine operation and implementing commercially available waste heat devices, without the introduction of novel technologies or innovative fuels (orange cloud configurations in Figure 6). The same emission target can be achieved by implementing a MCFC fuelled *with LNG*; however, considering a fuel cell of 1.4 MW_e (yellow cloud) or 2.8 MW_e (green cloud), the CAPEX increases significantly, up to 9 and 15 M€, respectively.
- 14.5% (by 2035) with *the implementation of a mix of technologies (Layout 6) including a fuel cell* capable of providing 2.8 MWe, *fuelled with bio-LNG* (sky-blue cloud). PES values (including propulsion) higher than 14.5% can be attained to achieve current energy efficiency goals. Intermediate targets (between 6% and 14%) can be reached by considering a smaller fuel cell of 1.4 MWe (violet cloud).

The results of this study demonstrate that short-term sustainability goals for ships can be achieved nowadays, whereas to reach long-term goals, each step must be planned with proper regulations and support for the advancement of technology and green fuel. By following a clear path, it is possible to achieve energy efficiency and environmental goals. Finally, the proposed holistic approach aims to pave the way for the successful integration and utilization of innovative technologies and fuels for fostering maritime energy transition through the energy efficiency of large ships.

ACKNOWLEDGMENTS

The research has been founded by the European Union through the HEMOS "Holistic heat energy management on ships by implementing innovative dynamic calculation models towards maximum waste heat capture and energy efficiency" project (101056909), within the Horizon Europe RIA program (HORIZON-CL5-2021-D5-01, https://hemosproject.eu/).

NOMENCLATURE

Symbols

c	energy price (€/kg)
DAC	Double stage Absorption Chiller
f	Pollutant emission factor (kg/kWh)
J	Capital cost (€)
LNG	Liquefied Natural Gas
m	Fuel consumption (kg/s)
MCFC	Molten Carbonate Fuel Cell
MSF	Multi Stage Flash machine
OC	Operating costs
ORC	Organic Rankine Cycle machine
PE	Primary energy (kWh)
RO	Reverse Osmosis machine
SAC	Single stage Absorption Chiller
WST	Wet Steam Turbine

Subscripts and superscripts:

c	*cooling*
e	*electrical*
PL	proposed layout
RL	reference layout

REFERENCES

[1] IMO. (2023). *Marine Environment Protection Committee (MEPC 80)*.

[2] (2023). *Fit for 55: deal on new EU rules for cleaner maritime fuels*.

[3] European Parliament, "Reducing carbon emissions: EU targets and policies," *https://www.europarl.europa.eu/news/en/headlines/society/20180305STO99003/reducing-carbon-emissions-eu-targets-and-policies*, 2023.

[4] J. Barreiro, S. Zaragoza, and V. Diaz-Casas, "Review of ship energy efficiency," *Ocean Engineering*, vol. 257, p. 111594, 2022/08/01/ 2022.

[5] A. Coraddu, M. Kalikatzarakis, J. Walker, D. Ilardi, and L. Oneto, "Chapter 7 - Data science and advanced analytics for shipping energy systems," in *Sustainable Energy Systems on Ships*, F. Baldi, A. Coraddu, and M. E. Mondejar, Eds.: Elsevier, 2022, pp. 303-349.

[6] G. Barone, A. Buonomano, C. Forzano, A. Palombo, and M. Vicidomini, "Sustainable energy design of cruise ships through dynamic simulations: Multi-objective optimization for waste heat recovery," *Energy Conversion and Management*, vol. 221, p. 113166, 2020/10/01/ 2020.

[7] V. Lepistö, J. Lappalainen, K. Sillanpää, and P. Ahtila, "Dynamic process simulation promotes energy efficient ship design," *Ocean Engineering*, vol. 111, pp. 43-55, 2016/01/01/ 2016.

[8] A. Godet, J. N. Nurup, J. T. Saber, G. Panagakos, and M. B. Barfod, "Operational cycles for maritime transportation: A benchmarking tool for ship energy efficiency," *Transportation Research Part D: Transport and Environment*, vol. 121, p. 103840, 2023/08/01/ 2023.

[9] M. Jensen. (2018). *BIM on the high seas?*

[10] J. Lampe, E. Rüde, Y. Papadopoulos, and S. Kabir, "Model-based assessment of energy-efficiency, dependability, and cost-effectiveness of waste heat recovery systems onboard ship," *Ocean Engineering*, vol. 157, pp. 234-250, 2018/06/01/ 2018.

[11] A. Dotto, R. Sacchi, F. Satta, and U. Campora, "Dynamic performance simulation of combined gas electric and steam power plants for cruise-ferry ships," *Next Energy*, vol. 1, no. 3, p. 100020, 2023/09/01/ 2023.

[12] Ç. Karatuğ, M. Tadros, M. Ventura, and C. Guedes Soares, "Strategy for ship energy efficiency based on optimization model and data-driven approach," *Ocean Engineering*, vol. 279, p. 114397, 2023/07/01/ 2023.

[13] M. A. Ancona *et al.*, "Efficiency improvement on a cruise ship: Load allocation optimization," *Energy Conversion and Management*, vol. 164, pp. 42-58, 2018/05/15/ 2018.

[14] M. Bakker, A. Coraddu, and R. Hijdra, "A model predictive control approach towards the energy efficiency of submerged dredging," *Ocean Engineering*, vol. 287, p. 115770, 2023/11/01/ 2023.

[15] A. M. Bassam, A. B. Phillips, S. R. Turnock, and P. A. Wilson, "Experimental testing and simulations of an autonomous, self-propulsion and self-measuring tanker ship model," *Ocean Engineering*, vol. 186, p. 106065, 2019/08/15/ 2019.

[16] N. L. Trivyza, A. Rentizelas, G. Theotokatos, and E. Boulougouris, "Decision support methods for sustainable ship energy systems: A state-of-the-art review," *Energy*, vol. 239, p. 122288, 2022/01/15/ 2022.

[17] A. Dotto, F. Satta, and U. Campora, "Energy, environmental and economic investigations of cruise ships powered by alternative fuels," *Energy Conversion and Management*, vol. 285, p. 117011, 2023/06/01/ 2023.

[18] G. Barone, A. Buonomano, C. Forzano, and A. Palombo, "Implementing the dynamic simulation approach for the design and optimization of ships energy systems: Methodology and applicability to modern cruise ships," *Renewable and Sustainable Energy Reviews*, vol. 150, p. 111488, 2021/10/01/ 2021.

[19] T. Ouyang, Z. Su, F. Wang, B. Jing, H. Huang, and Q. Wei, "Efficient and sustainable design for demand-supply and deployment of waste heat and cold energy recovery in marine natural gas engines," *Journal of Cleaner Production*, vol. 274, p. 123004, 2020/11/20/ 2020.

[20] E. Sciubba, L. Tocci, and C. Toro, "Thermodynamic analysis of a Rankine dual loop waste thermal energy recovery system,"

Energy Conversion and Management, vol. 122, pp. 109-118, 2016/08/15/ 2016.
[21] U. Larsen, O. Sigthorsson, and F. Haglind, "A comparison of advanced heat recovery power cycles in a combined cycle for large ships," *Energy*, vol. 74, pp. 260-268, 2014/09/01/ 2014.
[22] A. Brækken, C. Gabrielii, and N. Nord, "Energy use and energy efficiency in cruise ship hotel systems in a Nordic climate," *Energy Conversion and Management*, vol. 288, p. 117121, 2023/07/15/ 2023.
[23] D. V. Singh and E. Pedersen, "A review of waste heat recovery technologies for maritime applications," *Energy Conversion and Management*, vol. 111, pp. 315-328, 2016/03/01/ 2016.
[24] A. Buonomano, G. Del Papa, G. Francesco Giuzio, R. Maka, and A. Palombo, "Advancing sustainability in the maritime sector: energy design and optimization of large ships through information modelling and dynamic simulation," *Applied Thermal Engineering*, vol. 235, p. 121359, 2023/11/25/ 2023.
[25] A. Y. Kaya and K. E. Erginer, "An analysis of decision-making process of shipowners for implementing energy efficiency measures on existing ships: The case of Turkish maritime industry," *Ocean Engineering*, vol. 241, p. 110001, 2021/12/01/ 2021.
[26] CruiseMapper. *Allure Of The Seas*.
[27] G. Barone, A. Buonomano, G. Del Papa, R. Maka, and A. Palombo, "How to achieve energy efficiency and sustainability of large ships: a new tool to optimize the operation of on-board diesel generators," *Energy*, vol. 282, p. 128288, 2023/11/01/ 2023.
[28] S. Bhojwani, K. Topolski, R. Mukherjee, D. Sengupta, and M. M. El-Halwagi, "Technology review and data analysis for cost assessment of water treatment systems," *Science of The Total Environment*, vol. 651, pp. 2749-2761, 2019/02/15/ 2019.
[29] SEA-LNG. (2023). *BIO-LNG BUNKERING AVAILABLITY*.

A Case Study on the Heat Pump Integration for Enhanced Efficiency in Battery-Electric Short-Sea Ferries

Steffen Brötje[a*], Markus Mühmer[a], Thorben Schwedt[a], A. Phong Tran[b] and Sören Ehlers[a]

[a] Institute of Maritime Energy Systems, German Aerospace Center (DLR), 21502 Geesthacht, Germany
[b] Institute of Low-Carbon Industrial Processes, German Aerospace Center (DLR), Walther-Pauer-Straße 5, 03046 Cottbus
* Correspondence: steffen.broetje@dlr.de, +49 4152 8488-107

Abstract

This case study investigates the potential of incorporating water heat pumps into onboard thermal systems to utilize low-temperature waste heat for onboard heating and enhance the efficiency and economics of all-electric battery-driven ferries. We analysed a hybrid-driven roll-on/roll-off passenger ferry operating in the Baltic Sea, gathering data on vessel operation, power, and heat provision in low-temperature cycles. We integrated real-time measurement data, energy flow analysis, and thermodynamic calculations to draw conclusions for a potential battery retrofit scenario featuring an all-electric operation and a battery system capacity of 10 MWh. Our results indicate that the integration of heat pumps in battery-electric mode can cover more than 50 % of the onboard nominal heat capacity of HVAC systems, with a seasonal coefficient of performance (SCOP) of 3.5 during the heating season. The overall electric energy demand of the vessel during the 6-month heating period is reduced by approximately 8 % compared with direct-electric heating.

Keywords: Maritime heat pumps, battery-electric ships, low-temperature waste heat, energy efficiency, green maritime technologies

1 INTRODUCTION

The International Maritime Organization (IMO) aims to achieve net-zero GHG emissions from shipping by approximately 2050 [1]. Waterborne transportation produced 3-4 % of the EU's total CO_2 emissions by 2021 [2]. With the "Fit for 55" package and the European Green Deal, the European Commission targets a 55 % GHG reduction by 2030 and climate neutrality by 2050, with shipping emissions included in the EU's emissions trading system [3]. The IPCC highlights efficiency improvements as a key measure for vessels [4]. Legal measures for ship efficiency are the Energy Efficiency Existing Ship Index (EEXI) and the Carbon Intensity Indicator (CII). Integrating water-water heat pumps into heating systems and low-temperature (LT) cooling cycles of all-electric ferries presents a solution for enhancing energy efficiency, thus aligning with these environmental goals.

1.1 Electrification of Short-Sea Ferries

Ferries constitute nearly 10 % of the total commercial value of all types of ships and represent a significant share of the global maritime economy, particularly in Europe, where they conduct the majority of short-sea operations involving freight and passengers, due to the many islands and archipelagos in the region [3, 5–7].

Historically, electric ships have been smaller, resulting in less complex energy systems. However, the emerging trend of deploying high-capacity batteries in larger short-sea vessels allows the inclusion of more sophisticated energy systems and heat recovery equipment. This shift is evident in the increasing number of commissioned larger electric vessels. Over 2200 Ro-Ro and passenger ferries of 1000 gross tonnage and more are listed in Clarkson's "World Fleet Register" [5].

Harmful emissions from ships, such as SO_X and NO_X, are high, so interventions are needed to meet MARPOL Annex VI amendments and increasingly stringent Emission Control Area (ECA) requirements [6, 8–10].

One promising strategy for reducing these emissions is the electrification of ship energy systems. Battery-electric storage systems (BESS) are becoming increasingly popular, especially for short-range vessels [11]. The number of battery-powered and purely electric vessels in operation and on order is rising, particularly in ferries. The DNV's "Alternative Fuel Insights" database indicates 619 operational battery-powered ships, 158 of which are purely electric. In addition, there are 212 more ships in order, 43 of which are purely

@2023 Brötje, S. et al. published by TU Delft OPEN Publishing on behalf of the authors. Licensed under a Creative Commons Attribution CC BY license.
DOI: https://doi.org/10.59490/moses.2023.663

electric. Of the pure electric ships, 115 are ferries, with 33 more in the pipeline [12].

Electric vessels are primarily used in transportation and tourism, with Norway and Denmark leading electrified ferry operations [6, 13]. Two-thirds of electrified vessels operate in a hybrid mode, as battery-electric power is largely dependent on voyage distances [6].

Batteries in hybrid systems help reduce fuel consumption and emissions by allowing for load levelling, peak-shaving, and the potential for temporary engine shutdown [10]. However, deep-sea vessels may not find BESS financially viable because of their high energy needs and long journeys, making carbon-neutral fuels a more appropriate option [11].

Battery electric ships with onshore charging at berths present a significant opportunity to reduce pollutants in ports. Studies have shown potential reductions in fuel costs and emissions of 15–35 % by sourcing power for batteries from onshore grids that utilize renewable energy [8, 10]. Rapidly declining battery prices, now at an average of 100 USD/kWh, and the potential of renewable energy sources, such as wind and solar power, further enhance the viability of this approach [6, 14, 15].

However, the transition to electrification presents challenges like power system optimization and management strategies [10, 14, 16].

Recent advancements in battery systems, characterized by enhanced energy density and reduced weight [17], have facilitated electrification of larger vessels. Consequently, this technological progression has resulted in the elimination of the waste heat originating from combustion engines. Battery-electric vessels have different thermal management systems than diesel or diesel-electric systems because they do not reject high amounts of heat via exhaust gases and cooling water from combustion engines nor do they produce high temperatures (HT).

1.2 Waste Heat Utilization and Heating on Ferries

Diesel and diesel-electric hybrid ships utilize waste heat sourced from engine exhaust or HT cooling water. This heat is applied in various ways depending on the ship type and travel profile, generally through steam coils in fuel tanks and preheaters for different substances, such as fuel oil, lubricating oil, air, and water, along with other technological receivers [18]. On passenger ships, HT waste heat is used for steam generation, direct heating, hot water production, or electricity generation through steam turbines or the Organic Rankine Cycle (ORC). These vessels use waste heat for hot potable water production and can employ thermal storage to balance the generated and consumed heat [19].

The efficiency of waste heat recovery (WHR) systems is influenced by the temperature of the heat source, making them useful only when there is a corresponding demand. Owing to their customized systems and short distances between heat sources and consumers, ships are suitable for WHR.

Diesel engines running on carbon-neutral fuel are likely to continue to power bulk and container vessels, providing HT heat. Battery-electric ships can operate emission-free with the right renewable power mix, but they only provide low-exergy heat owing to their low cooling circuit temperatures. Heat loss from the propulsion and supply systems of these ships is typically discharged into seawater. Heating systems on board still demand heat at approximately 50 to 70 °C, while drivetrain devices are cooled to a maximum of approximately 40 °C, resulting in a significant energy loss.

The state of the art for heating battery-powered vessels primarily revolves around direct electric heating. In such systems, the electricity from the battery of the vessel is used to directly produce heat through electric heaters with resistive elements. This method is straightforward, simple, and reliable, but not the most energy-efficient [20], especially when compared to heat pumps.

1.3 Heat Pumps in Battery-Electric Ships

Heat pumps are a promising solution for enhancing the energy efficiency of battery-powered electric ships [20]. They can harness the low-temperature waste heat generated by electrical machinery, such as batteries and battery converters [17, 20], to provide heating for passenger ships and other vessels with significant heat and cooling demands. Compared to the benchmark of direct-electric heaters with resistive elements, the use of heat pumps reduces the operational costs of electricity and the required battery capacity. Heat pumps can provide both heating and cooling by reversing the cycle using reversing valves.

However, there are challenges in integrating heat pumps into ships, such as limited space, complexity, upfront costs, and the need to be installed near the heat source [21]. The speed of response of water heat pump systems also tends to be slower than with local direct-electric heating. A secondary heat source must be implemented to provide heat during low operation losses and high heat demands. Additionally, the refrigerants used in some heat pumps can have environmental implications if not properly managed.

The feasibility of heat pump integration is closely related to vessel size and heating requirements. Electric cabling is typically less expensive than fluid piping. As equipment costs do not scale linearly with size and electricity costs for heating are nearly proportional to power demand, the increasing size of ships and electric capacities favour the potential of utilising low-temperature waste heat, particularly on ferries with significant heat demand.

We assessed the use of water-water heat pumps to recover this waste heat in BESS-equipped all-electric ships, such as RoPax ferries. This can reduce energy use, emissions, and battery load for direct-electric heating. The upscaling of electric systems leads to an increase in LT waste heat, specifically originating from batteries and battery converters for the grid and consumers. This waste heat can be repurposed for onboard heating using specially designed heat pump systems.

To validate this, we investigate the integration of a heat pump system into a Baltic Sea ferry, recording heat and energy flows, and simulating the potential energy savings following a hypothetical conversion to a fully electric ferry.

2 HEAT FLOW ANALYSIS

2.1 Hybrid-electric ferry specifications

A measurement campaign was conducted on the hybrid-electric RoPax ferry "Schleswig-Holstein" over five days in November and December 2022 to assess the feasibility of using heat pumps for a potential retrofit to all-electric operation. This study does not evaluate the conversion itself but instead develops a theoretical model scenario for a possible system layout. Figure 1 shows the ferry in operation.

Figure 1: Hybrid-electric ferry “Schleswig-Holstein” (Source: Scandlines)

Table 1 presents the system. The ferry is powered by a 2,600-kWh NMC battery system and up to four diesel generators, ranging from 2,640 kW to 4,950 kW. The Corvus battery system provides low-speed propulsion, load balancing, and power for onboard operation. In normal operation, load levelling is achieved by running the 9-cylinder engine and the battery system, charging the ESS during port time, and discharging it during cruising. The 6-cylinder engine was used only once during the measurement period because of a scrubber system refill requirement. Diesel generators ensure safe manoeuvrability and compliance with the SOLAS regulations. Figure 2 shows all completed voyages between Puttgarden, Germany and Rødbyhavn, Denmark, undertaken during the measurement campaign.

Table 1: Specifications of investigated hybrid-electric ferry

Basic Specifications	
Length	142.0 m
Width	24.4 m
Gross tonnage	15,187 GT
Gross deadweight	2,904 t
Operational speed	18.5 kn
Machinery & Propulsion	
GenSet, MAK 9M32E + 3 Ph 50 Hz 6600 V/245 A	1 x 4,950 kW
GenSet, MAK 8M32 + 3 Ph 50 Hz 6600 V/330 A	2 x 3,520 kW
GenSet, MAK 6M32 + 3 Ph 50 Hz 6600 V/519 A	1 x 2,640 kW
ESS, Corvus	2,600 kWh 3,500 kW
Kongsberg Azimuth Thruster AZP 120 FP	4x 3,000 kW

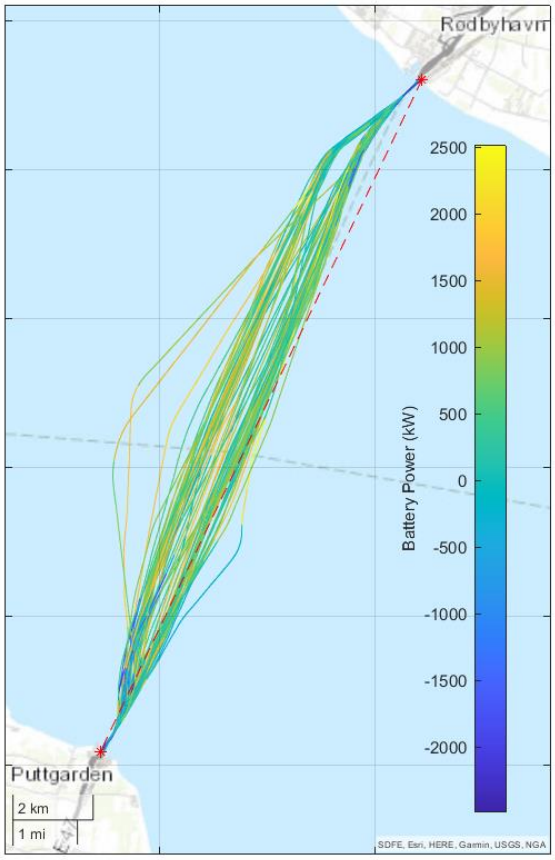

Figure 2: Voyage routes during measurements

2.2 Data acquisition

Measurements were collected from the NMEA interface, the monitoring and surveillance system in the engine control room, and via heat flow measurements on the low-temperature cooling circuit.

2.2.1 Navigational and power data

A custom Raspberry Pi data-logger, attached to the NMEA 0183 interface near the northern bridge, recorded time-dependent propulsion power, power consumption, navigation, and position data. Managed by the National Marine Electronics Association, NMEA 0183 enables communication between marine electronics. The text-based output was synchronized with the heat flow measurements and correlated with the ship operations. Figure 3 depicts the repeated route of the hybrid ferry during the main measurement activities, as indicated by the latitude position, along with the total energy consumption of each round trip. The repetitiveness of the cycle simplifies the measurement and modelling owing to the constant boundary conditions. The seawater and ambient air temperatures are also illustrated.

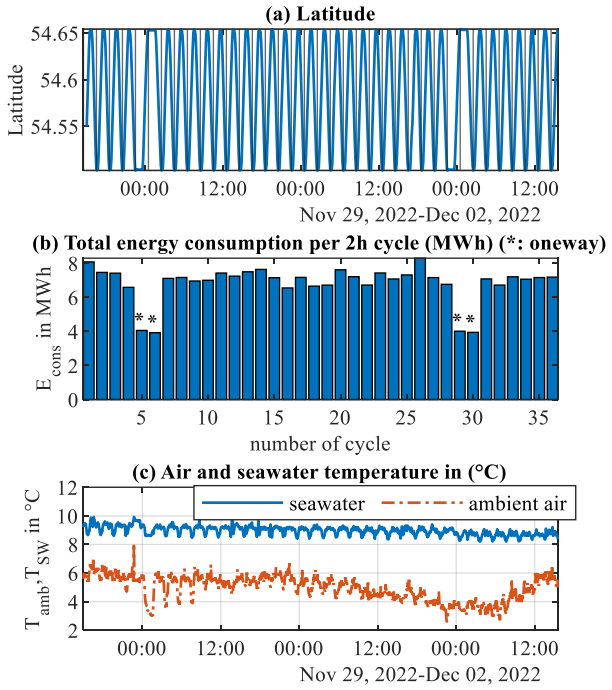

Figure 3: Round trips acc. to NMEA data:
(a) Latitude of ship in 2-hour cycles
(Puttgarden-Rødbyhavn-Puttgarden)
(b) Total energy consumption per round trip
(*: only one-way trip Putt.-Rødby./Rødby.-Putt.)
(c) Air and seawater temperature

2.2.2 Heat flow rate measurements

Four portable dual-channel ultrasonic flow meters were used to measure the heat flow rates in the LT cooling system of the hybrid-electric ferry, covering heat-rejecting components such as converters, ESS, and electric motors. Additionally, Surplus heat from the 9-cylinder diesel and 160 °C thermal recovery system was tracked for heat balance evaluation after electrification. Some electric drivetrain parts, such as transformers, are dry-cooled and not part the LT system. Ultrasonic sensors were clamped at either the inlet or outlet of the cooling cycle to acquire the volume flow rates $\dot{V}_\mathrm{i}$. The inlet and outlet temperatures T_1 and T_2 were measured using resistance thermometers of type Pt100. We used Eq. (1) to determine the enthalpy flow difference between two points in the cooling system, noting that the fluid properties of water, such as density $\rho(\bar{T})$ and specific heat $c_\mathrm{p}(\bar{T})$, remain relatively stable with temperature.

$$\dot{Q}_\mathrm{i} = \dot{m}\,\Delta H = \dot{V}_\mathrm{i}\,\rho(\bar{T})\,c_\mathrm{p}(\bar{T})\,(T_2 - T_1) \qquad (1)$$

Figure 4: Setup of heat flow rate measurement from cooling of the battery´s bidirectional converter

The heat flow rates rejected by each component are presented in Table 2. The primary LT cooling ranged between 26 and 30 °C, while the return was 30 to 35 °C before seawater cooling.

In addition to the listed points, enthalpy differences at key cooling system branches were measured but disregarded due to minimal temperature differences and the resulting high enthalpy rate uncertainties.

Figure 4 shows an exemplary measurement setup: the flow meter is at the bottom, temperature sensors T1 and T2 are at the inlet and outlet, respectively, and both the sending and receiving ultrasonic sensors are on the outlet pipe.

2.3 Measurement results

The power data and LT heat flow rates for the ship are listed in Table 3, with the overall mean weighted by the duration of each test.

Approximately 87 % of the LT heat originates from the diesel genset. Figure 5 displays the power rates in the hybrid-electric system and a comparison of overall LT heat transferred to seawater with the LT cooling waste heat of the diesel-generator during an exemplary set of measurements. Deducting the LT heat of the diesel genset and the HT surplus from the total LT heat rejected to seawater provides an estimate for potential battery-powered ships (Eq. 2).

$$\dot{Q}_{\mathrm{Test}} = \left|\dot{Q}_{\mathrm{SW}}\right| - \dot{Q}_{\mathrm{DG}} - \dot{Q}_{\mathrm{SP}} = 272\ \mathrm{kW} \qquad (2)$$

The uncertainty of the estimation was high owing to the fluctuation in the highest heat flow rates. Therefore, the potential LT heat available in the all-electric scenario is calculated by summing all the heat rejected by the electric drive system units, as shown in Eq. (3).

Table 2: Water-cooled heat sources and parameters in low-temperature cooling cycle

Location/unit	Type (cooling details)	Rated power per unit (kW)	Rated losses per unit (kW)	Diameter (ND)	Rated water flow rate (m^3/h)
Battery ESS	NMC Li-Ion (3-Stage compressor + water-air HEX)	3,500	60	50	11.9
ESS converter	Bidirectional (water-cooled)	4,000	40	60	5.3
Thruster Motor (4x) [a]	3-Phase (air-cooled, air-water HEX)	3,100	126	50	15.5
Azimuth Thruster	(valves closed during measurements)	3,000	150	65	21
Thruster frequency converter (4x) [b]	24 Pulse DFE Rectifier + Inverter	3,100	61	50	12.5
Provisions cooler	(provisions partially water-cooled)	16	16	50	3
HT Surplus[c]	Plate HEX (from 160 °C-system)	250	250	50	25
Diesel Genset 5 [c] (LT cycle only)	4-stroke recipro. piston inline engine + 3-Phase 50 Hz generator	4,950	3,500	100	93
Seawater HEX	Plate HEX	/	-11,098	300	342.0

[a] 4 Azipull Thrusters; heat flow rate at No. 2 and 4 was measured; losses for No. 1 and 3 assumed to be the same
[b] Heat flow rates of No. 1 and 2 were measured, losses for No. 3 and 4 assumed to be the same
[c] Diesel engines and HT surplus obsolete in all-electric scenario; DG 5 was only genset running during evaluation

Table 3: Measured power and heat flow rates

Location/unit	Name	Dimension	Source	Min.	Max	Weighted average
Power						
Diesel Generator 5	P_{DG5}	MW_{el}	NMEA	- [a]	- [a]	3.63
Battery Power	P_{ESS}	MW_{el}	NMEA	-2.39	2.12	-0.07
Consumption (total)	P_{Con}	MW_{el}	NMEA	0.22	6.61	3.56
Thrusters (sum)	P_{Thr}	MW_{el}	NMEA	0.00	4.66	2.18
Thermal system						
Seawater heat exchanger	$\dot{Q}_{\mathrm{SW}}$	kW_{th}	HFM	-3,356	329	-2,087
Diesel Genset 5 (LT heat rejected)	$\dot{Q}_{\mathrm{DG}}$	kW_{th}	HFM	-511	2,173	1,816
HT System (Surplus from 160°C-system)	$\dot{Q}_{\mathrm{SP}}$	kW_{th}	HFM	2	19	11
Heat to seawater (excl. $\dot{Q}_{\mathrm{DG}}$, $\dot{Q}_{\mathrm{SP}}$)	$\dot{Q}_{\mathrm{Test}}$	kW_{th}	HFM	-	-	272
Heat rejected by electric drive system units						
Battery ESS	$\dot{Q}_{\mathrm{ESS}}$	kW_{th}	HFM	8	90	32
Battery ESS converter	$\dot{Q}_{\mathrm{EC}}$	kW_{th}	HFM	1	20	9
Thruster Motor No. 2 & 4	$\dot{Q}_{\mathrm{Th2/4}}$	kW_{th}	HFM	6 / 3	37 / 32	23 / 21
Thruster frequency converter No. 1 & 2	$\dot{Q}_{\mathrm{TC1/2}}$	kW_{th}	HFM	7 / 9	38 / 43	20 / 24
Provisions cooler [b]	$\dot{Q}_{\mathrm{Pr}}$	kW_{th}	HFM		10	10

[a] Generator Power calculated indirectly from total power output and battery power. Min/Max values not reliable due to low frequency of battery power signal; [b] Assumption
NMEA: data achieved from NMEA Interface signals and own calculations
HFM: data achieved from heat flow rate measurements and own calculations

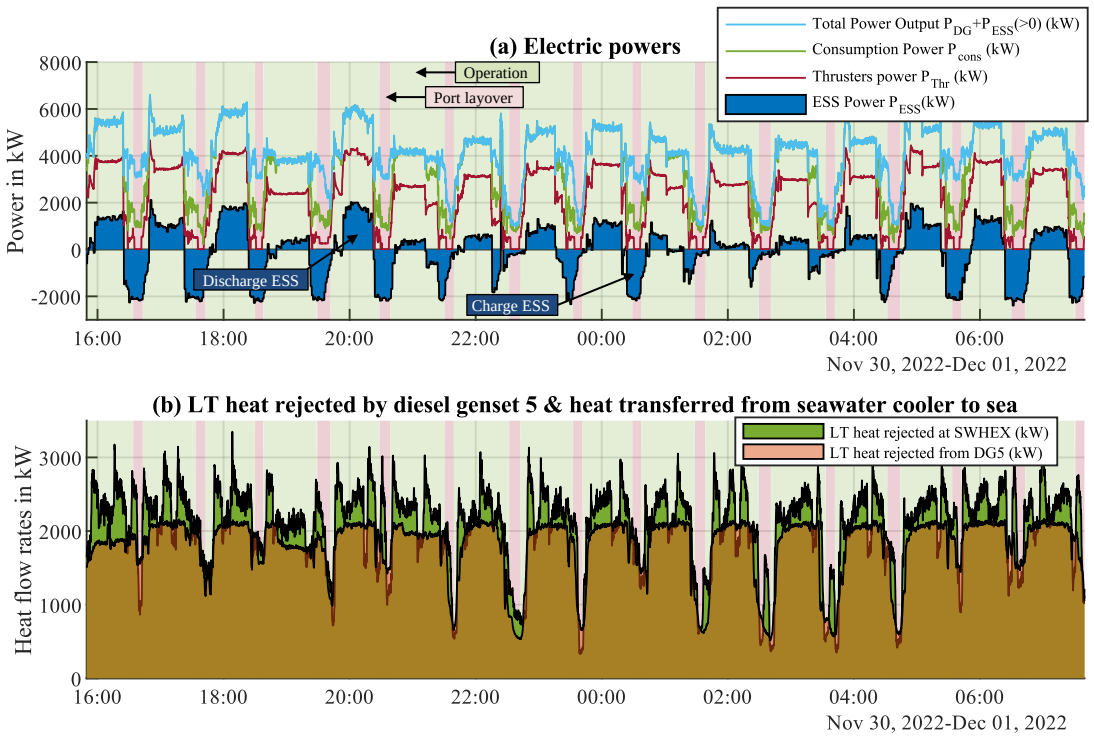

Figure 5: Exemplary signal plots
(a) Power rates of battery, consumers (propulsion + hotel), propulsion and total output
(b) LT heat flow rates at seawater heat exchanger and main engine 5

$$\dot{Q}_{\mathrm{LT,el}} = \dot{Q}_{\mathrm{ESS}} + \dot{Q}_{\mathrm{EC}} + 2\,\dot{Q}_{\mathrm{Th2}} + 2\,\dot{Q}_{\mathrm{Th4}} + 2\,\dot{Q}_{\mathrm{TC1}} + 2\,\dot{Q}_{\mathrm{TC2}} + \dot{Q}_{\mathrm{Pr}} = 227\ \mathrm{kW} \quad (3)$$

The 227 kW value represents the minimal LT heat in colder seasons for the present ship setup, excluding the fuel heat sources. The disparity between $\dot{Q}_{\mathrm{Test}}$ and $\dot{Q}_{\mathrm{LT,el}}$ indicates significant uncertainties in the major heat sources and heat transfer to the sea. In addition, the system also includes three more diesel engines in standby, contributing heat via a complex cooling and fuel preheating system of non-insulated HT parts next to the LT cooling pipes.
Notably, each thruster motor and its grid converter have approximately 4 % loss relative to the power of each thruster. 227 kW signifies a roughly 6 % loss in total consumption. In a fully electric battery-operated mode, crucial electric drivetrain elements, such as the battery system and converter, will increase, adding more LT heat for heat pumps. Moreover, more electric consumers are expected in all-electric vessels, including the heat pump system. This is further explained in Section 3.

3 ALL-ELECTRIC SCENARIO

The transition to fully electric operation poses a challenge considering that the Rødby-Puttgarden route covers 18.5 km, and the current schedule only allows for a 15-minute layover at each port for quick charging [22].

This chapter employs a basic voyage and charging profile to project LT heat availability in a hypothetical all-electric ferry. This scenario is unconfirmed, and decisions for such large retrofit and grid projects must consider factors beyond efficiency.

3.1 Battery losses

Heat losses from the upscaled battery system during charging, discharging, and pausing are accounted for and estimated through a basic correlation to power. [23]:

$$\dot{Q}_{\mathrm{ESS}} = k\,P_{\mathrm{ESS}}^2 \quad (4)$$

The loss factor k is defined as equal for both the charging and discharging processes. High losses diminish the benefits of high charging rates and accelerate battery cell aging. The actual power and heat losses of a battery system depend on cell type, cell size, cooling system, and topology. Losses have been described in several studies for different cell types such as LMO, NMC, LTO, and LFP. [15, 24–26]. MAN Energy Solutions observed that while charging a 1 MWh battery at a C-rate of 3, there is a heat loss power ranging from 4 % to 6 %. As the C-rate increases, the heat loss also increases [27]. A loss of 5 % at a C-rate of 3 is assumed for the following scenarios, resulting in k = 1.67e-6.

3.2 All-electric voyage profile

Switching to an all-electric system implies replacing diesel engines with larger battery systems. A scenario was created to assess how altered charging strategies and battery losses affect the heat released to the low-temperature cycle and its usability for heat pumps.

Table 4 details this scenario. A 10 MWh battery system is charged at both ports using 15 MW onshore power, indicating a 1.5 C-Rate as a near-future solution. To maintain manoeuvrability and energy levels, a 17-minute charge at each port with a 41 % DoD is needed.

Table 4: Modelled all-electric scenario in comparison to existing hybrid-electric operation

	Hybrid	All-electric
Route time and power profile		
Charging time per port t_{chg} (Min.)	-	17
Cruise time t_{op} (Min.)	45	45
Pause time in port t_{pause} (Min.)	15	3
One-way voyage time (Min.)	60	65
C-Rate (port charge)	-	1.5
Propulsion (cruise) P_{Thr} (kW)	2,907	2,907
Hotel loads P_{hotel} (kW)	1,380	1,780
Consumption (cruise) P_{op} (kW)	4,287	4,687
Consumption (mean) (kW)	3,560	3,792
Overall genset capacity (kW)	14,430	-
ESS capacity (kWh)	2,600	10,000
ESS power capacity (kW)	3,500	15,000
Energy balance		
Charging power P_{chg} (kW)	(919)	15,000
C-Rate charge	(0.35)	1.5
Losses charging ε_{chg} (%)	-	2.5
Cruise power P_{op} (kW)	(760)	4,687
C-Rate discharge	(0.29)	0.47
Losses discharge ε_{op} (%)	-	0.8
C-Rate hotel mode	(0.53)	0.18
Losses pause ε_{pause} (%)	-	0.3
Charged energy E_{chg} (kWh, excl. losses)		**4,144**
Required energy E_{req} (kWh, incl. losses)		**4,138**

The mean hotel load for the hybrid ship was 1382 kW. Further 200 kW are assumed for the heat pump consumption and 200 kW for new electric consumers expected on the all-electric ship. Thus, 1782 kW is considered a constant hotel load.

The charging and discharging losses are considered in the energy balance, according to Eq. (4). The scenario is set up to be potentially operated fully electric, as there is more energy charged than consumed due to losses. The charged and required energies for a one-way voyage (half-round trip) were calculated using Eq. (5) and (6), assuming that the EMS allows for the simultaneous charging and provision of hotel loads:

$$E_{chg} = P_{chg} \frac{t_{chg}}{60\ \mathrm{Min/h}} \cdot (1\text{-}\varepsilon_{chg}) \quad (5)$$

$$E_{req} = \frac{P_{op}}{(1\text{-}\varepsilon_{op})} \frac{t_{op}}{60\ \mathrm{Min/h}} + \frac{P_{hotel}}{(1\text{-}\varepsilon_{hotel})} \frac{t_{chg}+t_{pause}}{60\ \mathrm{Min/h}} \quad (6)$$

The change in the operation profile and battery upscaling from 2.6 to 10 MWh affect parts of the LT cooling cycle, particularly the battery cooling heat rates at the battery chiller and battery converter. The total LT heat rates available for the heat pump are listed in Table 5.

The battery chiller heat rates are acquired from the battery losses, as shown in Eq. (4) and Table 4, assuming heat transfer of the losses to the cooling water with 90 % efficiency. The presented heat flow rates are the mean values of all times of the standard route schedule, including cruise, charging, and additional port times. To assess the potential of heat pump applications, the mean values are considered sufficient because of the unresponsive slow behaviour of the thermal system.

In the all-electric mode, there is 346 kW of heat available at low-temperatures of approximately 30 °C. Excluding the diesel-genset losses, this is an increase of 50 % compared with the hybrid system.

Table 5: Available LT heat rates in all-electric mode

	Hybrid	All-electric
Heat rejected to LT cooling water system (kW)		
ESS (charge)	-	375
ESS (operation)	-	36.6
ESS (pause)	-	5.3
ESS (mean)	32	124 x 0.9
ESS Converter	9	39
Constant values (measured kW, see Table 3**)**		
Thruster Motor 2	2 x 23	
Thruster Motor 4	2 x 21	
Thr. frequency converter 1	2 x 20	
Thr. frequency converter 2	2 x 24	
Proviant	2 x 10	
Sum $\dot{Q}_{LT,av}$ (kW)	227 →	**346**

4 HEAT PUMP INTEGRATION

4.1 Heat pump model

To assess the performance of the proposed heat pump, a parametric study was conducted using a simulation model implemented in the Modelica Buildings library [28]. A constant second-law efficiency, denoted as η, is assumed for the heat pump, which relates the heat pump's coefficient of performance (COP) to the Carnot cycle COP using Eq. (7):

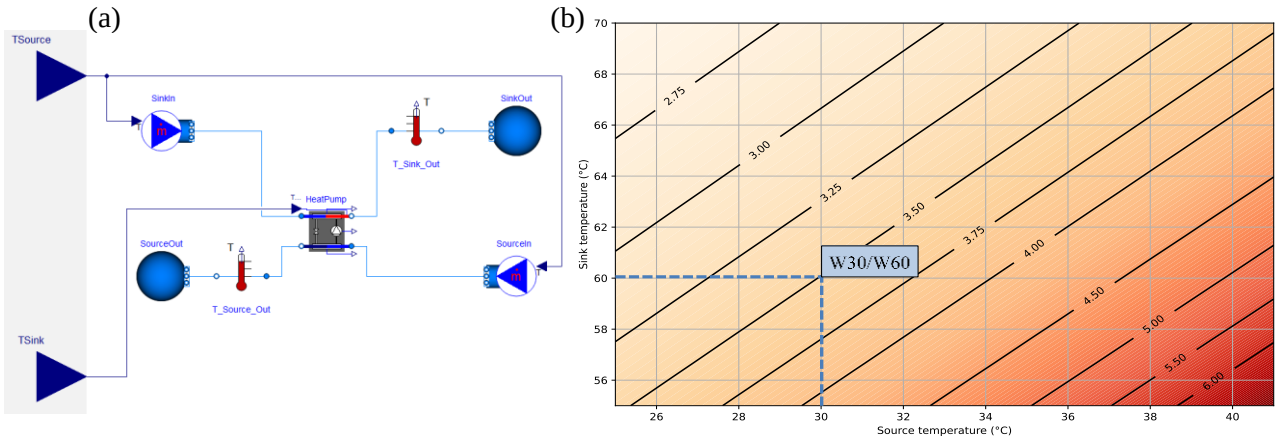

Figure 6: (a) Modelica-based model for presented heat pump study
(b) Coefficient of performance (COP) of the heat pump at various source and sink temperatures.

$$\mathrm{COP} = \eta \cdot \mathrm{COP}_{\mathrm{Carnot}} \qquad (7)$$

$$\text{where } \mathrm{COP}_{\mathrm{Carnot}} = \frac{T_{\mathrm{h}}}{T_{\mathrm{h}} - T_{\mathrm{l}}}$$

Arpagaus et al. [29] compiled the performance data of commercially available industrial heat pumps and reported Carnot efficiencies of 40 % to 60 % for most heat pumps. For this study, a Carnot efficiency of 50 % was assumed. Moreover, a terminal temperature difference of 2 K was considered for both the evaporator and condenser. The heat source temperature was varied between 25 and 41 °C, whereas the heat sink temperatures ranged between 55 and 70 °C. See the next section for a description of the chosen temperature ranges.

Figure 6 illustrates the COP of the proposed heat pump as a function of the source and sink temperatures as well as the system model used.

4.2 Estimation of energy savings

To estimate energy savings, a water-water heat pump with source/sink temperatures of 30 °C/60 °C (W30/W60) was considered. The ship could consistently maintain the 30 °C source. The system's design caps at 41 °C to safeguard equipment like lithium-ion batteries, from thermal runway. Although the hybrid ferry's heating system is designed for 65 °C to 70 °C, the considered HVAC systems can effectively operate at 55 °C to 60 °C.

With a COP of 3.5, the heat pump generates 3.5 times the heat for each kWh of electricity. Its energy demand is substantially lower than that of the direct-electric heaters. The energy savings for a 6-month heating period were estimated.

Table 6 illustrates the energy savings for the W30/W60 mode heat pump with a 3.5 seasonal coefficient of performance (SCOP). Used for the HVAC registers, the heat pump can supply 50 % of the peak design heat rate of the system. Because heating systems are typically designed for very cold winter days, the pump is expected to offer substantial heat, reducing the need for direct electric heating. This will be investigated in a future study.

The heat pump can substantially meet onboard heating needs, saving up to 0.5 million euros annually, depending on electricity costs. While decentralized renewables might cost less than 0.30 €/kWh, grid costs often increase the price.

Using only electric heaters instead of a heat pump for the heating of the ship means drawing all the energy from the ESS. The hotel load increased correspondingly to 2126 kW. Using Eq. (6), the required energy E_{req} per half-round trip would increase from 4138 to 4518 kWh, adding approximately 2 min of port-charging time. Correspondingly, the heat pump can cut energy requirements by approximately 8.4 % and decrease the battery capacity requirements by 380 kWh.

Table 6: Estimations of energy and cost savings, compared to 100 % electric heaters

	All-electric mode
Heat available at ca. 30 °C $\dot{Q}_{\mathrm{LT,av}}$	346 $\mathrm{kW_{th}}$
COP at W30/W60	3.5
Heat pump power demand	138 $\mathrm{kW_{el}}$
Heat available at 60 °C*	**484 $\mathbf{kW_{th}}$**
Assumed electricity price	0.30 €/$\mathrm{kWh_{el}}$
Days of heating period	182.5 days
Financial saving per year	**454,000** €
Savings of energy per round trip	**8.4 %**
Potential savings of ESS capacity	**380 kWh**
*Comparison: fraction of maximum (rated) heat for	
… HVAC (898 kW)	54 %
… Radiators (535 kW)	91 %

5 CONCLUSION

This study analysed the possible use of heat pumps in battery-electric ferries, particularly

considering retrofitting a hybrid-electric RoPax ferry. The main findings are as follows:

The ferry cooling system allows substantial heat recovery for onboard air-conditioning. In a fully electric system, the available low-temperature heat for heat pumps increases by 50 % compared to the existing hybrid setup.

Using a Modelica-based model, a heat pump was studied parametrically. With a Carnot efficiency of 50 %, the Coefficient of Performance (COP) of the heat pump was found to be significantly influenced by the source and sink temperatures. Notably, a COP of 3.5 was determined to be very likely for the heat pump, indicating its efficiency in energy conversion.

Integrating heat pumps into the heating system results in an 8 % reduction in the vessel's electric energy demand over a 6-month heating period compared to a benchmark of direct-electric heating with resistive elements. This reduction not only optimizes the energy consumption but also positively impacts the required battery capacity. For a 15,187 GT vessel, the potential annual savings approach 0.5 million euros, although these savings are highly sensitive to shore energy prices.

The operational and charging profiles of the ferry significantly influence the efficiency of an all-electric system. Although hypothetical, the model scenario highlights challenges in transitioning to fully electric operation. The integration of heat pumps into battery-electric ferries presents an energy-efficient and economically viable solution. This study offers guidance for future maritime retrofitting and sustainable operational decisions.

6 OUTLOOK

Heat pump integration necessitates a comprehensive design that links the onboard systems [30, 31]. Adaptation methods for retrofits can be sourced from sectors, such as buildings [32]. The design variables include the specific heating demand and cooling heat of battery systems and power electronics, which can fluctuate owing to elements such as cell size, cooling system, topology, and cell type [15, 24–26].

Future research should consider the dynamics of heat receivers and sources, influenced by passenger numbers, boundary conditions, operation schedules, and the impact of different route scenarios. Specific heat demand profiles will be the subject of future research.

Seasonal effects, especially cooling needs during the summer months, require further exploration of bidirectional heat pump usage. Exploring thermal storage for balancing heat production and demand and utilizing sustainable working fluids, such as CO_2 and NH_3 in heat pumps is aligned with sustainability objectives.

Demonstrators and system models provide invaluable performance data for optimizing these technologies. As highlighted in section 1.3, vessel size is essential in assessing the feasibility of heat pump integration, necessitating an analysis comparing upfront costs to potential savings.

APPENDIX

A.1 Nomenclature

ε	Losses	%
ρ	Density	kg/m^3
η	Second-law efficiency	-
c_p	Specific heat capacity	J/(kg K)
E	Energy	kWh
ΔH	Enthalpy difference	kJ/kg
k	Battery loss factor	√kW
$\dot{m}$	Water mass flow	kg/s
P_i	Electric power (of part i)	MW
$\dot{Q}_i$	Rejected heat flow rate (of part i)	kW
t_i	Time interval	Min.
$T_{1/2}$	Temperature inlet / outlet	°C
T_h	Temperature of hot reservoir	K
T_l	Temperature of cold reservoir	K
$\dot{V}_i$	Volume flow rate	m^3/s

A.2 Abbreviations

COP	Coefficient of Performance
DoD	Depth of discharge
EMS	Energy Management System
HEX	Heat exchanger
HT	High-temperature
HVAC	Heating, Ventilation and Air Conditioning
LT	Low-temperature
Ro-Ro	Roll-on/roll-off
RoPax	Roll-on/roll-off passenger vessel
SCOP	Seasonal coeff. of performance
SW	Seawater

REFERENCES

[1] IMO. “Revised GHG reduction strategy for global shipping adopted.” https://www.imo.org/en/MediaCentre/PressBriefings/pages/Revised-GHG-reduction-strategy-for-global-shipping-adopted-.aspx (accessed Jul. 8, 2023).

[2] European Comission. “European Green Deal: Agreement reached on cutting maritime transport emissions by promoting sustainable fuels for shipping.” https://ec.europa.eu/commission/presscorner/detail/en/ip_23_1813 (accessed Jul. 8, 2023).

[3] United Nations Conference on Trade and Development (UNCTAD), Navigating stormy waters, Review of maritime transport. Geneva, vol. 2022.

[4] M. Pathak, R. Slade, P. R. Shukla, J. Skea, R. Pichs-Madruga, and D. Ürge-Vorsatz, “Technical Summary. In: Climate Change 2022: Mitigation of Climate Change. Contribution of Working Group III to the Sixth Assessment Report of the IPCC,” IPCC, Cambridge and New York, 2022.
[5] Clarkson Research. “World Fleet Register.” www.clarksons.net (accessed Apr. 21, 2023).
[6] S. Anwar, M. Y. I. Zia, M. Rashid, G. Z. de Rubens, and P. Enevoldsen, “Towards Ferry Electrification in the Maritime Sector,” Energies, vol. 13, no. 24, p. 6506, 2020, doi: 10.3390/en13246506.
[7] M. Brambilla and A. Martino, The EU maritime transport system Focus on ferries: Research for Tran Committee. Brussels: European Parliament, doi: 10.2861/657769.
[8] H. Winnes, L. Styhre, and E. Fridell, “Reducing GHG emissions from ships in port areas,” Research in Transportation Business & Management, vol. 17, pp. 73–82, 2015, doi: 10.1016/j.rtbm.2015.10.008.
[9] A. Torvanger, J. Tvedt, and I. B. Hovi, “Carbon dioxide mitigation from public procurement with environmental conditions: The case of short-sea shipping in Norway,” Maritime Transport Research, vol. 4, p. 100085, 2023, doi: 10.1016/j.martra.2023.100085.
[10] H. P. Nguyen et al., “The electric propulsion system as a green solution for management strategy of CO 2 emission in ocean shipping: A comprehensive review,” Int Trans Electr Energ Syst, vol. 31, no. 11, 2021, doi: 10.1002/2050-7038.12580.
[11] M. Kolodziejski and I. Michalska-Pozoga, “Battery Energy Storage Systems in Ships’ Hybrid/Electric Propulsion Systems,” Energies, vol. 16, no. 3, p. 1122, 2023, doi: 10.3390/en16031122.
[12] DNV. “DNV "Alternative Fuels Insight" Database.” https://afi.dnv.com/statistics/(accessed May. 22, 2023).
[13] S. R. Sæther and E. Moe, “A green maritime shift: Lessons from the electrification of ferries in Norway,” Energy Research & Social Science, vol. 81, p. 102282, 2021, doi: 10.1016/j.erss.2021.102282.
[14] S. Wen et al., “Coordinated Optimal Energy Management and Voyage Scheduling for All-Electric Ships Based on Predicted Shore-Side Electricity Price,” IEEE Trans. on Ind. Applicat., vol. 57, no. 1, pp. 139–148, 2021, doi: 10.1109/TIA.2020.3034290.
[15] J. Kersey, N. D. Popovich, and A. A. Phadke, “Rapid battery cost declines accelerate the prospects of all-electric interregional container shipping,” Nat Energy, vol. 7, no. 7, pp. 664–674, 2022, doi: 10.1038/s41560-022-01065-y.
[16] V. M. Moreno and A. Pigazo, “Future Trens in Electric Propulsion Systems for Commercial Vessels,” Journal of Maritime Research, Vol. IV. No. 2, pp. 81–100, 2007.
[17] J. Verma and D. Kumar, “Recent developments in energy storage systems for marine environment,” Mater. Adv., vol. 2, no. 21, pp. 6800–6815, 2021, doi: 10.1039/D1MA00746G.
[18] D. Bocheński and D. Kreft, “Cargo Ships’ Heat Demand - Operational Experiment,” Polish Maritime Research, vol. 27, no. 4, pp. 60–66, 2020, doi: 10.2478/pomr-2020-0066.
[19] M. Manzan et al., “Potential of thermal storage for hot potable water distribution in cruise ships,” Energy Procedia, vol. 148, pp. 1105–1112, 2018, doi: 10.1016/j.egypro.2018.08.044.
[20] S. Trzebiński, “Technical Aspects of Using the Heat Pump at the Ship,” Scientific Journal of Polish Naval Academy, vol. 217, no. 2, pp. 5–15, 2019, doi: 10.2478/sjpna-2019-0009.
[21] A. Brækken, C. Gabrielii, and N. Nord, “Energy use and energy efficiency in cruise ship hotel systems in a Nordic climate,” Energy Conversion and Management, vol. 288, p. 117121, 2023, doi: 10.1016/j.enconman.2023.117121.
[22] Scandlines Deutschland GmbH. “Zero emission freight ferry.” https://www.scandlines.com/about-us/our-green-agenda/zero-emission-freight-ferry/(accessed Jul. 11, 2023).
[23] N. Murgovski, L. Johannesson, and J. Sjöberg, “Convex modeling of energy buffers in power control applications,” IFAC Proceedings Volumes, vol. 45, no. 30, pp. 92–99, 2012, doi: 10.3182/20121023-3-FR-4025.00009.
[24] Y. Abdul-Quadir et al., “Heat Generation in High Power Prismatic Li-Ion Battery Cell with LiMnNiCoO2 Cathode Material,” Intl J of Energy Research, vol. 38, no. 11, pp. 1424–1437, 2014, doi: 10.1002/er.3156.
[25] S. Madani, E. Schaltz, and S. Knudsen Kær, “Heat Loss Measurement of Lithium Titanate Oxide Batteries under Fast Charging Conditions by Employing Isothermal Calorimeter,” Batteries, vol. 4, no. 4, p. 59, 2018, doi: 10.3390/batteries4040059.
[26] Z. Gao, H. Xie, X. Yang, W. Niu, S. Li, and S. Chen, “The Dilemma of C-Rate and Cycle Life for Lithium-Ion Batteries under Low Temperature Fast Charging,” Batteries, vol. 8, no. 11, p. 234, 2022, doi: 10.3390/batteries8110234.
[27] MAN Energy Solutions, Batteries on board ocean-going vessels: Investigation of the potential for battery propulsion and hybridisation by the application of batteries on board. Denmark, 2019.
[28] M. Wetter, W. Zuo, T. S. Nouidui, and X. Pang, “Modelica Buildings library,” Journal of Building Performance Simulation, vol. 7, no. 4, pp. 253–270, 2014, doi: 10.1080/19401493.2013.765506.
[29] C. Arpagaus, F. Bless, M. Uhlmann, J. Schiffmann, and S. S. Bertsch, “High temperature heat pumps: Market overview, state of the art, research status, refrigerants, and application potentials,” Energy, vol. 152, pp. 985–1010, 2018, doi: 10.1016/j.energy.2018.03.166.
[30] F. Baldi, T.-V. Nguyen, and F. Ahlgren, “The Application of Process Integration to the Optimisation of Cruise Ship Energy Systems: A Case Study,” in ECOS 2016, Portorož, Slovenia, A. Kitanovski and A. Poredoš, Eds., 2016.
[31] O. Konur, O. Y. Saatcioglu, S. A. Korkmaz, A. Erdogan, and C. O. Colpan, “Heat exchanger network design of an organic Rankine cycle integrated waste heat recovery system of a marine vessel using pinch point analysis,” Intl J of Energy Research, vol. 44, no. 15, pp. 12312–12328, 2020, doi: 10.1002/er.5212.
[32] C. Vering, “Optimal design of heat pump systems for existing buildings,” Aachen, 2023.

Heat Pump as an Emission Reduction Measure for Ships: Environmental and Economic Assessment

Fayas Malik Kanchiralla[a*], Selma Brynolf[a] and Dinis Soares Reis de Oliveira[b]

[a] Chalmers University of Technology, SE-412 96, Gothenburg, Sweden
[b] Stena Rederi AB, SE-405 19, Gothenburg, Sweden
*fayas.kanchiralla@chalmers.se

Abstract

Greenhouse gas regulations from the International Maritime Organization, such as the Carbon Intensity Indicator and the Energy Efficiency Existing Ship Index are drawing attention to the implementation of energy efficiency technologies in ships to lower emissions. Presently, more attention is paid to energy efficiency measures related to propulsion (e.g. speed management) and auxiliary energy use (e.g. onshore power). This study compares the environmental impact and cost of replacing heat pumps as an energy efficiency measure instead of oil-fired boilers for two case study vessels by comparing the life cycle impact of different strategies to fulfill the thermal load of vessels while at the port. In terms of life cycle emissions, the heat pump operated using onshore power has the potential to reduce global warming potential by 88% compared to an oil-fired boiler. This accounts for saving 3% and 8% of annual greenhouse gas emissions from entire ship operations, including emissions from engines for the respective case study ships. In addition, shifting to a heat pump avoids NOx and SOx emissions, which adversely affect air quality in the populated areas near the port. Cost results show that the heat pump has an overall higher cost of ownership for case study vessel 1 and a lower cost of ownership for case study vessel 2 compared to oil-fired boiler. Depending on the energy use of specific ships, heat pumps can be cost-competitive at existing carbon emission allowance prices (approximately 90€/tCO_2) in the European emission trading system. For the assessed cases, with the emission trading scheme, the return on investment is less than six years and three years for case study vessels 1 and 2 respectively. The study also shows that operating a heat pump is more cost-effective than directly using electro-fuel in a boiler for thermal loads.

Keywords: Heat pump, Life cycle assessment, Cost assessment, Maritime, Energy efficiency.

1. INTRODUCTION

The shipping industry as a whole is responsible for a significant portion of the global greenhouse gas emissions due to its heavy reliance on fossil fuels. In addition to greenhouse gas emissions, air emissions from shipping, such as nitrogen oxides (NO_x), sulfur oxides (SO_x), and particulate matter (PM), have significant negative impact on both air quality and human health [1]. Impacts of air pollutants are especially critical for ships operating near populated areas such as ferries and cruise ships. When it comes to emission reduction measures from shipping, the focus is typically placed on the propulsion system and auxiliary loads rather than on the hotel heat load as the energy required for the hotel load is significantly less for most ship types. However, the hotel system for passenger ships is responsible for approximately 40 percent of the total energy consumption on board [2].

The International Maritime Organization (IMO) has regulations to reduce GHG emissions for shipping including the Carbon Intensity Indicator (CII), Energy Efficiency Existing Ship Index (EEXI), and Ship Energy Efficiency Management Plan (SEEMP) by promoting energy efficiency measures [3]. In the Fit for 55 legislative packages, the European Union (EU) adopted the FuelEU maritime regulation, which aims to increase the use of renewable and low-carbon fuels in the maritime sector and includes the shipping sector in the EU emission trading scheme (ETS) [4, 5]. In line with these, an increased number of studies have focused on alternative fuels and propulsion systems for ships [6]. Such changes in the ship system also imply changes in the availability of waste heat which is used extensively now for hotel loads, e.g. the waste heat will not be available with onboard reforming requirements [7] or electrification using fuel cells or batteries [8].

Presently the thermal energy for the hotel load is supplied largely from the waste heat from the engines and partially from the onboard auxiliary boiler [9]. The heat from auxiliary oil boilers is mainly required when the main engines are not operating while staying at the port or during winters when the hotel load is high [9]. In sectors such as industry, residential, and building, the role of heat pumps has been considered important for

@2023 Kanchiralla, F. et al., published by TU Delft OPEN Publishing on behalf of the authors. Licensed under a Creative Commons Attribution CC BY license.
DOI: https://doi.org/10.59490/moses.2023.668

decarbonization and energy efficiency, and recent improvements in performance has made heat pumps cost-competitive in these sectors [10]. However, in the shipping sector, few studies [9, 11, 12] have considered heat pumps as energy efficiency measures or emission reduction measures. With the increased interest in the electrification of ferries, heat pumps have been investigated by designers for marine applications. However, the main barrier to the use of heat pumps for larger ships is likely the low utilization of the auxiliary heat generation system owing to the availability of waste heat from engines and the high investment cost [11].

Heat pump feasibility would be different with the two new regulations on the horizon: 1) the ships moored at the quayside of the member state shall be connected to onshore power (OSP) supply for their electrical power demand [13] and 2) the cost of emission allowances within the EU ETS for GHG emissions from shipping [5]. In addition, to meet the GHG emission reduction targets set by the IMO, reliance on lower-priced fossil-based fuels should be reduced and the use of alternative fuels may increase in the future. None of the prior studies considered these factors, and there is a lack of life cycle knowledge on the application of heat pumps on ships, making it difficult to understand their environmental impact over the life cycle. The purpose of this study is to fill this gap by performing life cycle assessment and cost assessment considering scenarios including the above upcoming policies and future scenarios of using an electro-fuel instead of fossil fuel. The study is performed for two case study passenger ships to understand the variation in results between ships based on their operation and size.

2. METHODOLOGY

2.1 Case study ships

Two case study roll-on/roll-off passenger (RoPax) ferries with two different operation profiles and sizes were chosen for the life cycle assessment and costing. Table 1 summarizes the vessel parameters used in the assessment. Case 1 involves a vessel operating between Gothenburg, Sweden, and Kiel, Germany. The energy data for this vessel is obtained directly from the operator. Case 2 vessel operates between Oslo, Norway, and Kiel, Germany, and energy-use data is published by Brakken et al. [9]. Ships differ in terms of the time spent in ports, where boilers are predominantly used, and exhibit varying thermal loads. In addition, the thermal load varies widely for these vessels with seasons, with winter having a higher thermal load and summer having a lower thermal load for hotels. For instance, for case 1, the boiler consumes approximately 2% in summer and approximately 4% in winter of the total fuel used onboard. However, for simplification, the total annual energy use (including both summer and winter conditions) is considered for the assessment with a steady state for both vessels and only when the ship is at the port. Another assumption is that the heat demand is required only on ports as the excess heat from the engine is available while sailing at sea. It may be noted that during extreme winter days, the boiler needs to be operated while at sea which is not considered in this study. Heat pump and boiler power requirements listed in Table 1 were sized with an additional 20% more power than the measured peak demand. The purpose of this excess capacity is to ensure that heat can be supplied even in extremely cold climates.

Table 1: Key characteristics of the case study Cruiseferries

	Case 1	*Case 2*
Gross tonnage (GT)	52000	75 000
Passenger capacity (Number)	1300	2770
Vehicle capacity (cars)	1290	750
Length (m)	240	224
Width (m)	29	35
Connected to OSP	Yes	Yes
Peak thermal power (kW)	6000	4500
Annual thermal load at port (GJ)	156 000	288 000

2.2 Scenarios

Based on the three system configurations and two fuels, five scenarios are assessed to compare the results as shown in Fig. 1. In the first scenario (S1), the policy scenario when the ship is connected to the OSP and an air-to-water heat pump operates using the electricity from OSP. In the second scenario, it is assumed that the heat pump operated from the electricity produced by the auxiliary engines installed onboard. The second scenario is assessed in two parts: the first part (S2a) where the auxiliary engines are fueled using marine gas oil (MGO) and the second part (S2b) where the auxiliary engines are fueled by an alternative fuel. Electro-methanol is considered as the alternative fuel. In the third scenario, an oil-fired boiler is used for the thermal load. Similar to the second scenario, the third scenario is also divided into two parts. The first part (S3a) is a reference scenario or base scenario replicating the present situation where MGO is used as fuel in the boiler and the second part (S3b) considers electro-methanol as the fuel for the boiler. Electro-methanol is preferred over other electro-fuels such as electro-ammonia, electro-hydrogen, and electro-methane because of

its lower safety risks for onboard passengers [8]. The influence of the EU ETS for all the scenarios is included in the sensitivity analysis.

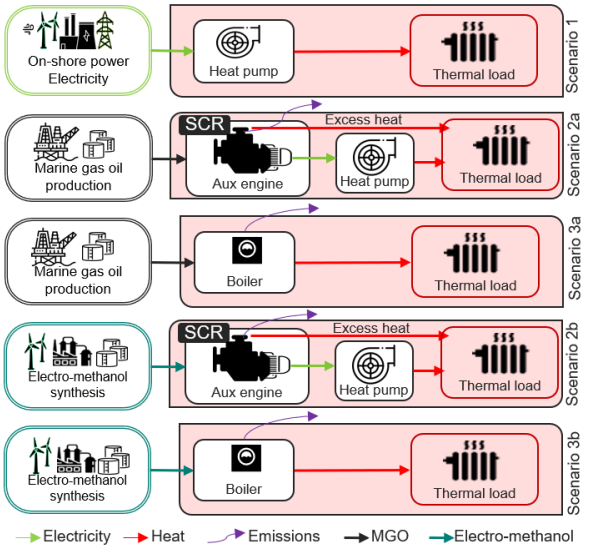

Figure 1: Five scenarios of heat system configurations accessed in the study Scenario 3a is base case scenario.

2.3 Environmental assessment

The environmental assessment of products and services can be evaluated over their lifecycle using the life cycle assessment (LCA) method, which is an established method usually performed under the framework provided by ISO 14040 and ISO 14044. In this study, the main focus is on the emission of GHGs over the life cycle (the extraction of raw material required for producing the component and fuel to the end of life and final use of energy in the ship). The functional unit of the assessment is 'the annual thermal energy required for the ship while at the port'. The scope is limited to the operation of a heat pump or boiler in the port by analyzing the operation profile and measured in 'GJ of energy'. As per earlier studies and analysis of the operation profile, during navigation at sea, excess heat from the main and auxiliary engines is sufficient to meet the thermal demand and the boiler is not operated. In addition, a comparative LCA is performed, hence only the major changes between different configurations are considered in the system boundary as the goal of the study is to provide insight into the environmental impact focusing on GHG emissions specifically addressing the use of heat pumps while ships are moored at ports.

Inventory analysis is performed by dividing the processes into foreground and background processes, where the foreground processes are processes that are focused on the study, and background processes are other processes whose inventory data are adopted from secondary datasets such as Ecoinvent (for raw materials and infrastructure) [14], GaBi (for electricity) [15] and various studies. The inventories used for the assessment are listed in Table 2. The life cycle emissions for the considered system are divided into three parts for simplification as shown in Fig. 2: i) Upstream including the production and distribution of the fuels and electricity generation and distribution usually referred to as well-to-tank. ii) Downstream including emissions from the boiler or auxiliary engine, no emissions are assumed from the heat pump operation, and iii) Manufacturing of the system components such as the oil boiler and heat pump.

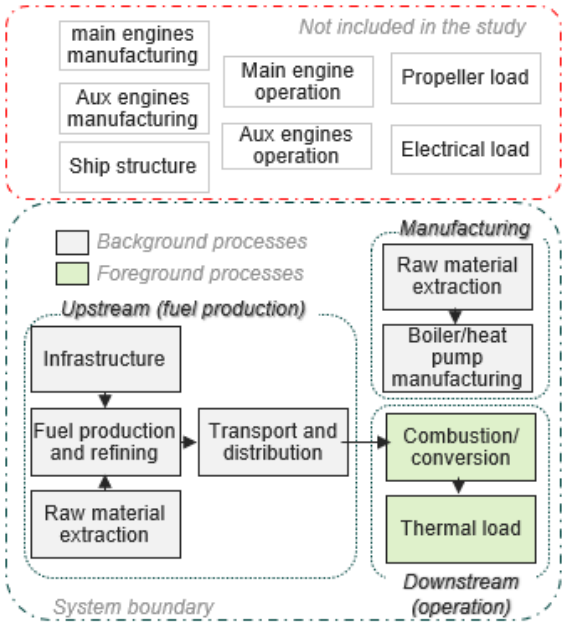

Figure 2: System boundary considered in the study showing background and foreground processes.

In the upstream stage for S1, the GHG intensity of the electricity mix varies with the port where the ship is moored (Gothenburg and Kiel for case 1, and Oslo and Kiel for case 2). Hence the GHG intensity of the electricity mix in Sweden, Norway, and Germany for Gothenburg, Oslo, and Kiel respectively are used. GHG intensity of the electricity mix for Sweden and Norway considered in this study is 30gCO_2eq/kWh [16, 17], and 280gCO_2eq/kWh for Germany [16]. The global volume-weighted average GHG intensity for crude oil production and refining is used (17.6 gCO_2eq/MJ) for the MGO production phase [18]. For electro-methanol production, it is assumed that the fuel would be produced from renewable electricity and is adopted from the study [8] and has a GHG intensity of (-)60gCO_2eq/MJ. The reference study for electro-methanol has included the cradle-to-grave impact of producing electro-methanol including the impacts from the infrastructure (electrolysis, direct air capture, and methanol synthesis), generation of electricity required for

various processes, production of consumables required for the processes, and process emissions. The negative value is because the CO_2 used in fuel production is sourced from direct air capture, where CO_2 is removed from the air and stored in the fuel [8].

Downstream, the main emissions are from auxiliary engines used to produce electricity for the operation of the heat pump for S2a and S2b, and for S3a and S3b the emissions are from oil boilers. Both vessels are fitted with selective catalytic reduction for NO_x abatement to meet the Tier 3 requirements. The emissions from engines and boilers 'per engine output, in kWh' are adjusted to the energy of the fuel 'per MJ fuel used'. MGO with 0.1 % sulfur content is considered with 75.08 g of CO_2, 0.05 g of SO_x, and 0.05 g of NO_x (after abatement) for 1 MJ of MGO burned (LHV of 42.7MJ/kg is assumed) [6, 19]. For 1 MJ of methanol, 69.10 g of CO_2 emission is considered. Other GHGs (methane and nitrous oxide) are not considered. These are simplified assumptions considering a 50% load and it may be noted that the emissions would vary with the engine or boiler load, air-fuel ratio, etc. The waste heat from the engines was assumed to be 20% of the engine output [7], while the heat pump is operated using an auxiliary engine thereby reducing the heat required from the heat pump and the peak power of the heat pump.

Table 2: Parameters and cost of the components considered in the study

	Efficiency	*Specific CAPEX*	*O&M cost*	*Refs*
Auxilary engine	35% [a]	350€/kW	2 %	[8,20]
Oil-boiler	90%	100€/kW	2 %	[21]
Heat pump	3.5 [b]	750€/kW	1 %	[21,22]

[a] assumed, [b] coefficient of performance

For manufacturing and end-of-life of components, the power rating of the component determines the size of the components (see Table 1). A heat pump with a lower power capacity is assumed for scenario 2 (calculated to be 90%) than for scenario 1 as the excess heat from the auxiliary engine is also used. The material composition of the heat pump and boiler for inventory analysis is assumed from the study by Miralles et al. [23]. It is assumed that additional auxiliary engine capacity is not required considering that the installed capacity that is used during navigation through the sea may be used at ports for supplying electricity to the heat pump. Since additional capacity is not assumed, the engine construction is not included in the assessment.

The total life cycle impact assessment (LCA) for global warming potential (GWP) (kCO_2eq/year) is calculated by combining the environmental impact from upstream (IA_{WTT} ($kgCO_2eq$ per MJ_{fuel})), downstream (IA_{TTW} ($kgCO_2eq$ per MJ_{fuel})), manufacturing with end-of-life recycling ($IA_{man,eol}$ ($kgCO_2eq$ per kW)) phases as shown in Equation 1. In addition, the emission of SO_x and NO_x are calculated for each option but not converted to a midpoint indicator such as acidification or eutrophication.

$$LCA = IA_{WTT} \times f_c + IA_{TTW,c} \times f_c + \frac{P_C \times IA_{man,eol}}{t} \quad (1)$$

where f_c is the annual fuel consumption in MJ, P_C is the capacity of the heat pump or boiler for each scenario (kW) *and t* is the service life of the engine, boiler, and heat pump which is assumed to be 25 years.

2.4 Economic assessment

The economic assessment is performed using the total cost of ownership (TCO) method based on the system boundaries in line with the LCA as shown in Fig. 2. In addition, the cost is calculated for the functional unit 'the annual thermal energy required for the ship while at port'. Three costs are considered: 1) operation cost related to the fuel or electricity use, ii) capital cost related to the cost of equipment, and iii) maintenance cost. The cost for components and maintenance costs are also shown in Table 2. The operational cost considered here is the cost of the fuel or electricity required for the operation, represented by C_F (€/MJ). Capital cost is the cost of capital equipment (heat pump or oil boiler) represented by E_C (€/kW) and the capital cost is converted to the net present value where the future cost is discounted to the present value using the capital recovery factor (*crf*) given in Equation 2, where *t* is the service life of the components, and *i* is the discount rate (5%).

$$crf = \frac{i\,(1+i)^t}{(1+i)^t - 1} \quad (2)$$

The annual maintenance cost is considered based on the capacity of the capital equipment (C_M) (€/kW/year). The total cost of ownership (TCO) (€/year) is the sum of all costs converted into annual costs as given in Equation 3.

$$TCO = C_F \times f_c + E_C \times P_C \times crf + C_M \times P_C \quad (3)$$

The following costs are considered for the fuel costs, for electricity (including the power tariff) 100€/MWh, for MGO 700 €/t, and for electro-methanol 1870 €/t [8].

2.5 Uncertainty and sensitivity analysis

The COP of the heat pump is sensitive to the sink and source temperatures which depend on the placement of the heat pump. For instance, a higher COP can be achieved if heat pumps can reuse low-temperature engine cooling water, which is normally discharged into the sea [11]. Hence, we include a range of possible outcomes in the analysis by considering COP values between 3 and 4 and included these uncertainty levels in the result. The influence of the EU ETS as a policy for individual scenarios is included in the sensitivity analysis. In the analysis, the price of the emission allowances varied between zero and 300 €/tCO_2. The analysis is performed individually for all scenarios as the policy applies to all configurations but will have an impact only on scenarios where marine gas oil is used. This can be considered similar to a carbon tax on fossil emissions from ships.

3. RESULT

3.1 Energy efficiency

The energy consumption results for the different scenarios are shown in Table 3 for both case study vessels. Significant savings in the energy required for different scenarios are observed. In S1, where the thermal load is supplied by a heat pump supplied with onshore port power, the energy required is 78% less than in S3a and S3b when the thermal load is supplied from an oil boiler. In S2a and S2b where the heat pump needs to be operated using electricity generated from the auxiliary engine the energy required is 31% less than that in scenarios where the thermal load is supplied from an oil boiler (S3a and S3b). The results show that installing a heat pump can reduce the energy use of the ship even if electricity has to be generated onboard using auxiliary engines. These case study vessels are already connected to the OSP, but installing a heat pump for other passenger ships that are not connected to the OSP is also beneficial from an energy use perspective.

Table 3: Energy consumption for different scenarios

	S1	*S2a & S2b*	*S3a & S3b*
Case study vessel 1			
Electricity from port (GJ)	3900	-	-
MGO required (GJ)	-	12000	17350
Case study vessel 2			
Electricity from port (GJ)	7200	-	-
MGO required (GJ)	-	22200	32000
% Energy saved compared to boiler	***78%***	***31%***	-

3.2 Emission results

The GHG emissions for all five scenarios are assessed from cradle to grave for the thermal load of the case study ships while moored at port. Fig. 3 shows the GWP results for the different scenarios accessed for the first case study vessel. The results show that GHG emissions can be significantly reduced when a heat pump connected to the OSP is used for the thermal load (S1). There is an 87% reduction in GHG emissions compared to the boiler powered by MGO. In S2a, when the heat pump operates using electricity from auxiliary engines run on MGO, the GHG emission reduction is approximately 38% compared to the case with MGO and an oil-fired boiler (S3a).

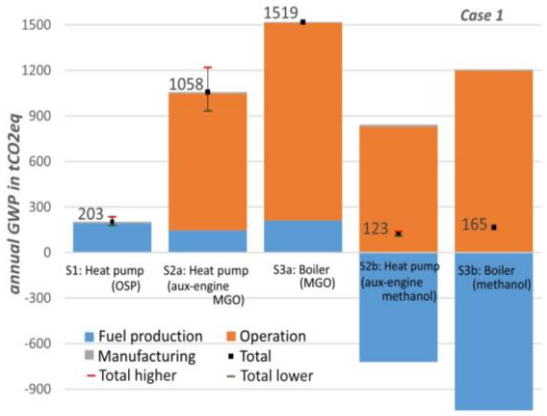

Figure 3: GWP of different scenarios for the first case study vessel. Total higher is total GHG emission considering heat pump COP 3 and lower is for COP 4.

Using electro-methanol in the boiler as in S3b and electro-methanol in the engine to power the heat pump as in S2b can have lower life cycle GHG emissions than a scenario where the heat pump is connected to an OSP (S1). This reduction is due to the assumption that the electro-fuel is produced from renewable electricity, whereas while using OSP about half of the electricity is considered from the electricity mix of Germany (GHG intensity of electricity mix is high). This scenario will be different in the future when more renewable energy is available in ports.

Fig. 4 shows the GWP for the different scenarios for the second case study vessel. The result is similar to the first case study with 87% GHG emission reduction for the S1 and 38% emission reduction in S2a compared to scenario S3a. In both cases, it can be noted that the impact of the manufacturing of the component is negligible for both the heat pump and the boiler. While using MGO and electro-methanol the emissions are primarily during the operation phase and for S1 there are no emissions during operation.

Apart from the GHG emission reduction that can be obtained using the heat pump, there are reductions in NO_x and SO_x emissions. For the first case study vessel, there is an emission reduction of 860 kg of SO_x and 900 kg of NO_x for S1 and an emission reduction of 330 kg of SO_x and 340 kg of NO_x for S2a. Because electro-methanol has no sulfur in the fuel, there will not be any significant SO_x emission in scenarios with electro-fuel. For electrofuel scenarios (S3a and S3b), NO_x emissions are not evaluated in the study.

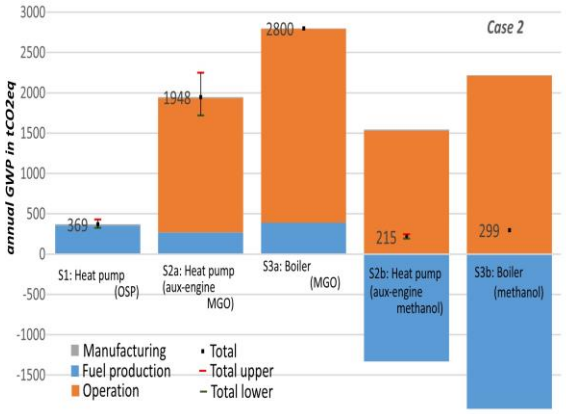

Figure 4: GWP of different scenarios for the second case study vessel. Total upper is total GHG emission considering heat pump COP 3 and lower is for COP 4.

The results on varying the COP of heat pumps are also shown in Fig. 3 and Fig. 4. Reduction of COP from 3.5 to 3 increases the emission by 16% for S1a and by 15% for S2a for both vessels. Increasing COP from 3.5 to 4 decreases the emission by 12% for S1a and S2a for both vessels. The results show that the detailed design of the heat pump system for optimizing the COP can affect the emission reduction potential.

3.3 Cost results

In this section, the results from the TCO for both case studies with different scenarios are analyzed. Fig. 5 shows the TCO for different scenarios accessed for the first case study vessel. The results show that S1 (heat pump with OSP) and S2a (heat pump with auxiliary electricity fueled by MGO) are more expensive than MGO-fired boiler. However, compared to the electro-methanol cases (S2b and S3b) S1 has a significantly lower cost. This shows that comparing the cost associated with GHG reduction, heat pumps connected to OSP have better prospects than other options such as switching to electro-fuels. It may be noted that the cost associated with EU ETS is not included in the result, and the effect of the EU ETS can make heat pumps more competitive which is detailed in section 3.4. The main cost associated with the heat pump is the cost of investment whereas it is the cost of fuel for the boiler option. With a higher cost of fuel as in S2b and S3b, the heat pump connected to the auxiliary engine has a considerable advantage over the boiler due to its higher overall efficiency.

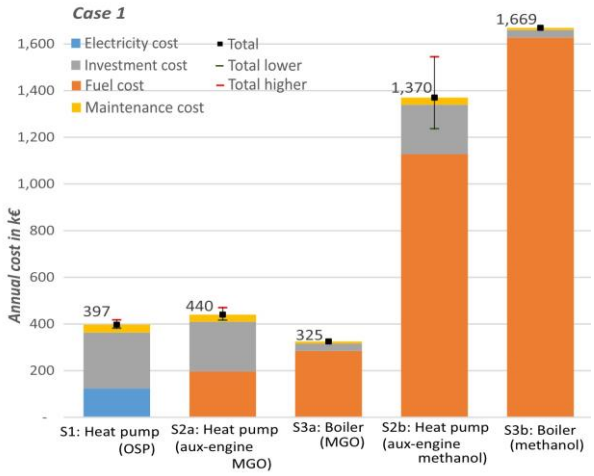

Figure 5: TCO of different scenarios for the first case study vessel. The higher represents the total cost considering heat pump COP 3 and the lower is for COP 4.

Fig. 6 shows the TCO for different scenarios accessed for the second case study vessel. For the second case study vessel, scenario 1 (the heat pump with OSP) has a similar cost to that of the MGO-fired boiler and has lower TCO when the COP of the heat pump is assumed to be 4. The difference in the results between the case studies highlights that the investment decision differs depending on the ship under consideration. With ships having a higher thermal demand (as in case 2), heat pumps would be competitive even without an incentive. This is because the higher investment cost is covered by decreased energy use (due to higher efficiency).

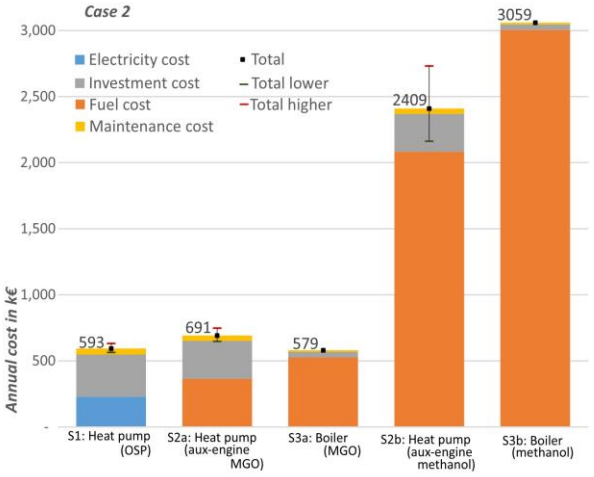

Figure 6: TCO of different scenarios for the second case study vessel. The higher represents the total cost considering heat pump COP 3 and the lower is for COP 4.

The uncertainties in the TCO results on different COPs of heat pumps are also shown in Fig. 5 and Fig. 6. A reduction in COP from 3.5 to 3 increases the TCO by 6% for S1a and by 8% for S2a for both vessels. Increasing the COP from 3.5 to 4 decreases the TCO by 5% for S1a and 6% for S2a for both vessels. The variation is lower compared with GHG emissions as the major cost associated with the heat pump is the investment cost.

3.4 Sensitivity analysis

In this section, TCOs are accessed for different carbon emission allowance prices if the EU ETS is introduced in the shipping industry. Fig. 7 shows the sensitivity analysis for different scenarios accessed for the first case study vessel. The results show that at the present allowance price level (about 90€/tCO_2), the heat pump connected to the OSP (S1) has significant cost benefits compared to S3a with an MGO-powered boiler. The return on investment calculation shows that with an allowance price of 90€/tCO_2, the payback period is six years. This indicates that retrofitting case study vessel 1 is economically desirable if ETS is introduced.

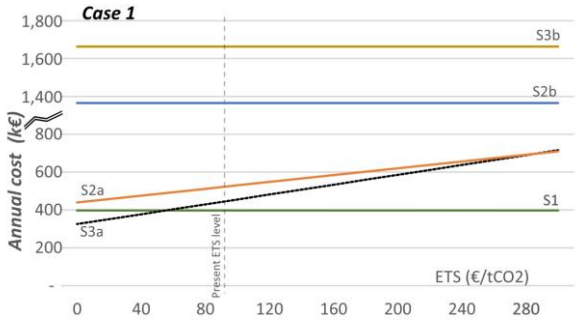

Figure 7:Sensitivity of TCO with different ETS prices for the first case study vessel

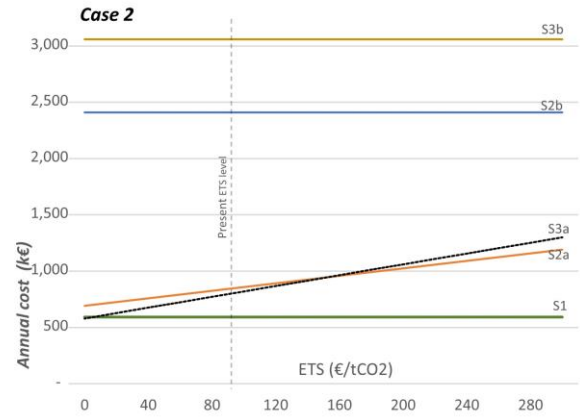

Figure 8: Sensitivity of TCO with different ETC prices for the second case study vessel

Fig. 8 shows a similar sensitivity analysis for the second case study vessel. For the second case study vessel already S1 has a TCO similar to that of base case S3a. Sensitivity analysis results show that S2a when the heat pump is operated using the auxiliary electricity also will be cost-competitive if ETS is considered. The return on investment calculation shows that heat pumps powered by OSP have a payback period of only 2.5 years with the present rate of ETS.

4. DISCUSSION

Similar to other sectors, such as industry, commercial, and residential sectors, the shipping sector especially the passenger segment can make use of heat pumps for decarbonization efforts to meet the heating demand. The utilization of heat pumps is mostly limited to the time at the port when the OSP is available due to the excess heat available from the engines in the shipping sector. The study accessed the possibility of using the heat pump directly from the OSP and using auxiliary generation sets from the energy, economic, and environmental perspectives.

Replacing oil boilers with heat pumps powered by OSP has multiple benefits from energy efficiency to the reduction of emissions such as GHGs, SO_x, NO_x, etc. This is particularly important for passenger ships as in the case study vessels as the ship operates the boiler in the port where air quality is a major concern [24]. There are also some emission reductions and fuel savings even if the electricity required for the heat pump is produced using auxiliary engines instead of being connected to the OSP. The life cycle result for the heat pump operated from OSP also shows a significant global warming potential reduction compared to oil-fired boilers, even considering the present electricity mix. With more renewables in the electricity mix available in the ports, these benefits would be even higher. The result also shows that the impact of the component production is negligible compared to the upstream (fuel production) and downstream (operation) emissions.

The total cost of ownership results show that cost competitiveness varies with the case study vessel parameters. However, the proposed regulations such as EU ETS can make a significant difference in the cost competitiveness of the heat pump system compared to the MGO boilers. The results show that for the second case study vessels can have a return on investment in less than three years if the price of carbon allowances in ETS is above 90€/tCO_2eq. The major cost item in the TCO is the investment cost of the heat pump, policies

that support investment in heat pumps can also be beneficial. In addition, the investment cost is for the total capacity to be installed onboard, and support systems such as thermal energy storage can reduce the capacity of the heat pump by avoiding peak demands. Combining such measures can further reduce investment and operating costs. However, this aspect was not assessed in the present study.

One of the major limitations of this study is that the complete operation profile of the case study vessels including variations in the season, was not considered. The study could have included an uncertainty analysis of the cost of the fuel and investment cost for these options as well as the size requirement of the components onboard. This study is restricted to a preliminary analysis, and a detailed analysis may be performed in future studies considering the above aspects. Other benefits such as the possibility of using heat pumps reversibly during summer for cooling, easier and safer operation of heat pump, and increasing efficiency further by utilizing the low-temperature heat from the engine could also be investigated in future studies.

5. CONCLUSION

This study provides a preliminary comparison of the economic and environmental implications of installing heat pumps on two passenger vessels. In terms of thermal load alone, the heat pump has a GWP that is 87 percent lower than that of an oil-fired boiler. In addition, switching to a heat pump eliminates the NO_x, and SO_x emissions, which have a negative impact on the air quality in the populated areas near the port. When connected to onshore power, the heat pump has a higher total cost of ownership without the emission trading scheme for the first case study vessel and less for the second case study ship. With the emission trading scheme, heat pumps are cost-effective for both case study vessels, and have a lower cost of ownership compared to using electro-fuel in a boiler. In summary, the replacement of a boiler with a heat pump is found to be an effective emission reduction measure for ships using onshore power, but the study observed that the payback period will vary depending on the vessel's energy needs and price level for emission allowances.

ACKNOWLEDGMENTS

This research was conducted as part of the project Assessment of hydrogen, ammonia, and battery-electric propulsion for future zero-carbon shipping funded by the Swedish Transport Administration through the industry program Sustainable shipping led by the Swedish Maritime Competence Center (Lighthouse), grant number FP2_E_2020,

APPENDIX A

A.1 Nomenclature

C_F	Cost of the fuel	(€/MJ)
E_C	Capital cost	(€/kW)
crf	Capital recovery factor	
i	Discounting rate	(%)
t	Service life	(years)
C_M	Maintenance cost	(€/kW/year)
TCO	Total cost of ownership	(€/year)
P_C	Heat pump or boiler capacity	(kW)
f_c	Annual fuel consumption	(MJ)
GWP	Global warming potential	($kgCO_2eq$)
IA	Impact assement result	

REFERENCES

[1] K. Andersson, S. Brynolf, F. Lindgren, and M. Wilewska-Bien, Shipping and the Environment : Improving Environmental Performance in Marine Transportation, 1st ed. Berlin, Heidelberg: Springer Berlin Heidelberg : Imprint: Springer,, 2016, pp. 1 online resource (XXIII, 426 pages 77 illustrations, 49 illustrations in color.

[2] F. Baldi, F. Ahlgren, T.-V. Nguyen, M. Thern, and K. Andersson, "Energy and Exergy Analysis of a Cruise Ship," Energies, vol. 11, no. 10, 2018, doi: 10.3390/en11102508.

[3] M. E. P. C. (MEPC). "Marine Environment Protection Committee (MEPC)." IMO. https://www.imo.org/en/MediaCentre/MeetingSummaries/Pages/MEPC-default.aspx (accessed 10 Jul, 2023).

[4] Regulation (EU) 2023/959 of the European Parliament and of the Council, C. o. t. E. U. European Parliament Directive (EU) 2023/959, 2023.

[5] C. o. t. EU;, "Fit for 55 package: Council adopts its position on three texts relating to the transport sector," D. Mammonas, Ed., ed: The European Council, 2022.

[6] F. M. Kanchiralla, S. Brynolf, E. Malmgren, J. Hansson, and M. Grahn, "Life-Cycle Assessment and Costing of Fuels and Propulsion Systems in Future Fossil-Free Shipping," Environ Sci Technol, vol. 56, no. 17, pp. 12517-12531, Sep 6 2022, doi: 10.1021/acs.est.2c03016.

[7] B. Thaler et al., "Optimal design and operation of maritime energy systems based on renewable methanol and closed carbon

cycles," Energy Conversion and Management, vol. 269, 2022, doi: 10.1016/j.enconman.2022.116064.
[8] F. M. Kanchiralla, S. Brynolf, T. Olsson, J. Ellis, J. Hansson, and M. Grahn, "How do variations in ship operation impact the techno-economic feasibility and life cycle environmental performance of fossil-free fuels? a life cycle study," Applied Energy, vol. 350, 2023, doi: 10.1016/j.apenergy.2023.121773.
[9] A. Brækken, C. Gabrielii, and N. Nord, "Energy use and energy efficiency in cruise ship hotel systems in a Nordic climate," Energy Conversion and Management, vol. 288, 2023, doi: 10.1016/j.enconman.2023.117121.
[10] S. Paiho, S. Pulakka, and A. Knuuti, "Life-cycle cost analyses of heat pump concepts for Finnish new nearly zero energy residential buildings," Energy and Buildings, vol. 150, pp. 396-402, 2017, doi: 10.1016/j.enbuild.2017.06.034.
[11] R. El Geneidy, K. Otto, P. Ahtila, P. Kujala, K. Sillanpää, and T. Mäki-Jouppila, "Increasing energy efficiency in passenger ships by novel energy conservation measures," Journal of Marine Engineering & Technology, vol. 17, no. 2, pp. 85-98, 2017, doi: 10.1080/20464177.2017.1317430.
[12] S. Trzebiński, "Technical Aspects of Using the Heat Pump at the Ship," Scientific Journal of Polish Naval Academy, vol. 217, no. 2, pp. 5-15, 2019, doi: 10.2478/sjpna-2019-0009.
[13] (2022). Council general approach.
[14] G. Wernet, C. Bauer, B. Steubing, J. Reinhard, E. Moreno-Ruiz, and B. Weidema, "The ecoinvent database version 3 (part I): overview and methodology," The International Journal of Life Cycle Assessment, vol. 21, no. 9, pp. 1218-1230, 2016/09/01 2016, doi: 10.1007/s11367-016-1087-8.
[15] Sphera, "GaBi Databases & Modelling Principles 2022," 2022.
[16] European Commission, "EU Reference Scenario 2020- Energy. transport and GHG emissions trends to 2050," European Commission, Brussels, 2021.
[17] M. Wråke, Karlsson, K., Kofoed-Wiuff, A., Folsland Bolkesjø, T., Lindroos, T.J., Tennbakk, B., Ogner Jåstad, E., Bosack Simonsen, M., Hagberg, M., Unger, T., Putkonen, N., Lehtilä, A. & Koljonen, T, "Nordic Clean Energy Scenarios," Nordic Energy Research, September 7 2021.
[18] L. Jing et al., "Carbon intensity of global crude oil refining and mitigation potential," Nature Climate Change, vol. 10, no. 6, pp. 526-532, 2020, doi: 10.1038/s41558-020-0775-3.
[19] International Maritime Organization, "Reduction of GHG emissions from Ships: Fourth IMO GHG Study 2020," International Maritime Organization, London, 2021.
[20] A. D. Korberg, S. Brynolf, M. Grahn, and I. R. Skov, "Techno-economic assessment of advanced fuels and propulsion systems in future fossil-free ships," (in English), Renew Sust Energ Rev, vol. 142, May 2021, doi: 10.1016/j.rser.2021.110861.
[21] Danish Energy Agency, "Technology data - generation of electricity and district heating. Updated April 2020," Copenhagen, 2016.
[22] Uniturbo® 34FY – Centrifugal Compressor for large scale refrigeration plants and heat pumps, G007-05, 2020.
[23] J. A. Lozano Miralles, R. López García, J. M. Palomar Carnicero, and F. J. R. Martínez, "Comparative study of heat pump system and biomass boiler system to a tertiary building using the Life Cycle Assessment (LCA)," Renewable Energy, vol. 152, pp. 1439-1450, 2020, doi: 10.1016/j.renene.2019.12.148.
[24] M. Sofiev et al., "Cleaner fuels for ships provide public health benefits with climate tradeoffs," Nature Communications, vol. 9, no. 1, 2018, doi: 10.1038/s41467-017-02774-9.

PROCEEDINGS OF MOSES2023 CONFERENCE
4TH INTERNATIONAL CONFERENCE ON MODELLING AND OPTIMISATION OF SHIP ENERGY SYSTEMS
26-27 OCTOBER 2023, DELFT, NETHERLANDS

Co-Design and Energy Management for Future Vessels

Steven Wilkins[a,*], Udai Shipurkar[b], Avedis Dadikozyan[a], and Christian Veldhuis[b]

[a]TNO Powertrains, Helmond, Netherlands
[b]MARIN, Wageningen, Netherlands
[*]steven.wilkins@tno.nl

Abstract

The maritime industry is undergoing a significant shift towards more sustainable and efficient forms of transportation. As a result, designing Power, Propulsion and Energy (PPE) Systems for future vessels presents new challenges that require a systematic approach that reduces the risk in development and implementation. This paper focuses on three aspects of such a systematic approach: Model-Based System Engineering (MBSE), Co-design, and Verification and Validation. The MBSE approach can be used to mitigate the risks associated with the transition by maintaining a clear traceability of user needs, functional requirements and physical realizations. A rigorous needs analysis and functional design reduces the optimisation design space that results in a significant reduction in the complexity of a design optimisation problem. Further, co-design is discussed as a methodology for a combined optimisation of the hardware and software design where the Modular Energy Management approach supports automated controller generation for the optimisation, a key challenge when optimising PPE systems. An important aspect of the MBSE approach is the use of models for the verification and validation of the developed designs. However, the successful use of models is contingent on their applicability. This paper proposes a way to categorise model confidence for verification and validation studies.

Keywords: PPE; MBSE; Co-Design; Energy Management; FMI.

1 INTRODUCTION

The use of fossil fuels significantly contributes to pollution and greenhouse gas emissions. To prevent further climate change, both the International Maritime Organisation (IMO) and the European Union (EU) have defined ambitious and compulsory targets for the reduction of emissions in the near future. The EU's objective is to reduce greenhouse gas emissions by at least 55 percent by 2030 and achieve climate neutrality by 2050 [1]. Similarly, the IMO aims to reduce CO_2 emissions per transport work, as an average across international shipping, by at least 40 percent by 2030, with efforts towards a 70 percent reduction by 2050, compared to 2008 levels [2].

Several regulations related to these targets have been introduced. The EU introduced the "Fit for 55" package, which includes measures such as the Emission Trading System (ETS). The ETS enables the direct reduction of greenhouse gases by setting an overall emission cap per sector and enabling emission credits trading between partners. The revised Renewable Energy Directive (REDII) focuses on greening fuel production and distribution. Additionally, FuelEU Maritime aims to increase the share of renewable and low-carbon fuels in the maritime fuel mix. In parallel the IMO regulates the energy efficiency of newly built ships by means of the Energy Efficiency Design Index (EEDI) and the energy efficiency of operational ships with the Ship Energy Efficiency Management Plan (SEEMP). These regulations become progressively more stringent over time, with the aim of achieving greater emission reductions.

Clearly, the transition from fossil fuels to cleaner and more sustainable alternatives implies a big challenge for the maritime sector. The introduction of many upcoming regulations adds to the complexity, and their precise impact is now always in advance. Furthermore, there are many unknown factors to consider — Which fuels to choose? Which power & energy systems are suitable for my operation? How reliable are these new systems considering that many techniques are not yet fully mature? What emission reductions can we achieve and do the solutions comply with the upcoming regulations?

Given that this energy transition in the maritime sector is rapidly evolving, the conventional approach to design may not be sufficient to keep up with the pace of change. It becomes essential to adopt a "first time right" approach and pursue parallel and multidisciplinary developments as much as possible. This paper aims to describe an ap-

@2023 Wilkins, S. et al. published by TU Delft OPEN Publishing on behalf of the authors. Licensed under a Creative Commons Attribution CC BY license.
DOI: https://doi.org/10.59490/moses.2023.666

proach that addresses the forthcoming challenges in the maritime sector. At the core of this approach is Model-Based System Engineering (MBSE), which provides a well-structured methodology to reduce the risks during the development and construction of future vessels. By establishing a clear traceability of user needs, functional requirements, and physical realizations, MBSE enables early-stage risk reduction in the design process. Additionally, this approach incorporates verification and validation test plans that can be traced back to these needs and requirements, further enhancing the reliability of the vessel development process.

Furthermore, the majority of new low- or zero-emission fuels present challenges in terms of weight or volume. Consequently, future vessel designs will need to be optimised to accommodate these fuels based on user needs, while also optimising operational efficiency. The complexity arises from the interplay between these two aspects: optimised design and optimised operation. To address this challenge specifically in the Power, Propulsion, and Energy System, the paper proposes the utilisation of co-design. Co-design is a methodology that integrates the design of the physical system with the design of the control system. This integrated approach necessitates an automated method for generating an appropriate Energy Management strategy. The Modular Energy Management Strategy (MEMS) effectively fulfills this requirement. A case study from the automotive sector that demonstrates this approach is also presented. By incorporating MEMS within a co-design framework, supported by an MBSE-based approach, this article presents a solution to address the upcoming challenges in the maritime sector.

This approach will be explained in this paper. The application and demonstration of this approach will be subject of future publications. This work is part of the Methanol as an Energy Step towards Zero-Emission Dutch Shipping (MENENS) project which aims to make a significant impact on the Dutch shipping industry and reduce CO_2 emissions by laying out the framework for equivalent safe use of methanol as a fuel in commercial shipping that is cost-effective and sustainable [3].

2 THE MBSE APPROACH: CHALLENGES AND OPPORTUNITIES FOR MARITIME

2.1 The MBSE Methodology

MBSE applies models to support system requirements, design, analysis, verification and validation activities beginning in the conceptual design phase and continuing throughout development and later life cycle phases [4]. MBSE replaces a document-centric engineering approach with a model that serves as a "single-source-of-truth". As stated by Friedenthal *et al.* [5], "The output of the systems engineering activities is a coherent model of the system (i.e., system model), where the emphasis is placed on evolving and refining the model using model-based methods and tools." This System Model or System Architecture Model is the hub for integrating data, engineering analysis, and simulation models used across the product life-cycle [6]. This integration improves consistency and traceability through the design process into operations.

The use of MBSE has several advantages. It results in more complete and consistent requirements when used for requirement development and engineering [7], [8]. The model-based approach can improve the design process by improving collaboration between stakeholders by providing a consistent model across domains and enabling multiple viewpoints from different perspectives [9], [10]. It improves quality by enabling rigorous traceability among requirements, design, analysis, and testing [11], [12]. Furthermore, it facilitates ongoing requirements validation and design verification from the early phases of a complex project [5], [13], [14]. All of these aspects reduce the risks associated with complex projects.

However, there are challenges in adopting the MBSE approach in organisations. Designers and engineers across all disciplines involved in the project need to understand the MBSE approach [15]. In addition, when working with a large diverse set of stakeholders across organisations, it is challenging to create a mechanism where stakeholders update the integrated architecture model rather than their own representations that they are used to [12]. Simpson *et al.* [16] stated that "The maximum benefit of employing a single integrated end-to-end description may only be realized if it serves as a single source of truth for capturing, representing, and communicating the description of the latest architecture design by the majority of the stakeholders involved." Feedback from MBSE users shows that it remains difficult to create an accessible single source of truth for multiple, multi-disciplinary stakeholders. The risk is that MBSE tool users become experts and external stakeholders need them to translate the MBSE model content, making the MBSE model just another dataset. Another challenge is interfacing the system architecting tool to

the existing tools being used in the design process. Many tools are already involved in the design, analysis, and testing of projects, and the integration of results from these tools in the system model should be automated to maintain consistency and prevent ambiguity by duplication. Despite these challenges, there is a clear advantage to applying the MBSE approach to complex projects. In a review, Carroll and Malina [7] reported a significant advantage in project performance by applying the SE/MBSE approach. They also report that an MBSE approach improves engineering efficiency and prevents costly rework.

The MBSE approach is built upon three pillars: modeling methods, modeling languages, and modeling tools/software, as illustrated in Fig. 1.

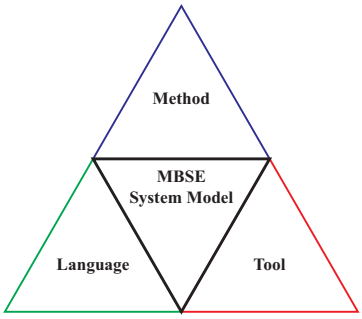

Figure 1: MBSE pillars. From [17]

MBSE Methods

MBSE modeling methods are conventions and step-wise procedures that describe the development and building of a system model. Methods usually define the amount of information and the sequence in which it is used. The most widespread MBSE modeling approaches are Harmony-SE, Object-Oriented System Engineering Method (OOSEM), System Modeling Method (SYSMOD), and Architecture Analysis & Design Integrated Approach (ARCADIA). Each of the listed methods has similarities to the rest but also unique characteristics. Some methods such as OOSEM are tool-independent, whereas others can be realized only with one specific tool.

MBSE Languages

A Model-Based Systems Engineering language refers to a specific modeling language that is used to logically describe and represent systems within the MBSE approach. Such a language provides a standardized set of notations, symbols, and rules for modeling elements and relationships that enable stakeholders to create and communicate system models without ambiguity. The most frequently-used MBSE languages are the Unified Modeling Language (UML) and the Systems Modeling Language (SysML), with the latter being an extension of the former. UML is applied in software engineering while SysML is better suited for systems engineering applications.

MBSE Tools

MBSE modeling tools are software platforms that enable the realization of the modeling procedures using the modeling languages. Tools provide user interface and may have a set of different functionalities, some being:

- Modeling and Diagramming - provide a visual environment for creating and editing system models using diagrams specific to the chosen modeling language. Commonly used tools are Capella, IBM Rhapsody, Cameo Systems Modeler, etc.
- Simulation and Analysis - system behavior analysis, system simulations, and assessment of system performance. Popular tools include MATLAB/Simulink and ANSYS.
- Requirements Management - management of requirements and dependencies. While IBM Rational DOORS is an example of a specialised requirement management tool, many modeling and diagramming tools are adopted for requirement management as well.

2.2 Application to maritime

Although models have been used extensively in the maritime sector, literature on the application of the MBSE approach is limited and most of these studies focus on naval applications. Poullis described prevalent ship design methodologies and explored the use of MBSE to address some of the shortcomings [13]. Furthermore, Tepper explored the use of MBSE in the design of the propulsion system for a naval ship [19]. The study highlighted the importance of beginning system architecture development at very early stages of ship design to ensure that the architecture is well-defined and addresses the needs of the stakeholders. Like experience from other industries, this study also identified the benefits of MBSE in enhancing communication, requirement traceability, and improved decision-making. Kerns *et al.* found that the complex relationships between systems and processes can be better managed by building a system architecture [20]. The system architecture can then be the single source reposi-

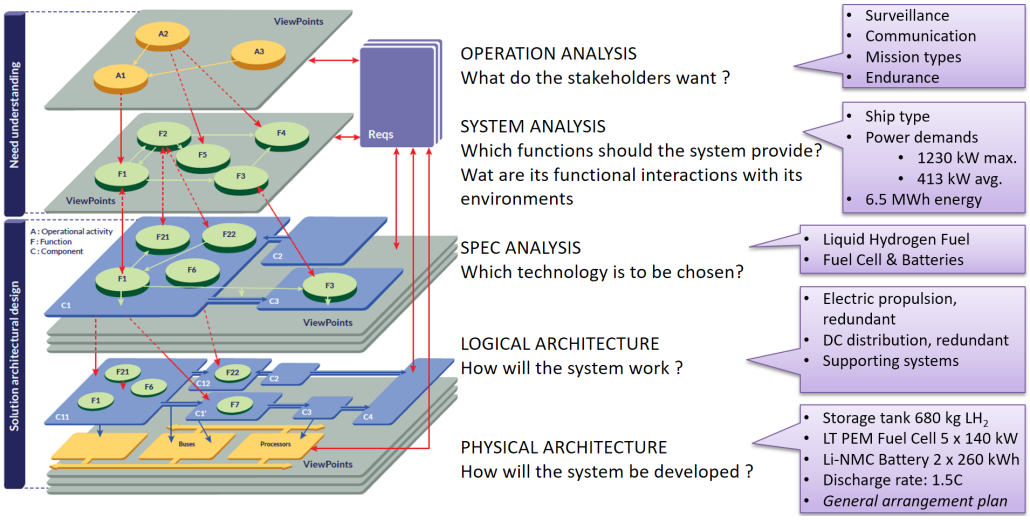

Figure 2: The Arcadia Capella MBSE approach (left) with its different steps (middle) and level of detail (right). The SPEC (Ship Power and Energy Concept) tool is a maritime sector design exploration tool that was integrated in the MBSE approach. From [18]

tory for all the information required for or produced by the ship design process. This was also found to be a useful tool for understanding the impacts of design decisions or changes on the physical design as well as on other aspects of the architecture like cost, function and capabilities. Similarly, Pearce *et al.* identified improved design consistency, precision, traceability, subsystem integration, and design evolution as key benefits attributed to the use of the MBSE approach [21].

More recently, the NAVAIS (New Advanced and Value-Added Innovative Ships) project used the MBSE approach in a modular system engineering-based ship design procedure [22], [23]. Veldhuis *et al.* reported the benefits of MBSE based design using a case study in [18]. The study used the Arcadia method in Capella for the Power, Propulsion and Energy (PPE) system architecture and requirements development for an Inland Patrol Vessel. Fig. 2 shows the structure of the method followed by the authors. The paper highlighted the importance of traceability and consistency in the design approach.

2.3 Lessons from other sectors

The maritime sector is not alone in its pursuit of MBSE and suitable methods towards a structured design process. One particular industry which as adopted and matured the MBSE approach is the automotive industry. Whilst there are many similarities in the challenges in this sector, it should be noted that not all of the manners in which the industry and market act is the same, and therefore a careful mapping of methods and solutions from this sector to maritime should be made.

For automotive, before model-based design, the development of new vehicles for the market would have gone through several prototype/mock-ups before series production. The onset of MBSE methodologies has reduced the need for full prototype development and testing. Tools and workflows such as utilising SysML have largely replaced the document-centered design process. Due to the relative scale of the industry, components (and models) have been standardised and modular solutions have been in focus for newer families of products.

The automotive development cycle traditionally follows a V-cycle, capturing the design process on the left, and the validation process on the right. The approach shown in Fig. 2 forms the left side of the V-cycle that results in a design in the form of a Physical Architecture. Due to the flexibility of the MBSE process, modern development also encompasses a V-cycle within the V-cycle wherein a virtual development loop is performed.

Within this inner V-cycle, the design is evaluated using virtual tests towards the compliance of specifications and requirements, as depicted in Fig. 3. This allows for optimisation of the design towards given criteria (such as cost, energy efficiency etc.). Several methodologies exist for virtually optimising the design of a system. One emergent technique highlighted in this paper, is that of co-design during this process. This is explained in the following section. Co-design is an emerging methodology finding place in both research and industrial contexts.

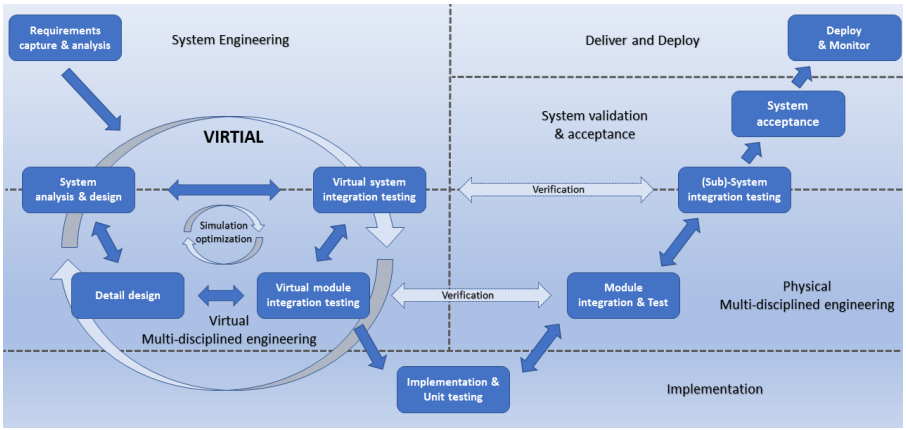

Figure 3: The new "V in V" process - early and continuous feedback in early systems design phases.

3 OPTIMISED DESIGN OF PPE SYSTEMS USING CO-DESIGN

Although the MBSE approach brings structure and traceability to the design process, the technical challenges in designing an effective power and propulsion system are addressed by the co-design of component topology, sizing and controller. In this paper co-design refers to the specific aspect of the concurrent optimal design of plant (as topology or size) and control as reported in [24].

Co-design is a methodology that combines the design of the hardware of a system, alongside its control. In so doing, control techniques can be used to overcome the limitations of the selected components, whereas choices in the powertrain topology can enable improved control application.

For the design of the hardware, the first design space is for the selection of the logical connection of components (i.e. the topology), as illustrated in Fig. 4. In the next layer, the choice of what technology of the components is made, after which the components can be sized in relation to the requirements of the system. Finally, the inner-most level, the control methodology can be defined.

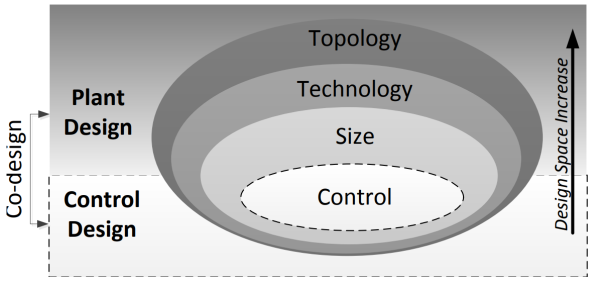

Figure 4: Co-Design Layered Approach. From [25]

It should be noted that there is some resemblance with the Arcadia method; in particular the Logical and Physical architecture from Arcadia match the Topology and Technology/Size layers in the Co-Design approach.

This layered view of system design can imply a nested approach to the design problem. The co-design methodology focuses on finding the optimal topology, sizing, configuration, and control of a power and propulsion system, based on a defined design objective function. The design objective functions are typically either a weighted equivalent function, or left open in terms of a multi-criteria approach.

Fig. 5 illustrates the availability of several variants of the co-design methodology. The most common co-design methodology exploits the alternating plant and control design architecture. Compared to nested and simultaneous schemes, this is seen to be more computationally efficient and easier to implement [25].

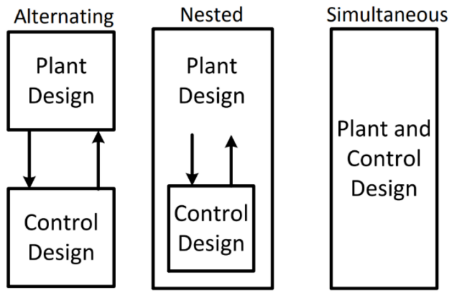

Figure 5: Co-Design Methodology Concepts. From [25]

Within an alternating co-design methodology, the plant design is fixed, allowing for the control design to take place at each stage. Once the control design is complete and evaluated, the results are used for the next iteration where the design of the plant is updated. Through an optimisation scheme, this methodology eventually converges into a plant

and control design, which is measured as optimum and satisfies any requirements or constraints placed on the system.

For the maritime sector important optimisation objectives include fuel consumption, emission, system volume and weight, lifetime, and cost. These aspects are also important for other modalities such as automotive. The constraints are more maritime specific, focusing on on-board safety typically in harsh environments, sizing constraints because of hydrodynamics and stability aspects and specific Class Rules. However, an overarching maritime objective is de-risking of a design that uses innovative, less mature technologies. In maritime a prototype is often going into service and needs to be "first-time-right". That asks for a robust solution with a clever balance of the optimisation objectives listed above. This also makes model-based verification and validation an important tool in de-risking the project.

The co-design approach represents an opportunity for virtual development and evaluation within the design process, representing a virtual V-Cycle within the usual V-Cycle of system development.

4 CO-DESIGN TOOLS WITHIN MBSE

To utilize co-design techniques effectively, the use of tools is necessary due to the typically extensive design possibilities. This section explores tools for plant modeling and control generation, both individually and in combination. It's important to note that in this context, the terms "plant" and "system" are used interchangeably.

4.1 Plant/System

Modeling, simulating, and analysing the plant behaviour requires an MBSE modeling tool. One of the most popular software platforms in the automotive and maritime industries is MATLAB/Simulink. Simulink is a visual programming environment that allows for model representation through block diagrams, thus enabling the design and optimisation of complex plants. Plant models can be classified on the basis of the direction of physical causality used to simulate the plant. Two main categories exist - backward (reversed causality) and forward (established causality) models. Forward models represent the plant with high accuracy and are suitable for developing control algorithms, but require higher computational power and calibration. Backward-facing models require less effort to set up and simulate, making them ideal in cases where a sizeable design space has to be explored. However, such models lack the accuracy of the forward ones and often neglect dynamic effects and physical limitations.

Selecting the appropriate type of model is crucial and it is dependent on the development phase. Backwards models can be very useful during the initial design stages where the design space is relatively large. As the development is progressing it would be logical to use more accurate models that are relevant for more elaborate testing.

The QSS Toolbox by ETH Zurich is an example of a Simulink implementation of a backward-facing modeling library [26]. ADVANCE is a modular vehicle and powertrain simulation environment developed by TNO [27]. The Simulink-based forward-facing type vehicle and powertrain components allow for easy set-up of the vehicle of interest due to the standardized input and outputs.

The ship plant design process typically involves several stakeholders. Therefore, sharing simulation models across stakeholders who may be using different simulation platforms is a technical challenge but essential for consistency. The Functional Mock-up Interface (FMI) is an industry standard for model exchange and co-simulation across different simulation platforms [28], that promotes the MBSE methodology. Within FMI, models are exported in a standardized Functional Mock-up Unit (FMU) format, i.e. an ADVANCE powertrain model can be exported as a single FMU and reused in a vessel system model. By allowing for platform-independent integration of models from several stakeholders, FMI manages the complexity of large systems and promotes collaboration. The standard originates from automotive but it is widely used in various industries, such as aerospace, energy, etc.

4.2 Control

Automation plays a critical role in facilitating a purely computational approach within the Co-Design methodology, as highlighted in [29]. Specifically, during the control design phase, it is imperative to automatically generate the controller that effectively operates on the plant. Although heuristic rule-based approaches can achieve this, it is widely acknowledged that these control techniques may not produce the optimal solution against a control objective function.

In the automotive domain, various methods of optimal control theory have been applied for many

years. However, defining, configuring, and calibrating these control regimes can be time-consuming and requires a high level of expertise from control engineers to implement reliably. As a result, rule-based control approaches have been dominant, and optimal control theory has yet to realize its full potential in the automotive domain.

The Modular Energy Management Strategy (MEMS) developed by TNO uses a dual decomposition to solve the Equivalent Consumption Minimization Strategy (ECMS) optimal control problem [30]. This innovative approach involves breaking down the optimal control problem into smaller subproblems, corresponding to subsystems or specific parts of the powertrain topology, such as the electric machine or the battery. By accurately modeling power flows within the system, MEMS ensures scalability and the ability to automatically generate solutions for various powertrain configurations, provided that the power balances at the nodes are known.

A crucial modification in MEMS, as opposed to ECMS, but equivalent, is that the optimisation objective involves minimising the total energy losses of each component. This redefined formulation allows for decomposition by considering the input and output powers of each subsystem.

The use of convex models to represent the powertrain components guarantees global optimality when the algorithm converges. To facilitate the automated generation of optimal control blocks, MEMS leverages a combination of a component library, an objective function, a component connectivity matrix, and a defined drive cycle. This streamlined process enables efficient generation of the control strategy in Simulink, making MEMS a powerful tool for optimising powertrain performance.

4.3 Plant/System & Control

Unlike plant modeling and control tools, few integrated plant and control tools for co-design are available. TNO has developed several powertrain co-design methodologies:

- TOPDSIGN - an automated tool for powertrain topology design and control, that aims at providing initial advice on the powertrain design and control for hybrid-electric vehicles [31]. The plant model is realized using the QSS Toolbox and it is controlled with MEMS.
- ADVANCE+MEMS - integration of an ADVANCE (forward) model and a MEMS controller within a co-design framework for (hybrid) electric vehicles [32]

4.4 Use-Case Study Co-Design

In this section, we consider a use-case of co-design applied in the automotive sector. The case considers the design optimisation of a hybrid truck, utilising the Modular Energy Management approach outlined in the European project ORCA [33]. The optimisation approach considered the sizing of key components in terms of maximum power, using a GA approach to find the optimal configuration for a given overall objective function expressed in terms of Total Cost of Ownership (TCO) [34]. It should be noted that the topology of the hybrid configuration was assumed, and as such the optimisation focused only on the control and optimal sizing.

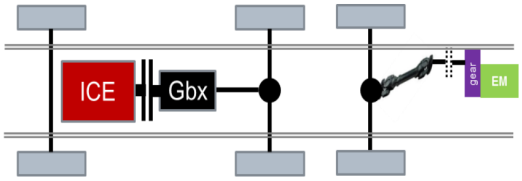

Figure 6: Schematic powertrain topology for hybrid truck [34].

The general approach was also considered by formulating the models within the co-design approach towards convex formulation, for a hybrid bus application [35]. The advantage of this approach is to guarantee global optimality of the optimisation approach. However, since the approach is a mixed integer problem (from the inclusion of gearing), the convex optimisation is combined iteratively with a dynamic programming approach.

Figure 7: Testing of the ORCA truck at the Vehicle Feature Lab [36].

Both approaches were ultimately used to govern the choice of hardware component sizes for two demonstration vehicles. These vehicles were assessed against the requirements formulated in the

MBSE approach through both virtual and physical testing, as illustrated in Fig. 7.

Such an approach that integrates MBSE, co-design for the optimisation of ship energy systems, and verification and validation can be benefitial in the maritime sector as well.

5 VERIFICATION AND VALIDATION

Using models to perform verification and validation testing through the design process can reduce project risks by identifying issues at early stages of the process. Simulation models can be used to test the requirements developed through the design process and ensure that the solution meets the user needs. However, as with the System Architecture model, the simulation model requires inputs and co-operation across disciplines and stakeholder which is a challenge. Furthermore, when working with multiple stakeholders on a common model, issues such as IP protection and the use of diverse modeling software and approaches often arise. While standards such as FMI described in 4.1 may offer a step towards a solution, it remains a challenge.

One essential aspect of using models within MBSE, is the understanding and confidence of their use from a verification and validation viewpoint. It should be recalled the clear distinction between the two, wherein [37]:

- Verification. The evaluation of whether or not a product, service, or system complies with a regulation, requirement, specification, or imposed condition. It is often an internal process. Contrast with validation.
- Validation. The assurance that a product, service, or system meets the needs of the customer and other identified stakeholders. It often involves acceptance and suitability with external customers. Contrast with verification.

When discussing the use of models, it is helpful to separate the concepts of the 'model' in terms of the implementation of the equations in terms of code, and 'modeling' in terms of the definition of how the physical system is represented by equations. Given this definition, it is possible to consider that a modeling approach might be novel, and therefore at a lower validity level, and where it has been implemented in code correctly. In that sense, the model can be less valid, but verified, and of course there can be situations where the converse is also true.

5.1 Model Confidence Level for Verification

As a way to categorise the level of verification of a model, the following classification is suggested in Table 1. Since the verification process is part of the model development, different types of virtual testing can be applied to verify that the model is correctly implemented.

Table 1: Verification Confidence categorisation.

Verification Confidence Level	Short Name	Description
1	Low	The code is implemented and executes, but not checked for valid output
2	Functional	The code is checked for a limited set of artificial functional tests, results are compared to expected outcomes
3	Domain	The code is checked within its domain of intended use, results are compared to expected outcomes
4	Independent	The code is independently verified with both functional and domain tests by third party

5.2 Modeling Confidence for Validation

In contrast to the model confidence, the modeling confidence represents the level of validity of the modeling approach. In general speaking, this is a measure of how widely the modeling method and representation of the physical system are accepted. Table 2 provides a suggestion for levels of categorisation for modeling confidence.

Table 2: Modeling Confidence categorisation.

Modeling Confidence Level	Short Name	Description
1	Novel	First of its kind, unproven technique
2	Adapted	Proven in one application, but applied in a domain where it is unproven
3	Adopted	Widely accepted technique, only partial evidence of real-world applicability
4	Proven	Widely accepted technique, validated through wide range of conditions and applications

5.3 Model Validation Confidence Level

After considering the modeling validity, and model verification, the level of confidence of the model validity needs to be determined. This is characteristically, that the model has been fitted with parameters for the specific system or component

Table 3: Model Confidence Level categorization.

Model Validation Confidence Level	Short Name	Description
1	Theoretical	The model is based on theoretical parameters/inputs only.
2	Derived	The model is based on a higher fidelity theoretical model.
3	Benchmarked	The model is based on or fitted against a matured simulation model
4	Empirical steady state lab	The model is based on experimental test data relating to steady state from lab tests in a narrow set of operating conditions, but combined with theoretical transient behavior and theoretical behavior in an extended range of operating conditions.
5	Empirical steady state lab extended	The model is based on experimental test data relating to steady state from lab tests in a wide set of operating conditions, but combined with theoretical transient behavior.
6	Empirical full lab	The model is based on experimental test data relating to both steady state and dynamic behavior in a wide set of operating conditions from lab tests
7	Combined	The model is based on subsystems that are individually validated to at least MCL 5-6.
8	Validated lab	The model is based on or fitted and validated against real-world emulated conditions within a lab environment.
9	Validated real-world non-domain	The model is based on or fitted and validated against real-world operational data for one application, but extrapolated for assessment in another.
10	Validated real-world domain	The model is based on or fitted and validated against real-world operational data for the relevant application.

which it represents, and that the combination of the modeling approach and fitted parameters adequately captures the designed accuracy required for the functional use of the model.

It is clear in this regard, that a model can be measured at different levels of validity. It is often useful to rank the level of model confidence. For system development, the confidence level of components can be high, but their combination as a system be at a lower level where the interactions of the models may be a source of inaccuracy.

A ranking system is suggested in Table 3, which can be referred as a Model Confidence Level (MCL). Since models by definition are a simplified representation of a physical system, it is important to track their validity through the design process. However, the availability of data for model validation, especially in the maritime domain, is a challenge.

5.4 Model Use through the MBSE Process

The MCL for components can be improved through the design process, or making use of pre-existing library of components with high MCL from prior development. In the early stages, relatively simple models can be used which have limited numbers of parameters to fit/scale.

Where laboratory test data, or field operational data becomes available, the parameters of these models can be re-fitted improving the MCL.

Further, as component or controller hardware becomes available, these components models can be replaced in the following methods:

- MIL – Model-in-the-Loop. The functional testing to abstract the behaviour of a system so that the model can be used to test, simulate and verify itself. Often for control development
- SIL – Software-in-the-Loop. The testing of a compiled software component, wherein the loop comprises of a simulated system
- HIL – Hardware-in-the-Loop. The testing of a single component, wherein the loop comprises of a simulated system. Controller (PIL) can be part of the hardware or separate.

The latter of these methods, hardware-in-the-loop allows for critical hardware to replace models in the system simulation. These tests can be completed by the vessel developer, or the component supplier, provided that the interfacing between the simulation models and hardware is well defined. One of the challenges of working in this form, is allowing for a system model to be made available to suppliers, or conversely allowing for models to be made available by suppliers for evaluation.

6 CONCLUSIONS

The maritime industry faces new challenges in terms of design and development of future vessels, meeting new emission requirements, and increasing complexity of design and control. These systems mean that a systematic approach is required to virtual explore design options, set against the overall requirements and design objectives. Model-Based System Engineering (MBSE) is a strong candidate approach emerging within the sector, already used in other industrial segments.

This paper has presented the principles of the MBSE approach as an overview for the methodology required for complex vessel development. Where models are used, care needs to be placed on understanding their use in terms of verification and the levels of validation. Several ranking schemes

are presented to indicate the level of confidence in the models being used.

Co-design is discussed as a methodology for optimising the design of the vessel in terms of both hardware and controller design, which yields high potential for complex system design. This methodology represents a V-cycle within a V-cycle for virtualised design and assessment. Finally, as a key enabling technology, the Modular Energy Management Approach is discussed, fulfilling the need for automated controller generation for a given plant design, as part of the co-design process. All that is put into context by presenting a use case from the automotive domain.

The use of the MBSE approach and the innovations presented in this paper still have challenges in terms of the widespread adoption. These are:

- A common approach for the handling of models and IP needs to be adopted between suppliers, vessel developers, and research partners.
- A willingness to share data, or validated models between stakeholders, with transparency over the validity
- MBSE approaches beyond the design process, extending into hardware evaluation via MIL and HIL methods
- Sharing of tools and methods from the research community to help accelerate the transition to MBSE

Overall, a strong and resilient maritime industry requires collaboration, and the tailoring of methods to the needs of the sector, and the tough emission targets ahead.

ACKNOWLEDGEMENTS

This work is part of the MENENS project, funded by the Netherlands Enterprise Agency (RVO) under grant number MOB21012.

REFERENCES

[1] "2030 climate target plan." (), [Online]. Available: https://climate.ec.europa.eu/eu-action/european-green-deal/2030-climate-target-plan_en (visited on 06/27/2023).

[2] "Initial imo ghg strategy." (), [Online]. Available: https://www.imo.org/en/MediaCentre/HotTopics/Pages/Reducing-greenhouse-gas-emissions-from-ships.aspx (visited on 06/27/2023).

[3] "Methanol as an energy step towards zero-emission dutch shipping (menens)." (), [Online]. Available: https://menens.nl/ (visited on 06/24/2023).

[4] I. C. on Systems Engineering (INCOSE), "Systems engineering vision 2020," INCOSE, San Diego, USA, Tech. Rep. INCOSE-TP-2004-004-02, 2007.

[5] S. Friedenthal, A. Moore, and R. Steiner, *A practical guide to SysML: the systems modeling language*. Morgan Kaufmann, 2014.

[6] Hart, L.E. "Introduction to model-based system engineering (mbse) and sysml: Presented at the delaware valley incose chapter meeting," Lockheed Martin, IS&GS. (Jul. 30, 2015), [Online]. Available: https://www.incose.org/docs/default-source/delaware-valley/mbse-overview-incose-30-july-2015.pdf (visited on 06/18/2023).

[7] E. Carroll and R. Malins, "Systematic literature review: How is model-based systems engineering justified?" Sandia National Laboratories, Albuquerque, USA, Tech. Rep. SAND2016-2607, 2016.

[8] K. Vipavetz, D. Murphy, and S. Infeld, "Model-based systems engineering pilot program at nasa langley," in *AIAA SPACE 2012 Conference & Exposition*, 2012, p. 5165.

[9] O. T. Holland, "Model-based systems engineering," in *Modeling and Simulation in the Systems Engineering Life Cycle: Core Concepts and Accompanying Lectures*, M. L. Loper, Ed. London: Springer London, 2015, pp. 299–306.

[10] M. Ryan, S. Cook, and W. Scott, "Application of mbse to requirements engineering - research challenges," in *Proceedings of the Systems Engineering/Test and Evaluation Conference*, Saporo, Australia, 2013, pp. 1–11.

[11] E. A. Bjorkman, S. Sarkani, and T. A. Mazzuchi, "Using model-based systems engineering as a framework for improving test and evaluation activities," *Systems Engineering*, vol. 16, no. 3, pp. 346–362, 2013.

[12] A. M. Madni and M. Sievers, "Model-based systems engineering: Motivation, current status, and research opportunities," *Systems Engineering*, vol. 21, no. 3, pp. 172–190, 2018.

[13] I. Poullis, "Application of model based system engineering (mbse) with ship design arrangement tool of advanced zero emissions power, propulsion and energy systems in maritime technology," MSc Thesis, Delft University of Technology, Delft, 2022.

[14] M. Khan, G. Dubos, J. Tirona, and S. Standley, "Model-based verification and validation of the smap uplink processes," in *2013 IEEE Aerospace Conference*, IEEE, 2013, pp. 1–9.

[15] H. Góngora, A. Dauron, and T. Gaudré, "A commonsense-driven architecture framework. part 1: A car manufacturer's (naıve) take on

mbse," in *INCOSE International Symposium*, Wiley Online Library, vol. 22, 2012, pp. 1410–1424.

[16] K. Simpson, O. Sindiy, and T. McVittie, "Orion flight test 1 architecture—observed benefits of a model based engineering approach," in *2012 IEEE Aerospace Conference*, IEEE, 2012, pp. 1–7.

[17] L. Delligatti, "SysML distilled : a brief guide to the systems modeling language," 2014.

[18] C. Veldhuis, A. Grasman, J. Willemsen, and U. Shipurkar, "Systematic design of future marine power & energy systems," in *Proceedings of the 15th International Symposium onPractical Design of Ships and Other Floating Structures (PRADS)*, Dubrovnik, Croatia, 2022, pp. 268–287.

[19] N. Tepper, "Exploring the use of model-based systems engineering (mbse) to develop systems architectures in naval ship design," MSc Thesis, Massachusetts Institute of Technology, 2010.

[20] C. Kerns, A. Brown, and D. Woodward, "Application of a dodaf total-ship system architecture in building a design reference mission for assessing naval ship operational effectiveness," in *ASNE Global Deterrence and Defense Symposium*, Bloomington, IN, 2011, pp. 1–22.

[21] P. Pearce and S. Friedenthal, "A practical approach for modelling submarine subsystem architecture in sysml," in *Submarine Institute of Australia Science, Technology & Engineering Conference*, vol. 2013, 2013.

[22] R. Audoire, "Platform-based modular product family design," in *Proceedings of the International Conference on Computer Applications in Shipbuilding*, Rotterdam, The Netherlands, 2019.

[23] NAVAIS. "New, advanced and value-added innovative ship." (), [Online]. Available: `https://www.navais.eu/` (visited on 06/24/2023).

[24] E. Silvas, T. Hofman, N. Murgovski, L. P. Etman, and M. Steinbuch, "Review of optimization strategies for system-level design in hybrid electric vehicles," *IEEE Transactions on Vehicular Technology*, vol. 66, no. 1, pp. 57–70, 2016.

[25] E. Silvas, "Integrated Optimal Design for Hybrid Electric Vehicles," Ph.D. dissertation, TU Eindhoven, 2015. [Online]. Available: `https://pure.tue.nl/ws/portalfiles/portal/8809090/20151130_Silvas.pdf`.

[26] *Downloads – Institute for Dynamic Systems and Control — ETH Zurich*. [Online]. Available: `https://idsc.ethz.ch/research-guzzella-onder/downloads.html` (visited on 06/30/2023).

[27] E. van den Tillaart, S. Mourad, and H. Lupker, "Tno advance: A modular simulation tool for combined chassis and powertrain analysis," in *Proceedings of the All Electric Combat Vehicle (AECV) Conference*, Noordwijkerhout, The Netherlands, 2002.

[28] Functional Mockup Interface, *Functional Mockup Interface*, 2018. [Online]. Available: `https://fmi-standard.org/` (visited on 06/19/2023).

[29] S. Wilkins, A. Dadikozyan, P. Mentink, and F. Kupper, "Applying modular energy management strategy to hev powertrain design & control," in *Proceedings of the 2022 JSAE Annual Congress (Spring)*, Yokohama, Japan, 2022.

[30] T. Romijn, T. Pham, and S. Wilkins, "Modular ecms framework for hybrid vehicles," in *Proceedings of the IFAC International Symposium on Advances in Automotive Control*, Orleans, France, 2019.

[31] A. Dadikozyan, M. Salazar, and S. Wilkins, "Applying modular energy management strategy to hev powertrain design & control," in *Proceedings of the 35th International Electric Vehicle Symposium (EVS35)*, Oslo, Norway, 2022.

[32] A. Dadikozyan, P. Mentink, and S. Wilkins, "Model-based methodology for co-design of refrigerated light-duty e-truck," in *Proceedings of the 2023 JSAE Annual Congress (Spring)*, Yokohama, Japan, 2023.

[33] D. D. Tran, O. Hegazy, J. Van Mierlo, *et al.*, "Modeling and co-design optimization for heavy duty trucks," *31st International Electric Vehicle Symposium and Exhibition, EVS 2018 and International Electric Vehicle Technology Conference 2018, EVTeC 2018*, 2018.

[34] S. Wilkins, T. Pham, D. Dai Tran, O. Hegazy, and N. Omar, "ORCA project: optimization framework for next generation heavy duty hybrids," in *15th International Symposium on Heavy Vehicle Transportation Technology*, 2017.

[35] D. P. H. Kolodziejak, T. H. Pham, T. Hofman, and S. Wilkins, "An Optimization and Analysis Framework for TCO Minimization of Plug-in Hybrid Heavy-duty Electric Vehicles," *IFAC-PapersOnLine*, vol. 52, no. 5, pp. 484–491, Jan. 2019.

[36] *Successful testing of the ORCA truck at the Vehicle Feature Lab – H2020-ORCA*. [Online]. Available: `https://h2020-orca.eu/news/update3-regional-distribution-truck/` (visited on 09/15/2023).

[37] *Project Management Body of Knowledge (PMBOK® Guide)*. PMI, 2008.

PROCEEDINGS OF MOSES2023 CONFERENCE
4TH INTERNATIONAL CONFERENCE ON MODELLING AND OPTIMISATION OF SHIP ENERGY SYSTEMS
26-27 OCTOBER 2023, DELFT, NETHERLANDS

Modelling and Simulation of a Wet Scrubber System

B.T.W. Mestemaker[a,*], E. Elmazi[b], L. van Biert[c], H.N. van den Heuvel[a], and K. Visser[c]

[a]Royal IHC, Kinderdijk, The Netherlands
[b]Heatmaster, Hendrik-Ido-Ambacht, The Netherlands
[c]Delft University of Technology, Delft, The Netherlands
[*]btw.mestemaker@royalihc.com

Abstract

Shipping is a relatively clean transport method with low emissions per ton-mile compared with road transport. However, harmful emissions emitted in coastal areas are a concern, as these affect local air quality and health. To reduce sulphur oxide (SO_X) emissions, the International Maritime Organization (IMO) implemented a global sulphur cap of 0.5 wt% and the 0.1 wt% limit in emission control areas (ECAs). Ship owners can opt for either low sulphur fuels or wet scrubber systems. Wet scrubber systems are a reliable method for reducing SO_X emissions with capture rates of up to 98%. These systems may use seawater alkalinity or caustic soda (e.g. closed-loop systems) to neutralise the SO_X emissions. However, the dynamic loading of engines can cause large fluctuations in the exhaust flow conditions, and it is unknown how these affect the effectiveness of the scrubber. This study explores the impact of dynamic loads on the SO_X removal efficiency of closed-loop wet scrubbers. A dynamic model of a closed-loop wet scrubber utilising fresh water and caustic soda is developed and verified using publicly available data. The model applies the two-film theory to model the gas-liquid interface. Billet and Schultes liquid hold-up theory is used to model the liquid film thickness in the packed bed. Maintaining scrubber efficiency with large load fluctuations or high-frequency fluctuations requires an increased liquid flow. The scrubber control system used a set-point of 75% of the equivalent compliance limit to ensure compliance with the 0.1% ECA limit during load fluctuations. The model and results can be used to develop a more advanced control system for improved scrubber operation and integration with a selective catalytic reduction (SCR) system to demonstrate compliance with the IMO NO_X Tier III limit when using high-sulphur heavy fuel oil (HFO).

Keywords: Dynamics simulation; Modelling; Wet scrubber; System integration.

1 INTRODUCTION

The environment has taken up a crucial role in all decisions made during the 21^{st} century. Many governments have implemented legislation to reduce greenhouse gas (GHG) emissions such as carbon dioxide (CO_2), methane (CH_4) and nitrous oxide (N_2O) emissions [1]. Shipping is currently a relatively clean form of transport with low emissions per ton-mile [2]. To ensure that the relative contribution of shipping does not increase in the future, the International Maritime Organization (IMO) has launched its initial GHG reduction strategy [3]. Additionally, the IMO has implemented measures such as the Energy Efficiency Design Index (EEDI), Energy Efficiency eXisting ship Index (EEXI), Ship Energy Efficiency Management Plan (SEEMP) and Carbon Intensity Indicator (CII) [4]–[6].

Harmful emissions such as nitrogen oxides (NO_X), sulphur oxides (SO_X) and particulate matter (PM) have become increasingly important due to their impact on human health, ecosystem acidification and eutrophication [7], [8]. The global sulphur cap of 0.5 wt% implemented by the maritime industry on January 1^{st} 2020 has significantly reduced the SO_X emissions. Shipping contributed about 5-8% of all global SO_X emissions before the implementation of the global sulphur cap in 2020 [9], [10].

There are several options to comply with the 0.5 wt% sulphur limit [11]. The solution may be found in the fuel choice such as a switch to very low sulphur fuel oil (VLSFO), distillate fuel, or liquefied natural gas (LNG). However, an abatement technology may also be applied to achieve the specified limit. The wet scrubber is the most widely applied SO_X emission reduction technology in the maritime sector and approximately 5000 ships are currently using such a system [12]. The three main wet scrubber types are as follows:

- An open-loop system with seawater used as the wash-water. The alkalinity of seawater is used to absorb and neutralise sulphur oxides.
- A closed-loop system in which fresh water and/or seawater is recycled. Caustic soda is used to absorb and neutralise the sulphur oxides.

@2023 Mestemaker, B. T. W. et al. published by TU Delft OPEN Publishing on behalf of the authors. Licensed under a Creative Commons Attribution CC BY license.
DOI: https://doi.org/10.59490/moses.2023.664

- A hybrid system that uses seawater for the open-loop and seawater and/or fresh water with caustic soda for the closed-loop.

An open-loop system is implemented in approximately 81% of the cases, a hybrid system is implemented in about 17% and the remaining systems are closed-loop systems [12]. The majority of vessels equipped with scrubbers are cargo vessels crossing the ocean, sailing from port to port. Work vessels, such as dredging vessels have not yet been equipped with wet scrubber systems because of the limited available space on these vessels. Additionally, dredging vessels experience significant load changes from the dredge equipment, which may also affect the effectiveness of the scrubber.

The objective of this study is to investigate the impact of dynamic loads on the effectiveness of operating a closed-loop wet scrubber system with caustic soda. This is done to evaluate the potential of implementing such a system on vessels with highly transient loads, such as dredging vessels. The modelling methodology is discussed in Section 2. In Section 3, the simulations results are discussed, followed by the conclusions in Section 4, and future work in Section 5.

2 METHODS

The wet scrubber investigated in this study cleans the exhaust gas of an internal combustion engine (ICE) fuelled with high-sulphur heavy fuel oil (HFO). The scrubber uses scrubbing water (water mixed with caustic soda) for the absorption and conversion of the SO_X from the exhaust gas. The modelling of the scrubber process has been split between the gas phase, the liquid phase and the interface between both phases in which the SO_X absorption, water evaporation and heat transfer occur. This section discusses the modelling of the gas phase, the liquid phase and the interface between the gas and liquid phases.

2.1 Gas phase

The gas phase of the scrubber is modelled as a combination of resistance and volume elements as shown in Fig. 1. This method has been discussed in more detail by Schulten [13]. These elements are used to build complex systems in which gas flows. The venturi, packed bed, and demister are resistance elements, and the lower and upper volumes (volume below and above the packed bed) are volume elements. The venturi and demister sections are assumed to be simple resistance models, while the packed bed is assumed to be the only location in which the SO_X absorption process occurs.

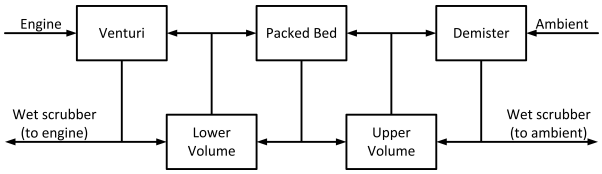

Figure 1: Schematic of wet scrubber model with resistance (upper row of blocks) and volume (lower row of blocks) elements

A resistance element as shown in Fig. 2 calculates the mass flow between the two volume elements as a function of the pressure drop. The element is modelled as an orifice, because there is no mass accumulation in it [13]. Equation 1 shows the mass flow calculation (ϕ^g) in the resistance element for an assumed incompressible flow [14] calculated using the effective area (A_{eff}) and resistance coefficient (ζ) of the orifice, pressure (p^g_{in}) and temperature (T^g_{in}) of the gas entering the resistance element, gas constant (R) and pressure ratio over the resistance element (π).

$$\phi^g = \frac{A_{eff}}{\sqrt{1+\zeta}} \cdot \frac{p^g_{in}}{\sqrt{R \cdot T^g_{in}}} \cdot \sqrt{2} \cdot \sqrt{1 - \frac{1}{\pi}} \quad (1)$$

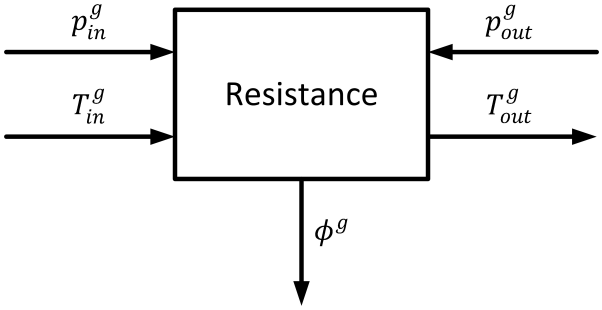

Figure 2: Resistance element (mass flow calculation)

A volume element as shown in Fig. 3 calculates the pressure in the element based on the mass flows entering and leaving the element, the temperature of the mass flow entering and the internal mass and energy balance [13]. The potential and kinetic energy terms are neglected in the volume element because these are small compared with the internal enthalpy [14].

The mass balance of the volume element is given by Eq. 2, where the mass change in the element ($\frac{dm^g_{cv}}{dt}$) is a function of the mass flow entering ($\phi^g_{cv,in}$) and leaving ($\phi^g_{cv,out}$) the element.

The temperature of the element is calculated using the energy balance of the control volume as shown in Eq. 3. The internal energy change ($\frac{d(m^g_{cv} \cdot u^g_{cv})}{dt}$) in this equation is calculated using the mass flow ($\phi^g_{cv,in}$) and enthalpy ($h^g_{cv,in}$) of the flow entering the element, mass flow ($\phi^g_{cv,out}$) and enthalpy ($h^g_{cv,out}$) of the flow leaving the element, heat loss (q^g_{cv}) and work (w^g_{cv}) in the element. The pressure (p^g_{cv}) in the element was calculated using the ideal gas law, as shown in Eq. 4 with the gas constant (R), mass (m^g_{cv}) and temperature (T^g_{cv}) of the content of the element and the volume (V^g_{cv}) as parameters.

$$\frac{dm^g_{cv}}{dt} = \phi^g_{cv,in} - \phi^g_{cv,out} \tag{2}$$

$$\frac{d(m^g_{cv} \cdot u^g_{cv})}{dt} = \phi^g_{cv,in} \cdot h^g_{cv,in} - \phi^g_{cv,out} \cdot h^g_{cv,out} + q^g_{cv} + w^g_{cv} \tag{3}$$

$$p^g_{cv} = \frac{m^g_{cv} \cdot R \cdot T^g_{cv}}{V^g_{cv}} \tag{4}$$

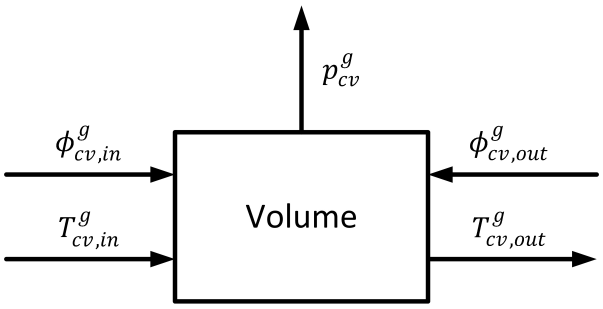

Figure 3: Volume element (pressure & temperature calculation)

The SO_X absorption, water evaporation and heat transfer between the gas and liquid phases occur in the packed bed section of the scrubber. The packed bed itself is modelled as a resistance element for the surrounding components. To improve the accuracy of the results, the packed bed was discretised using the same resistance and volume element approach, as shown in Fig. 4.

The removal of the SO_X, evaporation of water, and heat transfer occur in the internal volume elements of the packed bed. In these discretised elements, an interface between the gas and liquid phases is present, as shown in Fig. 5. The liquid (shown in blue) is fed to the top of the column and flows down owing to gravity, and the gas (represented in grey) is fed to the bottom and moves upward owing to pressure. Liquid and gas coexist in each discretised element. Absorption towers are often filled with packing materials to improve the water distribution and create a large gas-liquid interface area [15].

Gas and liquid have contact in each section (for example, random section m in Fig. 5), and there is simultaneous mass and heat transfer between both phases. Both phases have their own control volumes for calculating their respective properties. There is a bidirectional flow between the control volumes for the mass flows of the absorbed sulphur dioxide (ϕ_{SO_2}) and the evaporated water ($\phi^{evap}_{H_2O}$) and the transfer of heat (q). Each gas control volume (m) receives its gas input from the previous discretised element (m-1) and each liquid control volume (m) receives its gas input from the previous discretised element (m+1). The interface between the gas and liquid phase is discussed in more detail in Section 2.3.

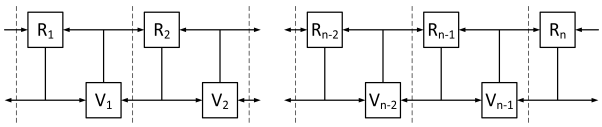

Figure 4: Packed bed gas phase discretisation to resistance and volume element

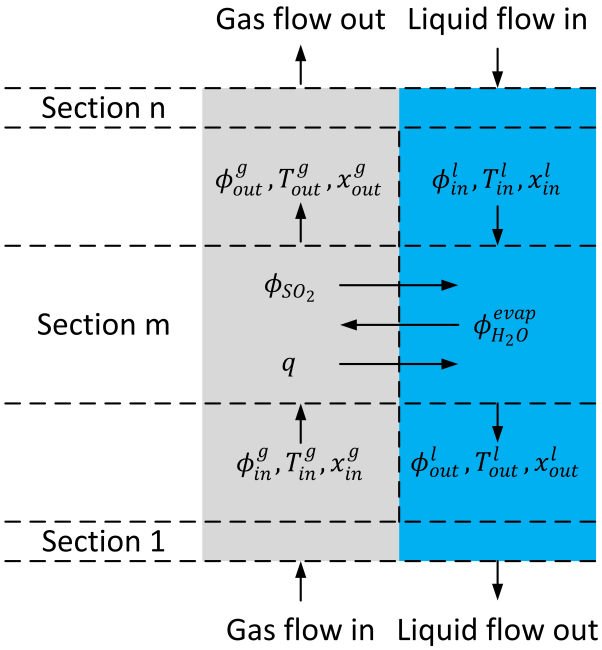

Figure 5: Packed bed presentation in n-sections with a detailed presentation of random section m

2.2 Liquid phase

The liquid water phase is modelled in the packed bed section of the scrubber to capture the adsorption process. Such an elaborate approach is omitted in the other sections because the majority of the SO_X

absorption takes place in the packed bed. The liquid phase of the other scrubber sections, as shown in Fig. 1, namely the venturi, lower and upper volumes, and demister, have not been modelled.

The liquid mass balance in the packed bed is governed by gravity alone. The slight pressure differences in the scrubber vessel that affect the gas phase are too small to affect water flow. Therefore, another approach must be applied to model the rate at which water flows through the packed bed. The mass balance of the liquid-phase ($\frac{dm^l_{pb}}{dt}$) is modelled according to Eq. 5 with the ingoing ($\phi^l_{pb,in}$) and outgoing flows ($\phi^l_{pb,out}$) and the water evaporating ($\phi^{evap}_{H_2O}$) as its parameters.

$$\frac{dm^l_{pb}}{dt} = \phi^l_{pb,in} - \phi^l_{pb,out} - \phi^{evap}_{H_2O} \tag{5}$$

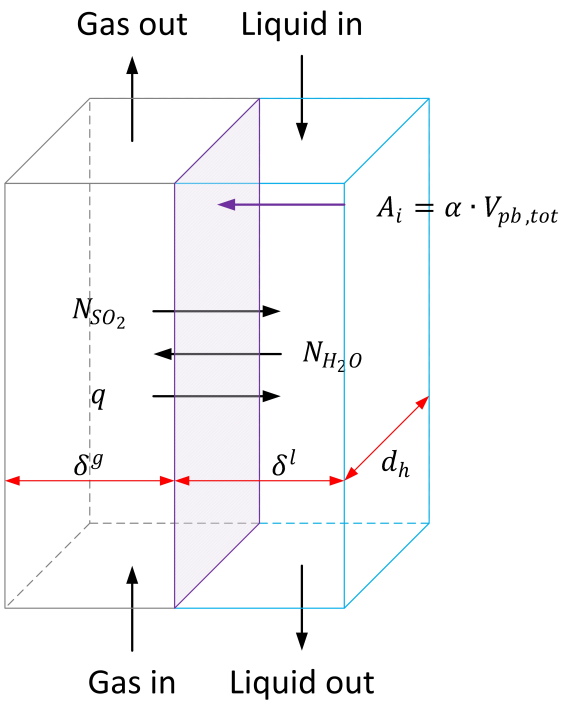

Figure 6: Schematic representation of the liquid gas interface in the model

The packed bed is irregular in shape and orientation, making it difficult to model. It is assumed that the packed bed may be modelled as a counterflow of liquid (downward) and gas (upward) in vertical flow channels (Fig. 6). The deviation between the real and modelled flows is the specific surface area (α) as shown in Eq. 6 to calculate the hydraulic diameter (d_h) of the vertical flow channels together with the void fraction (ϵ) [16].

$$d_h = 4 \cdot \frac{\epsilon}{\alpha} \tag{6}$$

The liquid film thickness (δ^l) in the packed bed is calculated using the ingoing ($\phi^l_{pb,in}$) and outgoing liquid flows ($\phi^l_{pb,out}$), water evaporating ($\phi^{evap}_{H_2O}$), liquid density (ρ^l), the specific surface area (α) and total volume of the packed bed ($V_{pb,tot}$) (Eq. 7).

$$\frac{d\delta^l}{dt} = \frac{\phi^l_{in} - \phi^l_{out} - \phi^{evap}_{H_2O}}{\rho^l \cdot \alpha \cdot V_{pb,tot}} \tag{7}$$

The liquid velocity in the packed bed (v^l_{cv}) is calculated using the empirical formula from Billet and Schultes for the liquid hold-up in packing materials [16]. Equation 8 calculates the velocity with the liquid hold-up (h^l), liquid density (ρ^l), cross-sectional area of the empty scrubber (A_{sc}), dynamic viscosity of the liquid (μ^l), specific surface area (α), hydraulic diameter (d_h) of the vertical flow channels, and liquid film thickness (δ^l).

$$v^l_{cv} = \frac{(h^l)^3 \cdot g \cdot \rho^l \cdot A_{sc}}{12 \cdot \mu^l \cdot \alpha^2 \cdot d_h \cdot \delta^l} \tag{8}$$

The changes in the liquid flow over the packed bed height are captured by discretisation of the packed bed model. The control volumes are assumed as ideally mixed elements. The mass flow leaving the control volume (ϕ^l_{cv}) is calculated using the liquid density (ρ^l), hydraulic diameter (d_h), liquid film thickness (δ^l) and liquid velocity in the packed bed (v^l_{cv}) (Eq. 9).

$$\phi^l_{cv} = \rho^l \cdot d_h \cdot \delta^l \cdot v^l_{cv} \tag{9}$$

2.3 Liquid-gas interface

The liquid-gas interface is where the heat and mass transfer between gas and liquid phases occurs. Sulphur oxides in the gas phase are absorbed by the liquid phase, where they react chemically with caustic soda (NaOH). Water evaporates from the liquid phase to the gas phase, while heat is transferred from the hot exhaust gases in the gas phase to the liquid phase.

The two-film theory introduced by Lewis and Whitman in 1924 is used to model the interface layers between the gas and liquid phases [17], [18]. The transport between both phases by molecular diffusion is limited by the mass-transfer resistance of the interface layers. The concentrations of the substances modelled are in equilibrium at the interface of both layers, but are not necessarily equal (Fig. 7). Figure 7 also shows a reaction plane for the chemical reaction between sulphur oxide and caustic soda. The chemical absorption of sulphur dioxide (SO_2) in the presence of hydroxide (OH^-) may

be considered instantaneous and irreversible [19]–[21]. Therefore, the model introduced by Danckwerts [22] for instantaneous and irreversible reactions will be adopted. The concentration of sulphur dioxide decreases from the bulk gas value ($c^g_{SO_2,b}$) in the gas film towards the interface value of ($c^g_{SO_2,i}$). On the liquid side of the interface, the concentration is ($c^l_{SO_2,i}$) and it is constantly reduced. The reaction plane at distance (δ^r) in the liquid film is the location where it encounters the hydroxide concentration ($c^l_{OH^-}$) which has diffused through the liquid film at distance ($\delta^l - \delta^r$) from the bulk concentration ($c^l_{OH^-,b}$). Fick's law is used to model diffusion in the liquid film [23].

It is assumed that the reaction between the (SO_2) and the (OH^-) is completely performed in the reaction plane and that the (SO_2) does not reach the bulk of the liquid ($c^l_{SO_2,b} = 0$).

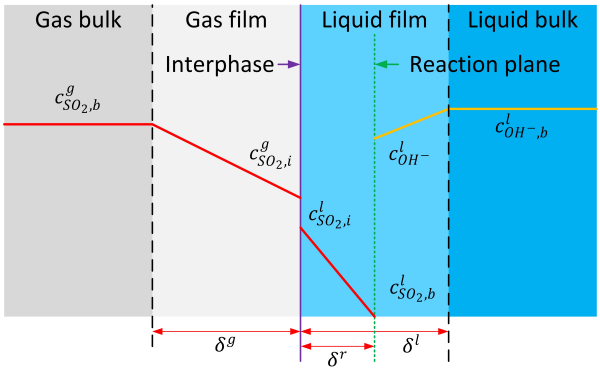

Figure 7: SO_2 and OH^- concentrations in the gas and liquid film and bulk

The mass transfer of sulphur dioxide (N_{SO_2}) is calculated using Eq. 10 and with the following parameters [24]–[26]: the mole fractions of sulphur dioxide ($y^g_{SO_2,b}$) in the gas and hydroxide ($y^l_{OH^-,b}$) in the liquid, the diffusion rate of sulphur dioxide ($D^l_{SO_2}$) and hydroxide ($D^l_{OH^-}$) in the liquid, Henry's constant for sulphur dioxide in the liquid ($H^l_{SO_2}$), the mass transfer coefficient for the gas (k^g_y) and the liquid (k^l_y), the gas pressure (p^g), the interface surface area (A_i) and the scrubber volume (V_{tot}).

Equation 11 is used to calculate the mass transfer of the water (N_{H_2O}) with the mass transfer coefficient for water (k^g_{y,H_2O}) in gas, the mole fractions of water in the gas ($y^g_{H_2O,b}$) and in liquid ($y^l_{H_2O,b}$), the saturated gas pressure (p^l_{sat}) and the gas pressure (p^g), the interface surface area (A_i) and the scrubber volume (V_{tot}) [26], [27].

$$N_{SO_2} = \frac{y^g_{SO_2,b} + \frac{H^l_{SO_2}}{p^g} \cdot \frac{D^l_{OH^-} \cdot y^l_{OH^-,b}}{2 \cdot D^l_{SO_2}}}{\frac{1}{k^g_y} + \frac{1}{k^l_y} \cdot \frac{H^l_{SO_2}}{p^g}} \cdot A_i \cdot V_{tot} \tag{10}$$

$$N_{H_2O} = k^g_{y,H_2O} \cdot (y^g_{H_2O,b} - y^l_{H_2O,b} \cdot \frac{p^l_{sat}}{p^g}) \cdot A_i \cdot V_{tot} \tag{11}$$

The heat transfer process from the (hot) gas to the (cold) liquid phase is illustrated in Fig. 8. The heat transfer follows from Eq. 12 with the following parameters [26]: the heat transfer coefficients for the gas (h^g_c) and the liquid (h^l_c) phases, the temperatures of the gas bulk (T^g_b), the interface area (T_i) and the bulk liquid (T^l_b), the specific surface area (α) and the total volume of the packed bed ($V_{pb,tot}$).

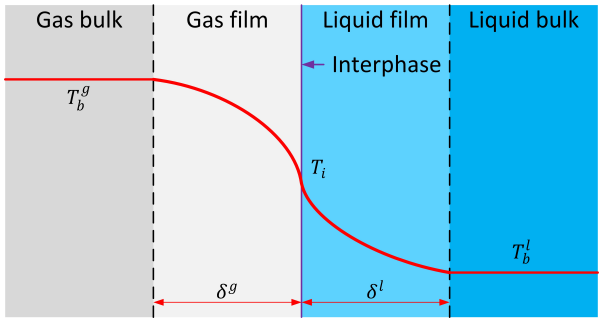

Figure 8: Temperature profile of the gas and liquid film and bulk

$$q = h^g_c \cdot \alpha \cdot V_{pb,tot} \cdot (T^g_b - T_i) = h^l_c \cdot \alpha \cdot V_{pb,tot} \cdot (T_i - T^l_b) \tag{12}$$

3 RESULTS

The simulations have been performed for a closed-loop wet scrubber suitable for a 6 cylinder 7.5 MW engine with the engine data provided in Table 1. The engine is assumed to operate at a constant excess air ratio of 2 and with an HFO with a fuel sulphur content of 3.5% [$\frac{m}{m}$].

The scrubber vessel has a diameter of 2.8 m and a height of 7.5 m of which it is assumed that the packed bed uses a height of 2.0 m. The packed bed in this study consists of a dumped packing of ceramic Hiflow rings with a diameter of 50 mm, resulting in 5120 rings per m^3 with a specific surface area (α) of 89.7 $\frac{m^2}{m^3}$ and a void fraction (ϵ) of 0.809 $\frac{m^3}{m^3}$. The liquid flow has a hydroxide mass fraction (x_{OH^-}) of 0.000145 $\frac{kg}{kg}$.

Table 1: Engine data used for the simulations.

$Load[\%]$	$\phi_{gas}[\frac{kg}{s}]$	$Temperature[K]$
25	5.08	573
50	8.91	538
75	10.9	565
100	13.0	611

The packed bed has been discretised to improve the accuracy of the model. A higher discretisation produces more accurate results, but also has longer simulation times. Figure 9 shows the effect of the discretisation on the liquid flow required to achieve the SO_2 removal efficiency. The scrubber must ensure compliance to the upper limit of 0.1% $\frac{m}{m}$ limit when operating in a Sulphur oxide Emission Control Area (SECA). The 0.1% $\frac{m}{m}$ limit is equivalent to 4.3 $\frac{ppmv_{SO_2}}{y_{CO_2}}$ [28].

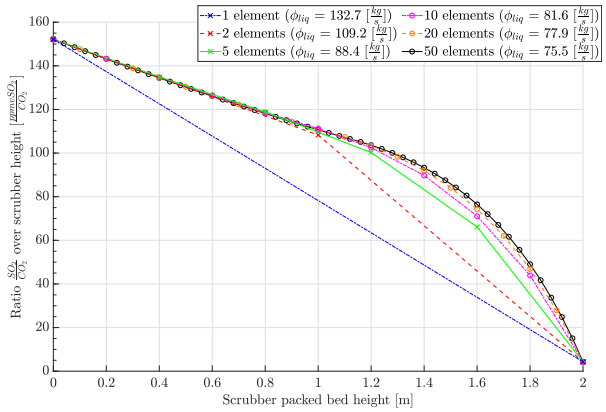

Figure 9: Liquid flow required to achieve the 4.3 $\frac{ppmv_{SO_2}}{y_{CO_2}}$ limit for different packed bed discretisation sizes

The simulations in the remainder of this study will be performed with a discretisation of 10 steps as the results for 1,2 and 5 deviate significantly from those of 10, 20 and 50 steps. The liquid flow required to achieve the limit with 10 discretisation steps is 81.6 $\frac{kg}{s}$, this is less than 5% higher than the 77.9 $\frac{kg}{s}$ for 20 discretisation steps and 8% higher than the 75.5 $\frac{kg}{s}$ for 50 discretisation steps while having a more acceptable calculation time.

Figures 10 and 11 show the longitudinal gas and liquid temperatures in the packed bed of the scrubber for each engine load point and the liquid flow required to achieve the 4.3 $\frac{ppmv_{SO_2}}{y_{CO_2}}$ limit. The exhaust gas enters at a packed bed height of 0 m and exits at 2 m with a temperature of about 300 K. This is about 5 K above the liquid temperature of 295 K for all gas mass flows. The liquid flow enters the packed bed at 2 meters with a temperature of 295 K and a flow of 81.6 $\frac{kg}{s}$ and exits at the bottom (0m) with a temperature increases of around 11-16K.

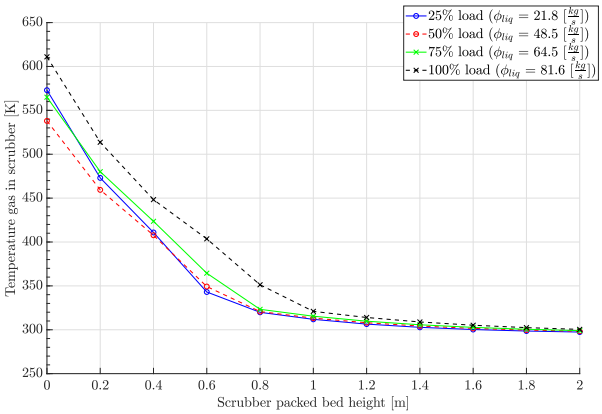

Figure 10: Longitudinal gas temperature for each engine load point

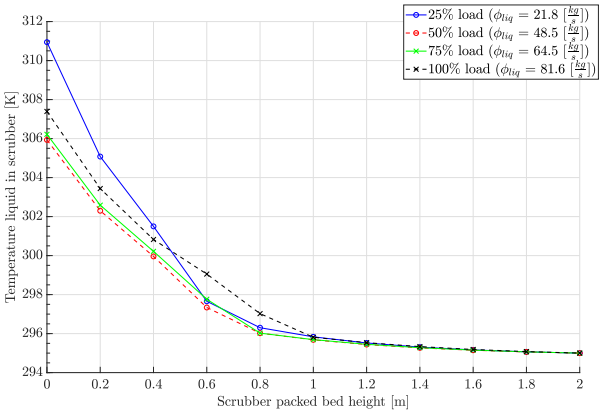

Figure 11: Longitudinal liquid temperature for each engine load point

The impact of transient engine loading on the scrubber performance is tested using the data given in Table 1 by cycling through these load points. The scrubber model is dynamic, but on the engine side a quasi-static approach is used which neglects the impact of among others the turbocharger behaviour on the exhaust gas mass flow, temperature and composition. The pump-pipe dynamics have been simplified with a rate limiter to include the effect of accelerating and decelerating the scrubber liquid flow. The liquid flow of the scrubber is controlled with a Proportional Integral (PI)-controller with a set-point of 3.225 ($= 4.3 \cdot 75\%$) $\frac{ppmv_{SO_2}}{y_{CO_2}}$ to ensure compliance to the 0.1 wt% SECA limit during the load fluctuations. This set-point requires a liquid flow of 82.5 $\frac{kg}{s}$ at 100% maximum continuous rating (MCR).

Several vessel types, such as dredging vessels, experience load fluctuations owing to the nature of their operation [29]. This may impact the effective

SO_X removal of the scrubber, and therefore, the impact of two fluctuation sizes will be tested, namely 25%-100% maximum continuous rating (MCR) and 75%-100% MCR.

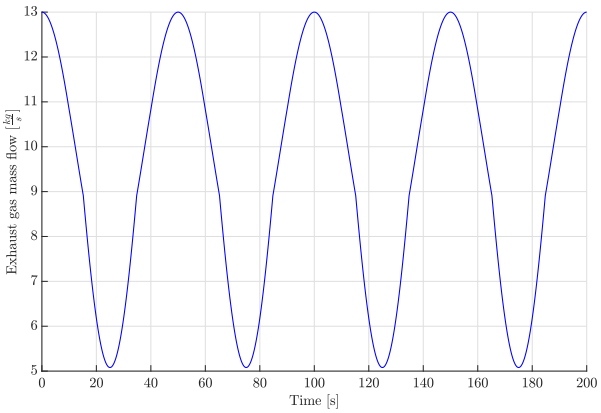

Figure 12: Exhaust gas mass entering the scrubber ($100\% - 25\% - 100\%$)

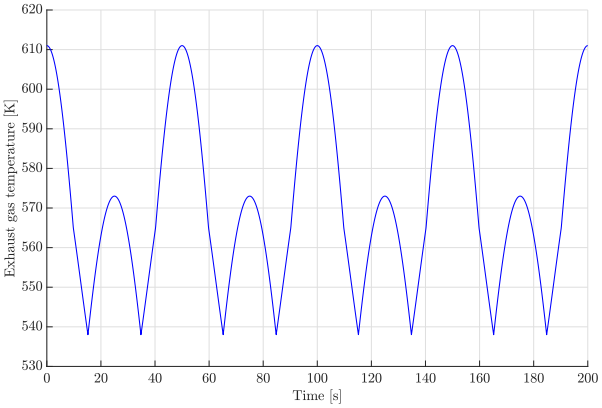

Figure 13: Exhaust gas temperature entering the scrubber ($100\% - 25\% - 100\%$)

Figures 12 and 13 show the exhaust gas mass flow and temperature entering the scrubber for fluctuations between 25% and 100% MCR with a period of 50 s. The liquid flow during the dynamics exceeds the flow required to achieve the set-point of 3.225 $\frac{ppmv_{SO_2}}{y_{CO_2}}$ (82.5 $\frac{kg}{s}$) at nominal load with about 7.0% (88.3 $\frac{kg}{s}$) for the simulation with evaporation and with about 2.7% (84.7 $\frac{kg}{s}$) if evaporation is not included as shown in Fig. 14. The scrubber remains within the compliance limit, as shown in Fig. 15.

The inclusion of evaporation in the simulation model appears to result in an instability of the liquid flow and the $\frac{ppmv_{SO_2}}{y_{CO_2}}$ ratio during this simulation. However, the validity of this instability is uncertain because the model has not been validated.

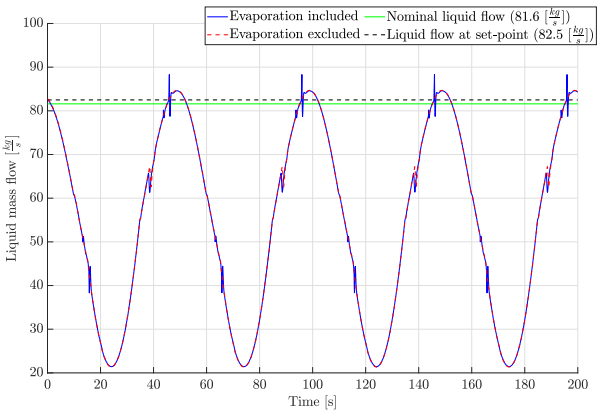

Figure 14: Scrubber liquid flow including and excluding the evaporation influence ($100\% - 25\% - 100\%$)

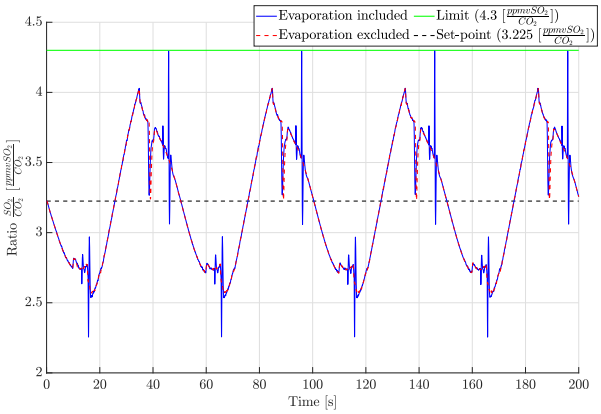

Figure 15: Fraction of $\frac{ppmv_{SO_2}}{y_{CO_2}}$ leaving the scrubber including and excluding the evaporation influence ($100\% - 25\% - 100\%$)

The 75%-100% MCR simulations have been performed with a period of 50 and of 10 s to observe the impact of a faster load change. The simulations include the effect of water evaporation. Figure 16 shows that the liquid flow exceeds the nominal value for the 50 s period by about 0.1% (82.6 $\frac{kg}{s}$) and by about 3.6% (85.5 $\frac{kg}{s}$) for the 10 s period.

Figure 17 shows that the ratio of $\frac{ppmv_{SO_2}}{y_{CO_2}}$ is more stable for the 50 second period than for the 10 second period. This means that for applications in which fast load changes occur a larger margin to the SECA limit is required to ensure compliance, whereas for applications with slower changes, a smaller margin will suffice. The application of a more advanced control system may result in a more stable $\frac{ppmv_{SO_2}}{y_{CO_2}}$ ratio, but it will not compensate for the slow response of the pump-pipe system, which must be overcome for the load changes.

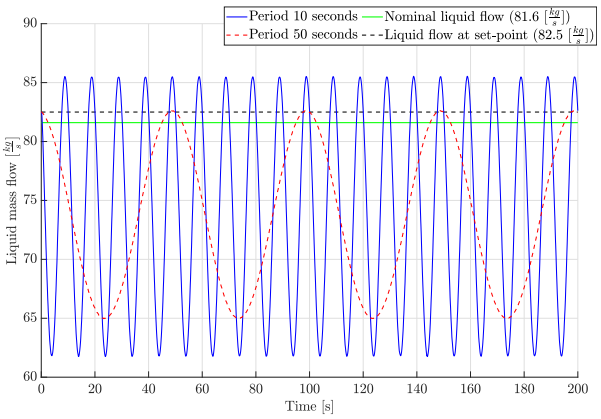

Figure 16: Scrubber liquid flow ($100\% - 75\% - 100\%$)

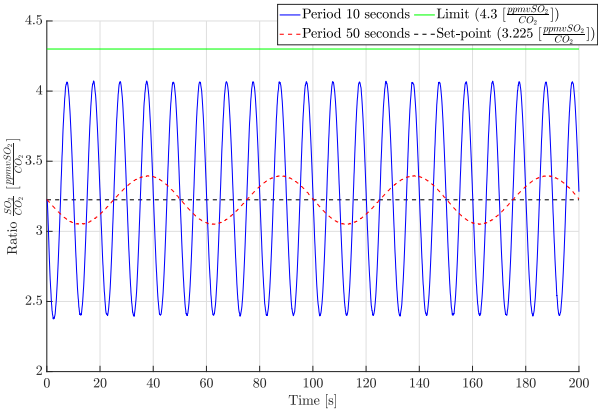

Figure 17: Fraction of $\frac{ppmv_{SO_2}}{y_{CO_2}}$ leaving the scrubber ($100\% - 75\% - 100\%$)

4 CONCLUSIONS

Wet scrubbers are capable of effectively removing sulphur oxide emissions from the exhaust gas of vessels with dynamically loaded engines. A feedback control system with a sufficient margin in the set-point is sufficient to maintain the SO_X emissions well within the dictated limit.

The inclusion of evaporation in the model results in instability of the $\frac{ppmv_{SO_2}}{y_{CO_2}}$ ratio in the model owing to the evaporation of liquid in the packed bed and condensation in the demister. This may result in a scrubber that momentarily exceeds the dictated limit.

discretisation of the packed bed model improves the accuracy of the SO_2 removal efficiency calculation. This increase in accuracy comes at the cost of additional calculation time. The calculation results converge from the discretisation of 10 steps, whereas for this number of discretisation steps, the calculation time is still acceptable.

5 FUTURE WORKS

The model and its results should be validated to examine the accuracy of the SO_X removal efficiency and the impact of evaporation on the scrubber performance. The impact of evaporation may have to be ignored in future research if the behaviour shown in the 25%-100% MCR simulations is an effect of the simulation and modelling approach and does not occur in actual systems.

A more advanced control system may be considered based on a feed-forward signal from the engine (e.g. engine load and fuel rack position), in combination with the feedback signal from the exhaust gas composition. This solution may result in a better controlled liquid flow without overshooting the nominal value. Additionally, this could result in the system operating with less margin in the liquid flow, which reduces the power consumption of the scrubber.

The scrubber model may also be integrated with an engine model and/or run measurement data to determine the impact of actual load fluctuations on the operation and sulphur oxide removal efficiency of the scrubber. This shows the impact of a combined change in the exhaust gas mass flow and mass fractions of sulphur oxide in the exhaust gas. In addition, integration with a selective catalytic reduction (SCR) system may to demonstrate compliance with the IMO NO_X Tier III limit when using high-sulphur heavy fuel oil (HFO).

The packed bed modelling method may be changed from a resistance-volume element system to a plug flow model. This allows for more discretisation of the packed bed and a higher accuracy of the simulation results without a significant impact on the calculation time.

ACKNOWLEDGEMENTS

This research is based on the work performed within the MSc thesis work of Enri Elmazi named: “Closed Loop Wet Scrubber System for Maritime Application: Dynamic Modelling and System Integration” at Delft University of Technology.

REFERENCES

[1] S. Gössling, C. Meyer-Habighorst, and A. Humpe, “A global review of marine air pollution policies, their scope and effectiveness,” *Ocean & Coastal Management*, vol. 212, p. 105 824, 2021, ISSN: 0964-5691.

[2] IMO, *Second imo ghg study 2009*, https://wwwcdn.imo.org/localresources/en/OurWork/Environment/Documents/SecondIMOGHGStudy2009.pdf, 2009.

[3] IMO, *Initial imo strategy on reduction of ghg emissions from ships, resolution mepc.304(72)*, https://wwwcdn.imo.org/localresources/en/KnowledgeCentre/IndexofIMOResolutions/MEPCDocuments/MEPC.304(72).pdf, 2018.

[4] IMO, *Amendments to the annex of the protocol of 1997 to amend the international convention for the prevention of pollution from ships, 1973, as modified by the protocol of 1978 relating thereto, amendments to marpol annex vi, procedures for sampling and verification of the sulphur content of fuel oil and the energy efficiency design index (eedi), resolution mepc.324(75)*, https://wwwcdn.imo.org/localresources/en/KnowledgeCentre/IndexofIMOResolutions/MEPCDocuments/MEPC.324(75).pdf, 2020.

[5] IMO, *Report of the marine environment protection committee on its seventy-fifth session*, https://www.mpa.gov.sg/docs/mpalibraries/mpa-documents-files/shipping-division/mepc-reports/mepc-75-18---report-of-the-marine-environment-protection-committeeon-its-seventy-fifth-session-(secretariat).pdf, 2020.

[6] IMO, *Report of the marine environment protection committee on its seventy-sixth session*, https://www.mpa.gov.sg/docs/mpalibraries/mpa-documents-files/shipping-division/mepc-reports/mepc-76-15---report-of-the-marine-environment-protection-committee-on-its-seventy-sixth-session-(secretariat).pdf, 2021.

[7] IMO, *Amendments to the annex of the protocol of 1997 to amend the international convention for the prevention of pollution from ships, 1973, as modified by the protocol of 1978 relating thereto (revised marpol annex vi), resolution mepc.176(58)*, https://wwwcdn.imo.org/localresources/en/OurWork/Environment/Documents/176(58).pdf, 2008.

[8] E. Ytreberg, S. Åström, and E. Fridell, "Valuating environmental impacts from ship emissions – the marine perspective," *Journal of Environmental Management*, vol. 282, p. 111 958, 2021, ISSN: 0301-4797.

[9] K. Cullinane and S. Cullinane, "Chapter 3 - policy on reducing shipping emissions: Implications for "green ports"," in *Green Ports*, R. Bergqvist and J. Monios, Eds., Elsevier, 2019, pp. 35–62, ISBN: 978-0-12-814054-3. [Online]. Available: https://www.sciencedirect.com/science/article/pii/B9780128140543000037.

[10] L. v. Biert, "Solid oxide fuel cells for ships: System integration concepts with reforming and thermal cycles," Ph.D. dissertation, Delft University of Technology, 2020, ISBN: 9789463662482.

[11] M. Tadros, M. Ventura, and C. Guedes Soares, "Review of current regulations, available technologies, and future trends in the green shipping industry," *Ocean Engineering*, vol. 280, p. 114 670, 2023, ISSN: 0029-8018.

[12] DNV. "Alternative fuels insight, scrubbers." (2023), [Online]. Available: https://afi.dnvgl.com/statistics/DDF10E2B-B6E9-41D6-BE2F-C12BB5660107.

[13] P. Schulten, "The interaction between diesel engines, ship and propellers during manouevring," Ph.D. dissertation, Delft University of Technology, 2005, ISBN: 9789040725791.

[14] D. Stapersma, "Diesel engines, a fundamental approach to performance analysis, turbocharging, combustion, emissions and heat transfer, part i, performance analysis and turbocharging, volume 2, turbocharging," Royal Netherlands Naval College, Tech. Rep., 2010.

[15] V. Bontozglou, *Introduction to Physical Processes, Theoretical Background and Basic Applications (translated from Greek)*, Greek. Kallipos Publications, 2015, ISBN: 9786188212473.

[16] R. Billet and M. Schultes, "Prediction of mass transfer columns with dumped and arranged packings: Updated summary of the calculation method of billet and schultes," *Chemical Engineering Research and Design*, vol. 77, no. 6, pp. 498–504, 1999, ISSN: 0263-8762.

[17] W. Lewis and W. Whitman, "Principles of gas absorption.," *Industrial & Engineering Chemistry*, vol. 16, pp. 1215–1220, 1924.

[18] R. A. Zaveri, R. C. Easter, J. E. Shilling, and J. H. Seinfeld, "Modeling kinetic partitioning of secondary organic aerosol and size distribution dynamics: Representing effects of volatility, phase state, and particle-phase reaction," *Atmospheric Chemistry and Physics*, vol. 14, no. 10, pp. 5153–5181, 2014.

[19] J. Dean, *Lange's handbook of chemistry*. McGraw-Hill, Inc., 1998, 1424 pp., ISBN: 9780070163843.

[20] G. Vázquez, G. Antorrena, F. Chenlo, and F. Paleo, "Absorption of so2 by aqueous naoh solutions in the presence of a surfactant," *Chemical Engineering & Technology*, vol. 11, no. 1, pp. 156–162, 1988.

[21] D. Flagiello, F. Di Natale, A. Lancia, *et al.*, "Experimental and modelling approach to the design of chemical absorption columns with fast gas-liquid reaction: A case-study on flue-gas desulfurization with h2o2 oxidative solutions," *Chemical Engineering Research and Design*, vol. 194, pp. 425–438, 2023, ISSN: 0263-8762.

[22] P. Danckwerts, *Gas-liquid reactions*. McGraw-Hill Book Company, 1970, ISBN: 9780070152878.

[23] W. Chen, Y. Chen, and C. Hung, "A simplified model of predicting SO2 absorption by single atmospheric raindrops with chemical dissociation and internal circulation," *Aerosol and Air Quality Research*, vol. 11, no. 7, pp. 860–872, 2011.

[24] M. Schultes, "Absorption of sulphur dioxide with sodium hydroxide solution in packed columns," *Chemical Engineering & Technology*, vol. 21, no. 2, pp. 201–209, 1998.

[25] M. Schlager, M. Baumfrisch, G. Haushofer, V. Wolf-Zöllner, and M. Lehner, "Mass transfer model of packed seawater scrubbers for marine exhaust gas cleaning," *Chemical Engineering Research and Design*, vol. 192, pp. 128–140, 2023, ISSN: 0263-8762.

[26] R. Bird, W. Stewart, E. Lightfoot, and D. Klingenberg, *Introductory Transport Phenomena*. Wiley, 2015, ISBN: 9781118953716.

[27] W. Johansson, J. Li, and L. Lin, "Module-based simulation model for prediction of convective and condensational heat recovery in a centrifugal wet scrubber," *Applied Thermal Engineering*, vol. 219, p. 119 454, 2023, ISSN: 1359-4311.

[28] IMO, *2021 guidelines for exhaust gas cleaning systems, resolution mepc.340(77)*, `https://puc.overheid.nl/nsi/doc/PUC_701345_14/1/`, 2021.

[29] B. Mestemaker, M. Goncalves Castro, H. van den Heuvel, and K. Visser, "Dynamic simulation of a vessel drive system with dual fuel engines and energy storage," *Energy*, vol. 194, p. 116 792, 2020, ISSN: 0360-5442.

PROCEEDINGS OF MOSES2023 CONFERENCE
4TH INTERNATIONAL CONFERENCE ON MODELLING AND OPTIMISATION OF SHIP ENERGY SYSTEMS
26-27 OCTOBER 2023, DELFT, NETHERLANDS

Decentralized Power Sharing with Frequency Decoupling for a Fuel Cell-Battery DC Shipboard Power System

Timon Kopka[*a], Foivos Mylonopoulos[a], Andrea Coraddu[a,b], and Henk Polinder[a]

[a]Department of Maritime and Transport Technology, Delft University of Technology, The Netherlands
[b]Netherlands Defence Academy, The Netherlands
[*]Corresponding author: t.kopka@tudelft.nl

Abstract

The maritime industry is under increasing pressure to reduce its carbon footprint by adopting new energy generation and storage technologies in shipboard power systems (SPS). Fuel cells (FCs) show great potential as primary power sources when hybridized with energy storage systems (ESS). Integrating different technologies in future SPS requires the coordination of power generation and storage modules, which can be facilitated by DC technology with power electronics interfaces. However, studies on FC integration have primarily focused on small-scale applications with centralized control architectures. There has been little research on the modular control of multiple FC and battery modules in SPS. This study proposes a decentralized droop-based power sharing approach with load frequency decoupling to efficiently utilize power system modules based on their dynamic capabilities. The proposed strategy further incorporates decentralized voltage regulation and state-of-charge (SoC) management functions. The methodology was applied to a short-sea cargo vessel with an FC-battery DC power system. The results indicate that the mission load profile can be satisfied while limiting fluctuations in the FC output power. Moreover, the proposed strategy achieves the same voltage regulation performance as a centralized proportional-integral (PI) controller and can be easily tuned to achieve load frequency decoupling with the desired time constant. Finally, a comparative analysis shows how the trade-off between the dynamic operation of the FC and the discharge depth of the ESS is affected by the choice of time constant.

Keywords: DC power distribution, Frequency decoupling, Fuel cells, Power sharing, Shipboard power system

1 INTRODUCTION

Whereas the maritime industry could rely on internal combustion engines and a direct-driven topology in the past, technological advances as well as regulatory and environmental challenges drive innovation in the design of shipboard power systems (SPSs) [1]. The electrification and incorporation of energy storage systems (ESSs) into an integrated power system (IPS) are among the key trends observed in power system designs [2]. Moreover, the aim of reducing the dependency on fossil fuels has brought fuel cells (FCs) into play as an alternative to diesel generators as power supplies [3], [4]. One central enabling technology facilitating the integration of FC-battery hybrid systems is the DC distribution technology. This is further supported by power electronics interfaces that achieve a high degree of controllability of power flows in the system [5]. Recent developments further point to the benefits of integrating these subsystems in a modular fashion, making them easily replaceable and allowing for an expansion of the SPS [6], [7].

A challenge lies in the question of how multiple power generation and storage modules with different dynamic and steady-state characteristics can be efficiently coordinated [8]. A power system is required to provide sufficient power under fluctuating loads while minimizing fuel costs and component wear [9]. FCs, in particular, suffer from high efficiency losses and lifetime degradation if not operated with low output gradient and within an efficient operation band [10]. Considering the presence of different power generation characteristics and the goal of achieving an easily reconfigurable power system with plug-and-play (PnP) capability, a suitable control strategy is required to meet these requirements. A decentralized control architecture is generally regarded as advantageous in terms of scalability and reconfigurability of the power system [11], [12]. Droop control using a virtual resistance is the most common method for achieving decentralized power sharing. However, this leads to voltage deviations and inefficient power sharing under transient loads [9], [13]. A goal in hybrid power systems is to decouple the load frequencies using the battery to cover high load gradients so that the main supply can operate efficiently and at low stress [2].

@2023 Walker & Coraddu & Savio & Oneto published by TU Delft OPEN Publishing on behalf of the authors. Licensed under a Creative Commons Attribution CC BY license.

DOI: https://doi.org/10.59490/moses.2023.670

The approaches for coordinated control in the FC-battery SPS found in the literature are dominated by centralized solutions, typically involving only a single FC and battery. This is realized, e.g., using PI-controllers as in [14]–[16] or via rule-based approaches as in [16]–[19]. Load-frequency separation is also a popular objective for the control of a hybrid energy storage system (HESS) [20]–[22]. The current literature fails to account for larger hydrogen-based DC SPS with multiple parallel components, in which one centralized controller is no longer feasible. Moreover, such centralized solutions do not offer the desired modular characteristics. Accordingly, this study aims to develop a method for dynamic power sharing among multiple FC and ESS in an SPS using a decentralized architecture as a scalable and reconfigurable solution.

A virtual impedance-based approach for decentralized HESS-control using capacitive droop elements was described in [23]. This concept is extended by an inductive droop controller in this study to achieve droop-based frequency decoupling for batteries and FCs. The decentralized architecture facilitates the extension of the power system with further components, which can be parameterized according to their dynamic characteristics to cover the total load demand. Additionally, each local controller's reference voltage is constantly adapted to achieve a secondary function. Whereas the reference of the FC droop control is adapted such that the DC bus voltage is regulated to its nominal value, the voltage adaption in the ESS aims to manage and balance their state of charge (SoC). Accordingly, the main contribution of this study is a decentralized coordinated control strategy for DC SPS, that achieves a simultaneous load frequency decoupling, voltage regulation, and SoC management. The developed methodology is finally showcased in numerical simulations at the example of a short-sea cargo ship.

The remainder of this paper is organized as follows. Section 2 elaborates on the SPS design considered in this study. The modeling is described in Section 3. The main contribution of this study, i.e., the coordinated control strategy, is detailed in Section 4. Finally, Section 5 presents the simulation scenarios and results, followed by an overview of the main conclusions of this study in Section 6.

2 SYSTEM DESCRIPTION

The proposed control strategy was developed for all-electric ships (AESs) with predominantly propulsive loads, which is the case for cargo vessels. Hence, the main power demand is for the electric propulsion. On the power generation side, a hybrid energy system, consisting of multiple main power supplies and ESSs, was considered. This work investigates an FC-battery hybrid SPS, however, the methodology is applicable to alternative generation and storage technologies as well. Furthermore, DC distribution offers several advantages, such as increased efficiency [24] and operational flexibility [5]. It is particularly suitable for DC sources, as is the case with FCs and batteries, which are interfaced via DCDC converters.

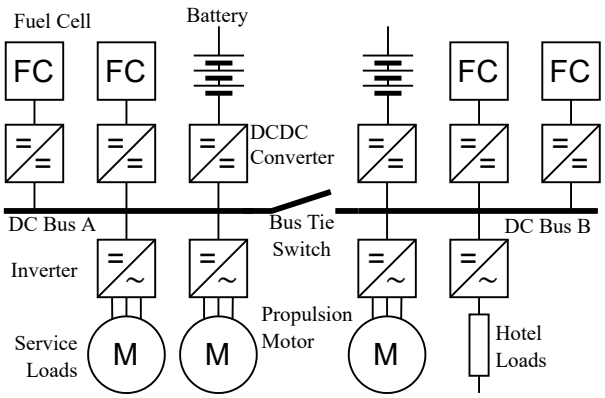

Figure 1: Power system topology of case study

A short-sea cargo vessel operating in the Baltic and North Sea, with a maximum propulsive power of 1.2 MW, serves as a case study. The original system was fitted with a diesel direct-drive propulsion. For this research, a virtual retrofit of its SPS was conducted by fitting the vessel with an FC-battery hybrid system. The resulting system, equipped with four FC and two battery systems in a dual-bus configuration, is shown in Fig. 1. The power and energy ratings of the components are listed in Table 1. Real propulsive power measurements from various missions of the original system are available and used as inputs for the simulation of the SPS model. The comparably low hotel loads of the cargo vessel are neglected in the scope of this study.

Table 1: Case study parameters

Param.	Description	Value
V_{DC}	DC-link voltage	700 V
P_{FC}	FC power rating (x4)	325 kW
P_{bat}	Battery power rating (x2)	325 kW
C_{bat}	Battery capacity (x2)	225 kWh
P_{em}	Prop. motor rating (x2)	600 kW

The power rating of the batteries is selected such that one battery can deliver the same output power

as an FC at its peak, i.e., 325 kW. This allows short-time compensation for the loss of one main power supply via the batteries while still having a second battery covering transient loads.

3 MODELING

The focus of this work is the development of control strategies. Power system and component models are required to evaluate these strategies. Because the emphasis is on system-level control, simple dynamic models are implemented to build a simulation environment for the complete SPS. The following sections describe the approaches for modeling FCs, batteries and converters, and how they interact with one another and the load current via the DC-link.

3.1 Fuel Cell

The FC models used in this work were implemented according to [25]. A beneficial feature of this model is that it can be parameterized using manufacturer data. Hence, the real components can be easily represented.

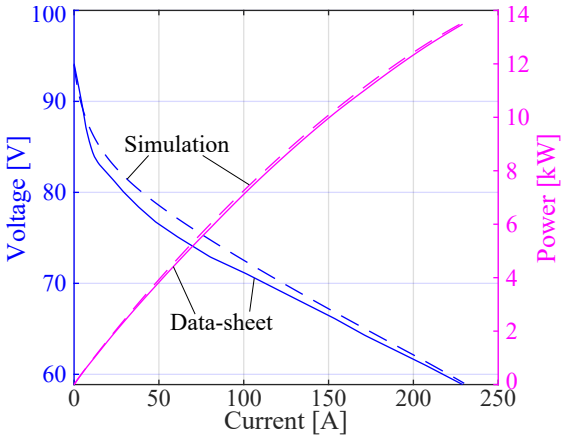

Figure 2: Polarization curve and power output of Nedstack FCS 13 XXL module, from data-sheet and simulation in steady-state

The FC systems investigated in this paper are based on the Nedstack FCS 13 XXL, a proton-exchange membrane fuel cell (PEMFC) module with a maximum output power of 13.6 kW [26]. To achieve the targeted 325 kW per FC system in the SPS, 24 modules are stacked together, with six parallel-connected strands of four modules in series. Figure 2 shows the polarization curves and power outputs of a single module from the manufacturer's data-sheet against the simulation results obtained using the described model in steady-state operation. The mean absolute percentage error (MAPE) of the output voltage between the simulation and data-sheet is 1.6 %, which is sufficiently accurate for the purpose of this research.

3.2 Battery

For the batteries, a model of similarly low fidelity as that for the FCs was used, as reported in [27]. It is based on single cell modeling, and in this study, generic values for Li-ion battery cells, as reported in the source, are used. Furthermore, multiple cells are connected in series and parallel such that the desired voltage, power, and energy levels of the battery packs are reached.

3.3 DCDC Converter

A dynamic model of a DCDC converter for maritime power systems is presented in [28]. It is an averaged model that describes the current dynamics while neglecting any losses in the system. Originally, the DCDC converter included a transformer stage. However, for the purpose of this paper, an averaged representation of a half-bridge is sufficient, and can be used as either a uni- or bi-directional converter, as in [29]. The dynamics of the average inductor current I_L in an ideal half-bridge topology can be computed as

$$\frac{dI_L}{dt} = \frac{1}{L}(V_{in} - (1-D)V_{out}) \qquad (1)$$

where V_{in} and V_{out} denote the source and output voltages, respectively; L is the main inductance and D the duty cycle of the switches, which functions as the control input. In the considered topology, the converter is directly interfaced to the DC bus, hence V_{out} equals the DC-link voltage V_{DC}. The DCDC converter is equipped with a PI current controller, tuned to operate at a bandwidth of 1 kHz. Hence, local controllers that generate the current reference for the DCDC converters can operate at 100 Hz.

3.4 DC-Link and Load

The DC distribution system in a ship is characterized by short lines with low impedance. For this reason, the DC-link can be modeled as a single capacitor, neglecting the losses and inductances in the network. The DC-link capacity C_{DC} is the sum of the output capacitors of all N adjacent DCDC converters $C_{out,i}$. Accordingly, the time derivative of the DC-link voltage $\dot{V}_{DC}$ can be computed as:

$$\dot{V}_{DC} = \frac{1}{C_{DC}}(\sum_{i=1}^{N} I_{out,i} - I_{load}) \qquad (2)$$

$$C_{DC} = \sum_{i=1}^{N} C_{out,i} \tag{3}$$

Furthermore, the load current can be derived from a given power profile P_{load} as

$$I_{load} = P_{load}/V_{DC} \tag{4}$$

4 COORDINATED CONTROL

The coordinated control in the FC-battery hybrid power system determines the current references for all integrated power generation and energy storage modules. This work focuses on the following three main functionalities of coordinated control in an SPS:

- (dynamic) Power sharing
- Voltage regulation
- SoC management

The importance of each of these three functionalities and a method for implementing them in a decentralized architecture are addressed in the following sections.

4.1 Dynamic Power Sharing

Virtual impedance-based droop control is used in this work to achieve the proposed modular characteristic for the coordinated control. The decentralized architecture of droop control schemes s fundamentally modular due to its lack of communication network. While traditional resistive droop control is appropriate for power sharing under steady-state conditions, additional capacitive or inductive droop elements can be used to improve power sharing under dynamic loads. The approach of using capacitive droop elements for DC microgrid control in [30] was applied to a HESS integrated into an SPS by [23] to achieve load frequency decoupling between different ESS technologies. Whereas a capacitive droop controller serves as a high-pass filter, this work proposes an extension of droop schemes with an inductive element to create a low-pass filter (LPF). Such a droop controller is an appropriate tool for controlling the power output of power supplies with slow dynamic capabilities, such as FCs. Figure 3 shows the equivalent circuits describing the functioning principle of different droop schemes. The corresponding transfer functions of the DC link voltage deviation $\Delta V = V_{ref} - V_{DC}$ to the current reference are as follows:

$$\frac{I_{d,R}}{\Delta V} = \frac{1}{R_{d,RL}} \tag{5}$$

$$\frac{I_{d,RC}}{\Delta V} = \frac{sC_{d,RC}}{sR_{d,RC}C_{d,RC} + 1} \tag{6}$$

$$\frac{I_{d,RL}}{\Delta V} = \frac{1}{R_{d,RL} + sL_{d,RL}} \tag{7}$$

where $I_{d,x}$ is the computed reference current for the droop-controlled source. $R_{d,x}$, $C_{d,x}$, and $L_{d,x}$ describe the virtual resistance, capacitance and inductance, C_{DC} isthe DC-link capacity; V_{ref} and V_{DC} are the reference and actual DC-link voltages, respectively.

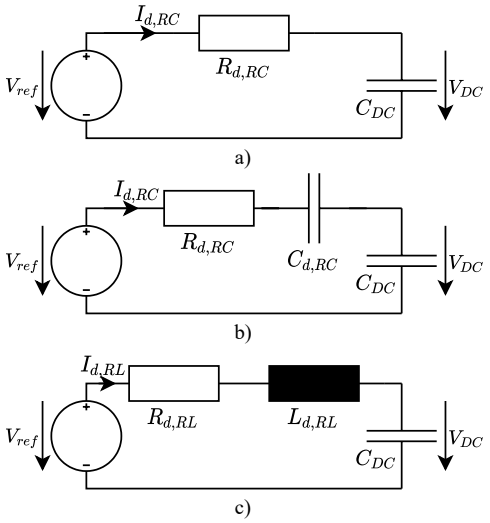

Figure 3: Virtual impedance control with a) classic resistive (subscript R) droop, b) resistive-capacitive (RC) droop, c) resistive-inductive (RL) droop

To achieve the desired frequency separation, a resistive-inductive droop scheme, as described by (7), is used in the local controllers of the FC systems. The battery controllers are equipped with a complementary resistive-capacitive droop controller according to (6). For the consistent behavior of the power system under dynamic operation, a series of guidelines for tuning the control parameters are proposed:

- The total droop resistance of the main power supplies and the ESS should be equal so that a consistent response of the power system in dynamic and steady-state operation is obtained.
- The total droop resistance should be selected such that the bandwidth of the DC bus voltage regulation is at least one order of magnitude slower than the current control of the DCDC converters.
- The droop resistances of the FC controllers should be inversely proportional to their rated power. The same approach shall be applied for the ESS.

- In the proposed FC-hybrid system, the time constants of the RC and RL filters should be equal, to allow a smooth transition from batteries to FC as a power source.
- Reducing the time constant will yield a higher dynamic capability, allowing the generation-side to cover higher load gradients, which would otherwise be inhibited by the limited power of the batteries. However, a higher time-constant lowers the output gradients of the FCs, reducing their degradation.

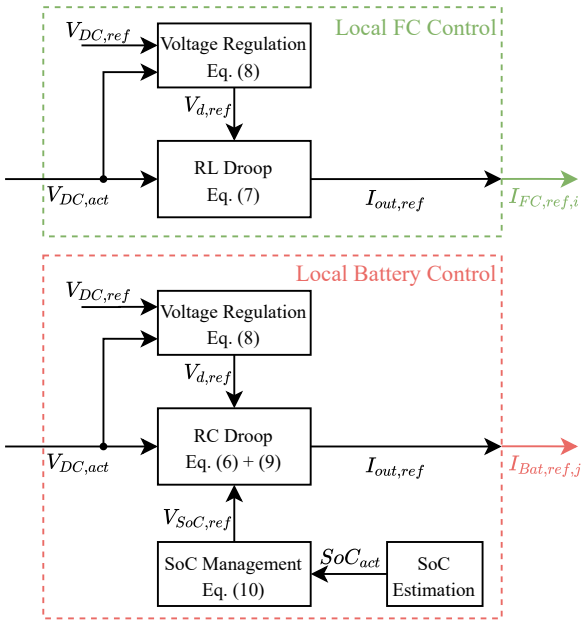

Figure 4: Decentralized control of FC and batteries with voltage regulation and SoC management

4.2 Voltage Regulation

It is desirable to maintain the DC link voltage at its nominal level to provide a certain quality of power supply and minimize transmission losses in the DC network. Traditional droop control schemes lead to a voltage drop on the main bus proportional to the delivered power [31]. For this reason, an additional voltage regulation function was added to the proposed droop-based power sharing strategy. A local implementation of this functionality maintains the modular control architecture. Hence, all the local controllers are equipped with an independent voltage regulation control. The proposed method is an integral adaptation of the reference voltage in the local droop controller based on the measured DC link voltage deviation. Accordingly, the voltage reference $V_{d,ref}$ in the local droop controllers of the sources is computed as:

$$V_{d,ref} = V_{DC,ref} + k_V \int V_{DC,ref} - V_{DC,act} dt \quad (8)$$

where k_V is the integral coefficient for voltage regulation and $V_{DC,ref}$ denotes the DC bus voltage reference. To avoid circulating currents between components, it is vital that deviations of $V_{d,ref}$ between local controllers are kept at a minimum. In the scope of this work, it is assumed that this can be achieved through an appropriate tuning of the control parameters. However, this challenge requires further attention in future research.

4.3 SoC Management

The limited energy capacity and power capability of battery storage systems act as constraints on the overall system control. The SoC management of ESS encompasses two main challenges.

First, it must be ensured that the SoC remains within certain boundaries, e.g. between 20 % and 80 % as in [32]. The usable energy is limited to account for capacity degradation, whereas deep discharge is avoided to prevent damagess and safety risks. Moreover, in steady-state the ESSs shall follow a reference SoC centered between the defined limits to withhold an equal positive and negative reserve for compensating load fluctuations.

Second, in the presence of multiple parallel ESS, differences in operation and parameter deviations lead to SoC imbalance. Hence, an additional objective of the power system control is to eliminate these imbalances under steady-state conditions.

These objectives imply the need for an extension of the control strategy by an SoC management functionality. As before, a decentralized approach is proposed. Because the SoC is an individual variable of every ESS, the coordination of this function between parallel devices is not required. An additional SoC-dependent term $V_{\mathrm{SoC},ref}$ is introduced to achieve the desired charge and discharge of the ESS. The adjusted reference voltage for the droop $V^*_{d,ref}$ is computed as:

$$V^*_{d,ref} = V_{d,ref} + V_{SoC,ref} \quad (9)$$

$$V_{\mathrm{SoC},ref} = k_{\mathrm{SoC}} \int (\mathrm{SoC}_{ref} - \mathrm{SoC}_{act})^{\alpha} dt \quad (10)$$

where SoC_{ref} and SoC_{act} are the reference and actual SoC values and k_{SoC} is the integral coefficient

of the SoC management strategy. The shape factor α describes the relationship between SoC deviation and charging current. Because the batteries use an RC droop controller, integration in (10) is required to produce the desired current.

Parameters k_{SoC} and α are selected such that the ESS provides its maximum discharge current $I_{ESS,max}$ at its maximum allowable charge. Accordingly, the minimum discharge current - $I_{ESS,max}$ is targeted at the lower SoC threshold to charge the ESS. Coefficient α determines the shape of the current reference over the SoC range. The curves for various values are plotted in Fig. 5. The smaller the value of $\alpha \in (0, \infty)$, the more stringently the SoC management function regulates the battery charge towards its reference value. A graphical representation of the local controllers for the FCs and ESSs is shown in Fig. 4.

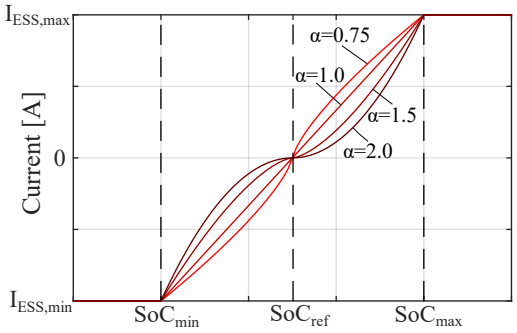

Figure 5: Relationship of individual battery SoC and targeted discharge current depending on shape factor α

5 SIMULATION RESULTS

The models of the SPS components as well as the methodology described in the previous section are implemented in MATLAB Simulink. Several simulation scenarios were constructed based on the case study described in Section 2 to evaluate and compare the proposed strategies to a benchmark controller.

5.1 Centralized Control with LPF

A centralized PI controller with an LPF was implemented as a benchmark, similar to the work in [21]. The central controller directly generates current references for all local controllers, requiring high-bandwidth communication. Furthermore, this strategy requires global awareness of all component parameters and states. The advantage of this architecture is that no coordination among the local controllers is required. It achieves accurate tracking of the reference DC link voltage as well as frequency decoupling according to the filter time constant τ_{LPF}.

The control strategy is illustrated in Fig. 6. The PI controller determines the reference current to stabilize and restore the DC link voltage. The low-frequency parts of this current are supplied by all FCs, while the batteries cover the remainder. The reference currents are distributed among parallel components proportional to their power rating.

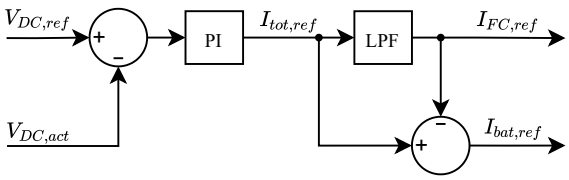

Figure 6: Centralized control strategy with LPF for frequency decoupling between FCs and batteries

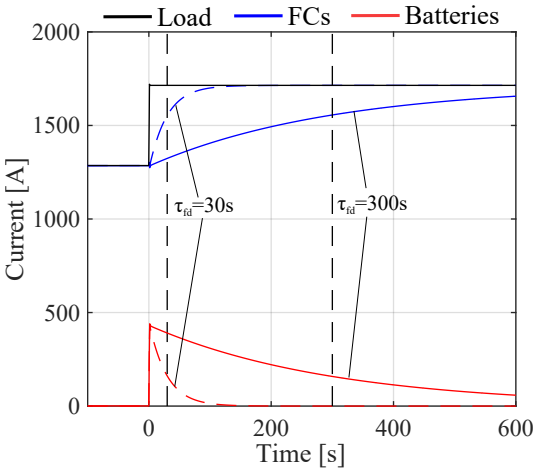

Figure 7: Total output current of FC and battery systems after a load step using the centralized PI control with LPF and time constants of 30s(dashed) and 300s(solid)

In the first simulation, the step response of the power system was investigated. Measurements of the propulsive power, taken during a mission of the reference cargo vessel, show an average load of 900 kW during cruising. Taking this value as the starting point, the step to full propulsive power of 1200 kW was investigated. In this scenario, the initial power load was assumed to be completely supplied by the FCs. To avoid high power gradients for the FCs, the LPF time constant τ_{LPF} was chosen to be in the range of multiple seconds to minutes. Two step responses with $\tau_{LPF} = 300\,\mathrm{s}$ and $30\,\mathrm{s}$ were analyzed to compare the effects of different time constants. The PI controller was tuned such that its poles are in the area of 10 Hz, approximately

10 times slower than the underlying current control.

The resulting step responses are displayed in Fig. 7. The FCs react to the load change according to the LPF; therefore at $t = \tau_{LPF}$ the output current reaches 63.2 % of its final value. The battery supplies the remaining difference between load and FC power, and additionally stabilizes the DC link voltage, which remains within 5 V of the nominal DC link voltage of 700 V.

5.2 Decentralized Control Strategy

The proposed strategy aims to achieve the same performance as the central controller using a decentralized architecture. For this purpose, the total droop resistance was chosen such that it equals the inverse of the proportional factor of the PI controller in the benchmark strategy. Furthermore, the time constant for frequency decoupling τ_{fd} is adjusted by sizing the virtual inductances and capacitances such that $\tau_{fd} = R_{d,rc}C_{d,rc} = L_{d,rl}/R_{d,rl}$.

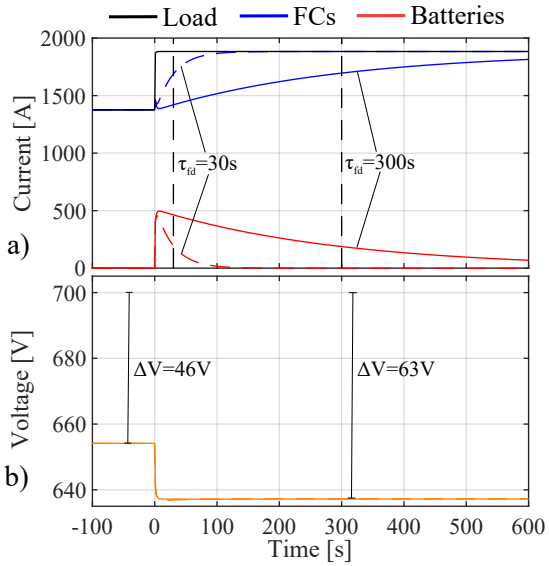

Figure 8: Load step response with decentralized strategy with τ_{fd}=30 s(dashed) and 300 s(solid) a) FC, battery and load currents, b) DC bus voltage

Initially, voltage regulation and SoC management are not implemented and the power system with the virtual impedance based droop is subjected to the same load step as the benchmark strategy in Section 5.1. The simulation results in Fig. 8 show that frequency decoupling is achieved as accurately as with the benchmark, matching the chosen τ_{fd}. The steady-state deviation resulting from the droop scheme, which lack an integral action, amounts to 63 V at full load. The reduced DC bus voltage requires higher currents and therefore increases conduction losses. Furthermore, the power quality can be insufficient for sensitive loads, and a sudden change in voltage is challenging for accurate current control in DCDC converters.

5.3 Voltage regulation

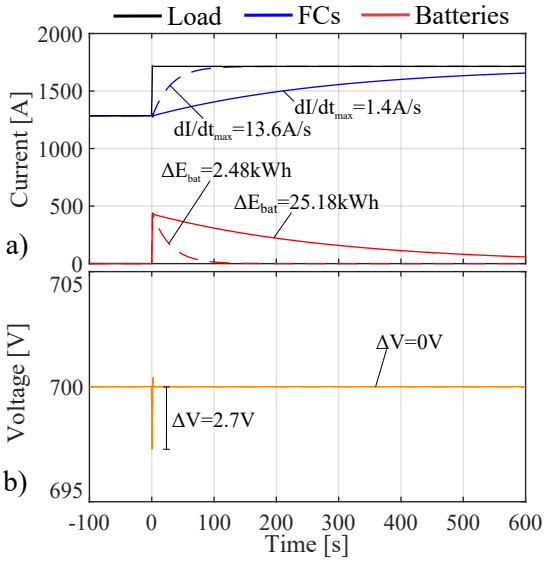

Figure 9: Load step response with decentralized strategy incl. voltage regulation with τ_{fd}=30 s(dashed) and 300 s(solid) a) FC, battery and load currents, b) DC bus voltage

In the next step, the same step response as before was simulated with the proposed strategy including the voltage regulation scheme described in Section 4.2. The gain k_V in (8) was selected to match the integral action of the benchmark's PI controller. Hence, the overall voltage control, tuned based on the DC bus capacitance, was designed to achieve a bandwidth of 100 Hz, ensuring that it is one order of magnitude slower than the local current control loops. It is vital to make k_V equal in all local controllers such that the same $V_{d,ref}$ is obtained. The differing dynamics and power ratings of the components are already represented in the virtual impedances. The step response obtained using this strategy is displayed in Fig. 9. The resulting curves of the FC and battery currents are equal to those of the benchmark, indicating that the same behavior of a centralized PI controller with an LPF can be achieved in a decentralized architecture. Additionally, this design of power sharing and voltage regulation achieves accurate tracking of the nominal DC bus voltage. Initially after the load step, a voltage drop of only 2.7 V can be observed with no steady-state error.

Furthermore, Fig. 9 shows the implications of changing the time constant τ_{fd}. With 300 s, a to-

tal of 25.18 kWh of battery charge is required to compensate for the difference between load and FC power, while the maximum current gradient of the FC systems is limited to 1.4 A/s. Reducing the time constant by a factor of ten, proportionally reduced the required battery charge. However, the current gradient of the FCs increased by the same factor, leading to higher degradation. This comparison highlights the underlying trade-off between the required battery charge and dynamic operation of the FCs when selecting the time constant.

5.4 SoC Management

To evaluate the SoC management function, described in Section 4.3, the SoCs of the two batteries were set to different initial values during the simulation. The constant load demand is entirely covered by the FCs, hence the batteries do not participate in load sharing and voltage regulation. The initial SoCs of batteries A and B are set to different values, as in [33]. Here, 70 % and 40 % were selected as the starting values. All batteries followed a reference SoC of 50 %. The shape factor α in (10) was set to 0.75, 1.0, 1.5 and 2.0, for a series of simulations.

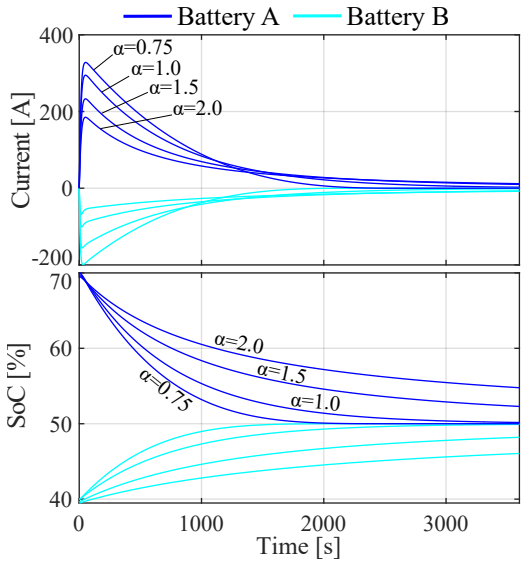

Figure 10: Convergence of two batteries' SoC towards reference value for different shape factors α

The resulting behaviors of the discharge current and SoCs over time for both batteries are shown in Fig. 10. As expected, a low shape factor yields a faster convergence towards the reference value. However, a high factor leads to a lower charging current, interfering less with other functionalities as long as the SoC is kept close to the reference. Additionally, the test case shows that different charges in parallel batteries are balanced over time.

5.5 Mission simulation

Finally, the complete proposed control strategy was evaluated using a realistic power profile from the reference short-sea cargo vessel. The considered mission, shown in Fig. 11, has a duration of ca. 30 h and was measured at 5 min intervals. For the simulation, running at 10 ms steps, the measured values were linearly interpolated.

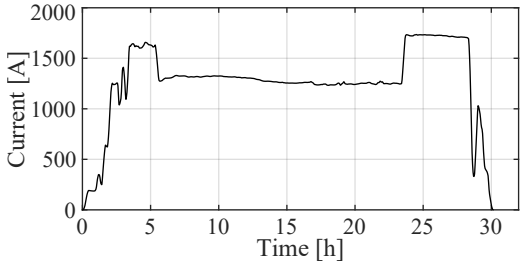

Figure 11: Power demand of exemplary mission used for the simulations

The focus of this investigation is to observe how the FCs' power output is adjusted when subjected to a real operating profile over a longer time and to what extent batteries are required to achieve a power balance. Three mission simulations were performed with varying time constants τ_{fd} for the frequency decoupling. Because multiple control functionalities act on the power system, it is key to ensure that they do not interfere with each other. As discussed in Section 5.3, the current and voltage control bandwidths are separated by tuning the control parameters. In the same manner, the slower control loops, i.e. the frequency decoupling and the SoC management, need to be separated to avoid them interfering with one another. For this purpose, the shape factor α was set to 2.0 so that the slope of the charging current around the target SoC was flat, reducing the charging dynamics as shown in Fig. 10. Doing so ensures that the SoC management acts more slowly than the frequency decoupling.

Figure 12 shows the resulting current curves of the FCs and batteries next to each other for the first segment of the mission profile until the vessel reaches a steady power demand at the cruising speed. Table 2 summarizes the key numbers from the simulations, including the batteries' SoC ranges, as well as maximum charge and discharge currents. Load cycling is reported to be detrimental to the health of PEMFC [34], [35]. In [36], a linear degradation factor for transient loads on the cell voltage decay was used. Hence, the average absolute value of the FC power gradient $|\dot{P}_{FC}|_{avg}$ is listed as a proxy for assessing the effect of FC operation on

degradation. Given the FC output $P_{FC,n}$ and time at the n-th simulation step t_n, it is computed as:

$$|\dot{P_{FC}}|_{avg} = \frac{1}{N}\sum_{n=1}^{N}\frac{|P_{FC,n} - P_{FC,n-1}|}{t_n - t_{n-1}} \quad (11)$$

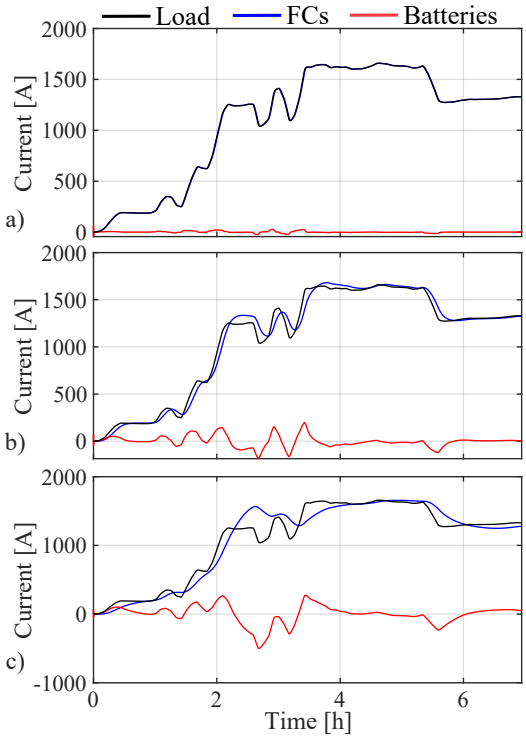

Figure 12: Total FC, battery and load currents with proposed strategy in mission simulation with τ_{fd}=30 s(a), 300 s(b) and 900 s(c)

Table 2: Evaluation of mission simulation

τ_{fd}	30 s	300 s	900 s
SoC_{min}	48.4 %	39.3 %	26.0 %
SoC_{max}	51.5 %	63.9 %	84.2 %
$P_{bat,min}$	−17 kW	−143 kW	−268 kW
$P_{bat,max}$	25 kW	121 kW	256 kW
$\|\dot{P_{FC}}\|_{avg}$	49.8 $\frac{W}{s}$	45.4 $\frac{W}{s}$	35.6 $\frac{W}{s}$

The results show that the FC follows the load closely, and little power and energy are demanded from the batteries with a low time constant. However, a higher time constant smoothens the power output of the FCs, reducing their power gradients and, consequently, their degradation. At a time constant of 900 s, the SoC-limits were fully exploited, leading to a minimized transient operation of the FCs. Overcharging above 80 % is caused by allowing a battery operation slightly above the batteries' ratings to avoid instability of the DC voltage. The results underscore the importance of selecting the time constant in a manner that aligns with the ship operator's objectives the trade-off between the discharge depth of the batteries and the transient loading of the FCs. It is important to note that an increased discharge depth negatively influences the battery lifetime, which must be considered in this trade-off. The simulated operation range of the batteries also shows that they may be sized significantly smaller when a small time constant is chosen to reduce capital expenditure.

6 CONCLUSIONS

Although FC-battery hybrid power systems with DC distribution are emerging as a promising solution for zero-emission shipping, the coordinated control of multiple power system resources remains a challenge. An appropriate control strategy can ensure power balance in the system while accounting for the different characteristics of the generation and storage technologies.

Especially in larger systems, a modular approach for integration and control appears to be a viable approach, as it can facilitate the reconfiguration and extension of the SPS by offering PnP capability. For this purpose, a decentralized coordinated control strategy based on virtual impedance droop controllers was presented as an alternative to centralized control. The proposed method achieves an excellent tracking of the DC bus voltage while decoupling the load power into low and high frequencies so that they can be covered by FCs and batteries, respectively. A trade-off is required between the dynamic operation of the main power supplies and the used power and energy of the batteries, affecting their degradation. This can be influenced by the time constant selection in the local droop controllers. It could be shown that the decentralized solution can achieve the same quality in dynamic power sharing and load tracking as a centralized PI controller with an LPF.

Hence, the developed method provides a decentralized control strategy capable of coordinating multiple power supplies and ESSs with different characteristics in large SPS. However, varying component parameters, e.g. owing to aging effects, and the effect of the operation strategy on system efficiency have not been accounted for in this study. Lack of awareness of specific system-wide parameters and variables in a decentralized architecture, e.g. the operating state and control parameters, are further challenges that will be addressed in future work. One possible solution is to investigate a low-

bandwidth communication network that can facilitate information sharing among local controllers. Furthermore. the introduction of a central controller enables the online adjustment of control parameters based on the operating conditions and changing component states and characteristics. The steady operation of FC already contributes to their efficient utilization. However, an explicit consideration and optimization of the overall system efficiency to reduce fuel consumption is planned.

ACKNOWLEDGMENTS

This research is supported by the *Sustainable Hydrogen Integrated Propulsion Drives (SH2IPDRIVE)* project, which has received funding from RvO (reference number MOB21013), through the RDM regulation of the Ministry of Economic Affairs and Climate Policy.

REFERENCES

[1] J. F. Hansen and F. Wendt, "History and State of the Art in Commercial Electric Ship Propulsion, Integrated Power Systems, and Future Trends," *Proceedings of the IEEE*, vol. 103, no. 12, pp. 2229–2242, Dec. 2015.

[2] M. U. Mutarraf, Y. Terriche, K. A. K. Niazi, J. C. Vasquez, and J. M. Guerrero, "Energy Storage Systems for Shipboard Microgrids—A Review," p. 32, 2018.

[3] C. Nuchturee, T. Li, and H. Xia, "Energy efficiency of integrated electric propulsion for ships – A review," *Renewable and Sustainable Energy Reviews*, vol. 134, p. 110 145, Dec. 2020.

[4] L. van Biert, M. Godjevac, K. Visser, and P. Aravind, "A review of fuel cell systems for maritime applications," *Journal of Power Sources*, vol. 327, pp. 345–364, Sep. 2016.

[5] L. Xu, J. Guerrero, A. Lashab, *et al.*, "A Review of DC Shipboard Microgrids—Part I: Power Architectures, Energy Storage, and Power Converters," *IEEE Transactions on Power Electronics*, vol. 37, no. 5, pp. 5155–5172, May 2022.

[6] M. S. Sadabadi, Q. Shafiee, and A. Karimi, "Plug-and-Play Robust Voltage Control of DC Microgrids," *IEEE Transactions on Smart Grid*, vol. 9, no. 6, pp. 6886–6896, Nov. 2018.

[7] H. Xing, C. Stuart, S. Spence, and H. Chen, "Fuel Cell Power Systems for Maritime Applications: Progress and Perspectives," *Sustainability*, vol. 13, no. 3, p. 1213, Jan. 2021.

[8] L. Xu, J. Guerrero, A. Lashab, *et al.*, "A Review of DC Shipboard Microgrids—Part II: Control Architectures, Stability Analysis, and Protection Schemes," *IEEE Transactions on Power Electronics*, vol. 37, no. 4, pp. 4105–4120, Apr. 2022.

[9] Y. Han, X. Ning, P. Yang, and L. Xu, "Review of Power Sharing, Voltage Restoration and Stabilization Techniques in Hierarchical Controlled DC Microgrids," *IEEE Access*, vol. 7, pp. 149 202–149 223, 2019.

[10] N. Shakeri, M. Zadeh, and J. Bremnes Nielsen, "Hydrogen Fuel Cells for Ship Electric Propulsion: Moving Toward Greener Ships," *IEEE Electrification Magazine*, vol. 8, no. 2, pp. 27–43, Jun. 2020.

[11] T. Dragicevic, X. Lu, J. Vasquez, and J. Guerrero, "DC Microgrids–Part I: A Review of Control Strategies and Stabilization Techniques," *IEEE Transactions on Power Electronics*, pp. 1–1, 2015.

[12] Z.-X. Xiao, Y.-Z. Guan, H.-W. Fang, Y. Terriche, and J. M. Guerrero, "Dynamic and Steady-State Power-Sharing Control of High-Efficiency DC Shipboard Microgrid Supplied by Diesel Generators," *IEEE Systems Journal*, vol. 16, no. 3, pp. 4595–4606, Sep. 2022.

[13] B. Zahedi and L. E. Norum, "Voltage regulation and power sharing control in ship LVDC power distribution systems," in *2013 15th European Conference on Power Electronics and Applications (EPE)*, Sep. 2013, pp. 1–8.

[14] C.-L. Su, X.-T. Weng, and Ching-Jin Chen, "Power generation controls of fuel cell/energy storage hybrid ship power systems," in *2014 IEEE Conference and Expo Transportation Electrification Asia-Pacific (ITEC Asia-Pacific)*, Beijing, China: IEEE, Aug. 2014, pp. 1–6.

[15] H. Chen, Z. Zhang, C. Guan, and H. Gao, "Optimization of sizing and frequency control in battery/supercapacitor hybrid energy storage system for fuel cell ship," *Energy*, vol. 197, p. 117 285, Apr. 2020.

[16] L. Balestra and I. Schjølberg, "Energy management strategies for a zero-emission hybrid domestic ferry," *International Journal of Hydrogen Energy*, vol. 46, no. 77, pp. 38 490–38 503, Nov. 2021.

[17] J. Han, J.-F. Charpentier, and T. Tang, "An energy management system of a fuel cell/battery hybrid boat," *Energies*, vol. 7, no. 5, pp. 2799–2820, 2014.

[18] A. M. Bassam, A. B. Phillips, S. R. Turnock, and P. A. Wilson, "Development of a multi-scheme energy management strategy for a hybrid fuel cell driven passenger ship," *International Journal of Hydrogen Energy*, vol. 42, no. 1, pp. 623–635, Jan. 2017.

[19] L. Zhu, J. Han, D. Peng, T. Wang, T. Tang, and J.-F. Charpentier, "Fuzzy logic based energy management strategy for a fuel cell/battery/ultracapacitor hybrid ship," in *2014 First International Conference on Green Energy ICGE 2014*, Mar. 2014, pp. 107–112.

[20] Z. Jin, L. Meng, J. C. Vasquez, and J. M. Guerrero, "Frequency-division power sharing and hierarchical control design for DC shipboard mi-

crogrids with hybrid energy storage systems," in *2017 IEEE Applied Power Electronics Conference and Exposition (APEC)*, Mar. 2017, pp. 3661–3668.

[21] K. Kwon, D. Park, and M. K. Zadeh, "Load Frequency-Based Power Management for Shipboard DC Hybrid Power Systems," in *2020 IEEE 29th International Symposium on Industrial Electronics (ISIE)*, Jun. 2020, pp. 142–147.

[22] P. Xie, S. Tan, N. Bazmohammadi, *et al.*, "A distributed real-time power management scheme for shipboard zonal multi-microgrid system," *Applied Energy*, vol. 317, p. 119 072, Jul. 2022.

[23] J. Khazaei, "Optimal Flow of MVDC Shipboard Microgrids With Hybrid Storage Enhanced With Capacitive and Resistive Droop Controllers," *IEEE Transactions on Power Systems*, vol. 36, no. 4, pp. 3728–3739, Jul. 2021.

[24] B. Zahedi, L. E. Norum, and K. B. Ludvigsen, "Optimized efficiency of all-electric ships by dc hybrid power systems," *Journal of Power Sources*, vol. 255, pp. 341–354, Jun. 2014.

[25] S. N. M., O. Tremblay, and L.-A. Dessaint, "A generic fuel cell model for the simulation of fuel cell vehicles," in *2009 IEEE Vehicle Power and Propulsion Conference*, Sep. 2009, pp. 1722–1729.

[26] *FCS 13-XXL — Nedstack*, https://nedstack.com/en/pem-fcs-stack-technology/fcs-13-xxl.

[27] O. Tremblay, L.-A. Dessaint, and A.-I. Dekkiche, "A Generic Battery Model for the Dynamic Simulation of Hybrid Electric Vehicles," in *2007 IEEE Vehicle Power and Propulsion Conference*, Sep. 2007, pp. 284–289.

[28] B. Zahedi and L. E. Norum, "Modeling and Simulation of All-Electric Ships With Low-Voltage DC Hybrid Power Systems," *IEEE Transactions on Power Electronics*, vol. 28, no. 10, pp. 4525–4537, Oct. 2013.

[29] A. Haseltalab, L. van Biert, H. Sapra, B. Mestemaker, and R. R. Negenborn, "Component sizing and energy management for SOFC-based ship power systems," *Energy Conversion and Management*, vol. 245, p. 114 625, Oct. 2021.

[30] X. Chen, J. Zhou, M. Shi, L. Yan, W. Zuo, and J. Wen, "A Novel Virtual Resistor and Capacitor Droop Control for HESS in Medium-Voltage DC System," *IEEE Transactions on Power Systems*, vol. 34, no. 4, pp. 2518–2527, Jul. 2019.

[31] S. Peyghami, H. Mokhtari, P. Davari, P. C. Loh, and F. Blaabjerg, "On Secondary Control Approaches for Voltage Regulation in DC Microgrids," *IEEE Transactions on Industry Applications*, vol. 53, no. 5, pp. 4855–4862, Sep. 2017.

[32] L. Balestra, "Design of Hybrid Fuel Cell/Battery Systems for Maritime Vessels," Doctoral Thesis, NTNU, 2022.

[33] M. U. Mutarraf, Y. Guan, Y. Terriche, *et al.*, "Adaptive Power Management of Hierarchical Controlled Hybrid Shipboard Microgrids," *IEEE Access*, vol. 10, pp. 21 397–21 411, 2022.

[34] E. Pahon, S. Jemei, N. Y. Steiner, and D. Hissel, "Effect of Load Cycling on the Performance of Fuel Cell Stacks," in *2019 IEEE Vehicle Power and Propulsion Conference (VPPC)*, Oct. 2019, pp. 1–4.

[35] M. Jourdan, H. Mounir, and A. El Marjani, "Compilation of factors affecting durability of Proton Exchange Membrane Fuel Cell (PEMFC)," in *2014 International Renewable and Sustainable Energy Conference (IRSEC)*, Oct. 2014, pp. 542–547.

[36] T. Fletcher, R. Thring, and M. Watkinson, "An Energy Management Strategy to concurrently optimise fuel consumption & PEM fuel cell lifetime in a hybrid vehicle," *International Journal of Hydrogen Energy*, vol. 41, no. 46, pp. 21 503–21 515, Dec. 2016.

PROCEEDINGS OF MOSES2023 CONFERENCE
4TH INTERNATIONAL CONFERENCE ON MODELLING AND OPTIMISATION OF SHIP ENERGY SYSTEMS
26-27 OCTOBER 2023, DELFT, NETHERLANDS

Equivalent Consumption Minimization Strategy for Full-Electric Ship Energy Management with Multiple Objectives

Charlotte Löffler[a*], Rinze Geertsma[b], Despoina Mitropoulou[c], Henk Polinder[a], and Andrea Coraddu[a]

[a]Delft University of Technology, Delft, Netherlands
[b]Netherlands Defense Academy, Den Helder, Netherlands
[c]RH Marine, Schiedam, Netherlands
[*]c.loeffler@tudelft.nl

Abstract

Optimal energy management is still a challenge in full-electric vessels. New degrees of flexibility in the energy management resulting from the load sharing between multiple, heterogenous power sources lead to a suboptimal solution using rule-based control. Therefore, advanced control strategies present a solution to the challenge of finding the optimal control input for a nonlinear multi-objective power and energy problem in sufficient time. As additional benefit, advanced control allows to incorporate multiple objectives in the optimization such as minimization of several emissions, operational costs, and component degradation. Equivalent Consumption Minimization Strategy (ECMS) is a strategy for instantaneous optimization, which is promising for applications in vessels with a high degree of uncertainty in the load profile. It incorporates multiple objectives by assigning equivalent cost factors in the cost function, allowing a flexible expansion of the control problem. In this paper, we present a novel ECMS-based control strategy for a full-electric vessel with the ability to react flexibly to changing mission conditions. First, we define the objectives for the control problem, in this study CO_2 production, hazardous emission production, fuel consumption, energy cost, and the degradation of the battery. Second, we develop a pareto-front approach for a-posteriori definition of the equivalent cost factors. To showcase energy consumption reduction, we use a benchmark control based on state-of-the-art control strategies. A full-electric case study vessel with high uncertainty in the load profile is chosen to evaluate the proposed controller. Several different load profiles are generated and tested to evaluate the performance of the ECMS controller in dealing with different types of loads. The results will demonstrate the effectiveness of the proposed novel control strategy in reducing energy consumption while minimizing other hazardous emission outputs and preserving the health of the battery.

Keywords: Energy Management; Full-Electric Vessel; ECMS; Multiobjective Optimization; NOx emission.

1 INTRODUCTION

The electrification of vessels is an important step in the direction of climate-friendly transportation [1]. Full-electric vessels often combine heterogeneous power generation and storage components, which allows for a more fuel-efficient operation and decreased CO_2 emission [2]. However, this enhanced flexibility of the power generation also leads to a raised complexity of the system [3]. This raised system complexity leads to a non-optimal control solution using rule-based control (RBC) [4]. A solution to this problem is to use advanced control strategies. An additional benefit of advanced control is the possibility to minimize several objectives alongside the control strategy.

The first step to change the propulsion system of a vessel towards zero-emission is to use battery-only systems [5]. However, the short autonomous travel distance limits the application of battery-only systems due to the relatively low energy density of batteries [6]. The autonomous travel distance can be increased by using alternative fuels in the propulsion system [5]. Alternative fuels can be used in a variety of technologies such as Internal Combustion Engines (ICE) or fuel cells (FC) [7]. The first step to introduce alternative fuels in the energy management of a full-electric vessel is the operation of different sets of diesel engines alongside to benefit from their individual characteristics. One major benefit of using ICE is the ability to provide high loads with comparatively fast dynamic response at low cost [8].

However, ICE still produce emission under operation. One emission, which is not often considered in current control research in the maritime is the production of NOx. Different than CO_2 output, which relates linear to the fuel consumption, the formation of NOx is not correlated to the fuel consumption but rather to the operational conditions in the en-

@2023 Löffler et al. published by TU Delft OPEN Publishing on behalf of the authors. Licensed under a Creative Commons Attribution CC BY license.
DOI: https://doi.org/10.59490/moses.2023.673

gine. Considering this in a control problem adds to the complexity of the developed control since several more objectives are relevant to vessel energy management. While another major cost factor for the control is the reduction of fuel consumption, the extension of components' lifetime due to optimal usage gains more interest with full-electric systems operating with batteries and fuel cells. This combination of several objectives in the same strategy is called multi-objective control. All the objectives of interest for the vessel control can be categorized into different categories. Depending on the type of objective, the optimal point of operation differs, so the control has to find the best possible compromise. Batteries introduce greater flexibility into the operation of energy systems. However, their degradation, influenced by time and improper usage, cannot be overlooked. This degradation leads to increased maintenance and replacement costs. One major problem of multi-objective control is that it expands the control problem further, leading to raised algorithm solution times.

Current approaches on multi-objective control mainly combine fuel consumption and CO_2 emission reduction [9]–[12]. Research also started to address the combination of fuel cost reduction with an extension of the battery lifetime [13]–[15]. The combination of objectives from more than two categories, such as fuel cost, emission production, and degradation, is rarely investigated [12], [15], [16]. However, even those only focus on the CO_2 production as emission output. The incorporation of emission production besides CO_2 ensures the protection of sensitive areas by specific optimization. For a holistic optimization of the operation, the aspects of battery degradation and fuel price have to be combined with the emission reduction.

One promising advanced control strategy, which is able to optimize between several objectives quickly, is Equivalent Consumption Minimization (ECMS). A main advantage of ECMS is the instantaneous optimization in one step, which makes it suitable for high degrees of uncertainty and fast dynamics. ECMS was already studied for its application in the automotive sector, where it is used to keep up with the quick dynamics in real-time [17]. For maritime application, Kalikatzarakis et al. [18] applied it for the reduction of fuel consumption, which showed promising first results. Even though the authors successfully apply ECMS to a marine energy management problem, the strategy's potential to minimise more than one objective needs further investigation.

2 PROPULSION LAYOUT

A full-electric vessel of the type Yacht is selected as the case for this paper. The vessel is operating with a DC-distribution system with two directly connected battery packs as energy storage system. The power generation uses two pairs of diesel generators of different sizes. The generator sets are connected via AC/DC converters to the DC grid, which allows for a variable speed operation of the engines.

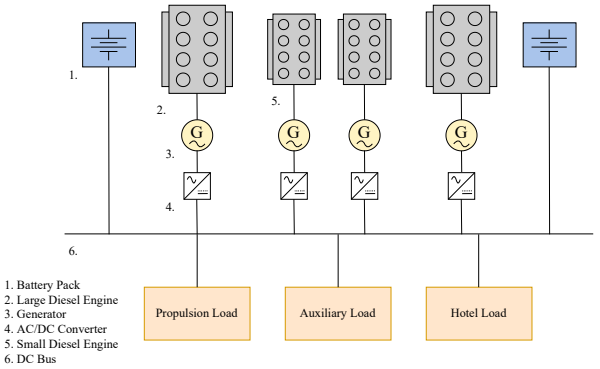

Figure 1: Propulsive layout of the usecase vessel

2.1 System Modelling

We model the behavior of the propulsion system using steady-state, first-principle equations. These models are derived from mathematical relationships combined with empirical measurements of the components. In the table below are the specifications of the propulsion system summarized. In the following, we introduce the models used to describe the component behaviour.

Table 1: Case study parameters

Parameter	Description	Value
V_{DC}	DC-bus voltage	$800 - 1000\,\mathrm{V}$
$P_{E,l}$	Engine power (x2)	$1430\,\mathrm{KWe}$
$P_{E,s}$	Engine power (x2)	$895\,\mathrm{KWe}$
E_{Bat}	Battery capacity (x2)	$2250\,\mathrm{KWh}$
η_{AC-DC}	Conversion efficiency	0.98
η_{DC-AC}	Conversion efficiency	0.98
η_{DC-DC}	Conversion efficiency	0.98
η_m	Motor efficiency	0.97
η_{gb}	Gearbox loss	0.97
η_{gen}	Generator efficiency	0.96

For the battery packs, we use the research of Tremblay et al. [19] for a generic battery model of a Lithium-Ion battery. The battery model is scaled to match the required size for the vessel battery packs. The control of the battery is indirect over the control of the engines using the power balance of the

system. No individual set point is required as the batteries are connected directly to the DC bus.

The system contains two sets of two combinations of engine and generator for the propulsion, which all operate using Diesel. We model the engines using performance maps, which are created over the engine's operating envelope. Since we combine the engines with a DC grid in this study, the engines can be operated flexibly using variable speed set points. For each type of engine, the specific fuel consumption (SFC) is mapped over speed in rounds per minute [rpm] and power [kWh]. The emission production is modelled in two different ways: while the CO_2 production can be related linearly to the SFC, the NOx formation is related to the engine's operational conditions and not the SFC. We model the NOx emission by creating a similar map over the operational envelope based on real-world measurements. The engines are controlled with a set point for the requested power and one for the speed.

The other power system components are modelled using transfer functions for the losses. This includes the gear box, generators, electrical motors, converters, and the DC grid. The selected values are derived from information provided by the shipbuilder and manufacturers; however, we cannot disclose the specific values due to confidentiality reasons.

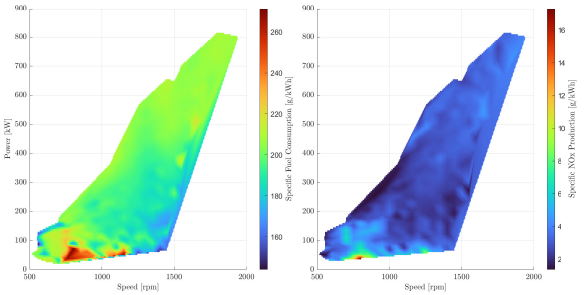

Figure 2: SFC and NOX maps for small engine [20]

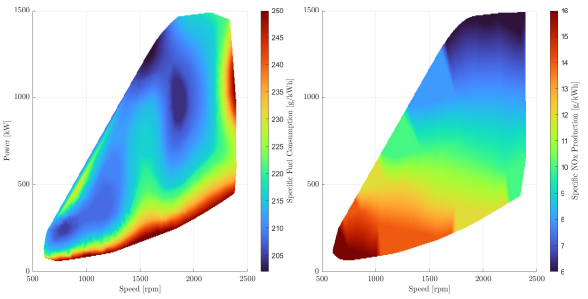

Figure 3: SFC and NOX maps for large engine [21]

3 CONTROL DEVELOPMENT

For the energy management of the vessel, a 2-level multi-objective ECMS controller is developed. While the first layer decides the optimal power scheduling combination of components, the second layer determines the optimal set points for the components in use. The controller uses a set of variables to describe the system's behaviour. The system is defined by four states: the engine current (I_{Eng}), the load current (I_{Load}), the battery current (I_{Bat}) as represented in the power balance on the DC bus, and the state of charge (SoC_{Bat}) for one of the battery packs. For clarity, these states are denoted as $I_{\text{Eng}} = x_1$, $I_{\text{Load}} = x_2$, $I_{\text{Bat}} = x_3$, and $SoC_{\text{Bat}} = x_4$. Additionally, there are eight control variables: four related to engine power ($P_{\text{Eng,i}} = u_i$ for $i \in 1,2,3,4$) and four to engine speed ($n_{\text{Eng,i}} = u_j$ for $j \in 5,6,7,8$). A comprehensive overview of these state and control variables, along with other inputs and parameters, is provided in Table 2.

Table 2: State and Control Variables, Input, and Parameters

Parameter	Description	Role
I_{Eng}	Engine Current	State
I_{Load}	Requested Load Current	State
I_{Bat}	Battery Current	State
SoC_{Bat}	Battery State of Charge	State
$P_{\text{Eng,i}}$	i^{th} Engine Power Reference	Control
$n_{\text{Eng,i}}$	i^{th} Speed Reference	Control
P_{Prop}	Propulsion Load	Input
P_{Aux}	Auxiliary Load	Input
V_{DC}	DC Voltage	Input
r_{CO2}	Release Rate CO_2	Const.
p_{D}	Price of diesel	Const.
p_{Bat}	Equivalent factor battery	Const.
n_{p}	Battery modules in parallel	Const.
Q_{nom}	Battery nominal power	Const.

It is worth noting that only one battery pack is considered since both behave identically due to the direct connection to the DC bus. The four states are shown in Eq. 1.

$$
\begin{aligned}
x_1 &= \frac{(u_1 + u_2 + u_3 + u_4) \cdot \eta_{gen}}{V_{\text{DC}}} \cdot \eta_{\text{AC-DC}} \\
x_2 &= \frac{P_{\text{Prop}} \cdot 1/\eta_{gb} \cdot 1/\eta_m + P_{\text{Aux}}}{V_{\text{DC}} \cdot \eta_{\text{DC-AC}}} \\
x_3 &= x_1 - x_2 \\
x_4 &= x_{4n-1} + \frac{1}{2} \frac{\Delta t \cdot x_3}{Q_{\text{nom}} \cdot n_p}
\end{aligned}
\tag{1}
$$

Using the relationships outlined in Eq. 1, the ref-

erences for the state variables can be determined, which must be matched by the controller's states to ensure the similarity to the real system. In addition, a set of objectives is defined to optimize special targets. First, the control variables of the problem are used to determine the SFC and the NOx production of the engines based on the maps in Fig. 2 and Fig. 3. With $i \in \{1, 2\}$ and $j \in \{3, 4\}$, the SFC and NOx of the engines 1-4 can be expressed as

$$\mathrm{SFC}_{\mathrm{Eng,i}} = f_1(u_i, u_{i+4}) \tag{2}$$
$$\mathrm{NOx}_{\mathrm{Eng,i}} = f_2(u_i, u_{i+4}) \tag{3}$$
$$\mathrm{SFC}_{\mathrm{Eng,j}} = f_3(u_j, u_{j+4}) \tag{4}$$
$$\mathrm{NOx}_{\mathrm{Eng,j}} = f_4(u_j, u_{j+4}) \tag{5}$$

where f_1 and f_2 are functions that represent the SFC and NOx formation of the small engines, and f_3 and f_4 are similar functions for the large engines. Using those references, we calculate the mass of fuel consumed (m_{D}) and emission produced ($m_{\mathrm{CO_2}}, m_{\mathrm{NOx}}$) as

$$m_{\mathrm{D}} = \sum_{i=1}^{4} \mathrm{SFC}_{\mathrm{Eng,i}} \cdot u_i \tag{6}$$
$$m_{\mathrm{CO_2}} = \sum_{i=1}^{4} \mathrm{SFC}_{\mathrm{Eng,i}} \cdot u_i \cdot r_{\mathrm{CO2}} \tag{7}$$
$$m_{\mathrm{NOx}} = \sum_{i=1}^{4} \mathrm{NOx}_{\mathrm{Eng,i}} \cdot u_i \tag{8}$$

where $r_{\mathrm{CO_2}}$ is the release rate of CO_2 from diesel during combustion.

3.1 Objective Function Definition

We introduce three objectives to account for the fuel consumption and emission production in the objective function. While the first objective C_1 represents the price of a kWh as a comparison between the engines and the batteries, the latter objectives C_2 and C_3 account for the mass of emission formatted under operation. The price of a kWh diesel is related to a pricing factor p_{D} representing the fuel's market value. To allow for comparison, an equivalent pricing factor for the battery p_{Bat} is defined. With this, the three objectives are set up as denoted in Eq. 9.

$$\begin{aligned} \mathrm{C}_1 &: m_{\mathrm{D}} \cdot p_{\mathrm{D}} + P_{\mathrm{Bat}} \cdot p_{\mathrm{Bat}} \\ \mathrm{C}_2 &: m_{\mathrm{CO_2}} \\ \mathrm{C}_3 &: m_{\mathrm{NOx}} \end{aligned} \tag{9}$$

The objectives are normalized to allow an equal comparison of the differently-natured targets.

We account for the battery's health by imposing constraints on the minimum and maximum of the SOC. Those boundaries ensure the operation to stay between 20% and 80% SOC. Further, we aim to avoid excessive battery currents by introducing a penalty for the depth of discharge (DoD) using a penalty factor c_{Bat}. This penalty term is $c_{\mathrm{Bat}} \cdot (x_4 - 0.5)$.

The three objectives are incorporated in a scalarized objective function function. Each of those objectives is combined with a weight λ_i with the index $i \in \{1, 2, 3\}$. This leads to

$$J(\mathbf{x}, \mathbf{u}) = \sum \lambda_i \cdot \mathrm{C}_i, \tag{10}$$

where $\mathbf{x}$ and $\mathbf{u}$ represent the state and control variables, as reported in Tab. 2.

3.2 Optimization Problem

We solve the multi-objective optimization problem to determine the optimal control input for the vessel energy system. For this purpose, the objective function, represented in Eq. 10, is expanded with two parts. The first one includes the controller's reference values of the state variables in the form of $\mathbf{x}_{\mathrm{ref}}$, which penalizes a deviation from the expected values of the real system. The second one adds the penalty for the depth of discharge DoD. Taking this into account, the final objective function can be expressed as:

$$J(\mathbf{x}, \mathbf{u}) = (\mathbf{x} - \mathbf{x}_{\mathrm{ref}}) + \mathrm{DoD} + \sum \lambda_i \cdot \mathrm{C}_i, \tag{11}$$

Additionally, constraints are imposed to further characterize the minimization problem. The first prominent constraint is the power balance between the requested and the generated power in the form of

$$P_{\mathrm{Load}} = P_{\mathrm{Gen}}. \tag{12}$$

Further constraints limit the operational range of system components as following

$$\mathcal{O}_{\mathrm{lower}} \leq \mathcal{O} \leq \mathcal{O}_{\mathrm{upper}}, \tag{13}$$

where $\mathcal{O}$ stands for the component with its respective lower $\mathcal{O}_{\mathrm{lower}}$ and upper $\mathcal{O}_{\mathrm{upper}}$ limits. The upper and lower limits of the two types of engines are characterized by non-linear functions describing the respective threshold. Therefore, the Eq. 13 for the constraints imposed on the engines are represented for $i \in \{1, 2, 3, 4\}$:

$$f_{\mathrm{lower,i}}(\mathbf{x}) \leq \mathcal{O}_{\mathrm{Eng,i}} \leq f_{\mathrm{upper,i}}(\mathbf{x}), \tag{14}$$

5 where $\mathcal{O}_{\mathrm{Eng,i}}$ stands for the i-th engine and $f_{\mathrm{lower,i}}(\mathbf{x})$ and $f_{\mathrm{upper,i}}(\mathbf{x})$ are the corresponding non-linear functions of the lower and upper limit.

Based on those constraints and our knowledge about the system behavior, we aim to identify the set of optimal control inputs $\mathbf{u}(\cdot|k)_{\text{opt}}$ that minimizes the objective function J, respective Eq. 11. This leads to the following minimization problem:

$$\begin{aligned} \text{Minimize:} \quad & J(\mathbf{u}(\cdot|k)) \\ \text{s.t.:} \quad & \\ & \mathbf{x}_{k+1} = f(\mathbf{x}_k, \mathbf{u}_k) \\ & \mathbf{u}_k = \mathbf{u}_{k-1} + \Delta\mathbf{u}_k \\ & g_{\text{in}}(\mathbf{x}_k, \mathbf{u}_k) \leq 0 \\ & g_{\text{eq}}(\mathbf{x}_k, \mathbf{u}_k) = 0 \end{aligned} \tag{15}$$

where $\mathbf{x}_{k+1}$ corresponds to the state at the next time step as a function of the current values of the state variables x_k and the control variables u_k. The value of the control u_k in time step k is formed by adding the difference in the control value $\Delta\mathbf{u}_k$ to the control value u_{k-1} of time step $k-1$. The equality and inequality constraints set is represented by g_{eq} and g_{in} in dependence on the control and state variables u_k and x_k.

Eq. 15 analysis shows the problem to be nonlinear and non-convex in combination with nonlinear constraints. A problem natured like this can be solved by applying different approaches [22]. According to Wolpert et Macready [23] and their no free lunch theorem, determining the optimal algorithm for an optimization problem a-priori is impossible. This decision is only possible by testing various ones and later comparing their performance. However, in this study, we decide to apply Sequential Quadratic Programming (SQP) [24], as it includes the required capabilities to solve problems of the nature of Eq. 15 [25]. This is based on the works and findings of [26] and [25]. To ensure algorithm convergence and finding the global minimum, we apply a multi-start approach [27]. In concrete, we define a set of 50 randomly distributed starting points inside the defined space for the optimization problem. We implement the described optimization framework inside a Matlab 2022b environment.

3.3 Pareto-Frontier Evaluation

The Pareto frontier represents solutions of the multi-objective optimization defined in Eq. 15 where improvement in one objective can only be achieved at the expense of another. Within this context, the skyline operator [28] plays a crucial role in assisting our algorithm in identifying dominant and non-dominant solutions at each timestamp. The skyline operator helps extract the subset of solutions not dominated by any other solution in our multi-dimensional space. In particular, a data point is said to be in the "skyline" if no other point is better than it in all dimensions. This makes it an efficient tool for sifting through vast solution spaces to highlight those solutions that might be of particular interest due to their dominance in certain objectives. When applied to our Pareto frontier obtained from the solution of Eq. 15 at each timestamp, the skyline operator was used to refine the Pareto frontier solutions set by highlighting those solutions that stand out in particular dimensions. By focusing on skyline solutions, it is possible to have a clearer view of the trade-offs involved and prioritize solutions that align closely with strategic objectives or users' preferences. As the number of objectives of Eq. 15 is large and the solutions space is large, the skyline operator provides a more computationally efficient way to isolate dominant solutions without exhaustively comparing every possible pair of solutions. Finally, the skyline operator doesn't require any a priori knowledge about the decision maker's preferences, making it a versatile tool for our multi-objective scenarios.

4 SIMULATION STUDY

A simulation study is carried out to investigate the performance of the proposed control framework. Further, we develop an RBC, which we use to evaluate the ECMS control against a benchmark. The chosen load profile has a length of 4 h, shown in Fig. 4. It incorporates both periods of low and high load demand. While the propulsion load is shown in blue, the auxiliary loads are represented in red.

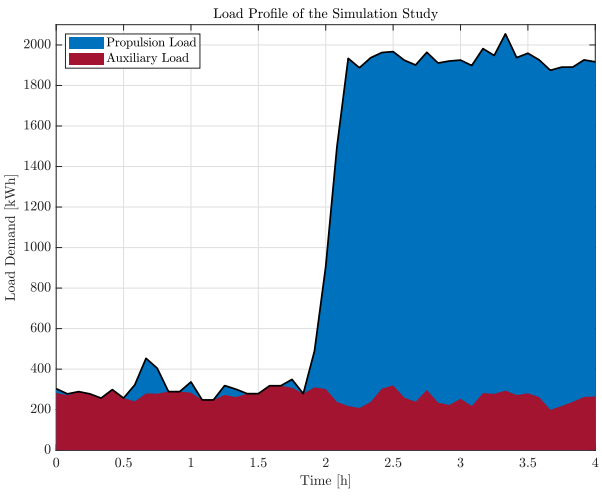

Figure 4: Load Profile

4.1 Benchmark Control

The RBC, shown as a schematic in Fig. 5, is developed with a single focus on fuel consumption while providing the requested load demand. For this, the batteries are used to buffer for fluctuation in the load and to allow a fuel-efficient operation of the engines. The engines are operated at fixed set points of the highest fuel efficiency along the propeller curve. The RBC takes the requested load demand and the current battery SoC as input values. The SoC is used to determine if the battery mode requires a change between charge and discharge. The change is initiated when the battery SoC approaches the upper or lower limit. We choose those limits to 20% and 80% SoC as a first step into battery lifetime beneficial operation. Further, we evaluate if the change in power request between the steps exceeds 350 kW. If the deviation does not exceed the limit and no change of battery mode is required, the controller keeps the previous set points. In case the set points need adjustment, the new set points are chosen according to the battery mode to either $P_{\text{Load}} \geq P_{\text{Set}}$ or $P_{\text{Load}} \leq P_{\text{Set}}$. This allows the operation of the engines at the most efficient points at all times while slowly charging or discharging the batteries.

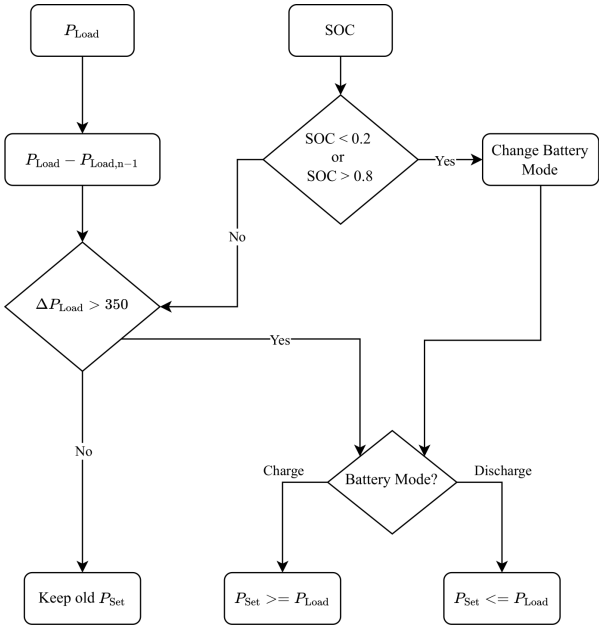

Figure 5: Decision tree of the RBC

We test the RBC on the load profile to create a benchmark. The discretization size is chosen to 5 min to allow a fair comparison with the ECMS controller. The smaller the step size of the discretization is chosen, the closer it resembles the real-world load profile in Fig. 4. In Fig. 6, the power balance at the DC bus is shown. The first subplot shows the balance between the engine and battery currents, while the second subplot compares the load demand and the provided power. The RBC is able to supply the required power demand while keeping the engines at constant power levels most of the time. The battery is used to buffer for fluctuation.

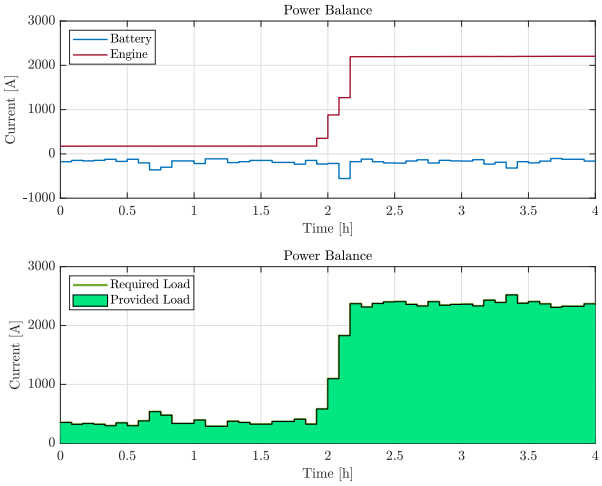

Figure 6: Current sharing and power balance with RBC. The current colors indicate the power source (engines = red, battery = blue, load = dark green, and light green = sum of produced power).

Fig. 7 shows the corresponding development of the battery SoC and the DC system voltage over the operation time. The battery behaviour is related to the left y-axis of the plot, while the voltage is depicted on the right y-axis. It is observable that the battery is slowly discharged but maintained between the upper and lower limits.

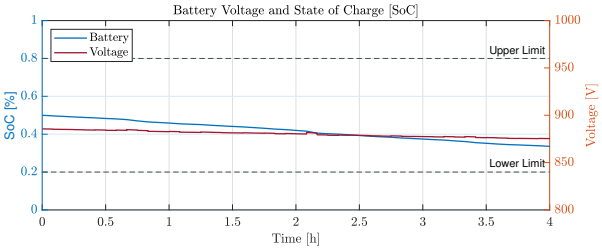

Figure 7: Battery SoC and DC system voltage using RBC. SoC is shown in blue, and Voltage in red.

In addition, the fuel consumption and the formated CO_2 and NOx emissions are calculated to compare the RBC to the ECMS in Section 5.

4.2 ECMS Control

The ECMS controller is tested with the same load profile, depicted in Fig. 4. The discretization

time step size is also chosen to 5 min. The density of diesel ρ_D is chosen according to [29] and the release rate of CO_2 from fuel r_{CO2} according to [30]. The price of diesel fuel is chosen based on an evaluation of the market as shown in Tab. 3. The equivalent pricing factor of the batteries is chosen to match the point of minimal fuel consumption of each engine to balance the power sources. Following, the equivalent factor equals the minimum SFC of the large engines when only operating those, while it corresponds to the minimum SFC of the smaller engines whenever they are involved in the power scheduling.

Some attention was spent on the choice of the penalty factor for the DoD of the battery, as a too-low factor will increase the gradient of the battery current, and a too-high factor will result in non-optimal use of the battery potential. While this factor should be investigated using a logarithmic scale to determine a good choice between flexibility and health preservation in theory, we choose a factor of $c_{\mathrm{Bat}} = 1$ in this study as a proof of concept after testing a limited amount of choices. This way, we can already showcase the performance of the ECMS control, while a full study on the effect of this parameter needs to be carried out to choose it optimally. Taking those parameters into account, the controller can determine the value of all defined objectives and minimizes the cost function Eq. 10.

Table 3: Control parameters

Parameter	Description	Value
ρ_D	Density diesel	0.838 kg/l
$r_{\mathrm{CO_2}}$	CO_2 release rate	2.7 t CO2/l
p_D	Price diesel	0.7 Euro/l
p_B	Battery equivalent cost	0.7 Euro/l
c_{Bat}	Battery penalty	1
SoC_0	Initial SoC	0.5

In our approach to determine the weights of the objectives, we employ the Pareto-Frontier combined with the skyline operator as reported in Section 3.3. This method serves as an initial step towards a deliberate a-posteriori weight selection, tailored to the end user's preferences.

5 RESULTS

In the following, we showcase the behaviour of the ECMS controller for the scenario in which we use the Pareto-Frontier combined with the skyline operator for weight selection. The power balance of the currents using the ECMS controller is shown in Fig. 8. The ECMS controller consistently meets the power demand throughout its operation. The battery serves as a buffer for load fluctuations and provides crucial support during significant power demand surges, especially during sailing.

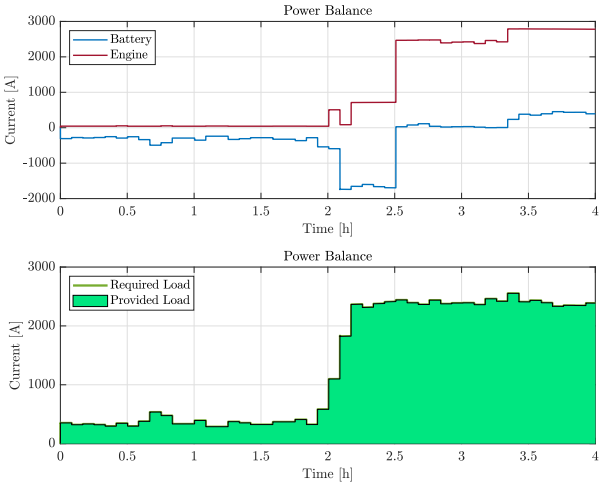

Figure 8: Current sharing and power balance with ECMS. The current colors indicate the power source (engines = red, battery = blue, load = dark green, and light green = sum of produced power).

The corresponding behaviour of the batteries and the DC system voltage is shown in Fig. 9. The SoC is represented in the left y-axis, while the voltage is connected to the right y-axis. The ECMS controller depletes the SoC fully during the large step in the load demand and slowly charges the battery again. Even though the ECMS controller breaches the lower limit of the SoC, we observe that it afterward schedules the load to charge the battery again.

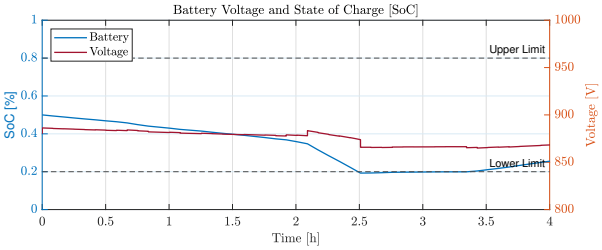

Figure 9: Battery SoC and DC system voltage using ECMS. SoC is shown in blue, and Voltage in red.

As an illustration, we assess the selected set points of the engines, as depicted in Fig. 10. In alignment with the load profile, it is evident that the controller relies solely on the smaller engines during periods of low loads. When the power demand increases drastically, the controller starts to use one of the large engines as an additional power source. Further, the controller adjusts the engine's rotational speed under operation to fully optimize the operation.

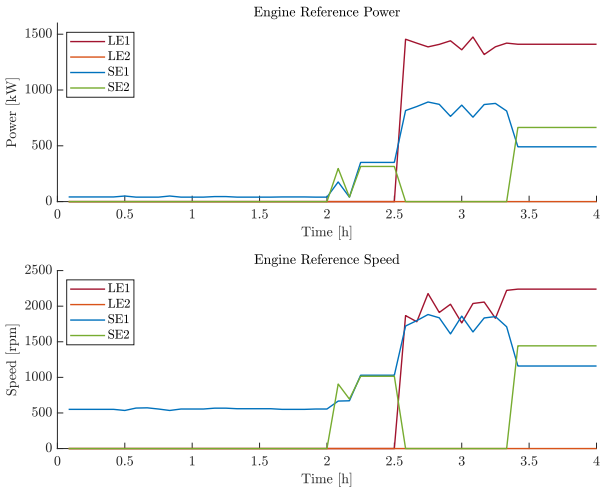

Figure 10: Power and speed reference set points for all four engines over the 4 h load profile. Each color represents a different engine.

5.1 Scenario Comparison

To further evaluate the performance of the proposed ECMS framework, we tested three scenario cases to compare with the RBC results. Two scenarios investigate edges of the Pareto-Frontier, meaning all weights besides one are set to zero, while this specific one is set to 1. The first one (SFC) is designed to singularly minimize the SFC, while the second one (NOx) only focuses on the produced NOx under operation. An overview of those scenarios' weights is presented in Tab. 4. The third scenario (Pareto) uses the Pareto-Frontier for the selection of the weights, as explained in Section 3.3.

Table 4: Scenario Design

Scenario	**SFC**	**CO_2**	**NOx**
	λ_1	λ_2	λ_3
SFC	1	0	0
NOx	0	0	1

We can evaluate the results for all three scenarios compared to the RBC. The results are presented in Tab. 5. We compare the scenarios in the aspects of consumed fuel, formatted CO_2 and NOx emissions, and the total operational cost in €. For the calculation cost, we take only the consumed fuel into account with the price assumed in Tab. 3. In addition, the percentage of deviation to the RBC is calculated for comparison and displayed in Tab. 6.

Table 5: Scenario Comparison

	Fuel	**Emission**		**Cost**
	Diesel [t]	**CO_2 [t]**	**NOx [t]**	**[€]**
RBC	0.8948	2.8829	0.0328	747.39
SFC	0.8815	2.8401	0.0223	736.33
NOx	0.9809	3.1606	0.0195	819.42
Pareto	0.9746	3.1402	0.0203	814.17

Table 6: Scenario Comparison (relative differences)

	Fuel	**Emission**		**Cost**
	Diesel [%]	**CO_2 [%]**	**NOx [%]**	**[%]**
SFC	-1.5	-1.5	-32	-1.5
NOx	+9.62	+9.6	-40	+9.6
Pareto	+8.9	+8.9	-38	+8.9

We observe a difference in the results between the three scenarios. The first scenario is the scenario that is the most similar to the setup of the RBC. Therefore, the results are relatively similar, with savings of about 1.5 % for fuel consumption, CO_2, and operational cost. This saving can be explained by a more efficient battery operation resulting in the complete discharge under operation. This result represents one edge of the Pareto-Frontier focusing only on SFC. Another edge of the Pareto-Frontier is shown in the NOx scenario. We report savings of 40 % compared to the RBC. Accompanied by that, we see an increase of about 9.6 % in fuel consumption. This is related to the fact that the most NOx efficient operating points are not equal to the fuel efficiency optima. Relating to this, the cost of the operation increases, which is basically the price paid for the saving in terms of emissions. Since the CO_2 production is linearly related to the fuel consumed, we observe an increase in CO_2 emissions alongside. The third scenario uses the Pareto-Frontier for the weight selection. We see a saving in terms of NOx formation of 38 % and a corresponding increase in fuel consumption, operational cost, and CO_2 emissions of about 8.9 %.

Evaluating the performance of the ECMS framework, we can state that the ECMS framework is able to outperform a well-designed RBC for a single-objective scenario. With the other edge of the Pareto-Frontier, we can account for maximum NOxemission savings and the corresponding price increase. Further, we showcase that a conscious decision for a compromise is possible using the Pareto-Frontier.

6 CONCLUSION

This paper presented an ECMS-based framework for multi-objective optimization of a vessel energy system. The control could fulfill the required load demand at all times while taking the fuel efficiency and emission formation of two sets of differently behaving engines into account. We implemented a Pareto-Frontier approach to allow for an a-posteriori selection of the objective weights. In three scenarios, we showed that the controller can optimize between the different optimal points for each objective based on the assigned weight in the objective function. We first tested the developed control on a $4\,\mathrm{h}$ load profile obtained from a real vessel. This allowed us to showcase the adaptation capability of the controller to adjust the performance based on the choice of objective weights. A comparison with an intelligent RBC with a focus on fuel efficiency showed the potential for up to $1.5\,\%$ savings of fuel or up to $40\,\%$ savings of NOx emissions under operation for the cases of single-objective focus.

Future work will focus on improvements in the battery handling in the control strategy. This includes more detailed research on the choice of the equivalent cost factor and the penalty factor for the DoD. Furthermore, handling delays in the system, such as engine start-up and cool-down times or set point switches, needs further study. Potential contribution can also be seen in handling the battery's health from the control perspective, which can be considered combined with a degradation model of the component. Last, further research is required on choosing the optimal objective combination from the Pareto-Frontier by implementing enhanced user selection.

ACKNOWLEDGEMENTS

This research is supported by the project MENENS, funded by the Netherlands Enterprise Agency (RVO) under the grant number MOB21012.

REFERENCES

[1] J. F. Hansen and F. Wendt, "History and State of the Art in Commercial Electric Ship Propulsion, Integrated Power Systems, and Future Trends," *Proceedings of the IEEE*, vol. 103, no. 12, pp. 2229–2242, 2015.

[2] V. Eyring, H. W. Köhler, A. Lauer, and B. Lemper, "Emissions from international shipping: 2. Impact of future technologies on scenarios until 2050," *Journal of Geophysical Research: Atmospheres*, vol. 11, no. D17, 2005.

[3] C. Nuchturee, T. Li, and H. Xia, "Energy efficiency of integrated electric propulsion for ships – A review," *Renewable and Sustainable Energy Reviews*, vol. 134, p. 110 145, 2020.

[4] P. Nema, R. K. Nema, and S. Rangnekar, "A current and future state of art development of hybrid energy system using wind and PV-solar: A review," *Renewable and Sustainable Energy Reviews*, vol. 13, no. 8, pp. 2096–2103, 2009.

[5] A. D. Korberg, S. Brynolf, M. Grahn, and I. R. Skov, "Techno-economic assessment of advanced fuels and propulsion systems in future fossil-free ships," *Renewable and Sustainable Energy Reviews*, vol. 142, p. 110 861, 2021.

[6] M. Perčić, I. Ančić, and N. Vladimir, "Life-cycle cost assessments of different power system configurations to reduce the carbon footprint in the Croatian short-sea shipping sector," *Renewable and Sustainable Energy Reviews*, vol. 131, p. 110 028, 2020.

[7] S. Atilhan, S. Park, M. M. El-Halwagi, M. Atilhan, M. Moore, and R. B. Nielsen, "Green hydrogen as an alternative fuel for the shipping industry," *Current Opinion in Chemical Engineering*, vol. 31, p. 100 668, 2021.

[8] M. Prussi, N. Scarlat, M. Acciaro, and V. Kosmas, "Potential and limiting factors in the use of alternative fuels in the European maritime sector," *Journal of Cleaner Production*, vol. 291, p. 125 849, 2021.

[9] F. D. Kanellos, A. Anvari-Moghaddam, and J. M. Guerrero, "A cost-effective and emission-aware power management system for ships with integrated full electric propulsion," *Electric Power Systems Research*, vol. 150, pp. 63–75, Sep. 2017, ISSN: 0378-7796. (visited on 08/31/2022).

[10] F. D. Kanellos, "Optimal Power Management With GHG Emissions Limitation in All-Electric Ship Power Systems Comprising Energy Storage Systems," *IEEE Transactions on Power Systems*, vol. 29, no. 1, pp. 330–339, Jan. 2014, ISSN: 1558-0679.

[11] D. Gao, X. Wang, T. Wang, Y. Wang, and X. Xu, "An Energy Optimization Strategy for Hybrid Power Ships under Load Uncertainty Based on Load Power Prediction and Improved NSGA-II Algorithm," *Energies*, vol. 11, no. 7, p. 1699, Jul. 2018, ISSN: 1996-1073. (visited on 01/20/2023).

[12] S. Fang, Y. Xu, Z. Li, T. Zhao, and H. Wang, "Two-Step Multi-Objective Management of Hybrid Energy Storage System in All-Electric Ship Microgrids," *IEEE Transactions on Vehicular Technology*, vol. 68, no. 4, 2019.

[13] C. Tsoumpris and G. Theotokatos, "A health-aware energy management strategy for autonomous ships power plants operation," *Transportation Research Procedia*, p. 8, 2019.

[14] M. Banaei, M. Rafiei, J. Boudjadar, and M.-H. Khooban, "A Comparative Analysis of Optimal

Operation Scenarios in Hybrid Emission-Free Ferry Ships," *IEEE Transactions on Transportation Electrification*, vol. 6, no. 1, pp. 318–333, Mar. 2020, ISSN: 2332-7782.

[15] K. Hein, Y. Xu, G. Wilson, and A. K. Gupta, "Coordinated Optimal Voyage Planning and Energy Management of All-Electric Ship With Hybrid Energy Storage System," *IEEE Transactions on Power Systems*, vol. 36, no. 3, pp. 2355–2365, May 2021, ISSN: 1558-0679.

[16] K. Hein, X. Yan, and G. Wilson, "Multi-Objective Optimal Scheduling of a Hybrid Ferry with Shore-to-Ship Power Supply Considering Energy Storage Degradation," *Electronics*, vol. 9, no. 5, p. 849, May 2020, ISSN: 2079-9292. (visited on 08/31/2022).

[17] H. Li, A. Ravey, A. N'Diaye, and A. Djerdir, "A novel equivalent consumption minimization strategy for hybrid electric vehicle powered by fuel cell, battery and supercapacitor," *Journal of Power Sources*, vol. 395, pp. 262–270, 2018.

[18] M. Kalikatzarakis, R. D. Geertsma, E. J. Boonen, K. Visser, and R. R. Negenborn, "Ship energy management for hybrid propulsion and power supply with shore charging," *Control Engineering Practice*, vol. 76, pp. 133–154, 2018.

[19] O. Tremblay, L.-A. Dessaint, and A.-I. Dekkiche, "A Generic Battery Model for the Dynamic Simulation of Hybrid Electric Vehicles," in *2007 IEEE Vehicle Power and Propulsion Conference*, 2007.

[20] F. Rosero, N. Fonseca, J.-M. López, and J. Casanova, "Real-world fuel efficiency and emissions from an urban diesel bus engine under transient operating conditions," *Applied Energy*, vol. 261, p. 114 442, Mar. 2020, ISSN: 0306-2619. (visited on 05/24/2023).

[21] R. D. Geertsma, R. R. Negenborn, K. Visser, and J. J. Hopman, "Design and control of hybrid power and propulsion systems for smart ships: A review of developments," *Applied Energy*, vol. 194, pp. 30–54, 2017.

[22] M. J. Kochenderfer and T. A. Wheeler, *Algorithms for decision making*. Mit Press, 2022.

[23] D. Wolpert and W. Macready, "No free lunch theorems for optimization," *IEEE Transactions on Evolutionary Computation*, vol. 1, no. 1, pp. 67–82, Apr. 1997, ISSN: 1941-0026.

[24] P. T. Boggs and J. W. Tolle, "Sequential quadratic programming," *Acta numerica*, vol. 4, pp. 1–51, 1995.

[25] Z. Khalik, G. Padilla, T. Romijn, and M. Donkers, "Vehicle energy management with ecodriving: A sequential quadratic programming approach with dual decomposition," in *2018 Annual American Control Conference (ACC)*, IEEE, 2018, pp. 4002–4007.

[26] S. Mennen, F. P. Willems, and M. Donkers, "A sequential quadratic programming approach to combined energy and emission management of a heavy-duty parallel-hybrid vehicle," *IFAC-PapersOnLine*, vol. 55, no. 24, pp. 335–341, 2022.

[27] R. Martí, "Multi-start methods," in *Handbook of Metaheuristics*, 2003.

[28] S. Borzsony, D. Kossmann, and K. Stocker, "The Skyline operator," in *Proceedings 17th International Conference on Data Engineering*, Apr. 2001, pp. 421–430.

[29] F. Murphy, K. McDonnell, E. Butler, and G. Devlin, "The evaluation of viscosity and density of blends of Cyn-diesel pyrolysis fuel with conventional diesel fuel in relation to compliance with fuel specifications EN 590:2009," *Fuel*, vol. 91, no. 1, pp. 112–118, 2012.

[30] A. Q. Jakhrani, A. R. H. Rigit, A.-K. Othman, S. R. Samo, and S. A. Kamboh, "Estimation of carbon footprints from diesel generator emissions," in *2012 International Conference on Green and Ubiquitous Technology*, 2012, pp. 78–81.

A Model-based Parametric Study for Comparison of System Configurations and Control of a Hydrogen Hybrid Cargo Vessel

Foivos Mylonopoulos[a*], Timon Kopka[a], Andrea Coraddu[a], and Henk Polinder[a]

[a] Department of Maritime and Transport Technology, Delft University of Technology, 2628 CD Delft, The Netherlands
* Corresponding Author: F.P.Mylonopoulos@tudelft.nl

Abstract
The current state of research in marine energy systems has concentrated on conventional diesel systems, while limited literature is available on the configuration and control of alternative energy sources such as hydrogen hybrid systems, which have attracted increasing interest recently owing to the energy transition. This paper presents a modelling and control study for conceptual retrofitting of a general cargo vessel to a hydrogen-hybrid version. Generic fuel cell, battery, and converter models are used, enabling easy adaptation to various powerplant sizes and ship types. A robustly coordinated Energy Management Strategy (EMS), which can be implemented for different vessel's power profiles, was developed for power sharing, DC bus voltage control, and battery State of Charge (SoC) regulation. The total installed fuel cell power and battery capacity were heuristically selected from a range of power profiles of the ship. A database of fuel cells with stacks from different manufacturers was created to test different combinations in terms of fuel consumption, cost, and weight, based on the framework of the problem. Uncertainties in terms of fuel prices are presented using normal distribution graphs. The system configurations and control results are presented for one power profile of the vessel and the average fuel costs. It is demonstrated that with the proposed control method, the power losses are less than 1%, the DC bus voltage fluctuations are less than 0.5%, and the battery SoC remains between 35-65% for the entire duration of the analysed power profile. The configuration with eight stacks of 150 kW has the lowest total fuel cost (730 $) with an average difference of 7.1% from the other solutions, and the lowest total weight (10.54 tons) with an average difference of 15.4% from the other configurations. Overall, this study demonstrates the efficient configuration and control of hybrid energy systems using parameterized components.

Keywords: Cargo Ship**,** Configurations**,** Control, Cost Uncertainties, Hydrogen--Fuel Cells, Parametric Study.

1. INTRODUCTION

The shipping industry is responsible for 3% of global Greenhouse Gas emissions. However, if no countermeasures are taken, this percentage may increase to 17% by 2050 [1]. Thus, the International Maritime Organization has imposed stringent regulations requiring a 50% emission reduction by 2050 compared to the 2008 levels [1]. One of the most promising alternative fuels for emission reduction is hydrogen, which can result in zero onboard emissions if fuel cells are utilised. They are scalable power sources with high efficiency at their rated level, and they produce power with reduced noise and vibrations compared to conventional engines without emitting harmful gases. Hybrid configurations of fuel cells and batteries have attracted increasing interest in recent years [2]. Batteries are used to cover the peak demands and transient loads that fuel cells cannot deliver owing to their limited power output and slow response. Such hydrogen hybrid configurations are more applicable for short ranges near recharging and refuelling infrastructure. Despite their higher cost and complexity compared to traditional configurations with diesel mechanical propulsion, hydrogen-hybrid systems offer increased flexibility, energy efficiency, and reliability in the case of failures [3].

Currently, most studies have focused on the modelling, control, and optimization of diesel-based (hybrid) ship systems because they have been in use for a long time and are well-established in the marine sector. In most cases, the objective is to increase the use of renewable sources by reducing the operation of diesel generators/engines to minimize onboard emissions. Zhu *et al*. [4],[5] modelled and optimized the sizes of the batteries,

@2023 Mylonopoulos, F. et al., published by TU Delft OPEN Publishing on behalf of the authors. Licensed under a Creative Commons Attribution CC BY license.
DOI: https://doi.org/10.59490/ moses.2023.671

generators, and e-motors of a diesel electric vessel using the Non-dominated Sorting Genetic Algorithm to reduce emissions, lifecycle costs and diesel consumption.

Vu *et al*. [6] proposed a Power Management Strategy using the interior point algorithm to optimally control the load splitting between the diesel generators and batteries of a hybrid tugboat.

Kanellos *et al*. [7],[8] developed models and control strategies using Particle Swarm Optimization algorithms to reduce the operational expenses and satisfy the emission requirements (operational indexes) for the case vessels.

The authors of [9],[10] modelled and sized the diesel generators, batteries, and supercapacitors to optimally control the highly fluctuating loads of the power profiles of vessels.

The modelling, control, and optimization studies for hydrogen-based vessels have focused on passenger vessels (i.e., small boats, high-speed ferries, roll-on-roll-off vessels). Because there are no emissions onboard, more focus is given to operational costs, capital expenses, and degradation of components.

Different studies have used the generic fuel cell and battery models from the Simscape library, which are also used in this study, focusing mainly on system control. Balestra and Schjølberg [11],[12] modelled the powertrain of a conceptually retrofitted hydrogen-based passenger vessel using real ship data. They tested the effects of component sizes on different Energy Management approaches, with a focus on hydrogen cost and component degradation.

Jaster *et al*. [13] modelled the propulsion and control systems of a hydrogen vessel and simulated them using the hardware-in-the-loop method to estimate the loads and fuel consumption.

Cha *et al*. [14] used an optimisation-based approach for the power management to maximize the efficiency of the fuel cells while constraining the battery State of Charge (SoC).

Bassam *et al*. [15] presented a multi-scheme Energy Management Strategy (EMS) that could switch to different control approaches based on the pre-defined instructions for varying battery SoC and operating profile, aiming to minimize the energy consumption.

Bassam *et al*. [16] presented an improved Proportional Integral strategy for a hydrogen-hybrid tourist boat and compared the optimization results of hydrogen consumption, cost, and component stresses with three other approaches: Classical Proportional Integral, Equivalent Consumption Minimization Strategy, and a rule-based method.

A summary of the main points and learnings from the above-mentioned studies, and the literature gaps addressed in this research are presented herein. There have been many studies on the design and control of diesel-based ship systems but very few have focused on system configurations and control for hydrogen hybrid vessels. In most cases, one fuel cell stack is considered for the analysis, with specifications from a specific manufacturer, without comparing the different system arrangements and fuel cell models in terms of fuel consumption and weights. To the best of the authors' knowledge, there are no studies on the selection of component sizes, configurations, and system control for vessels with multiple operating conditions and power profiles. Studies on hydrogen-hybrid ships usually consider a passenger vessel with a fixed route, schedule, and one power profile for the analysis, which simplifies the selection of component sizes and the EMS approach. Simple rule-based or PI-based approaches are usually implemented with a focus on power sharing between the components to minimize the energy losses for the considered load profile.

This is a model-based parametric study using generic fuel cell/battery models and average converters. A diesel-based general cargo vessel was conceptually retrofitted to a hydrogen-based version with hybrid power supply. Low-temperature proton-exchange membrane fuel cells and lithium-ion batteries are the power supply sources and electric motors are used for propulsion. The aim of this research is to compare different configurations of fuel cells and batteries in terms of fuel consumption/cost and weight, and to efficiently control the systems. The novelties and contributions of this study are summarized as follows. To the best of the authors' knowledge, this is the first such analysis for a general cargo vessel with various power profiles. A robustly coordinated EMS, that can be applied to different vessel profiles, was developed to control the DC bus voltage, SoC and for efficient power sharing. The installed fuel cell power and battery energy capacity were heuristically selected from a range of power profiles derived from real-time onboard measurements. Different combinations of fuel cells and batteries from various manufacturers were tested in terms of fuel consumption/cost, weight, Uncertainties in the fuel prices were considered for the calculations. The system configurations and control results are presented for one power profile of the vessel and the average hydrogen costs.

The remainder of this paper is organised as follows. In Section 2, the case study details for the vessel and its operating profiles are presented. The

proposed methodology, models and controllers are described in Section 3. The results of the simulations and discussions are presented in Section 4. Finally, the concluding remarks and directions for future research are presented in Section 5.

2. CASE STUDY

The specifications of the general cargo vessel considered in the analysis are listed in Table 1. The original version had one main diesel engine and a controllable pitch propeller.

Table 1. Case vessel specifications

Parameters	Values/Info
Length	89.9 m.
Width	12.5 m.
DWT	3638 t.
Year built	2007
Engine	Wartsila 9L20

The general cargo vessel does not have a fixed schedule and route. Instead, there are different operational areas and power profiles. The most energy-intensive (load fluctuating) and power-intensive load profiles are shown in Figure 1.

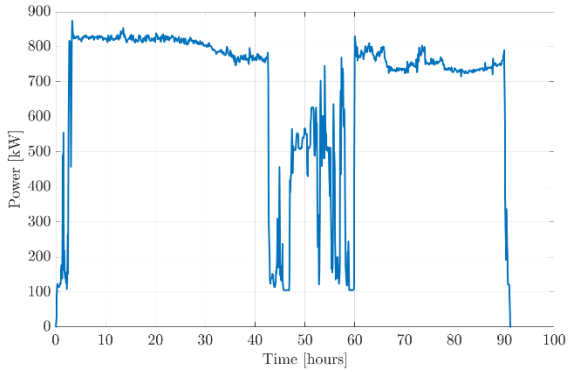

a) Energy intensive profile

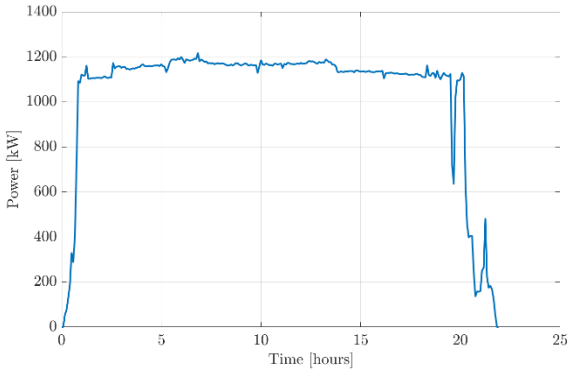

b) Power intensive profile

Figure 1: Power demand over time of the case vessel for different operating profiles

Data measurements were obtained for the propulsion loads from the main diesel engine of the original mechanical version of the cargo vessel with a frequency interval of 5 minutes. The engine's power output is the propulsion power demand for the retrofitted hydrogen-hybrid version developed in this study. The auxiliary loads have not been considered for the analysis since no measurement data is available.

3. METHODOLOGY

3.1 Framework

A simplified diagram of the methodology used in this study is shown in Figure 2. Detailed discussions of how the proposed methodology is applied to this case study are also presented in this section.

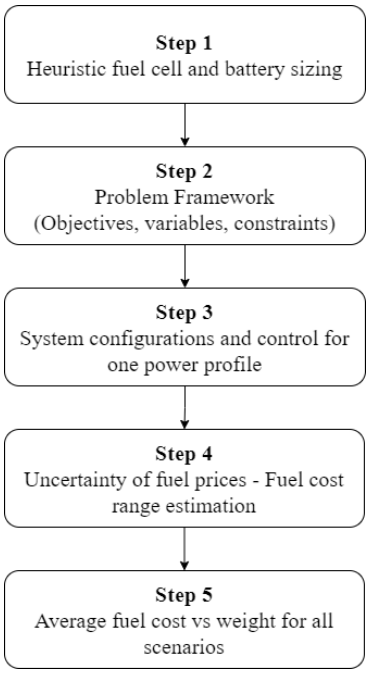

Figure 2: Steps of the proposed methodology

In the hydrogen version, the fuel cells and the batteries were sized according to the numerous power profiles of the vessel (Step 1). The sizes of the fuel cells, which are the main power sources, are such that they can cover the maximum recorded power output of 1200 kW (Figure 1b). The batteries were sized to deliver the highly fluctuating loads for energy-intensive profiles (Figure 1a). The selection of pack sizes was based on discussions with the vessel operators and industry experts. It was suggested that battery packs with a total energy capacity of 550 kWh and a total power of 800 kW could be sufficient for the

case vessel, considering its various operating profiles.

In Step 2, the problem framework is defined in terms of variables (i.e., number of batteries, number of fuel cells, and module selections from different manufacturers), objectives (i.e., fuel consumption/cost and system weight), and constraints. In particular, the following constraints were considered:

- $\text{Bus Voltage} = 1000\ \text{V} \pm 5\%$ [11]
- $20\% \leq \text{SoC (t)} \leq 80\%$ [12]
- $\text{P}_\text{L}(\text{t}) \leq \text{P}_\text{out}(\text{t}) \leq 1.01\text{P}_\text{L}(\text{t})$

where $\text{P}_\text{L}(t)$ is the power demand (load) as a function of time, and $\text{P}_\text{out}(\text{t})$ is the combined power output of the fuel cells and batteries as a function of time. The upper limit of the power output was constrained to be up to 1% higher than the load demand to minimize the power losses.

In Step 3, different combinations of batteries and fuel cells were tested to estimate the fuel consumption, costs, weights, and to control the voltage and power levels. The analysis was performed for one profile of the vessel, which is presented in Section 4.1.

In Step 4, variable and uncertain fuel prices are considered. The fuel cost range was obtained by multiplying the fuel price by the fuel consumption for each scenario. The mean and standard deviation for each case with a 95% confidence interval were also considered.

Finally, in Step 5, the average fuel costs were plotted against the system weights for all the considered scenarios. The results of the fuel consumption and system weights were compared with those of the original diesel-based version.

The different scenarios for the modelling, design, and control analysis of the considered power profile are discussed in Section 4.1.

3.2 Models and control approach

A simplified diagram of the powertrain layout for 'n' components is shown in Figure 3.

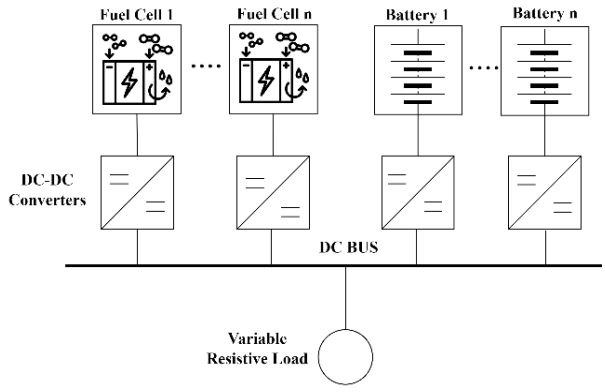

Figure 3: Powertrain configuration with varying number of fuel cells, converters, and batteries

Generic fuel cell and battery models from [17] and [18] respectively, have been used for modelling and integration of the systems into one powertrain. Average converter models have also been implemented, instead of detailed converters with pulse width modulation that would significantly increase the computational time. For system-level modelling, average models are sufficiently accurate [16].

The fuel cells are connected to the DC bus via unidirectional DC-DC converters, which increase the variable fuel cell voltage to the levels of the DC bus (1000 V).

For the batteries, the bi-directional converters enable discharging or charging onboard depending on the load demand. In this study, shore-charging was not considered. The DC bus is modelled with a single capacitance, which is obtained by the summation of all capacitances from the parallel-connected converters. The DC bus is connected to a single variable resistive load, which is equal to the bus voltage divided by the load current from the power profile.

The components after the DC bus, including inverters, AC motors, and propellers were not modelled in this study.

The implemented EMS developed for system control is shown in Figure 4.

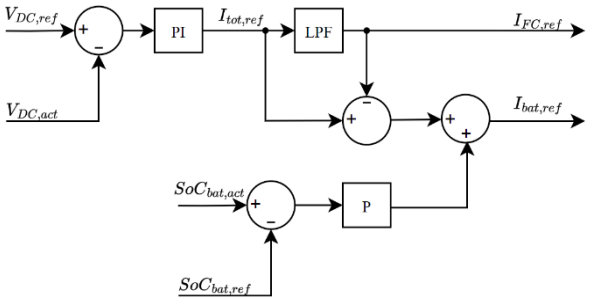

Figure 4: Developed EMS for power sharing, DC bus voltage control, and battery SoC regulation

In Figure 4, the DC bus voltage is controlled by a PI controller to its reference value of 1000 V. The total current output from the voltage regulation is then split into a low-frequency component for the fuel cells and a high-frequency component for the batteries. A low-pass filter is used before the fuel cell to limit the current gradients for degradation purposes [19]. The higher the time constant in the transfer function of the low-pass filter, the slower the fuel cell response and the smaller the fuel cell degradation. However, for a high time constant, the

batteries provide more power and degrade faster. A saturation block ensures that the fuel cell current remains within its limits. The fuel cell reference current is then split equally to the unidirectional DC-DC converters for current control.

The difference between the total current and fuel cell current is the battery current. For the batteries, the SoC is controlled with a P controller around a reference value of 50%, which is in the middle of the desired operating range of 20-80%. The P controller resulted in reduced oscillations compared to a PI controller around the equilibrium point. A PI controller with a high integral gain could be used if the aim was to keep the SoC almost constant at 50% SoC, but this would result in higher fuel consumption and fuel cell degradation, because almost all the power would be provided by the fuel cell stacks. With the P controller, if the SoC is below 50%, the system requires additional current to increase the SoC. The total battery current is a superposition of the voltage regulation and SoC regulation parts, and it is then split equally to the bi-directional converters of the battery packs that are connected in parallel. The SoC controller has much slower dynamic capabilities than those of the DC bus voltage controller. The limits for the battery charge and discharge currents are set in a saturation block. The developed EMS is robust and can be used for different power profiles of the vessel, because if the load profile changes, the fuel cell and the battery react to these changes.

The gains k_p and k_i for the DC bus voltage PI controller were estimated based on (1) and (2) as demonstrated in [20].

$$k_{p,DC} = \mathrm{C_{DC}}/\tau_{DC} \quad (1)$$

$$k_{i,DC} = 0.25k_{p,DC}^2/(4\mathrm{C_{DC}}) \quad (2)$$

where $k_{p,DC}$ and $k_{i,DC}$ are the proportional and integral gains, respectively, $\mathrm{C_{DC}}$ is the capacitance of the DC bus and τ_{DC} is a time constant for the voltage control which is set to 0.01 seconds for this study based on the authors' experience.

The gain of the P controller for battery SoC control was estimated based on (3) and (4).

$$k_{p,SoC} = \mathrm{I_{max}}/\Delta_{SoC} \quad (3)$$

$$\mathrm{I_{max}} = P_{Batt,max}/V_{DC} \quad (4)$$

where $k_{p,SoC}$ is the proportional gain of the SoC controller, $\mathrm{I_{max}}$ is the maximum battery current, Δ_{SoC} is the difference between the actual and reference SoC values, $P_{Batt,max}$ is the maximum battery power, and $\mathrm{V_{DC}}$ is the reference DC bus voltage which is 1000 V in this study.

3.3 Database of components

To test the different component sizes and system configurations, a small database of five actual fuel cell components with various power levels from different manufacturers was developed, as shown in Table 2.

Table 2. Fuel cell database

Components	Rated power (kW)	Stack weight (kg)
Zepp.Y50 [21]	50	212
HyPM HD90 [22]	100	327
Zepp. X-150 [21]	150	355
Powercell-200 [23]	200	1070
HyPM HD180 [22]	200	654

For the batteries, a single lithium-ion module from Toshiba was considered for the analysis [24]. The specifications of the modules are listed in Table 3.

Table 3. Battery module specifications

Parameters	Values (units)
Nominal voltage	24.6 V.
Rated capacity	45 Ah.
Weight	14.6 kg.

These modules are composed of numerous cells, and can be connected in series to increase the nominal voltage of the battery pack and in parallel to increase its rated capacity. The total installed energy capacity of the batteries was set equal to 550 kWh, as discussed in Section 3.1. Different numbers of battery packs were considered, ranging from 2 to 5 units, to investigate which configuration provides the required capacity with the lowest weight. A configuration with one battery pack was not considered because of the active redundancy requirements. Different total battery energy capacities will be considered in future work, where the optimal number and power/energy of components will be evaluated using an optimization algorithm.

4. RESULTS AND DISCUSSION

In this section, the results from the simulations are presented and discussed.

4.1 System configurations and control using the developed Energy Management

The analysis was conducted for a short power profile of 4.16 hours (15000 seconds) for computational reasons (Figure 5).

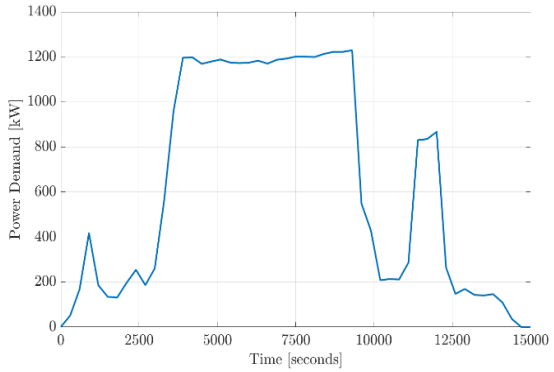

Figure 5: Power Profile for the simulations.

The battery weights for the different configurations with packs ranging from 2 to 5 units are listed in Table 4. The total weight was calculated by multiplying the module weight by the total number of modules in all packs. The total number of modules in each pack was calculated by multiplying the components connected in series with those connected in parallel.

Table 4. Number of battery packs and total weights for 550 kWh total battery capacity

Packs	Capacity of 1 pack [Ah]	Modules in each pack	Weight [tons]
2	343.7	264	7.7
3	229.2	198	8.6
4	171.8	132	7.7
5	137.5	132	9.6

Either two or four battery packs can provide 550 kWh of energy with the smallest system weight of 7.7 tons (Table 4). Hence, in each scenario, there are 2 battery packs of 275 kWh each.

Five scenarios were considered for the analysis: one for each fuel cell stack (Table 2). The total installed fuel cell power is limited to 1.2 MW which is the maximum power demanded by the diesel engine in the original mechanical version. Hence, for each scenario, the number of stacks required for onboard installation is presented in Table 5. All the fuel cells are used during operation in each scenario. No batteries or fuel cells are individually controlled and switched off during operation.

Table 5. Scenarios for different fuel cells

Scenario	Rated power (kW)	Stack no.
1	50	24
2	100	12
3	150	8
4	200	6
5	200	6

The results are presented for the power profile in Figure 5, for the 4th scenario with six fuel cell stacks of 200 kW from Powercell. The components from the different manufacturers of the fuel cells for each scenario and the nominal efficiencies at the beginning of the life cycle for each stack are presented in Table 6. Nominal efficiency is a required input parameter for the generic stack model, and for each fuel cell the nominal point is assumed to be at 80% of its rated power in this study. In two other parameterized generic stack models from the Simscape library, the nominal operating points are between 60-80% of the maximum power.

Table 6. Fuel cell nominal efficiencies

Scenario	Components	Efficiency (%)
1	Zepp.Y50	52.5
2	HyPM HD90	47.5
3	Zepp.X-150	53.5
4	Powercell-200	49.0
5	HyPM HD180	48.0

The purpose of the comparison of the different stacks is to compare the differences in fuel consumption/cost and weights for various configurations. In other words, the aim is to investigate the extent to which the hydrogen consumption and system weights vary for the same total installed power and battery capacity, but for various fuel cell component models with different parameters.

After running the simulations for the 4th scenario, the results for the DC bus voltage levels, the SoC, and the power outputs from the fuel cells and batteries were obtained.

The DC bus voltage was almost constant at 1000 V for the entire simulation time with fluctuations of less than 0.5%.

The battery SoC is shown in Figure 6. At the beginning, the SoC value remained close to the reference value of 50%. After t = 3500 seconds, the power demand increased and at approximately 4200 seconds it reached the maximum load of 1.2 MW. During the steady state, the battery SoC remained close to 40%. For the entire duration, the SoC value ranged between 35-65%, which lies within the recommended 20-80% range for degradation purposes.

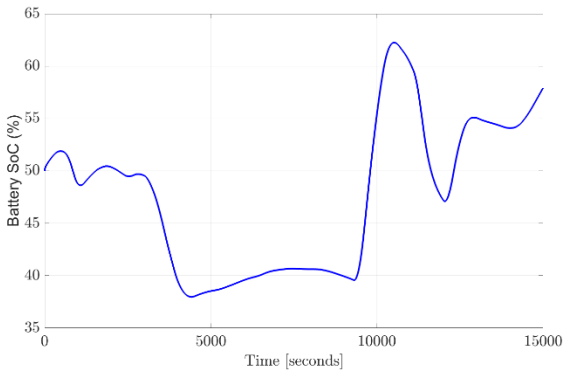

Figure 6: Battery SoC over time

In Figure 7, the power output from the fuel cells and batteries, and the analysed load profile are shown. The power losses were less than 1% for the entire voyage. The load of the fuel cells followed the power profile. A time constant of 360 seconds was used in the low-pass filter for the fuel cell current (Figure 4). Between 9,000-10,000 seconds the fuel cells provided the maximum power of 1.2 MW and the SoC is at 40% which is below the reference value of 50%. The difference between the fuel cell power and the load power in that interval is because the batteries need to be charged to reach the reference value. When the load drops, the fuel cells have extra power to charge the batteries. Between 14,500-15,000 seconds the fuel cell power converged to its lower limit which corresponds to 10% of the rated output for degradation and efficiency purposes [25]. At this interval the load profile was below the fuel cell power. If, in a different power profile, the load power was lower than the fuel cell power for a longer time interval, the battery SoC would increase until it reached the maximum limit of 80% SoC. Then, the fuel cell would have to be turned off. The condition of turning off the fuel cells is not accounted for by this strategy, but it will be considered in future work.

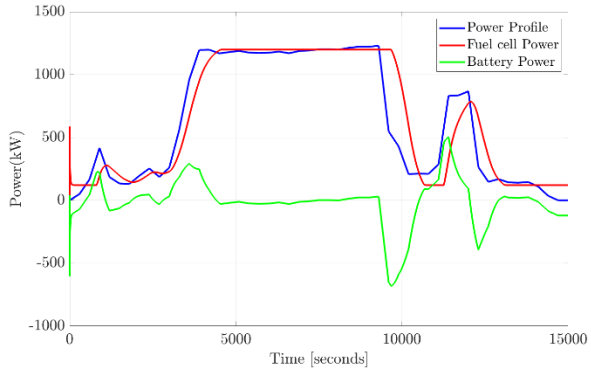

Figure 7: Power Profile vs Power output from fuel cells and batteries

A second limitation of the models and control approach is that battery efficiencies during charging and discharging were not considered. Hence, for total battery energy capacity higher or lower than the considered 550 kWh, and the same time constant in the low pass filter, the fuel consumption will remain the same, but the SoC range will change. For larger batteries, the SoC range will be smaller and for lower energy capacities than 550 kWh, the SoC range will be larger than in Figure 6.

The simulation results for the average hydrogen consumption for each of the five scenarios are summarized in Table 7. The same time constant in the low-pass filter was used for all scenarios. Hence, the differences in hydrogen consumption are due to the different fuel cell model parameters and stack efficiencies.

The detailed stack model requires the following parameters as inputs: voltage and current at 0 and 1 A, at nominal conditions and at the maximum operating point, the number of cells, nominal efficiency, nominal temperature, supply pressures of fuel and air, nominal air flow rate, and compositions of hydrogen, oxygen, and water.

The air and fuel flow rates are variable parameters that depend on the fuel cell current as shown in Equations (5) and (6) respectively, based on [17].

$$V_{air} = \frac{60{,}000RTNi_{fc}}{zFP_{air}Uf_{O2}y\%} \quad (5)$$

$$V_{fuel} = \frac{60{,}000RTNi_{fc}}{zFP_{fuel}Uf_{H2}x\%} \quad (6)$$

where V_{air} (litres/minute) and V_{fuel} (litres/minute) are the flow rates of air and fuel, R is the universal gas constant (J/molK), F is the Faraday's constant (C/mol), T is the operating temperature (K), N is the number of cells, i_{fc} is the fuel cell current which is controlled by the EMS, z is the number of moving electrons, P_{air} (atm) and P_{fuel} (atm) are the absolute supply pressures of air and fuel, Uf_{O2} and Uf_{H2} are the oxygen and hydrogen utilization rates, y% and x% are the percentages of oxygen in the oxidant and hydrogen in the fuel respectively. All the parameters on the right-hand side of (5) and (6) are assumed to be constant except for the current of the fuel cell i_{fc}.

The generic fuel cell model calculates the efficiency (η_{FC}) at various load points, as shown in (7), based on [14].

$$\eta_{FC} = \frac{P_{FC}}{V_{fuel}LHV} \quad (7)$$

where P_{FC} is the power of the fuel cell (W) at the different load points, V_{fuel} is the hydrogen flow rate calculated from (6) and converted from standard litres/minute to kg/sec, and LHV is the Lower Heating Value of hydrogen (J/kg).

Table 7. Average hydrogen consumption results

Scenario	Component	Fuel consumption [kg]
1	Zepp Y50	163.62
2	HyPM HD90	181.33
3	Zepp.X-150	162.29
4	Powercell-200	174.62
5	HyPM HD180	180.16

The lowest fuel consumption (162.29 kg) was obtained from the 3rd scenario with eight stacks Zepp.X-150 of 150 kW each, from Zepp. Solutions (Table 7). There is an 11.1 % difference with the scenario of the highest hydrogen consumption (181.33 kg), which corresponds to the case of 12 stacks of 100 kW from Hydrogenics.

At the same time interval of the considered power profile the average diesel fuel consumption of the original design was 156 kg/hour which corresponds to 649 kg of diesel required for the entire voyage of 4.16 hours. Thus, the diesel consumption was approximately 3.5-4 times higher than the hydrogen consumption, which was expected because of the Lower Heating Value of diesel, and the lower operating efficiency of the main propulsion diesel engine.

4.2 Uncertainties of fuel costs

Uncertainties have been considered for the fuel prices to investigate variations in the hydrogen cost. In Figure 8, the hydrogen price variations for 2023, based on [26], are presented using normal distribution graphs. The number of samples was set to 1,000,000, the mean was 4.5 ($/kg) and the standard deviation was 0.4472.

The vessel operates mainly in the Baltic Sea and the North Sea in European countries. It is important to note that these fuel prices are for green hydrogen production costs, so that the well-to-wake emissions are minimized. Hence, these are bare production costs and do not reflect the actual price paid by consumers, particularly when considering compressed hydrogen, liquefied hydrogen, liquid organic hydrogen carriers, or chemical hydrides. In 2023, the green hydrogen prices range between 3.5-5.5 $/kg (Figure 8) in the operational area. In general, the fuel prices in the vessel's operational area are higher than those in most parts of the world [26].

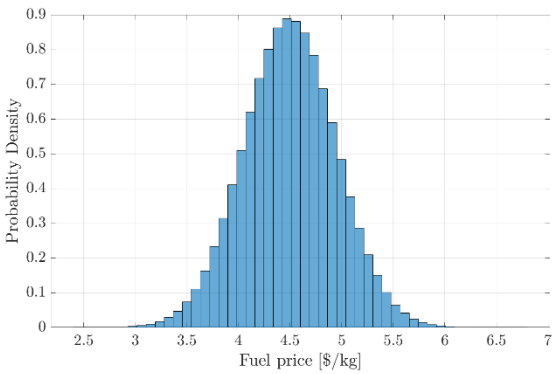

Figure 8: Hydrogen price variations for 2023

The fuel cost range ($) is presented in Figure 9. It was obtained by multiplying the fuel consumption (kg) for each scenario (Table 7) with the fuel price ($/kg) extracted from the normal distribution graph in Figure 8.

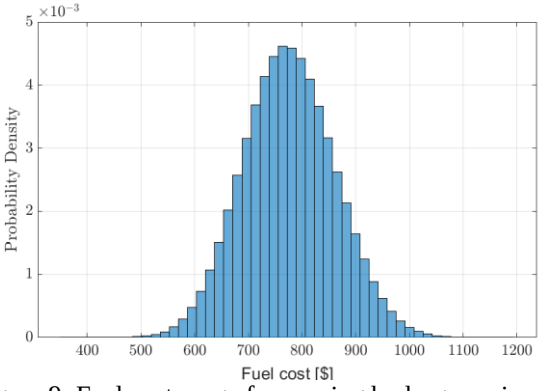

Figure 9: Fuel cost range for varying hydrogen price

Figure 10 presents the fuel cost range for each scenario with 95% confidence interval. The middle black line represents the mean (average) values, and the dotted lines represent the lower and upper limits of the fuel costs for each scenario.

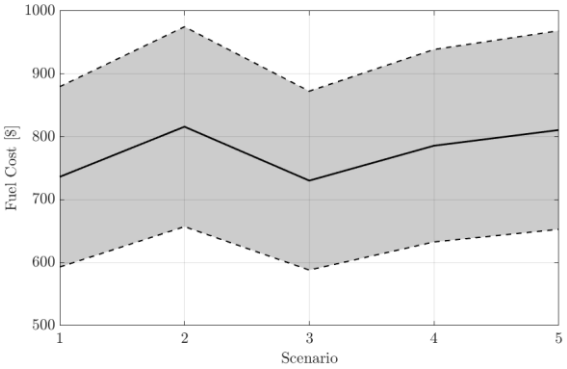

Figure 10: Fuel cost range for the 5 scenarios with 95% confidence interval

4.3 Average fuel costs vs weights

The solutions for the five scenarios, in terms of weight and average fuel cost, are presented in Table 8 and Figure 11.

Table 8. Fuel cost and weight for each scenario

Scenario	Fuel cost [$]	Weight [tons]
1	736.3	12.78
2	816.0	11.62
3	730.3	10.54
4	785.8	14.12
5	810.7	11.62

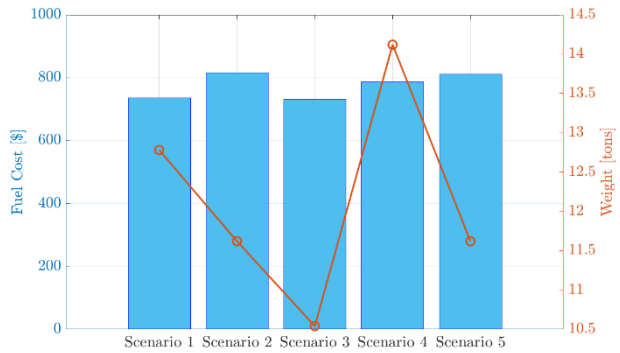

Figure 11: Weight-average fuel cost solutions for each scenario for 2023 hydrogen prices

It can be observed in Figure 11 that the configuration with eight stacks of 150 kW (Scenario 3) has the lowest total fuel cost (730 $) with an average difference of 7.1% from the other solutions, and the lowest total weight (10.54 tons) with an average difference of 15.4% from the other solutions.

The weight of the original diesel engine is equal to 11.6 tons. The weight of the considered fuel cells and batteries in the retrofitted version ranges between 10.54 – 14.12 tons from the five scenarios (Figure 11). The system weight of the hydrogen-hybrid version for the 3rd scenario is 1 ton less than that of the original system, without considering other components, apart from the main equipment that provides the propulsion loads.

5. CONCLUSIONS

This research focused on alternative energy sources in marine systems, specifically on a hydrogen-fuelled vessel, with hybrid power supply, obtained by conceptual retrofitting of a diesel-based cargo vessel.

Our work included a modelling and control study for the hypothetical retrofitting employing fuel cell, battery, and converter models that can be adapted for various power plant sizes and ship types, making our approach highly versatile.

The fuel cells and batteries were sized based on the most power and energy intensive (fluctuating) power profiles, but the modelling and control results were presented for a short voyage of approximately 4 hours for computational requirements. The developed robustly coordinated control strategy, which can be applied to different vessel power profiles, resulted in less than 0.5% DC bus voltage fluctuations from its reference value, and a battery SoC range of 35-65% by efficiently splitting the power between the fuel cells and batteries with power losses of less than 1% for the entire voyage.

A database of five fuel cell stacks, from different manufacturers, was considered in this model-based parametric study to investigate different combinations in terms of fuel consumption, cost, and weight. The fuel cost range was estimated with a 95% confidence interval for each case by multiplying the fuel price from the normal distribution graph (3.5-5.5 $/kg for 2023) with the hydrogen consumption for each scenario. Overall, the 3rd scenario with eight stacks/150 kW from Zepp. Solutions resulted in the lowest fuel cost of 703$ with an average difference of 7.1% from the other solutions. This configuration also resulted in the lowest combined fuel cell and battery system weight of 10.54 tons, which is 1 ton lighter than that of the original diesel engine.

In future work, an optimization algorithm will be implemented for the sizing and control problem, considering capital costs, system volumes, and component degradation. An optimization algorithm will explore a larger design space. Inverters, motors, and propeller models will also be developed, and a lifecycle analysis of the emissions and costs will be conducted.

ACKNOWLEDGEMENT

This research was supported by the Sustainable Hydrogen Integrated Propulsion Drives (SH2IPDRIVE) project, which has received funding from RvO (reference number MOB21013) through the RDM regulation of the Ministry of Economic Affairs and Climate Policy.

REFERENCES

[1] D. Gritsenko, "Regulating GHG Emissions from shipping: Local, global, or polycentric approach?", *Mar. Policy*, vol. 84, pp. 130–133, Oct. 2017.

[2] S. Fang, Y. Wang, B. Gou and Y. Xu, "Toward future green maritime transportation: An overview of seaport microgrids and all-electric ships", *IEEE Trans. Veh. Technol.*, vol. 69, no. 1, pp. 207-219, Jan. 2020.

[3] O. B. Inal, J. F. Charpentier and C. Deniz, "Hybrid power and propulsion systems for ships: Current status and future challenges", *Renewable and Sustain. Energy Rev.*, vol. 156, Mar. 2022.

[4] J. Zhu, L. Chen, B. Wang and L. Xia, "Optimal design of a hybrid electric propulsive system for an anchor handling tug supply vessel", *Appl. Energy*, vol. 226, pp. 423-436, Sept. 2018.

[5] J. Zhu, L. Chen, B. Wang and L. Xia, "Bi-objective optimal design of plug-in hybrid electric propulsion system for ships", *Energy*, vol. 177, pp. 247-261, Jun. 2019.

[6] T. L. Vu, A. A. Ayu, J. S. Dhupia, L. Kennedy and A. K. Adnanes, "Power Management for Electric Tugboats Through Operating Load Estimation", *IEEE Trans. on Control Syst. Technol*., vol. 23, no. 6, pp. 2375–2382, Nov. 2015.

[7] F. D. Kanellos, "Optimal power management with GHG emissions limitation in all-electric ship power systems comprising energy storage systems". *IEEE Trans. Power Syst*., vol. 29, no. 1, pp. 330-339, Jan. 2014.

[8] F. D. Kanellos, A. Anvari-Moghaddam and J. M. Guerrero, "A cost-effective and emission-aware power management system for ships with integrated full electric propulsion", *Electric Power Syst. Res*., vol. 150, pp. 63-75, Sept. 2017.

[9] Z. Wang and X. Li, "Research on multi-objective optimization of capacity allocation for marine hybrid energy storage systems", in *Proc. IOP Conf. Ser: Earth Environ. Sci*., vol. 692, 1st ed., Mar. 2021.

[10] C. Chen, X. Wang and J. Xiao, "An energy allocation strategy for hybrid ship DC power system based on genetic algorithm", *IETE J. Res.*, vol. 62, no. 3, pp. 301-306, Oct. 2015.

[11] L. Balestra and I. Schjølberg, "Modelling and simulation of a zero-emission hybrid power plant for a domestic ferry", *Int. J. Hydrogen Energy*, vol. 46, no. 18, pp. 10924-10938, Mar. 2021.

[12] L. Balestra and I. Schjølberg, "Energy management strategies for a zero-emission hybrid domestic ferry", *Int. J. Hydrogen Energy*, vol. 46, no. 77, pp. 38490-38503, Nov. 2021.

[13] T. Jaster, A. Rowe and Z. Dong, "Modeling and simulation of a hybrid electric propulsion system of a green ship", in *Proc. 10th IEEE/ASME Int. Conf. Mechatronic Embedded Syst Appl. (MESA)*, Senigallia, Italy, Sept. 10-12, 2014, pp. 1-6.

[14] M. Cha *et al.*, "Power Management Optimisation of a Battery/Fuel Cell Hybrid Electric Ferry", in *Proc. 31st Australasian Univ. Power Eng. Conf. (AUPEC)*, Perth, Australia, Sept. 26-30, 2021.

[15] A. M. Bassam, A. B. Philips, S. R. Turnock and P. A. Wilson, "Development of a multi-scheme energy management strategy for a hybrid fuel cell driven passenger ship", *Int. J. Hydrogen Energy*, vol. 42, no. 1, pp. 623-635, Jan. 2017.

[16] A. M. Bassam, A. B. Philips, S. R. Turnock and P. A. Wilson, "An improved energy management strategy for a hybrid fuel cell/battery passenger vessel", *Int. J. Hydrogen Energy*, vol. 41, no. 47, pp. 22453–22464, Dec. 2016.

[17] N. M. Souleman, O. Tremblay and L. A. Dessaint, "A generic fuel cell model for the simulation of fuel cell vehicles", in *Proc. 5th IEEE Veh. Power and Propulsion Conf. (VPPC)*, Dearborn, MI, USA, Sept. 7-10, 2009.

[18] O. Tremblay, L. A. Dessaint and A. I. Dekkiche, "A Generic Battery Model for the Dynamic Simulation of Hybrid Electric Vehicles", in *Proc. 4th IEEE Veh. Power and Propulsion Conf. (VPPC)*, Arlington, TX, USA, Sept. 9-12, 2007.

[19] K. Kwon, D. Park and M. K. Zadeh, "Load Frequency-Based Power Management for Shipboard DC Hybrid Power Systems", in *Proc. 29th IEEE Int. Symp. Ind Electron. (ISIE)*, Delft, Netherlands, Jun. 17-19, 2020, pp. 142–147.

[20] W. Yeetum and V. Kinnares, "PI Controller Based on Direct Synthesis Method for DC-Link Voltage Control of Active Power Filter", in *Proc. Int. Elect. Eng. Congr. (IEECON)*, Krabi, Thailand, Mar. 7-9, 2018.

[21] Maritime hydrogen fuel cell systems - zepp.solutions, https://zepp.solutions/en/maritime-fuel-cell-systems/ (accessed Feb. 1, 2023).

[22] Accelera | Powering the World with Clean Energy, https://www.accelerazero.com/ (accessed Feb. 5, 2023).

[23] Marine | PowerCell Group | Hydrogen Fuel Cell Solutions, https://powercellgroup.com/segments/marine (accessed Feb. 10, 2023).

[24] M. Boekhout, "Hydrogen Powered Ship Propulsion for High-Speed Craft: The implementation of Fuel Cell Battery Propulsion Systems", M.S. Thesis, Dept. 3mE, Delft Univ. of Technol., Delft, Netherlands, 2020.

[25] X. Wang *et al.*, "Sizing and Control of a Hybrid Ship Propulsion System Using Multi-Objective Double-Layer Optimization", *IEEE Access*, vol. 9, pp. 72587–72601, May 2021.

[26] Green hydrogen economy - predicted development oftomorrow:PwC, https://www.pwc.com/gx/en/industries/energy-utilities-resources/future-energy/green-hydrogen-cost.html (accessed Feb. 10, 2023).

A Method to Enable Reduced Sensor Capacitor Voltage Estimation in Modular Multilevel Converters

Eugene Tinjinui Ndoh[a*], Seongsu Byeon[a], Lotz Marc[b] and Soeren Ehlers[a]

[a] DLR Institute for Maritime Energy Systems, Geesthacht, Germany
[b] Technische Universität Braunschweig, Braunschweig, Germany
*eugene.ndoh@dlr.de

Abstract

Bulk power applications such as shipping increasingly consider multilevel converter topologies such as modular multilevel converters (MMC), which offers the advantages of scalability, good power quality, and reconfigurability. The internal functioning of MMC requires complete knowledge of the capacitor voltages that make up their submodules meaning a large number of sensors are needed and thus a high number of potential points of failure exist. To increase reliability and reduce investment costs, state estimation techniques such as KALMAN filters have been employed to replace the physical sensors. Analytical techniques based on the knowledge of arm current, arm voltage, and submodule states have also been developed. These techniques exploit the fact that at an insertion index of 1, the arm voltage equals the capacitor voltage on the submodule which permits the estimation algorithm to refresh periodically with measured data thereby increasing the accuracy. This method requires a long refresher time, especially when many submodules are used per arm. In this study, we propose an improved analytical estimation by not only using unity insertion indices, but also exploiting transitions between two successive insertion indices. The study was carried out on a 4 submodule per arm MMC system. The estimated capacitor voltages were then compared with sensor-based voltage measurements confirming the validity of the proposed method. It was then integrated into a complete MMC controller including the inner controls such as circulating current and capacitor voltage balancing.

Keywords: Modular Multilevel Converter, Insertion Index, Modulation index, Capacitor Voltage balancing, Circulating Current.

1. INTRODUCTION

The shipping industry is currently facing the challenge of achieving its climate goals through the adoption of new technologies. The electrification of ships is a critical factor in this regard, as it permits better integration of renewable energy and energy storage into the ship energy mix. Both academia and industry are seeking feasible ways to enable zero-emissions shipping. While direct current (DC) systems have shown benefits over conventional alternating current (AC) systems, their deployment has been limited to low-voltage direct current (LVDC) systems for small vessels, such as offshore support and inland vessels. To enable true DC transition in shipping, medium-voltage direct current (MVDC) systems [1] need to be developed, as the current electrical propulsion systems for large commercial vessels are based on medium-voltage alternating current (MVAC).

Modular Multilevel Converters (MMC) have been identified as the most promising power converter topology for medium-voltage direct current (MVDC) systems for large commercial vessels [2]. The full-bridge topology of MMC enhances the fault-limiting capabilities of shipboard power systems, which is one of the most critical design criteria for MVDC systems. Additionally, MMC offer modularity, flexible voltage levels, and low harmonic output voltages. However, one of the drawbacks of MMC is the high number of sensors required to measure numerous parameters, such as both AC and DC voltages/currents, arm currents, and capacitor voltages [3]. The high number of sensors lead to increase in the system size and cost as well as a reduction of the reliability. The sensors for capacitor voltage measurements account for a large portion of these sensors. Various studies have been conducted to address this challenge by adapting numerous estimation techniques for capacitor voltage estimation that could replace conventional sensors.

In this study, we propose an improved capacitor voltage estimation method for a grid tied MMC ship systems. Instead of utilizing a unity insertion index, the proposed method exploits the transitions between two successive insertion indices. In effect, insertion indices under normal operation change in steps of one. Knowing the changes in arm voltage,

@2023 Ndoh, E. T. et al., published by TU Delft OPEN Publishing on behalf of the authors. Licensed under a Creative Commons Attribution CC BY license.
DOI: https://doi.org/10.59490/ moses.2023.672

the arm currents as well as the state changes of the switches at the transition points permit capacitor voltage calculation. Analytical equations permit the estimation of the voltages between the transition instances. Given that state transitions occur throughout the period, the refreshing time for the proposed voltage estimation is shorter.

The rest of the paper is structured as follows: Section 2 provides an overview of the MMC topology, and control systems, Section 3 describes the state-of-the-art voltage estimation methods, Section 4 describes the proposed voltage estimation method, Section 5 presents the simulation results and an analysis of the obtained outcomes. Finally, in Section 6, the paper concludes with a summary of the main findings, a discussion of their implications, and possible future research directions.

2. MODELLING OF THE MMC

2.1. Topology descriptions

Figure 1 shows the architecture of a three-phase MMC consisting of half-bridge (HB) submodules. The MMC's DC bus or DC link are connected to the positive and negative bars of the three converter legs (a, b, c), each of which is made up of two arms. The arm connected to the positive bar is referred to as the upper arm (u), and the arm connected to the negative bar is referred to as the lower arm (l). Each arm contains a group of submodules (SM) and an inductor (L_{arm}). The inductor for each arm is serially linked to the arm SM group to reduce circulating currents arising from voltage disparities between the arms.

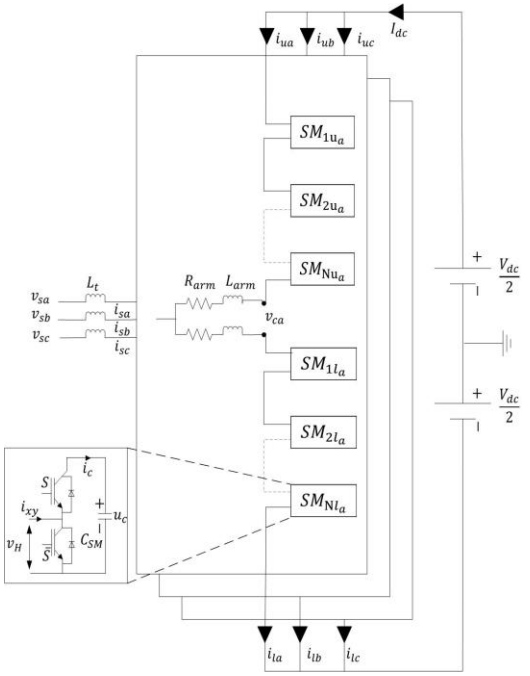

Figure 1: MMC architecture with HB submodule

Several types of MMC submodules [12] have been developed in the last few decades, such as Half-bridge and the Full-bridge submodules. The half-bridge (HB) submodule is often referred to as a chopper cell. It is composed of two MOSFET or IGBT switching devices with antiparallel diodes (S and $\overline{S}$) and a capacitor (C_{SM}). The two switching devices are operated in a complementary manner to regulate the capacitor voltage at a value of u_C. The capacitor voltage is given by:

$$u_c = \frac{1}{C}\int_{0+}^{t} i_c(t)\, dt \quad (1)$$

The capacitor current (i_c) in terms of the arm current (i_{xy}) and the switching state, S, is given by

$$i_c = S\, i_{xy} \quad (2)$$

Depending on the state of the top switch, the effect on the capacitor voltage for different directions of the arm current are listed in Table 1. The output voltage of the HB has two voltage levels, "0" and "u_c". When the top switch is "on", the output voltage is equal to u_c. In this mode, the capacitor voltage increases for positive arm currents and decreases for negative arm currents. When the top switch is "off", the output voltage is equal to "0", In this mode, the capacitor voltage remains constant, irrespective of the current direction. The output voltage of the HB can be represented in terms of the voltage and switching state of the top switch as $v_H = S\, u_c$.

S	v_H	i_{xy} >0	i_{xy} ≤0
1	u_c	$u_c \uparrow$	$u_c \downarrow$
0	0	$u_c \approx$	$u_c \approx$

Table 1. Switching states of HB SM

2.2. Modelling of the MMC

In Figure 2, the MMC is modelled using variable arm voltages, which are determined based on the states of the SMs and their corresponding capacitor voltages. In this study, an MMC inverter connected to a strong ship grid is considered. All three phases are controlled to inject balanced power into the grid, and normal operation (no fault) is assumed.

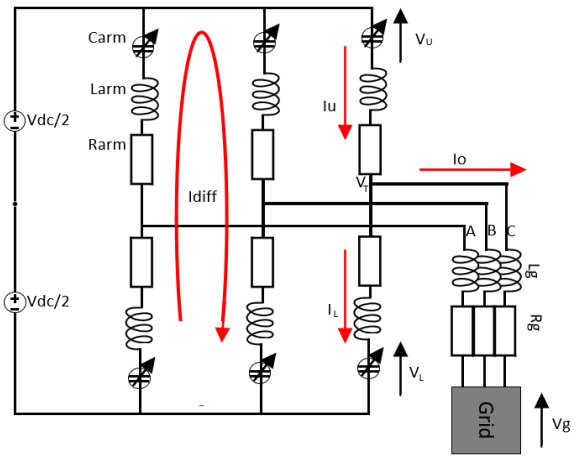

Figure 2: MMC single line diagram

In particular, for one phase, equation (3) and (4) can be established.

$$\frac{V_{dc}}{2} - V_U = V_T + \left(R_{arm} * I_U + L_{arm}\frac{dI_U}{dt}\right) \quad (3)$$

$$\frac{V_{dc}}{2} - V_L = -V_T + \left(R_{arm} * I_L + L_{arm}\frac{dI_L}{dt}\right) \quad (4)$$

As seen in equations (5) and (6) the arm currents consist of a DC component, an AC component, and a second-harmonic component known as the circulating current (I_{cc}). This circulating current flows between the arms and is caused by the differential voltages on each arm, resulting from their distinct switching patterns. The differential Current (I_{diff}) is the sum of the DC and second harmonic current.

$$I_U = \frac{I_{dc}}{3} + I_{cc} + \frac{I_o}{2} \quad (5)$$

$$I_L = \frac{I_{dc}}{3} + I_{cc} - \frac{I_o}{2} \quad (6)$$

I_{dc} represents the current from the DC link. Adding and subtracting equation (5) from equation (6) yields equation (7) and (8), respectively.

$$I_o = I_U - I_L \quad (7)$$

$$I_U + I_L = 2 * \left(\frac{I_{dc}}{3} + I_{cc}\right) = 2 * I_{diff} \quad (8)$$

By subtracting and adding equations (3) and (4), equations (9) and (10) are derived.

$$V_T = \left(\frac{-V_U + V_L}{2}\right) - \left(\frac{R_{arm}}{2} * I_o + \frac{L_{arm}}{2}\frac{dI_o}{dt}\right) \quad (9)$$

$$V_{dc} = (V_U + V_L) + 2\left(R_{arm} * I_{dif} + L_{arm}\frac{dI_{dif}}{dt}\right) \quad (10)$$

2.3. MMC control systems

The MMC control scheme illustrated in Figure 3 is divided into two main components: outer power control and inner grid current control. The output power control determines the power exchange between the MMC and the AC grid. It provides the reference current levels that will be tracked by the inner grid current control. Given that the grid voltage and frequency at the point of common coupling are fixed, power is controlled by controlling the injected currents.

In addition to the modulation strategy, MMC specific control algorithms also exist. One such algorithm is the circulating current suppression control (CCSC), which mitigates the presence of second-harmonic currents in the arms. Circulating currents lead to underutilization of the SM current-handling capacity, higher power losses, and a requirement for larger heat sinks.

Another critical MMC-specific algorithm is the capacitor voltage sorting and balancing (CVSB). It ensures the equalization of all SM capacitor voltages within an arm. Failure to maintain a balance leads to SM divergence, resulting in extreme voltage breakdown in capacitors that are constantly charging, or voltage collapse in capacitors that are constantly discharging. Thus, the CVSB algorithm ensures safe and uninterrupted MMC operations.

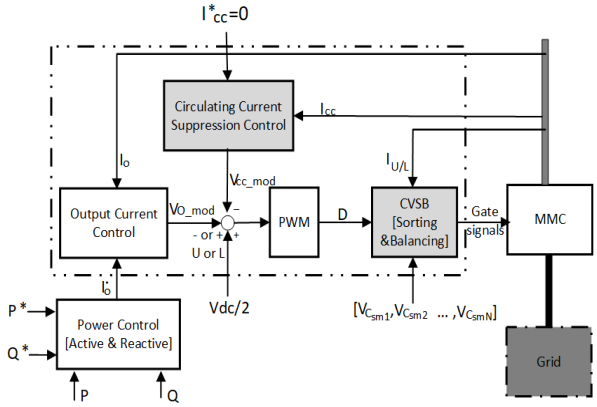

Figure 3: MMC control scheme

This study uses PI controllers for the MMC controls. To ensure the optimal performance of these controllers, it is necessary to transform AC quantities into the DQ coordinate system using Clark and Park transformations. This ensures the proper functioning of the controllers. Furthermore, the synchronization of the MMC with the ship grid is achieved through the utilization of a Phase-Locked Loop (PLL), which extracts the electrical angle from the grid voltage signals. We chose to align the grid voltage along the D-axis.

2.3.1. Output current control

Based on the single-line diagram in Figure 2 the equivalent circuit for the AC output current is shown in Figure 4.

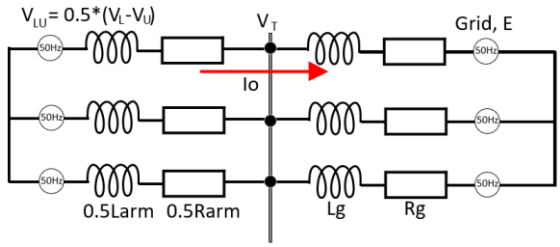

Figure 4: Equivalent circuit for the grid current

By deriving equation (11) from Figure 4, the design equation (12) for the control system in the ABC reference frame is obtained.

$$V_{LU} = \left(R_g + \frac{R_{arm}}{2}\right) * I_o + \left(L_g + \frac{L_{arm}}{2}\right) * \frac{dI_o}{dt} + E \quad (11)$$

With $R = \left(R_g + \frac{R_{arm}}{2}\right)$ and $L = \left(L_g + \frac{L_{arm}}{2}\right)$,

$$\begin{bmatrix} V_a \\ V_b \\ V_c \end{bmatrix} = R * \begin{bmatrix} I_{o_a} \\ I_{o_b} \\ I_{o_c} \end{bmatrix} + L * \begin{bmatrix} \frac{dI_{o_a}}{dt} \\ \frac{dI_{o_b}}{dt} \\ \frac{dI_{o_c}}{dt} \end{bmatrix} + \begin{bmatrix} E_a \\ E_b \\ E_c \end{bmatrix} \quad (12)$$

The equation (13) represents equation (12) in DQ coordinates.

$$\begin{bmatrix} V_d \\ V_q \end{bmatrix} = R * \begin{bmatrix} I_{o_d} \\ I_{o_q} \end{bmatrix} + L * \begin{bmatrix} \frac{dI_{o_d}}{dt} \\ \frac{dI_{o_q}}{dt} \end{bmatrix} + L\omega * \begin{bmatrix} -I_{o_q} \\ I_{o_d} \end{bmatrix} + \begin{bmatrix} E_d \\ E_q \end{bmatrix} \quad (13)$$

The plant model for the output current can be obtained by applying the Laplace transform to the equation, resulting in equation (14).

$$\begin{bmatrix} V_d(s) \\ V_q(s) \end{bmatrix} = (R + sL) * \begin{bmatrix} I_{o_d}(s) \\ I_{o_q}(s) \end{bmatrix} + L\omega * \begin{bmatrix} -I_{o_q}(s) \\ I_{o_d}(s) \end{bmatrix} + \begin{bmatrix} E_d(s) \\ E_q(s) \end{bmatrix} \quad (14)$$

To enable independent control of the D-axis and Q-axis currents, the coupling term $-L\omega I_{o_q}(s)$, $L\omega I_{o_d}(s)$ and the grid voltage values E_d and E_q are fed forward. By employing pole-cancellation techniques, the PI gains can be determined using the following equation:

$$K_{p\_c} = 2\pi L f_{bw}, \quad (15)$$
$$K_{i\_c} = 2\pi R f_{bw}, \quad (16)$$

In these equations, f_{bw} represents the controller bandwidth, which is typically set to 1/10th of the switching frequency.

2.3.2. Output power control

The output D and Q current references are determined based on active and reactive power controls respectively. Considering the chosen alignment of the grid voltage with the D-axis ($E_q = 0$), equation (17) represents the active power and equation (18) represents the reactive power.

$$P = \frac{3}{2}\left(E_d I_d + E_q I_q\right) = \frac{3}{2}\left(E_d I_d\right) \quad (17)$$
$$Q = \frac{3}{2}\left(E_q I_d - E_d I_q\right) = -\frac{3}{2}\left(E_d I_q\right) \quad (18)$$

2.3.3. Circulating current suppression

In an MMC, the second-harmonic circulating current primarily circulates within the converter itself. This has AC component of twice the fundamental frequency which must be suppressed. Figure 5 shows the equivalent circuit of the differential current. With $V_{cc} = V_u + V_L$

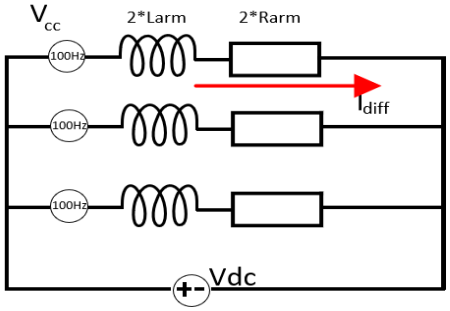

Figure 5: Equivalent circuit for differential current

The circulating current part of the differential current [100 Hz] is governed by equation (19).

$$V_{cc} = \left(R_{arm} * I_{cc} + L_{arm}\frac{dI_{cc}}{dt}\right) \quad (19)$$

Given that the second harmonic is a negative sequence, the synchronization signal from the PLL is multiplied by -2 before the DQ transform. The circulating current plant model in DQ coordinates is given by equation (20).

$$\begin{bmatrix} V_{cc_d} \\ V_{cc_q} \end{bmatrix} = R_{arm}\begin{bmatrix} I_{cc_d} \\ I_{cc_q} \end{bmatrix} + L_{arm}\begin{bmatrix} \frac{dI_{cc_d}}{dt} \\ \frac{dI_{cc_q}}{dt} \end{bmatrix} + 2L_{arm}\omega * \begin{bmatrix} I_{cc_q} \\ -I_{cc_d} \end{bmatrix} \quad (20)$$

The circulating current control equation is identical to that of the output current control. Pole placement was also used to tune the PI gains.

2.4. Modulation and arm capacitor voltage sorting and balancing (CVSB)

2.4.1. Modulation

Pulse width modulation (PWM) was used to translate the control output into gate signals. By adjusting the duty cycles of the switching devices, the targeted output can be achieved. MMC use multi-carrier modulation schemes (N carrier signals) such as phase-shifted carrier (PSC-PWM)

and level-shifted carrier (LSC-PWM) modulations. In PSC-PWM, triangular carrier signals with unity magnitudes but phase-shifted from one another are compared with the modulating signal. In LSC-PWM, triangular carrier signals with magnitudes equal to 1/N of unity are compared with the modulating signal. Another modulation technique used in this study is the nearest level modulation (NLM) which is based on approximating the insertion indices to the nearest step level based on the modulating signal.

2.4.2. Arm capacitor voltage sorting and balancing (CVSB)

To avoid the collapse of the MMC or the breakdown of capacitors due to the divergence of capacitor voltages, the capacitor voltages are strictly supervised and adjusted. The voltages are first read, sorted in ascending order, and then the SM to be switched are chosen based on their relative voltages, the current insertion index and direction of the arm current as shown in Figure 6. For any insertion index, D, if the arm current is positive, the D submodules with the least charged capacitors are switched on so that they can charge up, whereas for negative arm currents, the D submodules with the highest charged capacitors are discharged.

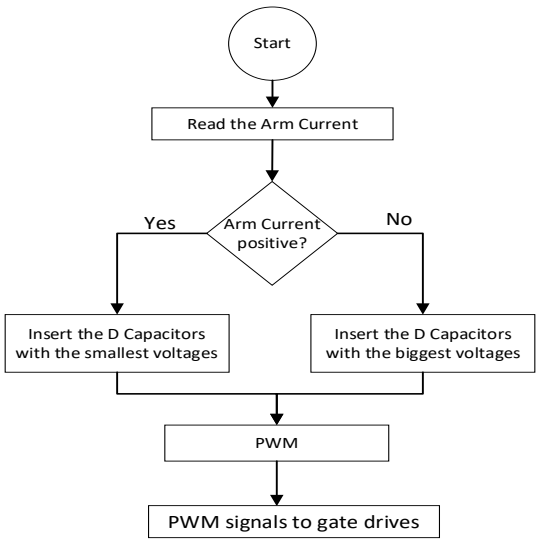

Figure 6: CVSB algorithm

3. CURRENT CAPACITOR VOLTAGE ESTIMATION METHODS FOR MMC.

Several methods have been proposed most of which rely on the state-space model of the MMC system. In [4] an adaptive back-stepping observer was proposed, whereas in [5] the authors used Kalman filter estimation. In [6], a sliding mode observer and state estimator were used, considering currents and capacitor voltages as state variables. In [7] the authors used an adaptive filter, but this time included capacitances as an uncertain parameter as capacitances of electrolytic capacitors may vary greatly. This increases the accuracy but also the complexity of the problem which has to be solved in near real time in order to provide the gate signals on time. In [8], an observer was directly integrated into model predictive control of the MMC. In [9] a modified sliding-mode observer was proposed.

Analytical methods based on SM states have also been proposed and have the advantage of being both simple and able to periodically correct the estimation errors by using real measurement data. In [10] and [11], the authors used the analytical expression of the capacitor voltage in equation (21). The total arm voltage was measured and compared to the sum of the estimated arm-capacitor voltages. The estimation error was then redistributed among all "on" state capacitors either equally or based on their duty cycles or their average switching function.

$$V_{c_{xyn}}(k+1) = \frac{1}{C_{sm}} \int_{t_k}^{t_{k+1}} S_{xyn}\, i_{xy} dt + V_{c_{xyn}}(k) \quad (21)$$

For this technique, refreshment with accurate values from arm voltage measurement only takes place when the insertion index (D) of the arm is one. At this index, the arm voltage equals the capacitor voltage of the SM in "on" state minus the small voltage drop across the active SM in the arm.

The validity of all the above-mentioned methods, and thus the accuracy and stability of the control loops built up on them depends on the accuracy of the underlying models used by these estimators. Often, these methods must pass through model linearization which reduce model fidelity. Furthermore, the model parameters are usually assumed to be constant, however, in reality, they fluctuate. In particular, observer-based methods provide a filtering property that estimates the states of variables values from their previous values and measurable outputs. They rely entirely on the mathematical model of the system and are thus very vulnerable to changes in parameters due to ageing or temperature changes. Analytical techniques on their part also rely on the accuracy of the model. However, this dependence can be eliminated using sufficiently high refreshment. For example, simple interpolation techniques other than the analytical equation of capacitor (dis)charging could be used between measurement points if the refreshment was sufficiently fast. As a matter of fact, analytical techniques amount to the digital equivalent of signal sampling and using

approximation techniques to estimate the values between samples. The higher the sampling rate, the better the quality of the reconstructed signal. However, the current methods have a low refreshing frequency, as this is only possible if the arm insertion index equals unity. That is, for an MMC with N+1 steps and period T, we have a window of less than d_1*T, where we can apply this technique, as shown in Figure 7 by the red window. d_1 is the arm duty cycle at unity insertion index. Furthermore, these refreshments are not uniformly distributed throughout the period, but are regrouped within the red band corresponding to the unity insertion index, as shown in Figure 7.

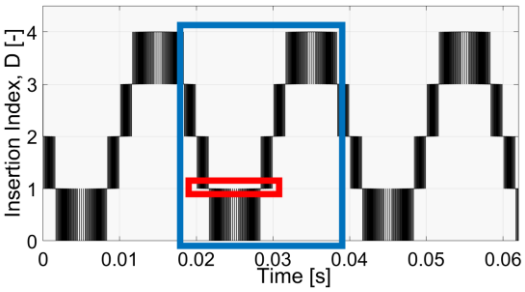

Figure 7: Insertion index of upper arm

Analytical techniques are a good option if a method can be found that increases the refreshment frequency and if these refreshments are uniformly distributed throughout the period irrespective of the insertion index. This is the purpose of the proposed method.

4. PROPOSED CAPACITOR VOLTAGE ESTIMATION

Unlike current analytical estimation algorithms, the proposed algorithm is a state transition-based technique that uses the change in the measured arm voltage and attributes it to a particular arm SM capacitor. Gate-state changes provide a unique identification of the SM.

As shown in Figure 7, the insertion index of an MMC changes by one under normal operation. This means that optimally, one SM goes on or off at any given time. Therefore, the change in arm voltage corresponds to the contribution of the SM. Given that switching occurs through the period and in the sub-second range, the refresh rate is high and distributed over most of the period on the insertion index graph, as shown by the blue window in Figure 7. For this algorithm, first the capacitor voltages were initialized. The signals from the gates were monitored to detect any state transitions. At any time, a state transition is retained if no other state transition is simultaneously detected. The SM undergoing the change is attributed the corresponding change in arm voltage minus a negligible voltage drop as illustrated in Figure 8.

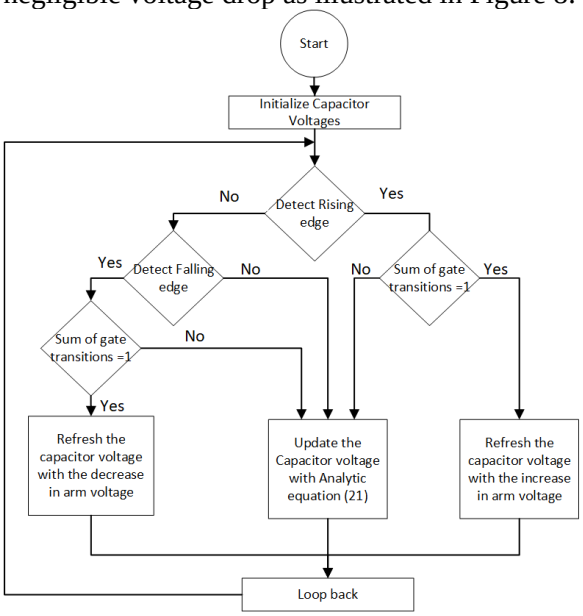

Figure 8: Proposed CVE algorithm

5. SIMULATION VERIFICATION

5.1. MMC simulation model

The performance of the proposed CVE was tested through simulations using MATLAB/Simulink software. The MMC test parameters are listed in Table 2. The sensor measurements were used as benchmarks.

Parameters	*Value*
DC link Voltage (kV)	10
AC grid RMS Voltage (kV)	3.54
AC grid frequency (Hz)	50
Submodule Capacitance (mF)	2
Arm inductance (mH)	1
Grid inductance (mH)	2
Switching frequency (Hz)	2000
Number of submodules per arm	4

Table 2: System Parameter

5.2. Results and discussions

5.2.1. Accuracy of the proposed method

The proposed CVE algorithm was analyzed in steady state condition using LSPWM and compared with sensor-based measurements. As shown in Figure 9, the estimated capacitor voltage matches that of the sensor-based method. The error reached up to 0.02 %.

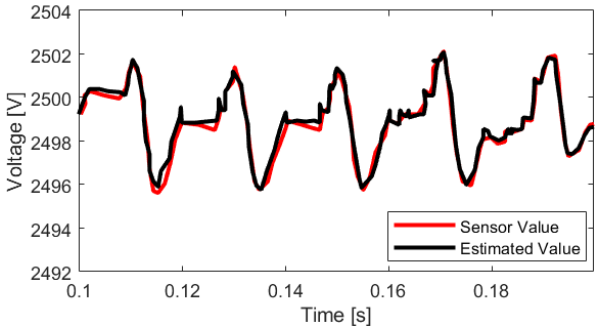

Figure 9: Proposed CVE performance

5.2.2. Dynamic performance in a closed loop

The proposed method was integrated into the MMC closed loop control. Figure 10 to Figure 13 show that the estimation seamlessly blends into the MMC controls. The proposed CVE estimation accuracy and speed were thus sufficient for MMC control. The settling time for the outer power controls are less than 0.1s as shown in Figure 10 and Figure 11. In Figure 12, the circulating current suppression control was triggered at the 0.1s thereby suppressing the 100 Hz currents in less than 0.03s. Figure 13 shows the output voltage and current of the converter. Figure 14 shows that the capacitor voltage for all the SM within the arms don't diverge meaning, the values provided by the proposed CVE estimation algorithm are sufficiently accurate to maintain stable operation in the CVSB block.

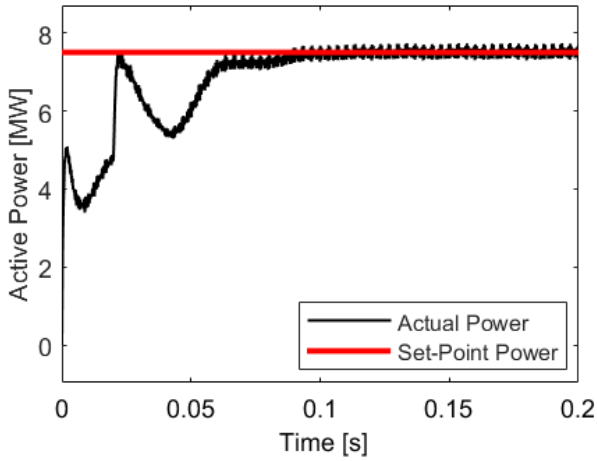

Figure 10: Active power controller time response

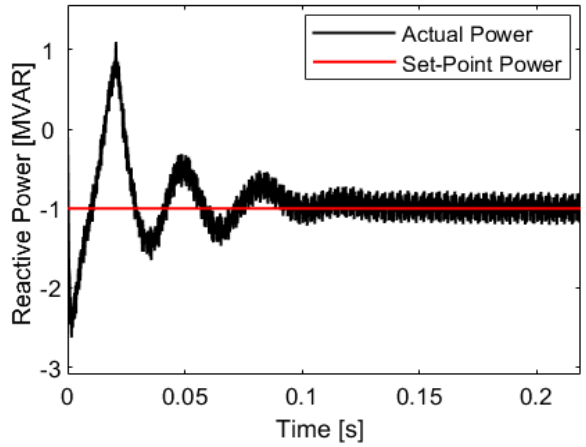

Figure 11: Reactive power time response

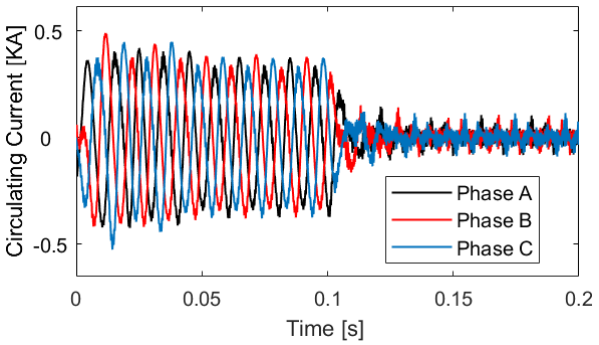

Figure 12: Circulating current suppression control

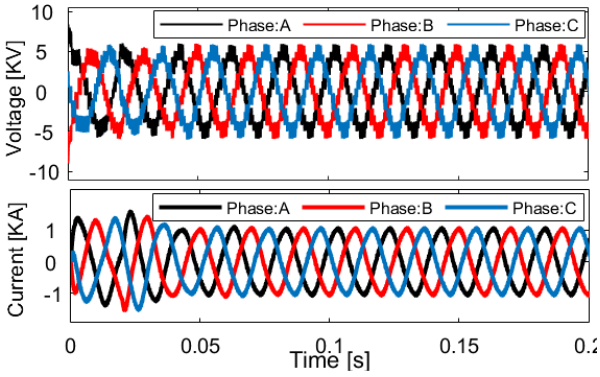

Figure 13: Converter output voltage and current

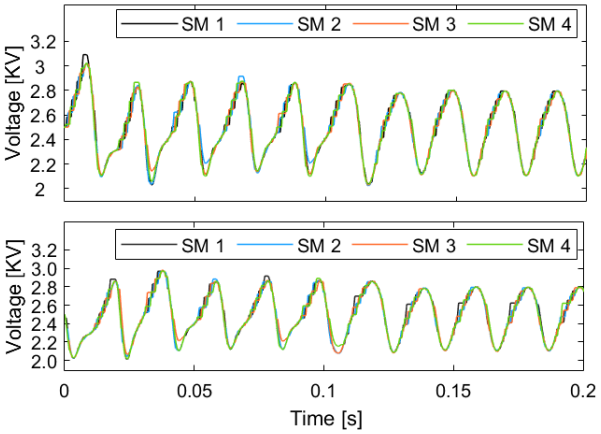

Figure 14: Capacitor Voltages for an MMC leg.

5.2.3. Performance evaluation under different conditions

The next step of the simulation studies involved studying the influence of different parameters on the tracking performance of the proposed CVE relative to the sensor-based method.

5.2.3.1. Influence of modulation type

As seen in the Figure 15 and Figure 160 for PSPWM and NLM, respectively, the tracking error is much reduced with the PSPWM scheme but much worse with NLM. This is because there is a natural balancing of capacitor voltages with the PSPWM technique, whereas the NLM technique needs the CVSB algorithm.

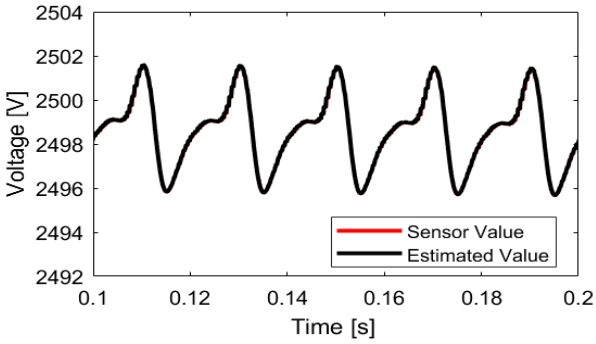

Figure 15: Sensitivity to modulation (PSPWM)

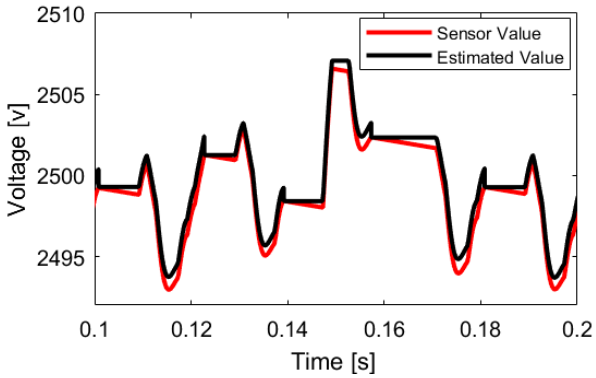

Figure 16: Sensitivity to modulation (NLM)

5.2.3.2. Influence of Switching frequency:

To investigate the effect of switching frequency, the LSPWM technique was utilized. It is seen that lowering the switching frequency still permits the estimation of the voltage although the error worsens as the switching frequency reduces as shown in Figure 17 and Figure 18 for switching frequencies of 600 Hz and 300 Hz respectively. The proposed algorithm is principally based on periodic reading of the arm voltage changes and attributing it to the changes in the submodule gate states meaning that the accuracy is improved if the arm voltage sampling frequency is increased. However, as seen from the different tracking errors, a high switching frequency does not necessarily lead to a large increase in tracking accuracy; on the other hand, it leads to an increase in switching power losses. However, high switching frequency also improve the harmonic content of the output AC voltage. The choice of the switching frequency is a compromise between the switching power losses, power quality, and voltage estimation accuracy.

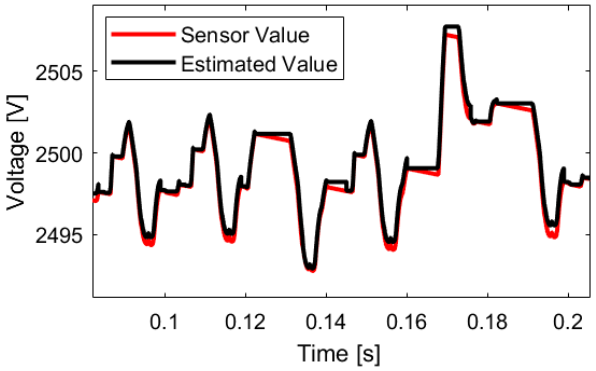

Figure 17: Effect of switching frequency (600Hz)

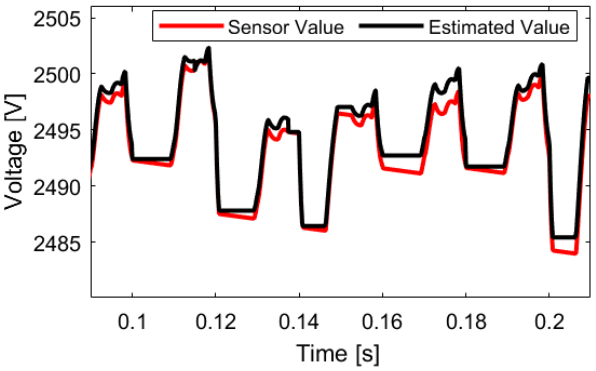

Figure 18: Effect of switching frequency (300Hz)

5.2.3.3. Influence of AC frequency:

At low AC frequencies, MMC usually underperforms as the capacitor voltages have longer charge/discharge periods, leading to the need for extra mitigation efforts in addition to the CCSC and CVSB. This is the case for MMC motor drives at low speeds. In the experiment, an RL load was used with a 5 Hz AC output. Figure 19 and Figure 20 show that compared to the sensor-based measurement, the proposed method is more accurate. This is because the proposed algorithm depends primarily on the switching frequency. The standard CVE algorithm used for comparison was the analytical technique employed in [10] and [11] as described in section 3 and depends on the unity

insertion index which in tend depends on the output AC frequency.

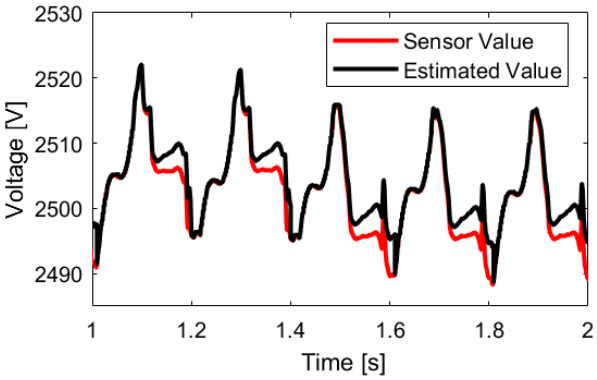

Figure 19: Standard CVE for low frequency AC.

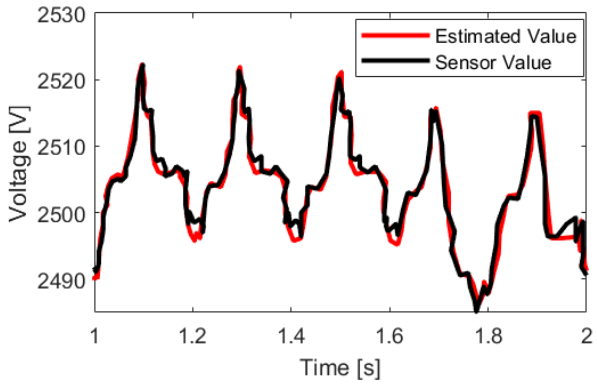

Figure 20: Proposed CVE for low frequency AC.

6. CONCLUSION

In this study, we propose an improved capacitor voltage estimation method for modular multilevel converters. The conventional method relies on a unity insertion index for estimation, which results in a long refresher time and limited accuracy, particularly in systems with a high number of submodules per arm. To address these limitations, we explored not only unity insertion index but also the transitions between successive insertion indices.

By utilizing the arm voltage at the transition points and the state changes of the switches, we developed an estimation algorithm that allows for periodic refreshing with measured data, thereby increasing the accuracy of the capacitor voltage estimation.

To validate the proposed method, we conducted a study on a four-submodule per-arm MMC system. The estimated capacitor voltages were compared with the sensor-based voltage measurements, confirming the validity of the proposed method. Furthermore, the proposed method was integrated into a complete MMC controller, including inner controls, such as circulating current and capacitor voltage balancing. Sensitivity studies were also conducted on different algorithm parameters and showed that the algorithm for a given switching frequency is immune to errors from model parameters, such as submodule capacitance, and also functions well at for low frequency applications.

The proposed capacitor voltage estimation method offers several advantages for MMC technology: by reducing the reliance on sensors, the method helps to decrease the number of potential points of failure and overall investment costs. Moreover, the improved accuracy of the voltage estimation contributes to enhanced system performance opening perspectives for operation under fault.

Though the proposed method thus provides a solution for a reliable and cost-effective capacitor voltage estimation in MMCs, the operation of the MMC critically relies on the availability of the arm voltage sensor and the accurate knowledge of the actual gate signals in near real time. Lack of data leads to faulty operations. Future research directions include extension to operation under fault conditions, further incorporation of the modified capacitor voltage sorting and balancing into the simulation to ensure cycling of all SM in the arms especially in fault operations. In addition, power hardware in the loop simulation on a test bench to validate this method will be the next step.

REFERENCES

[1] U. Javaid, F. D. Freijedo, D. Dujic and W. van der Merwe, "*MVDC supply technologies for marine electrical distribution systems*," in CPSS Transactions on Power Electronics and Applications, vol. 3, no. 1, pp. 65-76, March 2018, doi: 10.24295/CPSSTPEA.2018.00007

[2] L. Hong, Q. Xu, Z. He, F. Ma, A. Luo and J. M. Guerrero, "*Fault-Tolerant Oriented Hierarchical Control and Configuration of Modular Multilevel Converter for Shipboard MVdc System*," in IEEE Transactions on Industrial Informatics, vol. 15, no. 8, pp. 4525-4535, Aug. 2019, doi: 10.1109/TII.2018.2879981.

[3] G. Konstantinou, H. R. Wickramasinghe, C. D. Townsend, S. Ceballos and J. Pou, "*Estimation Methods and Sensor Reduction in Modular Multilevel Converters: A Review*," 2018 8th International Conference on Power and Energy Systems (ICPES), Colombo, Sri Lanka, 2018, pp. 23-28, doi: 10.1109/ICPESYS.2018.8626987.

[4] V. Najmi, H. Nademi and R. Burgos, "*An adaptive backstepping observer for modular multilevel converter*," 2014 IEEE Energy Conversion Congress and Exposition (ECCE), Pittsburgh, PA, USA, 2014, pp. 2115-2120, doi: 10.1109/ECCE.2014.6953682.

[5] O. Abushafa, S. Gadoue, M. Dhaidah and D. Aktinson, "*Capacitor voltage estimation in modular multilevel converters using a Kalman*

filter algorithm," 2015 IEEE International Conference on Industrial Technology (ICIT), Seville, Spain, 2015, pp. 3016-3021, doi: 10.1109/ICIT.2015.7125543.

[6] A. Al-Wedami, K. Al-Hosani and A. R. Beig, "*Sliding mode observer of submodular capacitor voltages in Modular Multilevel Converter*," 2015 International Workshop on Recent Advances in Sliding Modes (RASM), Istanbul, Turkey, 2015, pp. 1-6, doi: 10.1109/RASM.2015.7154650.

[7] H. Nademi, A. Das and L. E. Norum, "*Modular Multilevel Converter With an Adaptive Observer of Capacitor Voltages*," in IEEE Transactions on Power Electronics, vol. 30, no. 1, pp. 235-248, Jan. 2015, doi: 10.1109/TPEL.2014.2301879.

[8] M. Trabelsi, M. Ghanes, O. Ellabban, H. Abu-Rub and L. Ben-Brahim, "*An interconnected observer for modular multilevel converter*," 2016 IEEE Energy Conversion Congress and Exposition (ECCE), Milwaukee, WI, USA, 2016, pp. 1-7, doi: 10.1109/ECCE.2016.7854853.

[9] G. S. da Silva, R. P. Vieira and C. Rech, "*Modified sliding-mode observer of capacitor voltages in Modular Multilevel Converter*," 2015 IEEE 13th Brazilian Power Electronics Conference and 1st Southern Power Electronics Conference (COBEP/SPEC), Fortaleza, Brazil, 2015, pp. 1-6, doi: 10.1109/COBEP.2015.7420217.

[10] S. D'Arco and J. A. Suul, "Estimation of sub-module capacitor voltages in modular multilevel converters," 2013 15th European Conference on Power Electronics and Applications (EPE), Lille, France, 2013, pp. 1-10, doi: 10.1109/EPE.2013.6631931

[11] L. A. Grégoire, Weihua Wang, S. I. Seleme and M. Fadel, "*High reliability observers for modular multilevel converter capacitor voltage evaluation*," 2016 IEEE 8th International Power Electronics and Motion Control Conference (IPEMC-ECCE Asia), Hefei, China, 2016, pp. 2332-2336, doi: 10.1109/IPEMC.2016.7512661.

[12] L. A. M. Barros, A. P. Martins, and J. G. Pinto, "*A Comprehensive Review on Modular Multilevel Converters, Submodule Topologies, and Modulation Techniques*," Energies, vol. 15, no. 3, p. 1078, Feb. 2022, doi: 10.3390/en15031078.

[13] A. A. Ferreira, C. C.Rodríguez, and O. G. Bellmunt, "*Modulation techniques applied to medium voltage modular multilevel converters for renewable energy integration: A review*," in Proceedings of the Electric Power Systems Research, vol. 155, pp. 21-39, February 2018, doi: 10.1016/j.epsr.2017.08.015

Paving the Way Towards Zero-Emission and Robust Inland Shipping

A. Kirichek[a*], J. Pruyn[a,b], B. Atasoy[a], R. R. Negenborn[a], R. Zuidwijk[c], J.H.R. van Duin[a,b], K. Tachi[d] and M. van Koningsveld[a,e]

[a] Delft University of Technology, Delft, the Netherlands
[b] Rotterdam University of Applied Sciences, Rotterdam, the Netherlands
[c] Erasmus University Rotterdam, Rotterdam, the Netherlands
[d] Expertise and Innovation Centre Barging, Rotterdam, the Netherlands
[e] VanOord, Rotterdam, the Netherlands
*Corresponding Author o.kirichek@tudelft.nl

Abstract

Several measures have been developed to prevent emissions from inland water transportation. However, it is challenging to weigh all the aspects to identify the pathway that will ultimately result in zero-emission inland shipping. A data-driven virtual representation of the inland shipping system can be used to evaluate zero-emission strategies, effectiveness of policies and technologies, and consequences of their implementation. This multi-level digital twin can realistically represent the system with all relevant components, which needs to be validated using real-world data. Subsequently, future scenarios can be imposed on the digital twin, and the proposed intervention measures can be applied, based on which their efficiency can be assessed together with the inland shipping sector.

This study discusses the essential aspects of designing a digital twin for an IWT. Three aspects are considered essential: individual ships, logistics chains, and infrastructure. As these research topics span various scales, ranging from a single vessel to an entire infrastructure network, an agent-based approach is suitable for forming the basis of the digital twin. Consequently, potential interventions can be considered, ranging from the application of new technologies to individual vessels to policy measures implemented for an entire shipping corridor or various bunker infrastructure strategies in the network. Additionally, the impact of the implemented interventions can be evaluated at any desired scale, ranging from the individual ship level and its emissions to the network level and aggregated emissions in an entire area, or the impact on the logistics chain.

Keywords: Emissions, PATH2ZERO, Multi-level digital twin, inland waterway transport, Energy transition, Sustainability.

1. INTRODUCTION

Inland waterway transport (IWT) is vital to the European economy. This mode of transport is highly efficient and contributes significantly to a region's trade volumes. Furthermore, the IWT is one of the most energy-efficient modes of transport per ton of transported goods, consuming only 17% of the energy required by often-congested road transport and 50% of rail transport. This sector already plays an important economic role in transporting goods and passengers in Europe. Despite its efficiency, IWT contributes to greenhouse gas emissions. Given the projected growth in the European economy, emissions from IWT will rise unless proactive measures are taken. The Paris Agreement set the ambition to limit global warming to 1.5 °. In line with the Paris Agreement, the EU aims to become a carbon-neutral economy by 2050, with a 55% reduction in CO_2 emissions by 2030. To achieve these goals, the 2019 European Green Deal reaffirmed that the EU transportation sector must reduce its emissions by 90% by 2050. A significant proportion (75%) of the inland freight transported by road today should be shifted to inland waterways and rail. The Green Deal also called for measures to increase the unused capacity of inland navigation. With the Sustainable and Smart Mobility Strategy of December 2020, the European Commission outlined the planned transformation of the EU transport system, including a 25% increase in IWT and short-sea shipping by 2030, and 50% by 2050. This will require measures, such as improved connections and a more modern shipping infrastructure that ensures year-round navigability. Its untapped potential to increase capacity justifies the renewed attention it has recently received in terms of sustainable development.

Several emission reduction measures have been developed in recent decades [1], [2], [3], [4]. Currently, there are no obvious pathways toward zero-emission shipping because of the many

@2023 Kirichek et al., published by TU Delft OPEN Publishing on behalf of the authors. Licensed under a Creative Commons Attribution CC BY license.
DOI: https://doi.org/10.59490/moses.2023.675

uncertainties regarding all aspects of zero-emission shipping. The aim of this study is to address the challenges of shipping, transport chains (logistics), and infrastructure in the transition to zero-emission (ZE) IWT. The remainder of this paper is organized as follows. First, up-to-date emission reduction measures for inland navigation were categorized. Second, the challenges in accelerating the transition and filling the remaining knowledge gaps are discussed. Third, the potential of digital twin solutions for accelerating the transition to zero-emission and robust inland navigation is discussed. Finally, conclusions are summarized.

Table 1. Average annual emission factors of the inland navigation fleet for diesel engines and total emissions of IWT reported by CCNR [4].

Emissions	g/kWh	Total (kt)	Sources
CO_2	673-771	4149	[4],[5],[7]
CO	1.3-5.3	38	[4],[5],[6]
NO_x	3.75-10.8	61	[4],[5],[6],[7]
N_2O	0.017-0.019	-	[5]
NH_3	0.0021-0.0024	-	[5]
PM	0.01-0.6	2	[5],[6],[7]
SO_2	0.004-0.486	-	[5]
VOC	0.2-1.2		[5],[6]
CH_4	-	0.2	[4]

2. EMISSION REDUCTION MEASURES FOR IWT

2.1 Types of emissions from IWT

The vast majority of inland ships today use diesel engines, which are similar in principle to those used in non-road mobile machines, locomotives, and small-sea vessels. However, it is essential to note that IWT uses low-sulfur diesel (EN590), which is similar to automotive fuel. The distinction between non-road mobile machines, including IWT and road transport, is evident in the regulatory standards. Until NRMM STAGE V, regulations for non-road machines were less stringent than those for road transport, particularly concerning emission limits for air pollutants. For instance, the permissible levels of pollutants such as NO_x and PM are much higher. The combustion of fuels produces emissions of various greenhouse gases, including carbon dioxide (CO_2), methane (CH_4), and nitrous oxide (N_2O). In addition, inland shipping generates other air pollutants such as carbon monoxide (CO), nitrogen oxides (NO_x), non-methane volatile organic compounds (NMVOC), and particulate matter (PM).

Table 1 summarizes the emission factors of the diesel engines of the inland navigation fleet and total emissions of the IWT. In terms of absolute weight, CO_2 emissions were the most dominant emissions from the IWT. However, external costs or air pollutant emissions may be higher depending on the area in which they are emitted.

2.2 Current strategies for emission reduction from IWT

The main strategy for achieving ZE IWT is to use energy carriers with a low well-to-wake carbon intensity. Substantial leaps in emission reduction for the IWT can be achieved by a transition to renewable and/or low-carbon fuels complemented by alternative energy converters. Various alternatives to diesel can be considered. These can be divided into three groups.

- Biofuels: biomass-based energy sources;
- E-Fuels: fuels produced by renewable electricity;
- Electricity.

Figure 1, adapted from [8], shows well-to-wake CO_2-equivalent emissions for current fossil fuels and alternative fuels that are considered for reducing emissions from IWT. The data suggests that biofuels can substantially decrease the emissions from IWT as tank-to-wake emissions can be minimized as confirmed by a number of studies [9]. At the same time, a long-term strategy can be focused on minimizing the emissions to zero by drawing more attention to E-Fuels and electricity. The storage of the latter can provide a promising alternative to other types of fuels for IWT as battery systems can either be integrated into the hull of the ship or can be installed in a standard container that could then be inter-changeably stored on the ship.

Other emission reduction strategies mainly focus on ship-related or logistics-related measures. Ship-related measures include technologies that can be incorporated into a ship to reduce the ship's emissions compared to the original ship design. These measures focused on novel designs, retrofits, or newly built ships. With the support of sensing, computation, and communication technologies, new techniques for decision support and control can be developed to optimize operational decisions from an emission-aware/sustainability perspective. Furthermore, new technologies include solutions for a ship's propulsion system, which consists of the ship's hull and propeller. The measures aim to optimize energy consumption by reducing ship resistance, improving thrust efficiency, improving power generation efficiency or retrofitting current engines.

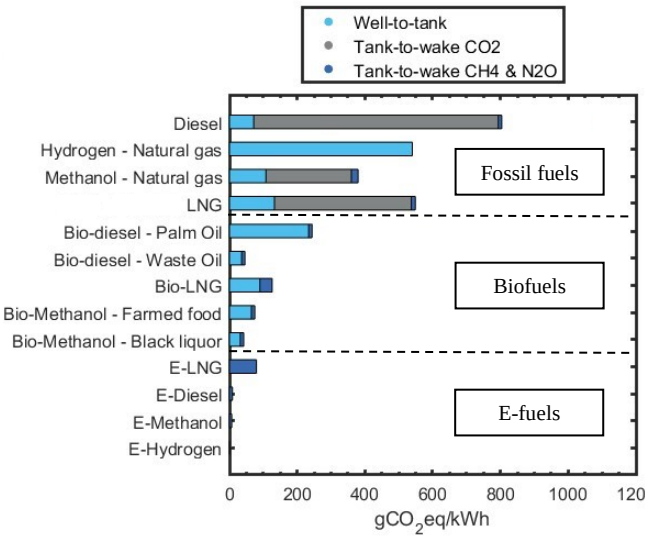

Figure 1: Reported well-to-wake CO_2-equivalent emissions for current and alternative energy carriers for IWT (adapted from [8])

Logistics-related measures include optimizing sailing routes to ensure that the most efficient paths are taken, minimizing empty voyages to enhance transport efficiency, and maximizing cargo loading to ensure optimal utilization of available capacity. Furthermore, other operational measures can involve advanced scheduling to avoid congestion at ports, terminals, and locks.

Over the past two decades, several measures have been developed to reduce emissions from IWT. These measures can be divided into ZE measures that lead to ZE IWT and measures that can reduce emissions from the IWT to a certain level. Both categories can be further categorized into technical (ship-related) and operational (logistics-related). An overview of the currently available emission reduction measures for IWT is shown in Figure 2.

Apart from measures related to alternative fuels and retrofitting/replacing existing engines to use these fuels, other measures offer a smaller impact than alternative energy carriers. However, these measures are important to achieve robust energy consumption during the transition to renewable and/or low-carbon fuels supplemented by alternative energy converters.

2.3 Ship's emission reduction measures

2.3.1 Retrofitting and replacing engines

One of the short-term emission reduction strategies can be focused on retrofitting or replacing existing engines with alternative fuels. Currently, there are two types of engines for introducing new fuels.

1) Compression ignition engine: Air is compressed so much that it heats up and ignites the fuel. Fuels with different auto-ignition temperatures require different engine types. The following fuels can potentially replace diesel in this type of engine [10]: vegetable oil, DME (dimethyl ether), GTL (gas-to-liquid), BTL (biomass-to-liquid), and HVO (hydrotreated vegetable oil).

2) Spark ignition engine: the fuel-air mixture will not ignite until a spark is created. The compression ratio is much lower (typically 1:11) than 1:20 for compression ignition in compression ignition engines. The following fuels are used in engines [10]: gasoline, ethanol, methanol, natural gas, biomethane (both CNG and LNG), and hydrogen.

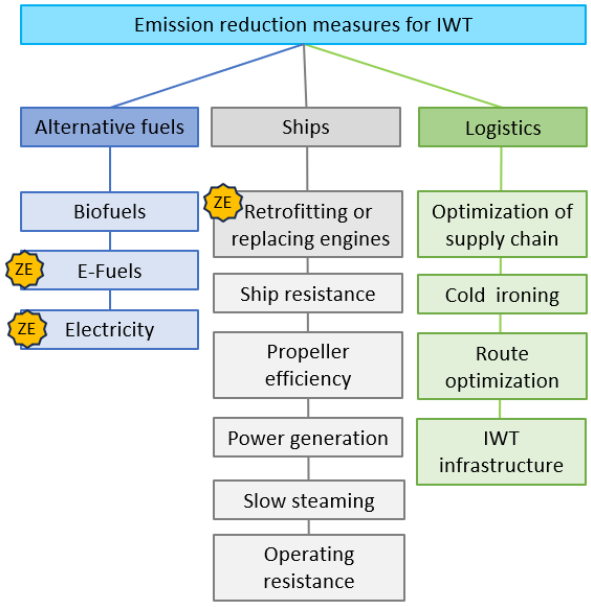

Figure 2: Overview of the current emission reduction measures for IWT. ZE indicates zero-emission measures.

Alternative fuels can be used in three main ways:

1) Mono-fuel: Changing the engine type requires major adjustments because parts of the engine must be rebuilt. Therefore, it is easier to install new engines.

2) Dual-fuel: Two fuel systems on a ship. Typically, a small amount of diesel fuel is used as the pilot fuel to initiate the ignition process, followed by combustion of the selected alternative fuel. The side-to-side use of two mono-fuel engines is also considered an emission-reduction strategy.

3) Designing new ships: selecting the right energy convertors and energy carriers for new ships (e.g. electric drive using batteries, fuel cells).

For energy carriers, the focus is on ZE tailpipe emissions (batteries, hydrogen, and hydrogen carriers), although bio or synthetic diesel combined with internal combustion engines is considered because of their high TRL and positive impact in the short term. Further reduction of air pollutant emissions from combustion engines can already be achieved with available Stage V engines (e.g., Euro VI and NRE engines); however, a comparison with ZE tailpipe solutions from a full well-to-wake and

life cycle viewpoint still has to be made. Matching power configurations (internal combustion, fuel cells, and batteries) are also included, while bunkering is limited to the traditional transfer or charging and swapping of containers and tanks as the two most likely options.

2.3.2 Ship resistance

Reducing the ship's resistance lowers the power required for a given speed and thus lowers fuel consumption and emissions. Considering the current weather conditions, currents, and hull fouling, an extra effective propeller power is required to overcome the additional resistance. Ship resistance is particularly affected by ship design, design speed, and hydrodynamics of the hull.

The structural design of the hull of an IWT ship should be optimized based on the specific route and dimensions of the waterway, as well as hydrodynamic conditions (e.g., low water level and current velocities) that affect the ship's resistance.

The ship design and propeller selection can be optimized through better structural design and advanced materials. Fiber-reinforced plastic composites, high-strength steels, and aluminum alloys are the primary lightweight materials currently used in the maritime industry [11]. Research and application of metal sandwich panels and lightweight steel-composite sandwich panels with novel joining methods have shown their advantages. These novel arrangements and lightweight materials are expected to be widely used in superstructures, secondary structures, and components for all types of inland vessels.

In addition, advanced hull coatings can reduce frictional resistance, resulting in fuel savings.

2.3.3 Propeller efficiency

The main opportunities for optimizing propulsion efficiency in an IWT relate to hull efficiency and relative rotative efficiency, which depend on high-efficiency propellers, improving wake distribution, and recovering rotational energy.

A more homogeneous wake translates into better propeller efficiency. Wake equalizing devices, such as ducted propellers, wake equalizing ducts, and nozzles, aim to improve wake distribution and reduce flow losses around the working propeller. Another group of power-saving devices is aimed at recovering rotational energy from the water downstream of the propeller and converting it into thrust. Many devices have also been proposed to recover some of the rotational energy of water.

2.3.4 Power generation efficiency

Currently, there are some opportunities for fuel savings in the main and auxiliary engines, as well as in the various energy-consuming equipment on board ships. New technologies are currently targeting traditional diesel engines. However, all of these engine technologies have nearly reached their limits in terms of improving energy efficiency. The potential for further fuel savings is typically less than 1%. However, converting to battery-electric sailing can save approximately 50% of the energy, because the thermal loss in the conversion of electrical power to mechanical power at the propeller shaft is much lower.

In addition, more emphasis is being placed on reducing NO_x and particulate matter emissions from IWT engines. For CCNR Stage II engines, this reduction is achieved at the cost of a reduced fuel efficiency. Flexible power options, such as power-take-off/power-take-in configurations and hybrid propulsion, can be considered to save fuel. However, the new Stage V engines use SCR to reduce NO_x emissions, which allows engine management systems to be tuned for maximum fuel efficiency while reaching even higher NO_x reduction levels.

2.3.5 Slow steaming

Slow steaming is the practice of operating ships at speeds lower than the design speed. This measure was introduced in the maritime industry to reduce fuel costs and is used by nearly all global shipping companies in the current context of the sluggish shipping market. Slow steaming has been shown to be the most energy-efficient operational measure for individual maritime vessels because fuel savings and emission reductions of up to 60% can be achieved, depending on the extent of speed reduction. Although mandatory speed reduction may directly lead to emission reductions from the IWT, speed restrictions for inland vessels may be difficult to apply because of safety concerns.

2.3.6 Operating resistance optimization

The main objective of operating resistance optimization is to minimize the calm water ship resistance (i.e., frictional and residual resistance) for specific shipping routes and payloads using draft, trim, and ballast optimization. The hull form is usually optimized for a single speed and load condition, which is normally the design speed at the design draft. With the different speeds and loading conditions encountered in practice, the resistance can be optimized. Varying ship drafts or trims will change the wetted surface area, waterline length, and resistance, and can be considered for more robust ship designs, considering the specific

routes and conditions expected during the lifetime of the ship.

2.4 Logistics' emission reduction measures

Transport chain measures for emission mitigation are focused on using operational efforts that include reducing power demand and improving energy efficiency. Several promising operational measures for navigation, supply chains, and logistics have been developed by the industry [12]–[14]. Typically, these measures can be grouped into the following sub-groups: optimization of supply chains, cold ironing, route optimization, and optimized usage of infrastructure, all of which need to be considered in relation to the energy supply.

2.4.1 Optimisation of supply chains

The measures related to the supply chain can be grouped into the following sub-groups: trading network design, economies of scale, and port services.

The design of the trading network, in terms of the number of vessels, size of vessels, and commercial speed, has an important impact on IWT emissions. Shipping companies must find solutions for fleet deployment from different perspectives. Another challenge is to determine the shipment frequency, shipment size, and schedules that need to be assigned to many constraint conditions.

Cargo capacity utilization is another important consideration when designing capacity deployment in service networks. Trade demand may fluctuate owing to various factors, and shipping companies need to alter their service networks accordingly to achieve higher capacity utilization with the objective of minimizing costs and emissions. However, considering various factors such as freight rates, operations, ports, and logistical systems, there should be an optimal ship size and deployment for different trading routes.

An efficient turnaround in ports results in more voyages or the same voyage number with a slower and more fuel-efficient sailing speed. Therefore, the time spent at the port significantly affects the operational costs, benefits, and level of energy efficiency. Reducing the time in the port and anchorage is an important consideration for reducing fuel consumption and ship emissions, which depends primarily on the operation and service of port terminals. Improvements in berth allocation planning, assignment, and scheduling of quay cranes; integrated planning to improve loading/unloading efficiency; and reduction of unproductive time through faster document processing and check procedures would lead to a reduction in energy use.

2.4.2 Cold ironing

Cold ironing is the practice of supplying shoreside electrical power to a ship at the berth, while its diesel generators are turned off. As shoreside electrical power can be from low-carbon or zero-carbon energy sources, such as wind power, hydropower, solar power, or nuclear power, cold ironing is an important option for reducing shipping emissions. Although the fuel consumption while berthing at ports is a small proportion of the total energy consumption in the life of a ship, the overall benefits of cold ironing are significant because they simultaneously reduce emissions, toxic exhaust gas emissions, and noise pollution from ship berthing at ports, with benefits for the coastal ecosystem and the physical and mental health of people living nearby. In the future, cold ironing may also be used to recharge batteries as an energy source for the propulsion of vessels that have daytime operations and stay long in ports during the night. A clear example of this is the short-distance ferry operation.

2.4.3 Route optimization

Route optimization could be an overall name for the concept, as well as ship routing, scheduling, speed optimization, and trim optimization. More often, different kinds of optimization measures are currently used together and even combined with slow steaming, supply chain, and logistics to optimize energy consumption, thus reducing emissions.

Ship routing and scheduling methods were initially employed to shorten distance, optimize time, improve safety, and reduce costs. Recently, they have become important focal points for energy efficiency and emissions reduction. The main objective of ship routing is to choose the route of minimized ship resistance (e.g., at low water conditions and narrow sections), waiting times for passing locks and bridges, and undesirable vessel disturbance by selecting calm weather conditions. However, ship scheduling also considers temporal aspects, that is, the time of cargo loading/unloading, sailing, bunkering and refueling, anchoring, and hoteling. The use of different energy sources implies that the optimization for routing and scheduling needs to consider not only the transportation flow, but also the energy flow. where and when to visit an energy facility, for example, a charging station or any energy supply location, by which the ship becomes part of the decision-making process. For routine shipping lanes, ship particulars, water level conditions, currents, and specific waterway dimensions on the route, service, and waiting times at bridges and locks are also considered.

2.4.4 IWT infrastructure

Inland navigation can only function optimally if there is a new or existing infrastructure that is always navigable, properly maintained, suitable for use by existing and future fleets, and meets traffic needs.

To enable quantification of opportunities and bottlenecks, new research should focus on shallow water effects and payload vs. draught, and account for squat, ambient currents, engine age, partial engine loads, and alternative energy carriers on a transport graph that contains information on depth, current, and IWT infrastructure. Linked to waterways, locks, bridges, terminals, and berth services should be considered to allow operational improvements and achieve realistic fuel usage.

2.5 Fuel infrastructure for IWT

The transition to ZE energy carriers for IWT requires the construction of new facilities and infrastructure that are necessary to support the use of alternative fuels. The IWT offers valuable opportunities for being close to land-based infrastructures and operating within a regulatory regime that is less complex than international shipping in terms of developing a sufficient network for clean energy (including electricity). An IWT can have better access to a dedicated network of fuelling locations (energy hubs). Simultaneously, the current technical regulations for IWT fuel infrastructure (CESNI/ES-TRIN) are more complex than international shipping (IMO). In addition, for the placement of a new fuel infrastructure, riverbank properties, including safety, should be considered.

3. KEY CHALLENGES

There is a stalemate where the ship owners (demand) and energy producers (supply) are not daring to commit to a solution for the future ZE energy carrier. Thus, the energy transition is at its core in terms of the uncertainty of the best choice for a future energy carrier. Looking at the best choice for a vessel within a given logistical concept leads to suboptimal patchwork of energy carriers. However, selecting a single carrier might be beneficial from the production and supply perspective, but not the overall best solution, as different vessel types will have different possibilities to adapt, depending also on their sailing profile and the type of business they are in (e.g., long-term contracts for fixed routes versus ad hoc spot-market-driven assignments). There is deep uncertainty surrounding the actual benefits of potential solutions (new energy carriers or powering options). All solutions are still in the demonstrator or single application phase, and not market-ready development. This means that their performance will improve in the future, and thus, no reliable selection can be made. Methods that consider this uncertainty in the transport chain, design, and retrofitting are required to address this issue.

Second, there is a lack of coherent action or a clear vision towards the future. While only at the demonstrator level, each research project or pilot promotes its solution as the best option. Currently, research rarely looks beyond pilot projects and remains unaware of integration issues for other stakeholders in the sector. To alleviate this issue and reduce overall uncertainty, a broad approach is required. An action to integrate insights and bring together all types of stakeholders is required.

Furthermore, there is insufficient uptake and use of available data. In the last decade, many new sources of data have been introduced (Satellite, AIS, Engine data), and it will become even easier to collect (and communicate) in the coming years. This could lead to an Industry 4.0 revolution, but currently, this data is only sparsely used. Unlocking these data to improve vessels and transport operations will empower the sector to improve its efficiency and sustainability.

Next, the cross-sectoral transition toward a ZE fleet and the required development of cutting-edge green technologies in vessel design and equipment can be addressed. Such technology development projects involve formidable investments, the returns of which include high levels of technology, demand, and regulatory uncertainty. Faced with such uncertainty, companies should seek to form joint development alliances with other companies, academic institutions, non-profit organizations, and governmental bodies.

Finally, and most importantly, there is a lack of economic incentive to go green. Except for operational measures, all further investments in lowering emissions and environmental impacts have not yet offered any return. Going green has become a feasible business model in other sectors (built environment, cars, and even food). As IWT is mostly a sector that deals with business-to-business operations, it is further away from the consumer, and there is less pressure to go green. Cargo owners, such as Heineken and Ikea, need to take the lead in green transport and require effective incentives to support this movement.

4. DESIGNING DIGITAL TWIN FOR ZE AND ROBUST IWT

Evaluating the effectiveness of ZE policies, strategies, and technologies for emission reduction

and assessing the consequences of their implementation in the broadest sense of the inland shipping system is a challenging task.

A data-driven virtual representation of the inland shipping system can be potentially used to assess the efficiency of the proposed solutions and capture the potential trade-offs of the interventions in the system. This digital twin can model the present system with all relevant components in a realistic manner, which can be validated using real-world data. Subsequently, future scenarios can be imposed on the digital twin, and the proposed intervention measures can be applied, based on which their effectiveness can be assessed.

To speed up the transition and cover the remaining gaps in knowledge, an approach that considers the diversity of the inland fleet and its operators, which looks at the individual options for vessels at various time horizons, the interactions of vessels in the corridor, and the bunkering infrastructure, is required. An approach that is data-driven, not only from a technological or logistical perspective but also from a social perspective, that not only supports questions of ship owners, cargo owners, bunker operators, terminal operators, and policymakers but also brings the sector together for the discussion. This approach does not reinvent the wheel but aims to integrate knowledge from previous projects and projects on IWT and the energy transition that runs in parallel, providing an integrated living lab built on diligent research.

Three aspects are regarded as vital components of the digital twin: individual ships, transport chains (logistics), and infrastructure (see Figure 3). The input from the community in terms of policies, current pilots, and data is the key to developing a digital twin. The questions identified by the community can be answered through the development of a multilevel digital twin in scientific development. This digital twin consists of the lowest level of heterogeneous agents representing individual vessels to study the potential of measures at the vessel level. A combination of these agents forms traffic at the corridor level and can be used to study more complex interactions and the resulting environmental impact. In addition, transport and energy infrastructure models allow the investigation of policies, business concepts, and more strategic actions at the highest level. This complex model and community are supported by data collected from open sources, project partners, and dedicated experiments. This leads to a holistic approach, which means that the entire transport chain will be considered.

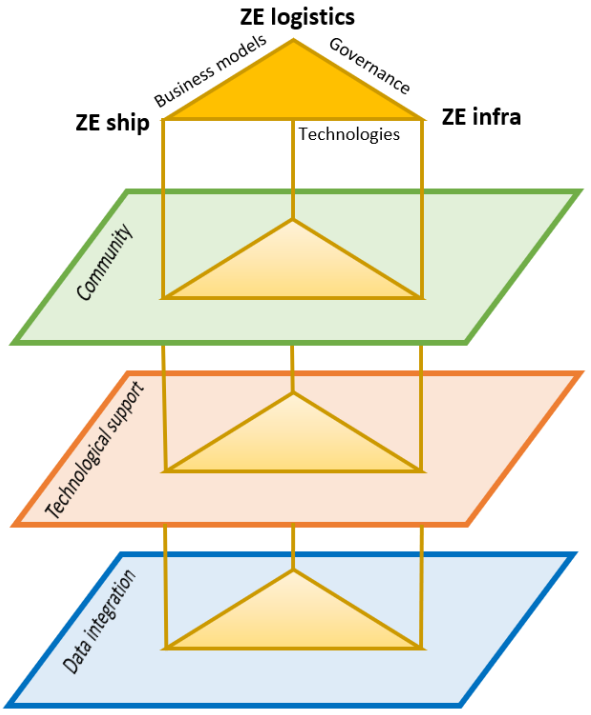

Figure 3: A schematic representation of the interaction between the individual ships, the transport chains (logistics), and the infrastructure in the Multi-Level Digital Twin.

As the main aspects of a digital twin span various scales, ranging from a single vessel to an entire infrastructure network, an agent-based approach can form the basis of a digital twin. Consequently, potential interventions can be considered, ranging from the application of new technologies to individual vessels to policy measures implemented for an entire shipping corridor or various bunker infrastructure strategies in the network. Additionally, the impact of the implemented interventions can be evaluated at any desired scale, ranging from the individual ship level, for example, its emissions or travel time, to the network level, for example, the aggregated emissions in an entire area, or the impact on the logistics chain.

The first attempt to make a prototype of a digital twin for nautical and port traffic and transport was made by the “Digital Twin Vaarwegen,” which used a fairway information system as the digital representation of the fairways, particularly of the Rotterdam-Duisburg corridor. An agent-based approach was used to model the vessels in the fairway network. This digital twin provides insights into the performance of several fleet operation strategies in terms of fleet occupancy on one hand, but it can also be used to evaluate the impact of water discharge variations on operational performance, important emission hotspots, and zoom-in, providing insights into the underlying causes.

Using an agent-based approach in a digital twin, the relevant processes at the individual vessel level can be modeled in detail, and their performance can be tracked in time and space. The agents operate on a graph consisting of nodes and edges that realistically represent the Dutch/European fairway network. Fairway characteristics were derived from the Dutch fairway information system ("Vaarweginformatie"). The developed basic infrastructure provides a necessary foundation for multilevel digital twins. The concrete theme for the multilevel digital twin can be focused on the interaction between nautical traffic-related emissions and user functions. Direct triggers motivating the need for this twin appear at operational, tactical, and strategic timescales:

• Operational: The localized spread of emissions is a health concern in port cities. Research on road traffic and fine dust is currently underway. We aim to extend the current approaches by linking them to nautical traffic. Based on operational vessel data (e.g., AIS data and engine rates), estimates can be made of energy use, fuel consumption, and emissions, close to real time. We aimed to develop algorithms for generating emission patterns (specified in space and time). These patterns can be crosschecked by measuring various emissions. This research can be used to make navigation more sustainable and can be an important input for policymakers.

• Tactical: An important part of nautical traffic and its emissions is driven by the need to move freight. Transport and handling services are provided by transport and terminal operators, and the planning of associated operations has the potential to manage localized emissions. For example, emissions are capped in time and place, thereby constraining planned operations. The findings in the operational arena will inform the management of localized emissions by adaptive planning, which will need to be a collaborative effort by transport and inland terminals, whether on the inland waterway side or the land side.

• Strategic: A major development concern for ports is the restriction of emissions on port expansion and development. Simulation algorithms for predicting shifts in emissions associated with port development and comparing them with current emission patterns should be developed. By including developments in scenarios, such as engine developments, autonomous vessels, and traffic management measures, we can generate insight into the extent to which new developments contribute to future emission patterns.

4.1 ZE ship

The challenges surrounding emission minimization for IWT can be addressed in the digital twin, starting from the ship perspective. The digital twinning hereby brings together new insights into the role of the digital/cyber ship aspects (ship digitization, communication, and decision making) on the one hand, and the link to the physical ship aspects (new alternative fuels, engines, ship designs) on the other.

To improve the vessel agent and vessel fleet behaviors, the important role that digitization and communication technology will have in improving the operational emission profiles of the future vessel fleet should be addressed. With the advent of more accurate information from a more diverse range of sources (onboard ships, as well on the infrastructure side) [16], and ease of communication between different transport chain systems, it becomes important to consider what information is needed where, when, and at what level of accuracy. This needs not to be considered only from a general efficient navigation perspective, but especially with an integrated view of sustainability and operational emission profile optimization. This is important in addressing both the enhancement of navigation systems onboard existing ships ('digital retrofitting') and when considering design choices for the next generation of (newly built) ships. A key challenge is to consider emission profiles in trade-off with levels of ensuring alignment with expectations regarding, for example, arrival times and other indicators for ship quality of service. As such, this task will result in new methods for emission-minimized ship decision-making (navigation, power, and energy management). The overall methodology pursued here is based on the model predictive control concept [17]. In this concept, links between digital twin representations of a ship and corridor dynamics and reduced-order mathematical representations thereof are encapsulated inside a rolling horizon framework to optimize set performance objectives. In addition to the individual (single-agent) ship control perspective, specific attention is given to the distributed (multi-agent) fleet management perspective, in which ships make use of shared information (e.g., for emission-minimized collaborative navigation).

Three different situations can be considered for digital twinning: current ships sailing on diesel, new ships starting on diesel but converting to green energy in the future, and ships built specifically for a single green fuel. Some degree of modularity is seen by many as the best option to deal with this, and MBSE has been shown in Aerospace and Car manufacturing to support this. However, a ship is a

much more integrated system in which the performance of subsystems can only be evaluated once the design is complete. The Dynamic Alternative Policy Pathways [18] will be used as a measure to deal with uncertainty in combination with Model-Based Systems Engineering [19] to deal with the modularization of the layout together to ensure the layout optimality of retrofitted, future-ready, and future ships. This will not be possible without the use of Artificial Intelligence principles in layout generation and assessment.

4.2 ZE logistics

A logistics digital twin model should be developed for strategic, tactical, and operational decisions for integrated logistics and energy systems based on various constraints and requirements. In particular, when a hybrid fleet using a variety of energy sources is deployed, challenging decision-making problems arise. The transition toward a ZE fleet and development of the corresponding energy distribution infrastructure not only requires an integrated design, planning, and execution, but also repositioning of several organizational strategies of the parties involved, and realignment of relationships between those parties.

At the strategic level, the integration and matching of viable ZE logistics systems and ZE energy systems deal with network design; the adaptations required for both the terminal and fleet towards ZE energy carriers. Gradual stages of adaptation should be considered to increase support for new energy carriers. Although studied for trucks and ships, the gradual adoption of multiple possible energy sources at the transport chain or network level remains understudied. At the tactical level, the service frequency and scheduling are also affected by the choice of ZE energy carrier. New carriers may change the number of transport types required to operate parts of the network, and the alignment of cargo and energy needs is required. Although a heterogeneous fleet has been studied [20], the consideration of energy in these problems introduces new challenges that will be addressed here. Finally, at the operational level, the routing of the vessels and the required energy distribution, which involves the swapping and charging of container batteries or fuel bunkering operations, must be decided in a similarly integrated way. In particular, ZE energy swapping options, such as battery containers, integrate a second cargo stream, including empty container repositioning [21], into the routing, requiring optimization of charging-related decisions [22] for a fleet. To our knowledge, integral decision support for intermodal transport and energy systems with multiple energy sources has been studied only sparsely and requires further modeling.

The interplay between demand and supply is an important factor for leveraging these uncertainties. Pricing not only leverages the supply and demand of transportation capacity, but also for energy supply. Integral pricing models that incorporate these aspects have received little attention, especially in the context of synchromodal transportation, and require further research. Instead of purchasing expensive assets and forcing a buy-in into a specific design and energy technology, innovative financing models need to be introduced that allow MSEs to purchase options on assets managed as a portfolio. This relates to investment in a green fleet of vessels, which is considered from a technological perspective. In addition to technology and the market, regulations also play an important role in the transition to a ZE IWT. Market parties are calling for regulations that support forerunners, and governments are progressing such regulations, but there are risks that regulations also have rebound effects. Therefore, new business models in the IWT ecosystem are challenged to address the technological, market, and regulatory uncertainties. Requiring new chartering and greening options that reap the benefits of new technologies and market opportunities addresses the uncertainties at hand to be developed.

To achieve ZE IWT, technology alliances will most likely involve cross-sector partnerships, such as partnerships among companies and academic institutions that have very different objective sets as well as organizational processes and norms. Since alliances involve separate independent institutions, they require significantly more coordination than internal R&D projects. Furthermore, the complete alignment of partner incentives is hardly achieved, which makes full cooperation unlikely. In this case, parties tend to follow their private benefits even when they are contradictory to common objectives. The benefits and inherent disadvantages of alliances have spurred research into the determinants of alliance performance. For instance, formal and informal governance, trust, re-evaluation and re-adjustment, partner similarity, and alliance experience play important roles in fostering alliance performance. However, little is known about inter-partner cooperation when alliance benefits involve a mix of commercial gains and social responsibility. In other words, the question remains whether alliances in green technologies perform worse than alliances in technology development for purely

commercial motives. To address this, data on technology development projects by leading-vessel builders should be collected.

4.3 ZE fuel infrastructure

To pave the way for a transition to ZE fuel infrastructure, it is crucial to develop knowledge at the infrastructure level (e.g., for the functional design and first-order dimensioning of individual bunkering stations) and at the network level (e.g., to understand the interactions with upstream energy flow and downstream transport behavior). Connecting the infrastructure level to the network level requires practice-oriented insights into the present energy demand and realistic perspectives on potential future energy demand [23], [24].

A promising and widely used starting point is to estimate the resistance experienced by vessels traveling over the network, for example based on the Holtrop and Mennen approach [25]. This resistance can be used to estimate the power that must be provided by a ship's engine. Empirical relationships are available to translate this power into fuel use and emissions. This enables the estimation of network-wide energy-use footprints as a function of time and space.

To enable the quantification of opportunities, bottlenecks, new policy perspectives, and new sustainable business models, the traditional method of Holtrop and Mennen needs to be expanded. Recent research [26], [27] developed a method that includes the latest insights into shallow water effects [28] and payload vs. draught [29], and can account for squats, ambient currents, engine age, partial engine loads, and alternative energy carriers on a transport graph that contains information on depths, currents, and infrastructure (such as bridges, locks, etc.).

Key questions regarding the ZE fuel infrastructure include where bunkering stations should be positioned and their capacity (both in terms of the total amount of energy to be supplied and in terms of desired service levels/allowable waiting times). Several associated knowledge gaps need to be addressed: How can the required bunkering capacity be translated into space requirements? What safety zones should be accounted for when designing infrastructure for different energy carriers? What are the suitable fuel loading concepts and how will these affect the network performance (tank-to-tank)? To what extent can new energy carriers be integrated into the existing infrastructure, or is a separate infrastructure required? etc.

To evaluate the wider feasibility of the new bunkering infrastructure, it is important to connect it with upstream energy flow models, downstream transport, and logistic models. An upstream energy flow model will reveal (changes in) the overall energy flows (well-to-tank), following the selection of a specific mix of alternative fuels combined with future transport scenarios. In practice, decisions for alternative energy carriers may typically be taken up (e.g., when a vessel owner or fleet operator sees certain advantages of a given solution). Recent developments in the global energy market have revealed that it is also important to have a top-down and long-term view of how much energy is required and from where it will be sourced. Downstream transport and logistic models are important to show how alternative energy carriers and energy conversion systems affect the performance of the transport chain. What is the impact of alternative energy carrier/energy converter solutions on the range, speed, and maximum payload of vessels (tank-to-wake)? How will alternative energy carrier/energy converter solutions affect the competitiveness of the IWT mode compared with other transport modes, as well as alternative transport corridors?

Practice-oriented methods should be provided to design zero-emission bunkering infrastructure, such as bunker locations (well-to-tank) and first-order functional designs of bunker facilities (tank-to-tank), as well as upstream energy flow consequences and downstream transport and logistics performance (tank-to-wake).

The investigation of ZE fuel infrastructure includes vessel transportation behavior in time and space, transport capacity and frequency, tank volume, vessel and route combinations, trade flow, handling capacity and time for bunkering sustainable fuel, and fairway information (depth, water flow, wind, wave, locks, bridges, etc.). The digital twin model for ZE fuel infrastructure should be able to simulate two-way traffic in waterways and output energy consumption and ZE fuel demand for different routes. The refueling point density can be determined based on the sailing-range capacity of the vessel.

5. CONCLUSIONS

A number of strategies and technologies are available for reducing emissions from inland waterway transport (IWT). The main strategy for achieving a ZE IWT is the use of alternative energy carriers with a lower well-to-wake carbon intensity. Other ship- and logistics-related measures had a smaller impact than alternative energy carriers. However, these measures are important to achieve robust energy consumption during the transition to ZE fuels.

There is deep uncertainty surrounding the benefits of alternative energy carriers and ZE technologies. A data-driven virtual representation of an inland shipping system can potentially be used to assess the efficiency of the proposed solutions and strategies. This digital twin can model the present system with all relevant components in a realistic manner, which can be validated using real-world data. The input from the community in terms of policies, strategies, and data can be processed by the digital twin, and the proposed intervention measures can be applied to assess their effectiveness.

The multi-level digital twin model for the ZE IWT should be developed for strategic, tactical, and operational decisions for integrated ships, logistics, and fuel infrastructure. This will have important implications for the management of technology development projects that involve a mix of commercial, environmental, and social objectives. Decision-makers on technology investments will exercise better judgment in the design and governance of technology development projects.

ACKNOWLEDGMENTS

This research was conducted within the project PATH2ZERO, which is financed by the NWA L2-Thema 2020 Zero Emission Shipping (ZES) program of the Netherlands Organization for Scientific Research (NWO) with Grant NWA.1439.20.001.

REFERENCES

[1] P. Miklautsch and M. Woschank. "*A framework of measures to mitigate greenhouse gas emissions in freight transport: Systematic literature review from a Manufacturer's perspective*". In: Journal of Cleaner Production 366 (2022), pp. 132883.

[2] H. Xing, S. Spence and H. Chen. "*A comprehensive review on countermeasures for CO2 emissions from ships*". In: Renewable and Sustainable Energy Reviews 134 (2020), pp. 110222.

[3] K. Moirangthem. "*Alternative fuels for marine and inland waterways: an exploratory study*". Tech. rep. JRC 100405, 2016, pp. 1-43.

[4] CCNR. "*Roadmap for reducing inland navigation emissions*". Tech. rep, 2022, pp 1-73.

[5] N.E. Ligterink et al. "*Emissiefactoren wegverkeer - Actualisatie 2019*". Tech. rep. TNO 2019 R10825v2, 2019, pp 1-54.

[6] H. Denier van der Gon and J. Hulskotte. "*Methodologies for estimating shipping emissions in the Netherlands A documentation of currently used emission factors and related activity data*". Tech. rep. 500099012, 2009, pp. 1-56.

[7] F. Dahlke-Wallat, B. Friedhoff and S. Martens. "*Assessment of technologies in view of zero-emission IWT*". Tech rep. 2293, 2020, pp. 1-100.

[8] E. Lindstat et al. "*Reduction of maritime GHG emissions and the potential role of E-Fuels*". In: Transportation Research Part D. 101, (2021), pp. 103075.

[9] E. van der Heuvel. "*Master plan for CO2-reduction in the Dutch shipping sector – Biofuels for Shipping*". E4tech rep. v4.0, 2018, pp.1-80.

[10] A. Florentinus et al. "*Potential of biofuels for shipping*", Tech. rep. BIONL11332, 2012, pp. 1-97.

[11] A. Singh et al. "*Evaluation of mechanical behavior of multifilament discarded fishnet/glass fiber and polyester composites for marine applications*". In: Mar. Struct. 58 (2018), pp. 361-366.

[12] R. Halim, L. Kirstein, O. Merk and L. Martinez. "*Decarbonisation pathways for international maritime transport: a model-based policy impact assessment*". In: Sustainability 10 (2018), pp 2243.

[13] E.A. Bouman, E. Lindstad, A.I. Rialland and A.H. Stromman. "*State-of-the-art technologies, measures, and potential for reducing GHG emissions from shipping-a review*". In: Transport Res. Transp. Environ 52 (2017).

[14] M.S. Eide, C. Chryssakis, O. Endresen. "*CO2 abatement potential towards 2050 for shipping, including alternative fuels*". In: Carbon Manag. 4 (2013).

[15] T. van Dijk, H. van Dorsser, R. van den Berg, H. Moonen and R.R Negenborn "*Smart ships and the changing maritime ecosystem*". Tech. rep. SmartPort, 2018, 1-31.

[16] L. Wang, Q. Wu, J. Liu, S. Li and R.R. Negenborn. "*State-of-the-art research on motion control of maritime autonomous surface ships*". In: Journal of Mar. Sc. and Eng. 7.12 (2019).

[17] J. Maestre and R.R. Negenborn. "*Distributed Model Predictive Control Made Easy*." 2014 Dordrecht. Springer, 2014, pp. 1-600.

[18] M. Haasnoot, J. Kwakkel, W. Walker, and J. Ter Maat. "*Dynamic adaptive policy pathways: A method for crafting robust decisions for a deeply uncertain world*". In: Global environmental change 23 (2013), pp. 485-498.

[19] H. Gaspar, D. Rhodes, A. Ross and S. Ove Erikstad. "*Addressing complexity aspects in conceptual ship design*: A systems engineering approach" In: Journal of Ship Production and Design 28 (2012), pp.145-159.

[20] J. Pasha, M. Dulebenets, A. Fathollahi-Fard, G. Tian, Y. Lau, P. Singh and B. Liang. "*An integrated optimization method for tactical-level planning in liner shipping with heterogeneous ship fleet and environmental considerations*." In: Advanced Engineering Informatics 48 (2021).

[21] T. Hjortnaes, B. Wiegmans, R. R Negenborn, R. Zuidwijk and R. Klijnhout. "*Minimizing cost of empty container repositioning in port hinterlands, while takin g repair operations into account*". J. of Transp. Geogr. 58 (2016), pp. 209-219.

[22] M. Dalmijn, B. Atasoy, P. Bijl, and R.R. Negenborn. "*Charge Scheduling of Electric Vehicles for Last-Mile Distribution of an E-grocer*" In: Proceedings of the 2020 Forum on Integrated and Sustainable Transportation Systems, 2020, pp. 236-241.

[23] M. Pourbeirami Hir, A. Kirichek, N. Pourmohammadzia, M. Jiang and M. van Koningsveld. "*Zero-emission fueling infrastructure for IWT: optimizing the connection between upstream energy supply and downstream energy demand*". In Proceedings of MOSES2023 conference, 2023.

[24] D. van der Kroft, and J. Pruyn. "*A Study into the Availability, Costs and GHG Reduction in Drop-In Biofuels for Shipping under Different Regimes between 2020 and 2050*". In Sustainability 13 (2021), pp. 9900.

[25] J. Holtrop and G. Mennen. "*An approximate power prediction method*". In: International Shipbuilding Progress 29 (1982), pp. 166-170

[26] L. Vehmeijer. "*Measures for the reduction of CO2 emissions, by the inland shipping fleet, on the Rotterdam-Antwerp corridor*". MSc thesis, TU Delft, 2019.

[27] M. van Koningsveld, H. Verheij, P. Taneja and H. De Vriend. *Ports and Waterways - Navigating the changing World*. TU Delft Open, 2023.

[28] F. Vinke, M. Van Koningsveld, C. Van Dorsser, F. Baart, P. Van Gelder and T. Vellinga. "*Cascading effects of sustained low water on inland shipping*." In: Climate Risk Management 3 (2022), pp.1-15.

[29] C. Van Dorsser, F, Vinke, R. Hekkenberg and M. van Koningsveld. "*The effect of low water on loading capacity of inland ships*". In: European Journal of Transport and Infrastructure Research 20 (2022).

Zero-emission Fueling Infrastructure for IWT: Optimizing the Connection between Upstream Energy Supply and Downstream Energy Demand

M. Pourbeirami Hir[a], A. Kirichek[a*], N. Pourmohammadzia[a], M. Jiang[a] and M. van Koningsveld[a,b]

[a] Delft University of Technology, Delft, the Netherlands
[b] VanOord, Rotterdam, the Netherlands
[*] Corresponding Author o.kirichek@tudelft.nl

Abstract

A key challenge in the energy transition for Inland Water Transport is the functional design of bunker networks and first-order dimensioning of individual bunker stations. A fundamental ingredient for this is an improved understanding of how upstream energy supply ('well-to-bunker-station') and downstream demand ('bunker-station-to-tank') may interconnect. In this paper we discuss an approach to the design of bunkering networks that takes logistic modelling to estimate network scale energy demand as a starting point. Depending on the vessels that use the network and the anticipated fuel mix for the overall fleet, logistical modelling may be used to estimate the magnitude of the energy demand along the network. Estimates of the operational range of vessels per energy carrier help to estimate maximum bunker station inter-distances. Insight into the potential supply chains that connect the source of each energy carrier to a physical bunker facility is needed to close the loop. Energy carriers may be needed on board in a gaseous or liquid form, or in the form of electrons. Transfer may take place in the form of loading (e.g., filling the fuel tank, charging the battery pack) or swapping (e.g., exchanging fuel containers, exchanging battery containers). Depending on the energy carrier, transfer method(s) and demand quantities, functional designs of bunker stations (in terms of required system elements and their order-of-magnitude dimensions) can be made. Depending on service level requirements both the dimensions of individual bunker stations and their spread over the network may be optimized. Key contribution of this work is a thorough overview of aspects that play a role in the design of bunker infrastructure for the decarbonisation of inland shipping. Based on this overview steps for further research are recommended.

Keywords: Inland Water Transport, Bunkering, Well-to-Bunker-Station, Bunker-Station-to-Tank.

1. INTRODUCTION

In line with the Climate Act and Paris Agreement, representing significant global efforts to combat adverse impact of climate change through mitigation, governments are actively working towards reducing greenhouse gas emissions to ensure a global temperature rise below 2ºC by 2030 [1]. In this regard, a commitment to a sustainable future includes a shift from fossil fuels to more clean and renewable energy resources. Inland shipping is a promising sector for reducing emissions in transportation, exhibiting higher energy efficiency and lower pollutant emissions compared to road or air transport. With the promotion and expansion of inland shipping, countries can leverage its potential to mitigate the environmental impact of transportation and carbon emissions. Furthermore, this shift can alleviate road congestion and reduce dependence on long-haul trucking, further aiding in emissions reduction.

Exploiting renewable resources as alternative fuels presents several challenges. One key challenge involves the construction of new facilities and infrastructures necessary to support the use of alternative fuels. This endeavor often requires significant investment, both in terms of financial resources and planning efforts. It involves establishing charging or refueling stations, upgrading existing ports and terminals, and adapting vessels to accommodate new fuel and propulsion systems. These considerations are closely intertwined with the Supply Chain Network (SCN) of bunkering, playing a crucial role in understanding the flow of fuels, associated costs, and other influential factors that contribute to the success of the network.

In order to achieve optimal network planning, strategic considerations play a crucial role. These considerations include factors such as the number, location, capacity levels, and technology employed

@2023 Pourbeirami Hir, M. et al. published by TU Delft OPEN Publishing on behalf of the authors. Licensed under a Creative Commons Attribution CC BY license.
DOI: https://doi.org/10.59490/moses.2023.674

in network facilities. These aspects directly impact the efficiency and responsiveness of the network. Designing bunkering infrastructure for inland shipping within a supply chain involves determining the location of bunkering facilities and devising strategies for fuel supply from resources to production locations, then to bunkering infrastructure, and finally connecting to downstream vessels. The choice of the location, capacity, and the type of bunkering are controlled by factors such as demand congestion, the amount of demand, the state of the waterway, the state of the fleet from the downstream side and the production, distribution, and resource locations from the upstream side. Availability and accessibility of alternative fuels, the feasibility in terms of production, distribution, the adequacy of supply facilities, and safety regulations are also of paramount importance.

The extensive literature on the location of bunkering infrastructure for different fuel types is noteworthy. However, it is crucial to highlight that these studies frequently overlook the condition of waterways and fleets in their analyses. Additionally, many of these studies tend to exclusively focus on a single fuel type, which limits their ability to offer comprehensive insights for future planning and decision-making processes. In 2022, Vilchez [2] conducted a comprehensive examination of the ongoing initiatives in Europe aimed at mitigating greenhouse gas emissions arising from navigation activities. Their focus was on the deployment of low- and zero-emission vessel technologies, with particular attention to alternative fuels such as electricity, hydrogen, and natural gas. The study also identified a range of policy measures and research and development actions put forth by European governments to facilitate these environmental efforts. In 2021, Grosso [3] assessed European research and innovation projects using the TRIMIS system and highlights the need for a combination of innovations to achieve carbon reduction goals. These potential innovations include lightweight materials, hull repair methods, wind-assisted propulsion, engine efficiency, hydrogen, and alternative fuels, emphasizing both technological and non-technological solutions to mitigate environmental impacts. Moreover, Prussi [4] explored the maritime industry's environmental concerns and its transition towards alternative fuels to meet decarbonization targets. This study proposed sector segmentation to assess fuel consumption and availability in Europe, highlighting factors like cost, GHG savings, safety regulations, and infrastructure reliability play vital roles in fuel adoption. Amaph [5] utilized bibliometric analysis to examine research trends in cleaner alternative marine fuels for reducing emissions in the shipping industry. He believed that the research field is growing significantly, with the USA as a major contributor, and Liquified Natural Gas being the most studied alternative fuel. However, recent trends indicate increased attention to methanol, ammonia, and hydrogen fuels, offering insights for future research on shipping industry decarbonization. Additionally, Moirangthem [6] highlighted the importance of alternative fuels in reducing emissions in the marine transport sector, driven by MARPOL regulations and stricter emission standards. Their report provided an overview of various alternative fuels, including methanol and LNG, while addressing sustainability and safety concerns. Furthermore, the report suggested the development of testing standards and policies to further promote the adoption of cleaner fuels in the shipping industry.

A comprehensive understanding of the upstream and downstream components of the SCN, along with the interdependencies, enables more efficient infrastructure planning. By connecting infrastructure and network levels, stakeholders can better respond to current energy needs and anticipate future demand, thereby facilitating a smoother transition to alternative fuels.

Considering the importance of inland shipping and connecting the upstream and downstream of the supply chain network, this paper examines three different forms of fuel (i.e., liquid, gaseous, and electricity) in order to demonstrate the challenges faced in developing the SCN of bunkering infrastructure for various kinds of fuel. Furthermore, a comprehensive assessment of the respective supply chains is presented. By analyzing the upstream and downstream elements, the paper aims to provide a comprehensive understanding of the complexities involved. Then, the challenges associated with considering the use of these alternative fuels in inland shipping are discussed, allowing for a realistic appraisal of the situation. Finally, the paper concludes with recommendations based on the findings, highlighting potential strategies to overcome the identified challenges and accelerate the transition towards sustainable inland shipping.

2. FOCUS ON THE SUPPLY SIDE

To gain a comprehensive understanding of the bunkering infrastructure, it is crucial to delve into the upstream side of the fuel SCN for inland shipping. This involves focusing on bunkering infrastructure located at terminal stations, which act as vital links between the upstream and

downstream parts of the fuel supply chain. For a fuel type to be made available to inland shipping, important decisions (and investments) need to be made in the upstream supply chain to facilitate adequate supply. To analyze the upstream part of the fuel SCN for bunkering, it is essential to consider the feedstock and raw materials of alternative fuels, suppliers, and the distribution between different parts of the supply chain. Zero-emission fuels predominantly depend on renewable energy sources for production, including solar power, wind energy, hydroelectric power, geothermal energy, and biomass. The availability of resources, scalability, accessibility, sustainability, and the feasibility of production are crucial factors to be considered. Additionally, resources capacity, regulations, and safety issues should be considered.

The environmental impact of alternative fuels also holds significant importance. Zero-emission fuels must exhibit minimal to no emissions of greenhouse gases throughout their entire life cycle, including extraction, production, distribution, and utilization. It is necessary to consider the total life cycle emissions of a particular fuel, including indirect emissions from upstream processes. The energy density is also an important factor to consider. Fuel with a higher energy density allows for longer sailing ranges and reduces bunkering frequency, making it more desirable for use.

Existing infrastructure and compatibility with current vessels and engines are other key parameters that should be identified. The shift to alternative fuels may require substantial investments in infrastructure both economically and technically, comprising investments in refueling stations, bunkering equipment, charging points, distribution facilities, storage facilities, supplier plant as well as modifications to vehicles and engines.

Alternately, government policies, incentives, and regulations are of paramount importance in promoting the widespread adoption of zero-emission alternative fuels. By implementing supportive policies, governments can stimulate investments, research, and development in alternative fuels, while fostering a favorable market environment

Furthermore, it is critical to consider economic viability of alternative fuels. Assessing the cost of production, distribution, and utilization of fuels is crucial in determining competitiveness on the market. Factors such as economies of scale, technological advancements, and market demand control fuel cost-effectiveness.

Fuel suppliers also play a crucial role in the SCN of bunkering infrastructure for inland shipping. A well-established infrastructure for procuring, storing, and distributing the required fuels, meeting the demands of inland vessels, should be available. In terms of fuel procurement, suppliers engage in sourcing fuels from diverse sources, establishing relationships with fuel producers to ensure a reliable supply. The production technology used to convert feedstock into alternative fuels should be efficient, scalable, and environmentally friendly. Different technologies are utilized based on the type of fuel involved. For example, biofuel production involves fermentation or chemical processes, while hydrogen production relies on electrolysis. Storage facilities and infrastructure should be maintained to store and handle the fuels. These facilities typically consist of large tanks or storages designed for storing different types of fuels. The infrastructure includes systems for fuel quality testing, blending, and customization based on customer requirements. Suppliers manage the logistics and transportation aspects of fuel delivery from resources to plants or from storage to bunkering terminals and vessels. They coordinate the movement of fuel through various modes of transportation, such as pipelines, train, trucks, trailers, container trailers, cables, or dedicated fuel barges, depending on the fuel types. If production sites have access to either inland or seaports, choosing short sea or inland waterway transportation can be a cost-effective and environmentally friendly choice. Alternatively, truck transportation is a flexible option with excellent connectivity, particularly suitable for smaller ports that lack multimodal connections to the hinterland. Even though pipeline transport does not currently appear to be viable for all fuel types, it should not be ruled out as an option. It might be a good business case to build one.

Efficient logistics planning and optimization of transportation routes are essential to ensure timely and cost-effective fuel delivery. It is important to note that the costs incurred by fuel suppliers in their SCN can affect the price of fuel at bunkering stations. The capital and operational expenditures encompass various components, including supply costs, distribution costs, construction costs, maintenance and operational costs, handling costs, inventory costs, shortage costs, raw material prices, and fuel prices.

Suppliers of alternative fuels can be categorized as centralized or on-site. Centralized suppliers utilize existing infrastructure, while on-site suppliers are employed in situations where distribution is impractical or expensive, or when building a plant incurs significant investment. On-site suppliers ensure fuel accessibility and

convenience for vessels by establishing an adequate number of production sites near stations.

This paper examines three types of fuels based on their physical appearance: gaseous, liquid, and electricity. The assessment of the technological feasibility of a fuel SCN is vital to determine the viability of each fuel type. It is important to note that zero-emission fuel alternatives, such as green hydrogen, electric batteries, biofuels, and methanol, have distinct infrastructure requirements. To ensure efficient implementation of the necessary bunkering infrastructure, it is crucial to analyze the SCN for each type of fuel.

2.1 Gaseous fuels

Figure 1 illustrates the Green Hydrogen supply chain, which involves the process of electrolyzing water using electricity that could be derived from renewable sources such as wind farms, solar panels, hydropower, biomass energy, geothermal energy, or tidal energy. To enable this process, electrolyzing plants need to be constructed. The feasibility of establishing these expensive plants depends significantly on the availability and accessibility of natural resources [7].

The output of the electrolysis process is hydrogen gas, which has a low energy density and occupies a considerable amount of space. Therefore, specialized storage technology is required to facilitate its storage. Gas can be transferred through pipelines, trailer trucks, or swappable containers. Pipelines are suitable for gas and liquid forms but require high levels of safety measures and initial investments in materials. It is important to note that if the distance between the stations and plants is significant, the cost of pipeline construction and maintenance increases due to the amount of material needed. However, pipelines are more convenient for distribution and provide significant capacity [8].

Gas trailers or swappable containers have lower initial costs compared to pipelines since they do not require additional infrastructure. However, they are typically used for short-term storage and rely on road infrastructure, which can increase hazards on the road. When using swappable containers, it is crucial to consider container dimensions, equipment for container displacement (such as cranes) to ship, loading and unloading times, and charging schedules. Station facilities should be designed to accommodate the containers adequately or provide specific storage facilities if containers require special handling properties. Additionally, optimizing the timing of distributing container transfers to charging facilities and charging time minimizes waiting times and network shortages.

Different storage and charging facilities can be constructed near stations, plants, or even between plants and stations. The choice of capacity of these facilities depends on the pressure and temperature requirements for storing gaseous fuels. Direct dispensing of this fuel to ships requires high-pressure compressors, and temporary storage necessitates low-pressure buffer storage. Bunkering operations can be carried out using hoses from gas trailers, storage facilities, or fuel-containing trucks.

The main challenges associated with gaseous fuels include the production or supply risks from limited renewable resources, the need for sufficient bunkering infrastructure and suitable ports, the relatively low energy content and price volatility influenced by the upstream part of the SCN.

2.2 Liquid fuels

Figure 1 also illustrates the fuel SCN of liquid hydrogen, which is obtained through the liquefaction of gaseous hydrogen and offers improved energy density compared to its gaseous form. Currently, there is a scarcity of infrastructure for liquefaction plants, making it economically impractical due to the high fuel costs until the installation of such facilities begins. Liquid hydrogen resembles LNG (liquefied natural gas) and holds promise for mid-term applications. Its transportation can be achieved through specialized liquid trucks that account for boil-off losses,

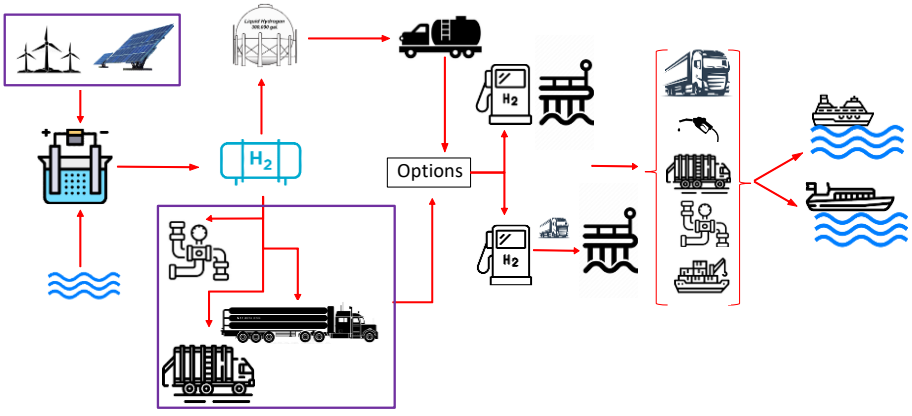

Figure 1 Green hydrogen supply chain network

necessitating the construction of dedicated facilities at a high cost. Bunkering operations can be conducted using hoses connected to trucks, fixed stations, or even bunker barges.

Biofuel is a liquid fuel, depicted in Figure 2, that can be derived from various sources including natural gas, gasified biomass, renewable sources (such as residual plant and animal fractions), and rapeseed oil. It offers several advantages as an alternative fuel. Firstly, it is non-toxic to humans and the environment. Secondly, there are no specific policies governing its usage, and finally, the infrastructure changes required for implementing biofuel usage are relatively minor, with costs negligible compared to other alternative fuels, making it a convenient option for replacing traditional fuels. However, it is important to note that biofuel is not a completely emission-free solution and only reduces greenhouse gas (GHG) emissions by approximately 60% [9].

It is similar to diesel/gasoil, and primarily utilized in heavy road vehicles. It exhibits comparable energy density and storage characteristics to diesel fuel. Storage of biofuel is recommended at ambient temperature and atmospheric pressure. In terms of energy density, viscosity, volume, and refueling time, biofuel is comparable to other alternative fuels. Currently, bunkering operations for biofuel can be conducted using trucks or direct drum transfers. There are, however, several challenges associated with biofuel usage. Ensuring long-term availability is one such challenge, as well as addressing competition between transportation modes and other industrial sectors. Additionally, the production rate of biofuel is relatively low, and it still contributes to emissions. Consequently, biofuel is considered a transitional fuel rather than a zero-emission solution.

Figure 3 presents an overview of the Methanol supply chain, which is more widely available compared to hydrogen and electricity. Methanol can be produced through four primary pathways: grey methanol (derived from fossil sources), bio methanol (obtained from wet biomass), carbon-recycled methanol (generated from fossil-based solid waste through gasification), and e-methanol (produced using green hydrogen and carbon sources). To achieve future greenhouse gas (GHG) targets, the transition to carbon-neutral fuels like bio-methanol and e-methanol is crucial. However, during the ongoing shift to methanol-based maritime transport, grey methanol may still be necessary in the short-term and medium-term.

The infrastructure costs associated with Methanol are comparable to diesel/gasoil and lower than other alternative fuels. It can also be used in various applications with minimal modifications. Methanol distribution can be carried out by train, which is cost-effective; trailers, although expensive and suitable for low volumes and short distances; barges; and pipelines, which are suitable for transporting large volumes and offer energy and cost efficiency during operation. Bunkering options for Methanol include ship-to-ship, shore-to-ship, and truck-to-ship methods. Currently, these methods are available for ferries in inland shipping, but they face challenges such as limited demand, high costs, and inadequate infrastructure [10].

While methanol does not face significant technological barriers and is considered a climate-neutral fuel, one of the main challenges is the high cost of producing methanol from renewable resources. Additionally, methanol has a lower energy density compared to gasoil and diesel, and it also exhibits higher toxicity. Furthermore, it requires more frequent bunkering stops compared to conventional fuels.

2.3 Battery Electric

Figure 4 illustrates a battery electric supply chain, which offers a lower energy density compared to diesel and gasoil, making it suitable for short-distance transportation. The charging stations within this chain should be capable of serving vessels with distances up to 100 km. There are two types of vessels that utilize batteries: fixed battery vessels and vessels with exchangeable batteries.

For fixed battery vessels, the charging time and capacity of the charging points are crucial factors. Therefore, charging facilities should be available at the stations to accommodate these requirements. The majority of vessels are charged during midnight hours, and the charging points should be located near the electricity grid. However,

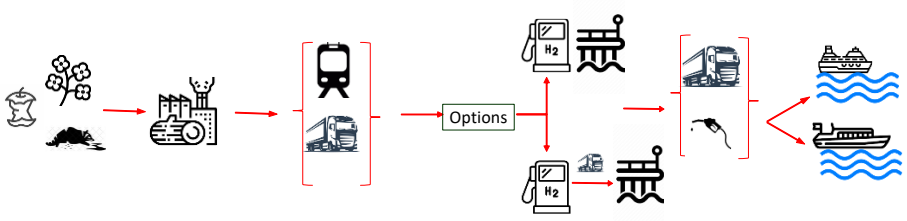

Figure 2 Biofuel supply chain network

distribution is necessary in areas without grid congestion. It is also possible to consider modifying the grid if necessary vessels with pre-installed electric batteries can be charged either through a cable or by induction.

Alternatively, exchangeable power packs or swappable batteries can be employed, which offer benefits such as time savings, reduced potential loss of revenue, and lower initial investment for the shipper. However, the infrastructure cost associated with exchangeable power packs is high, with limited economies of scale, requiring the development of entirely new infrastructure. Currently, this approach is restricted due to certain drawbacks, including longer charging times and time-consuming processes. The existing capacities do not support long or medium routes, necessitating a significant amount of power. While the risk of battery fires is generally low, if they occur, they can lead to significant issues.

3. FOCUS ON SPECIFYING DEMAND

In order to identify suitable locations for bunkering infrastructure for zero-emission inland shipping, it is crucial to conduct an analysis of the demand for alternative fuels. This analysis entails evaluating the current and future traffic flow requirements of vessels operating on inland waterways. By understanding patterns of demand, planners can prioritize the placement of bunkering facilities along specific waterways or regions. The placement of refueling points is determined based on the minimum sailing range of the representative fleet in the corridor. This ensures that all types of ships in the corridor can reach the next refueling point, with the maximum distance between two refueling points not exceeding this minimum range.

Estimating the required capacity of each refueling point can be done by considering the total energy consumption at various time scales, and the allocation of energy supply can be based on the direction of energy consumption. Accurately quantifying the energy demand for the entire route and corridor network necessitates reliable estimation of energy demand, taking into account variations in sailing conditions such as water depth, which affect energy demand [11]. It is also important to examine the potential effects of alternative fuels on a vessel's sailing range, payload capacity, and sailing velocity. Accordingly, if the sailing range is the only aspect impacted, the primary effect on transport efficiency would be an increased frequency of bunker stops. On the other hand, if the range remains unchanged but the payload capacity is affected, the main impact on transport efficiency would be the need for more trips to transport the same cargo volume [12].

Additionally, factors such as vessel types, their energy requirements, and the anticipated growth of the shipping industry should be taken into consideration. Two commonly used methods for estimating global bunker demand are the top-down and bottom-up approaches. To estimate energy consumption, information on transport demand (including volumes, origins, and destinations), waterway network conditions (such as water depths and currents), and fleet characteristics (such as composition and engine ages) is necessary. Vessel resistance algorithms can be utilized for this estimation [13-16].

Algorithms for energy consumption calculations, both at the individual ship and corridor network levels, have been implemented in the Python package OpenTNSim. Aggregating the results from multiple vessels allows for mapping the energy consumption of the corridor network and determining energy consumption at different time scales. The state of the waterway, including water depth and current, directly impacts the energy demand and congestion for transportation. The classification of waterways determines the maximum vessel size that can be used. It is important to note that alternative fuels have a lower energy density compared to diesel, which may require larger tanks or more frequent refueling [11].

Understanding the state of the available fleet for transportation on the waterway network, as defined by PIANC and RVW [12], is crucial. Factors such as available air draught, maximum width, length, and draught, as well as bottlenecks related to width and depth, typically impose limitations on the maximum vessel class allowed on a waterway.

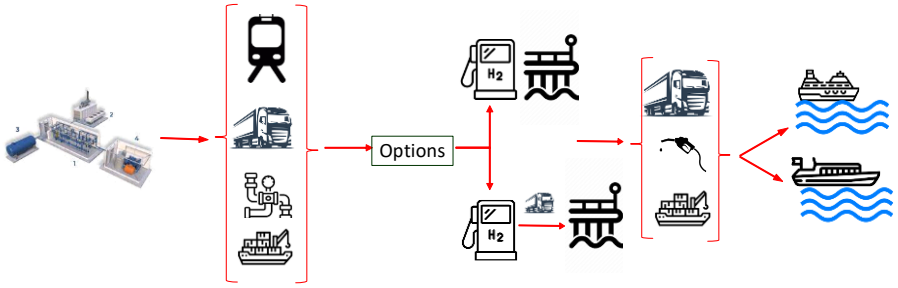

Figure 3 Methanol supply chain network

Traffic intensity and environmental conditions such as reduced water levels due to low discharge extremes can also influence the assessment [17,18]. It should be recognized that not all vessels in the fleet will be of maximum size, and smaller vessels will require more trips to transport the same cargo volume compared to larger ships. Older vessels might have outdated engines that perform less efficiently in terms of emissions. Additionally, evaluating the availability of alternative modes of transportation, such as road, rail, and pipelines, is important. If these alternatives can accommodate a significant shift in transportation, it will increase the pressure on the inland shipping sector to adopt or transition to other energy solutions [12].

4. MATCHING SUPPLY AND DEMAND

The bunkering terminal plays a crucial role as a key node within the inland shipping fuel SCN. These terminals are strategically located along inland waterways to facilitate efficient distribution of fuel. Upon receiving fuel shipments from suppliers, bunkering terminals store them temporarily before transferring them to vessels. Bunkering operations involve the transfer of fuel from storage facilities to vessels or direct supply from a grid (either available fuel pipelines or electricity).

The upstream side of the inland shipping SCN focuses on the production of fuel using various feedstocks and production methods, as well as the transportation of these fuels to bunkering stations or transferring fuel to vessel without using bunkering stations. This analysis considers feedstock suppliers, transportation companies, and fuel handling procedures. It also considers emerging trends in fuel production, such as the use of renewable energy sources or the adoption of cleaner fuel technologies, to align with environmental sustainability goals. Furthermore, the decision-making process regarding fuel selection and sourcing involves assessing the availability and reliability of different renewable resources. Evaluating the scalability and long-term viability of these resources is crucial, as it impacts the stability and resilience of the bunkering network. Additionally, the production plants and suppliers capable of producing and supplying the desired fuel with the best feasible distribution to bunkering stations need to be identified. Collaboration with renewable energy providers, research institutions, and regulatory bodies can help identify emerging technologies and advancements in renewable energy production, ensuring the availability of sustainable fuel sources for bunkering operations.

However, the capacity of these renewable resources is limited, necessitating careful decision-making regarding the quantity and type of fuel to be used and where it should be deployed. This decision also affects the selection of suppliers and production sites, which can be categorized into on-site and centralized facilities. Conversely, the downstream side addresses the efficient transfer of fuel from bunkering stations or other bunkering methods to end consumers, which are the vessels. This analysis involves commodity traders or brokers, transportation companies, storage facilities, bunkering operators, and vessels. It also considers the evolving needs and regulations in the shipping industry, such as the transition to low-emission vessels or the implementation of stricter fuel quality standards.

Efficient planning and coordination of the fuel SCN from the perspective of decision-makers at the bunkering station side are crucial to finding an acceptable trade-off between the upstream and downstream sides of the supply chain. This requires careful consideration of factors such as fuel production, transportation logistics, storage facilities, and bunkering operations to ensure the smooth flow of fuel from suppliers to end consumers. Additionally, assessing the availability and accessibility of bunkering locations, as well as the infrastructure requirements, plays a vital role in optimizing the bunkering network for inland shipping. Effective collaboration among stakeholders, including government bodies, shipping companies, fuel suppliers, and terminal operators, is essential to develop sustainable and resilient bunkering solutions.

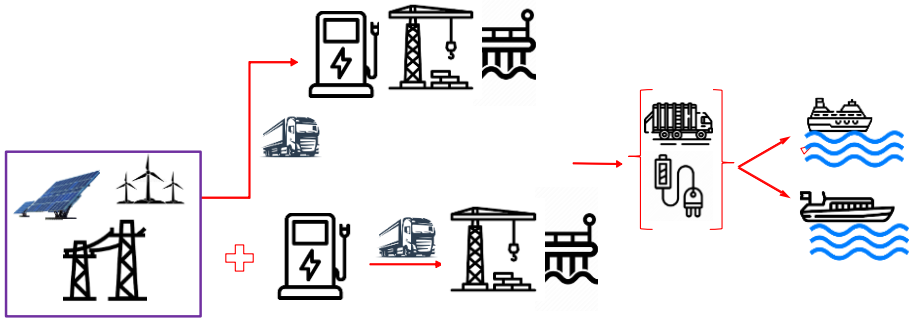

Figure 4 Electric battery supply chain network

In addition to cost considerations, the design of bunkering locations for inland shipping requires a comprehensive analysis of various factors to ensure an efficient and sustainable supply chain. This analysis includes evaluating the accessibility and proximity of potential bunkering sites to key shipping routes, as well as considering the infrastructure requirements for fuel storage, handling, and transfer operations. By integrating these factors, the bunkering network can be designed to support the seamless flow of fuels, promote environmental sustainability, and contribute to the overall growth and resilience of the inland shipping industry.

When determining the bunkering transfer method to be used, a combination of factors comes into play. These factors include the location of bunkering sites, which define the availability of infrastructure and the rules and regulations specific to each fuel and bunkering procedure. The amount of fuel to be bunkered and the operating costs of the vessel being fueled are also crucial considerations. Additionally, time and capacity considerations are important in determining the desired service level, aiming to minimize unmet demand, bunkering time, waiting time at the station, and traveling time. Factors such as traffic on waterways and demand congestion need to be carefully considered to optimize the bunkering process.

The bunkering type selected significantly impacts the required infrastructure. Ship-to-ship bunkering, for instance, is a flexible solution suitable for a wide range of fuel volumes, but only for liquid fuels. In this case, storage or production sites should be located within a certain distance of the port to support the bunkering barge. Ship-to-ship bunkering can take place at various locations, including along the quayside, at anchor, or at sea. Compared to other bunkering methods, ship-to-ship bunkering offers greater flexibility in terms of capacity and bunkering location.

Truck-to-ship bunkering, on the other hand, has capacity limitations due to the truck's capacity. However, it offers the lowest investment costs, making it suitable for short-term phases or smaller fuel volumes. For truck-to-ship bunkering, the location of the truck (either at a station or along the river) should be carefully determined, taking into account the availability of safe mooring places for vessels. Fixed bunkering stations enable bunkering volumes of any size and support multi-fuel bunkering, where a bunker vessel can carry multiple fuels or grades to serve several vessels. These fixed stations can be located specifically for bunkering purposes or serve other functions as well. They may incorporate storage facilities for handling swappable containers or charging facilities for electric vessels. Other components related to bunkering operations, such as cranes for container swapping, compressors, fuel quality testing facilities, and fuel blending facilities, may also be present. Fixed bunkering stations should be constructed to accommodate multiple fuels since other bunkering types are limited to supporting only one type of fuel.

In addition to carefully considering the selection of bunkering methods, various costs need to be calculated, including equipment, construction, distribution, installation, land, legal, and bunkering maintenance, and operations expenses. By integrating cost considerations, environmental sustainability, technological advancements, and regulatory compliance, the design of bunkering locations for inland shipping can contribute to establishing a robust and future-proof fuel SCN. This enables the seamless flow of fuels, supports the transition towards cleaner

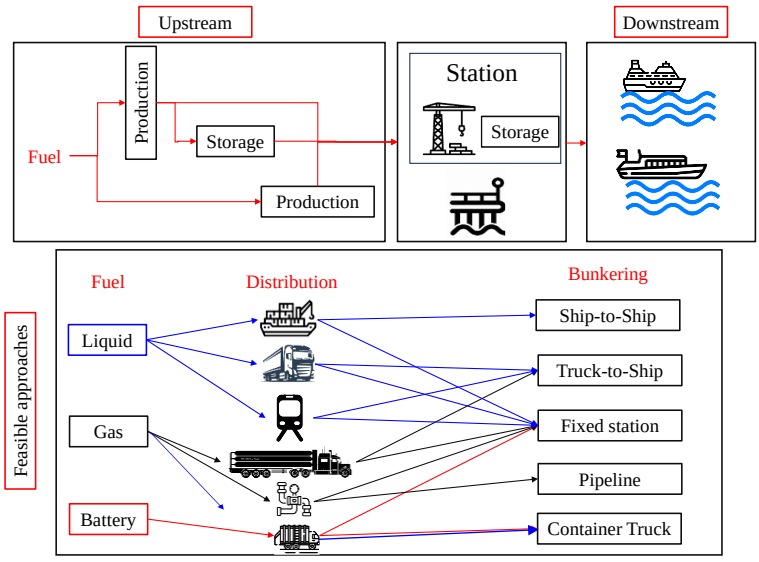

Figure 5 Inland shipping supply chain network

energy sources, and fosters the overall growth and sustainability of the inland shipping industry. Furthermore, it is important to assess whether the entire corridor has the necessary infrastructure and fleet capabilities to support vessels using the same type of fuel at the corridor's origin. These factors, including waterway infrastructure and fleet characteristics, influence the demand and feasibility of different bunkering types and distribution methods.

In designing bunkering locations for inland shipping, the distribution between components of the upstream side (resources, production plants, storages) and bunkering stations should be carefully considered based on the feasibility of different distribution types for fuels. Distribution options include truck, trailer, gas trailer, container trailer (utilizing road infrastructure and currently suitable for liquid, gas fuels), pipeline (suitable for gas and liquid fuels), train (using rail infrastructure and currently suitable for liquid fuels), container trailer (use road infrastructure and currently is suitable for fuels in the form of gas and electricity) and barges (utilizing waterway infrastructure and suitable for liquid fuels). Assessing the accessibility of distribution infrastructure in relation to waterway infrastructure and its feasibility for the desired fuels is crucial.

Distributing fuels by road can be employed for both centralized and on-site production with limited capacity. After distributing the fuels, bunkering can be done either by truck-to-ship transfer or by storing the fuels in fixed stations. Container trailers are suitable for distributing gas fuels and battery electricity, which need to be transferred to stations. These stations should have storage facilities to handle the containers. Another distribution option is by train, which is suitable for liquid fuels. If the rail infrastructure is not located near waterways, an additional distribution method, such as trucking the fuel to ports, needs to be considered. The third distribution type, which is pipeline, is more suitable for on-site production, reducing the huge costs of needed infrastructure. After distribution, the fuel can be stored in fixed stations, and bunkering can be done through pipelines. Another distribution option is by barges, suitable for liquid fuels. It allows for shipping fuels from both on-site and centralized production. After distribution, bunkering can be conducted either by ship-to-ship transfer or by storing the fuel at fixed stations. Fixed bunkering stations offer another option, where vessels can moor at jetties or pontoons, and storage facilities can be incorporated within the station. The capacity of these stations may vary depending on the demand. Additionally, swapping containers is another distribution option worth considering. This method offers lower delivered costs, eliminates the need for expensive land-based infrastructure, reduces bunker time, and allows for charging facilities to be co-located with loading operations. This can be achieved by utilizing cranes and similar port infrastructure, or the containers can be transported to separate charging facilities [12]. So, the selection of the most appropriate distribution method depends on factors such as fuel type, infrastructure availability, cost considerations, and the specific requirements of the bunkering operation.

Cargo owners often prioritize cost over greener transport options if cheaper conventional alternatives are available. However, higher costs that affect the entire industry can potentially be passed on to customers, leading to a shift in price willingness for greener transport [10]. Bunker prices significantly impact ship owners, operators, and charterers, and high bunker prices incentivize the adoption of alternative energy sources in the shipping industry. Fuel prices for shipping are influenced not only by production costs but also distribution costs and sellers. Additionally, bunker prices depend on the availability of the product in the market. Quay operators generally prefer to avoid occupying their premises with vessels that require truck-based bunkering. This is due to limited space availability for loading/unloading activities and environmental permit restrictions. As the market demand increases, ship-to-ship transfers become more attractive for vessels with a fuel demand of 200 metric tons or more (equivalent to more than four tank trucks). Compliance with regulations governing fuel quality, safety, and environmental standards is a vital aspect of the bunkering supply chain. Fuel suppliers, bunkering terminals, and transportation entities must adhere to relevant regulations to ensure safe and sustainable bunkering operations. Emphasis on compliance with emission regulations and the use of low-emission or alternative fuels is increasingly important to promote environmental sustainability.

The objective of the inland shipping supply chain analysis is to compare multiple scenarios and address the following key questions:

1. What can evaluate the essential changes or expansions needed in the current bunkering infrastructure to facilitate a seamless shift from traditional fuels to alternative fuels?
2. How can it be determined whether there is a need for new bunkering locations or if optimizing existing facilities is sufficient?
3. What are the key determinants influencing the bunkering supply chain network components in order to achieve zero emissions and how can they influence?

4. How can a bunkering network effectively incorporate multiple alternative fuels, and what would be the logistical and operational considerations in managing such a mixed fuel within the network?
5. How do waterway and fleet properties, including fleet composition, water depth, route traffic, waiting times, and bunkering procedures, influence the design and optimization of a sustainable bunkering network for inland shipping?
6. Which bunkering types are currently suitable and feasible, and how will their suitability evolve over time?

By examining these questions and conducting a comprehensive supply chain analysis, we aim to provide valuable insights into the design and optimization of bunkering locations for inland shipping.

5. CHALLENGES

Designing bunkering locations for inland shipping involves several challenges. Construction costs, facility location planning, and relocation projects require long-term investments. To ensure profitability, decision-makers should prioritize long-term facilities designed to remain operational for extended periods. It is crucial to select locations with sufficient capacity to accommodate not only the current demand for alternative fuels but also the future transition towards achieving net-zero emissions. Therefore, assessing the demand location and its congestion level is critical in estimating the required supply volume to prevent shortages within the network. Major waterways, such as core ports and main corridors, are expected to experience higher demand and may necessitate additional resources compared to other areas. Consequently, the network should aim to maintain the capacity of new facilities while meeting all demands. For the primary steps towards zero-emission, instead of constructing new plants near resource sites, investing in distribution is often more economically viable.

Additionally, reliability is a vital aspect to consider in the bunkering supply chain. Road congestion, weather conditions, and maintenance can significantly increase travel time for road transport. Rail transport generally operates on fixed schedules but can experience delays due to train failures or track repairs. River transport may face obstacles during the dry season when shallow sections become impassable. Addressing bottlenecks is crucial to improve the reliability of inland shipping. Road transport, favored by small transport companies, can be more competitive due to fuel subsidies and the preference for smaller trucks. Rail transport tends to have more cost but allows larger volumes per shipment, while river transport is generally the most cost-effective option for carrying significant cargo volumes.

Moreover, for swappable containers, the duration for which containers should remain on-site at fixed bunkering stations is an important consideration as their storage capacity in stations can change over time. Additionally, considering the capacity of suppliers is crucial. Centralized supply chains offer advantages, with suppliers benefiting from economies of scale, large-scale storage facilities, and well-established logistics networks to efficiently serve high-demand areas. However, transportation costs for centralized suppliers can increase due to longer distances and lead times to reach bunkering stations. On the other hand, on-site production may face challenges in scaling up production and meeting increased demands if existing infrastructure has limited capacity. The choice between on-site and centralized production depends on factors such as operational scale, geographic distribution, cost considerations, infrastructure availability, and responsiveness requirements. A combination of both approaches can be adopted to optimize the bunkering supply chain. Finding the right balance between centralized and on-site production, along with considering distribution factors such as lead time, transportation feasibility, and investment costs, is crucial for optimizing the bunkering supply chain and ensuring efficient fuel delivery to meet the demands of inland shipping.

6. DISCUSSION AND CONCLUSION

The following discussion focuses on key aspects related to the design of bunkering infrastructure for inland shipping. One crucial consideration is the exploration of alternative storage options derived from natural resources, particularly temporal or unconventional options. For example, utilizing salt caverns as storage facilities for gases like hydrogen offers a secure and efficient means of storing alternative fuels. This approach reduces costs and expedites the implementation of alternative fuels for inland shipping. Additionally, modifying or extending existing infrastructure can facilitate the integration of alternative fuels into the current system, minimizing the need for significant investments in new facilities, albeit at the expense of functionality for other fuels.

The distribution of bunkering locations should be guided by vessel traffic density to ensure that high-traffic areas receive adequate service without overinvesting in low-traffic regions. Implementing these design considerations involves establishing

fuel production capacities, adhering to specific policies and regulations, and accounting for uncertainties and resilience within the supply chain network. It is crucial to consider fuel diversity to accommodate the varying needs of inland vessels, as different vessels may require different fuel types. Therefore, a range of fuels, including traditional and alternative options, should be available at bunkering locations.

Uncertainties within the supply chain network present challenges for bunkering infrastructure design. Fluctuating fuel prices, changes in demand, and potential disruptions in the supply chain must be taken into account. Building resiliency into the network, such as incorporating redundant storage capacities or diversifying fuel sources, helps mitigate the impact of uncertainties and ensures a reliable and continuous fuel supply. It is worth noting that prioritizing factors in the supply chain network is crucial due to the time and cost involved.

The first step involved projecting demand to determine if the existing infrastructure described in the literature could meet current and future needs, and whether there were any fluctuations in demand. This assessment considered not only the quantity of demand but also the specific requirements for alternative fuels. Additionally, demand can vary daily and weekly, as well as across different corridors within a day. Such variability can also impact the supply side. In their research, Momenitabar [19] utilized machine learning methods, including Random Forest, Extreme Gradient Boosting Method, and Ensemble learning algorithms, to project bioethanol demand. In 2022, Kazi and Eljack [20] employed an RNN-LSTM prediction model to identify future hydrogen demand from the maritime sector. To forecast demand, various approaches such as time series analysis and machine learning algorithms can be applied based on historical data patterns.

Among the available methodologies, utilizing real-time data in an agent-based simulation proves to be a more reliable approach. This simulation method focuses on the development, capacity, and interactions within the waterway system. By employing agent-based simulation, it becomes possible to examine interactions between social systems, stakeholders, and the natural environment. This approach is particularly useful for identifying key stakeholders, such as vessel operators, port authorities, fuel providers, and regulatory bodies. Agents represent different vessel types, routes, schedules, fuel requirements, and decision criteria for selecting bunkering locations. The multi-agent simulation simulates vessel movements, routes, and stops for bunkering, while capturing data on fuel consumption, emissions, and operational costs for various vessel scenarios. Additionally, a framework should be designed to identify the trade-offs between dynamically changing scenarios. This Digital Twin could provide detailed information regarding waterway conditions, traffic patterns, vessel types, and sizes. To identify potential locations for bunkering infrastructure within the digital twin of the network, it is necessary to conduct an assessment using the results obtained from the multi-agent simulation. In addressing the questions about alternative fuels outlined in section 4, it is crucial to acknowledge that numerous factors influence decision-making regarding them. However, at this stage, determining which factors are superior remains uncertain. To gain a better understanding of these influential factors and to identify the trade-offs among them, the techniques mentioned earlier can be instrumental. These methods enable decision-makers to explore design scenarios, simulate the behavior of the supply chain, evaluate feasibility, identify bottlenecks, and optimize configurations. By leveraging these techniques, a resilient and efficient bunkering infrastructure can be achieved.

In conclusion, this paper explores the challenges and complexities associated with developing the supply chain network of bunkering infrastructure for alternative fuels in inland shipping, focusing on three different fuel forms: liquid, gaseous, and electricity. By analyzing the upstream and downstream components of the supply chain, this study establishes a comprehensive understanding of the interdependencies and considerations for infrastructure planning, including influential factors.

ACKNOWLEDGMENTS

This research is conducted within the project PATH2ZERO that is financed by NWA L2-Thema 2020 Zero emission shipping (ZES) program by Netherlands Organization for Scientific Research (NWO) with Grant NWA.1439.20.001.

REFERENCES

[1] J. Rogelj, et al., “Paris Agreement climate proposals need a boost to keep warming well below 2 C”. In: Nature (2016), 534(7609): pp. 631-639.

[2] J. J. Gómez Vilchez, et al., “An analysis of trends and policies promoting alternative fuel vessels and their refueling infrastructure in Europe”. In: Frontiers in Energy Research (2022), 10: p. 904500.

[3] M. Grosso, et al., “The role of research and innovation in europe for the decarbonisation of waterborne transport”. In: Sustainability (2021), 13(18): p. 10447.
[4] M. Prussi, et al., “Potential and limiting factors in the use of alternative fuels in the European maritime sector”. In: Journal of cleaner production (2021), 291: p. 125849.
[5] J. D. Ampah, et al., “Reviewing two decades of cleaner alternative marine fuels: Towards IMO's decarbonization of the maritime transport sector”. In: Journal of Cleaner Production (2021), 320: p. 128871.
[6] K. Moirangthem, “Alternative fuels for marine and inland waterways: An exploratory study”. In: Publications Office of the European Union (2016), EUR 27770, JRC100405.
[7] K. R. Kim, J. H. Cho, “Prioritization and Optimal Location of Hydrogen Fueling Stations in Seoul: Using Multi-Standard Decision-Making and ILP Optimization”. In: Processes (2023), 11(3): p. 831.
[8] D. Calandra, et al., “Management of hydrogen mobility challenges: A systematic literature review”. In: Journal of Cleaner Production (2023), p. 137305.
[9] R. Damwijk, “Towards the implementation of Bunkering Infrastructure for New Energy Carriers for Inland Navigation in The Netherlands”, 2022.
[10] G. Zomer, et al., “Green Maritime Methanol; operation aspects and the fuel supply chain”, TNO: Tech. Rep, 2020.
[11] M. Jiang, et al., “Corridor Scale Planning of Bunker Infrastructure for Zero-Emission Energy Sources in Inland Waterway Transport, in Smart Rivers”, Springer (2022), p. 334-345.
[12] M. Van Koningsveld, G. Pauli, “Infrastructure for the Decarbonisation of IWT in Smart Rivers”, Presenting the Work of PIANC TG234, Springer (2022), p. 122-134.
[13] E. Bolt, “Schatting energiegebruik binnenvaartschepen”, Rijkswaterstaat AdviesdienstVerkeer en Vervoer, Rotterdam, 20030.
[14] L. Vehmeijer, “Measures for the reduction of CO2 emissions, by the inland shipping fleet, on the Rotterdam-Antwerp corridor”, 2019.
[15] L. Segers, “Mapping inland shipping emissions in time and space for the benefit of emission policy development: a case study on the Rotterdam-Antwerp corridor”, 2021.
[16] M. van Koningsveld, et al., “Ports and waterways: navigating the changing world”, TU Delft Open, 2021.
[17] C. van Dorsser, et al., “The effect of low water on loading capacity of inland ships”. In: European Journal of Transport and Infrastructure Research (2020). 20(3): p. 47-70.
[18] F. Vinke, et al., “Cascading effects of sustained low water on inland shipping”. In: Climate Risk Management (2022). 35: p. 100400.
[19] M. Momenitabar, et al., “An integrated machine learning and quantitative optimization method for designing sustainable bioethanol supply chain networks”. In: Decision Analytics Journal (2023). 7: p. 100236.
[20] M. K. Kazi, F. Eljack, “Practicality of Green H2 Economy for Industry and Maritime Sector Decarbonization through Multiobjective Optimization and RNN-LSTM Model Analysis”. In: Industrial & Engineering Chemistry Research (2022), 61(18): p. 6173-6189.